https://researchcommons.waikato.ac.nz/

Research Commons at the University of Waikato

Copyright Statement:

The digital copy of this thesis is protected by the Copyright Act 1994 (New Zealand).

The thesis may be consulted by you, provided you comply with the provisions of the Act and the following conditions of use:

- Any use you make of these documents or images must be for research or private study purposes only, and you may not make them available to any other person.
- Authors control the copyright of their thesis. You will recognise the author's right to be identified as the author of the thesis, and due acknowledgement will be made to the author where appropriate.
- You will obtain the author's permission before publishing any material from the thesis.

Electronic circuitry for shaping current pulses for small scale transcranial magnetic stimulation coils

A thesis submitted in fulfilment
of the requirements for the degree of
Doctor of Philosophy
in Science
University of Waikato
by

Soniya Raju

THE UNIVERSITY OF
WAIKATO
Te Whare Wānanga o Waikato

2025

(INTENTIONALLY BLANK)

Abstract

Transcranial magnetic stimulation (TMS) uses electromagnetic induction to induce electric currents in brain tissue via a time-varying magnetic field from a coil, stimulating neuronal activity. While TMS is widely studied and utilized in humans, its adaptation for small animal research is limited, primarily due to the technical challenges associated with generating high-current pulses through miniature coils and managing associated heating issues. Existing TMS pulse generators are typically large, expensive, and designed for human use, with limited availability of compact, cost-effective systems suited for small-scale experiments. Furthermore, accurate modeling of TMS pulse generation circuits, particularly those incorporating dynamically controlled switching devices, remains underdeveloped.

This thesis presents the design, development, and validation of a new supercapacitor-based pulse generator and accompanying dynamic modeling framework specifically tailored for small animal TMS applications. The proposed system leverages a pre-charged commercial supercapacitor module as the primary energy storage unit, eliminating the need for external high-voltage DC supplies or multipliers traditionally used in TMS systems. This approach offers significant advantages in terms of size, cost, and safety, while maintaining the ability to deliver high-current, high-magnetic-field pulses essential for effective stimulation.

The pulse generator architecture integrates a MOSFET device, which is operated not as a simple switch, but as a dynamically varying resistive element. By applying a triangular gate voltage waveform, fine control over the MOSFET's resistance is achieved, allowing precise shaping of pulse parameters including rise time, fall time, pulse width, and peak current. The generated magnetic field amplitudes ranged between 200–400 mT with coil current amplitudes reaching up to 50 A with an input of 1 V. Pulse durations could be tuned between 50–250 μs by adjusting the gate waveform characteristics, providing flexibility to mimic different TMS protocols.

A significant contribution of this research is the development of a novel MATLAB-based model for simulating the dynamic behavior of the pulse generator circuit. The MOSFET is modeled as a variable resistance whose value changes at every instant, capturing its behavior across subthreshold, threshold, and above-threshold regions. A new governing equation was modified from existing equation to accurately represent this time-dependent resistance, allowing for the solution of the coupled differential equations governing the RLC circuit dynamics. The model was tested against experimental data using triangular, sinusoidal, and quadrilateral gate voltages.

Experimental characterization demonstrated the generator's ability to produce consistent, repeatable pulses without requiring recharge after every pulse, due to the high instantaneous power

delivery capability of the supercapacitor module.

The key outcomes of this work are:

1. The successful design of a compact, supercapacitor-based TMS pulse generator suitable for small animal research, capable of delivering flexible, controlled magnetic pulses without the need for high-voltage supplies.

2. The introduction of a dynamic pulse shaping strategy using a triangular gate voltage applied to a MOSFET operated as a variable resistor.

3. The development of a new MOSFET-RLC model that accurately predicts circuit behavior, validated against experimental results with various waveform inputs.

4. Demonstration of adjustable pulse amplitudes (200–400 mT), tunable pulse widths (50–250 μs), and efficient system operation suitable for low-to-moderate repetition rates.

This research demonstrates the supercapacitor-based pulse generator and its accompanying MATLAB model for small-scale TMS applications. The flexibility in pulse generation and the ability to create custom pulse shapes provide a strong foundation for future exploration in TMS research, particularly for animal studies. Additionally, the dynamic modeling approach introduced provides a foundation for more advanced simulation and optimization of TMS pulse generation systems in both preclinical and clinical research contexts.

Dedication

To my **Home** .....

AKSHAY

I will always remember this PhD journey with a smile and as one of the best times of my life because of you.

(INTENTIONALLY BLANK)

Acknowledgment

I would like to express my sincere gratitude to the University of Waikato for the opportunity to pursue my PhD and for the support provided through the doctoral scholarship.

First and foremost, I would like to thank my primary supervisor, Dr. Marcus Wilson. He has been a constant source of support and guidance since I received my admission offer in 2019. When the COVID-19 pandemic hit soon after, preventing me from traveling, he went above and beyond to help me start my studies online, understanding my situation and ensuring my admission was secure. His feedback and encouragement throughout my thesis, particularly in the writing process, have been invaluable. His patience and dedication in helping me improve my work continuously pushed me to achieve more than I thought possible. I truly appreciate all his effort in shaping this thesis. His constant support made a significant difference in my journey.

I am also deeply grateful to my second supervisor, Dr. Nihal Kularatna, whose practical insights and hardware training were crucial in developing my experimental skills. His mentorship helped me engage in hands-on research, and thanks to him, I was able to attend conferences and publish my work, which has been an incredible experience.

Although Dr. Alistair Steyn-Ross was not officially on my supervisory panel, I had the privilege of working closely with him. His disciplined approach, organizational skills, and attention to detail greatly influenced my research. We developed the MOSFET model together, which was a valuable learning experience. His guidance significantly improved my experimental setup and thesis writing skill, for which I am truly thankful.

I extend my heartfelt thanks to all three of my supervisors for their support and guidance throughout my PhD journey. Completing this within three years was made possible by their combined expertise, and I am truly grateful for their invaluable help.

I would also like to extend my heartfelt thanks to Chamara Dassanayake, Nirashi Polwaththa Gallage and Chamila Naligama. Their support and encouragement made a significant difference, and I am truly grateful for their friendship throughout this journey.

Last but certainly not least, I extend my heartfelt gratitude to my family, especially my mom, for never questioning my decisions and always supporting me. I am especially grateful to my partner, Akshay, whose steadfast encouragement and care made my PhD journey both enjoyable and stress-free. His support allowed me to focus entirely on my research, as he took care of everything else with remarkable ease. I could not have achieved this without him, and I will always be deeply thankful for his love and encouragement.

To everyone who has supported me on this journey, I extend my deepest thanks.

(INTENTIONALLY BLANK)

Table of Contents

List of Figures

List of Tables

(INTENTIONALLY BLANK)

Chapter 1

Introduction

1.1 Transcranial Magnetic Stimulation (TMS)

Transcranial magnetic stimulation (TMS) is a non-invasive technique that electrically stimulates neural tissue, including the cerebral cortex and peripheral nerves. Developed in the mid-1980s by Barker and colleagues [1–4], TMS has become an invaluable tool in both experimental neuroscience and clinical applications [5–9]. It allows for the modulation of neuronal activity, offering insights into brain function, and providing therapeutic benefits for various neurological and psychiatric conditions [10–19].

TMS has emerged as a valuable noninvasive tool for modulating brain function in both research and clinical settings. It holds promise for treating various neurological and psychiatric disorders such as major depressive disorder [20–26], Parkinson's disease [27–31], stroke [32–35] and anxiety disorders [25, 36–40].

1.1.1 Principles of TMS

TMS operates on the principle of electromagnetic induction, a process explained by Ampère's circuital law and Faraday's law of induction. The technique involves placing a stimulation coil over the head, which generates a rapidly changing magnetic field. These pulses penetrate the scalp and skull, inducing secondary ionic currents in the brain tissue, leading to neuronal depolarization at specific points along nerve fibers. Unlike direct electrical stimulation, which requires current to flow between electrodes placed on the scalp, TMS uses magnetic fields to induce currents without direct electrical contact. This allows TMS to non-invasively stimulate specific brain regions [41–43]. This is demonstrated in Fig. 1.1, which illustrates how the TMS mechanism works. The spatial distribution of the magnetic field is largely determined by the design and configuration of the stimulation coil. Commonly used coil shapes include figure-eight and circular designs, each offering different focal points and depths of penetration [44–46]. The induced electric field, however, is affected by the brain anatomy and the varying electrical conductivity of different tissues. At the interfaces between tissues with different conductivity, charge accumulations occur, generating secondary electric fields that influence the overall electric field distribution [47, 48].

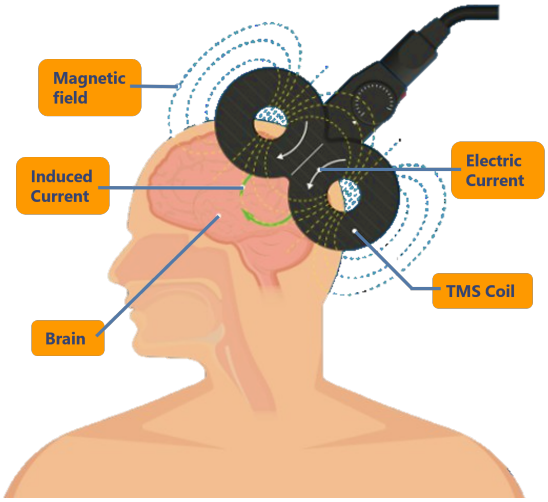

Figure 1.1: Principle of transcranial magnetic stimulation where the coil and its magnetic field induces current in the brain tissues. Source: Image used under license from shutterstock.com

1.1.2 Applications of TMS

TMS can be administered in various forms, such as single pulses, pairs of stimuli, or repetitive stimuli (rTMS) at different frequencies, allowing for the modulation of excitability in the cerebral cortex. This versatility makes TMS a significant tool in understanding the pathophysiology of neural circuitry underlying neurological and psychiatric disorders. In clinical settings, rTMS protocols can produce long-lasting changes in brain activity, providing therapeutic benefits for patients with treatment-resistant disorders such as depression and chronic pain. TMS has also been introduced as a non-invasive and safe method for activating the human motor cortex and assessing the integrity of central motor pathways, with applications in clinical neurophysiology, neurology, neuroscience, and psychiatry [49–52].

1.1.3 Importance and future directions

The effectiveness of TMS is influenced by both the spatial and temporal characteristics of the induced electric field. The spatial distribution of the magnetic field is largely determined by the pulse input, configuration and shape of the stimulation coil, while the induced electric field is also affected by the brain anatomy and varying electrical conductivity of different tissues [53–56]. Temporally, the response of neurons to TMS depends on their intrinsic properties, such as membrane excitability and geometry, making the temporal modeling of TMS responses complex yet crucial for understanding its mechanisms and optimizing its applications. However, despite the promising studies supporting its potential [50, 57], more research is necessary to establish the precise role of TMS in clinical neurology and to determine its full clinical value. Understanding the precise interaction of TMS induced fields with brain tissue is essential for improving its efficacy and safety. The main challenges with efficacy include variability in patient response and the difficulty in precisely targeting the desired brain regions. Safety concerns primarily revolve around the risk of seizures, discomfort during treatment, and potential long-term effects that are not yet fully

understood [6, 58–62]. Theoretical and computational modeling play a crucial role in advancing TMS technology. By simulating the induced electric fields and their interaction with brain anatomy [63–71], researchers can optimize coil designs, predict outcomes of TMS interventions, and tailor treatments to individual patients [72, 73].

During the application of TMS procedure, the cortical and sub-cortical tissue adjacent to the target area may also receive the stimulation at a lower intensity [74–76]. The underlying mechanisms of TMS and optimal application strategies remain incompletely understood. The main reason for the gaps in TMS studies is due to its initial acceptance stage. Unlike other clinically accepted procedures, TMS lacks a substantial body of non-human data, which has hindered its early development and broader acceptance. Most clinical procedures undergo extensive testing in animal models before being applied to humans, providing a wealth of data that supports their efficacy and safety. TMS, however, primarily advanced through direct human studies, resulting in a limited understanding of its mechanisms and long-term effects.

In summary, users are often driven more by practical concerns than by an interest in the technology's internal functioning [77–79]. As a result, users operate based on presumptions and inadequate information [7]. Therefore, it is crucial to conduct detailed studies on TMS to understand its actual effects comprehensively. By doing so, we can identify the specific factors that influence its outcomes and enhance the overall process. This detailed understanding will enable us to optimize TMS protocols, improve efficacy, and ensure safer application in clinical and research settings.

1.2 Significance of small animal TMS

Human studies have provided critical insights into the therapeutic potential of TMS. However, ethical concerns and practical challenges limit comprehensive investigations into TMS neurological mechanisms in humans. This limitation underscores the significance of utilizing animal models, particularly mice, in TMS research. Small animal models offer controlled environments to explore fundamental neurophysiological mechanisms that are difficult or impossible to study directly in humans [59, 80–83].

In light of the US government approval of magnetic stimulators for peripheral nerve stimulation, animal safety studies were not carried out. As a result, the device was used experimentally and unofficially for brain stimulation without the typical preliminary animal testing that usually supports clinical applications. This led to its use on the brain without the extensive safety and efficacy data typically gathered from non-human studies, contributing to its experimental status and initial gaps in understanding [5, 7, 9, 84–87]. The food and drug administration (FDA) approval of the rTMS device to treat depression in the absence of data on animal safety has limited the potential for animal studies that could reveal more about the device internal workings and improvements [1, 2, 5, 88–95].

Animal studies are crucial for probing beyond the effects of TMS on action potentials and understanding the basic cellular mechanisms underlying TMS stimulation. It is essential to determine the specific effects of TMS excitation and identify the contributing tissues. Additionally, assessing

potential adverse effects on nearby tissues and elucidating the exact mechanisms by which action potentials are produced remain unclear in human studies. These critical data can only be obtained through animal experiments, improving our overall understanding [96].

Animal models face challenges due to physical differences; human TMS equipment cannot easily scale down for smaller brains, potentially stimulating a significant portion of the animal body. Historically, this mismatch has hindered effective TMS animal studies, delaying direct applications in humans. Successfully validating new treatments effectiveness and safety through animal studies is essential for advancing novel therapeutic techniques and reducing research costs. Despite extensive research on coil enhancements, TMS stimulator circuits in mice remain understudied [84].

There is considerable variability in how TMS affects excitability and other performance measures across individuals and sessions. Animal experiments aim to comprehensively understand the nature, mechanisms, and causes of TMS effects. Much research has focused on developing small animal coils, especially for mice, given that human coils are unsuitable for animal use.

TMS response variation is influenced by the interaction between cortical neurons and the electric field induced by the magnetic pulse. Understanding these variables is crucial for exploring the diverse mechanisms underlying TMS activities, many of which remain unexplored. Effective experimental control over these mechanisms, including variations in stimulus amplitude, coil design, frequency, and duration of input pulse, is vital for understanding the polarity and degree of modulation (magnitude of changes in brain activity) induced by TMS.

Small animal TMS studies are pivotal for several reasons:

1. Mechanistic insights: Small animal models provide a platform to study the precise effects of TMS on neuronal circuits and synaptic plasticity at a cellular and molecular level. Unlike human studies, where direct investigation of these mechanisms is limited, small animal models allow for invasive methods to explore changes in synaptic efficacy, neurochemical profiles, and gene expression patterns induced by TMS.

2. Translational relevance: Findings from small animal TMS studies can inform and optimize clinical TMS protocols for humans. By mimicking human TMS conditions as closely as possible in small animals, researchers can better understand how different stimulation parameters affect brain function and tailor therapeutic strategies accordingly.

3. Technical advancements: The development of specialized TMS coils and experimental setups for small animals is crucial. Current commercial TMS systems designed for humans are often too large and lack the spatial resolution required for precise stimulation of mice brains. Innovative coil designs and input pulse configurations, such as those optimized for inducing specific electric field strengths with minimal energy consumption, are advancing the field of small animal TMS studies.

4. Cost and efficiency: Conducting initial studies in small animals is more cost-effective and time-efficient compared to human trials. Small animal models allow researchers to conduct systematic studies with larger sample sizes, evaluate safety profiles, and optimize stimulation parameters before translating findings into clinical trials.

5. Ethical considerations: Utilizing animal models for TMS research helps address ethical concerns associated with direct experimentation on human subjects. Small animal studies provide essential preliminary data to justify and refine clinical trials, ensuring that human participants receive safe and effective TMS treatments.

6. Exploring cellular mechanisms: Animal studies allow researchers to delve into the fundamental cellular mechanisms underlying TMS effects. These include understanding how TMS-induced magnetic fields interact with neurons to alter their membrane potentials and trigger action potentials. Factors such as intrinsic neuronal excitability, cell morphology, and orientation relative to the magnetic field are critical in determining the neural response to TMS, which can be systematically studied in animal models.

7. Assessing tissue effects: It is essential to evaluate the effects of TMS not only on neurons but also on surrounding tissues. Animal models provide an opportunity to investigate potential adverse effects and to optimize stimulation parameters to minimize unintended consequences. This includes studying whether TMS affects tissues beyond the targeted cortical regions and how different coil designs or stimulation protocols can mitigate such effects.

8. Scaling challenges: Scaling down human TMS equipment for use in animals has historically presented challenges due to the disparity in brain size and anatomy. This limitation has necessitated the development of specialized coils and experimental setups tailored to small animals like mice. Innovations in coil design and experimental techniques are crucial for achieving spatial precision and replicating human-like TMS conditions in small animals.

9. Variability in TMS response: TMS responses can vary significantly between individuals and sessions, influenced by factors such as coil geometry, stimulation frequency, intensity, and duration [43, 57, 84, 97–103]. Animal studies allow for controlled experiments to systematically manipulate these variables and elucidate their effects on neuronal excitability and plasticity.

10. Enhancing clinical translation: Insights gained from animal studies are indispensable for optimizing TMS protocols before clinical trials in humans. They provide a foundation for developing safer and more effective treatment strategies, thereby accelerating the translation of TMS research into clinical practice [104, 105].

In conclusion, small animal models play a crucial role in advancing the understanding of TMS and its application in both research and clinical settings. By providing a controlled environment, small animal studies enable exploration into intricate cellular mechanisms, assessment of tissue interactions, and understanding of variability in TMS responses. These insights are fundamental for refining TMS protocols and translating discoveries into clinical applications. Ultimately, small animal TMS research bridges the gap between basic science and clinical application, offering promise for developing targeted and effective interventions for neurological and psychiatric disorders in human patients.

TMS stands out among medical treatments due to its minimal reliance on animal studies compared to other scientifically and clinically accepted therapies. This unique approach stems from

several key factors. Firstly, TMS is fundamentally noninvasive, meaning it does not require surgical procedures to deliver magnetic pulses to the brain. This safety profile allowed for early human trials without extensive preclinical testing on animals. Moreover, TMS was initially adopted by neurophysiologists who had a long-standing tradition of using various forms of stimulation on experimental subjects, including themselves. This tradition of self-experimentation and direct application to human subjects contributed to the early acceptance and exploration of TMS without the extensive non-human testing typically seen with other clinical procedures. This familiarity with stimulation techniques facilitated its early human experimentation, bypassing the need for extensive animal studies.

The clinical adoption of TMS further reduced the emphasis on animal studies. TMS gained popularity in clinical psychiatry and neuroscience due to its therapeutic potential, rather than a comprehensive understanding of its neural mechanisms. Positive therapeutic outcomes in human trials, coupled with regulatory approvals based on safety data from these trials, decreased the urgency for detailed animal studies aimed at explaining its mechanisms.

Despite its clinical success, there remains a limited understanding of the precise neural mechanisms underlying TMS. Therefore, while TMS has demonstrated efficacy and safety in human trials, further research into its neural effects and optimization of stimulation techniques could lead to enhanced therapeutic outcomes and broader applications in the future [7].

1.3 Mouse coil development

A major challenge in small animal TMS studies is the lack of coils specifically designed for mouse. Most research relies on commercial human coils, such as "small" figure-of-eight or round coils, which are larger than the mouse brain. These coils can deliver high-intensity stimulation (1–2 T) similar to human studies, but they often lack the spatial resolution required for effective small animal brain stimulation [106–108]. To address this issue, some researchers have attempted to improve focality by offsetting the coil positions, though this method can be complex. An alternative approach involves scaling down the coil size to enhance focality. Recent advancements have demonstrated that smaller coils can maintain high-intensity capabilities but still often result in relatively unfocused stimulation. Conversely, mouse-specific coils with diameters as small as 8 mm have been successful in inducing structural and molecular plasticity in mouse brain regions [109, 110]. However, these low-intensity coils may not fully replicate the effects achieved with the higher intensity TMS used in human studies [111].

Rodent models of TMS are essential for understanding the cellular and molecular mechanisms of TMS-induced plasticity. Traditionally, mouse-specific TMS delivered focal stimulation at low intensities (12 mT). Two new TMS coils have been developed to deliver repetitive TMS (rTMS) at higher intensities while maintaining spatial resolution [80]. These coils, one with an air core and the other with a pure iron core, can generate peak magnetic fields of 90 mT and 120 mT, respectively. The iron-core coil, though less focal, increased motor evoked potential amplitudes in rats, showing its potential for studying rTMS effects in experimental settings. Similar-sized coils for

peripheral-nerve stimulation have been demonstrated in a figure-of-eight configuration by Colella et al. [112].

Recent studies have aimed to reduce heating effects during magnetic resonance imaging (MRI) scans, which are often exacerbated by deep brain stimulation (DBS) involving direct metal contact with brain tissue. Micro coils (μMS) have emerged as a promising alternative, offering electromagnetic induction without direct metal contact. Compared to traditional metal wires, μMS coils cause significantly less heating during MRI scans. Numerical simulations and experimental measurements show that μMS technology can substantially lower local specific absorption rate (SAR) and heating, making brain stimulation techniques safer [113].

Recent advancements have produced smaller TMS coils, such as Bonmassar et al. [113] sub-millimeter coil (0.5 mm diameter), which generated 10 mT B-fields and 6 V/m E-fields, affecting action potential production in retinal ganglion cells with minimal heating during MRI use. Minusa et al. developed implantable magnetic stimulators for mice with coils (1 mm long, 0.5 mm diameter) that provided highly focused 5 mT B-fields. Novel designs like tilted coil cores, demonstrated by Meng et al. [114], and stream function methods for focused stimulation with minimal heating, as shown by Sanchez et al. [115], offer improved field focus and reduced thermal effects [116].

While these advancements have significantly improved the capabilities of mouse-specific TMS coils, challenges remain in balancing high stimulation intensity with spatial resolution. There is ongoing research to develop coils that can deliver high-intensity stimulation while maintaining good focality, addressing physical constraints such as thermal and mechanical stress.

1.4 Importance of pulse shaping

While the importance of pulse shaping in TMS has been a latest research area, the specific pulse shape characteristics critical for neural stimulation require clearer definition. Studies have shown that both pulse width and intensity significantly influence facilitation and inhibition effects, with variations in pulse width producing outcomes similar to changes in intensity [117]. Moreover, pulse strength can be modulated through adjustments in either amplitude or duration, highlighting the need for precise control over these parameters [118]. In repetitive stimulation paradigms, such as quadro-pulse stimulation, carefully timed sequences of monophasic pulses have proven more effective than conventional paired pulses in inducing neuroplastic changes [119]. These findings underline that key controllable features, particularly pulse width, peak amplitude, rise and fall times, and pulse train timing are critical to optimizing stimulation outcomes.

There are a number of techniques to regulate the TMS response [57, 80, 120, 121, 121]; nonetheless, the input provided to the TMS coil is the most significant and vital component [122–127]. Since this is the primary source of excitation, altering the input pulse that generates stimulation may have a greater impact than other modifications. We now have flexibility in creating the necessary pulse shapes and adjusting them to improve response owing to the fast developing electronics field. Pulse shaping in TMS circuits is of paramount importance due to its direct influence on the efficacy and precision of neural stimulation [78, 117, 120, 128–135]. The pulse shape refers to the

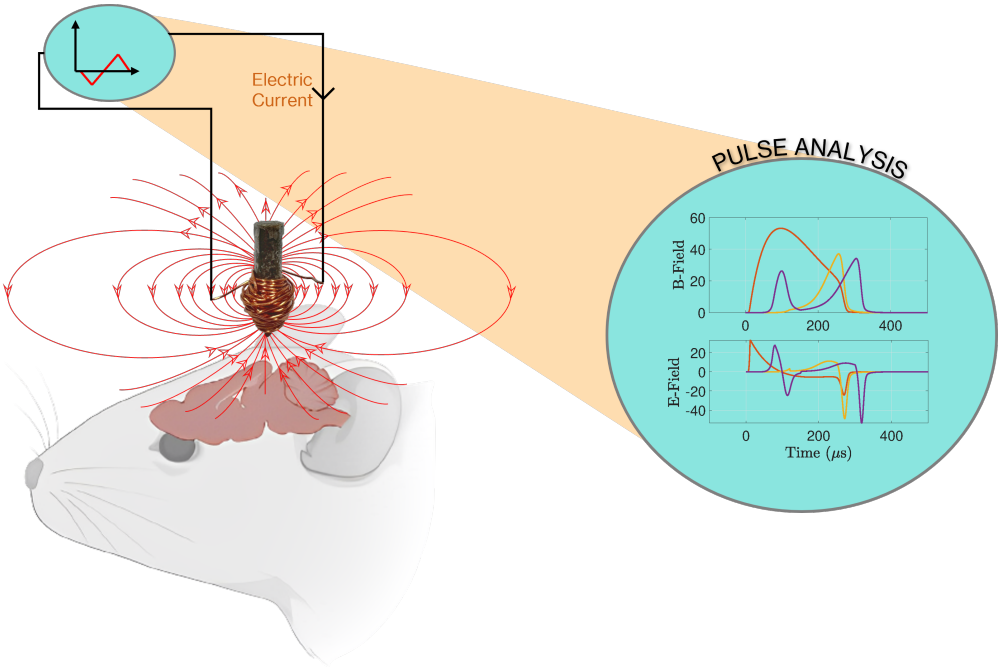

Figure 1.2: Schematic representation of the mouse TMS pulse shaping concept. This illustrates how different pulse shapes and amplitudes affect magnetic and electric fields in neurons. The diagram highlights the TMS coil's position on the mouse head and the resultant magnetic field.

specific waveform of the electrical current to the TMS coil, which generates the magnetic field used to stimulate the brain.

Figure 1.2 illustrates the schematic representation of the mouse TMS pulse shaping concept. This figure demonstrates how various pulse shapes and amplitudes can produce different magnetic and electric fields in the neurons. The diagram includes a mouse head with a TMS coil (developed by Khokhar et al. [136]) positioned to deliver the pulse. The coil generates magnetic field. Additionally, the figure zooms in on the pulses, showing different pulse widths and their respective effects on the magnetic and electric fields. This depiction emphasizes the importance of precise control over pulse characteristics in TMS applications, highlighting the impact on neuronal stimulation. Pulse shaping is crucial because:

1. Targeted neural activation: The shape of the electrical pulse determines the characteristics of the induced magnetic field and, consequently, the spatial and temporal distribution of the electric field in the brain [14, 87, 128, 129, 137–140].

2. Modulation of stimulation parameters: Pulse shaping allows for precise control over various stimulation parameters such as pulse duration, amplitude, and frequency. These parameters can significantly influence the physiological response of neurons to TMS. For example, altering the pulse duration can affect the depth of penetration of the induced electric field and the extent of neural activation. Similarly, adjusting the pulse amplitude can modulate the strength of stimulation delivered to neurons [117, 120, 139, 141, 142].

3. Enhanced therapeutic efficacy: In clinical applications, such as treating psychiatric disorders

or neurological conditions, optimizing pulse shape can enhance the therapeutic efficacy of TMS. Fine-tuning the pulse characteristics based on individual patient factors or specific treatment goals may lead to improved patient outcomes and reduced side effects [143–146].

4. Advanced research capabilities: Pulse shaping capabilities in TMS circuits have expanded with advancements in electronics and computational modeling [147, 148]. Researchers can now design complex pulse waveforms for human coils that mimic physiological patterns or explore novel stimulation paradigms. This capability opens doors to investigating new mechanisms of action and optimizing TMS protocols for both research and clinical purposes.

5. Safety and comfort: Tailoring pulse shapes can also contribute to improving the safety and comfort of TMS procedures [6, 58–62]. By minimizing unnecessary stimulation outside the target area and optimizing energy delivery, researchers can mitigate adverse effects and improve tolerability, thereby enhancing the overall feasibility and acceptance of TMS as a therapeutic tool.

In summary, pulse shaping in TMS circuits represents a critical advancement that facilitates precise control over neural stimulation parameters. This capability not only enhances our understanding of brain function through research but also holds promise for optimizing therapeutic outcomes in clinical settings. As technology continues to evolve, further innovations in pulse shaping will likely continue to expand the capabilities and applications of TMS in neuroscience and medicine.

1.5 Strategy of the research

This research employs a systematic approach to enhance pulse circuitry tailored for small-scale TMS coils. Initially, the study identifies existing gaps in TMS technology concerning its application in small animal studies. Subsequently, the methodology focuses on circuit design, aiming to develop a robust pulse generation system capable of delivering precise and adjustable stimuli. Experimental validation plays a pivotal role, where hardware setups are tested to ensure functionality and safety. The study innovates further by improving gate voltage control mechanisms, facilitating the production of tailored pulse shapes crucial for effective neuronal stimulation. A MATLAB simulation model is then developed to analyze and refine MOSFET behaviors within the circuit, enabling deeper insights into pulse characteristics under various conditions. Finally, optimization efforts concentrate on fine-tuning pulse parameters such as amplitude, duration, and symmetry, aiming to maximise the pulse-shaping function capability of the developed system in TMS applications. This comprehensive methodology integrates theoretical research with practical experimentation. Figure 1.3 illustrates the strategy of the research encompassing gap identification, circuit design, experimental testing and verification, gate voltage innovation, MATLAB modeling, and pulse optimization, aimed at enhancing small-scale TMS coil functionality.

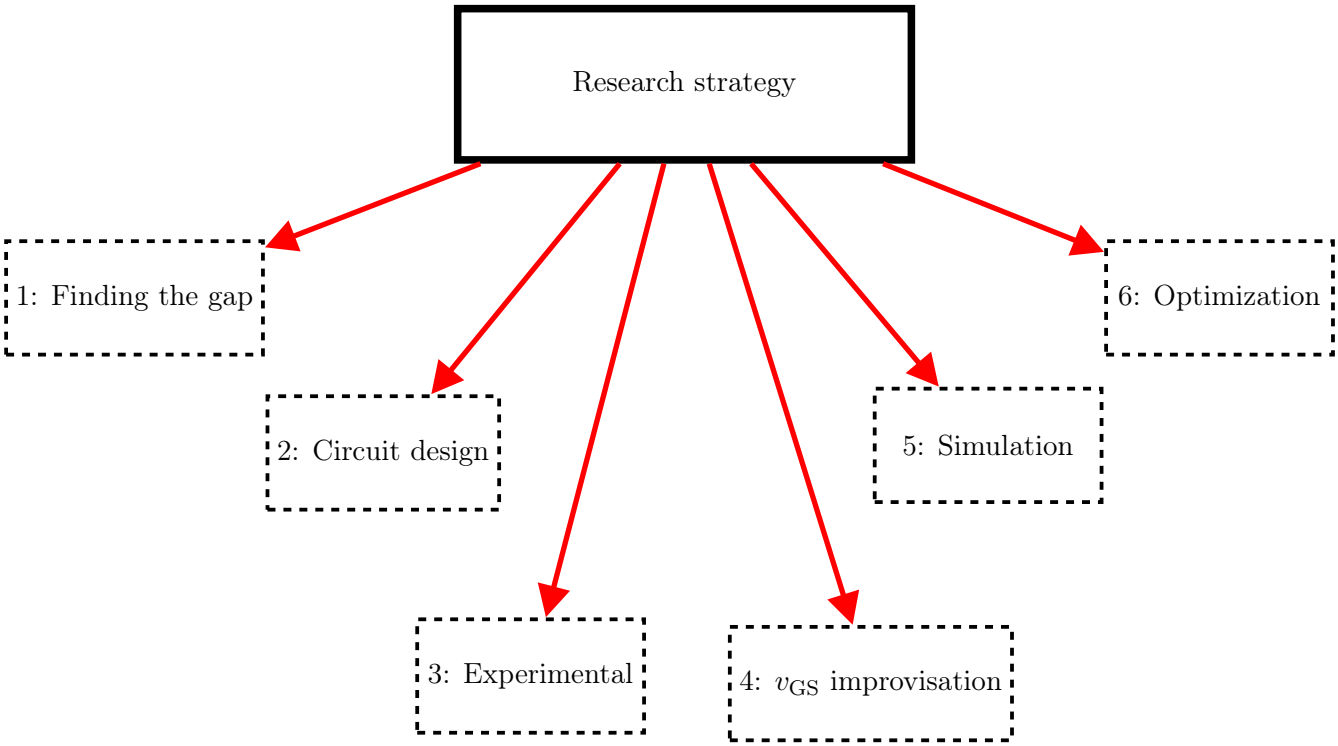

Figure 1.3: Methodology used for this research. Here v_{GS} refers to the gate source voltage of the MOSFET

1.6 Structure of the thesis

This thesis investigates the development of electronic circuitry for shaping current pulses specifically tailored for small-scale transcranial magnetic stimulation coils. The research aims to address two primary objectives: first, to design a current pulse circuit capable of generating sufficient field strength for effective neuronal stimulation in small animals; second, to establish a control over the pulse shape. This entails exploring various parameters such as pulse duration, amplitude, shape, and pulse-width, and their impact on stimulation efficacy and safety. The thesis will delve into the complexities of pulse shaping in TMS circuits, emphasizing the importance of precise control over key pulse characteristics. This precision is crucial for achieving reliable experimental outcomes and effective clinical applications, enabling other groups to carry forward this research and test it in clinical experiments. By bridging fundamental research with practical applications, this research seeks to contribute novel insights into advancing TMS technology for neuroscientific research and therapeutic interventions. Figure 1.4 illustrates the structure of the thesis, outlining the key chapters and their main topics. Each box represents a chapter, with arrows indicating the flow and progression of the content.

Chapter 1 introduces TMS as a principal tool in neuroscience and clinical applications, emphasizing its importance in non-invasive brain stimulation. It highlights the significance of TMS in small animal research and explores the role of pulse shaping in enhancing precision and efficacy.

Chapter 2 provides an overview of foundational TMS stimulation circuit layouts used in both

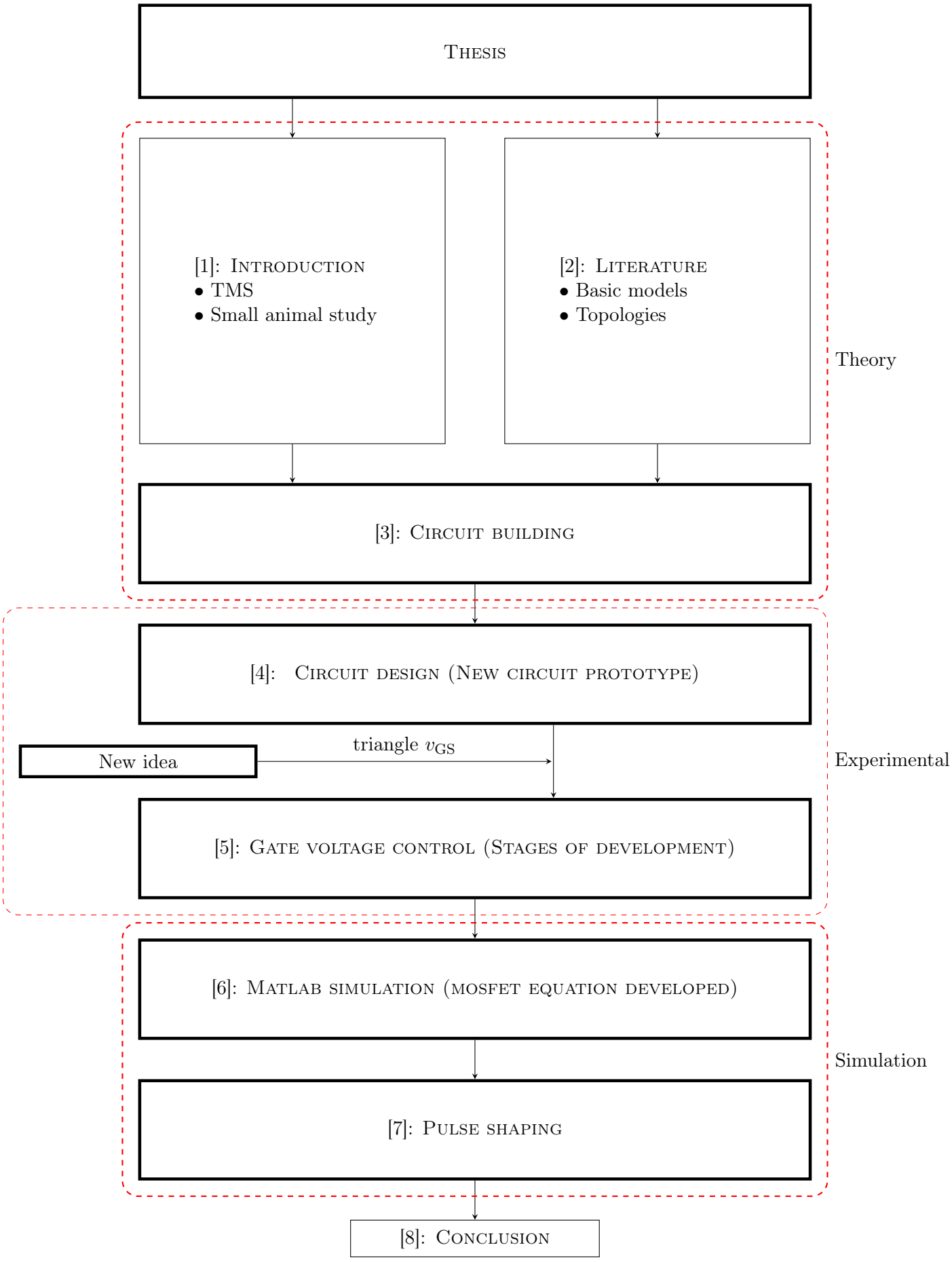

Figure 1.4: Summary of the chapter contents presented in this thesis

research and medical applications. It discusses various circuit topologies and advancements in pulse shaping techniques, focusing particularly on developments relevant to mouse TMS circuits.

Chapter 3 details the components used in TMS circuit design, providing structural insights and operational principles. It includes a comprehensive explanation of each component.

Chapter 4 covers the development and experimental validation of a pulse generation prototype aimed at improving TMS applications. It progresses from initial design stages to a functional prototype, highlighting the circuit's evolution and operational modes. Published results from IECON (IEEE Industrial Electronics Society Conference) 2023 underscore its advancements.

Chapter 5 explains the control mechanism for generating gate voltages, particularly for shaping TMS output pulses. It examines the transition to triangular waveform gate voltages and evaluates their impact on pulse characteristics. Experimental results demonstrate the circuit's efficacy in producing precise and adjustable pulses.

Chapter 6 details the development of a MATLAB simulation to model MOSFET behavior within the TMS circuit. It outlines the background study, modifications to existing equations, and the creation of a comprehensive simulation model capable of predicting output characteristics based on gate voltage inputs.

Chapter 7 explores the optimization of TMS pulses through parameter adjustments in the developed pulse generator prototype and corresponding MATLAB model. It focuses on understanding how changes in capacitor voltage, gate voltage amplitude, and pulse symmetry affect pulse outputs. Experimental validations and simulations validate these modifications, enhancing flexibility and effectiveness in TMS protocols and providing a better understanding of pulse shape. This chapter also outlines the process of recreating the existing TMS pulse shape using the prototype, along with exploring various pulse shaping possibilities.

Chapter 8 provides a comprehensive summary of the thesis, highlighting the key findings and contributions made throughout the research. It reflects on the main outcomes, including the development and validation of the proposed circuit design and its implications for TMS applications.

Chapter 9 addresses the limitations of the current work and proposes future research directions to overcome these challenges.

1.7 Publications

The research presented in this thesis has led to the following publications. Author attribution forms are included in Appendix E.

1. Published in IEEE IECON 2023, the 49th Annual Conference of the IEEE Industrial Electronics Society (IES) – Included in Chapter 4, Section 4.5.1

2. Poster presented at the Australasian Winter Conference on Brain Research (AWCBR), Queenstown, Aug/Sep 2023 – Included in Appendix A

3. Poster presented at NZIP & PHYSIKOS 2023 Conference, Massey University - Albany Campus, Auckland, 3-5 July 2023 – Included in Appendix A

4. Presented and publicated in IEEE IECON 2024, the 50th Annual Conference of the IEEE Industrial Electronics Society (IES) – Included in Chapter 5, Section 5.6

5. Presentated and will be published at APEC 2025, IEEE Applied Power Electronics Conference and Exposition – Included in Chapter 6, Section 6.5.1

6. Published in Biomedical Physics & Engineering Express journal. Included in Chapter 4, Section 4.5.2

7. Published in IEEE Transactions on circuits and systems I-Regular papers – Included in Chapter 6, Section 6.5.2

(INTENTIONALLY BLANK)

Chapter 2

Literature review & existing TMS pulse generator topologies

Introduction to chapter

In this chapter, an introduction will be given to the basic layouts used for TMS stimulation circuits in research and medical applications. These foundational circuits serve as the basis for all existing topologies, which are often expansions or modifications of these models. The discussion will then focus on various topologies developed by researchers, along with advancements in pulse shaping achieved with these circuits. Following this, a dedicated section will cover mouse TMS circuits, given the focus of this research on small animal coils. Finally, a proposal will be made to explain the aim of my research, highlighting new innovations and differences intended to be brought to the field of TMS circuits.

2.1 Basic Models for stimulation of TMS coils

2.1.1 Source-free series RLC circuit with precharged capacitor

The source-free series RLC as shown in Fig. 2.1(a) is a basic electrical circuit which can be used as a oscillator, also in the absence of a resistor. The analysis of the RLC circuit is as follows: Applying Kirchhoff's law to the Figure 2.1

$$v_c + Ri(t) + L\frac{di(t)}{dt} = 0, \tag{2.1}$$

$$\text{where } i(t) = \frac{dq(t)}{dt} = C\frac{dv_c}{dt} \tag{2.2}$$

where L is the inductance of the TMS stimulation coil, $v_c(t)$ is the voltage at the capacitor. Substituting $i(t)$ in Eq. (2.1) gives

$$\frac{d^2v_c}{dt^2} + \frac{R}{L}\frac{dv_c}{dt} + \frac{1}{LC}v_c = 0 \tag{2.3}$$

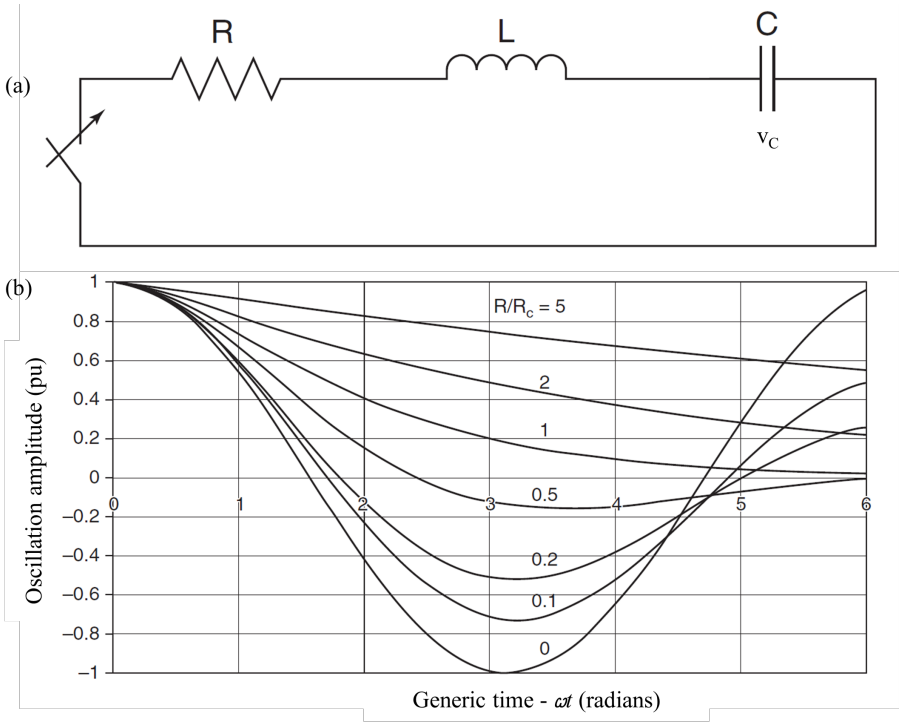

Figure 2.1: Source-free series RLC circuit with precharged capacitor & its generic damping curves. Here R_c is the value of R to give critical damping[149]. © 2020, John Wiley and Sons.

Solving we obtain, for the initial condition $i = 0$ *at* $t = 0$, and for $\frac{1}{LC} > \left(\frac{R}{2L}\right)^2$

$$v_c(t) = Ae^{-\alpha t} sin\omega t \tag{2.4}$$

where

$$\alpha = \frac{R}{2L} \tag{2.5}$$

$$\omega = \sqrt{\frac{1}{LC} - \left(\frac{R}{2L}\right)^2} = \sqrt{\omega_o^2 - \alpha^2} \tag{2.6}$$

where ω_o is the undamped resonant frequency. This circuit ability to resonate at a particular frequency, the resonance frequency f, is one of its key characteristics.

The solution can be divided into 3 cases

1.The circuit is overdamped $\alpha > \omega$

2.The circuit is critically damped $\alpha = \omega$

3.The circuit is underdamped $\alpha < \omega$

This circuit produces a harmonic oscillator for current and resonates similarly to an LC circuit. These oscillations reduce in frequency more quickly when the resistor is added; this phenomenon is called damping. The resistor also reduces the peak resonance frequency. Resistance cannot be entirely eliminated, even in situations when a resistor is not explicitly defined as a component [150].

Many researchers [78, 105, 136, 151] have been using RLC models and improvised RLC circuits for the TMS stimulation but they lack the provision of wave shaping or control over the pulse. In RLC circuit the pulse width only depends on the values of components (R,L & C). In [136], a similar circuit was utilized, lacking the capability for pulse shaping, and despite the TMS coil being inherently inductive, a resistance of 240 mΩ resulted in damping. This illustrates that even small resistances in the order of milliohms can significantly affect the pulse shape of the circuit, even in the absence of any physical resistance intentionally inserted into the circuit.

2.1.2 Single phase voltage source inverter

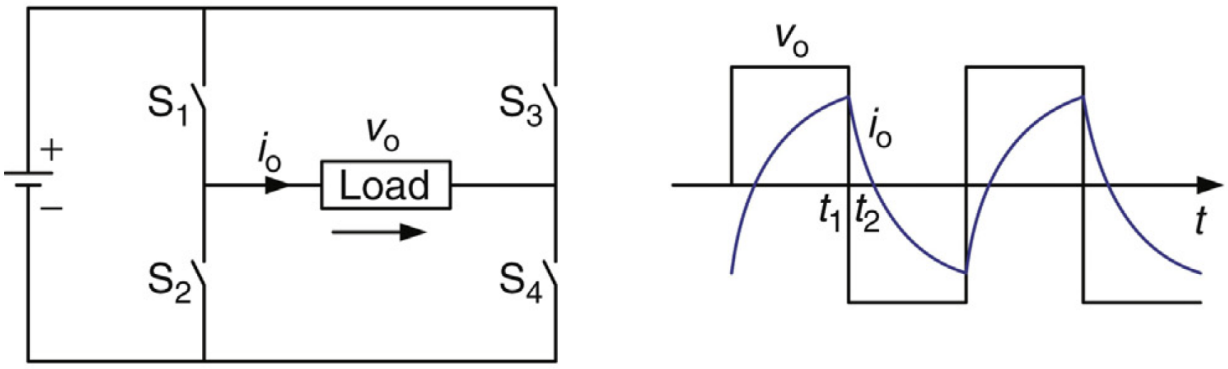

(a) (b)

Figure 2.2: (a) Basic inverter topology; (b) Output voltage and current waveform. Source - [152] © 2016 Elsevier Inc. All rights reserved.

A detailed explanation of the inverter circuit which is the second most commonly used topology in TMS stimulation is presented here. Some use the same inverter circuit, while others modify on it.

The inverter architecture is a popular and widely used topology when it comes to producing an alternating output waveform from a constant input. There are three categories based on the source-impedance source inverters (ISI), voltage source inverters (VSI), and current source inverters (CSI). Among these, VSI offer precise control over the voltage magnitude and frequency of the output waveform, making them highly versatile and suitable for various applications. In comparison to VSI, low-power commercial or medium-voltage industrial applications tend to use the other topologies.

The common operation of an inverter is addressed here. In any basic inverter as shown in Figure 2.2, when a switch or a pair of switch (here, S_1S_4) is turn on, current flows from the source through the load causing a positive voltage as shown in Figure 2.2(a), V_o direction (arrow). When the other pair (S_3S_2) is on, the current flows from source to through the load in the opposite direction as earlier causing a negative voltage during this time. This square alternating voltage is shown in the Figure 2.2(b) waveform. The waveform of the current always depends on the load which will be explained in detail in next subsection. When the load is changed from a purely resistive to inductive load, there will be a phase delay in the current compared to the voltage.

The half bridge and full bridge topologies are the conventional designs for single-phase VSI. Capacitors, switches, and diodes make up the converter. An array of two switches is referred to as the "inverter leg". For example, S_1 and S_2 make up the inverter leg of the half bridge in Figure 2.2. For the proper operation of the inverter, following rules must be followed.

1. Switches on the same leg cannot be turned on at the same time since doing so would induce a short circuit across the voltage source of the DC connection.

2. To give inductive loads a current path, a diode must be installed in opposition to each switch.

   When the switch turns off, the current through the inductor drops suddenly, causing a rapid collapse of the magnetic field. This rapid change induces a voltage in the coil, known as back electromotive force (EMF) or simply back EMF. This back EMF tries to maintain the current flow in the same direction as before, which can cause voltage spikes and damage to the switches if not properly managed.

   To prevent this, a diode is installed in opposition to each switch. These diodes are called freewheeling or fly-back diodes. When the switches turn off, the diodes provide a path for the current to continue flowing through the inductive load, allowing the energy stored in the inductor to dissipate gradually rather than causing voltage spikes.

   By placing the diodes in opposition to the switches, it ensures that when switch is on, the diode is reverse-biased, blocking any current flow through it. But when the switch turns off, the diode becomes forward-biased, allowing the current to flow through it and provide a path for the inductive load. The diode operation will be explained in detail in the next sub-section.

3. To prevent violating rule 1, a dead time needs to be taken into account in the control signals of the leg switches during the actual installation.

2.1.3 Half-bridge inverter

For the half bridge inverter, there are two defined (state 1-2) and one undefined switching state (state 3) as listed in Table 2.1. The voltage source charges up the capacitors to half of its voltage ($0.5V_\mathrm{d}$) respectively. Whenever Q_1 is turned on, upper capacitor C is connected to the load via the switch Q_1 as in the Figure 2.3(a). This is the state 1 where output will be $0.5V_\mathrm{d}$. Similarly, when Q_2 turn on, state 2 will occur in which output is -$0.5V_\mathrm{d}$. During this time, conduction is through the lower capacitor to load then to Q_2. This makes an alternating output which toggles from $0.5V_\mathrm{d}$ to -$0.5V_\mathrm{d}$ as shown in the waveform in Figure 2.3(b).

Table 2.1: Switching states of half bridge inverter

State	State no:	V_o	Components conducting
Q_1 is on, and Q_2 is off	1	$0.5V_\mathrm{d}$	Q_1, D_1
Q_2 is on, and Q_1 is off	2	-$0.5V_\mathrm{d}$	D_2, Q_2
Q_1 and Q_2 are all off	3	-$0.5V_\mathrm{d}$, $0.5V_\mathrm{d}$	D_2, D_1

In the following, we look at how the circuit in Figure 2.3 works for an RL load.

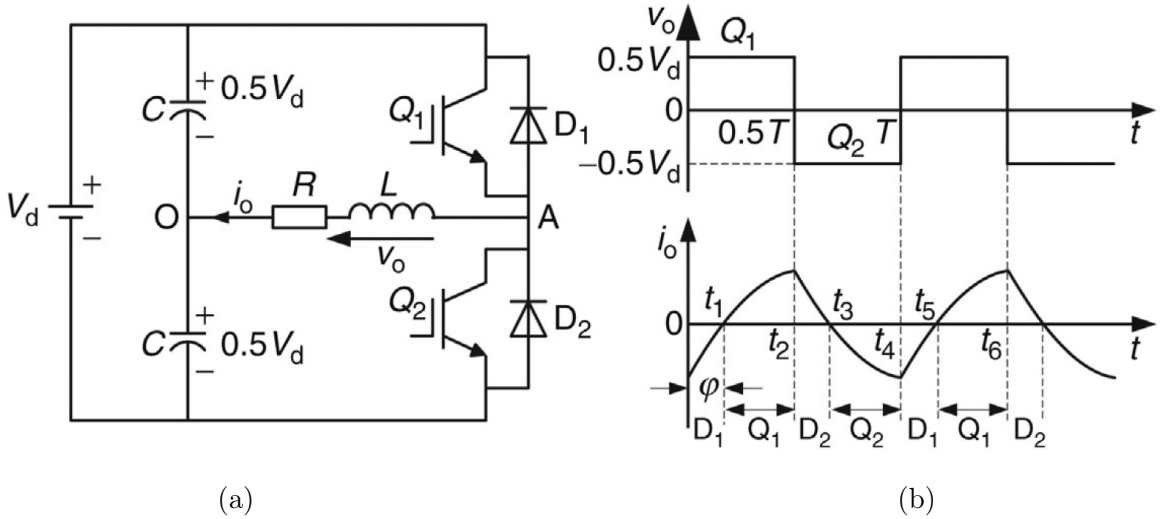

(a) (b)

Figure 2.3: (a) Half bridge inverter topology; (b) Output voltage and current waveforms. The fundamental component of the load current i_0 delays the fundamental component of the load voltage V_0 by ϕ. Source- [153] © (2018), with permission from Elsevier.

1. $0 \leq t < t_3$: During the initial half-cycle, when Q_1 is on and Q_2 is off, the output voltage is $0.5V_d$, causing the load current i_o to slowly rise. At time t_2, signals are sent to switch off Q_1 and switch on Q_2. At this moment, Q_1 turns off, but Q_2 does not immediately start conducting. Instead, the energy stored in the load inductor forces the diode D_2 to conduct, maintaining the load current i_o in the same direction.

2. $t_3 \leq t < t_5$: At the time instant t_3, the energy stored in the load inductor is depleted, causing the current i_o to drop to zero. At this point, diode D_2 turns off, allowing Q_2 to be triggered and turned on. After t_3, the current i_o reverses direction and gradually increases. At t_4, trigger signals are sent to switch Q_1 on and Q_2 off. Consequently, Q_2 turns off, but Q_1 cannot immediately turn on because the inductor forces diode D_1 to conduct. Therefore, the current i_o flows through D_1 back to the positive terminal of the supply voltage. By t_5, the current i_o drops to zero, allowing Q_1 to be triggered on and reversing the direction of the current i_o.

When either Q_1 or Q_2 is engaged, both the load voltage V_o and load current i_o share the same polarity, indicating the inverter is functioning in active mode, during which the power supply delivers energy to the load. Conversely, when either D_1 or D_2 conducts, the load voltage V_o and load current i_o exhibit opposite polarity, meaning the inverter is in feedback mode. In this mode, the energy stored in the load inductor is fed back to the DC side, where it is stored as reactive power in the DC side capacitors.

2.1.4 Full-bridge inverter

Full bridge inverter is more complicated than a half bridge. It has 4 switches which conduct as a pair to make a closed loop. The different state of operation when each pair of switches are on is given in Table 2.2. In short, when Q_1 and Q_4 are turned on, there is a positive voltage developed

across the load and when Q_2 and Q_3 are on, it make a negative voltage since the direction of current get reversed. There is 4 defined states (state 1-4) and 1 undefined state (state 5) for this inverter. In order to avoid an undefined output voltage condition, state 5 should be used just for the dead time. Silicon controlled rectifiers (SCR) were formerly employed as switches for high and medium-power inverters, and in order to turn the SCR off, commutation circuits were needed. Currently, the majority of power switches are fully-controlled models like gate turn-Off thyristor (GTO), insulated gate bipolar transistor (IGBT) for medium-power inverters, and IGBT for high-power inverters. When the load is inductive in nature, the role of diodes in these circuit become more crucial. It act as a freewheeling diode. The switches cannot be switched on immediately as the energy stored in the inductor forces the diode to conduct so that the load current i_o maintains the same direction[154, 155].

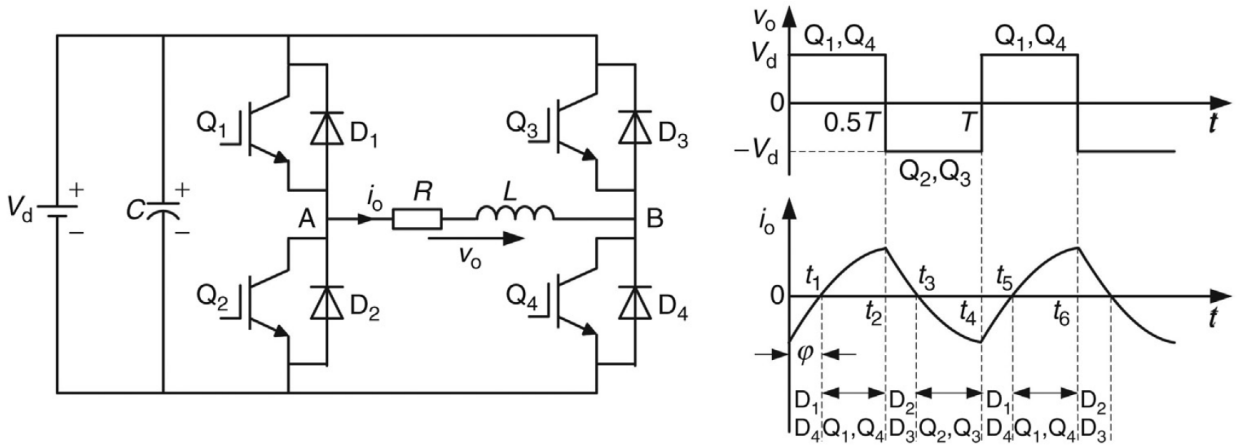

(a) (b)

Figure 2.4: (a) Full bridge inverter topology; (b) Output voltage and current waveforms. Source from [153] © (2018), with permission from Elsevier.

Table 2.2: Switching states of full bridge inverter [153]

State	State no:	V_o	Components conducting
Q_1 and Q_4 are on, and	1	V_d	Q_1 and Q_4
Q_2 and Q_3 are off			$D_1$and D_4
Q_2 and Q_3 are on, and	2	$-V_d$	Q_2 and Q_3
Q_1 and Q_4 are off			D_2 and D_3
Q_1 and Q_3 are on, and	3	0	Q_1 and D_3
Q_2 and Q_4 are off			D_2 and Q_3
Q_2 and Q_4 are on, and	4	0	D_2 and Q_3
Q_1 and Q_3 are off			Q_2 and D_4
Q_2 and Q_1 are off	5	Depends on Q_4, Q_3	D_2
			D_1
Q_4 and Q_3 are off		Depends on Q_2, Q_1	D_4
			D_3

The operation principle of the single-phase full-bridge inverter is as follows. Figure 2.4(a) illustrates the full bridge topology, while Fig. 2.4(b) presents the corresponding current and voltage waveforms.

1. $0 \leq t < t_1$: During the interval $0 \leq t < t_1$, both switch pairs (Q_1, Q_4) and (Q_2, Q_3) are off. However, the diode pair (D_1, D_4) is forced to conduct due to the energy stored in the load inductor. As a result, the output voltage V_o is V_d, and the inductor current i_o gradually decreases in amplitude. At time instant t_1, the load current i_o reaches zero, causing the diodes D_1 and D_4 to turn off, while the switches Q_1 and Q_4 are activated by triggering.

2. $t_1 \leq t < t_3$: During the time interval $t_1 \leq t < t_2$, the load voltage V_o remains at V_d, but the current i_o changes direction to positive. At time instant t_2, trigger signals are sent to turn off Q_1 and Q_4 and turn on Q_2 and Q_3. Consequently, Q_1 and Q_4 turn off immediately, but Q_2 and Q_3 cannot turn on immediately due to the energy stored in the load inductor, which forces the diodes D_2 and D_3 to conduct.

   At this point, the load voltage V_o switches to $-V_d$, while the load current i_o maintains its direction but gradually decreases in magnitude. When the time reaches t_3, the load current drops to zero, causing the diodes D_2 and D_3 to turn off, and the switches Q_2 and Q_3 are then turned on by triggering.

3. $t_3 \leq t < t_5$: During the interval $t_3 \leq t < t_4$, the output voltage across the load remains at $-V_d$, while the load current reverses direction and gradually increases in amplitude. At time instant t_4, trigger signals are sent to turn off Q_2 and Q_3, but Q_1 and Q_4 cannot turn on immediately because the energy stored in the load inductor forces diodes D_1 and D_4 to conduct.

   Therefore, during the interval $t_4 \leq t < t_5$, the output voltage V_o switches to V_d, but the load current retains its previous direction and decreases in amplitude over time. Essentially, the inverter operation during $t_4 \leq t < t_5$ mirrors the inverter process during the interval $0 \leq t < t_1$.

When the switch pairs (Q_1, Q_4) or (Q_2, Q_3) are activated, both the load voltage V_o and the load current i_o exhibit the same polarity, signifying that the DC source is supplying power to the load. Conversely, when the diode pairs (D_1, D_4) or (D_2, D_3) are conducting, the load voltage V_o and the load current i_o have opposite polarities, indicating that power is being returned from the load to the DC source.

In the discussions of both the half-bridge and full-bridge inverter operations, only continuous conduction mode (CCM) has been considered, where the load current remains non-zero throughout each switching cycle. This assumption is valid under the chosen operating conditions, where the switching frequency is sufficiently high to maintain continuous current flow. It is important to note that operation at lower switching frequencies could lead to discontinuous conduction mode (DCM), where the load current falls to zero for a portion of the cycle. The dynamics and additional switching states associated with DCM are beyond the scope of this discussion and have not been addressed here.

2.2 TMS pulse topologies for human stimulation

Here, I discuss the various topologies that have been developed and studied in the TMS application field, along with my perspective on these circuits.

TMS requires electronic circuitry which is a technical challenge for the design of a practical, flexible pulse. A pulse has to be delivered to the coil very rapidly in the range of one-tenth of a millisecond. Since TMS operates on the principle of electromagnetic induction, only a small portion of the energy produced by the pulse circuit is actually transferred to the brain. Most of the energy is dissipated as heat within the coil itself.

This occurs because the rapid change in current through the coil induces a strong magnetic field, which in turn induces an electric field in the brain. However, the brain conductivity limits the amount of energy that can be effectively transferred, leading to inefficiencies in the system. Furthermore, the coil resistance also contributes to energy loss in the form of heat. As current passes through the coil, it encounters resistance, converting electrical energy into heat energy. To mitigate these issues, various techniques are employed, such as using high-performance materials for the coil to minimize resistance and optimizing the pulse waveform to enhance energy transfer efficiency. However, despite these efforts, a significant portion of the energy produced by the pulse circuit is still wasted as heat, highlighting a key challenge in TMS circuit building.

This section aims to explore the existing topologies in the TMS field. While primarily used for humans, it can also be miniaturize for use with small animals. These fundamental topology ideas have been utilized in most TMS circuits up to now.

2.2.1 Circuits similar to RLC oscillator

The conventional method for producing a pulse is by using an RLC/oscillator circuit [78]. This technique involves an energy oscillation between the precharged capacitor and the inductor (TMS coil) to create the TMS pulse. There are currently many types of circuits available, such as monophasic, biphasic, and polyphasic pulse circuits.

A conventional monophasic TMS simulator (Fig. 2.5(a)) is built with a silicon-controlled rectifier (SCR), which lacks precise control over the switching. This design was improved to develop a controllable pulse width (PW) TMS, known as cTMS, as depicted in Fig. 2.5(b). When the stimulating coil and energy-storage capacitor are connected by the switch, the coil current increases, inducing an electric field in the brain proportional to the rate of change of the coil current. The operator sets the pulse width (PW) by selecting when to turn off the switch.

For a small PW, the induced electric field pulse is almost rectangular, and the coil current rise is approximately linear. This allows for a wide range of PW control and near-rectangular starting phases of the induced pulses by selecting an adequately large capacitance. These circuits lack much control over the output pulse because they use thyristors as shown in Fig. 2.5(a). Thyristors, unlike some other semiconductor devices, cannot be controlled to turn off at a particular point in time. Once triggered into conduction, thyristors continue to conduct until the current flowing through them drops to zero, at which point they turn off automatically.

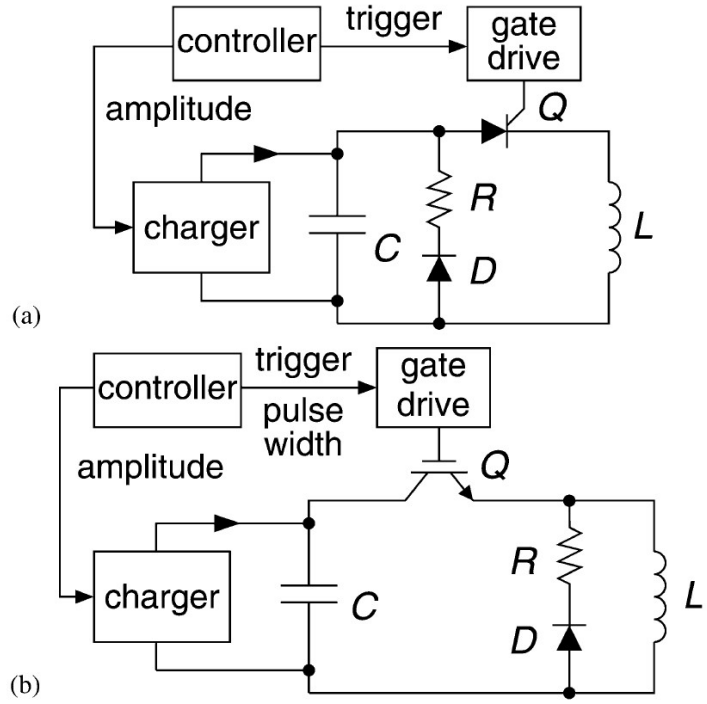

Figure 2.5: Circuit topology of (a) conventional monophasic TMS device; (b) Controllable TMS (cTMS) device. Source: [78]. © [2008] IEEE.

The monophasic circuit consists of an LC circuit with a controlled switch between them and a freewheeling diode path to eliminate the negative half cycle as shown in Fig. 2.5(b). It is similar to a half-wave power electronics converter in which we get an output of a positive half-sinusoidal waveform. The freewheeling diode shunts the negative cycle, and the output is damped with the resistor to slowly return to zero. The only way to shape the pulse is by adding a resistor, which leads to more energy loss due to heating. Due to the high heating and the need to charge the capacitor after each pulse, they are limited to low repetitive pulse rate applications only.

The key improvement in cTMS (cTMS device induces near-rectangular electric field pulses with controllable PW) is the use of an insulated gate bipolar transistor (IGBT), which allows for precise control over the turn-off timing for the gate signal, providing control over the pulse width. The IGBT connects the TMS coil and the energy storage capacitor, causing the coil current to ramp up and induce an electric field in the brain proportional to the rate of change of the coil current [77].

The biphasic pulse circuit generates waveform that terminate after one period, and any value can be controlled by the firing angle. The firing angle refers to the phase angle at which a thyristor or other controlled semiconductor device is triggered to conduct current in an alternating current (AC) circuit. It is a crucial parameter in power electronics, particularly in circuits involving controlled rectification or AC voltage control. The user controls the induced electric field amplitude by adjusting the capacitor voltage via the device controller and the switch-on time, determine the positive phase PW of the produced pulse.

All TMS systems inherently suffer efficiency losses due to the resistive heating in the current-carrying coil, which limits their overall electrical efficiency regardless of circuit design

Disadvantages of RLC oscillator circuits

1. Switching transients: Rapid switching of the IGBT can lead to switching transients, causing voltage spikes and electromagnetic interference (EMI). These transients can affect the performance of other electronic devices and may require additional filtering or shielding measures.

2. Limited pulse width range: While the circuit allows for adjustable pulse width, there may be limitations on the maximum and minimum pulse widths achievable. This could restrict the range of stimulation parameters available for certain applications.

3. Safety concerns: The rapid changes in current and voltage in the circuit pose safety risks when dealing with high voltage, particularly if not properly controlled. Over-voltage or over-current conditions could potentially damage the device or cause harm to the user.

2.2.2 Circuits similar to half and full-bridge inverter

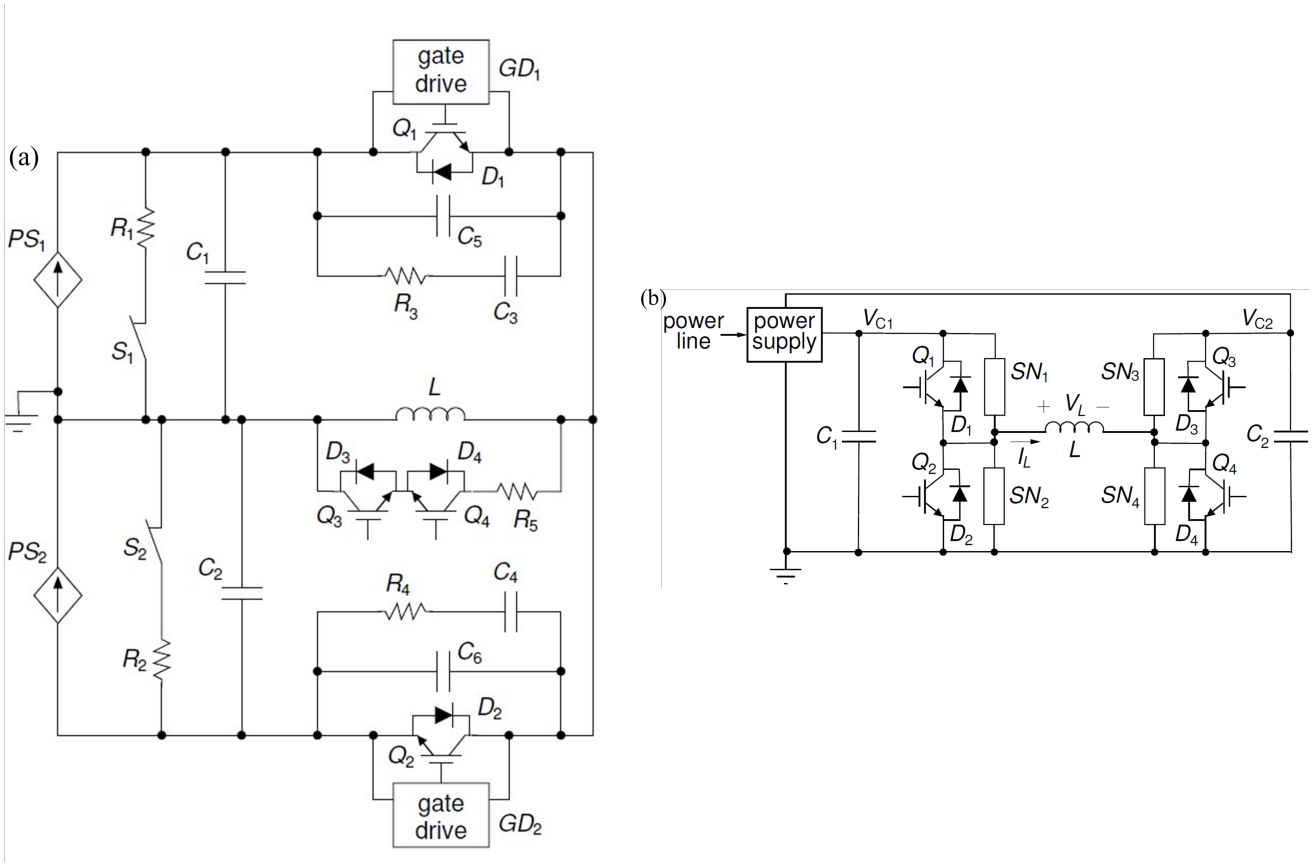

Figure 2.6: Circuit diagram of the cTMS (a) Half bridge and (b) full bridge model. Source:[156, 157]. © [2010,2011] IEEE.

The cTMS half-bridge circuit (Fig. 2.6(a)) consists of two large capacitors, C_1 and C_2, charged to positive and negative voltages respectively. These capacitors are connected to a TMS stimulation coil, L, via bidirectional switches, Q_1/D_1 and Q_2/D_2. Unlike conventional TMS devices that

use silicon-controlled rectifiers (SCR), the switches in cTMS are IGBT that can be electronically controlled to determine the pulse duration.

During the TMS pulse, either C_1 or C_2 is connected to the stimulation coil L, depending on which switch is turned on. This controls whether the induced electric field is positive or negative. The beginning and duration of the electric field phases can be adjusted by the timing of switches Q_1 and Q_2, and the amplitude can be controlled by adjusting capacitor voltages.

When switch Q_1 is turned on, capacitor C_1 supplies energy to the coil, causing the coil current to increase linearly. When Q_1 is turned off, the coil current is forced to flow through diode D_2 to capacitor C_2, producing a negative electric field. Similarly, when switch Q_2 is turned on, capacitor C_2 supplies energy to the coil, resulting in a negative electric field, and when Q_2 is turned off, the coil current flows through diode D_1 to capacitor C_1, producing a positive electric field [120, 138, 156].

The circuit operates efficiently, as the energy transferred during the pulse is not dissipated but rather transferred between capacitors C_1 and C_2 via the coil L. Despite some energy loss due to conduction and switching losses, a substantial portion of the energy is recovered on the capacitors at the end of the pulse, enabling energy-efficient operation. This recovery of energy allows for the reuse of energy in subsequent pulses.

The full-bridge topology (see Fig. 2.6(b)) used in cTMS applications provides superior control over stimulation parameters compared to the half-bridge circuit. It employs the same energy storage capacitors, C_1 and C_2, as the half-bridge setup, with C_2 charged to a positive voltage V_{C2}. However, the full-bridge configuration features four bidirectional current switches, Q_1/D_1–Q_4/D_4, which allows for the application of two different voltage levels to each terminal of the stimulation coil L. This setup enables the coil to be operated at four distinct voltage levels: V_{C1}, $-V_{C2}$, V_{C1}, $-V_{C2}$, and 0. While V_{C1} and $-V_{C2}$ are also used in the half-bridge circuit, the additional levels V_{C1}, $-V_{C2}$ and 0 are specific to the full-bridge topology.

Similar to the half bridge, the full bridge pairs IGBT with passive snubbers, SN1–SN4, to control voltage spikes and provide protection. However, unlike the half-bridge circuit, there is no need for an active coil snubber in the full bridge. This is because the 0 coil voltage condition (when Q_2/D_2 and Q_4/D_4 are on) can be used for the same purpose. In short, the full-bridge topology simplifies the circuit design while maintaining precise control over the output pulses [77, 158].

During operation, the full-bridge circuit enables the coil to generate positive and negative electric field pulses by selectively applying the voltage levels across the coil. When Q_1/D_1 and Q_3/D_3 are on, V_{C1} and $-V_{C2}$ are applied across the coil, resulting in a positive coil current. Conversely, when Q_2/D_2 and Q_4/D_4 are on, V_{C1}, $-V_{C2}$ and 0 are applied across the coil, resulting in a negative coil current.

Overall, while the full-bridge topology offers enhanced functionality and flexibility, it may come with increased complexity and cost compared to the half-bridge circuit [78, 131].

Disadvantages of half and full-bridge inverter

1. Cost: The use of multiple capacitors and sophisticated electronic components, such as IGBT, may increase the cost of the cTMS device.

2. Limited pulse shaping: While the circuits offer precise control over turn-off timing, there are no specific contributions to elements of pulse shaping such as rise or fall times.

2.2.3 Cascaded model

The high-voltage pulse shape shown in Fig. 2.7(b) is generated by combining multiple smaller voltage steps. Each step is produced by an independent two-pole module, all of which are connected in series as shown in Fig. 2.7(a). Each module contains an electrical energy storage capacitor (C_M), four semiconductor switches, and corresponding free-wheeling diodes. These modules operate using four switching states: (a) positive polarity, (b) negative polarity, (c) shorted terminals enforcing 0 V, and (d) passive mode where no switch is closed and the diode rectifier feeds the capacitor. Each module can generate a voltage of either $-V_C$, 0, or $+V_C$.

In its simplest mode, this results in a staircase waveform as illustrated in Fig 2.7(b). The entire column of modules acts as a high-power parallel digital-to-analog converter (DAC), capable of generating multiple quantization levels.

The voltage in each module is limited by the capacitor maximum level. The capacitors, along with the free-wheeling diodes, form a dynamically balanced voltage divider and act as snubber circuitry. This allows the use of common low-voltage power components like field-effect transistors, which support higher switching rates. Switching modulation is distributed among all modules, with each module responsible for only a fraction of the effective switching rate.

The passive mode (mode of operation using passive elements) can be helpful for magnetic stimulation, as it ensures precise control over the pulse duration without requiring exact knowledge of the pulse timing or current direction changes. This is achieved by using rectifying semiconductors that automatically turn off when the current direction changes [121, 159].

Disadvantages of cascaded model

1. Complexity: The circuit involves multiple modules, each containing several components, which increases the overall complexity of the system.

2. Cost: The high number of components and modules can lead to increased manufacturing and maintenance costs.

3. Control complexity: The distributed switching modulation and selection of modules for specific operations increase the complexity of the control system.

2.2.4 Pulse shaping

Pulse shaping in TMS research is an important and relatively unexplored aspect that focuses on the ability of the circuit to shape the waveform of the induced pulse. Pulse width has been a relatively understudied aspect in TMS research due to limitations in conventional stimulators, which often lacked the capability to vary pulse width. Additionally, many studies [120, 147, 148] have not explicitly mentioned the type of pulse used to trigger the switches, with the assumption being that a square voltage gate is typically employed. In pulse shaping circuits, extra components were often required for pulse shaping, necessitating the use of separate pulse shaping circuits.

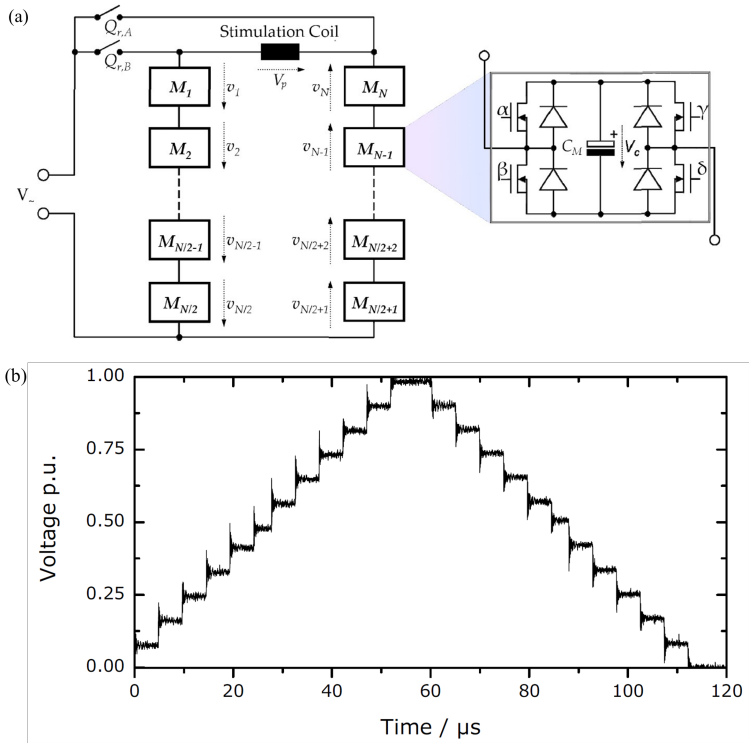

Figure 2.7: (a) Cascaded topology with N number of modules and topology of individual model (right) (b) Output voltage waveform obtain using cascaded model. Source: [147]. © [2012] IEEE

A cascaded H-bridge based pulse generator for TMS has been developed to provide flexibility in generating various stimulus pulses. This system is capable of producing pulses with different shapes, durations, directions, and repetition rates, similar to existing systems. However, each module of the generator has its own charging circuit, resulting in increased cost and size [160].

Third generation controllable pulse parameter device that uses a novel full bridge circuit topology is cTMS3 [120]. With cTMS3 (Fig 2.8), researchers can precisely adjust the amplitude, duration, and ratio between positive and negative phases of the pulse, allowing for tailored stimulation protocols to suit various applications. The device can adjust the peak amplitude of the pulse, allowing for variations in the strength of the magnetic field induced by the TMS coil. This amplitude control is essential for targeting specific brain areas and achieving desired stimulation effects.

cTMS3 enables the adjustment of the duration of each phase of the pulse. This means that the positive and negative phases of the electric field pulse can be independently controlled, allowing for customization of the pulse shape. Longer or shorter duration can be set based on the desired stimulation outcome.

The device actively snubs waveform ringing, which is a significant issue in TMS devices with enhanced pulse shape control. By mitigating waveform ringing, cTMS3 ensures cleaner and more precise stimulation pulses.

By generating lower internal voltage differences and using lower voltage IGBT modules, cTMS3 ensures safer operation while reducing costs, making it more accessible for commercial implemen-

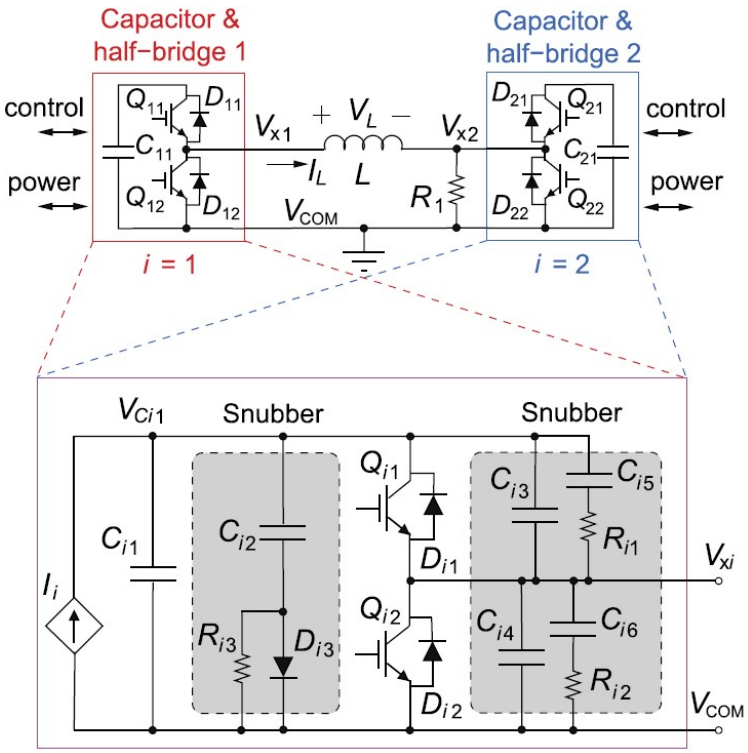

Figure 2.8: cTMS3 topology Source with the snubber circuit: [120]. © [2013] IEEE

tation. Additionally, the inclusion of zero coil-voltage levels enables active snubbing of waveform ringing. Moreover, cTMS3 exhibits high energy efficiency, enabling the generation of powerful rapid pulse sequences with large capacitor energy storage, which was not feasible with conventional TMS devices [120].

Disadvantages of cTMS3 circuit

1. Complexity and cost: Implementing active snubbing with the main IGBT modules in cTMS3 increases complexity and cost compared to passive snubbing methods. The use of additional voltage levels and control mechanisms may also add to the overall complexity of the device.

2. Technical optimization challenges: Achieving optimal pulse shaping requires careful technical optimization. Adjusting parameters such as duty ratio of IGBT switching during snubbing may present challenges in practice.

3. High-voltage source: All these circuits require a high-voltage source for generating high-voltage/current pulses. This necessitates either a separate circuit for high-voltage production or the use of a costly high-voltage source.

In the study [117], investigation was done on the strength-duration relationship in paired-pulse TMS and its implications for optimizing repetitive paired-pulse stimulation (rPPS) protocols. It was found that variations in pulse width (PW) had a similar effect on the degree of facilitation

or inhibition in brain as variations in intensity. By manipulating PW, it was able to control the electric field, which influenced the excitability of the motor cortex.

In conclusion, the investigation of the strength-duration relationship in paired-pulse TMS highlights the crucial role of pulse shaping in optimizing stimulation protocols. By manipulating pulse width, researchers can control the amount of pulse that can be given to the brain cells, thereby modulating neural excitability. This emphasizes the importance of pulse shaping techniques in TMS, as they offer a means to fine-tune stimulation parameters and achieve more targeted effects on brain activity. Ultimately, understanding and utilizing pulse shaping techniques can lead to the development of more effective and personalized therapeutic interventions for neurological disorders [117, 161].

2.3 TMS pulse topologies for mouse stimulation

Human TMS topologies are unsuitable for mouse stimulation coils for several reasons. Firstly, constructing a medium to high voltage circuit for a small coil is challenging. Additionally, it is crucial to address heating and losses associated with the small animal coil and ensure adequate protection.

The literature provides mouse-specific TMS circuits designed to address these challenges [58, 59, 80, 104, 105, 136]. These circuits are tailored to accommodate the smaller size of the coil, provide appropriate voltage levels for stimulation, and mitigate heating and losses associated with the smaller coil size. There are very few circuits specifically designed for mouse TMS stimulation.

2.3.1 Circuit of Tang et al.

The work done by Tang et al. [80] focuses on developing TMS coils specifically for rodent models to better understand how TMS affects brain plasticity. This research involved constructing two novel rodent-specific TMS coils designed to deliver repetitive TMS at higher stimulation intensities while maintaining spatial resolution. The coils; one with an air-core and the other with a pure iron-core generated peak magnetic field strengths of 90 mT and 120 mT respectively. Finite element modeling suggested a peak electric field of 85 V/m within the skull and 12.7 V/m within the brain. Stimulation with the iron-core coil on anesthetized rats significantly increased motor evoked potential amplitudes, indicating altered cortical excitability. These results suggest that the novel coils can induce modest magnetic and electric fields capable of modulating cortical excitability in rodents.

The circuit used to excite the TMS coil involved constructing two custom circular coils with dimensions of 8 mm in height and 8 mm in outer diameter, wound with insulated copper wire around steel cores. Stimulation parameters were controlled by a waveform generator (Agilent Technologies 335141B, CA, USA), connected to a bipolar voltage programmable power supply (KEPCO BOP 100-4M, TMG Test Equipment, Melbourne, Australia). This setup utilized a pulse generator to excite the mouse coil, limiting the pulse shapes to those provided by the pulse generator itself.

2.3.2 Circuit of Selvaraj et al.

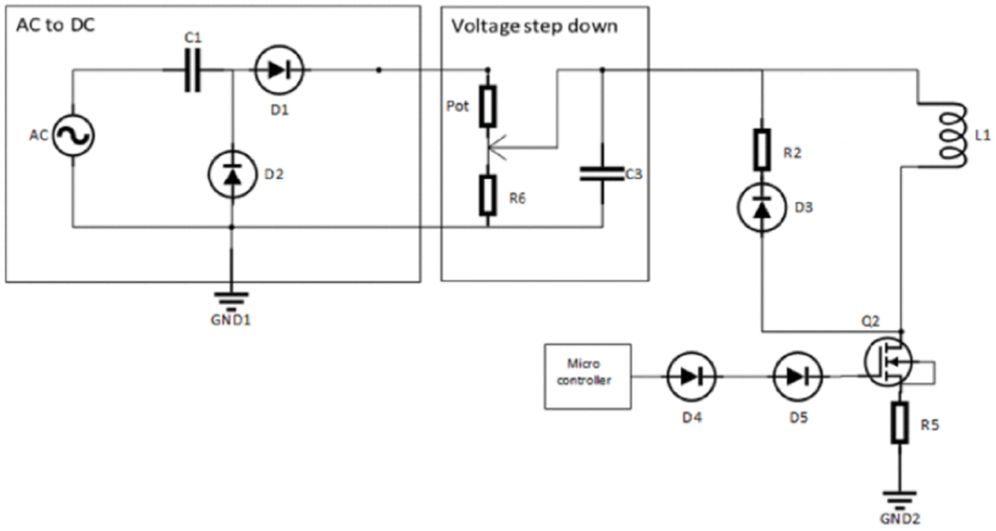

Figure 2.9: TMS circuit used for mouse brain stimulation by Selvaraj et al. [105] © [2018] IEEE

Selvaraj et al. [105] describe a TMS stimulator circuit detailed in Fig. 2.9. The design comprises three primary components: an AC-to-DC converter, a voltage reduction stage, and a load with feedback. The AC-to-DC section converts a 120V AC signal into a DC voltage using diodes and a capacitor. This DC voltage is then applied to two resistors, one being a variable potentiometer, which adjusts the voltage across the discharge capacitor. In the final stage, the discharge capacitor (C3) is linked to an inductive load (L1), with feedback implemented through resistors for power dissipation. Diodes are used to ensure unidirectional current flow during discharge. A transistor (Q2), controlled by a microcontroller, handles switching operations, and a current sensing resistor (R5) monitors the current through the transistor [105].

Disadvantages of Selvaraj et al. circuit

1. High voltage requirement: The circuit requires a high-voltage source (120 V AC) for operation, which may pose safety risks during handling and maintenance. Additionally, obtaining or generating high-voltage signals can be costly and may require specialized equipment.

2. Limited control: While the circuit allows for control over the voltage developed across the discharge capacitor through the potentiometer resistor, it may lack finer control features needed for precise stimulation protocols. This limitation could restrict its applicability in certain research or medical settings where precise control over stimulation parameters is required.

2.3.3 Circuit of Nieminen et al.

A study of Nieminen et al. on the mouse brain stimulation [104] used a previously developed [162] human TMS circuit. The custom stimulator electronics unit enables the generation of a controllable pulse waveform, similar to existing devices discussed in Section 2.2.2.

2.3.4 Circuit of Senda et al.

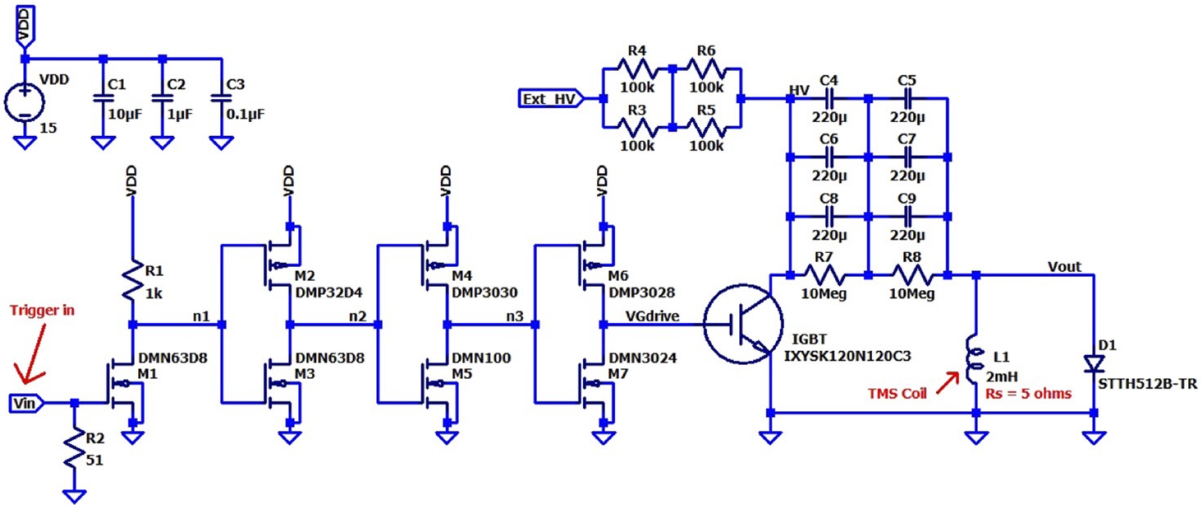

Figure 2.10: TMS circuit used for mouse brain stimulation by Senda et al. [151] © [2021] IEEE

Figure 2.10 illustrates an IGBT pulse generator designed for repetitive TMS studies in small animals, such as mice [151]. This generator employs an IGBT capable of handling 700 A for 1 ms with a DC breakdown voltage of 1200 V. The pulse duration is regulated by an input trigger pulse, while the output voltage is controlled via an external high-voltage power supply and a 330 μF capacitor bank.

The operation of the pulse generator involves charging the capacitor bank to a high voltage and then discharging it through a TMS coil to generate a pulse. Here's a breakdown of the process:

1. Charging stage: Before the pulse is triggered, the IGBT collector is charged by the external high-voltage supply (Ext HV) via resistors (R3-R6). These resistors regulate the current drawn from the high-voltage supply, ensuring that it does not trip or shut down. With a 1200 V supply, the collector of the IGBT will charge up to 1200 V.

2. Triggering stage: When the trigger input signal is activated, the IGBT turns on, causing the output voltage (V_{out}) at the top of the TMS coil to reach 1200 V. As the pulse is delivered, the output voltage decreases due to the limited energy stored in the capacitor bank. To minimize this voltage drop, additional capacitance can be added to the bank.

3. Discharging stage: Once the IGBT turns off, a freewheeling diode (D1) facilitates the removal of energy stored in the TMS coil. This diode prevents the output voltage from increasing uncontrollably, which could otherwise lead to circuit breakdown and failure.

4. Driver circuit: The driver circuit (M1-M7 and R1) ensures proper control and switching of the IGBT. When the trigger input signal goes low, the MOSFET (M1-M7) in the driver circuit control the gate voltage of the IGBT, turning it on. When the trigger input signal goes high, the MOSFET turn off, allowing the IGBT to turn off.

5. Output pulse: The output pulse is generated across the TMS coil when the capacitor bank discharges through it. The pulse width and amplitude can be controlled by adjusting the voltage level of the capacitor bank and the timing of the trigger input signal.

Overall, the circuit operates by charging a capacitor bank to a high voltage, triggering the discharge of this voltage through the TMS coil, and controlling the pulse generation process using a driver circuit. The resulting pulse is then delivered to the TMS coil for brain stimulation [151].

Disadvantages of Senda et al. circuit

1. Complexity and cost: The use of IGBT and associated driver circuitry adds complexity and cost to the design, making it less accessible for some applications.

2. High voltage source: Requirement of a external high voltage source adds up the complexity and cost.

3. Limited scalability: The design may have limitations in scalability, particularly when higher currents or voltages are required, which may necessitate additional circuitry or modifications.

These disadvantages highlight the challenges in designing high-voltage and high-current pulse generators for TMS applications, particularly when considering factors such as speed, cost, and scalability.

2.3.5 Circuit of Khokhar et al.

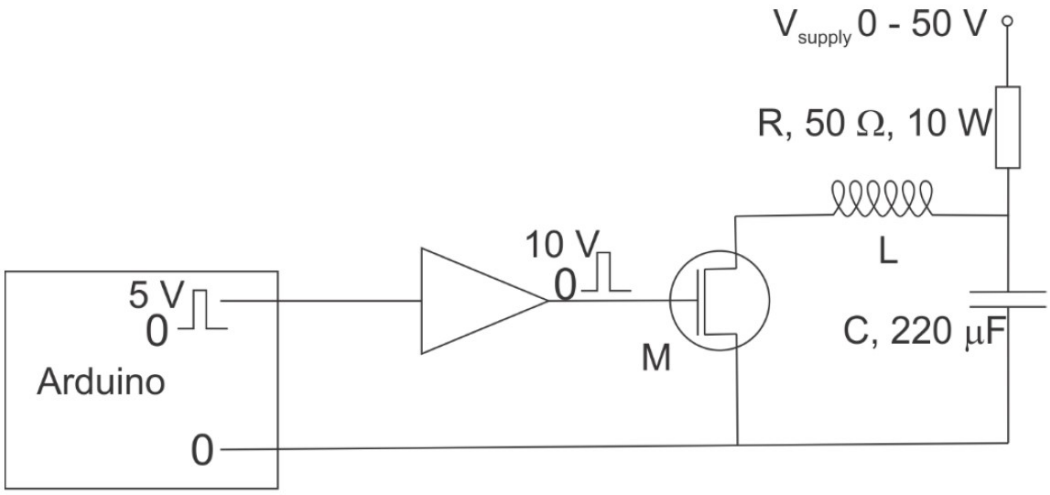

Figure 2.11: TMS circuit developed by Khokhar et al. [136] © [2021] IEEE

The circuit shown in Fig. 2.11 was used by the research team at the University of Waikato for mouse brain stimulation [136]. It consists of a basic RLC circuit as in Fig. 2.1 with a MOSFET for controlling the charging and discharging path. This MOSFET is controlled using an Arduino, which allows for easy programming to develop the required pulse pattern. They were able to supply pulses

in cTBS (continuous theta burst stimulation) pattern directly from Arduino. However, the pulse shape was not modifiable, meaning they were limited to the default pulse shapes (square pulse) provided by the Arduino and did not have the provision to alter the pulse width or amplitude.

Most small animal brain stimulation research discussed here has relied on existing or common circuits rather than specially designed ones. Upon reviewing the circuits in Figures 2.9, 2.10, and 2.11 they all appear quite similar. They typically employ basic capacitor discharging and freewheeling through diodes or inverters. One main drawback is the lack of a specific input source for these circuits. They may require either a high-voltage supply or high-voltage capacitor, depending on the application needs, or simply a basic DC lab supply for smaller circuits. The main differences among these circuits lie in the driving circuitry or control mechanisms, and there is often no provision for pulse shaping.

2.4 "Pulse shaping for mouse stimulation" — my proposal

In this chapter, I have discussed various types of TMS circuits for both human and mouse applications. One major gap identified is the lack of specific mouse TMS circuits with pulse shaping capabilities. Existing literature highlights the requirement for a high voltage source to charge the input capacitor in all TMS circuits, or a stand-alone high voltage input. This presents a significant challenge in designing circuits for small animals like mice.

The objective of my research is to develop a circuit capable of shaping output pulses without the need for additional components or separate circuits for pulse control. This innovation aims to eliminate the high voltage source requirement, thereby simplifying the circuit design. Achieving pulse shaping without extra blocks would be a significant advancement in both electronics and TMS field, as it reduces complexity. This involves building a simple and cost-effective prototype that functions effectively as both a pulse generator and a pulse shaping circuit for mouse coils, without the need for a separate high voltage source which can be expensive. This approach aims to simplify the design and reduce costs while maintaining the functionality needed for effective TMS in small animals.

Specifically, the aims of the research are:

1. **Design a TMS oriented pulse generator and to effectively control the MOSFET for pulse control**: I decided not to pursue inverter or cascaded-type topologies because they involve more than two switches, making individual control complex. Instead, I opted for a circuit with a reliable source capable of continuously providing output pulses, which can be step up to achieve the medium/high voltage required for stimulation. The focus is to effectively control the available MOSFET to explore various possibilities of MOSFET gate control effects on the circuit and stimulation. This aspect of gate voltage exploration has not been addressed by any researchers in the TMS field before.

2. **Alternative high-voltage sources**: Most existing circuits rely on external high-voltage sources or high-voltage capacitors. I aim to replace these with a more reliable and cost-effective source that can provide similar to a normal high-voltage source. This source should

not necessarily be high voltage and should be affordable while being able to withstand the required pulse duration.

3. **Cost and maintenance efficiency**: My aim is to develop a prototype that is low-cost (less than 500 NZD) and low-maintenance prototype achieved by minimizing the number of MOSFET, thus reducing the driver and control circuit complexity.

4. **Innovative gate pulse control**: There has been no innovation in the gate pulse given to the MOSFET switch that controls TMS excitation. Most researchers have used square pulses. I intend to go beyond the typical on/off of gate voltage and explore the effects of changing the gate voltage shape/pattern.

5. **Control over pulse parameters**: Precise control over pulse width (50–250 μs) and the amplitude of the output voltage and current is essential. Additionally, the generated magnetic field amplitudes should range between 200–400 mT. Control requirements also include managing the time interval between pulses as well as the rise and fall times of each pulse.

6. **Flexible pulse shaping**: Flexibility in pulse shape within the circuit without requiring additional circuits such as snubber or wave shaping is another objective.

7. **Simulation model**: A simulation model of the prototype is essential. Since the circuit requires high/medium voltage, having a circuit model will enable testing of further aspects and exploring more possibility of pulse pattern and its effects using simulation. A good model will be a valuable tool for analysis and development.

8. **Protection and isolation measures**: Incorporation of voltage protection and isolation measures is necessary to ensure the safe operation of the circuit.

9. **Modifiable prototype**: Developing an easy and modifiable prototype is important for facilitating adjustments and improvements during the research process.

Chapter 3

Circuit building

3.1 Introduction to components in prototype

Here, I present details for most of the components used in the circuit design, detailing their structure and operations.

3.2 Electrolytic capacitor

A capacitor holds electrical charge between two parallel conductive plates that are separated by an insulating material known as a dielectric. When a DC voltage is applied across the plates, one plate gains a positive charge (+Q), while the other plate acquires an equal but opposite negative charge (−Q). This charging process continues until the voltage difference between the plates equals the applied voltage.

Charging and discharging an electrolytic capacitor involve the accumulation and release of electrical charge on the capacitor plates. When a voltage is applied to an electrolytic capacitor, electrons flow onto one of its plates, causing it to become negatively charged while the other plate becomes positively charged. This process stores electrical energy in the form of an electric field across the capacitor. During discharging, the stored energy is released as the capacitor is connected to a load or circuit. Electrons flow from the negatively charged plate to the positively charged plate, generating an electric current. In a typical charging circuit for a capacitor, as shown in Fig. 3.1, a constant

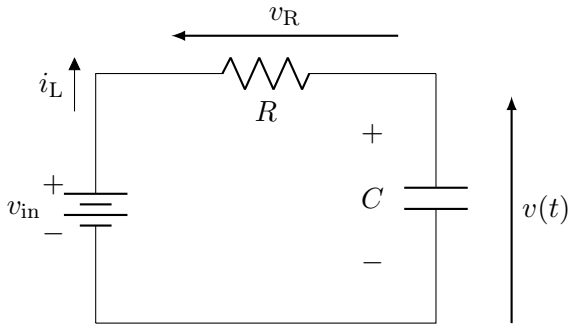

Figure 3.1: Charging of a capacitor from a constant DC voltage v_{in} through a series resistor R.

DC voltage is applied across the capacitor through a series resistor R. This resistor accounts for various resistances such as the equivalent series resistance (ESR) of the capacitor, external leads, and any deliberately introduced resistance. Initially, the voltage across the capacitor, v_0, is zero.

Using Kirchoff's voltage law, we can solve for the current $i(t)$ flowing through the circuit. Solving the equation for current, we obtain:

$$i(t) = \frac{v_{\text{in}}}{R} \exp(-\frac{1}{RC}) \tag{3.1}$$

Similarly, using this current equation, we can determine the voltage across the capacitor at any given time during the charging process:

$$v(t) = v_{\text{in}}[1 - \exp(-\frac{t}{RC})) \tag{3.2}$$

Figure 3.2 shows the charging/discharging current and voltage curve of the capacitor. The rate at which the capacitor charges is determined by the product of the resistance (R) and capacitance (C), which is commonly referred to as the time constant, denoted by

$$\tau = RC \tag{3.3}$$

It typically takes more than 5 time constants for a capacitor to fully charge or discharge. This time constant governs how quickly the capacitor reaches its maximum charge.

When the DC supply is replaced with a short circuit, the capacitor will discharge through the load resistance. During discharging, the current behaves similarly to charging, but flows in the opposite direction. The voltage across the capacitor will decay exponentially towards zero. The discharge current and voltage expressions are:

$$i(t) = \frac{v_{\text{fin}}}{R} \exp\left[\frac{-t}{RC}\right] \tag{3.4}$$

$$v(t) = v_{\text{fin}} \exp\left[\frac{-t}{RC}\right] \tag{3.5}$$

where v_{fin} is the voltage at the start of capacitor discharge.

In DC circuits, it acts as an energy storage device, while in AC circuits, it behaves as a frequency-dependent resistor. The energy storage capacity of an electrolytic capacitor is determined by its capacitance and the square of its voltage. Electrolytic capacitors typically have higher energy storage capabilities compared to other types of capacitors. The total energy stored in a capacitor:

$$E = \frac{1}{2}Cv^2 \tag{3.6}$$

In circuits, capacitors can be connected in series or in parallel. When capacitors are connected in series, the total capacitance decreases. The total capacitance for capacitors connected in series

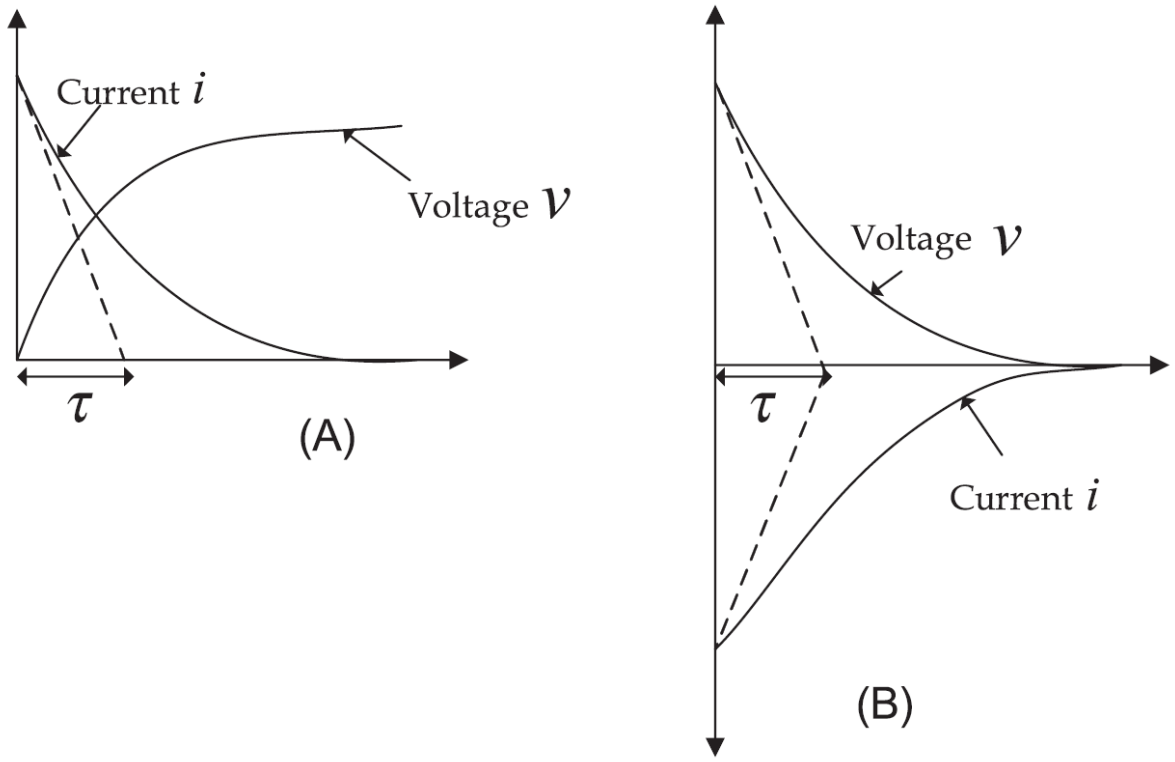

Figure 3.2: (a) The charging current and voltage curve (b) discharging current and voltage curve of the capacitor. Source - [163] © (2018), with permission from Elsevier.

is calculated using the formula:

$$\frac{1}{C_{\text{total}}} = \frac{1}{C_1} + \frac{1}{C_2} + \frac{1}{C_3} \ldots + \frac{1}{C_{\text{n}}} \tag{3.7}$$

When capacitors are connected in parallel, the total capacitance (C_{total}) increases. The total capacitance for capacitors connected in parallel is the sum of the individual capacitances:

$$C_{\text{total}} = C_1 + C_2 + C_3 \ldots + C_{\text{n}} \tag{3.8}$$

ESR is the total resistance of an electrolytic capacitor, including the resistance of the capacitor electrodes, electrolyte, and any other internal components. ESR affects the performance of electrolytic capacitors by influencing their charge and discharge rates, efficiency, and power handling capabilities. Voltage is a critical parameter for electrolytic capacitors and is usually specified as the rated voltage, which is the maximum DC voltage or peak pulse voltage that can be continuously applied without causing damage.

Electrolytic capacitors can deliver power to a circuit or load when discharged. However, their power handling capabilities may be limited compared to other types of capacitors due to factors such as ESR and internal resistance.

3.3 Supercapacitors

Supercapacitors have unique applications beyond traditional energy storage. It is a special kind of capacitor known for its ability to store a large amount of energy. In fact, it can store 10 to 100 times more energy than regular capacitors. One of its key advantages is its fast charging and discharging capability, which makes it ideal for applications requiring rapid energy transfer.

Capacitance values for supercapacitors, denoted as "rated capacitance", are typically much larger than those of electrolytic capacitors, often in the range of Farads. This high capacitance allows supercapacitors to store a significant amount of energy when loaded with a DC voltage.

A capacitor with a large capacitance, like a supercapacitor, in a circuit with finite series resistance, can safely absorb energy from a high-voltage transient source with a short-duration occurrence. This capability makes supercapacitors valuable in applications where rapid energy absorption and release are needed [164, 165].

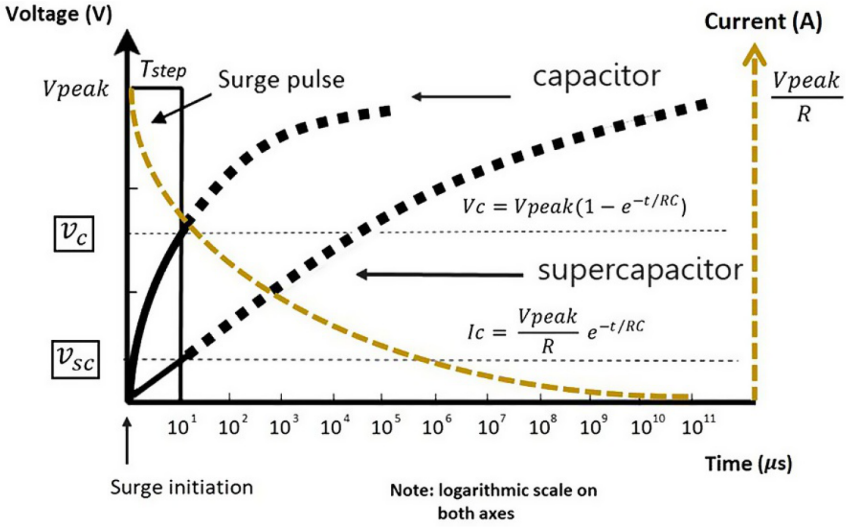

Figure 3.3: Depicts the case of a normal capacitor versus a supercapacitor working in an RC circuit activated by a 10 microsecond step pulse waveform. Source - [163] © (2018), with permission from Elsevier.

To ensure safe operation, supercapacitors have specific voltage limits known as the rated voltage. Exceeding this voltage can lead to damage. Operating supercapacitors below their rated voltage improves their long-term performance, stabilizing capacitance values and internal resistance during cycling, thus extending their lifetime and charge/discharge cycles.

When higher application voltages are needed, supercapacitors can be connected in series. However, variations in capacitance value and internal resistance among components necessitate active or passive balancing to stabilize the applied voltage.

Charging and discharging a supercapacitor involve the movement of ions in the electrolyte to and from the electrodes through their porous structure. This movement results in losses, which are measured as the internal DC resistance along with capacitance, determines the time constant and thus affects the charge/discharge time.

Table 3.1: Comparison of electrolytic capacitor and supercapacitors

Feature	Electrolytic capacitors	Supercapacitors
Energy storage	Accumulate charge on dielectric	Movement of ions between electrolyte and electrodes
Charging/discharging	Relatively slow	Rapid
Equivalent series resistance (ESR)	Higher	Lower
Voltage rating	Higher voltage rating	Lower voltage rating, need series connection for high voltage
Lifespan	Finite lifespan	Long lifespan with millions of cycles
Size and weight	Larger and heavier	Smaller and lighter
Specific energy/power	Lower specific energy/power	Higher specific energy/power
Application range	Low-frequency circuits, power supply filtering	High power density, rapid energy transfer applications
Environmental impact	May contain hazardous materials	Generally more environmentally friendly

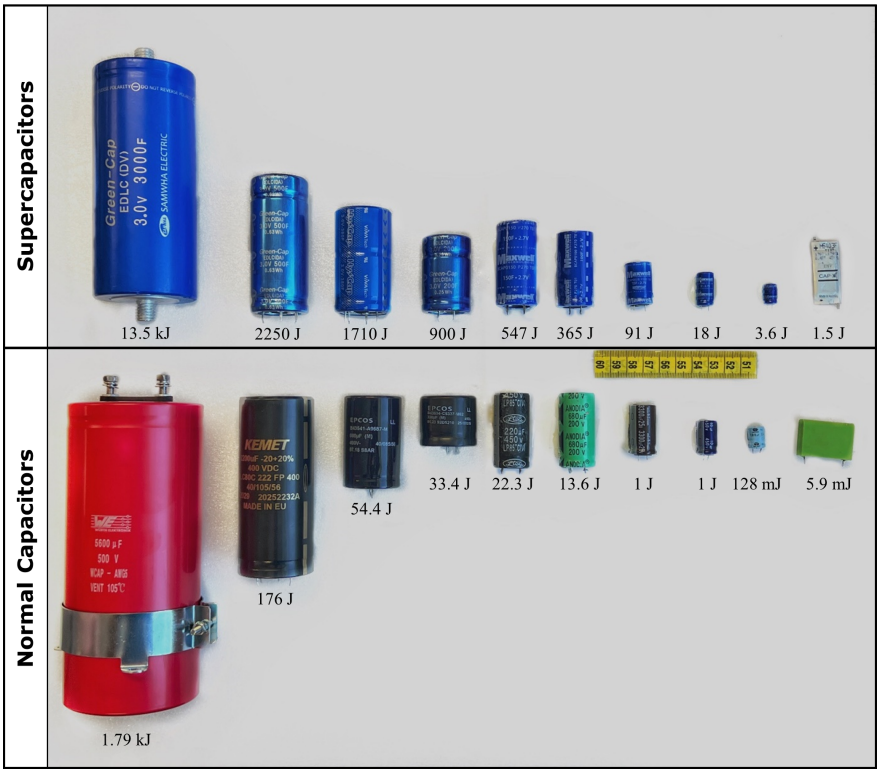

Figure 3.4: Comparison of supercapacitors and similarly-sized electrolytic capacitors with associated energy capacity (ruler scale in cm)

Supercapacitors, unlike batteries, are not constrained by chemical reactions but are limited by internal resistance, which can be much lower. This characteristic allows them to endure over one million charge/discharge cycles without significant degradation in capacity or increase in internal resistance, offering a substantial advantage over conventional batteries. Figure 3.3 compares a regular capacitor with a supercapacitor in an RC circuit subjected to a 10 μs pulse waveform. By controlling the duration of a high-voltage (HV) source to a sufficiently brief period, the voltage across the capacitor's terminals can remain within its maximum rating. This suggests that a supercapacitor, with its large capacitance, can effectively absorb energy from a high-voltage transient source for a short duration. Furthermore, using lower current loads can further enhance the longevity and life cycle of the capacitor.

Supercapacitors bridge the gap between high-power, low-energy electrolytic capacitors and low-power, high-energy rechargeable batteries. While they may have lower specific energy compared to batteries, they compensate with higher specific power. Specific power, measuring how quickly energy can be delivered to a load, can be 10 to 100 times greater than batteries, reaching values up to 15 kW/kg. Table 3.1 presents a comparison between capacitors and supercapacitors.

The specific energy of a capacitor is the amount of energy it can store per unit mass, while energy density is the energy stored per unit volume. Commercial supercapacitors typically have energy densities ranging from 5 to 8 Wh/L and specific energies ranging from 0.5 to 15 Wh/kg. Ragone charts [166] allow for easy comparison of energy storage technologies.

Supercapacitors offer advantages such as high power density, rapid charging and discharging, long cycle life, and excellent performance at low temperatures. However, they still face challenges such as limited specific energy and high self-discharge rates compared to batteries. Ongoing research aims to improve these aspects and expand the applications of supercapacitors in various fields, including transportation, renewable energy, and electronics.

The amount of energy a supercapacitor can store is determined by its capacitance and the square of its voltage. Supercapacitors are known for their high power density, allowing them to charge and discharge rapidly. Figure 3.4 shows a representative set of paired supercapacitors and electrolytic capacitors having similar canister volumes.

3.4 Transformer and magnetic core

Transformers and inductors are essential components in power supply circuits, but they can be bulky due to their physical construction and operational characteristics. Transformers are used to step up or step down voltages in AC circuits.

Increasing the operational frequency allows for a reduction in the number of turns required for a specific voltage across the winding, provided the core material can handle the higher frequency without saturating. This is because higher frequency operation requires less time for each cycle, allowing for faster energy transfer.

Inductors, on the other hand, are used primarily for energy storage and filtering in power supply

circuits. The impedance of an inductor is:

$$Z = R + j(2\pi f)L \tag{3.9}$$

At higher frequencies, the impedance of an inductor increases, which helps filter out high-frequency noise or ripple in circuits. However, this also introduces challenges such as increased core and copper losses, not necessarily due to impedance itself but due to frequency-dependent effects. These losses can lead to heating and efficiency issues. Depending on the application and required inductance, higher-frequency inductors may require careful design; sometimes resulting in larger components or specialized materials to minimize losses.

To understand the proposed topology, it is important to grasp the theoretical concepts behind the transformers, which necessitate the use of a transformer as a basic building block. Figure 3.5 illustrates the case of an ideal transformer, while Figure 3.6 considers practical conditions, including winding resistances, leakage inductance, and a superficial winding to represent the magnetizing requirement of the core. Figure 3.7 simplifies the case assuming small voltage drops across the windings are negligible and equivalent model for calculations in circuits. For a deeper discussion on transformers, particularly applicable to high-frequency switching transformers, refer to [167].

Magnetic materials used in electronic applications can be broadly categorized into three types, each with its own unique characteristics:

Magnetic metals and alloys: These materials, such as silicon steel, mumetal, permalloy, and amorphous metals, are typically in tape or laminated form. They have high saturation flux density and high permeability. Due to their high electrical conductivity, they are used in laminated or tape form to reduce eddy current losses. They are suitable for line frequency (50–400 Hz) transformers and inductors but have limited use at high frequencies due to eddy current losses.

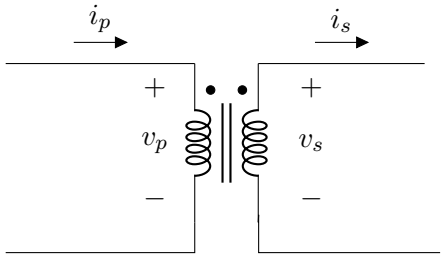

Figure 3.5: Equivalent circuit of the transformer in ideal case

Powdered magnetic metals: These materials consist of magnetic metals that are ground into a fine powder, coated with an insulating layer, and then shaped through pressing and sintering. The small particle size helps to minimize eddy currents, allowing these materials to operate effectively at frequencies up to several megahertz. They generally have low permeability, ranging from 8 to 80, making them ideal for filter inductors used at medium frequencies, typically between 1 and 100 kHz.

Ferrites: Ferrites are ceramic materials that are typically dark gray or black, and they are known for their hardness, brittleness, and chemical inertness. Common types, such as MnZn and NiZn ferrites, display excellent magnetic properties below their Curie temperature (T_c). These materials

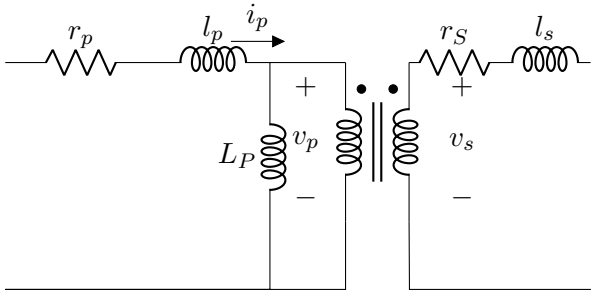

Figure 3.6: Equivalent circuit of the transformer with components indicating winding resistances, leakage inductance, and magnetizing inductance

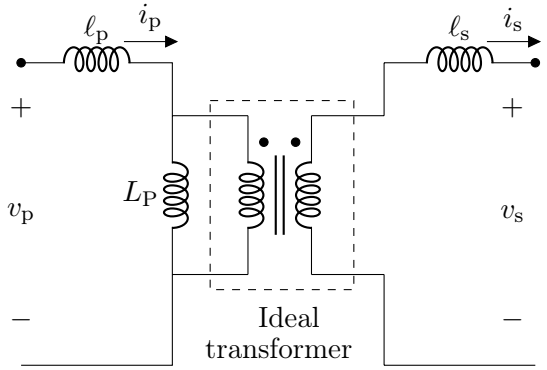

Figure 3.7: Equivalent circuit of the transformer suitable for switching regulator calculations, neglecting all losses in transformer

have high resistivity, which makes them well-suited for transformers and inductors operating at high frequencies (up to several tens of MHz) with minimal losses and high Q factors. Although their saturation flux densities are relatively low and permeability ranges from a few hundred to 15,000, ferrites come in a wide variety of core shapes, enhancing their versatility for different applications. Unlike magnetic metals, ferrites can be used at very high frequencies without the need for laminating.

Overall, the choice of magnetic material depends on the specific application requirements such as frequency, permeability, and saturation flux density. Ferrites are often preferred for high-frequency applications due to their low loss and high resistivity, while magnetic metals are suitable for low to medium-frequency applications where high saturation flux density is required.

3.5 Power MOSFET

A metal-oxide-semiconductor field-effect transistor (MOSFET) is a type of transistor that is widely used in electronic devices and circuits. It operates by controlling the flow of current between the source and drain terminals using an electric field generated by the voltage applied to the gate terminal.

Initially developed in the mid-1970s, the vertical power MOSFET was created to address limitations in existing power bipolar transistors, such as low current gain and inability to operate at high frequencies. Power MOSFETs replaced these by offering voltage-controlled operation, high input

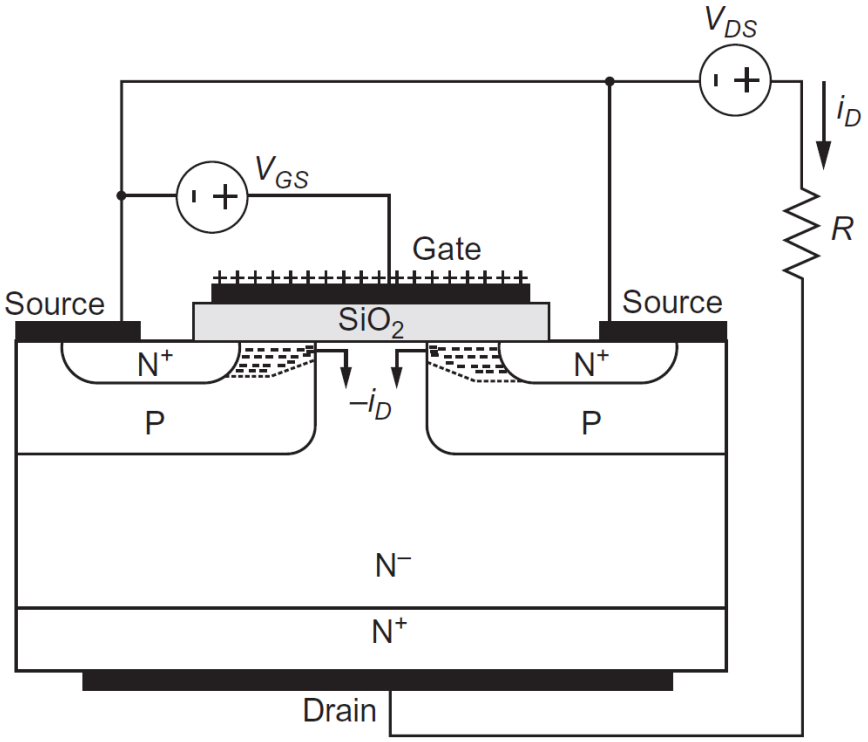

Figure 3.8: Structure of an n-channel MOSFET. Source - [153]© (2018), with permission from Elsevier.

impedance, and faster switching speeds, making them ideal for a wide range of applications.

MOSFETs are key components in modern electronics, offering advantages such as voltage-controlled operation, high input impedance, and fast switching speeds. Over the years, advancements in MOSFET design have focused on reducing internal resistance and improving performance for various applications, from power supplies to switch-mode power supplies, and beyond.

3.5.1 Structure & operation

A MOSFET consists of three primary components: the drain (D), source (S), and gate (G). As depicted in Fig 3.8, the MOSFET's operation is controlled by these elements:

Gate insulator: The gate is separated from the semiconductor material by a silicon dioxide (SiO_2) layer, serving as an insulator.

PN junction diode: There is a PN junction diode situated between the source and drain. This diode allows current to flow when the voltage between the drain and source is negative, and it can withstand reverse voltages applied to the MOSFET.

Transistor function: The MOSFET functions as a transistor when a positive voltage is applied between the drain and source.

Channel formation: Applying a positive voltage to the gate-source terminals repels positive charges in the P-type regions and attracts electrons. When the gate-source voltage surpasses a certain threshold, it forms a conductive path, or channel, between the source and drain.

Current flow: This channel permits current to flow from the drain to the source. Increasing the gate-source voltage attracts more electrons, enhancing the current flow.

Carrier movement: The conduction current consists of electrons moving from the N+ source region through the channel and into the N+ and N- drain regions.

Without gate voltage: When no voltage is applied to the gate, the MOSFET behaves like an open switch, preventing current from flowing between the source and drain.

With positive gate voltage: Applying a positive voltage to the gate generates an electric field that draws electrons into the channel between the source and drain. This creates a conductive channel, allowing current to pass through. At lower drain voltages, the MOSFET acts as a variable resistor, with resistance controlled by the gate voltage. At higher gate voltages, the resistance of the drift region (the area between the channel and the drain) may become significant.

Current saturation: When the drain voltage reaches and exceeds the gate voltage, the MOSFET enters saturation, where the current flow stabilizes. This saturation is beneficial for switching inductive loads, as it limits current during transitions but can result in substantial power dissipation.

In summary, the N-channel MOSFET operates as a transistor when a positive voltage is applied to the gate-source terminals. This voltage induces a channel that facilitates current flow from the drain to the source. When the gate voltage is applied, it enables current conduction through the channel.

Talking particularly about power MOSFET, they operates the same way by controlling the flow of current between its source and drain terminals using a gate bias voltage. It supports high voltage and high current, and its behavior can be controlled by the gate voltage, making it suitable for various applications including power switching. Power MOSFETs and regular MOSFETs (sometimes called small-signal MOSFETs) are both types of metal-oxide-semiconductor field-effect transistors, but they are designed for different applications and have different characteristics. Power MOSFET have:

1. High power handling: Power MOSFETs are designed to handle higher currents and voltages compared to regular MOSFETs. They are used in power electronics applications where high power levels are involved, such as in power supplies, motor control, and audio amplifiers.

2. Low on-resistance: Power MOSFETs typically have lower on-resistance compared to regular MOSFETs. This is important in power applications because it reduces power losses and improves efficiency.

3. High input capacitance: Power MOSFETs often have higher input capacitance, which can affect their performance in high-frequency applications.

In summary, the main differences lie in their power handling capabilities, on-resistance, switching speeds, and intended applications. Power MOSFETs are optimized for high-power applications, whereas regular MOSFETs are used in low-power applications where fast switching speeds and small size are more important.

3.6 TMS coil

In this study, the TMS coil constructed by Khokhar et al. [136] was utilized. As an initial phase, resistance and inductance measurements of the coil (Fig. 3.9) were conducted. The coil comprises 50 turns of copper wire with a conductive diameter of 0.4 mm wound around a 5 mm diameter carbonyl powdered iron core (Micro Metals, U.S.A).

The inductance of the coil was measured to be 22 μH. Using Agilent E4980A four-point impedance meter, resistance and reactance value for the various frequency ranging from 50 Hz to 2 MHz was observed. It gives an idea about in which range of frequency we need to pulse the TMS coil so that its electrical characteristics are unaltered.

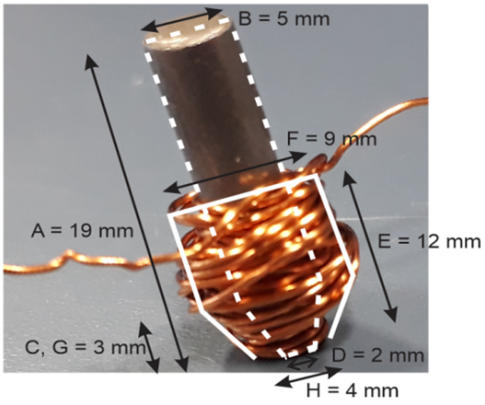

Figure 3.9: Geometry of the mouse coil designed by khokhar et al. [136] © [2021], IEEE

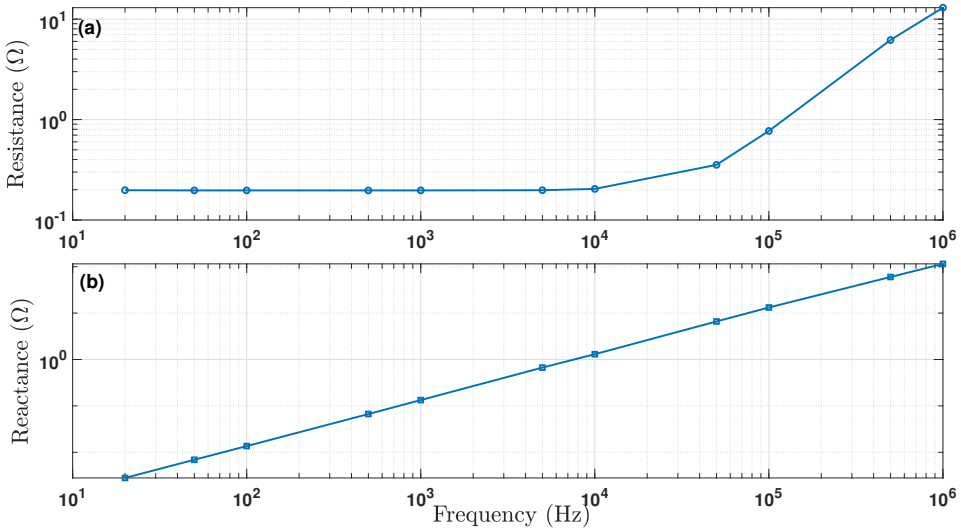

Figure 3.10: Measurement of the TMS mouse coil inductance and resistance taken using Agilent E4980A four-point impedance meter

As depicted in Fig. 3.10, the resistance remains constant throughout the low-frequency range whereas the reactance varies linearly to frequency.

(INTENTIONALLY BLANK)

Chapter 4

Circuit design

Introduction to chapter

This chapter provides a comprehensive overview of the development and experimental validation of the pulse generation prototype designed to enhance TMS applications. It begins with a detailed explanation of the block diagram representation of the prototype, followed by a full circuit diagram and a description of the components used. The development process is outlined in stages, illustrating the evolution from initial design to a successful prototype. The modes of operation are discussed, with each circuit block explained in detail. Notably, the initial successful stage of the prototype was published in the proceedings of IECON 2023 (flagship annual conference of the IEEE Industrial Electronics Society), and the corresponding publication is included at the end of this chapter.

4.1 Block diagram of the prototype

Figure 4.1 depicts the overall block diagram of my proposed supercapacitor-based high-power pulse generator. In the block diagram representation, there are two stages highlighted by red and blue dotted rectangles. The first stage (red dashed block) is the power stage, which handles high voltage and current. The second stage (blue dashed block) is the switching control stage, which operates at low voltage. An opto-isolator is used to isolate these two stages, ensuring electrical protection and safety. I aimed to design a circuit that diverges from existing literature, focusing on a self-sufficient and low-cost solution. Traditionally, high-voltage/high-power pulse generators in the power electronics field are constructed using a high-voltage power supply combined with a pulse shaping stage [66, 168, 169]. Upon reviewing various traditional techniques, I identified that supercapacitors (SCs) can serve as the core energy supply element for pulse generators due to their exceptionally low equivalent series resistance (ESR), which translates to a maximum power capability of $\frac{V^2}{R}$, where V is the rated capacitor voltage and R is the ESR.

I initially tested the circuit using a 12 V, 12.8 mΩ supercapacitor bank of 95 Farads (four 380 F SCs in series) with a power capability of 2.8 kW and a total energy delivery of 6.8 kJ. This setup produces enough TMS pulses per discharge to effectively excite the TMS coil. The key advantage of SCs over electrolytic or film capacitors is their combined energy storage and power delivery

capability, making them a crucial component of this low-cost pulse generator.

During the design and build approach, I could not find any papers or articles on supercapacitor-based pulse generators for even high-power pulse applications. Therefore, developing a new and modifiable circuit for TMS took precedence over being guided by existing literature. Additionally, creating a circuit with fewer switches was a priority because controlling multiple switches may become complex and difficult. Consequently, I designed a high-voltage pulse generator using a single MOSFET control and explored various ways to utilize the MOSFET in pulse shaping beyond its typical on/off functionality.

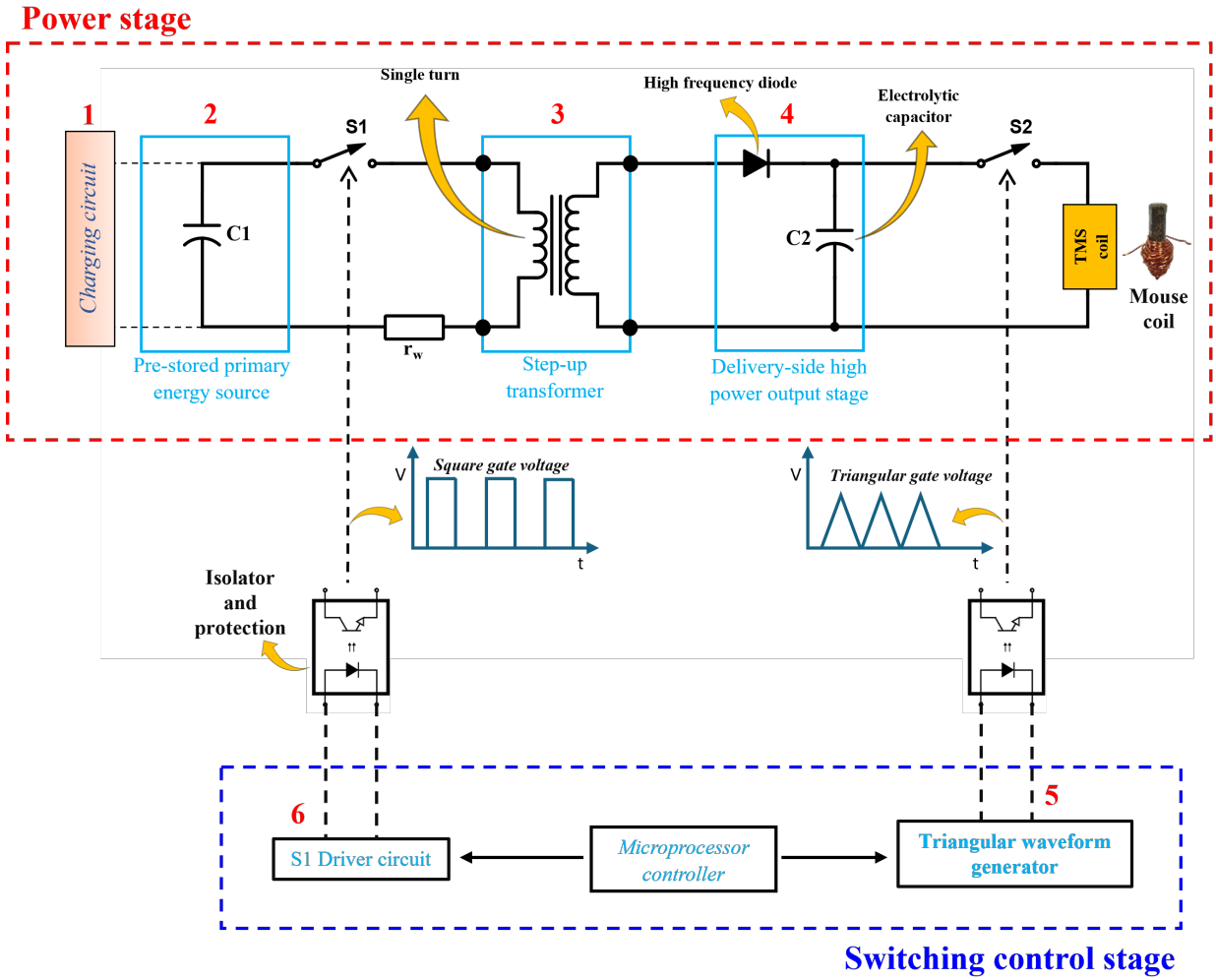

Figure 4.1: Block diagram of TMS pulse generator prototype . Power stage (high voltage/current) and switching control stage (low voltage) highlighted by red and blue dotted rectangles. An opto-isolator isolates the stages for protection and safety.

4.1.1 Charging circuit (Block 1)

For this prototype, the supercapacitor bank is charged to 5 V using a standard 3 A, 0–30 V laboratory DC power supply (BK precision 1670A).

4.1.2 Pre-storage primary energy source (Block 2)

The Block 2 (Fig. 4.1) primary energy source is a supercapacitor bank (C1) constructed from four 3-V, 380-F supercapacitors connected in series to give a net capacitance of 95 F, and a maximum working voltage of 12 V. When charged to 5 V, this bank can store a total energy of $\frac{1}{2}CV_{\text{oc}}^2 = 1188$ J. This energy is sufficient to generate approximately 20 TMS pulses of 100 μs pulse width per discharge, even with a 1 V input, and a voltage drop of only 0.2 V per discharge in the supercapacitors. Utilizing a higher capacity supercapacitor (SC) could produce significantly more pulses with an even smaller voltage drop ($\approx$ 0.02 V with a 3000 F SC). This will be discussed in detail in Section 4.4.1.

Total ESR of the capacitor bank is 12.8 mΩ which can provide a maximum short circuit current of 937 A. This potentially high short circuit DC current capability indicates that it can drive a very high current into the primary of the step-up transformer (Block 3), subject to additional loop resistances created by the connectors and the other parasitic resistance.

Our broader power electronics research team at the University of Waikato focuses on supercapacitor-assisted (SCA) techniques and their applications [165, 170–173]. This foundation of knowledge on supercapacitors inspired me to develop this new approach.

4.1.3 Step-up transformer (Block 3)

Given that a mouse TMS coil requires an excitation voltage of 200 to 500 V [105], we need to upscale the output voltage of the supercapacitor bank by a significant factor. For this purpose, we have tested the suitability of a step-up transformer with a single-turn primary and large turns ratio (1:60 range).

This single turn primary coil allows very high primary loop current which will be within the short circuit current of the SC bank. If we build the secondary winding with a very large number of turns (several thousands), we can get high voltage at the secondary. However, from the detailed equivalent circuit of the transformer, ohmic resistance of the secondary will limit the maximum current deliverable to the load.

Since the designed transformer has higher secondary turns, secondary winding resistance will be dominant, and it will reduce the current into the load. To overcome this issue, we opted to charge an electrolytic capacitor from this stepped-up voltage. The maximum power delivered to the secondary will depend on the total resistance of the secondary (given a single turn case, primary resistance can be neglected).

4.1.4 Delivery-side high-power output stage (Block 4)

Theoretically we should be able to drive the TMS coil directly from the secondary via the series switch. Given that the secondary referred magnetizing inductance and the ohmic resistance of the secondary coil dominate, achieving high current capability will not be possible. For that reason, I have inserted a high voltage electrolytic capacitor-based charging circuit block in series with an electronic switch controlled by the processor board. As the ESR of a SC decreases with capacitance value, if a higher current is required we could simply use a high value SC to improve the circuit.

A high-frequency diode and a high-voltage rated electrolytic capacitor (C2) are coupled to the secondary of the transformer to achieve a DC output voltage which is sufficient to drive a high-power pulse into the TMS coil. During each ON period of Switch-1 (MOSFET S1 in Fig. 4.1), the transformer's secondary winding, possessing high self-inductance, forms a series path with the rectifier diode and the output electrolytic capacitor. The transformer secondary resistance limits the rate of current change, thereby restricting the amount of charge that can accumulate on the capacitor during the ON interval. In order to charge the capacitor to the required voltage it is necessary to repetitively trigger S1. So the processor (Block 6) drives the gate of S1 with a pulse repetition rate of 8 kHz for a total integration time of 2 s. During this charging time, MOSFET S2 is OFF.

The energy stored in the electrolytic capacitor is then delivered to the TMS coil by driving the output MOSFET (S2 in Fig. 4.1) with a triangular gate-control voltage (Block 5).

4.1.5 Variable slope triangular waveform generator for S2 (Block 5)

Creating a versatile waveform generator that can produce a triangular waveform with adjustable rise and fall slope is an important part of this circuit. One effective method involves utilizing constant current sources to charge and discharge a capacitor. This approach ensures that the rate of change of voltage across the capacitor remains constant, resulting in a triangular waveform. This setup provides precise control over the generation of a triangular waveform with adjustable slope. The use of constant current sources, analog switches, capacitor selection based on frequency, and feedback mechanism through the comparator ensures reliable and accurate waveform generation.

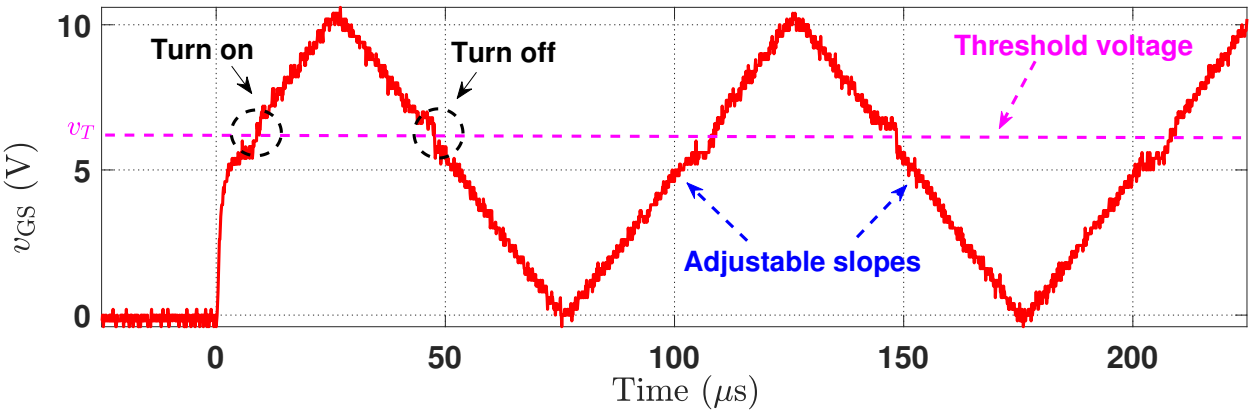

Figure 4.2: Triangle gate voltage showing the adjustable slope and threshold voltage (v_T)

Using a triangular gate voltage for a MOSFET offers several advantages:

1. **Reduced switching losses**:

   Smooth transition: A triangular gate voltage provides a smoother transition between the on and off states of the MOSFET compared to a square pulse. In the case of the triangular wave gate signal, the benefit is being able to control the output current pulse waveform through control over the rate of MOSFET on-off transitions. Figure 4.2 shows the MATLAB-captured

triangle gate voltage generated by the arbitrary waveform generator with adjustable slopes and the threshold voltage marked.

Controlled dv/dt and di/dt : The gradual increase and decrease in gate voltage control the rate of change of voltage (dv/dt) and current (di/dt) more effectively, minimizing losses due to rapid switching transients.

2. **Lower electromagnetic interference (EMI)**:

   The softer switching characteristics of a triangular gate pulse reduce the high-frequency components generated during switching. This results in lower EMI, which is beneficial for compliance with electromagnetic compatibility (EMC) standards and reduces interference with nearby electronic devices.

3. **Enhanced gate control**:

   A triangular gate pulse allows for more precise control over the gate charge, leading to better control of the MOSFET switching behavior. This can be particularly useful in applications requiring precise timing and control.

4. **Reduced ringing and oscillations**:

   The smoother transition provided by the triangular gate pulse helps to minimize ringing and oscillations that can occur during switching events. This leads to more stable operation and reduced risk of false triggering or noise issues.

5. **Improved efficiency**:

   By reducing switching losses and EMI, and improving thermal management, the overall efficiency of the power conversion process is improved. This can be particularly important in high-efficiency power supply designs and other power electronics applications.

The TMS coil voltage is determined by the rate of change of current (di/dt). The maximum voltage is achieved when the MOSFET is turned off as rapidly as possible (fast switching), which is maximized by using a sharp (rectangular) gate signal. In contrast, a triangular wave gate signal allows for control over the output current pulse waveform by adjusting the rate of the MOSFET's on-off transitions, enabling more precise shaping of the current pulse.

In my circuit, using a triangular gate voltage offered the added benefit of producing higher voltage across the TMS coil. Additionally, by adjusting the symmetry of the triangular waveform, I was able to further increase the voltage output without making any changes to the circuit components. This flexibility in tuning the gate voltage allows for optimizing the performance of the TMS coil, achieving higher voltages as needed for effective stimulation.

The next chapter will provide further details of this waveform generator, including circuit diagrams, equations, and a thorough explanation of its operation. This will offer a comprehensive understanding of how this method results in a triangular waveform with an adjustable slope.

4.1.6 Arduino controlled driver circuit for S1 (Block 6)

The S1 pulse is generated by an Arduino program, which is then routed through a driver circuit designed to interface with the primary side of a transformer. The driver circuit employs an opto-isolator, specifically the 4N25, to achieve electrical isolation between the low-voltage control side and the high-voltage side of the transformer. This isolation is crucial for ensuring the reliability and safety of the design, as it protects the low-voltage control electronics from potential high-voltage spikes.

The Arduino generates the initial control pulse, which is then fed into the driver circuit. Within this circuit, a transistor is used to amplify the voltage of the control signal, ensuring that it is strong enough to drive the subsequent stages. After amplification, the signal passes through the opto-isolator. The opto-isolator uses an LED and a phototransistor to transfer the control signal across an insulating barrier, maintaining electrical isolation while allowing the signal to be transmitted.

This combination of the Arduino-controlled pulse generation, voltage amplification via the transistor, and signal isolation using the opto-isolator ensures that the driver circuit can reliably control the primary side of the transformer. The opto-coupler not only provides protection but also enhances the robustness of the design, making it suitable for applications involving high voltages.

4.2 Circuit diagram & component list

In this section, the complete details of the developed hardware prototype are presented, accompanied by photographs of the various components. The Table 4.1 included in this section provide a breakdown of the cost of each component used in the prototype, with the total amount reaching 170 NZD, highlighting the affordability and cost-effectiveness of the design. The total cost of 170 NZD demonstrates that the design is economically viable for research or small-scale manufacturing purposes.

Table 4.1: List of components and the associated costs

Component	Assignment	Nominal rating	Cost (NZD)
C1	Electrolytic-capacitor	330 μF, 450 V	12
C2	Supercapacitor	380 F, 3 V, 3.2 mΩ, 257 A	20
S1	Charging switch	40 V, 1.35 mΩ, 350 A	8
S2	Discharging switch	650 V, 24 mΩ, 120 A	39
D	High-frequency diode	1.2 kV, 75 A	8
T	Step-up transformer	1:60 Turns ratio	3
A	ARDUINO UNO	5 V, 14 digital I/O pin	50
	Others (Resistance, transistors)		30
		Total cost	170

Figure 4.3 displays the full circuit diagram, which includes the S1 and S2 driving circuits, as well as the Arduino microcontroller that controls the switching operations. The diagram provides a comprehensive view of how the different components are interconnected to create the pulse generator for transcranial magnetic stimulation. Table 4.2 lists the entire component set used in the circuit. Figure 4.4 offers a more detailed look at the prototype through three subfigures: Fig. 4.4(a) shows the circuit diagram, laying out all key elements, including the power supply, MOSFET switches, control circuitry, and the step-up transformer used for generating the necessary voltage for TMS applications. Fig. 4.4(b) presents a photograph of the hardware setup, displaying the actual prototype of the main circuit. This image provides a visual reference for how the circuit components have been physically arranged and connected. Fig. 4.4(c) depicts the entire system, including the coil holder, which is used for measuring the magnetic field generated by the TMS coil.

Overall, this section offers a comprehensive overview of the prototype's design and construction, from the circuit diagrams and component lists to the physical hardware setup.

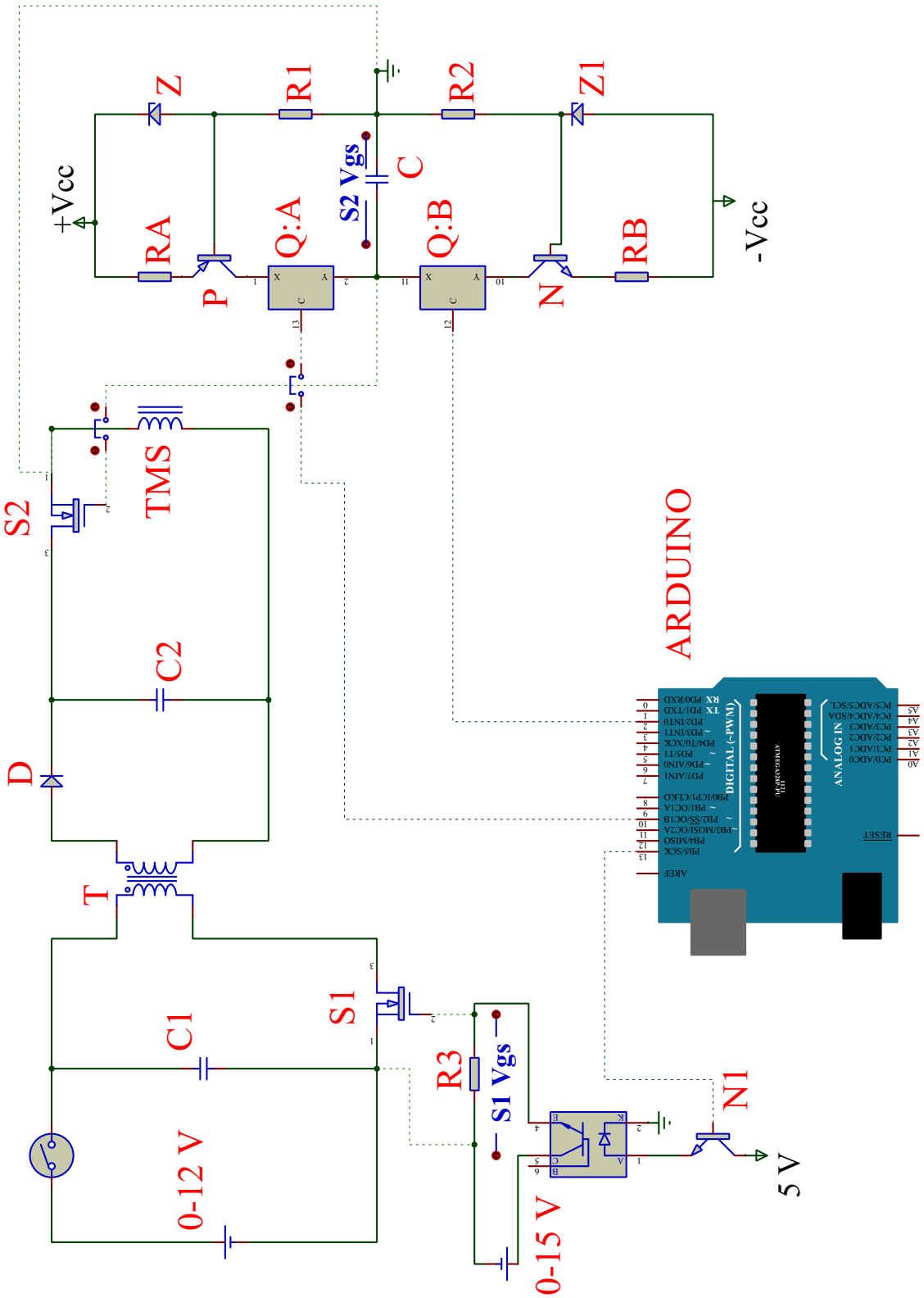

Figure 4.3: Circuit topology of the prototype

Table 4.2: Key components of the prototype

Component	Assignment	Nominal rating	Part number	Manufacturer
C1	Electrolytic-capacitor	330 μF, 450 V	B43634C5337M062	EPCOS
C2	Supercapacitor	380 F, 3 V, 3.2 mΩ, 257 A	VEC3R0387QG	VINA Tech
S1	Charging switch	40 V, 1.35 mΩ, 350 A	IRFP4004PbF	Infineon Technologies
S2	Discharging switch	650 V, 24 mΩ, 120 A	IXFK120N65X2	IXYS-Littelfuse
L	TMS coil	27 μH, 200 mΩ	Carbonyl powder iron core- P1224-340/9	Micrometals
D	High-frequency diode	1.2 kV, 75 A	STTH75S12W	STMicroelectronics
T	Step-up transformer	1:60 Turns ratio	Ferrite core ZW42207TC	Magnetics
		S1 driver circuit		
A	ARDUINO UNO ATMEGA328P board	5 V, 14 digital I/O pin	A000066	Arduino
O	Optocoupler	5 kV, 6 DIP	4N25	Vishay Semiconductor Opto Division
N	NPN transistor	NPN 45 V, 0.1 A	BC547	Onsemi
		S2 driver circuit		
C	Capacitor	15 nF 100 V	2A153J	Nichicon
Z	Zener diode	3.3 V 1 W	1N4728A	Onsemi
P	PNP transistor	PNP 80 V 1.5 A	BD140	STMicroelectronics
S	IC quad bilateral switch	125 Ω, 14 DIP	CD4066BE	Texas Instruments
R	Digital potentiometers	256 position variable resistance	8403A1	Analog devices

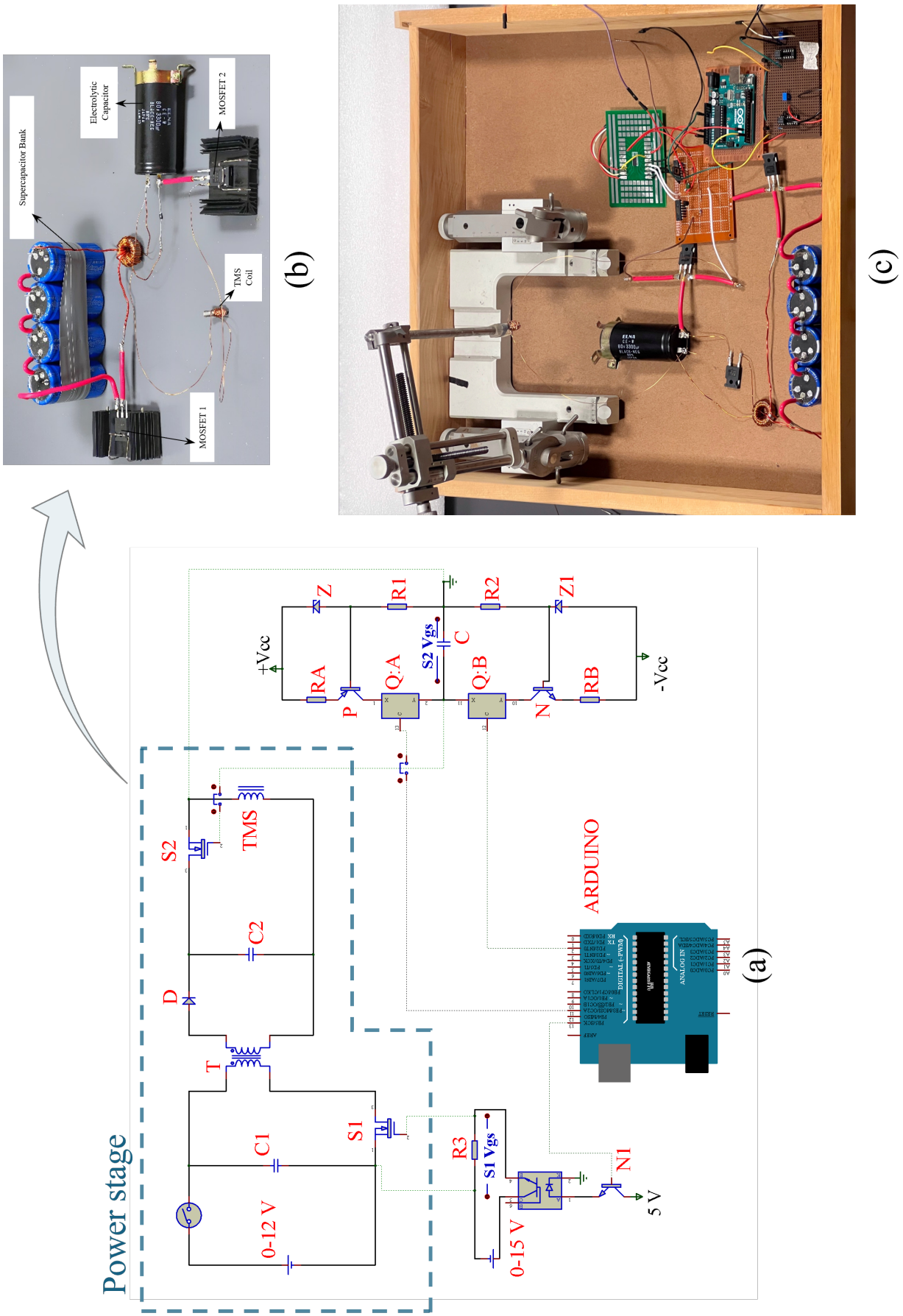

Figure 4.4: Proof-of-concept of prototype- (a) Overall system showing external drivers to S1 from Arduino processor board and triangle voltage waveform generator for S2; (b) experimental power stage; (c) Full circuit prototype setup

4.3 Main circuit development idea

1. Supercapacitor (SC) as energy source: The initial phase of this project involved experimenting with supercapacitors as the primary energy source. Supercapacitors, despite their invention in 1957, have seen significant advancements in their application in electronics. These devices offer substantial advantages due to their high energy density and capacity to deliver high currents. The last decade, particularly from 2010 to 2020, was critical for the development and commercialization of supercapacitors [174]. Although their operating voltage is typically below 5 V, their low internal resistance minimizes energy loss, making them highly efficient for TMS application. Their capability to provide high current is particularly beneficial for applications requiring rapid discharge rates.

2. Step-up transformer: Given the low voltage output of supercapacitors, a step-up transformer was employed to increase the voltage. The transformer design was critical, necessitating careful selection of the magnetic core material and the winding ratio to ensure optimal performance. By designing the transformer with a single primary turn and multiple secondary turns, the voltage output was significantly increased, facilitating higher voltage operations necessary for the circuit.

3. MOSFET for chopping DC: To utilize the step-up transformer, which operates with alternating current (AC), it was essential to convert the direct current (DC) from the supercapacitors into a form compatible with AC. This was achieved using a MOSFET, which chops the DC into pulsating DC, mimicking an AC signal suitable for transformer operation.

4. Rectification and capacitor storage: The pulsating DC voltage generated was subsequently rectified and stored in an electrolytic capacitor. This storage mechanism allows the converted voltage to be switched and utilized according to the desired pulse patterns for the application.

5. Controlling pulse sequences: Precise control over the pulse sequences delivered to the coil was essential. The stored high or medium voltage in the electrolytic capacitor was manipulated to deliver in any required pulse pattern, ensuring accurate and controlled delivery of energy to the coil.

6. Rigorous testing of prototype circuit: The prototype circuit demonstrated effective physical excitation of the coil, indicating that sufficient current and magnetic field were generated for the intended application. This successful operation validated the initial design and functionality of the circuit.

7. Pulse shaping with MOSFET: Further refinement involved shaping the pulses to achieve the desired waveform characteristics. Various pulse shapes were tested, with triangular gate voltage showing particularly promising results in optimizing the pulse delivery.

8. Development of software model: To mitigate the risks and costs associated with testing high voltage components and to test pulse shaping with different gate input/wave shapes, a software model was developed to predict circuit behavior. This model allowed for extensive

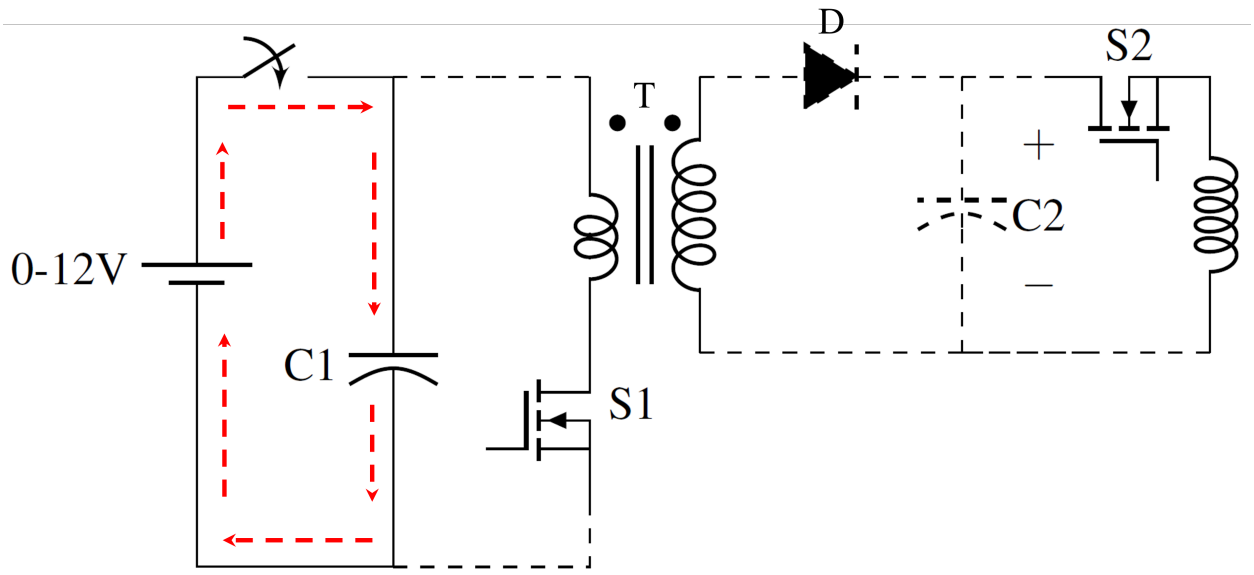

Figure 4.5: Mode-1 (red dashed lines) of the circuit topology of the power stage

experimentation and refinement of the prototype in a virtual environment. By correlating the experimental results with simulations, a robust software model was established that accurately predicts the circuit performance.

Overall, the development approach combined practical experimentation with simulation-based refinement, providing a systematic and efficient pathway to optimize the pulse generator prototype. This methodology facilitated tailored adjustments based on software model predictions, enhancing the prototype to meet specific user needs effectively.

4.4 Modes of operation

The prototype circuit operates in three modes: charging the supercapacitor, charging the electrolytic capacitor, and excitation of the TMS coil. I will now discuss each mode in turn.

4.4.1 Mode-1: Charging the supercapacitor bank

Figure 4.5 shows mode 1. In this mode, I utilize a standard laboratory power supply to charge the supercapacitor bank C1, Comprising four 3 V, 380 F supercapacitors connected in series to achieve a maximum voltage of 12 V and an effective capacitance of 95 F (380/4), the bank exhibits minimal voltage drop per discharge. Hence, recharging the supercapacitor bank C1 after each discharge is unnecessary, even though it is charged to only 2 V. The utilization of larger supercapacitor will allow for a prolonged operation without recharging. The conducting path for Mode-1 is depicted in Figure 4.5 with red dashed lines.

Over the last two decades, many capacitor manufacturers have started manufacturing supercapacitors, consequently the prices of these devices have started coming down, particularly for the

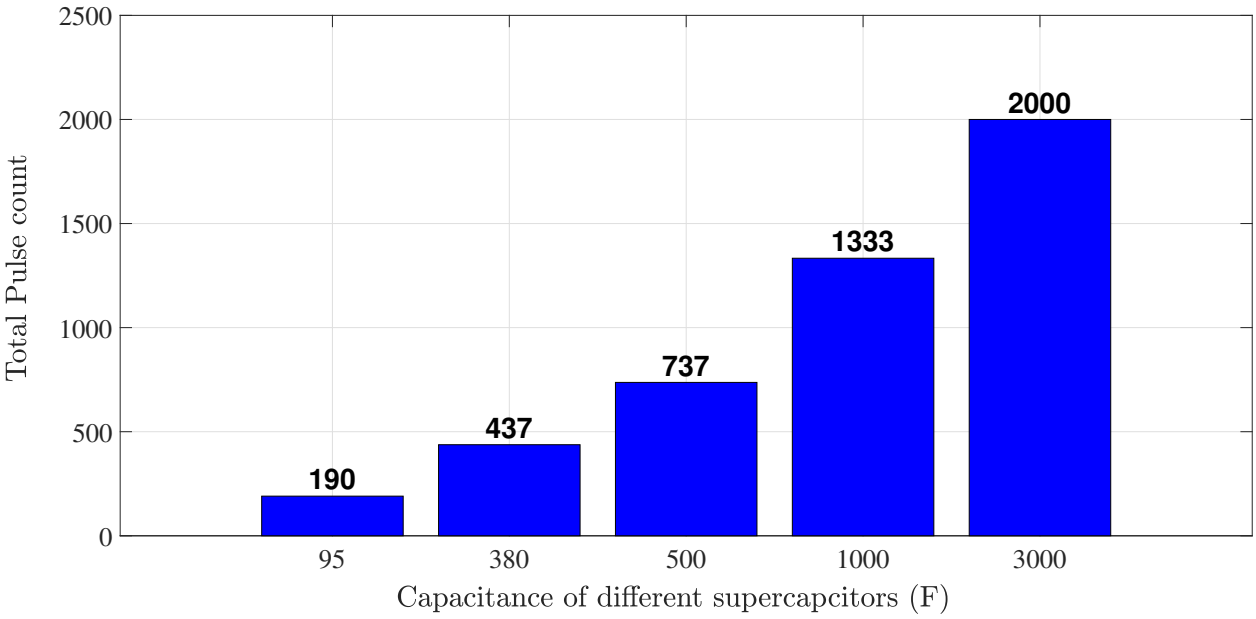

Figure 4.6: Total pulse count of the respective supercapacitors with an initial voltage of 2 V used as a source for the prototype to test the SC's ability as a pulse generator source.

lower capacitance devices from 1 F to 500 F [6]. The most useful properties of supercapacitors are: (i) very long life compared to limited life-cycle batteries, and (ii) low equivalent series resistance (ESR) which results in high power delivery capability.

The experimental results generated by the use of different sizes of supercapacitors (SC), detailing the overall pulse capacity of each capacitor type is shown in Fig 4.6. The supercapacitor bank has the capacity to charge upto 12 V but in this experiment, all supercapacitors were charged to 2 V and utilized as a primary power source for the prototype. The initial excitation of the TMS coil resulted in a reduction in the input supercapacitor voltage in the range of 0.02 to 0.2 V only. The experiment was conducted over 8 discharge sequences to provide insights on pulse count and energy. Notably, supercapacitors with higher capacitance exhibited a lower reduction in voltage, enabling a greater number of excitation with the supply voltage of 2 V.

This observation is particularly promising, as even at a voltage of 2 V, a high capacitance supercapacitor can generate up to 2000 pulses. In contrast, continuous theta burst stimulation or intermittent theta burst stimulation (iTBS) typically use only 600 to 1200 pulses. Therefore, this makes the supercapacitor an excellent option as a source for the circuit to generate enough pulses for TMS. This capability ensures that the supercapacitor can provide a stable and sufficient pulse count for effective therapy sessions, demonstrating the potential for supercapacitors in advanced medical devices. The cumulative pulse count for different supercapacitors, depicted in Fig. 4.6, further underscores their suitability as a superior power source for pulse generation.

The voltage drop, representing energy loss in 95 F and 3000 F supercapacitors, is shown in Fig. 4.7. The 3000 F supercapacitor maintains high energy levels throughout discharge with minimal

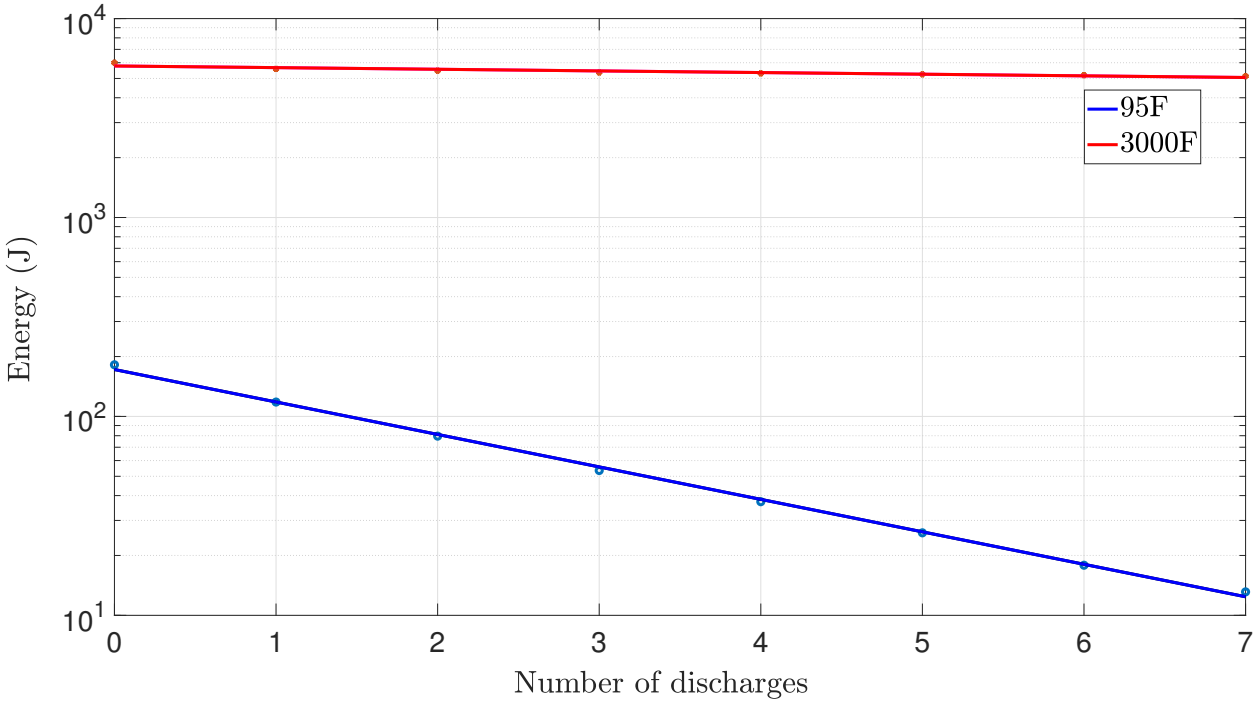

Figure 4.7: Energy discharge of 95 F (blue) and 3000 F (red) supercapacitors with 2 V initial voltage. This illustrates that the 3000 F supercapacitor can sustain high energy levels throughout the discharge process with minimal losses.

losses. Supercapacitors have very low and constant equivalent series resistance (fractional milliohms to a few milliohms), resulting in a high power density far superior to rechargeable batteries. By combining the series supercapacitor module with a low ESR, you can use a step-up transformer to output a high secondary voltage (v_S).

The supercapacitor's equivalent circuit model is a capacitor in series with an equivalent series resistor, with the latter proving crucial in determining instantaneous current through the load. Supercapacitors exhibit low ESR in the milliohm range, ensuring efficient energy transfer. The Ragone plot [175] indicates that supercapacitors are approaching the energy density of lead-acid batteries, offering higher life cycle capabilities. Despite the limitation of a 3 V DC voltage rating per cell, supercapacitors outperform other capacitors in energy storage and delivery, as evidenced by their Farad rating. By connecting supercapacitors in series, the low voltage issue can be mitigated.

As depicted in Fig. 4.6, by increasing the size of the supercapacitor module from 95 F to 3000 F with a precharged voltage of 2 V, the total number of pulses keep increasing with the size of the supercapacitor. This illustrates that for a given TMS experiment there is no necessity to have a specially designed DC power supply for the input supercapacitor stage. Once the SC module is precharged, the low voltage DC source can be disconnected by opening the switch.

4.4.2 Mode-2: Charging the electrolytic capacitor

Figure 4.8 shows the mode 2. Utilizing the advantageous properties of supercapacitors as discussed above, I have successfully constructed a prototype [79] with the TMS coil developed by Khokhar

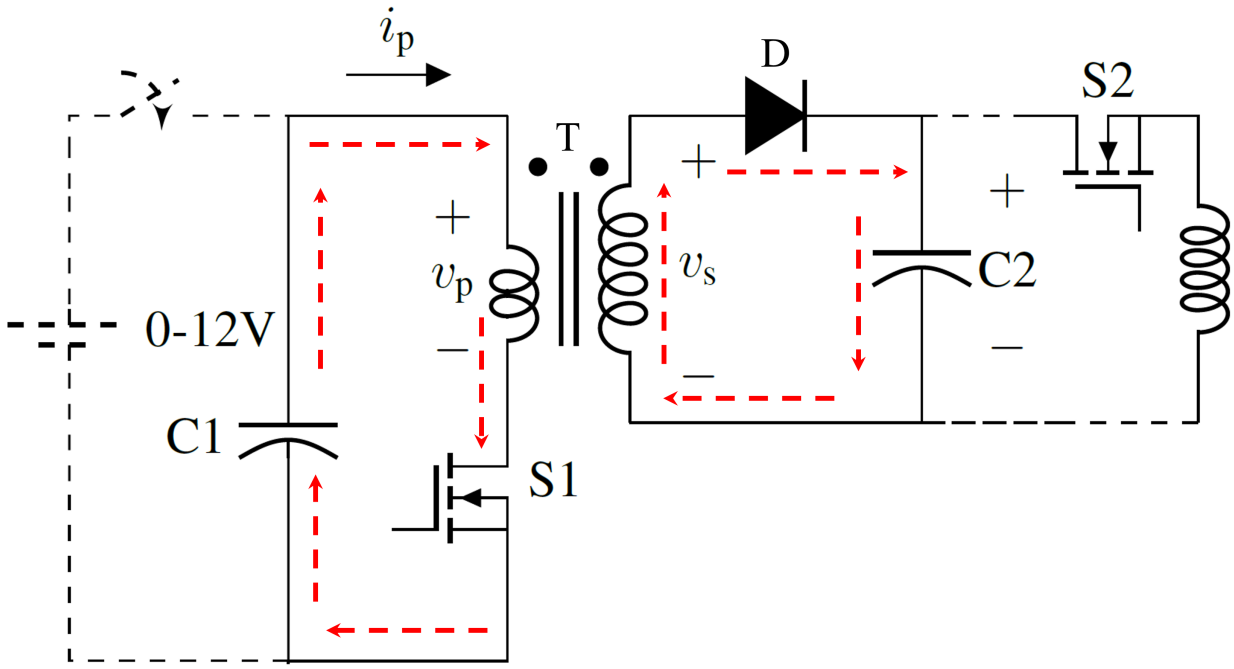

Figure 4.8: Mode-2 (red dashed lines) of the circuit topology of the power stage

et al. [136]. The circuit topology involves the utilization of a precharged supercapacitor, initially charged to a low voltage, such as 2 V.

The operation begins by activating MOSFET S1 at a frequency of 8 kHz. This high-frequency switching pumps energy into a step-up transformer. The transformer's high-voltage secondary winding feeds a rectifier circuit, which charges a high-voltage electrolytic capacitor. A processor subsystem, not depicted in the circuit diagram (Fig. 4.8), manages the operation of MOSFET S1 [79].

In this mode, the high-frequency switching of DC voltage from the supercapacitor bank results in a pulsed DC voltage. Because the transformer operates solely with AC, this alternating DC voltage functions equivalently to AC, allowing for voltage step-up. To achieve the required voltage across the capacitor C2, MOSFET S1 is operated for 2 seconds at an 8 kHz frequency. A ferrite toroidal core is used for the transformer, with a self-wound 1:60 turns ratio to achieve the necessary voltage step-up. The operational path for Mode-2 in the circuit is illustrated in Figure 4.8 with red dashed lines.

The inductance of an inductor can be measured by analyzing its impedance at a specific frequency. Accurate RLC meters are used for this purpose, as they can measure both the real and imaginary components of the impedance, effectively providing the R-L series equivalent network. Measurement of the transformer parameter was important in this stage of research. In the open circuit test of a transformer, where the secondary winding is left open and no current flows through it, the primary winding inductance measured using an LCR meter primarily reflects the magnetizing inductance (L_p). This is because the absence of current in the secondary winding ensures that the primary winding inductance measurement is not influenced by the leakage inductance, which

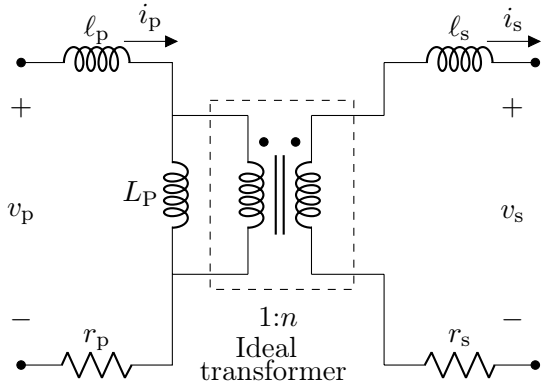

Figure 4.9: Equivalent circuit of the transformer

is typically negligible under these conditions due to the minimal coupling between winding (fewer primary turns).

Conversely, in the short circuit test, the secondary winding is short-circuited, resulting in maximum current flow through the winding. Here, the inductance measured from the primary winding reflects the total primary leakage inductance (ℓ_p) of the transformer. This includes the inductance associated with the magnetic flux that does not directly link both winding due to leakage paths, such as gaps or imperfect coupling between primary and secondary winding.

These tests provide essential insights into transformer characteristics crucial for designing efficient and reliable electrical systems and power electronics applications, ensuring that the transformer operates within specified parameters and minimizes losses [167].

Given that a TMS coil requires an excitation voltage of several hundred volts, we need to upscale the output voltage of the supercapacitor bank by a significant factor, of order sixty-fold. For this purpose, I have tested the suitability of a step-up transformer with a single-turn primary and large turns ratio (1:60 range). The single turn primary allows a high drive current into the transformer primary winding. Referring to Figures 4.1 and 4.9, and symbol definitions in Table 4.3, the initial voltages appearing across the primary and secondary coils are:

$$v_p = V_{oc} - (r_c + r_w + r_p) i_p$$
$$v_s = n\ v_p, \qquad \text{where } n = N_s/N_p$$

If the parasitic resistances r_c (internal resistance of supercapacitor), r_w (wire resistance) and r_p (primary winding resistance) are too large, the primary voltage will be too low to create a high-power output pulse. V_{oc} represents the open-circuit voltage of the supercapacitor bank.

As per the definition of self-inductance [167], the total self-inductance of primary (L_1) and secondary (L_2) windings can be expressed as the sum of magnetizing and leakage components:

$$L_1 = L_p + \ell_p$$

Table 4.3: Symbol definitions and values for the transformer equivalent circuit

Symbol	Description	Measured values primary, secondary
L_p, L_s	Magnetizing inductance for primary, secondary	8.33 μH, 32.5 mH
ℓ_p, ℓ_s	Leakage inductances	0.29 μH, 977 μH
r_p, r_s	Winding resistance	5.8 mΩ, 12 Ω
N_p, N_s	Number of turns	1, 60
v_p, v_s	Transformer voltages	–, –
i_p, i_s	Transformer currents	–, –

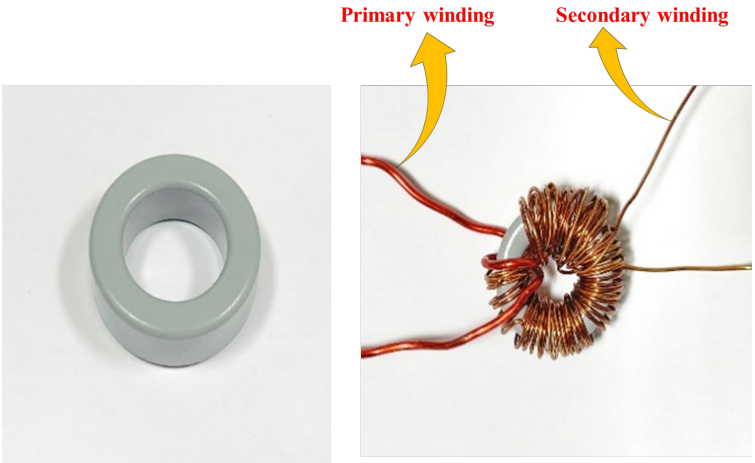

(a) (b)

Figure 4.10: (a) Ferrite core ZW42207TC and (b) wound transformer with 1:60 turns ratio.

$$L_2 = L_\mathrm{s} + \ell_\mathrm{s}$$

By referring all inductive components to the secondary, the total self inductance of the secondary side takes the form:

$$L_2 = n^2(L_\mathrm{p} + \ell_\mathrm{p}) + \ell_\mathrm{s} \tag{4.1}$$

Open-circuit and short-circuit measurements of the transformer core were carried out to estimate the relevant transformer parameters. Inductance for both windings were measured using a Agilent E4980A four-point impedance meter at 10 kHz; see Table 4.3. From Eq (4.1), the secondary winding will have a total self-inductance of $L_2 = 32$ mH, thus the secondary circuit is highly inductive. In this preliminary design, the transformer was wound on a highly-permeable toroidal ferrite core type ZW42207TC (Magnetics) using a turns ratio of 1:60. Figure 4.10 depicts the toroidal core and the wound transformer.

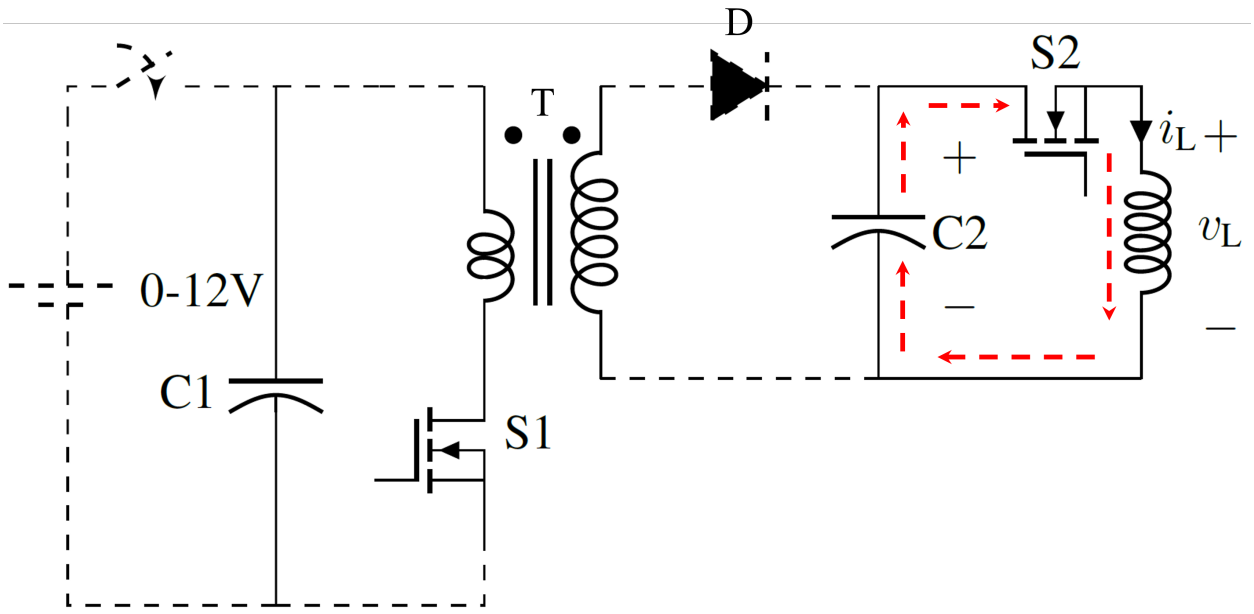

Figure 4.11: Mode-3 of the circuit topology. Gate control signals for S1 and S2 ensure that these switches are never ON at the same time

It should be noted that the transformer used in this design was not fully optimized, with only basic sizing and turns ratio considerations applied based on preliminary requirements. A comprehensive transformer design, including optimization of core material selection, winding configuration, leakage inductance minimization, and loss reduction strategies, was not undertaken. As a result, the energy transfer efficiency across the transformer could be substantially improved through a more detailed design approach.

4.4.3 Mode-3: Excitation of TMS coil

Figure 4.11 shows Mode 3. Upon reaching the required voltage, MOSFET S2 is triggered to initiate the excitation of the TMS coil. At this time, MOSFET S1 is turned off. Triggering S2 can be accomplished using various gate voltage waveforms. By employing different waveform types, we can regulate the coil current and voltage pulse parameters of the TMS coil, thus providing the pulse generator circuit with an additional pulse-shaping feature.

In the final stage of the TMS excitation circuit, a crucial element is introduced to control the output pulse through power MOSFET. The power MOSFET can be treated as a variable resistor, with its gate voltage determining its resistance, thereby altering the discharge rate of the capacitor. Using a MOSFET as a dynamic element rather than a simple switch is innovative in TMS applications.

By manipulating the resistance of the MOSFET, we can effectively change the discharging rate of the capacitor, allowing us to modify the output pulse without the need for additional components. This not only simplifies the circuit but also enhances its versatility, enabling precise control over the pulse characteristics. This means that by adjusting the gate voltage, we can control how quickly or slowly the capacitor discharges, effectively shaping the output pulse which opens up new possibilities

for pulse generation.

The MOSFET as a variable resistor has been successfully modeled, with simulation results matching experimental data as demonstrated in Chapter 6. This validates the effectiveness of the approach and ensures its reliability in practical applications. The model developed for one MOSFET can be expanded to include multiple MOSFET, allowing for greater flexibility in circuit design. This approach involves modeling the MOSFET as a variable resistor, which acts as a dynamic element in the circuit, and can be applied to other types of existing circuit topologies in literature [80, 104, 105, 136].

In summary, by treating the MOSFET as a variable resistor in the TMS excitation circuit, I have unlocked a new level of control and versatility. This innovative approach not only simplifies the circuit but also enhances its performance and adaptability, paving the way for advancements in neuromodulation and related fields.

Conclusion

In conclusion, the development of the pulse generator prototype for TMS demonstrated innovative integration of supercapacitors, step-up transformers, MOSFET, and pulse-shaping techniques to achieve efficient energy conversion and controlled pulse delivery. The selection of supercapacitors as the primary energy source proved effective for the prototype. Extensive research into developing a simple and efficient prototype, distinct from existing circuits and literature, was successful. The circuit successfully operated with effective pulse shaping.

Two main achievements emerged from this research. Firstly, the identification and utilization of a reliable power source were crucial, as the existing circuits utilized a high-voltage source, which can be costly. Secondly, the precise timing control of MOSFET for on-off switching, coupled with the triangular gate voltage providing a high rate of voltage change, potentially influencing the magnetic and electric fields developed by the TMS coil.

The successful validation of the prototype demonstrated its ability to generate sufficient current and magnetic field for TMS applications, affirming the effectiveness of the designed circuit in meeting operational requirements. This work was published and presented at the 49th Annual Conference of the IEEE Industrial Electronics Society (IECON 2023) [79], and is included below.

4.5 Publications

4.5.1 Paper published in proceedings of IECON 2023

The following paper was presented at 49th IECON23 (IEEE Industrial Electronics Society Conference), held from October 16-19, 2023, at Marina Bay Sands Expo and Convention Centre, Singapore, and published in the IEEE proceedings of the conference [79]. An attribution detailing the contributions from the authors is included in the Appendix E.

Supercapacitor based adjustable high power pulse generator for medical research applications

Soniya Raju
School of science
University of Waikato
Hamilton, New Zealand
sr231@students.waikato.ac.nz

Nihal Kularatna
School of Engineering
University of Waikato
Hamilton, New Zealand
nihalkul@waikato.ac.nz

Dr. Marcus Wilson
School of Science
University of Waikato
Hamilton, New Zealand
marcus.wilson@waikato.ac.nz

IECON 2023- 49th Annual Conference of the IEEE Industrial Electronics Society | 979-8-3503-3182-0/23/$31.00 ©2023 IEEE | DOI: 10.1109/IECON51785.2023.10311985

***Abstract*— High power pulse generators with variable parameters are helpful in many applications in the industrial and medical fields. The traditional approach to design these pulse generators is to start with a high voltage DC power supply, energy storage capacitor, and a wave shaping circuit. However, building a high-voltage DC power supply itself is a complex task and it ends up in a complicated circuit with several high-voltage components hence adding to the total cost.**

This paper presents a unique new approach to designing a supercapacitor-based high-voltage pulse generator with a lower number of components and simple two-winding transformer. First experimental circuit developed based on this new approach is presented here with variable pulse generator capable of several hundred volts peak voltage with loop current capability of several hundred amperes.

Keywords—Supercapacitors, High voltage engineering, Pulse generator, Transformer, transcranial magnetic stimulation.

I. INTRODUCTION

High voltage, high power pulse generators are used in many applications such as medical research, fence energizers and lightning surge simulators. There are many different approaches to design and build high power pulse generators. Some start with a high voltage DC power supply followed by wave-shaping circuits. Marx type pulse generators use voltage multiplier techniques [1]. Similar to Marx generator, a Tesla transformer [2] is also used to charge a pulse forming circuit.

Commercial versions of pulse generators come from many sources. Barth Electronics supply systems up to 2 kV, Kentech up to 12kV and Integrated Technologies using spark gap up to 120kV [2]. These versions provide single shot excitations of 10 to 20 pulses, but are not affordable in some applications due to excessive costs. With the evolution of power electronic switches with high voltage capabilities, numerous solid-state based high voltage pulse generators have also been proposed. Examples of power electronics-based pulse generators (PG) vary from mimicking the classical generators, such as the Marx generator to emerging new topologies and converters. Utilizing basic switched-mode power supply (SMPS) circuits like boost, buck-boost and the isolated buck-boost or the flyback in high voltage (HV) pulse generation topologies were being used a lot due to their voltage step-up capabilities. Sungwoo Bae [3] presents a high-voltage bipolar rectangular pulse generator using a solid-state boosting front-end and an H-bridge output stage. This circuit has more than 4 switches and many capacitors with high-voltage resistors. This is also an extended version of the Marx generator. Soo-Hong Kim [4] gives a model consisting of a capacitor charging power supply using a series-connected full-bridge pulse width modulation (PWM) converter for pulsed power applications. In [5] an input buck-boost converter feeds a stack of low voltage (LV) switch–capacitor units at the output stage. But a complicated control algorithm is required, and only unipolar pulses are generated. Xin Zan [6] proposes a medium voltage pulse power generator for the accurate current interruption. The authors have presented a module in a 4.5kV pulse generator using a high voltage switch stack, an insulated-gate bipolar transistor (IGBT) half-bridge module, and a high-voltage diode stack.

A single-stage LC resonant pulse generator can also be configured to boost the output voltage and current from the input voltage source, which can reduce the cost of the input high-voltage switches and high-voltage dc sources. A pre-charged capacitor bank can be used by an LC resonant capacitor bank pulse generator to create a pulse through an inductor. Some papers also describe replacing the pre-charged capacitor bank with the Marx generator. LC circuit with a boost circuit module is also used for high-voltage pulse generation [7].

Based on the literature review on various pulse generators, most have used pre-charged capacitors combined with various DC-DC converters to step up the voltage. Pulse generators should be compact, modular, and easy to step up to higher values. As a general observation from the study, high voltage pulses are generated mostly using low voltage switches connected in series which results in a huge number of switches and the losses associated with them. Also, some have used high-voltage switch modules, resistors, and diodes which comes at a high cost. With the development of solid-state pulse power technology, it plays a crucial role in industrial applications, biotechnology, and medical research. So far, the standard and available high-voltage pulse generators such as lightning surge simulators have very costly and complex circuits. Pulse generators are also used in the electric fencing circuits by companies like Gallagher [8] for the animal management systems. These systems use circuits with a high voltage DC source and shaping circuits.

In Section III of the paper, we develop a completely new design approach to a high-voltage pulse generator in a cost-effective manner and simple design approach based on a supercapacitor module as the starting energy source. With our wider power electronics research team at University of Waikato focus on supercapacitor assisted (SCA) techniques [9] and applications the background knowledge on supercapacitors motivated us to develop this new approach.

Authorized licensed use limited to: Univ of Waikato. Downloaded on January 09,2024 at 01:42:54 UTC from IEEE Xplore. Restrictions apply.

II. PULSE GENERATOR FOR MEDICAL RESEARCH APPLICATIONS

Our research project is aimed at developing a pulse generator for transcranial magnetic stimulation (TMS).

A. Specific requirements of the pulse generator for medical applications

High voltage supply or pulse generator is often used for medical applications such as Cell Electroporation Therapy (EPT), genetic therapy, ultrasonic cleaning, chemical-free bacterial decontamination, medical imaging and transcranial magnetic stimulation (TMS) [10]. All these systems' effectiveness may depend on i) pulse voltage ii) duration iii) pulse shape and iv) adjustability of shape. The references used so far mostly have used design approaches based on an electrolytic capacitor with high voltage rating and high voltage metal oxide silicon field effect transistors (MOSFET) [11].

As we are specifically focused on transcranial magnetic stimulation (TMS) application, so far mainly the conventional way of pulse generation is based on an LC oscillator circuit and an inverter topology [12]. TMS requires electronic circuitry which is a technical challenge for the design of a practical flexible pulse. The produced pulse should have high voltage and high current with the required magnetic field that can energize the small animal brain in TMS coil application. Here we have considered small animals because at a preliminary stage, we aim at producing several hundred volts at a high current only. Our aim was for a 10 – 20 J per pulse for small animal brain excitation for a short duration (a few hundred microseconds) and this can easily be discharged from a capacitor for each pulse. Section III of the paper provides the background of supercapacitors and a supercapacitor-based approach. Then Section IV provides a background to innovative approach used in this design. Section V summarizes the characteristics of the first prototype and its testing. Finally Section VI gives an insight to the potential application of TMS and then follows with the conclusion and future development plans for this design.

III. SUPERCAPACITOR & SUPERCAPACITOR-BASED APPROACH

Supercapacitors (SC) are a new form of energy storage devices with a very high power density and a long life cycle compared to rechargeable battery chemistries. Today there are supercapacitors with single cell capacitance values from 0.2 F to over 70,000F [13]. Their only weakness compared to electrolytic or film capacitors is the low DC voltage rating in the range of 2.5 to 4.2 V in general. When a high voltage capability supercapacitor bank is required, several cells are connected in series, similar to building battery banks with single cells.

Fig. 1 shows the equivalent of a rechargeable battery and a supercapacitor feeding a variable resistive load R_L. A rechargeable battery is basically a voltage source with internal resistance, which can be quantified by a DC source and lumped resistance r_{int}. Similarly a SC is also shown by its charged capacitance and the equivalent series resistance (ESR) as in Fig 1(b). For the cases here, load voltage V_{R_L} is given by,

$$V_{R_L} = \frac{V}{1+\frac{r_{int}}{R_L}} \tag{1}$$

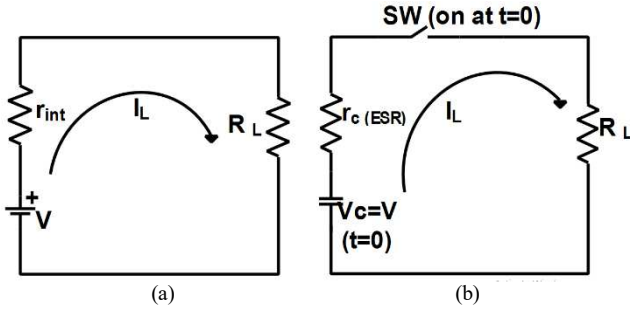

Fig. 1. Equivalent model of (a) rechargeable battery (b) supercapacitor

From equation (1) it is clear that the load voltage keeps on reducing as the internal resistance increases. So, a good energy source should have very low internal resistance with a high open circuit voltage. Power delivered to load can be written as

$$P=\frac{V^2}{R_L}\left[\frac{1}{\left(1+\frac{r_{int}}{R_L}\right)^2}\right] \tag{2}$$

For the maximum power condition $\frac{dP}{dR_T}=0$,

$$P_{max}=\frac{V^2}{4r_{int}} \tag{3}$$

when the internal resistance is equal to the load resistance.

Given this discussion, maximum power is restricted by the internal resistance. In many rechargeable batteries, the internal resistance increases with the discharge in general. Even though we get a near-constant open circuit voltage due to the electrochemistry in the cell, the available power keeps reducing due to the increase in internal resistance (Fig. 2).

As Fig.2 depicts, a battery's internal resistance keeps increasing with the discharge. However, in a similar size supercapacitor (SC) the ESR is much lower and it does not increase with the discharge. For this practical reason, if we select a suitable SC or a bank of SCs based on the previous maximum power delivery discussion, it can pump out a significantly high power. Moreover, a SC has the energy storage capability given by Equation (4) and this translates to a significant amount of Joule energy capability even for a very small SC. Given that a SC can be simplified as a Model in Fig.1(b), and the capacitor is initially charged to V_c, the total energy stored in the capacitor is given by.

$$E=\frac{1}{2}CV_c^2 \tag{4}$$

When the switch is activated at t=0, the instantaneous current through the load is

$$I_{R_L\ t=0}=\frac{V_c}{R_L+r_c} \tag{5}$$

This equation shows how important is the ESR in supercapacitors. Compared to other capacitors and energy storage device (ESD), supercapacitors have ESR in the range of milliohms. In a general R-C loop, including the ESR, time constant becomes

$$\tau=(R_L+r_c)C \tag{6}$$

Within 2 time constants, nearly all energy can be discharged [13]. As per information in Table 1, physically small and lower-cost SCs have significantly high energy storage capability, high current capability and high maximum power delivery based on Equation (3). Fig. 3 physically compares

Authorized licensed use limited to: Univ of Waikato. Downloaded on January 09,2024 at 01:42:54 UTC from IEEE Xplore. Restrictions apply.

electrolytic capacitors and small SCs. If the internal series resistance of the device is too large, while extracting energy from the energy source, a significant share of it is wasted within the source in the form of heat. This can adversely affect the lifetime of the devices too.

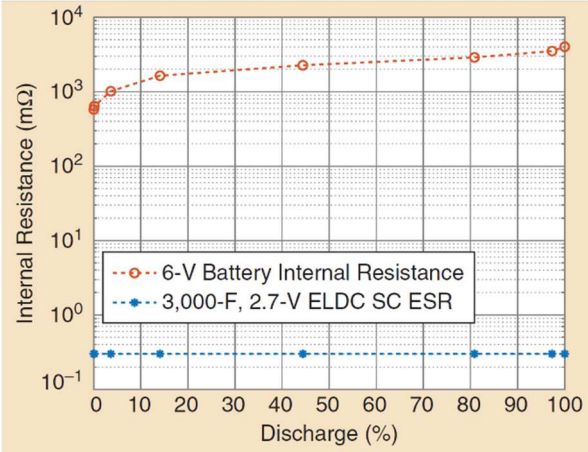

Fig. 2. Comparison of internal resistance variation with the percentage discharge—6V energizer battery and a 3000F 2.7V EDLC from VINATech.[13]

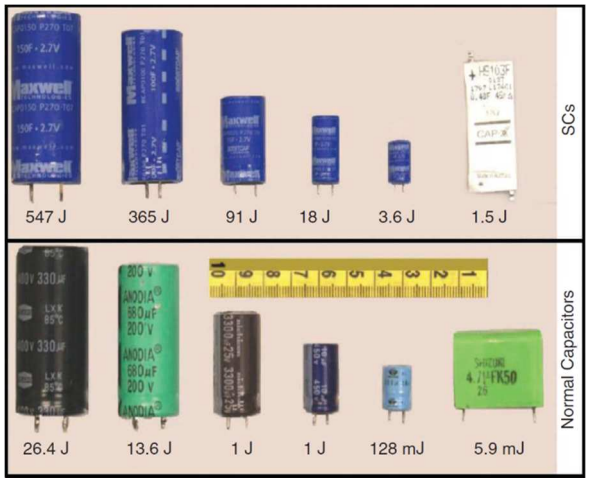

Fig. 3. Comparison of symmetrical double-layer capacitors (low-cost devices) with electrolytic capacitors of the similar canister sizes [13]

As per [14], supercapacitors are gradually trying to reach the energy density of lead -acid batteries while providing much higher life cycle capability than all rechargeable batteries. However, the only limitation is its DC voltage rating is not more than 3V per cell. Referring to Table 1, we can appreciate that a single SC in the range of few Farads to 500 Farads can store adequate energy to generate several pulses of the range of 10 to 20 J per pulse, based on a single full charge.

IV. SUPERCAPACITOR TRANSFORMER COMBINATION FOR HIGH VOLTAGE PULSE GENERATOR.

Fig. 5 indicates the block design approach for the Pulse generator prototype. Block A is a low voltage DC power supply to charge the SC bank B. In Block B, right now we have used 4 series connected supercapacitors of the size 380F/3 V which creates a total capacitance of 95 F. Total ESR of the capacitor bank is 12.8 mΩ which can provide a maximum short circuit current of 937 A as in Fig. 4. This potentially high short circuit DC current capability indicates that it can drive a very high current into the primary of the step-up transformer (Block C), subject to additional loop resistances created by the connectors and the other parasitic resistance.

TABLE I. SUMMARY OF VARIOUS HY-CAP NEO 3V SUPERCAPACITORS (VINATECH) AND ITS MAXIMUM POWER CAPACITY (SOURCE VINATECH DATASHEET [15])

Part Number	Capacitance (F)	ESR (mΩ)	Max. Current* (A)	Short circuit Current * (A)	Max Power (W)	Max Energy (J)
WEC3R0106QG	10	45	10	66.67	50	45
WEC3R0156QG	15	55	12	54.55	41	67.5
WEC3R0256QG	25	30	21	100	75	112.5
WEC3R0606QG	60	20	40	150	113	270
VEC3R0107QG	100	8	78	375	281	450
VEC3R0407QG	380	3.2	250	937.5	703	1800
VEC3R0507QG	500	3.2	288	937.5	703	2250

*Max. current-continuous Rated current given by the datasheet

*Short Circuit current -Instantaneous short-circuit current $\left(\frac{V_c}{ESR}\right)$

To achieve high secondary current capability, governed by the turns ratio, we have used just one turn in the primary. This single turn primary coil allows very high primary loop current which will be within the short circuit current of the SC bank. If we build the secondary winding with a very large number of turns (several thousands), we can get very high voltage at the secondary. However, from the detailed equivalent circuit of the transformer in Fig. 6, ohmic resistance of the secondary will limit the maximum current deliverable to the load. Following mathematical relationships provide the basis of the design calculations.

Maximum current possible from the supercapacitor (SC)

$$I = \frac{V_C}{r_c + r_l + R_P} \tag{7}$$

Where r_c -ESR of supercapacitors, r_l – loop resistance, Rp-primary winding resistance

If $r_l=0$,

$$I = \frac{V_C}{r_c + R_P} \tag{8}$$

Since we have designed a single turn and large diameter primary winding, R_P can be neglected.

By Kirchoff law,

$$V_C = Ir_c + L\frac{dI}{dt}, \text{ if } r_l=0 \quad \text{where } L=Ls+\frac{M}{N} \tag{9}$$

$$\text{Secondary Load voltage, } V_L = N*V_P \tag{10}$$

$$\text{So, approx. maximum current, } I_L = \frac{N*V_P}{R_L+R_S} \tag{11}$$

Since the designed transformer has higher secondary turns, secondary winding resistance will be dominant, and it will reduce the current into the load.

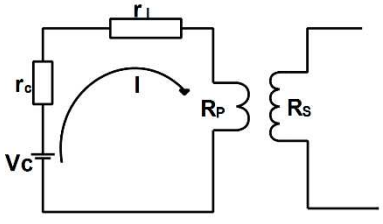

Fig. 4 Primary side of the transformer with SC source

Authorized licensed use limited to: Univ of Waikato. Downloaded on January 09,2024 at 01:42:54 UTC from IEEE Xplore. Restrictions apply.

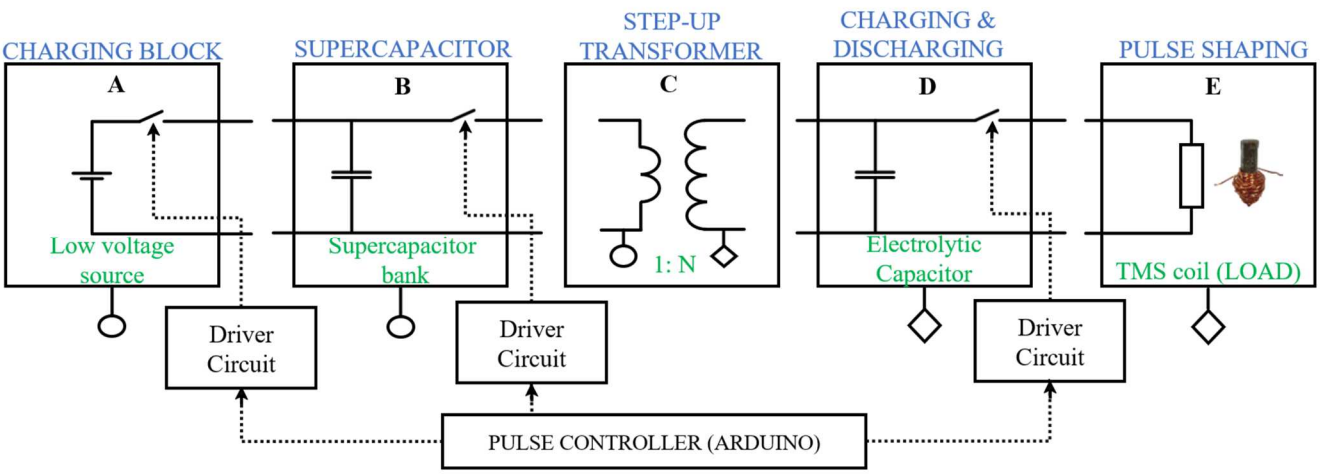

Fig. 5. Design flow/block approach for the prototype

To overcome this issue, we opted to charge an electrolytic capacitor from this stepped-up voltage. In Figure 6(b), the maximum power delivered to the secondary will depend on the total resistance of the secondary (given a single turn case, primary resistance can be neglected). Magnetizing inductance contributes to the open circuit's maximum voltage.

Open-circuit and short-circuit measurements of the transformer core were carried out to estimate the relevant transformer parameters referring to Fig 6. All inductance measurements of both windings were carried using an LCR meter (Fluke PM6304) over a range of frequencies from 1 to 10 kHz. Measurements carried out at 10 kHz, resulted in approximate values of Lm = 8.6µH; Lp =0.29µH; Ls=977µH and Lm'=33.5mH.

Theoretically we should be able to drive the TMS coil in block E directly from the secondary based on the series switch. Given that secondary referred magnetizing inductance and the ohmic resistance of the secondary coil starts dominating as in Figure 6, the high current capability will not be achieved. For that reason, we have inserted a high voltage electrolytic capacitor-based charging circuit block in series with an electronic switch controlled by the processor board. As indicated in Table I, with the ESR of a SC decreasing with capacitance value, if a higher current is required we could simply use a high value SC to improve the circuit.

A. Selection of the magnetic core.

The transformer was wound over a ZW42207TC core, which is a high-permeability ferrite material from MAGNETICS. Table II presents a summary of the magnetic parameters of the selected core material. With reference to Figure 7, the pulsating DC across the primary is magnified by the turns ratio. Then this voltage is rectified by a diode and electrolytic capacitor of high voltage to energize the TMS coil which is turned on by the second switch in block D.TMS coil is made by winding 50 turns of 0.4 mm copper wire on 19 mm long Carbonyl Powder iron core. This is the coil used to excite the nerve cells of small animals.

Future improvements will include pulse shaping circuits which is an important aspect of a perfect pulse generator. Fig.7 indicated the overall circuit with an Arduino microprocessor board used as a controller to drive MOSFETs (one in block A, B, and block D in Fig. 5).

B. Working pulse generator prototype building

A string of 4 series connected supercapacitors acting as the DC source is connected to the step-up transformer through a switch that operates at high frequency (>10kHz). The stepped-up transformer's output voltage is rectified using IN4007 and stored in the electrolytic capacitor. Once fully charged, the capacitor is discharged to the TMS coil (load) through a MOSFET. The pulse for each switch is programmed in a microprocessor in such a way that it complements each other.

Driver circuit using Opto isolator 4N25 is used in the primary side of the transformer. Isolation from the high voltage is an added advantage of using optocoupler in driver circuit for reliability of the design.

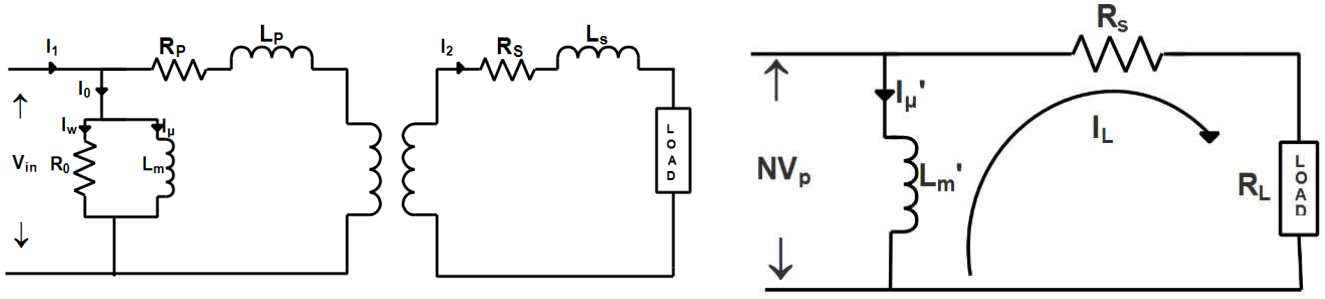

(a) (b)

Fig. 6. (a) Detailed equivalent circuit of a transformer (b) simplified model of the transformer referred to secondary side

Authorized licensed use limited to: Univ of Waikato. Downloaded on January 09,2024 at 01:42:54 UTC from IEEE Xplore. Restrictions apply.

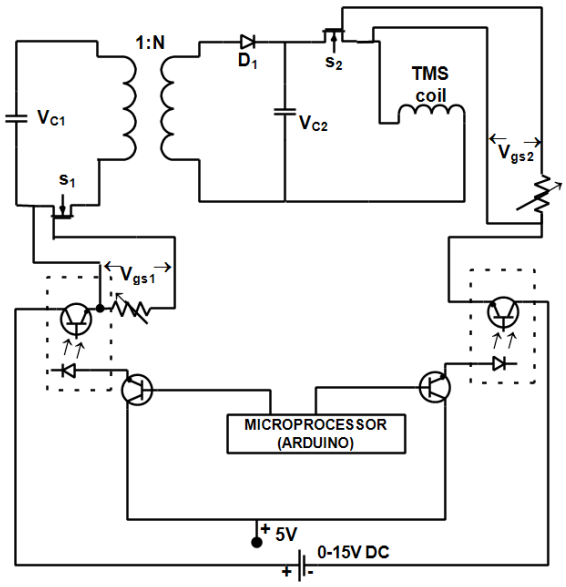

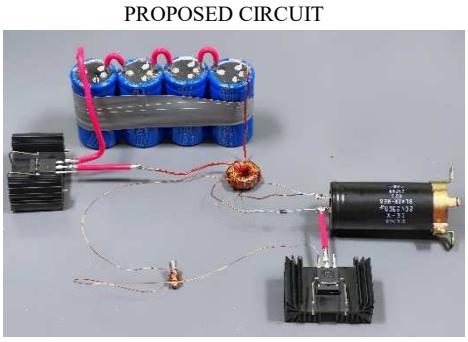

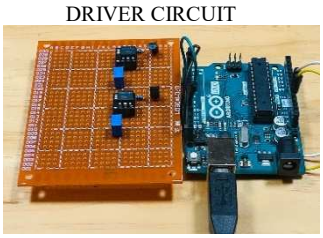

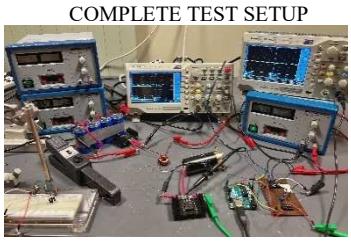

Fig. 7. Proposed prototype & experimental setup. (a) Circuit Diagram (b) Experimental set up

TABLE II. MAGNETIC PROPERTIES OF **W** FERRITE MATERIALS MANUFACTURED BY MAGNETICS, USA [16]

MATERIAL	***W***
Initial permeability(μ)	10,000
Max. Usable frequency (MHz)	≤ 0.5
Relative loss factor	≤ 7 (10kHz)
Curie Temperature (°C)	> 135
Flux density (mT)	390

V. PULSE GENERATOR PROTOTYPE TESTING

In this section we analyse our experimental results. Since hardware operates at higher voltage, we tested with lower voltage as a preliminary effort to ensure that the circuit is working as per designed. The capacitor voltage of 30V and Coil current of 40A from an input of 3 V from test setup is shown in Figure 8. The capacitor voltage was measured throughout the charging time and quick discharge through the TMS coil when switch 2 is turned on. The coil current is measured using Tektronix A622 AC/DC current probe during the discharge time of 1.5 ms. It was observed that we could charge the capacitor in the charging block to 400 V from 10V SC supply using the test setup. Even with low voltage stored in a capacitor (50 V), we could energize the mouse coil with a 250 mT magnetic field.

VI. APPLICATION

Over the last few decades, there are many research and improvements on the Human TMS that have been carried out. Whereas in small animals, TMS coils are less explored. This is a challenging area to work with because of the small size coil and to develop electric and magnetic field intensity required to stimulate the neurons. TMS, Transcranial Magnetic Stimulation, works on the principle of Faraday's law of electromagnetic induction. A time-varying current-carrying coil placed on the surface of the brain produces a magnetic field. This magnetic field which permeates a conductive medium (e.g., brain tissue), can induce an electric current in the tissue. The brain is a potential electrical conductor, in which we have neurons that are inherently excitable and can produce action potential when stimulated. So, this induced magnetic field may produce an eddy current in the brain sufficient to stimulate the axon hillock of each neuron [17][18][19]. Many aspects come into the picture as we design a circuit since there are a lot of constraints. These include that there should be a balance between high current and low heating, the inductance of the coil should be low, and whether a long or short-duration pulse is to be used.

Since it's a very useful and less explored area in the field of medical science, this prototype is designed to excite the

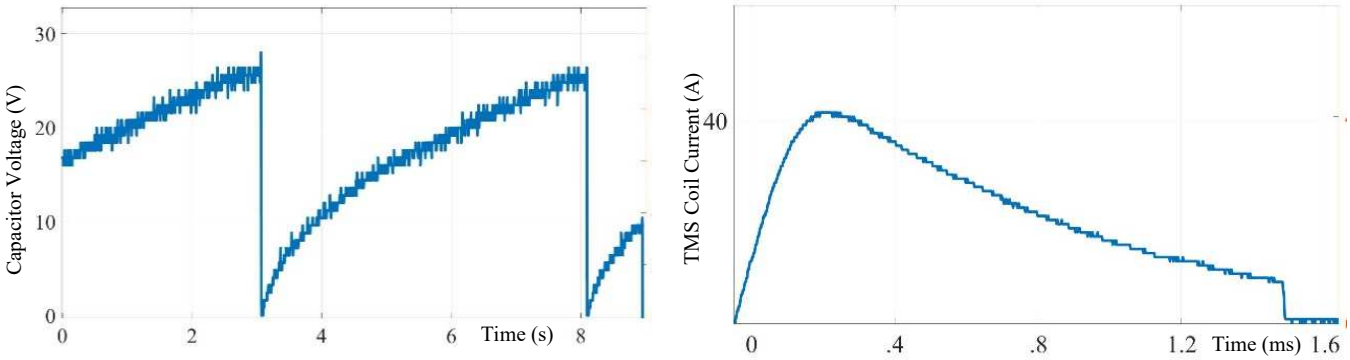

Fig. 8. Oscilloscope waveforms of charging/ discharging capacitor voltage and TMS coil current during the discharge

Authorized licensed use limited to: Univ of Waikato. Downloaded on January 09,2024 at 01:42:54 UTC from IEEE Xplore. Restrictions apply.

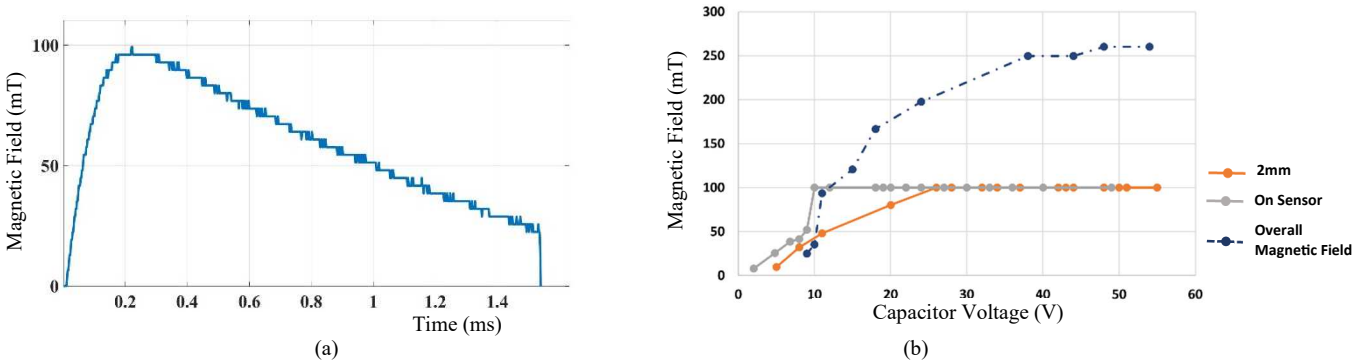

(a) (b)

Fig.9. (a) The magnetic field of the TMS coil measured 2mm above the coil during a single pulse (b) Overall magnetic field along with measurements taken on the sensor and 2mm above the coil

small animal brain. Figure 9 (a) shows the test result of the 30V charged capacitor and its corresponding magnetic field measured during the discharge period using the SS496A1 solid state hall effect sensor by Honeywell. Since the sensor is of low sensitivity, the field gets saturated at low voltage. So, we scale up various readings by placing the coil i) on the sensor ii) 2mm above iii) 3mm above iv) 4mm above, etc. The graph shown in Figure 9(b) gives a conclusion that 250mT is obtained at 2mm below the coil using the above method.

VII. CONCLUSION AND FUTURE WORK

This research proved that SC based Pulse generator (PG) can be designed without extra high-voltage transistors and diodes. The very basic version developed proved that it can energize a TMS coil adequately. Further improvements will allow a much higher performance variable PG based on the same basic prototype. Further work is in progress.

As this is the preliminary stage of the research, there are many limitations that are to be removed and updated in the next stage. The main changes include discharging the fully charged capacitor (400V) through an appropriate MOSFET that can withstand high currents. Next is to change the input SC to two parallel strings of series supercapacitors and to observe whether the increase in input current can increase the charging rates, or whether replacing it with higher capacitance can cause any effects. This circuit can also be designed to have higher voltage and current by changing the turns ratio and stepping up to a higher voltage. The pulse shaping block is the major area needed to be implemented in the next stage.

REFERENCES

[1] Z. Zhong, J. Rao, H. Liu, and L. M. Redondo, "Review on Solid-State-Based Marx Generators," in IEEE Transactions on Plasma Science, vol. 49, no. 11, pp. 3625-3643, Nov. 2021, doi: 10.1109/TPS.2021.3121683.

[2] J. Mankowski and M. Kristiansen, "A review of short pulse generator technology," in IEEE Transactions on Plasma Science, vol. 28, no. 1, pp. 102-108, Feb. 2000, doi: 10.1109/27.842875.

[3] S. Ba e, A. Kwasinski, M. M. Flynn and R. E. Hebner, "High-Power Pulse Generator With Flexible Output Pattern," in IEEE Transactions on Power Electronics, vol. 25, no. 7, pp. 1675-1684, July 2010, doi: 10.1109/TPEL.2010.2041012.

[4] S. -H. Kim, M. Ehsani and C. -S. Kim, "High-voltage power supply using series-connected full-bridge PWM converter for pulsed power applications," in IEEE Transactions on Dielectrics and Electrical Insulation, vol. 22, no. 4, pp. 1937-1944, August 2015, doi: 10.1109/TDEI.2015.004978.

[5] S. Zabihi, F. Zare, G. Ledwich and A. Ghosh, "A novel high voltage pulsed power supply based on low voltage switch capacitor units," 2009 IET European Pulsed Power Conference, Geneva, 2009, pp. 1-4, doi: 10.1049/cp.2009.1655.

[6] X. Zan et al., Daniel Román Torres, Reza Kheirollahi, Xiaonan Lu, "Medium Voltage Pulse Power Generator for Accurate Current Interruption," in IEEE Transactions on Industrial Electronics, vol. 70, no. 4, pp. 3604-3615, April 2023, doi: 10.1109/TIE.2022.3174234.

[7] A. Elserougi, S. Ahmed and A. Massoud, "A boost converter-based ringing circuit with high-voltage gain for unipolar pulse generation," in IEEE Transactions on Dielectrics and Electrical Insulation, vol. 23, no. 4, pp. 2088-2094, August 2016, doi: 10.1109/TDEI.2016.7556482.

[8] https://am.gallagher.com/en-US/Solutions/Case-Study Listings/Electric-Fencing-Basics

[9] S. T. S. Udayanga, S. Kokuhennadige, J. Fernando, N. Kularatna and D. A. Steyn-Ross, "Supercapacitor assisted surge absorber (SCASA) technique: selection of magnetic components based on permeance," 2021 IEEE Applied Power ElectronicsConference and Exposition (APEC), Phoenix, AZ, USA,2021,doi:10.1109/APEC42165.2021.9487254.

[10] S. J. Beebe, P. M. Fox, L. J. Rec, E. L. K. Willis, and K. H. Schoenbach, "Nanosecond, high-intensity pulsed electric fields induce apoptosis in human cells," The FASEB Journal, vol. 17, no. 11, 2003.

[11] Kasri, Nur Faizal & M. Piah, M. Afendi & Adzis, Zuraimy. (2020). Compact High-Voltage Pulse Generator for Pulsed Electric Field Applications: Lab-Scale Development. Journal of Electrical and Computer Engineering. 2020. 1-12.

[12] A. V. Peterchev, "Circuit topology comparison and design analysis for controllable pulse parameter transcranial magnetic stimulators," 2011 5th International IEEE/EMBS Conference on Neural Engineering, Cancun, Mexico, 2011, pp. 646-649, doi: 10.1109/NER.2011.5910631.

[13] N. Kularatna and D. Jayananda, "Supercapacitor-Based Long Time-Constant Circuits: A Unique Design Opportunity for New Power Electronic Circuit Topologies," in IEEE Industrial Electronics Magazine, vol. 14, no. 2, pp. 40-56, June 2020, doi: 10.1109/MIE.2019.2959199.

[14] Nihal Kularatna, Kosala Gunawardane, Energy Storage Devices for Renewable Energy-Based Systems (Second Edition), Academic Press, 2021

[15] https://www.vinatech.com/eng/product/supercapacitor-3v0.php

[16] Magnetics "Ferrite core documents," Mag-inc.com, 2017. Accessed: Dec. 10, 2022. [Online]. Available: https://www.mag-inc.com/Design/ TechnicalDocuments/Ferrite-Core-Documents

[17] Koponen L.M., Peterchev A.V. (2020) Transcranial Magnetic Stimulation: Principles and Applications. In: He B. (eds) Neural Engineering. Springer, Cham. pp 245-270 https://doi.org/10.1007/978-3-030-43395-6_7

[18] F. A. Khokhar, L. J. Voss, D. A. Steyn-Ross and M. T. Wilson, "Design and Demonstration In Vitro of a Mouse-Specific Transcranial Magnetic Stimulation Coil," in IEEE Transactions on Magnetics, vol. 57, no. 7, pp. 1-11, July 2021, Art no. 5800511, doi: 10.1109/TMAG.2021.3077976.

[19] M. T. Wilson, A. D. Tang, K. Iyer, H. McKee, J. Waas, and J. Rodger, "The challenges of producing effective small coils for transcranial magnetic stimulation of mice," Biomed. Phys. Eng. Exp., vol. 4, no. 3, Apr. 2018, Art. no. 037002, doi: 10.1088/2057-1976/aab525.

Authorized licensed use limited to: Univ of Waikato. Downloaded on January 09,2024 at 01:42:54 UTC from IEEE Xplore. Restrictions apply.

4.5.2 Journal of Biomedical Physics & Engineering Express

The paper titled "Supercapacitor-Based Pulse Generator with Waveform Adjustment Capability for Transcranial Magnetic Stimulation (TMS)" has been published in the journal Biomedical Physics & Engineering Express. An attribution detailing the contributions from the authors is included in the Appendix E.

Biomedical Physics &
Engineering Express

Endorsed by IPEM Institute of Physics and Engineering in Medicine
PURPOSE-LED PUBLISHING™

PAPER • **OPEN ACCESS**

Supercapacitor-based pulse generator with waveform adjustment capability for small animal transcranial magnetic stimulation

To cite this article: Soniya Raju *et al* 2025 *Biomed. Phys. Eng. Express* **11** 015045

View the article online for updates and enhancements.

You may also like

- Blindly separated spontaneous network-level oscillations predict corticospinal excitability
Maria Ermolova, Johanna Metsomaa, Paolo Belardinelli et al.
- High inductance magnetic-core coils have enhanced efficiency in inducing suprathreshold motor response in rats
Hieu Nguyen, Sergey N Makaroff, Charlotte Qiong Li et al.
- Modular pulse synthesizer for transcranial magnetic stimulation with fully adjustable pulse shape and sequence
Z Li, J Zhang, A V Peterchev et al.

This content was downloaded from IP address 203.211.73.235 on 24/04/2025 at 07:31

Biomedical Physics & Engineering Express

PAPER

Supercapacitor-based pulse generator with waveform adjustment capability for small animal transcranial magnetic stimulation

Soniya Raju[1], Nihal Kularatna[2], Marcus Wilson[1] and D Alistair Steyn-Ross[2]

[1] Te Aka Mātuatua School of Science, University of Waikato, New Zealand
[2] Te Kura Mata-Ao School of Engineering, University of Waikato, New Zealand

E-mail: sr231@students.waikato.ac.nz and marcus.wilson@waikato.ac.nz

Keywords: transcranial magnetic stimulation, Pulse circuits, supercapacitor, pulse shaping

OPEN ACCESS

RECEIVED
12 September 2024

REVISED
9 December 2024

ACCEPTED FOR PUBLICATION
16 December 2024

PUBLISHED
26 December 2024

Original content from this work may be used under the terms of the Creative Commons Attribution 4.0 licence.

Any further distribution of this work must maintain attribution to the author(s) and the title of the work, journal citation and DOI.

Abstract

In transcranial magnetic stimulation (TMS), pulsed magnetic fields are applied to the brain, typically requiring high-power stimulators with high voltages and low series impedance. TMS pulse generators for small animal coils, are underexplored, with limited dedicated circuits and simulation models. Here, we present a new design for a high-power TMS pulse generator for small animals, utilizing a pre-charged supercapacitor that is sufficient to produce repeated pulses for TMS applications without the need for recharging. This approach eliminates the need for expensive high-voltage components and a high-voltage power supply. In this paper, we detail the design approach and basic block diagrams of a supercapacitor (SC) based TMS pulse generator, along with its experimental results. The findings indicate that the new circuit enables a complete test using just a single charge of an SC module. The proposed circuit functions as a versatile pulse-shaping device, where the MOSFET is treated as a dynamically varying resistor element rather than a traditional switch; allowing pulse parameter variations. We analyze a novel circuit for generating and controlling TMS pulses in small animal coils, and demonstrate its effectiveness through experimental results.

1. Introduction

Transcranial magnetic stimulation (TMS) is a non-invasive technique that uses electromagnetic induction to electrically stimulate neural tissue, including the cerebral cortex and peripheral nerves. Developed in the mid-1980s by Barker and colleagues (Barker *et al* 1985, 1991), TMS has become an essential tool in both experimental neuroscience and clinical practice (Wassermann and Zimmerman, 2012; Valchev et al 2018; Peterchev *et al* 2015). By modulating neuronal activity, TMS provides valuable insights into brain function and offers therapeutic benefits for various neurological and psychiatric disorders, including major depressive disorder, Parkinson's disease, stroke, and anxiety disorders (Iglesias 2020; Somaa 2022; George *et al* 2010; Menzies *et al* 2008; Osuch *et al* 2009; Camera *et al* 2024; Smith and Stinea 2016). TMS works by placing a stimulation coil over the head to generate rapidly changing magnetic fields. These pulses penetrate the scalp and skull, inducing secondary ionic currents in the brain tissue. Unlike direct electrical stimulation, which requires electrodes on the scalp, TMS induces currents non-invasively, offering high spatial and temporal precision (Gomez-Tames *et al* 2020).

High-voltage and high-power pulse generators are used in many applications such as transcranial magnetic stimulation (TMS), lightning surge simulators and fence energizers (Peterchev *et al* 2007). Typically these pulse generators are designed by combining a high-voltage DC source with pulse-shaping circuits and high-voltage semiconductor switches (Mankowski and Kristianse 2000; Elserougi *et al* 2016; Zan *et al* 2023). Given the requirement for safety-related isolation within the circuits and the high cost of high-voltage components, the development of a high-power pulse generator poses significant challenges. Most human TMS pulse generators (Goetz *et al* 2012; Peterchev *et al* 2007; Koponen and Peterche 2020) are based on inverter topologies to generate a high-voltage pulse. Due to the constrained affordability of commercial pulse generators, research groups are motivated to develop their own high-power pulse generators (Selvaraj *et al* 2018; Peterchev and Murph 2013; Sorkhabi *et al* 2021; Ali *et al* 2023).

There are various approaches to designing and building high-power pulse generators in other applications as well (Yan *et al* 2020; Cheng *et al* 2021; Li *et al* 2015; Jiang *et al* 2022; Elgenedy *et al* 2017). Some start with a high voltage DC power supply followed by

© 2024 The Author(s). Published by IOP Publishing Ltd

wave-shaping circuits (Peterchev and Murph 2013). Marx type pulse generators use voltage multiplier techniques (Cheng *et al* 2022). Similar to the Marx generator, a Tesla transformer is also used to charge a pulse forming circuit (Zhao *et al* 2019). Despite innovations like solid-state Marx generators and Tesla transformers aimed at enhancing efficiency, these systems remain complex, expensive, and require multiple stages and components.

Moreover human TMS topologies are unsuitable for small-animal stimulation coils for several reasons. Firstly, constructing a medium to high voltage circuit for such a small coil is challenging. Additionally, it is crucial to address heating and losses associated with the small animal coil and ensure adequate protection. The literature provides mouse-specific TMS circuits designed to address these challenges (Wilson *et al* 2018; Tang *et al* 2017; Selvaraj *et al* 2018; Nieminen *et al* 2022; Khokhar *et al* 2021; Tang *et al* 2016). These circuits are tailored to accommodate the smaller size of the coil, provide appropriate voltage levels for stimulation, and mitigate heating and losses associated with the smaller coil size. Additionally, TMS pulse generators, especially those for small animals, are under-explored, with limited dedicated circuits and simulation models. A supercapacitor-based pulse generator (Raju *et al* 2023) offers a promising solution, leveraging higher energy density, rapid charging and discharging capabilities, and longer lifetimes. The supercapacitor approach could provide efficient, cost-effective, TMS pulse generation for small animals.

Most small animal brain stimulation research (Selvaraj *et al* 2018; Khokhar *et al* 2021; Nieminen *et al* 2022) has relied on common circuits rather than specifically designed ones. These circuits typically use capacitor discharging and free-wheeling through diodes or inverter topologies. A significant drawback is the lack of a specific input source, necessitating either a high-voltage supply or a high-voltage capacitor, depending on the application, or a basic DC lab supply for smaller circuits. The primary differences among these circuits are found in the driving circuitry or control mechanisms, and they often lack provisions for pulse shaping.

Here, we describe the development of a pulse generator prototype for small animal TMS coils (Wilson *et al* 2018; Khokhar *et al* 2021; Tang *et al* 2015, 2018). A new supercapacitor-based pulse generator approach for TMS (Raju *et al* 2023) draws from research on supercapacitor use in power converters and protection systems (Kularatna and Jayanand 2020; Udayanga *et al* 2021). This design leverages the energy storage capabilities of supercapacitors to deliver consistent and reliable pulses for TMS without the need for traditional high-voltage components.

This article details our research on developing an electronic circuit for TMS pulse shaping. There are currently very few dedicated circuits (Tang *et al* 2016; Khokhar *et al* 2021) designed specifically for mouse coils, and the ones that exist offer limited pulse-shaping capabilities. Addressing this gap in the literature, we have developed a novel prototype circuit with wave-shaping functionality and a self-sufficient power source capable of producing continuous TMS pulses. Traditional TMS circuits typically employ MOSFETs as simple switches (Peterchev *et al* 2007; Goetz *et al* 2012; Sorkhabi *et al* 2021). However, MOSFETs can also be utilized to achieve finer control over coil current and voltage. This study introduces an innovative pulse-shaping method that involves dynamically varying the gate voltages of MOSFETs, enabling them to act as dynamic elements rather than only switches. This approach significantly enhances TMS pulse-shaping capabilities without requiring substantial additional hardware.

2. Adequacy of a low-cost SC module as the primary energy source for a TMS pulse generation

2.1. General properties of commercial SC compared to electrolytic capacitors

Within the past decade, supercapacitors (SCs) have rapidly developed as a long-life energy storage solution. Technically, an SC can be considered to have a capacitance that is one million times larger than that of a typical electrolytic or film capacitor of the same canister size.

Compared to a rechargeable battery, an SC is capable of delivering very high power due to its extremely low equivalent series resistance (ESR). When a capacitor is connected to a load the maximum power delivery is governed by the internal resistance of the capacitor. The power transfer theorem (Kularatna and Gunawardan 2021) predicts that the maximum power deliverable by the capacitor is

$$P_{\max} = \frac{V_{oc}^2}{4r_c} \tag{1}$$

However, the primary limitation of an SC is its low DC rating compared to an electrolytic capacitor. Table 1 compares the key specifications of these two device families from a designer's perspective.

2.2. Power and energy delivery capabilities of supercapacitors and normal capacitors

Supercapacitors are designated as high power-density devices owing to their remarkably low ESR, typically 1 to 2 orders of magnitude smaller than that of electrolytic capacitors. Table 1 compares power delivery capability and maximum energy content for a representative set of paired supercapacitors and electrolytic capacitors having similar canister volumes.

Supercapacitors have medium energy density with high-power density (calculated by $\frac{V_{oc}{}^2}{4r_c}$ /mass). A similarly-sized electrolytic capacitor has higher power delivery capability but lower energy storage capacity.

Table 1. comparison of the supercapacitors and electrolytic capacitors.

Capacitor (F)	Rated voltage (V)	ESR (mΩ)	Max current[a] (A)	Short circuit current[b] (A)	Max power[c] (W)	Max energy (J)
25	3	30	21	100	75	112.5
100	3	8	78	375	281	450
[d]**380**	**3**	**3.2**	**250**	**937.5**	**70**	**1800**
500	3	3.2	288	937.5	703	2250
3000	3	0.23	2663	13 k	9.7 k	13.5 k
220 μ	450	1206	2.34	0.37 k	42 k	22.3
[d]**330 μ**	**450**	**340**	**3.62**	**1.3 k**	**148.9 k**	**33.4**
680 μ	200	36	4.15	5.5k	277.7 k	13.6
2200 μ	400	60	16	6.7 k	666.7 k	176
5600 μ	500	49	21	10.2 k	1275 k	700

[a] continuous rated current given by the data sheet.
[b] estimated instantaneous short-circuit current V_{oc}/r_c.
[c] maximum instantaneous power.
[d] highlighted rows correspond to the capacitors used in the TMS stimulation circuit described in this manuscript.

Electrolytic capacitors are unable to sustain high power delivery over an extended period due to their low time constant.

2.3. Concept behind the SC-based TMS pulse generator

As shown in table 1, a SC can store enough energy to generate a series of TMS pulses, based on its energy storage capacity, as listed under the maximum energy column. For example, a 95 F SC can store approximately 45 J with 1 V voltage, which is sufficient to generate over 190 TMS pulses. If we use a 3000 F SC, the number of pulses would significantly increase to 2000. This energy storage capacity can be further increased by charging the supercapacitor to a higher voltage, allowing it to store even more energy and thereby generate a greater number of TMS pulses. However, given that SCs typically have a low rated voltage, a voltage step-up circuit is necessary to raise the voltage to the required level for stimulation.

In Khokhar *et al* (2021), a DC supply with an output impedance of 10 Ω was used, while Tang *et al* (2016) employed a bipolar voltage-programmable power supply (KEPCO BOP 100-4M, TMG Test Equipment, Melbourne, Australia) with an output impedance of 4 mΩ. In comparison, using a supercapacitor results in significantly lower equivalent series resistance (ESR), with values as low as 0.23 mΩ as the capacitance increases (see table 1).

In section 3, we demonstrate how a supercapacitor-based primary energy source can be connected to an electrolytic capacitor-based output stage using inexpensive magnetic components and solid-state switches.

3. Prototype construction

Figure 1 depicts the overall block diagram of this supercapacitor-based high-power pulse generator. In the block diagram representation, there are two stages highlighted by red and blue dotted rectangles. The first stage (red dashed block) is the power stage, which handles high voltage and current. The second stage (blue dashed block) is the switching control stage, which operates at low voltage. An opto-isolator is used to isolate these two stages, ensuring electrical protection and safety. Since this research focuses solely on the development of the electronic circuit, without involving any animal testing, only circuit protection measures have been implemented.

3.1. Charging circuit (Block 1)

For this prototype, the supercapacitor bank is charged to 5 V using a standard 3 A, 0–30 V laboratory DC power supply (BK precision 1670A). This block can be disconnected once the supercapacitor module has reached the required voltage level, as the supercapacitor is capable of producing pulses without the need for recharging.

3.2. Pre-storage primary energy source (Block 2)

The Block 2 (figure 1) primary energy source is a supercapacitor bank (C_1) constructed from four 3-V, 380-F supercapacitors connected in series to give a net capacitance of 95 F, and a maximum working voltage of 12 V.

It can produce up to 6840 pulses with a 12 V input with each pulses of 2 J of energy and a voltage drop of only 0.2 V per discharge in the supercapacitors. Utilizing a higher capacity supercapacitor (SC) could produce significantly more pulses with an even smaller voltage drop ($\approx$ 0.02 V with a 3000 F SC). With larger capacitance, the energy density is also higher, allowing the supercapacitor to sustain a greater number of pulses with a single charge. Figure 2 presents the experimental results obtained using the prototype with a 1 V supply, demonstrating pulse count capacity across supercapacitors with different capacitance values.

One key advantage of this design is that the series-connected SC module can be pre-charged by any suitable laboratory power supply and the SC module can

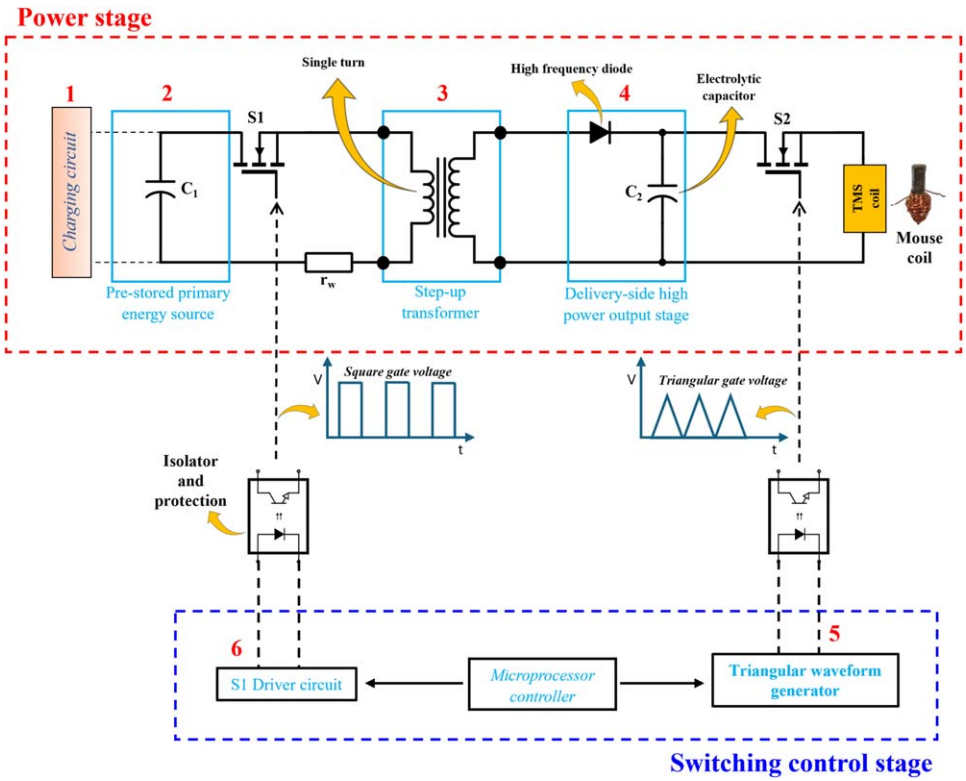

Figure 1. Block diagram of prototype TMS pulse generator. Power stage (high voltage) and switching control stage (low voltage) highlighted by red and blue dotted rectangles respectively. An opto-isolator isolates the stages for protection and safety.

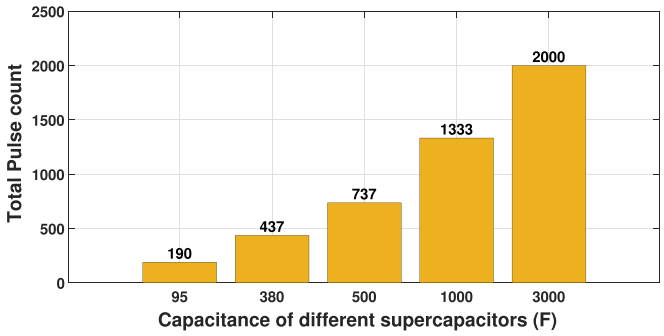

Figure 2. The total TMS pulse generated using the prototype with a 1 V input and tested with supercapacitors of varying capacitances. Pulses of 100 μs duration with a 200 V (1st pulse) amplitude were observed.

be used for repeated sets of pulses for a given experiment without the need for the DC power supply to be connected continuously.

3.3. Step up transformer (Block 3)

Given that a TMS coil requires an excitation voltage of several hundred volts, we must increase the output voltage of the supercapacitor bank by a significant factor. For this purpose, we have tested the suitability of a step-up transformer with a single-turn primary and large turn ratio (1:60 range). The single-turn primary allows a high drive current into the transformer's primary winding. The equivalent circuit of a transformer, as discussed in Valchev and den Bossch (2018), is shown in figure 3. Referring to figure 1 and figure 3, and symbol definitions in table 2, the initial voltages appearing across the primary and secondary coils are:

$$v_p = V_{oc} - (r_c + r_w + r_p) i_p \quad (2)$$

$$v_s = n \quad v_p \quad (3)$$

where $n = N_s/N_p$ and V_{oc} is the open-circuit voltage of the supercapacitor bank. If the parasitic resistances r_c, r_w (wire resistance) and r_p are too large, the primary voltage will be too low to create a high-power output pulse.

As per the definition of self-inductance (Valchev and den Bossch 2018), the total self-inductance of primary (L_1) and secondary (L_2) windings can be expressed as the sum of magnetizing and leakage

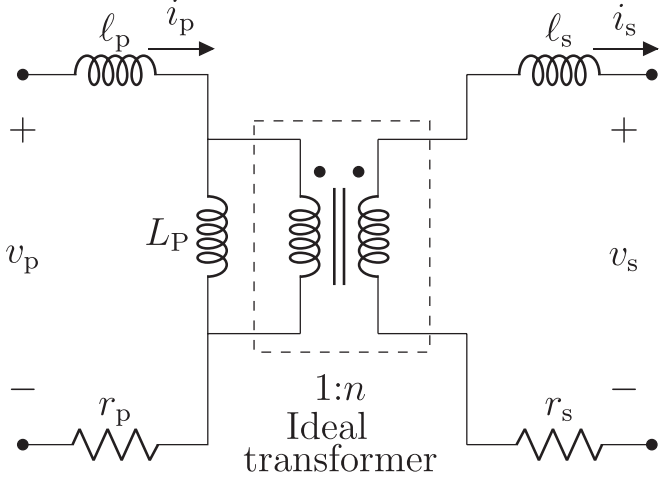

Figure 3. Equivalent circuit of the transformer.

Table 2. Symbol definitions and values for the transformer equivalent circuit.

Symbol	Description	Measured values primary, secondary
L_p, L_s	Magnetizing inductance for primary, secondary	8.33 μH, 32.5 mH
ℓ_p, ℓ_s	Leakage inductances	0.29 μH, 977 μH
r_p, r_s	Winding resistance	5.8 mΩ, 12 Ω
N_p, N_s	Number of turns	1, 60
v_p, v_s	Transformer voltages	–
i_p, i_s	Transformer currents	–

components:

$$L_1 = L_p + \ell_p, \tag{4}$$

and

$$L_2 = L_s + \ell_s. \tag{5}$$

By referring all inductive components to the secondary, the total self-inductance of the secondary side is:

$$L_2 = n^2(L_p + \ell_p) + \ell_s. \tag{6}$$

Inductance for both windings was measured using a Fluke PM6304 LCR meter at 10 kHz; see table 2. From equation (6), the secondary winding will have a total self-inductance of $L_2 = 32$mH, thus the secondary circuit is highly inductive. In this preliminary design the transformer was wound on a highly-permeable toroidal ferrite core type ZW42207TC (Magnetics) using a turns ratio of 1:60.

3.4. Delivery-side high-power output stage (Block 4)

A high-frequency diode and a high-voltage rated electrolytic capacitor (C_2) are coupled to the secondary of the transformer to achieve a DC output voltage which is sufficient to drive a high-power pulse into the TMS coil. Given that the transformer secondary has a high inductance which comes in series with the diode and capacitor in the secondary side, during each 'on' period of Switch-1 (MOSFET S1 in figure 1) there will be limited charge accumulation in the electrolytic capacitor. In order to charge the capacitor to the required voltage it is necessary to repetitively trigger S1. So the processor (Block 6) drives the gate of S1 with a pulse repetition rate of 8 kHz for a total integration time of 2 s. During this charging time, MOSFET S2 is 'off'. The energy stored in the electrolytic capacitor is then delivered to the TMS coil by driving the output MOSFET (S2 in figure 1) with a triangular gate-control voltage (Block 5). A full circuit diagram is shown in figure 4. The analysis of a resistor-diode combination placed in parallel with the TMS coil is explained in section 6.

The TMS coil is modeled as an inductance L in series with an internal resistance r_L (see figure 5). The coil is energized by discharging the electrolytic capacitor (C_2) via the non-linear resistance r_{DS} of MOSFET S2. The time-varying current i_L is measured with a current-clamp probe (Tektronix A622), then validated with MATLAB by integrating the measured inductor voltage ${v_L}^{meas}$. Figure 6 shows (a) the gate voltage, (b) the voltage over the C_2 and the current through the coil, and (c) the voltage over the coil and the drain-source voltage, as a function of time. We first identify from figure 6 the voltage over the coil (without resistance) as:

$$v_L(t) = L\frac{di_L}{dt} = {v_L}^{meas}(t) - i_L(t)r_L \tag{7}$$

We map this first-order differential equation to a finite difference equation approximation by mapping $di_L \rightarrow \Delta i_L = ({i_L}^{n+1} - {i_L}^n)$, and $dt \rightarrow \Delta t$, the oscilloscope time base resolution (time between consecutive samples). This

$$L\ \frac{{i_L}^{n+1} - {i_L}^n}{\Delta t} = ({v_L}^{meas})^n - {i_L}^n r_L \tag{8}$$

giving an Euler update equation for ${i_L}^{n+1}$,

$${i_L}^{n+1} = {i_L}^n + \frac{\Delta t}{L}(({v_L}^{meas})^n - {i_L}^n r_L) \tag{9}$$

where $n = 1 \ldots N$ is the time-step index for a total of $N = 2500$ samples. The initial condition is

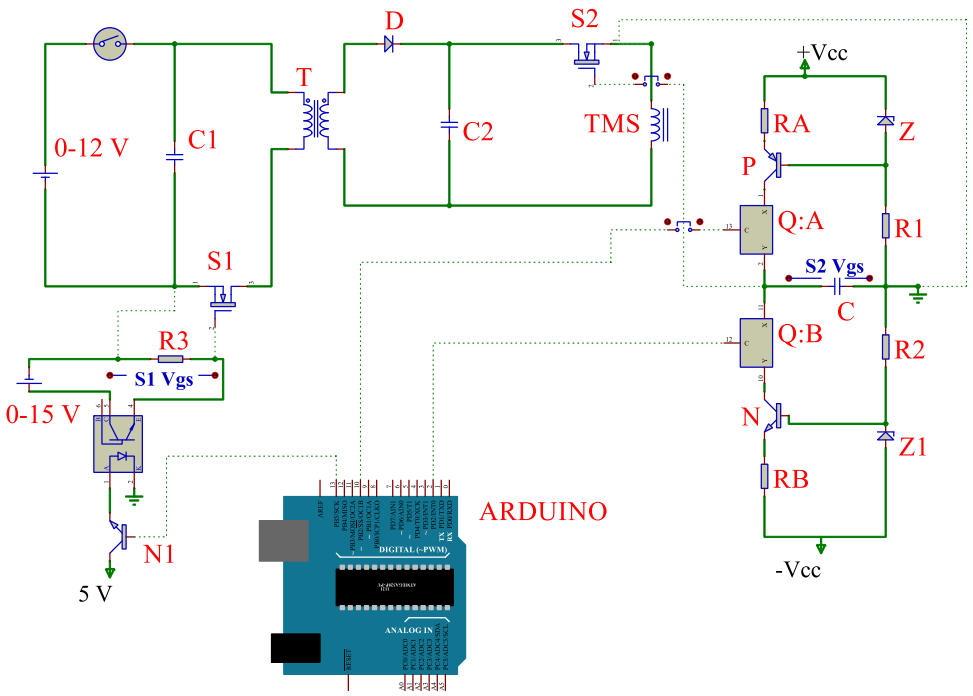

Figure 4. Circuit topology of the prototype.

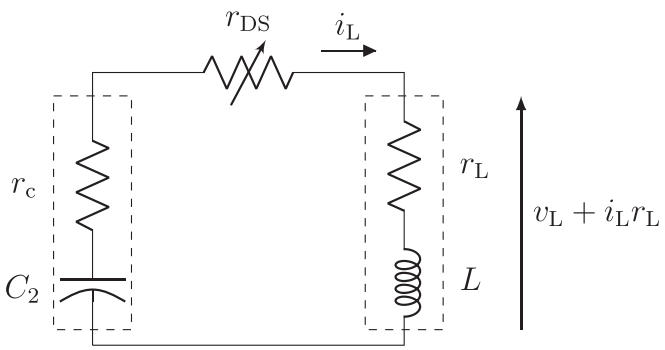

Figure 5. Equivalent model of the RLC circuit in the prototype consisting of the electrolytic capacitor C_2 with internal resistance r_C, non-linear resistance r_{DS} of MOSFET S2, and TMS coil with inductance L with internal resistance r_L.

$i_L(t=0) = 0 \rightarrow {i_L}^{n=1} = 0$. We can thus predict the current at the $(n+1)^{th}$ step given a measurement of coil voltage and current at the n^{th} step.

The comparison between modelled and measured currents is shown in figure 6. The current-probe has a bandwidth of dc-100 kHz, so gives a much slower response than the ${v_L}^{meas}(t)$ oscilloscope reading (bandwidth 0-10 MHz). To correct for current probe delay, we advanced the measured current trace by 2 μs prior to plotting (figure 6). This leftwards timing offset was also applied to the current traces displayed in MATLAB plots of figure 6, figure 7, figure 8, and figure 9.

3.5. Other requirements

There was no need for AC decoupling capacitors in the supply lines, as the circuit operates exclusively on DC power. The supercapacitors are charged using a DC power supply, and all wire lengths in the circuit have been kept as short as possible. Our goal was to design a low-cost and reliable pulse generator. To achieve this, we employed an optocoupler (figure 1), which performed exceptionally well. The optocoupler provided the correct gate voltage while ensuring effective isolation, thereby eliminating the need for a biasing resistor.

4. Circuit testing

In this proof-of-concept experiment, the S1 driver circuit with microprocessor block (Block 6 in figure 1) generates an 8 kHz square-wave voltage to repetitively trigger S1 until the output electrolytic capacitor (C_2) attains a predetermined voltage set at 30 V for this experiment. The gate voltage to S2 is provided by an adjustable triangular generator creating a triangular voltage waveform of variable slope.

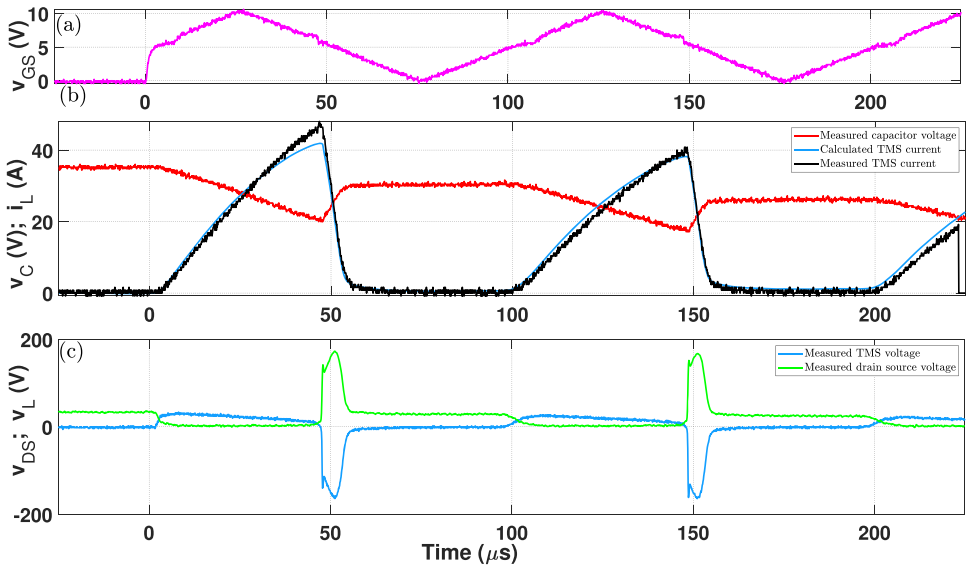

Figure 6. Circuit response measured during TMS coil excitation obtained with 1 V of input to the supercapacitor (a) Triangular control voltage of MOSFET 2 gate (the triangular wave is not captured for the initial 25 μs due to configuration of the triggering mechanism in the oscilloscope); (b) Measured electrolytic capacitor voltage (red) and measured/calculated TMS coil current (black/blue); (c) Drain-source voltage of MOSFET (green) and measured TMS coil voltage (blue).

In this study, the TMS coil constructed by Khokhar *et al* (2021) was utilized. As an initial phase, resistance and inductance measurements of the coil were conducted. The coil comprises 50 turns of copper wire with a conductive diameter of 0.4 mm wound around a 5 mm diameter carbonyl powdered iron core (Micro Metals, U.S.A). The inductance of the coil was measured to be 23 μH and resistance as 212 mΩ using an Agilent E4980A four-point impedance meter.

As shown in figure 6, the electrolytic capacitor (C_2) has a starting voltage of 30 V. This C_2 starting voltage was obtained by energy transfer (at 8 kHz for 2 s) from the C_1 supercapacitor that had been precharged to 1 V. C_2 is subsequently progressively discharged to the TMS coil by periodically triggering S2 with a 10 kHz triangular gate voltage with 50% symmetry (meaning the rise time is 50% of the total rise and fall time), generating a TMS pulse with a peak voltage 150 V, peak current 40 A, and peak instantaneous power 6 kW. The peak voltage is the inductive response to the rapid reduction in current when MOSFET S2 switches off.

We then increased the supercapacitor voltage to 3 V and activated S1 for a duration of 4 s, allowing the electrolytic capacitor to reach 100 V. Employing the same 50% symmetry and 10 V peak-to-peak triangular waveform to activate S2, we observed a TMS pulse with a peak negative voltage of amplitude 276 V, peak current 124 A, and a peak instantaneous power 34.2 kW. Results are shown in figure 7.

As illustrated in figure 8, by altering the symmetry of the 10 kHz triangular voltage drive to MOSFET S2, the circuit can generate significantly higher output voltages without re-configuring the hardware. Testing the configuration with 80% (80:20 rise-fall) symmetry resulted in a voltage pulse of amplitude 508 V. As well as amplitude, the system enables convenient adjustment of TMS pulse shape, including rise and fall time. A pronounced increase in peak coil voltage and the emergence of oscillations around 1 MHz, caused by fast switching transitions (dv/dt and di/dt) as well as parasitic inductance and capacitance, are observed in figure 8. This behaviour results from rapid turn-off and can be mitigated using an RC circuit in the TMS output stage and an improved gate driver circuit to mitigate the gate capacitance. Further investigation is required to fully understand and address this problem.

In addition, modification of gate-voltage amplitude allows further changes in the TMS current and voltage pulse characteristics. Figure 9(a) depicts the impact of varying the gate-voltage amplitude on the rise, fall, and pulse width of the TMS current waveform. Increasing the peak gate voltage from 7 V to 10 V increases the pulse width and pulse height of the TMS coil current. Figure 9(d) shows how the symmetry of the gate voltage influences the TMS voltage and current pulse shape, as well as the pulse width. A shorter fall time results in a shorter pulse duration but produces higher amplitude voltage pulses.

5. Magnetic field measurement

To measure the magnetic field produced, the coil was placed in an adjustable holder above a Hall effect sensor, figure 10(a). Existing literature (Tang *et al* 2016; Wilson *et al* 2018) indicates that magnetic field strengths of less than 200 mT are typically achieved for mouse coils. However, magnetic fields as high as 800 mT with a 50 V input have also been reported (Khokhar *et al* 2021), accompanied by an electric field

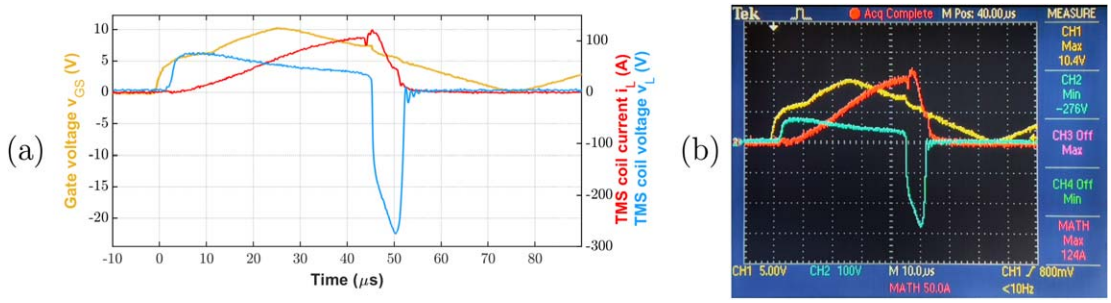

Figure 7. (a) Gate voltage, TMS coil current and TMS coil voltage against time. The raw traces captured from the oscilloscope (b) have been smoothed with a Whittaker filter (Weinert, 2007; Eilers, 2003) to reduce oscilloscope 8-bit digitization noise; (b) Oscilloscope measurement of MOSFET gate voltage (yellow), TMS coil voltage (blue) and TMS coil current (red). Symmetry is set at 50% with with a 3 V input in the supercapacitor bank.

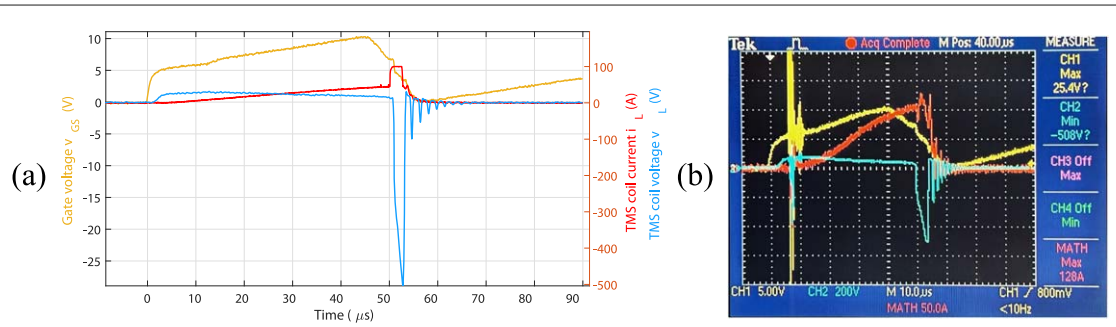

Figure 8. Gate voltage (yellow), TMS coil voltage (blue), and TMS current (red) for gate voltage symmetry at 80%. (a) MATLAB capture of oscilloscope traces of gate, voltage and current smoothed with a Whittaker filter; (b) Oscilloscope measurement. Note pronounced increase in peak coil voltage and emergence of $\approx$ 1 MHz oscillations arising from reduced gate-voltage fall time.

intensity of 10 V/m. However, with 80% symmetry and only with 1 V input from the supercapacitor, we were able to generate a magnetic field exceeding 200 mT, which may be sufficient to stimulate brain cells in small animals (Selvaraj *et al* 2018; Khokhar *et al* 2021). The magnetic field (B-field) measurement process utilized an SS496A1 Hall effect sensor. The Hall effect sensor was calibrated using a Helmholtz coil (Khokhar *et al* 2021). Figure 10(b) illustrate the magnetic flux density (B-field) from 0 mm to 4 mm distance from the coil with 80% symmetry gate voltage input.

For the 0 mm and 1 mm cases, the magnetic field exceeded the sensor's maximum range of 200 mT. To estimate the magnetic field beyond this range, a scaling factor was applied to the 2 mm results, ensuring that the estimated field aligns with the measured field below 200 mT (Khokhar *et al* 2021). Increasing the input voltage would enhance the output voltage and magnetic field strength. Higher input voltages would lead to increased C_2 voltage, resulting in higher induced voltages across the inductor and stronger magnetic fields.

6. Enhanced pulse shaping with resistor-diode combinations

Most TMS circuits incorporate a discharge path into the TMS coil circuit. This is often for the purpose of preventing high voltages over the switches, but also has the advantages that, the circuit gains additional control over the energy release from the coil, allowing for more precise manipulation of the pulse characteristics, such as width, amplitude, and overall shape.

The addition of a resistor-diode combination in parallel with the TMS coil (figure 11) serves a role in controlling the discharge rate of the coil when the MOSFET (S2) is turned off. This setup functions similarly to a snubber circuit, which is commonly used in electronic circuits to protect components and shape waveforms by controlling the voltage and current transitions.

When the switch S2 is on, the current flows through the TMS coil, storing energy in the magnetic field of the inductor. Without the R-diode (figure 4), upon turning off the switch S2, the current flow through the coil would typically drop rapidly leading to a high, potentially damaging voltage over S2. However the diode parallel to TMS coil (figure 11) allows the current to continue flowing through the resistor, rather than abruptly stopping. This creates a path for the inductor's stored energy to discharge more gradually. The resistor in the combination sets the rate at which the energy is dissipated. A higher resistance shortens the time it takes for the current to decay to zero, manifested through the $\frac{L}{R}$ time constant. Conversely, a lower resistance results in a more prolonged

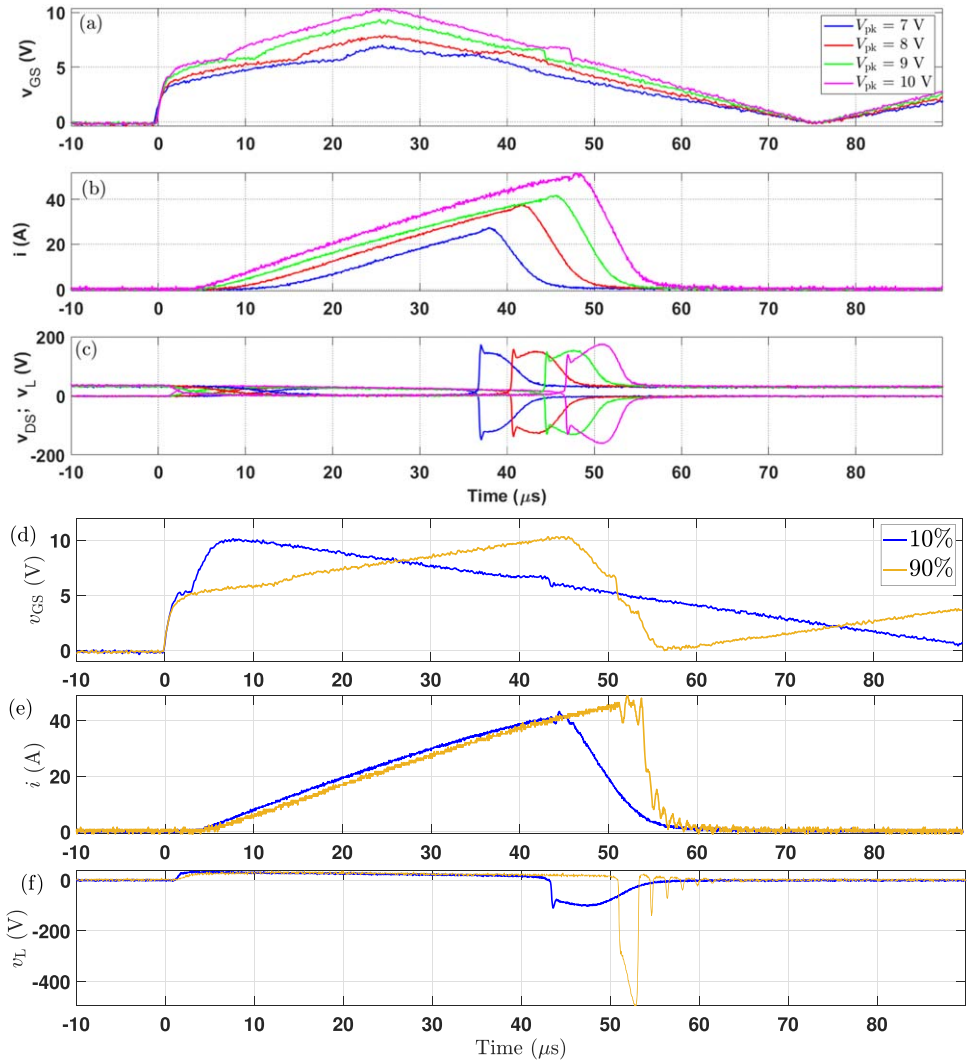

Figure 9. (a) Peak gate voltage is stepped from 7 V to 10 V; (b) TMS coil current pulse for respective gate voltage; (c) Drain-source voltage (above the zero reference) and TMS coil voltage; (d) 10% and 90% symmetry gate voltage; (e) TMS coil current pulse for respective gate voltage; (f) TMS coil voltage.

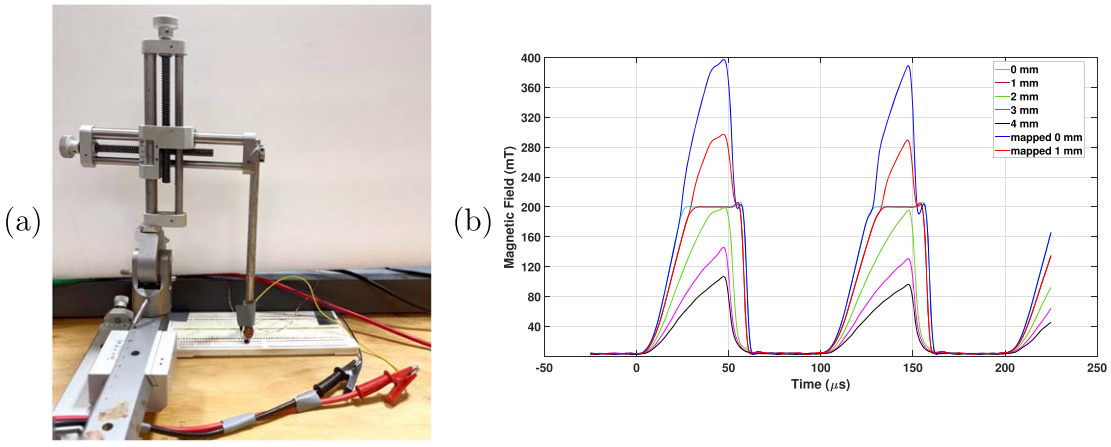

Figure 10. Laboratory setup for B-field measurement featuring an SS496A1 Hall effect sensor and a TMS coil mounted on an adjustable stand with vernier scale; (b)Experimental trials were conducted using an 80% symmetric triangular gate voltage with a 1 V SC input, measuring the magnetic field generated by the TMS coil at distances ranging from 0 mm to 4 mm from the sensor.

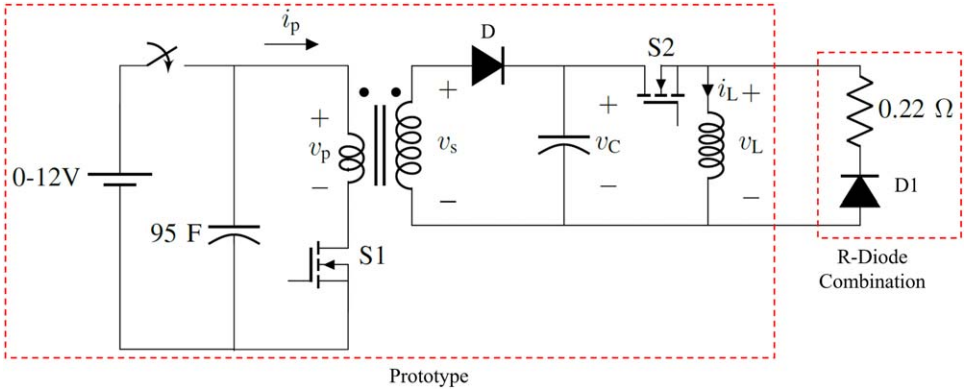

Figure 11. Circuit modification involves adding an R-diode combination in parallel to the existing prototype. For simplicity, only the main circuit of the prototype is illustrated, omitting the gate driver circuits for S1 and S2.

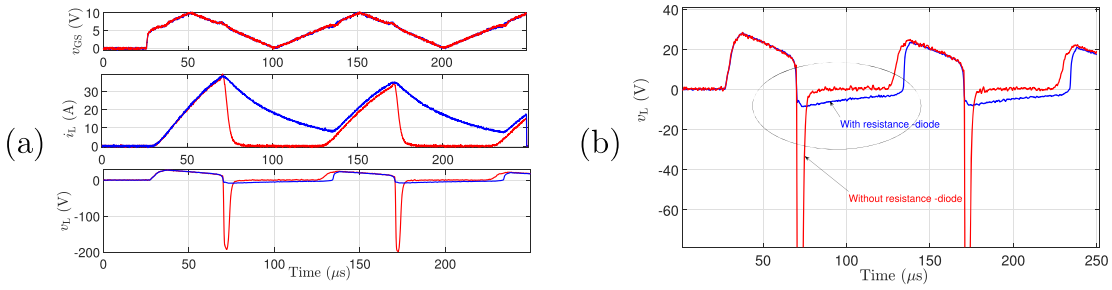

Figure 12. (a) Voltage Pulse TMS comparison between RLC prototype and enhanced version with resistor-diode combination (b) The zoomed-in view of the negative phase is presented, comparing the waveform with and without the resistor-diode combination.

discharge. This controlled discharge extends the duration of the negative phase of the voltage waveform across the TMS coil, allowing you to shape the pulse more effectively.

Figure 12 clearly shows the difference between the original prototype (figure 4) and the modification with the resistor-diode combination (figure 11). When the MOSFET S2 turns off, the current drop is delayed, allowing for more gradual energy dissipation. This delay in current reduction translates into a longer-lasting and more controllable negative phase of the TMS pulse.

7. Discussion

We have presented a new design approach for a supercapacitor-based pulse generator providing a test-bed for a low-cost flexible pulse generator for applications such as TMS excitation. This system can generate a tension of several hundred volts across the TMS coil using a low-voltage supercapacitor bank, and allows wave-shaping adjustment of the TMS current and voltage pulse, by varying the rise-fall symmetry of the triangular gate voltage. All experiments were conducted using a 1 V input from the supercapacitor (SC) during the initial testing phase of the prototype (figure 4). With this low input voltage, the design achieved a peak output voltage pulse of 500 V and generated a magnetic field exceeding 200 mT for a pulse of 100 μs width. These initial experiments served as a proof of concept, demonstrating the design's effectiveness and confirming its suitability for TMS applications, meeting the necessary requirements for successful stimulation. Using a supercapacitor bank with a 12 V input allows for the generation of multiple TMS pulses without the need to recharge the energy source. Due to the very low equivalent series resistance (ESR) of the supercapacitors, the voltage drop is minimal, enabling the voltage to be maintained across several pulse sequences, making it well-suited for reliable TMS applications. In the initial stage, with a 1 V input, we are generating 20 pulses per discharge. However, if there is a need to increase the number of pulses, we can replace the supercapacitor with one that has a higher capacitance value and charge it to a higher voltage (like 12 V). This modification would allow the circuit to continuously generate pulses in the range of 2000 pulses. The pulse count, however, is also dependent on the pulse width; a wider pulse width would reduce the total number of pulses.

An Arduino was chosen for this prototype design because it is easy to program and offers great flexibility in controlling various components. It is ideal for rapid

development and experimentation, allowing us to send control signals to the S1 gate and manage the triangle waveform generator for S2, as shown in figure 4. The key advantage of using a programmable processor like the Arduino than any electronic circuit is its precise control, adaptability for future changes, and the convenience of integrating multiple functions into a single unit, making it a cost-effective and efficient solution for the prototype stage. While the Arduino is a suitable choice for this development, the possibility of using other micro-controllers/software will also be explored in the future.

Our prototype demonstrates that a supercapacitor (SC) can serve as a reliable and low-cost energy source for a TMS pulse generator, effectively replacing the high-voltage sources used in existing topologies (Peterchev *et al* 2011; Goetz *et al* 2012). By treating the MOSFET as more than just a switch, and using a triangular pulse, we observed that the TMS voltage and current pulse parameters could be controlled through adjustments in the rise and fall times of the triangular pulse. This approach confirms the SC's suitability as an alternative energy source and the enhanced functionality of the MOSFET in pulse shaping.

The pulses presented in this study are of smaller pulsewidth. This serves as a preliminary test to evaluate the suitability of the design for TMS applications. Higher power applications can be achieved with the same prototype, although this would necessitate additional safety measures, such as sealing the components to prevent accidental contact.

8. Conclusion

This article presents a new design technique for TMS pulse generator based on a small supercapacitor bank as the primary energy source, eliminating a high voltage DC power supply. We use medium-canister size supercapacitors with common low-cost passive components such as a step-up transformer based on an inexpensive core, medium voltage electrolytic capacitors and low-cost MOSFETs. The SC has proven to be an excellent energy source, capable of retaining its voltage across many pulse sequences without needing to be recharged. Additionally, in this approach, the MOSFET is treated as a dynamic element, enabling effective pulse shaping. Pulse shaping is an under-explored area in TMS, and by adjusting the symmetry of the triangular gate voltage, the pulse width can be varied, offering control over TMS pulse. The circuit prototype has the ability to adjust the pulse parameters which adds an innovative dimension previously under-explored in TMS pulse generators.

Acknowledgments

Soniya Raju gratefully acknowledges the University of Waikato Doctoral Scholarship for research support.

Data availability statement

All data that support the findings of this study are included within the article (and any supplementary files).

ORCID iDs

Soniya Raju https://orcid.org/0009-0001-1619-6736
Marcus Wilson https://orcid.org/0000-0001-6214-7727

References

Ali K, Wendt K, Sorkhabi M M, Benjaber M, Denison T and Rogers D J 2023 xtms: A pulse generator for exploring transcranial magnetic stimulation therapies *2023 IEEE Applied Power Electronics Conference and Exposition (APEC)* 1875–80

Barker A T, Garnham C W and Freeston I L 1991 Magnetic nerve stimulation: the effect of waveform on efficiency, determination of neural membrane time constants and the measurement of stimulator output *Electroencephalogr Clin. Neurophysiol. Suppl.* **43** 227–37

Barker A T, Jalinous R and Freeston I L 1985 Non-invasive magnetic stimulation of human motor cortex *The Lancet* **325** 1106–7

Camera F, Colantoni E, Casciati A, Tanno B, Mencarelli L, Di Lorenzo F, Bonnì S, Koch G and Merla C 2024 Dosimetry for repetitive transcranial magnetic stimulation: a translational study from alzheimers disease patients to controlled in vitro investigations *Phys. Med. Biol.* **69** 185001

Cheng L, Chen Z, Wang H, Guo F, Wu G, Xie L, Xiao J, Wang Y, Shen S and Ding W 2021 A novel avalanche transistor-based nanosecond pulse generator with a wide working range and high reliability *IEEE Trans. Instrum. Meas.* **70** 1–14

Cheng L, Mei K, Chen Z, Jia W, Wang Y, Wang H, Xie L, Shen S and Ding W 2022 High-voltage repetitive nanosecond pulse generator utilizing power synthesis of modified avalanche transistorized marx circuits *IEEE Trans. Instrum. Meas.* **71** 1–16

Eilers P H 2003 A perfect smoother *Anal. Chem.* **75** 3631–6

Elgenedy M A, Massoud A M, Holliday D, Ahmed S and Williams B 2017 Low-voltage dc input, high-voltage pulse generator using nano-crystalline transformer and sequentially charged mmc sub-modules, for water treatment applications *2017 IEEE Energy Conversion Congress and Exposition (ECCE)* 2144–9

Elserougi A, Ahmed S and Massoud A 2016 A boost converter-based ringing circuit with high-voltage gain for unipolar pulse generation *IEEE Trans. Dielectr. Electr. Insul.* **23** 2088–94

George M S *et al* 2010 Daily left prefrontal transcranial magnetic stimulation therapy for major depressive disorder: a sham-controlled randomized trial *Archives of General Psychiatry* **67** 507–16

Goetz S M, Pfaeffl M, Huber J, Singer M, Marquardt R and Weyh T 2012 Circuit topology and control principle for a first magnetic stimulator with fully controllable waveform *2012 Annual International Conference of the IEEE Engineering in Medicine and Biology Society* (IEEE) 4700–3

Gomez-Tames J, Laakso I and Hirata A 2020 Review on biophysical modelling and simulation studies for transcranial magnetic stimulation *Phys. Med. Biol.* **65** 24TR03

Iglesias A H 2020 Transcranial magnetic stimulation as treatment in multiple neurologic conditions *Curr. Neurol. Neurosci. Rep.* **20** 1–9

Jiang S, Zhang W, Wang Y, Li Z and Rao J 2022 A solid-state pulse adder for high-voltage short pulses and low-voltage long pulses *IEEE Trans. Plasma Sci.* **50** 3107–12

Khokhar F A, Voss L J, Steyn-Ross D A and Wilson M T 2021 Design and demonstration in vitro of a mouse-specific transcranial magnetic stimulation coil *IEEE Trans. Magn.* **57** 1–11

Koponen L M and Peterchev A V 2020 Transcranial magnetic stimulation: principles and applications *Neural Eng.* ed B He (Springer) 245–70

Kularatna N and Gunawardane K 2021 *Energy Storage Devices for Renewable Energy-Based Systems: Rechargeable Batteries and Supercapacitors* (Academic)

Kularatna N and Jayananda D 2020 Supercapacitor-based long time-constant circuits: A unique design opportunity for new power electronic circuit topologies *IEEE Industrial Electronics Magazine* **14** 40–56

Li L, Ning M, Dehuai C, Lun L, Qiang K, Mingjia L, Yong C and Yuan P 2015 Study on double resonant performance of air-core spiral tesla transformer applied in repetitive pulsed operation *IEEE Trans. Dielectr. Electr. Insul.* **22** 1916–22

Mankowski J and Kristiansen M 2000 A review of short pulse generator technology *IEEE Trans. Plasma Sci.* **28** 102–8

Menzies L, Chamberlain S R, Laird A R, Thelen S M, Sahakian B J and Bullmore E T 2008 Integrating evidence from neuroimaging and neuropsychological studies of obsessive-compulsive disorder: the orbitofronto-striatal model revisited *Neuroscience & Biobehavioral Reviews* **32** 525–49

Nieminen J O, Pospelov A S, Koponen L M, Yrjölä P, Shulga A, Khirug S and Rivera C 2022 Transcranial magnetic stimulation set-up for small animals *Frontiers in Neuroscience* **16** 935268

Osuch E A, Benson B E, Luckenbaugh D A, Geraci M, Post R M and McCann U 2009 Repetitive tms combined with exposure therapy for ptsd: a preliminary study *Journal of Anxiety Disorders* **23** 54–9

Peterchev A V, Deng Z-D and Goetz S M 2015 Advances in transcranial magnetic stimulation technology *Brain Stimulation: Methodologies and Interventions* ed I M Reti (Wiley) 10 165–89

Peterchev A V, Jalinous R and Lisanby S H 2007 A transcranial magnetic stimulator inducing near-rectangular pulses with controllable pulse width (cTMS) *IEEE Trans. Biomed. Eng.* **55** 257–66

Peterchev A V and Murphy D L 2013 Controllable pulse parameter transcranial magnetic stimulator with enhanced pulse shaping, in '2013 *6th International IEEE/EMBS Conference on Neural Engineering (NER)* (IEEE) 121–4

Peterchev A V, Murphy D L and Lisanby S H 2011 Repetitive transcranial magnetic stimulator with controllable pulse parameters *J. Neural Eng.* **8** 036016

Raju S, Kularatna N and Wilson M 2023 Supercapacitor based adjustable high power pulse generator for medical research applications *IECON 2023-49th Annual Conference of the IEEE Industrial Electronics Society* (IEEE) 1–6

Selvaraj J, Rastogi P, Prabhu Gaunkar N, Hadimani R L and Mina M 2018 Transcranial magnetic stimulation: Design of a stimulator and a focused coil for the application of small animals *IEEE Trans. Magn.* **54** 1–5

Smith M-C and Stinear C M 2016 Transcranial magnetic stimulation (TMS) in stroke: ready for clinical practice? *Journal of Clinical Neuroscience* **31** 10–4

Somaa F A, de Graaf T A and Sack A T 2022 Transcranial magnetic stimulation in the treatment of neurological diseases *Frontiers Neurol.* **13** 793253

Sorkhabi M M, Benjaber M, Wendt K, West T O, Rogers D J and Denison T 2021 Programmable transcranial magnetic stimulation: A modulation approach for the generation of controllable magnetic stimuli *IEEE Trans. Biomed. Eng.* **68** 1847–58

Tang A D *et al* 2018 Low intensity repetitive transcranial magnetic stimulation modulates skilled motor learning in adult mice *Scientific Reports* **8** 4016

Tang A D *et al* 2016 Construction and evaluation of rodent-specific rTMS coils *Frontiers in Neural Circuits* **10** 47

Tang A D, Makowiecki K, Bartlett C and Rodger J 2015 Low intensity repetitive transcranial magnetic stimulation does not induce cell survival or regeneration in a mouse optic nerve crush model *PloS One* **10** e0126949

Tang A, Thickbroom G and Rodger J 2017 Repetitive transcranial magnetic stimulation of the brain: mechanisms from animal and experimental models *The Neuroscientist* **23** 82–94

Udayanga S T S, Kokuhennadige S, Fernando J, Kularatna N and Steyn-Ross D A 2021 Supercapacitor assisted surge absorber (SCASA) technique: Selection of magnetic components based on permeance *2021 IEEE Applied Power Electronics Conference and Exposition (APEC)* (IEEE) 2299–304

Valchev V C and Van den Bossche A 2018 *Inductors and Transformers for Power Electronics* (CRC press)

Van Rooij S J, Arulpragasam A R, McDonald W M and Philip N S 2024 Accelerated tms-moving quickly into the future of depression treatment *Neuropsychopharmacology* **49** 128–37

Wassermann E M and Zimmermann T 2012 Transcranial magnetic brain stimulation: therapeutic promises and scientific gaps *Pharmacology & Therapeutics* **133** 98–107

Weinert H L 2007 Efficient computation for Whittaker-Henderson smoothing *Computational Statistics & Data Analysis* **52** 959–74

Wilson M T, Fulcher B D, Fung P K, Robinson P A, Fornito A and Rogasch N C 2018 Biophysical modeling of neural plasticity induced by transcranial magnetic stimulation *Clin. Neurophysiol.* **129** 1230–41

Wilson M, Tang A, Iyer K, McKee H, Waas J and Rodger J 2018 The challenges of producing effective small coils for transcranial magnetic stimulation of mice *Biomed. Phys. Eng. Express* **4** 037002

Yan J, Shen S and Ding W 2020 High-power nanosecond pulse generators with improved reliability by adopting auxiliary triggering topology *IEEE Trans. Power Electron.* **35** 1353–64

Zan X, Torres D R, Kheirollahi R, Lu X, Zheng S, Lu F and Avestruz A-T 2023 Medium voltage pulse power generator for accurate current interruption *IEEE Trans. Ind. Electron.* **70** 3604–15

Zhao Y, Xie W, Jiang J, Chen L, Feng S, Wang M and Wang Z 2019 Replacement of marx generator by tesla transformer for pulsed power system reliability improvement *IEEE Trans. Plasma Sci.* **47** 574–80

4.5.3 Poster presented

I presented posters detailing the early stages of my research at several key conferences in 2023. At the NZIP (New Zealand Institute of Physics) & Physikos 2023 Conference, held at Massey University's Albany Campus in Auckland from July 3-5, I shared initial findings and developments in my research. Additionally, I showcased my early work at the Australasian Winter Conference on Brain Research (AWCBR) in Queenstown during August/September 2023. These presentations provided a platform for discussing preliminary results and engaging with the scientific community, reflecting my commitment to advancing research in the field.

Both posters from these conferences are attached in the Appendix A for reference.

Chapter 5

Gate voltage control

Introduction

This chapter explains the control mechanism for generating gate voltages for S1 and S2, focusing primarily on the S2 switch. By controlling S2, we can effectively shape the TMS output pulse. The development process of the gate voltage is detailed, highlighting the transition from conventional square gate voltages to the triangular shape. The impact of the symmetry in the triangular pulse waveform, specifically the rise and fall times, on the output pulse is examined. The chapter also discusses the successful operation of the prototype, outlining the development stages and experimental results with various gate voltages. These findings demonstrate the circuit effectiveness in producing precise and adjustable pulses. The research advancements are documented in the attached conference papers, underscoring the practical benefits and innovative approaches of this work.

5.1 Sequence of S1 and S2

5.1.1 Switching mechanism of S1

S1 switch is operated at 8 kHz, and its main function is to control the charging of the electrolytic capacitor. When S1 is closed, the supercapacitor begins charging the electrolytic capacitor. This process takes only 2 seconds to charge the capacitor from 1 V to 30 V. Once the electrolytic capacitor reaches the required voltage, S1 is switched off. Any high frequency can be used here approximately between 1 kHz to 10 kHz. This switching is to make a pulsating DC equivalent to AC as input to the transformer primary so that it can step up the voltage.

The switching mechanism of S1 is crucial in ensuring that the capacitor is charged efficiently within the desired time frame. It allows for precise control over the charging process, ensuring that the capacitor reaches the desired voltage level effectively.

5.1.2 Switching mechanism of S2

The S2 switch operates once the electrolytic capacitor (C2) reaches the required voltage of 30 V. Its purpose is to control the discharge of the capacitor (C2), thereby providing the necessary excitation to the TMS coil. In my setup, I used an 10 kHz switching frequency for the S2.

Initially, the circuit is started with a low voltage input, and C2 charges up to 30 V. Since the energy stored at 30 V is relatively low (even less than 1 J), for testing purposes, I employed a smaller pulse-width gate voltage of 100 μs (10 kHz) so that I can have prolonged pulses. However, this same circuit can be adapted to use millisecond pulse-widths, which will be discussed in detail in Chapter 7. The prototype can also be scaled up by using capacitors with higher capacitance values, allowing for greater energy storage. This makes it suitable to use in existing continuous theta burst stimulation (cTBS) patterns which uses pulse-width of 500 μs.

When S2 is closed, the charged electrolytic capacitor discharges its stored energy through the coil. This results in the generation of medium to high voltage across the coil, creating a strong magnetic field for coil excitation.

The decision to operate S2 at 30 V is strategic. Although the capacitor can handle higher voltages (up to 100 V), the prototype testing is kept conservative at 30 V to avoid stressing the MOSFET excessively. This ensures the reliability and longevity of the components.

5.1.3 Pulse sequence

In the test setup, the pulse sequence involves operating S1 for 2 seconds to charge the electrolytic capacitor, followed by closing S2 to discharge the capacitor to the TMS coil. This setup ensures that both switches never turn on simultaneously; when S1 is on, S2 is off, and vice versa. This alternating operation prevents any overlap in their functions and ensures the proper sequence of charging and discharging required for the TMS pulse generation. The 8 kHz (125 μs) pulses for 2 seconds ensure efficient charging (C2), while the subsequent 10 kHz (100 μs) pulses maintain the discharge until the capacitor (C2) is fully discharged. This typically results in about 20 pulses from single discharge, but increasing the capacitor voltage can yield more pulses.

Figure 5.1 depicts the S1 and S2 pulse pattern in the operation of the pulse generator prototype. It provides a conceptual representation of the pulse pattern rather than precise measurements of pulse width and frequency, as the original measurements of pulse width are too fast to be accurately shown. Therefore, Figure 5.1 serves as an illustrative depiction of the operational sequence of S1 and S2 in the prototype.

In summary, the switching mechanism of S1 and S2 plays a critical role in controlling the charging and discharging processes of the circuit, ensuring precise timing and efficient operation. The pulse sequence facilitates effective excitation of the TMS coil.

5.2 Shaping of gate waveform

This section details the progressive development and enhancement of a circuit prototype designed for TMS coil excitation. It covers the initial design and successful construction of the prototype,

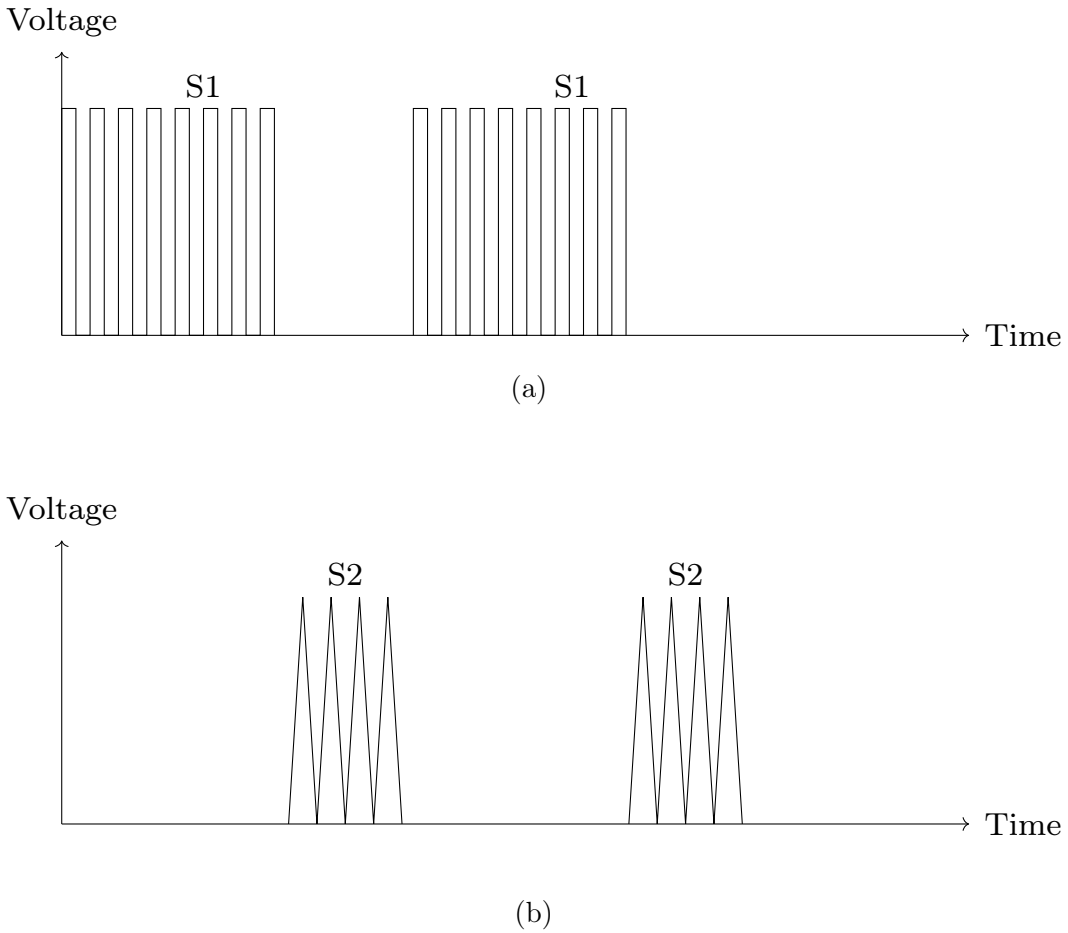

Figure 5.1: Graphical representation of the S1 and S2 MOSFET gate patterns (pulse-widths are approximate and intended solely to illustrate the pattern); (a) S1 gate pattern: An 8 kHz pulse is applied to the S1 MOSFET for 2 seconds, followed by an off state. (b) S2 gate pattern: After 2 seconds, the S2 MOSFET is triggered with a 10 kHz pulse.

subsequent stages of pulse shaping, and advancements in voltage handling and scalability. The journey from conceptualization to practical implementation is documented, highlighting significant milestones and experimental insights that contributed to the research success.

5.2.1 Stage I

The first stage of the circuit prototype was successfully designed and built. This design, along with the results, was published and presented at the 49th Annual Conference of the IEEE Industrial Electronics Society (IECON 2023) [79], held at the Marina Bay Sands Expo and Convention Centre in Singapore from October 16-19, 2023. The conference paper titled "Supercapacitor based adjustable high power pulse generator for medical research applications" is included before this chapter.

In the initial phase, the circuit utilized standard components, including IN4007 diodes and MOSFET rated at 100 V and 200 A. Although these were not high-power components, they effectively charged an electrolytic capacitor (C2) to 30 V from a 3 V input supplied by a supercapacitor. This setup successfully generated a magnetic field of 250 mT, causing the coil to vibrate. These results

provided a proof-of-concept that the circuit could function as a pulse generator for exciting the TMS coil.

5.2.2 Stage II

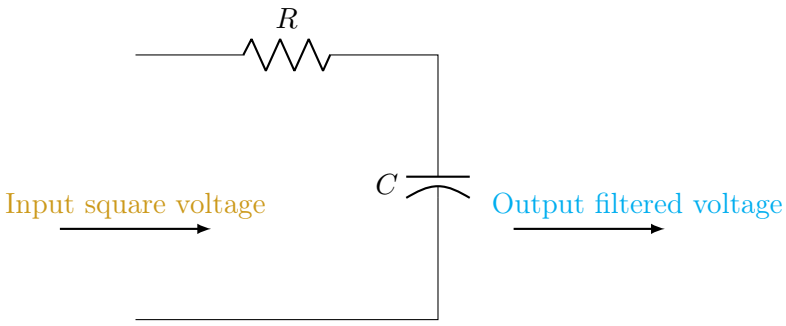

Figure 5.2: Low-pass filter topology

Figure 5.3: The oscilloscope output displays the square gate voltage (yellow) and the filtered output (blue). The low-pass filter, designed with a cutoff frequency of 800 Hz, is tested using a medium-range frequency input to demonstrate its filtering capabilities.

Following the successful pulse generation and TMS coil excitation, efforts were directed towards pulse shaping within the existing circuit, exploring whether the circuit's intrinsic ability to shape pulses was feasible; if not, consideration was given to adding extra components. The motivation to use filters initially stemmed from the idea of shaping the pulse by altering the excitation pulse (gate voltage to S2) rather than directly modifying the output voltage/current pulse. By focusing

on changing the shape of the gate voltage pulse, it was possible to control the on/off pattern of the gate voltage, thereby influencing the resulting TMS pulse shape. Initially, a square gate voltage was generated directly using an Arduino program. To achieve more nuanced waveform shapes, such as slope types, the simplest and most straightforward approach seemed to be using filters. Therefore, RC differentiator/integrator filters were employed to transform the square waveform into various slope waveforms. This approach sparked the realization that there is significant potential in manipulating the input signal to S2 using filters or other methods. This aligns with the goal of effectively and efficiently shaping the TMS pulses.

I designed a low-pass filter (Fig 5.2) with a cutoff frequency of 800 Hz and tested its response using input signals of 1 kHz and 2 kHz. The input signal, initially a square wave, was transformed into triangular and sawtooth waveform using the filter. The low-pass filter effectively smoothed the input signal as shown in Fig 5.3 and 5.4, demonstrating its ability to filter out higher frequency components.

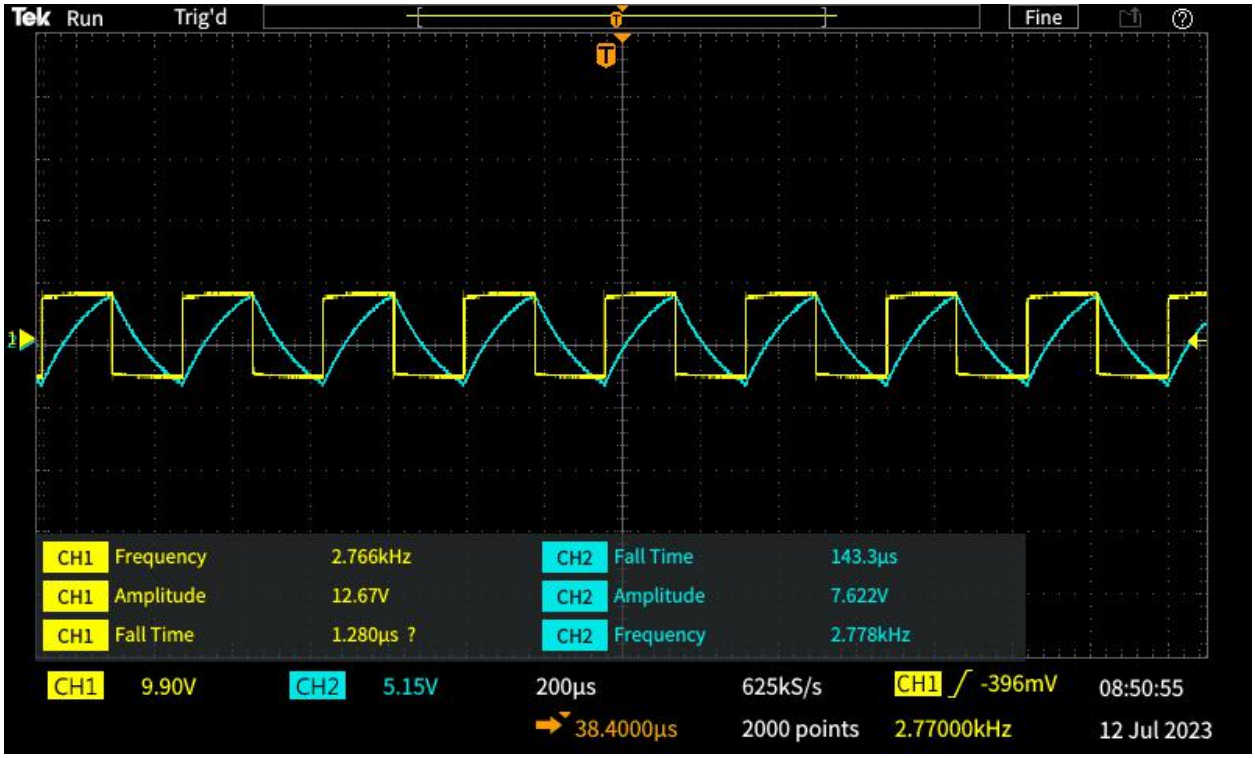

Figure 5.4: The oscilloscope output illustrates the square gate voltage (yellow) alongside the filtered output (blue). Designed with a cutoff frequency of 800 Hz, the low-pass filter is tested using a higher frequency input, effectively demonstrating its filtering capabilities.

Next, I designed a high-pass filter (Fig. 5.5) with a cutoff frequency of 8 kHz. When applied square wave input, the high-pass filter acted as a differentiator, producing an output with a sharp rise and a slow fall. This behavior is characteristic of high-pass filters, which emphasize rapid changes in the input signal. The output featured in Fig 5.7 and 5.6, a sharp rise and a slow fall, highlighting the filter differentiator-like behavior.

By varying the duty cycle of the square wave input voltage, I was able to modify the output

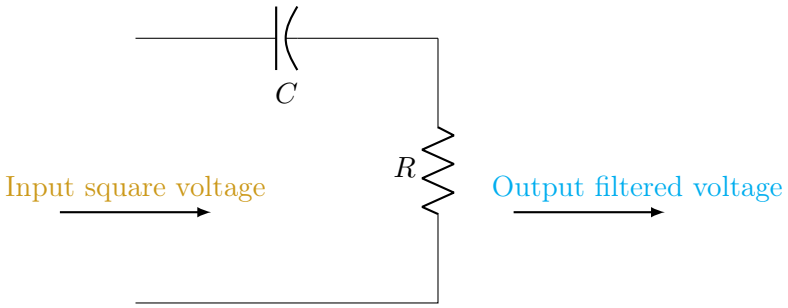

Figure 5.5: High-pass filter topology.

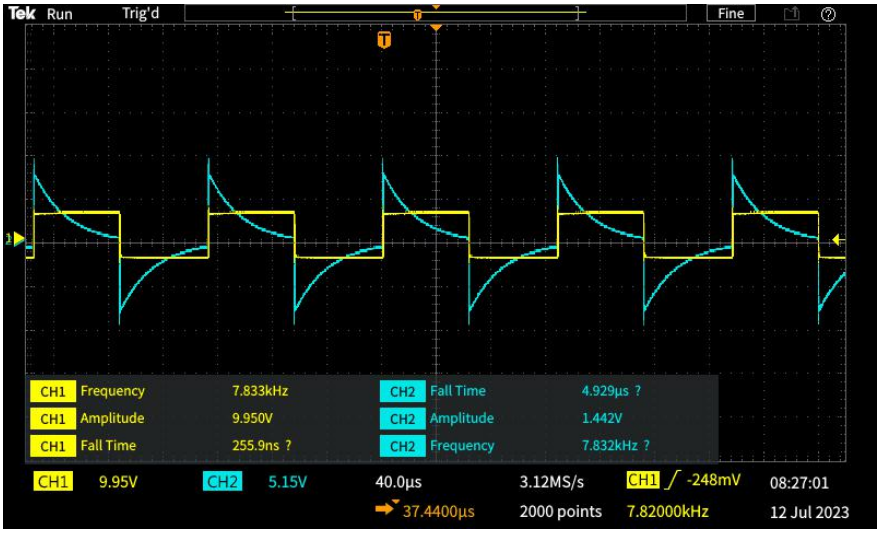

Figure 5.6: The oscilloscope output displays the square gate voltage (yellow) and the filtered output (blue). The high-pass filter, designed with a cutoff frequency of 1 kHz, is tested using a higher frequency input to demonstrate its filtering capabilities.

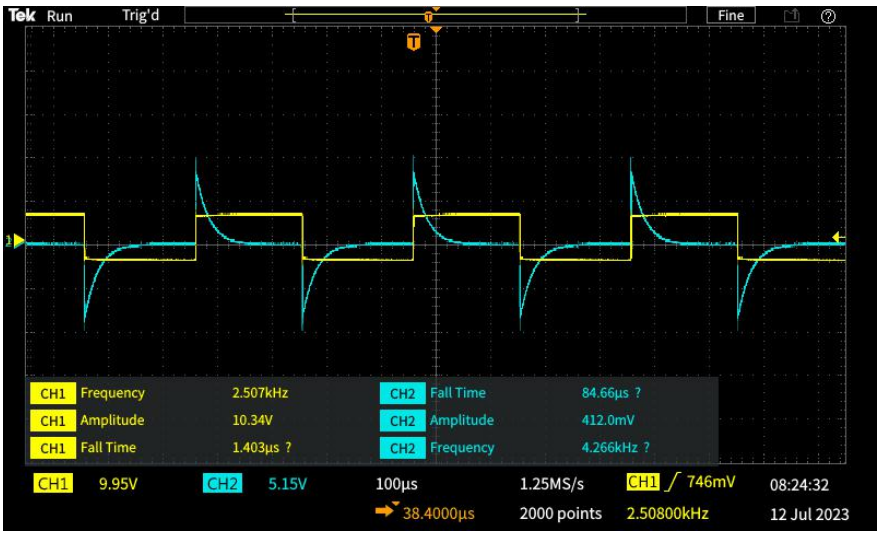

Figure 5.7: The oscilloscope output displays the square gate voltage (yellow) and the filtered output (blue). The high-pass filter, designed with a cutoff frequency of 1 kHz, is tested using a medium-range frequency input to demonstrate its filtering capabilities.

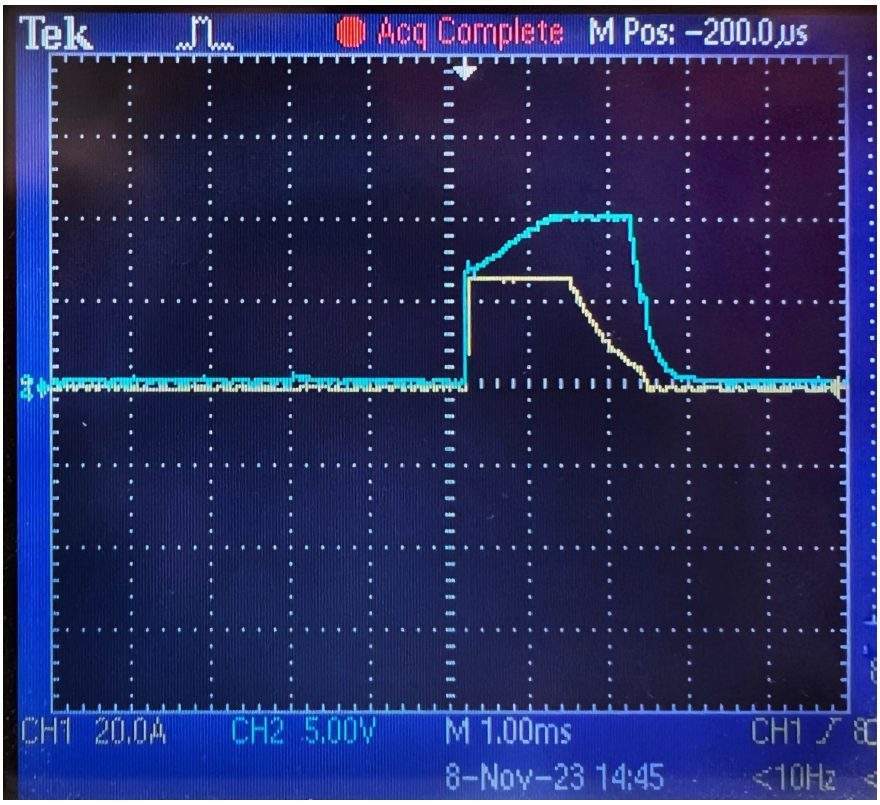

Figure 5.8: Oscilloscope demonstration of a 90% pulse applied to S2 switch from the filter (blue waveform) and the resulting TMS current pulse (yellow waveform) measured using Tektronix A622 current clamp

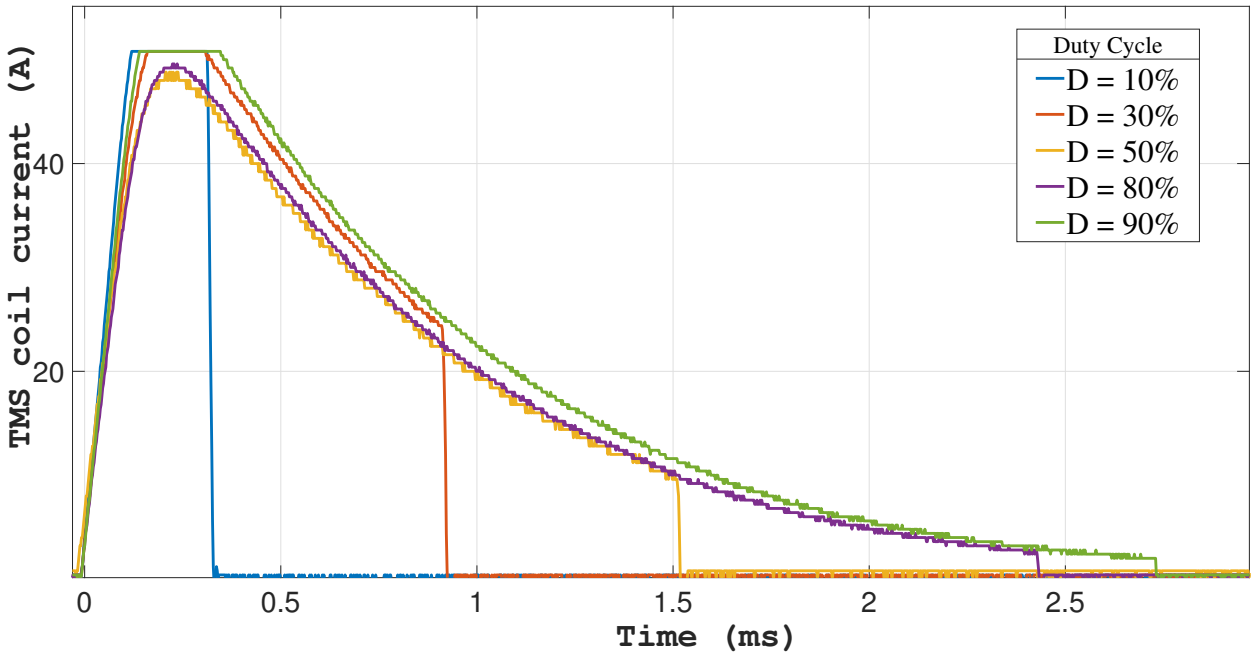

Figure 5.9: The pulse width variation is achieved by controlling the duty cycle of S2 (filtered square gate voltage) within the circuit. This gave the idea of using the gate voltage slope to adjust pulse parameters.

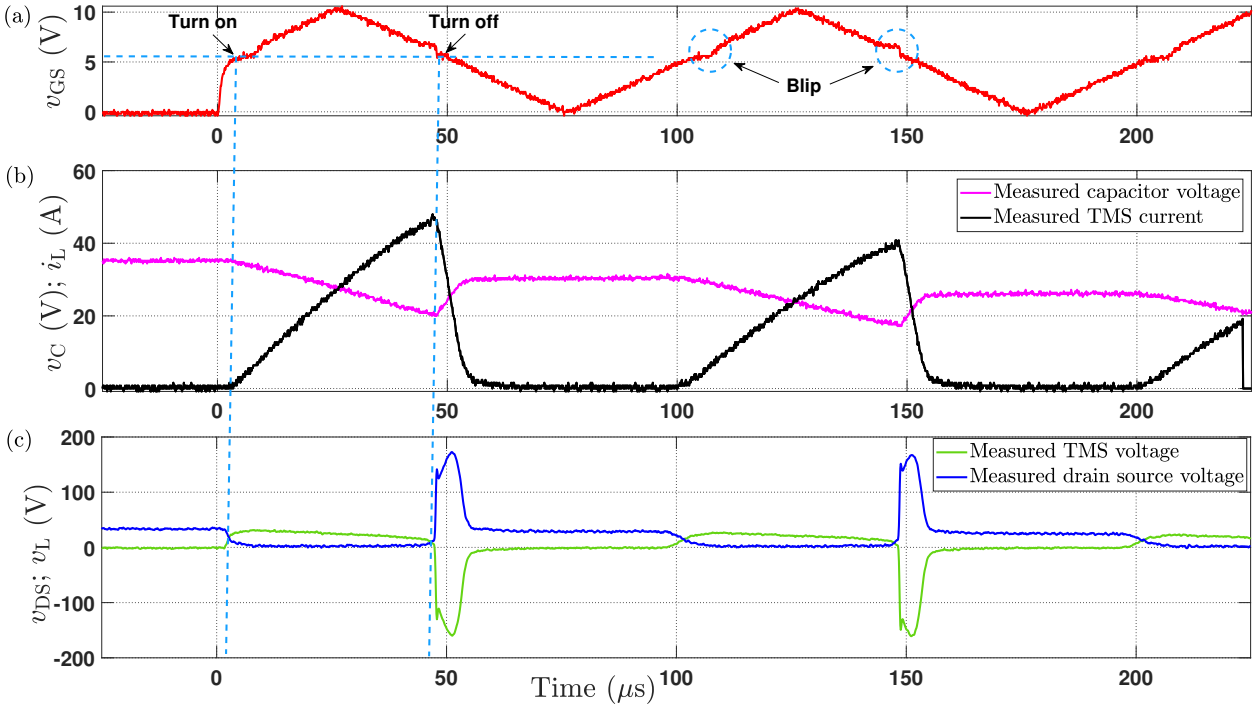

Figure 5.10: Circuit parameters measured during TMS coil excitation (a) Triangular control voltage of MOSFET 2 gate with turn on/off points marked. Blips due to input capacitance are also shown. Note that the triangular wave is not accurately captured for the initial 25 μs due to the configuration of the triggering mechanism in the oscilloscope. (b) Measured electrolytic capacitor voltage (magenta) and measured TMS coil current (black); (c) Drain-source voltage of MOSFET (blue) and measured TMS coil voltage (green).

of the high-pass filter. This allowed some control over the characteristics of the filtered output signal. Specifically, adjusting the duty cycle changed the timing of the sharp rise and slow fall in the output waveform, demonstrating the filter responsiveness to changes in the input signal duty cycle. A higher duty cycle resulted in a longer duration of the sharp rise, while a lower duty cycle shortened this duration.

The high-pass filter was particularly useful in generating specific current pulse shapes when driving a gate voltage with varying duty cycles. Oscilloscope measurement with 90% square Arduino output, filtered and applied to S2 switch, with the resulting TMS current pulse shown in Fig. 5.8. By adjusting the duty cycle, I was able to control the characteristics of the TMS current pulses effectively, achieving the change in pulse shape as shown in Fig 5.9.

By adjusting the duty cycle of the square gate voltage, the duration of the filtered output changed, demonstrating that modifying the MOSFET gate voltage allowed control over the output pulse than simply using it as an on/off switch.

From these filter experiments, I developed the idea that varying the slope of the gate voltage waveform can significantly influence the behavior of the MOSFET. Unlike traditional square wave gating, which operates primarily as an on/off switch, controlling the slope variation offers a more nuanced approach to modulating the output pulse. This insight opens up possibilities for more sophisticated control strategies, where the timing and duration of pulse characteristics can be finely

tuned to suit specific application requirements.

Experimentation with different waveform from the pulse generator, including arbitrary waveforms and triangular shapes, revealed further potential for pulse shaping. Adjusting the symmetry of the triangular waveform altered the slope angle, changing the instant at which the MOSFET turned off and thereby modifying the TMS pulse shape. Notably, the highest voltage was attained when the MOSFET turned off. When the positive slope of a triangle gate waveform crossed the threshold voltage, the electrolytic capacitor C2 discharged, and the inductor stored energy. As the negative slope crossed the threshold voltage, the MOSFET turned off, causing a rapid current fall. This rapid di/dt induced a high voltage across the inductor in the TMS coil. The measurements and points of turn on and turn off are showed in Fig 5.10.

The current-probe has a bandwidth of DC-100 kHz, so gives a much slower response than the measured $v_{\mathrm{L}}(t)$ oscilloscope reading (bandwidth 0-10 MHz). To correct for current probe delay, I advanced the measured current trace by 2 μs prior to plotting (Fig. 5.10). This leftwards timing offset is applied to the current traces throughout this thesis. In the course of analyzing the circuit behavior, a distinct blip was observed in the gate voltage response, as marked in Fig. 5.10. This anomaly is believed to be associated with the gate capacitance, as the blips exhibit a curvy structure similar to capacitor charging and discharging. Gate capacitance is a parameter in high-speed switching applications as it directly influences the switching behavior and overall performance of the circuit. Rapid charging and discharging of the gate capacitance can also lead to voltage spikes, contributing to the observed blip

Initially, a laboratory pulse generator was used for the triangular waveform, later replaced by a dedicated triangular waveform generator. The generated voltage across the inductor not only has a high amplitude but also increased rapidly which will induced a high rate of change in the electric field, of significance for TMS coil performance for brain stimulation. These improvements and insights were detailed in the 2024 Annual Conference of the IEEE Industrial Electronics Society (IECON) held on 3-6 November, 2024 in Chicago, Illinois. The text of the conference paper is included after this chapter.

5.2.3 Stage III

Building on the successful prototype implementation and pulse shaping, the next phase tested the circuit capability to handle higher voltages. Initially, C2 was charged to 30 V from 1 V, and subsequent testing involved charging C2 to high voltage from 5 V input, resulting in higher voltage and current across the TMS coil. These advancements are discussed and published in the attached journal paper (Section 4.5.2), illustrating the circuit versatility and scalability.

To further enhance the versatility and effectiveness of the circuit design, I embarked on developing a predictive MATLAB model. The model is described in detail in Chapter 6. This model aims to anticipate the performance and effects of incorporating high voltage components into the system.

The development and refinement of this pulse generator for TMS coil excitation demonstrate significant progress, from initial prototype stages to advanced pulse shaping and up-scaling capabilities.

5.3 Control circuit for generation of S1 and S2 pulse

The control mechanism for the gate pulse generation of the S1 MOSFET utilizes an Arduino microcontroller. The Arduino generates a square gate pulse with a frequency of 8 kHz. This pulse is then amplified using a Bipolar Junction Transistor as shown in the corresponding Fig 5.11 (left side). The amplification stage ensures that the gate pulse has sufficient power to drive the MOSFET.

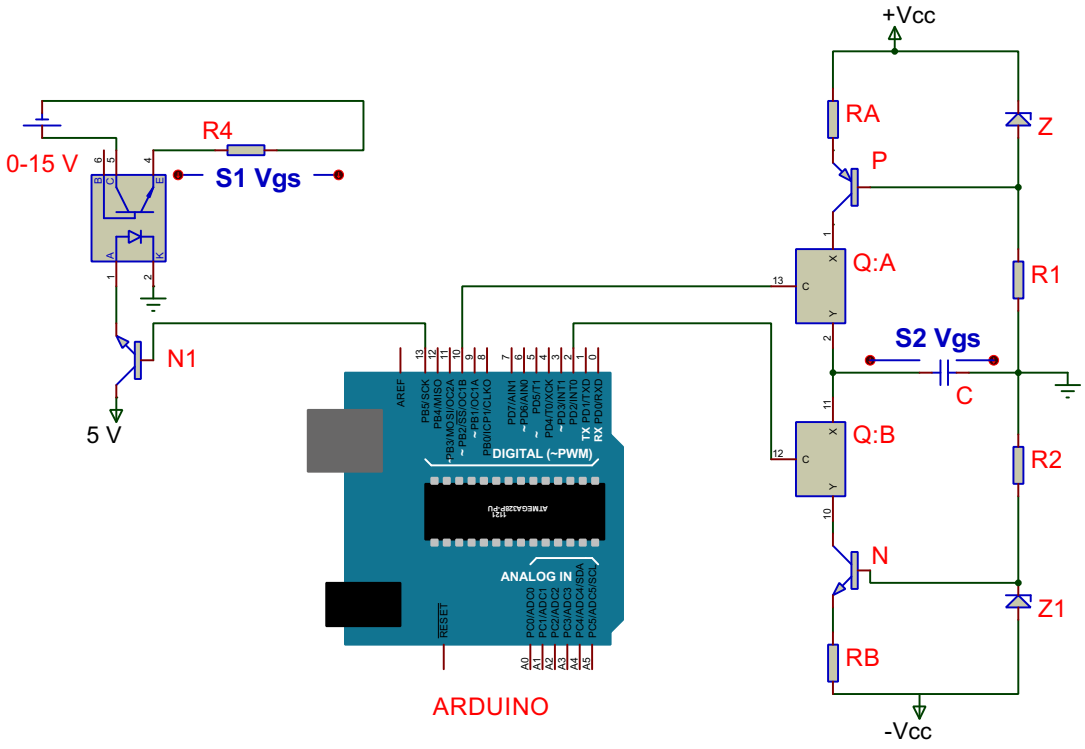

Figure 5.11: Gate voltage generation for S1 and the triangular waveform generator for S2, both controlled by Arduino

To achieve isolation between the main power circuit and the control circuit, the amplified gate pulse is fed into an opto-isolator. This isolation is crucial for protecting the Arduino and other control components from high voltages and currents present in the main power circuit. The output from the opto-isolator is then directed to the gate of S1 through a variable resistor (R4). The variable resistor allows for adjustment of the gate voltage amplitude, enabling either soft or hard switching of the MOSFET. Soft switching reduces switching losses and electromagnetic interference (EMI), while hard switching can provide faster transitions.

The S2 MOSFET requires a triangular gate voltage for its operation. To generate this, a variable slope adjustable triangular waveform generator is employed as shown in Fig. 5.11 (right side). This generator allows for the adjustment of both the slope and symmetry of the triangular waveform. The core of this generator is a constant current source circuit, which includes zener diodes, resistors,

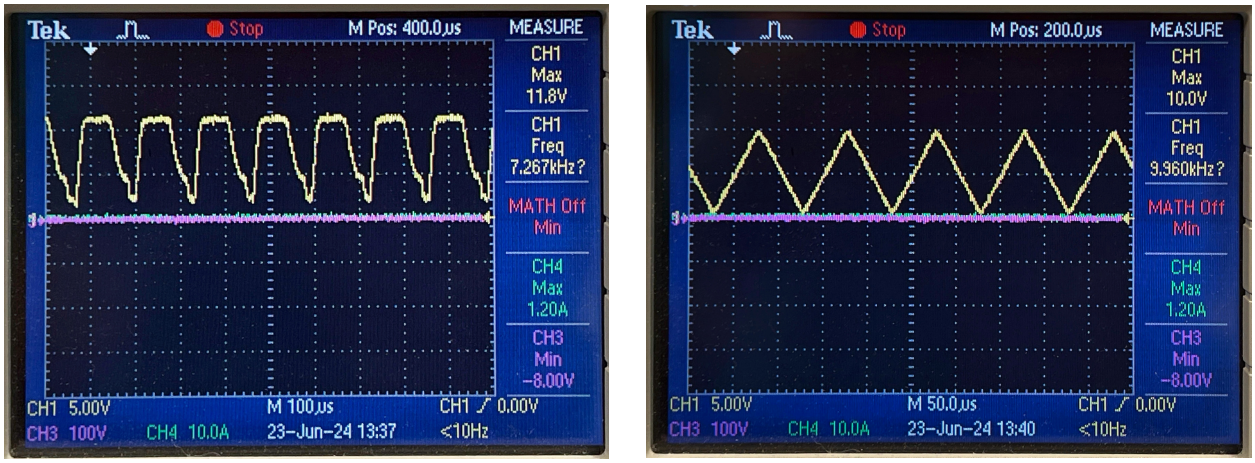

Figure 5.12: S1 (left) and S2 (right) gate voltage oscilloscope measurements from the driver circuit

and transistors.

The constant current source is designed to charge and discharge a capacitor linearly, creating a triangular voltage waveform across it. The zener diode (Z) and a resistor divider network provide a stable reference voltage, which is applied to the base of NPN (N) and PNP (P) transistors. This configuration ensures a constant current flow through the capacitor, controlled by the emitter resistor. The direction of the current, whether positive (charging) or negative (discharging), is controlled by the switches Q:A and Q:B. When Q:A is activated (on) and Q:B is deactivated (off), the current flows through the capacitor, resulting in the charging of the capacitor. Conversely, when Q:A is deactivated (off) and Q:B is activated (on), the current flows through the capacitor in the opposite direction, causing it to discharge. This switching mechanism allows for the generation of a stable triangular wave with a controllable slope. By varying the emitter resistor (RA & RB), the current, and hence the slope of the triangular waveform, can be adjusted. The mathematical relationship governing the triangular waveform is given by:

$$Q = I\Delta t = C\Delta V \tag{5.1}$$

$$\frac{\Delta V}{\Delta t} = \frac{I}{C} \tag{5.2}$$

where Q is the charge stored in the capacitor, C is the capacitance, Δt is the charging or discharging time which is approximately 5RC (time constant), and ΔV is the voltage change across the capacitor. Therefore, the voltage of the capacitor over time can be expressed as:

$$V_{(t)} = \frac{1}{C}\int_{-\infty}^{t} I(t)dt \tag{5.3}$$

Two current sources are utilized to manage the charging and discharging cycles of the capacitor. These sources provide a constant current, ensuring a linear change in voltage over time, crucial for generating a precise triangular waveform. The choice of capacitor is critical as it determines the frequency of the triangular waveform. Since the time constant determines the rise time and fall

time, it directly influences the pulse width of the waveform. The inverse of the pulse width gives the frequency. Higher frequencies necessitate smaller capacitors to achieve shorter charging and discharging times, while lower frequencies require larger capacitors. Analog switches control the flow of current for charging and discharging the capacitor. During the charging phase, one switch closes to allow current flow into the capacitor, while the other remains open. During the discharging phase, the roles reverse. The control signal to turn on the switches for the charging and discharging paths is provided by an Arduino. The pulse output from the driver circuit for S1 and S2 is shown in Fig. 5.12.

In conclusion, the control circuits for S1 and S2 MOSFETs are designed to ensure precise gate pulse generation and isolation from the main power circuit. The Arduino and BJT amplifier setup for S1 and the constant current source-based triangular waveform generator for S2, combined with appropriate control mechanisms, provide robust and adjustable control suitable for various experimental conditions.

5.4 Demonstrating control over TMS coil current pulse shape

This section delves into the experimental evaluation of using triangular waveform to control pulse shapes for TMS applications. By manipulating the symmetry and amplitude of the triangular gate voltage, significant variations in the resulting voltage and current pulses in the TMS coil were observed. These experiments demonstrate the potential for precise control over pulse characteristics, crucial for optimizing TMS efficacy. The investigation also explores the generation of biphasic pulses and the effects of symmetry change, highlighting the versatility and scalability of the circuit prototype. Detailed measurements of the magnetic field generated by the TMS coil at various distances further illustrate the practical implications of these findings.

5.4.1 Experimental results

In practical testing, the circuit was primarily operated using the supercapacitor input due to observations of achieving approximately 500 V output with a 3 V input, suggesting that further increases in input voltage could potentially damage the circuit. Experimental analyses were successfully conducted within this medium voltage range. Even with lower input voltages, notably larger magnetic fields were observed compared to previous literature findings [136].

Moreover, the exploration of pulse shaping aspects necessitated sufficient voltage, affirming the adequacy of the chosen voltage range for conducting comprehensive research. While the circuit can be adapted for higher voltage operations by adjusting component specifications, the medium voltage range proved sufficient and conducive for effective experimentation and analysis.

Experimental data shown in Fig 5.13 highlight the effects of different symmetry configurations of the triangular gate voltage on the resulting voltage and current pulses in the TMS coil. For instance, a 50% symmetry (50:50 rise -fall) results in a voltage amplitude of 164 V, whereas an 80% (80:20 rise-fall) symmetry produces a voltage amplitude of 320 V. These results were achieved with the capacitor C2 charged to 30 V from a 1 V SC input, demonstrating the significant impact of

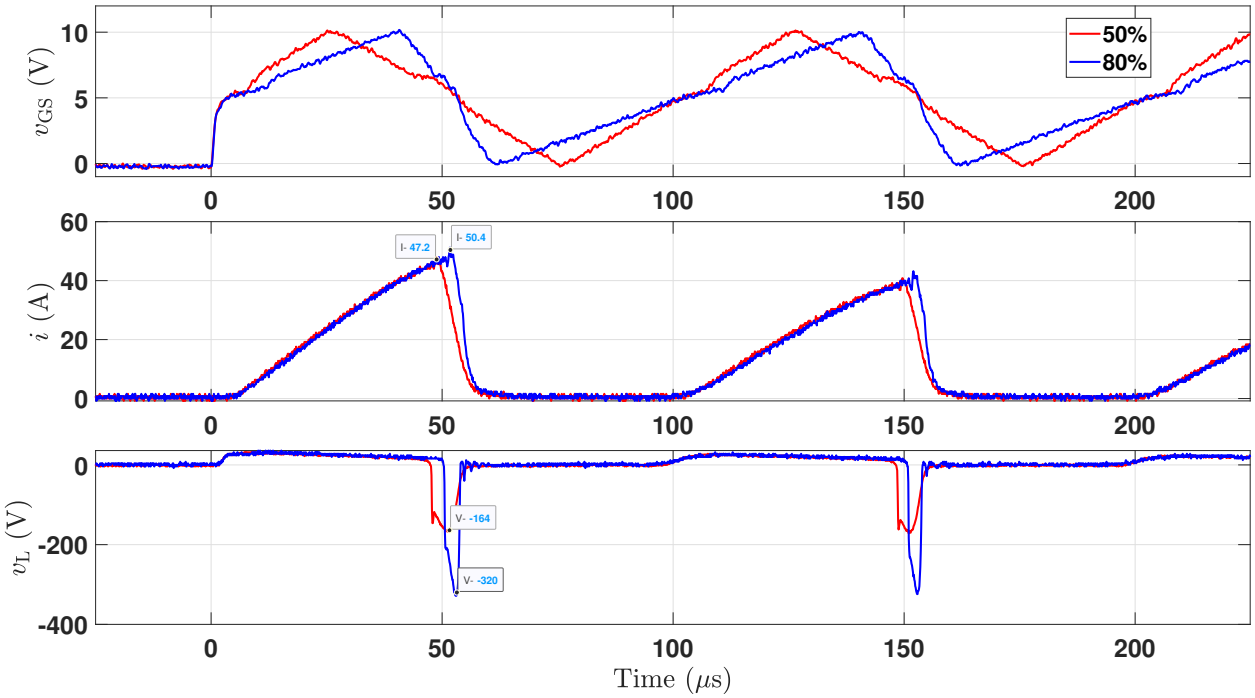

Figure 5.13: Experimental results of 50% and 80% symmetry of the triangular gate voltage (10 kHz) given to S2 and its TMS coil current and voltage pulse respectively. 50% symmetry causes a current pulse of amplitude 47.2 A and voltage ≈200 V. Whereas, 80% symmetry gate voltage produces a current pulse of amplitude 50 A and ≈320 V voltage. Raw traces have been smoothed with a Whittaker filter [176, 177] to reduce oscilloscope 8-bit digitization noise.

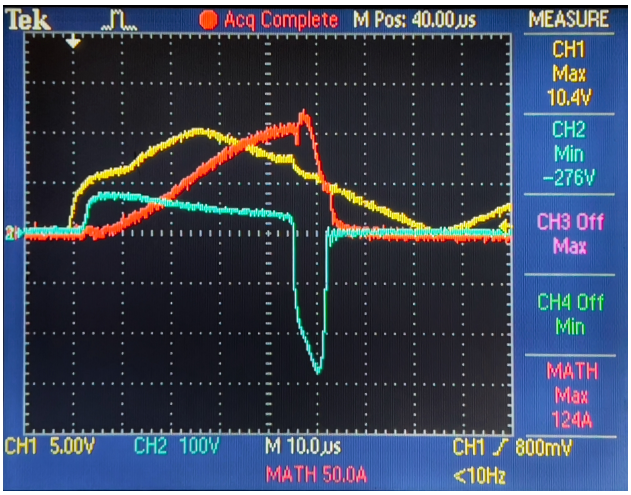

Figure 5.14: Oscilloscope measurement of 50% triangular gate voltage (yellow), TMS coil current measured using Tektronix A622 (red), voltage across the TMS coil (green)

waveform symmetry on pulse amplitude. With a 90% symmetry (90:10 rise-fall), the voltage could reach up to 500 V, although the MOSFETs were not heavily strained during these experiments, indicating the potential for even higher voltages with increased input. The figure 5.14 depicts the oscilloscope output demonstrating 50% symmetry as a proof of concept. High voltage capabilities will be demonstrated using a developed MATLAB model in Chapter 7, showcasing the detailed potential of the circuit prototype.

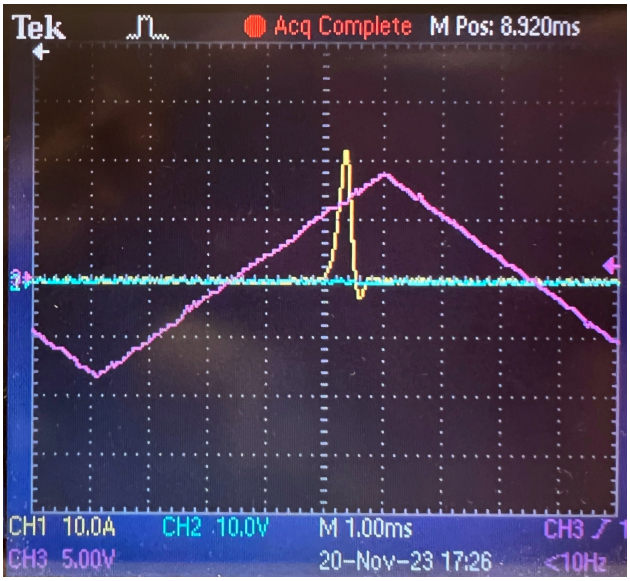

Figure 5.15: Oscilloscope demonstration of biphasic pulse. Magenta waveform represents the gate voltage, while yellow waveform shows the TMS current pulse

To explore the generation of biphasic pulses, experiments were conducted by varying the capacitance of C2 from 330 μF to 100 μF. The oscilloscope measurements captured the waveform shown Fig. 5.15, illustrating how changes in C2 affected the shape and characteristics of the output pulses. This investigation aimed to optimize the pulse generation process, ensuring compatibility with TMS applications. The results, depicted in Fig. 5.16, provide insights into the capacitor role in shaping the output waveform for enhanced TMS efficacy.

The investigation explored the effects of varying the symmetry and amplitude of the triangular gate voltage on the current and voltage pulses of a TMS coil, revealing significant changes in their characteristics. The amplitude variations, as shown in Figure 5.17, influenced the rise and fall times of the corresponding coil current and voltage pulses. However, the more intriguing aspect was the variation in the symmetry of the triangular waveform, which had a pronounced effect on the slope of the falling edge of the triangle, thereby impacting the rate of change of current (di/dt) and the inductor voltage.

In my thesis, "symmetry" refers to the balanced rise and fall characteristics of the triangle waveform used, ensuring uniformity in the waveform's transitions and facilitating predictable signal modulation and pulse shaping in circuit applications. A perfectly symmetric triangular waveform has equal rise and fall times, while an asymmetric waveform has unequal rise and fall times. In the experiment, the symmetry was varied from 10% to 90%, as illustrated in Figure 5.18. The

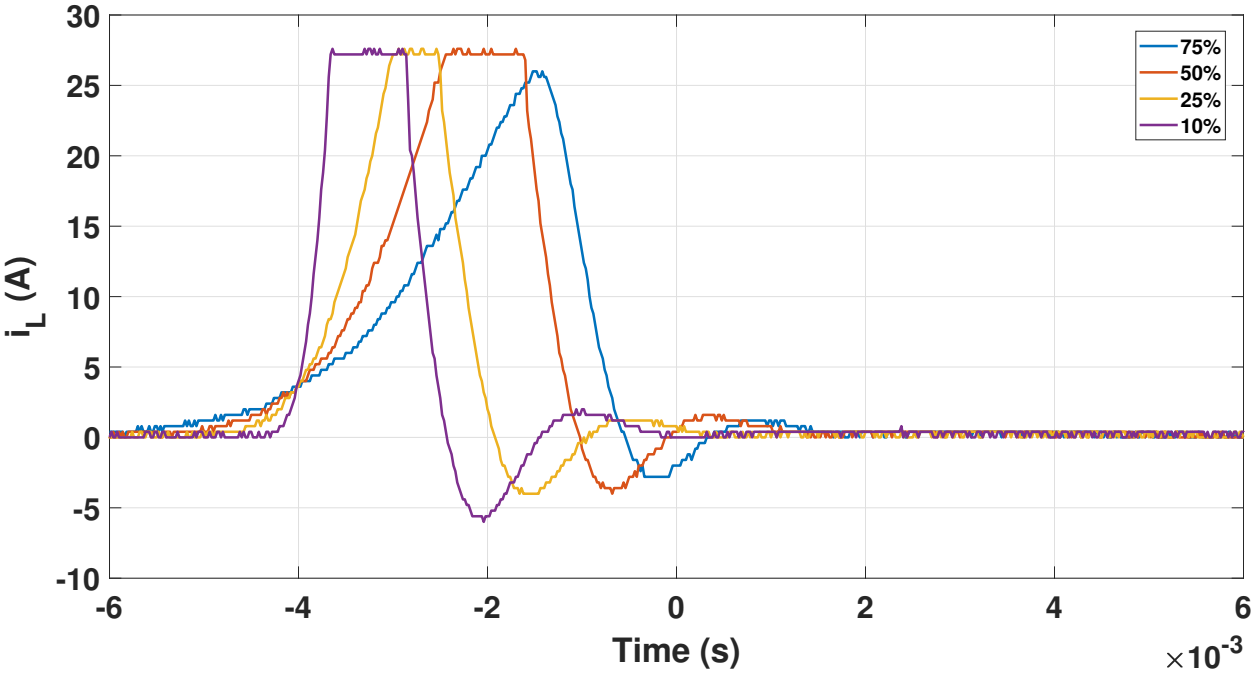

Figure 5.16: The measured coil current for different symmetry gate voltage waveform when C2 = 100 μF capacitor is used (The observed waveform clipping is attributed to measurement limitations with the current clamp)

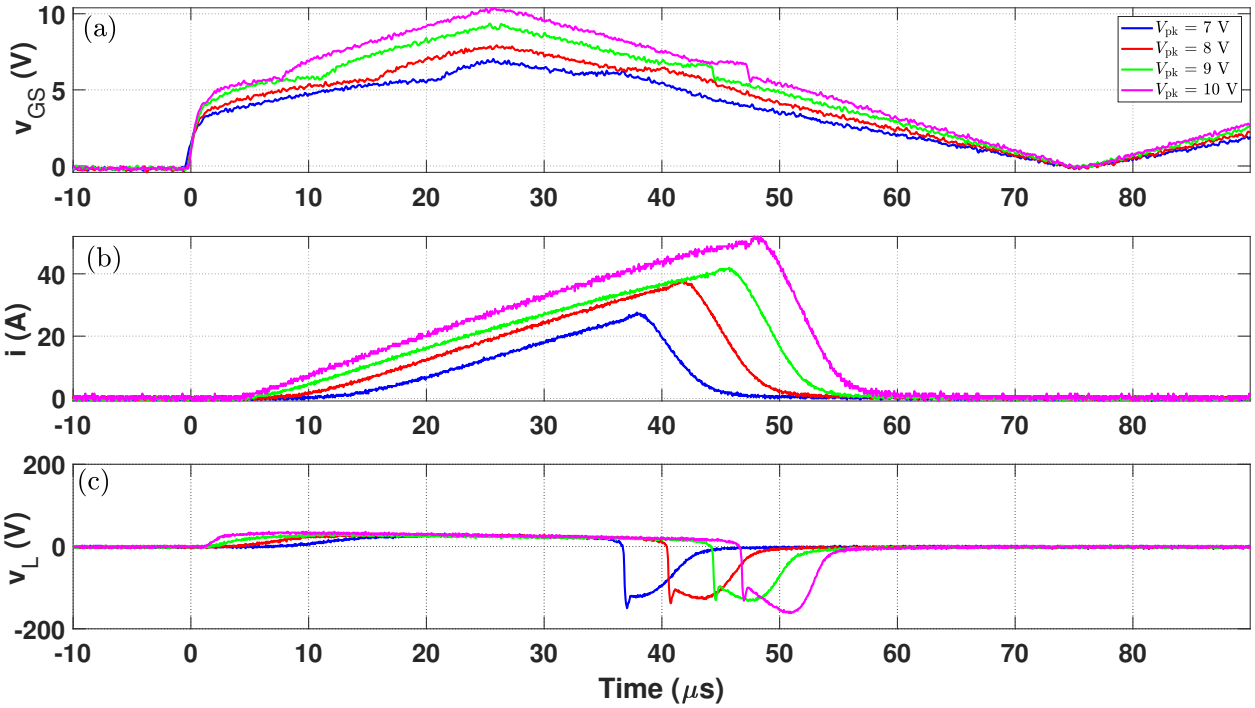

Figure 5.17: Dependence of TMS pulse characteristics on peak gate voltage (a) Peak gate voltage is stepped from 7 V to 10 V; (b) TMS coil current pulse for respective gate voltage; (c) TMS coil voltage.

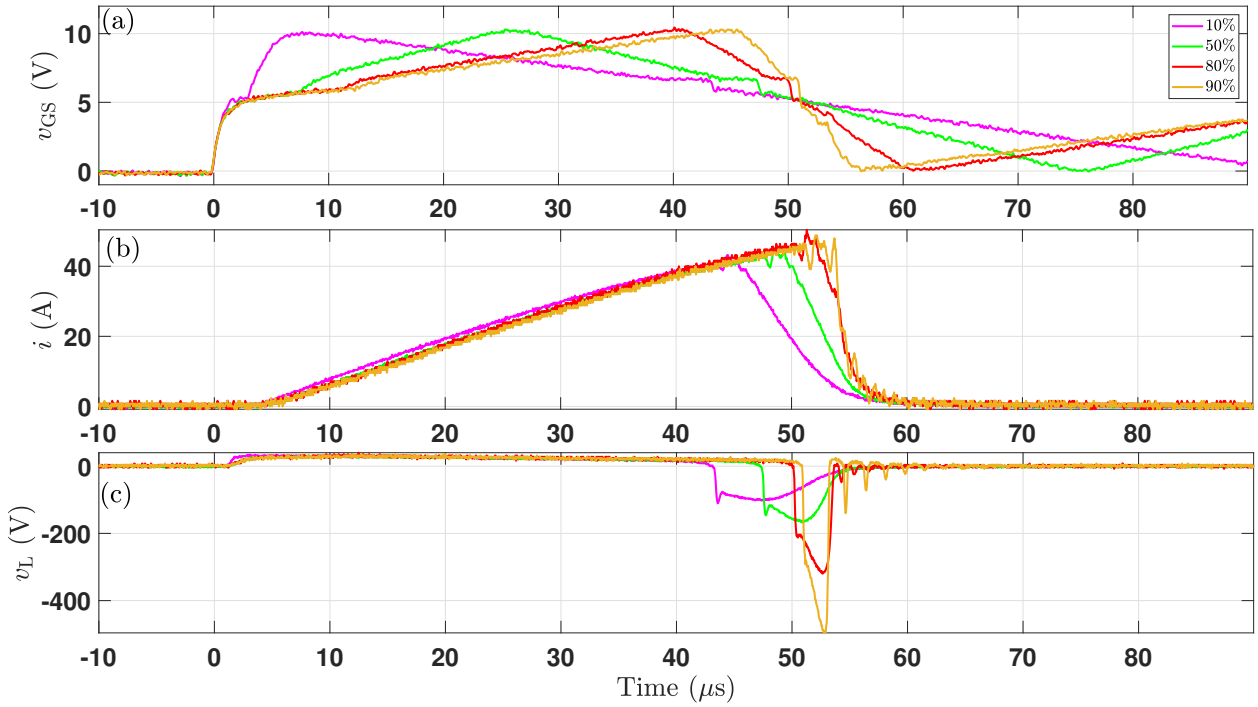

Figure 5.18: Dependence of TMS pulse characteristics on gate voltage symmetry (a) Gate voltage is varied from 10% to 90% symmetry; (b) TMS coil current pulse for respective gate voltage; (c) TMS coil voltage.

experiment results can be summarized as:

1. Triangle waveform dynamics- At 10% symmetry, the rise time is very short, and the fall time is relatively long. This creates a waveform where the voltage quickly reaches its peak and then slowly returns to the baseline. Conversely, at 80% symmetry, the rise time is extended, and the fall time is significantly shortened. This results in a waveform where the voltage rises gradually and then rapidly drops back to the baseline. So clearly, here the gradient dv_{GS}/dt influences the strength and duration of the negative v_L component.

2. Impact on current waveform (di/dt)- The steepness of the falling edge of the triangular waveform directly affects the rate of change of voltage over time (dv/dt). At higher symmetry percentages (such as 80%), the falling edge becomes much steeper. This increased dv/dt translates to a higher di/dt (rate of change of current) in the TMS coil because the voltage across an inductor (v_L) is proportional to the rate of change of current through it (di/dt), as described by the equation:

$$v_L = L\frac{di}{dt} \tag{5.4}$$

where L is the inductance of TMS coil. Therefore, with a steeper fall slope at 80% symmetry, the current slope (di/dt) increases sharply, indicating a rapid change in current.

3. Inductor voltage and pulse width- The sharp increase in di/dt due to the steep fall slope generates a higher voltage across the inductor. This is because the voltage induced in the

inductor is directly proportional to the rate of change of current. As the fall time shortens, the current reaches its peak and then quickly returns to zero. This change in pulse width affects the timing and intensity of the pulses generated by the TMS coil.

The effectiveness of the circuit is demonstrated by its capability to generate high-voltage pulses from relatively low input voltages. As observed in the experimental results, a voltage of 500 V was achieved at 90% symmetry with just a 1 V input from the supercapacitor. This indicates that by adjusting the symmetry of the triangular gate voltage, the circuit can be fine-tuned to achieve the desired pulse characteristics, making it highly efficient for applications requiring precise and powerful pulse generation.

In my experiments, I observed that using a 10% symmetry for the triangle gate voltage results in an increased fall time. This adjustment also leads to a longer voltage pulse width due to the slower decay of the current. Conversely, when the symmetry is increased to 90%, the fall time of the current pulse is significantly decreased. This change causes a reduction in the pulse width of the voltage pulse. At this high symmetry, the gate voltage drops very quickly, which generates higher voltage peaks. Additionally, during my tests at 90% symmetry, I encountered 1 MHz oscillation harmonics, indicating potential issues with stability and higher frequency noise. Due to these rapid voltage drops and associated harmonics, I limited my experiments to a maximum of 90% symmetry to avoid excessive oscillations and ensure more reliable measurements.

In summary, the variation in the symmetry of the triangular gate voltage has significant effects on the current and voltage pulses in the TMS coil system. Increasing the symmetry to 90% creates a much steeper fall slope in the triangular waveform, resulting in a higher rate of change of current (di/dt) through the coil. This increased di/dt generates a higher voltage across the inductor. The experimental results, depicted in Figure 5.18, underscore the circuit efficiency in generating high-voltage pulses from low input voltages, highlighting its potential for applications that require high field (electric/magnetic) intensity pulse generation. This investigation provides valuable insights into how waveform symmetry can be leveraged to optimize the performance of TMS coils and similar electromagnetic systems.

5.5 Magnetic field Measurement

To measure the magnetic field produced, a setup (Fig. 5.19) was arranged with the coil placed in an adjustable holder above a Hall effect sensor that convert output voltage into equivalent magnetic field measurements. Experiments conducted with a 50% symmetry triangular gate voltage at various distances from the sensor showed the magnetic field generated by the TMS coil.

The magnetic field (B-field) measurement process utilized an SS496A1 Hall effect sensor, which was selected for its capability of measuring B-fields up to approximately 200 mT. The Hall effect sensor was calibrated using a Helmholtz coil setup by Dr. Marcus Wilson [136].

For the measurement of the B-field along the axis of the coil, which was expected to be purely axial, the sensor was oriented accordingly as in the Fig. 5.19. Measurements were taken as a function of both axial distance (z) and radial distance (r) from the coil axis. However, close to the coil at

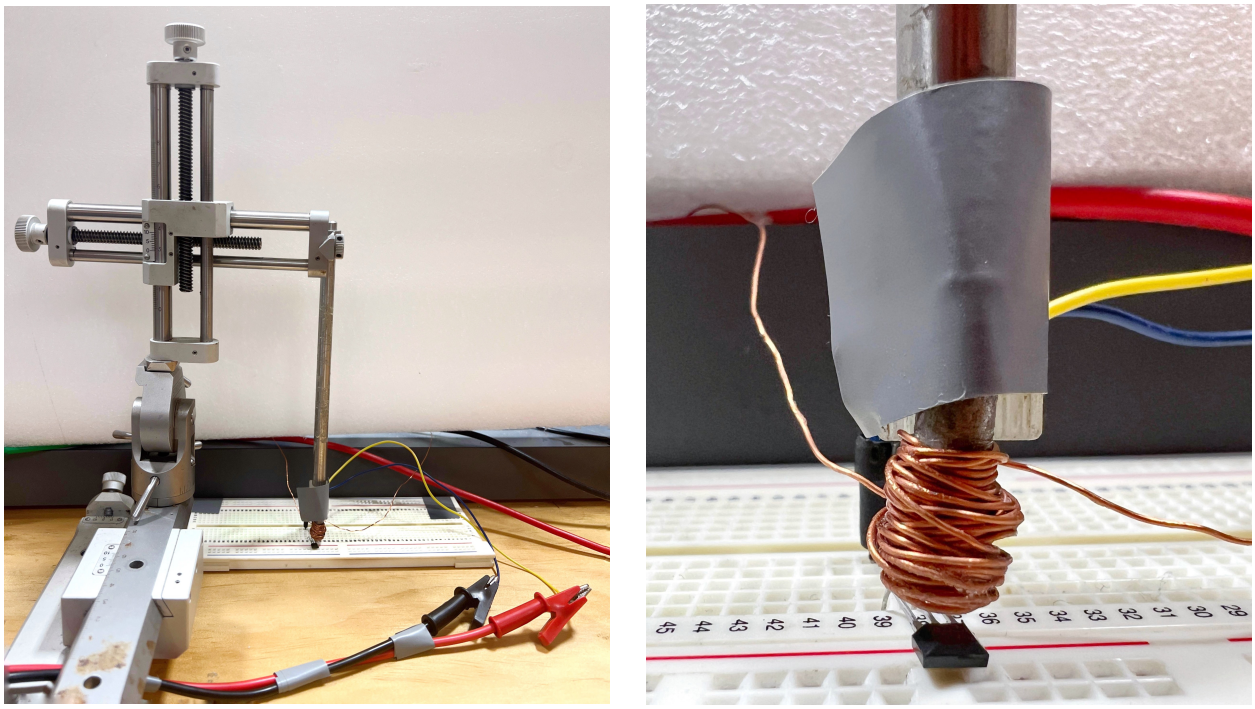

Figure 5.19: Laboratory setup for B-field measurement featuring an SS496A1 Hall effect sensor and a TMS coil mounted on an adjustable stand, enabling precise distance adjustments between the sensor and the coil (left). A zoomed-in view of the Hall effect sensor and the coil within the measurement setup (right).

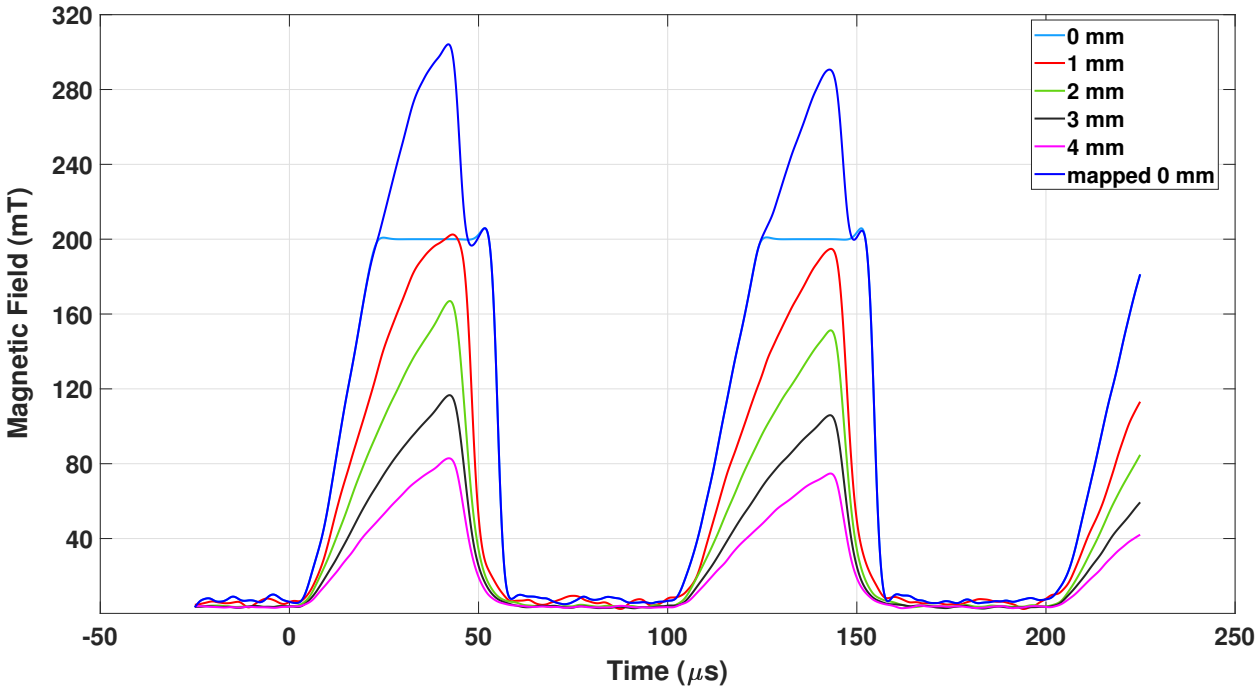

Figure 5.20: Experimental trials conducted with a 50% symmetric triangular gate voltage at distances ranging from 0 mm to 4 mm from the sensor, illustrating the observed magnetic field generated by the TMS coil.

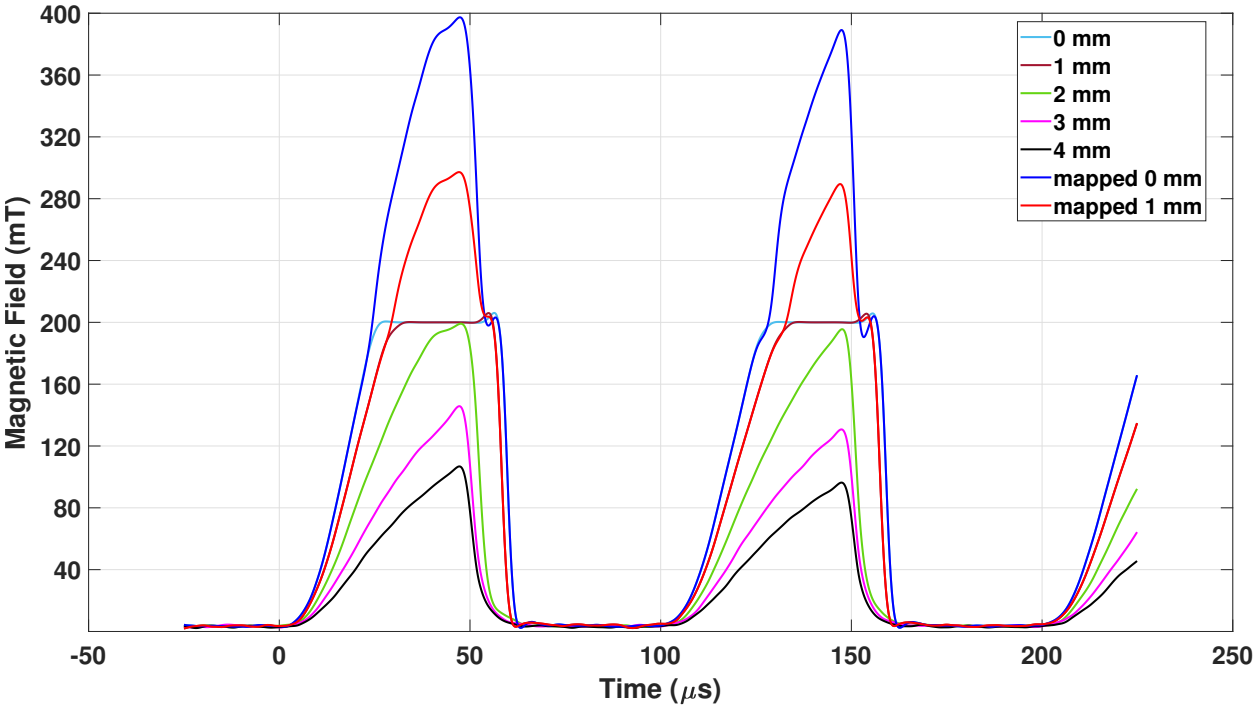

Figure 5.21: Experimental trials conducted with a 80% symmetric triangular gate voltage at distances ranging from 0 mm to 4 mm from the sensor, illustrating the observed magnetic field generated by the TMS coil.

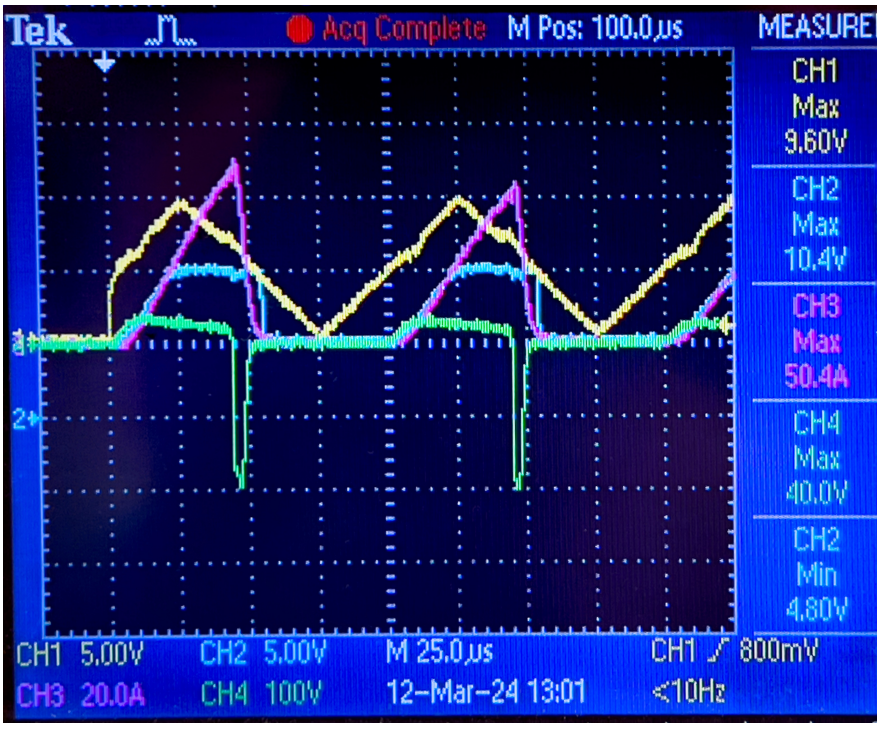

Figure 5.22: Oscilloscope measurement of 50% triangular gate voltage (yellow), TMS coil current (magenta), voltage across the TMS coil (green), magnetic field equivalent voltage measured by SS496A1 solid-state Hall effect sensor (blue) at 0 mm distance

Figure 5.23: Oscilloscope measurement of 80% triangular gate voltage (yellow), TMS coil current (magenta), voltage across the TMS coil (green), magnetic field equivalent voltage measured by SS496A1 solid-state Hall effect sensor (blue) at 0 mm distance

higher supply voltages, the B-field exceeded the sensor maximum measurable field of 200 mT. To address this, an indirect estimation method was employed for high-intensity fields. This method was based on the assumption that the B-field on the axis (r = 0) could be expressed as a product of two functions: $B(z, V) = f(z)g(V)$, where $f(z)$ is a function of distance from the coil, and $(g(V))$ is a function of the supply voltage. In the direct measurement phase, the B-field at the base of the coil (z = 0 mm) was measured, at which point the sensor reached its maximum measurable field. Additionally, the B-field 2 mm below the coil was measured, providing a reference measurement at a location where the B-field was weaker and within the sensor measurable range. To facilitate comparison, a scale factor (α) was determined such that $B(z = 0 \text{ mm}, V) = \alpha B(z = 2 \text{ mm}, V)$. This scaling accounted for the reduction in field strength due to the increased distance from the coil. Using the determined scale factor α, the B-field at the base of the coil was estimated by multiplying the measurements made 2 mm below the coil by α. This method allowed for the estimation of the B-field in high-intensity regions where the field strength exceeded the sensor direct measurement capability.

In summary, the magnetic field measurement process involved a combination of direct calibration using known B-fields, direct measurement within the sensor range, and an indirect estimation method for high-intensity fields. The calibration ensured accurate sensitivity determination, while the indirect method allowed for the extrapolation of B-field strengths in regions exceeding the sensor direct measurement capabilities. This comprehensive approach enabled detailed mapping of the B-field around the coil, ensuring accurate measurements even in high-intensity regions.

Given that TMS is a contactless procedure, understanding the field strength at around 2 mm

distance is crucial. Figures 5.20 and 5.21 illustrate the magnetic flux density (B-field) in milli-Tesla at different distances from the coil by the above measurement technique. The oscilloscope output in Figures 5.22 and 5.23 for 50% and 80% symmetry is presented as proof of concept.

Increasing the input voltage would proportionally enhance the output voltage and magnetic field strength. Higher input voltages would lead to increased C2 voltage, resulting in higher induced voltages across the inductor and stronger magnetic fields, thus further optimizing the system performance for generating high-intensity pulses.

Limitations & conclusion

One of the primary limitations of the prototype arises from the use of a MOSFET as a resistive element rather than a traditional switch. When the MOSFET is treated as a dynamic element, it is gradually turned on, causing its resistance to vary depending on the applied voltage. This operation often pushes the MOSFET into its threshold region, where it functions more as a variable resistor than a switch. As a result, there is inherent energy loss due to resistive heating, which consequently reduces the amplitude of the output pulse.

Additionally, the entire analysis and development of this prototype have been conducted using a single TMS coil. The coil inductance and resistance values play a crucial role in determining the overall system performance. Changes in the coil characteristics, such as different inductance or resistance values, could introduce new effects and alter the pulse shape, and magnetic field strength. This means that while the prototype works effectively with the current coil configuration, it may behave differently if other TMS coils with varying electrical properties are used. Testing with different coils would be necessary to understand the broader applicability of this approach across different setups. These factors should be considered for further optimization and potential expansion of the prototype's capabilities.

This chapter provides an overview of the development of the full prototype and the evolution of using a triangular gate waveform for S2. It explores how the triangular gate voltage shapes the output TMS pulses, emphasizing the effects of symmetry and amplitude changes on the rise, fall, and pulse width of these pulses. By manipulating the amplitude and symmetry of the triangular pulse, the research demonstrated significant alterations in the temporal characteristics of generated pulses. Notably, achieving a voltage of 500 V at 90% symmetry from a modest 1 V SC input highlights the prototype efficiency in converting low voltages into high-voltage pulses. Additionally, observations show that changes in symmetry can result in magnetic fields exceeding 300 mT. Furthermore, I have demonstrated the ability to transform pulse shapes from monophasic to biphasic through capacitance adjustments although I have not developed bipasic pulses further. These findings underscore the critical relationship between gate waveform characteristics and the resulting TMS output, contributing to advancements in magnetic stimulation technologies.

5.6 Paper published in proceedings of IECON 2024

The following paper was presented at 50th IECON24 (IEEE Industrial Electronics Society), held from November 3-6, 2024, in Chicago, Illinois, and has been published in the IEEE proceedings of the conference titled "Effects of Different Triggering Mechanisms on Pulse Shaping of a TMS Pulse Generator Based on Supercapacitor Energy Storage". A poster detailing the paper was also presented and is included in Appendix A. An attribution detailing the contributions from the authors is included in the Appendix E.

IECON 2024 - 50th Annual Conference of the IEEE Industrial Electronics Society | 978-1-6654-6454-3/24/$31.00 ©2024 IEEE | DOI: 10.1109/IECON55916.2024.10905940

Effects of different triggering mechanisms on pulse shaping of a TMS pulse generator based on supercapacitor energy storage

Soniya Raju
School of science
university of Waikato
Hamilton, New Zealand
sr231@students.waikato.ac.nz

Nihal Kularatna
School of Engineering
University of Waikato
Hamilton, New Zealand
nihalkul@waikato.ac.nz

Marcus Wilson
School of Science
University of Waikato
Hamilton, New Zealand
marcus.wilson@waikato.ac.nz

Alistair Steyn-Ross
School of Science
University of Waikato
Hamilton, New Zealand
alistair.steyn-ross@waikato.ac.nz

***Abstract*—High-voltage pulse generators are useful in many applications such as transient surge simulators, electric fence energizers, and transcranial magnetic stimulation (TMS) systems. Traditionally they are based on a high-voltage DC power supply with or without voltage multipliers for raising the voltage to several thousand volts. In contrast to these complex and costly approaches, we use a pre-charged supercapacitor followed by a step-up transformer and associated output circuitry to develop an inexpensive and flexible high-voltage pulse generator for applications in transcranial magnetic stimulation. Our new approach is to use the high-power delivery capability of commercial supercapacitors. In this work, we explore the advantages of different waveforms applied to the MOSFET associated with the secondary stage of the circuit topology and how they affect the final pulse shape.**

***Index Terms*—Electrical stimulation, Magnetic stimulation, Pulse circuits, Supercapacitors, Transcranial magnetic stimulation (TMS)**

I. Introduction

Traditional high-voltage and/or high-power pulse generators are used in miscellaneous engineering and scientific applications such as (i) TMS, which is used clinically to treat depression, anxiety, Parkinson's disease and multiple sclerosis [1], (ii) electric fence energizers and (iii) transient surge simulators also known as lightning surge simulators [2]. Generally, these high power pulse generator designs are based on the conventional Marx generator [3], and Tesla transformer [4]. Nowadays, these circuits are modified by incorporating switched-mode power supply (SMPS) circuits such as boost, buck-boost, and the isolated buck-boost or flyback converter for various applications.

In TMS, a coil carrying a time-varying current is placed on the surface of the scalp to produce a magnetic field that stimulates the brain. To energize the TMS coil, a high-power pulse generator is required, and designing one is a technical challenge. The pulse needs to be delivered to the coil very rapidly, in the range of one-tenth of a millisecond. The conventional way of producing a TMS pulse consists of an RLC-oscillator circuit, where the interaction between the pre-charged capacitor and the inductor (TMS coil) produces the TMS pulse. Many circuits, categorized as monophasic, biphasic, and polyphasic pulse circuits [5–8], have been used in TMS applications; these circuits are mainly improved versions of inverter topologies. Pulse width is an aspect that has not been studied much before because the variation of pulse width was not possible in conventional stimulators. In order to delve into the intricacies of TMS action on brain cells, small animal TMS studies play a crucial role, allowing for a detailed understanding of its mechanisms [1, 9–11]. Therefore, our initial focus has been on developing a prototype of a small animal TMS coil.

Given that there are two types of TMS experiments (i) for human brain excitation (ii) for small animal studies, our project aims the second type, where few hundred volts peak and a current range of 50 to 100 A is adequate. Most TMS pulse systems are built around a high voltage source (which could be expensive) and associated pulse shaping circuits, which can generate a specific number of repeated pulses for given experimental sequence. With the background expertise of our wider research team on supercapacitors and supercapacitor applications, we recognized that we can eliminate this expensive high voltage source, by the use of a pre-charged low voltage supercapacitor (SC) module and a suitable step up converter and a pulse shaping circuit, concentrating on the design aspects of the SC module and the pulse shaping stage, while maintaining the low cost aspects of the implementation.

Our research presents a novel approach to high-power pulse generation for TMS, eliminating the need for traditional high-voltage DC power supplies. By leveraging the high-power delivery capabilities of supercapacitors, we have created a cost-effective and flexible design that significantly reduces the overall system complexity and expense. This design offers precise control over pulse parameters such as amplitude, width, and rise and fall times, providing versatility previously unexplored in TMS pulse circuit design. We have successfully tested a proof-of-concept prototype, demonstrating its efficacy through experimental measurements and MATLAB-

Authorized licensed use limited to: Univ of Waikato. Downloaded on April 24,2025 at 06:31:49 UTC from IEEE Xplore. Restrictions apply.

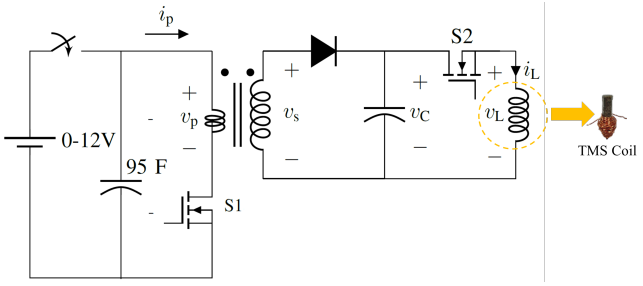

Fig. 1: Circuit topology with TMS coil

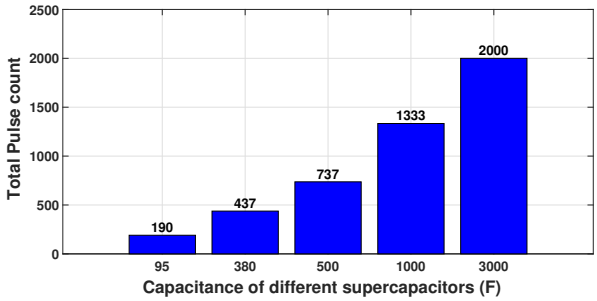

Fig. 2: Total pulse count of the respective supercapacitors with initial voltage of 2 V

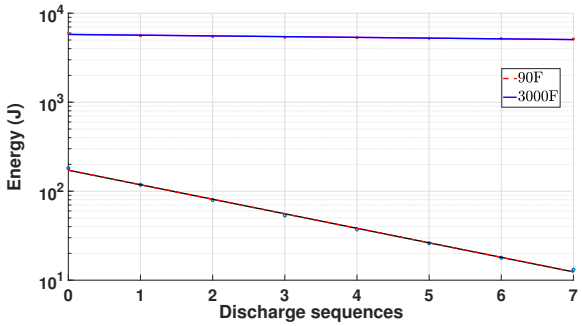

Fig. 3: Energy discharge of 90 F and 3000 F supercapacitor with 2 V initial voltage

based theoretical calculations. Fine-tuning the triangular gate voltage supplied to the final switch allows easy adjustment of the voltage and current pulse in the inductive magnetic coil used in TMS experiments. This innovative methodology introduces a new dimension to TMS pulse generation, offering significant advantages over conventional approaches.

Our team has successfully developed a supercapacitor-based pulse generator [12], enabling the production of a magnetic field of approximately 100 mT suitable for small animal brain excitation. To enhance the flexibility of our prototype, we conducted tests with various shapes of gate voltage waveforms, discovering their capability to deliver high-power pulses and adjust pulse shape. This paper presents a detailed study documenting our incremental improvements in different waveform configurations and their respective effects. In Section II, we emphasize the significance of utilizing supercapacitors as a power source in our circuit by experimental data, while Section III elucidates the operational modes of our pulse generator. Sections IV, V, and VI explain the effects of square, triangular, and sinusoidal waveform gate voltages on the transcranial magnetic stimulation (TMS) coil, respectively. Section VII encapsulates our findings and their implications for future advancements in supercapacitor-based pulse generators.

II. Importance of Supercapacitor as Source in Pulse Generator

Over the last two decades, many capacitor manufacturers have started manufacturing supercapacitors, consequently the prices of these devices have started coming down, particularly for the lower capacitance devices from 1 F to 500 F [6]. The most useful properties of supercapacitors are: (i) very long life compared to limited life-cycle batteries, and (ii) low equivalent series resistance (ESR) which results in high power delivery capability.

A. Supercapacitor based pulse generator implementation; A circuit design summary

Utilizing the advantageous properties of supercapacitors as discussed above, we have successfully constructed a prototype [12], simplified circuit diagram of which is depicted in Fig. 1 with the TMS coil developed by our team [9]. The circuit topology involves the utilization of a precharged supercapacitor, initially charged to a low voltage, such as 2 V. By activating MOSFET S1 at a frequency of 8 kHz, we pump energy to a step-up transformer where the high voltage secondary winding feeds a rectifier circuit charging a high-voltage electrolytic capacitor. A processor subsystem (not depicted in the circuit diagram) manages the operation by halting the function of S1 and activating the output switch S2, which drives the TMS coil [12]. For comprehensive details regarding the circuit design, refer to [12].

B. Commercial supercapacitors and their useful attributes

Table I illustrates the experimental results generated by the use of different sizes of supercapacitors (SC), detailing the pulse generated in each discharge and the overall pulse capacity of each capacitor type. The supercapacitor bank has the capacity to charge till 12 V but in this experiment, all supercapacitors were charged to 2 V and utilized as a primary power source for our prototype. The initial excitation of the TMS coil resulted in a reduction in the input supercapacitor voltage, as indicated in Table I. The experiment was conducted over 8 discharge sequences to provide insights on pulse count and energy. Notably, supercapacitors with higher capacitance exhibited a lower reduction in voltage, enabling a greater number of excitations with the supply voltage of 2 V.

The consistent number of pulses per sequence, ranging between 17 and 20, is also documented in the Table I. Increasing the input voltage in the supercapacitor bank leads to a rise in the number of pulses produced. As depicted in Fig. 2,

Authorized licensed use limited to: Univ of Waikato. Downloaded on April 24,2025 at 06:31:49 UTC from IEEE Xplore. Restrictions apply.

TABLE I: Generated pulse details from supercapacitor.

SUPERCAPACITOR capacitance, ESR	Supercapacitor voltage/ maximum pulse count at each discharge sequence									Avg. voltage reduction (V)	Avg. No:of pulses in single discharge
		1st	2nd	3rd	4th	5th	6th	7th	8th		
90F, 12.8mΩ	V_{SC} (V)	2.01	1.62	1.33	1.09	0.91	0.76	0.63	0.54	0.21	
	Pulse count	22	20	20	18	19	13	13	13		17
280F, 3.2mΩ	V_{SC} (V)	2.02	1.91	1.80	1.70	1.61	1.53	1.45	1.38	0.09	
	Pulse count	17	21	17	19	19	17	20	20		19
500F, 3.2mΩ	V_{SC} (V)	2.002	1.94	1.89	1.83	1.78	1.72	1.67	1.62	0.05	
	Pulse count	20	18	20	18	21	17	16	20		19
1000F, 1.6mΩ	V_{SC} (V)	2.004	1.96	1.92	1.89	1.86	1.83	1.80	1.79	0.03	
	Pulse count	16	19	21	19	20	16	19	19		19
3000F, 0.23mΩ	V_{SC} (V)	2.00	1.93	1.91	1.89	1.88	1.87	1.86	1.85	0.02	
	Pulse count	18	16	20	21	20	21	20	20		20

TABLE II: Key components of the prototype

Component	Assignment	Nominal rating	Part number	Manufacturer
C1	Electrolytic-capacitor	330 μF, 450 V	B43634C5337M062	EPCOS
C2	Supercapacitor	380 F, 3 V, 3.2 mΩ, 257 A	VEC3R0387QG	VINA Tech
S1	Charging switch	40 V, 1.35 mΩ, 350 A	IRFP4004PbF	Infineon Technologies
S2	Discharging switch	650 V, 24 mΩ, 120 A	IXFK120N65X2	IXYS-Littelfuse
L	TMS coil	27 μH, 200 mΩ	Carbonyl powder iron core- P1224-340/9	Micrometals
D	High-frequency diode	1.2 kV, 75 A	STTH75S12W	STMicroelectronics
T	Step-up transformer	1:60 Turns ratio	Ferrite core ZW42207TC	Magnetics

by increasing the size of the supercapacitor module from 95 F to 3000 F with a precharged voltage of 2 V, the total number of pulses keep increasing with the size of the supercapacitor. This illustrates that for a given TMS experiment there is no necessity to have a specially designed DC power supply for the input supercapacitor stage. Once the SC module is precharged, low voltage DC source can be disconnected. The number of output pulses and the associated voltage drop for each case of supercapacitor module is detailed in Table I.

It may be asked why a lithium rechargeable battery is not a good fit for the design instead of a supercapacitor. A comparison between rechargeable batteries and supercapacitors as energy storage devices shows that efficiency and power delivery are significantly influenced by internal resistance. The energy discharge due to the release of TMS type pulses based on two different sized supercapacitor is depicted in Fig. 3. The internal resistance of rechargeable batteries increases with discharge, resulting in a decrease in available power despite a constant open circuit voltage; in contrast supercapacitors maintain a constant equivalent series resistance (ESR) that is about one to two orders of magnitude smaller than that of lithium rechargeable batteries of comparable size. As a result, supercapacitors can deliver very high currents into an external circuit.

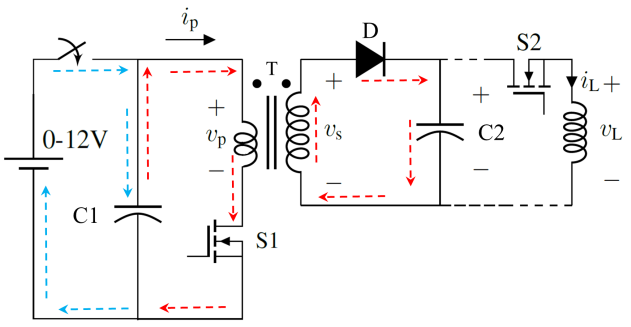

Fig. 4: Mode-1 (blue dotted line) and Mode-2 (red dotted lines) of the circuit topology of the power stage

III. Modes of Operation

Figures 4 and 5 shows the modes of operation of the prototype designed with the hardware components in Table II. This circuit operates in three modes: charging the supercapacitor, charging the electrolytic capacitor, and excitation of the TMS coil.

A. Mode-1: Charging the supercapacitor bank

In this mode, we utilize a standard laboratory power supply to charge the supercapacitor bank. Comprising four 3-V, 380-

Authorized licensed use limited to: Univ of Waikato. Downloaded on April 24,2025 at 06:31:49 UTC from IEEE Xplore. Restrictions apply.

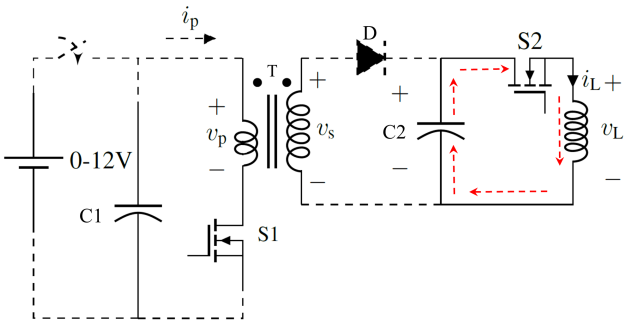

Fig. 5: Mode-3 of the circuit topology. Gate control signals for S1 and S2 ensure that these switches are never ON at the same time

F supercapacitors connected in series to achieve a maximum voltage of 12 V and an effective capacitance of 95 F (380/4), the bank exhibits minimal voltage drop per discharge, as indicated in Table I. Hence, recharging the supercapacitor bank C1 after each discharge is unnecessary, even though it is charged to only 2 V. The utilization of larger supercapacitor will allow for a prolonged operation without recharging. The conducting path for Mode-1 is depicted in Figure 4 with blue dotted lines.

B. Mode-2: Charging the electrolytic capacitor

In this mode, high-frequency switching of DC voltage from the supercapacitor bank results in an pulsed DC voltage. Utilizing a transformer that operates solely with AC, this alternating DC voltage is equivalent to AC and undergoes voltage step-up. To attain the required voltage across C2, MOSFET S1 is operated for 2 seconds at 8 kHz frequency. A ferrite torroidal core is employed for the transformer, with a self-wound 1:60 turns ratio to achieve the necessary step-up. The operational path for Mode-2 in the circuit is illustrated in Figure 4 with red dotted lines.

C. Mode-3: Excitation of TMS coil

Upon reaching the required voltage, MOSFET S2 is triggered to initiate the excitation of the TMS coil. The operational mode is depicted in Figure 5. Triggering S2 can be accomplished using various gate voltage waveforms, with their effects discussed in Sections IV, V, and VI. By employing different waveform types, we can regulate the current and voltage pulse parameters of the TMS coil, thus providing the pulse generator circuit with an additional pulse-shaping feature.

IV. Effect of square gate voltage to S2- initial testing

We initially conducted tests using a 50-Hz square-shaped gate voltage generated by an Arduino microprocessor, leading us to conclude that the circuit [12] is capable of creating a high-voltage pulse generator suitable for TMS applications. Our experiments revealed that this setup generates a magnetic field of 100 mT, sufficient to excite neurons in the mouse brain

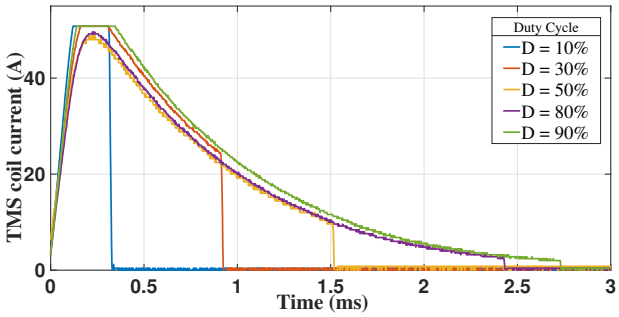

Fig. 6: The pulse width variation by controlling the S2 duty cycle (filtered square gate voltage) within the circuit

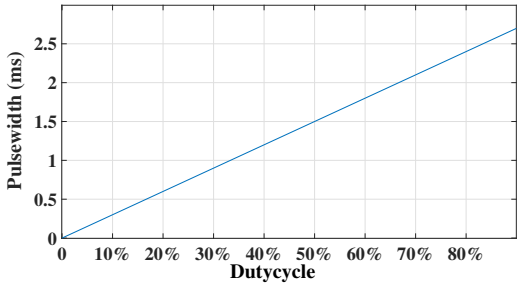

Fig. 7: The variation in pulse width with respect to the duty cycle

[14]. However, since our initial tests did not yield significant pulse shaping results, we explored various possibilities using different types of gate voltage waveform. To achieve this, we filtered the square voltage from the Arduino using a filter consisting of an RC differentiator with a cutoff frequency of 80 Hz, with a square input voltage of 333 Hz. By adjusting the duty cycle of the square voltage from the Arduino, we observed variations in the pulse width of the TMS coil current. Figure 6 illustrates the pulse-width variation at different duty cycles, while Fig. 7 demonstrates that this change in pulse width is directly proportional to the change in duty cycle. This phase showed promising results, indicating that altering the gate voltage waveform could facilitate pulse shaping without

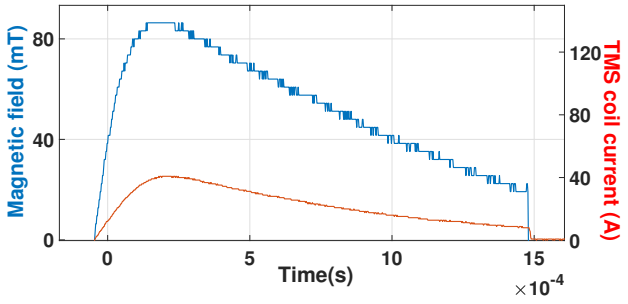

Fig. 8: Current and magnetic fields are proportional implying the TMS core is linear

Authorized licensed use limited to: Univ of Waikato. Downloaded on April 24,2025 at 06:31:49 UTC from IEEE Xplore. Restrictions apply.

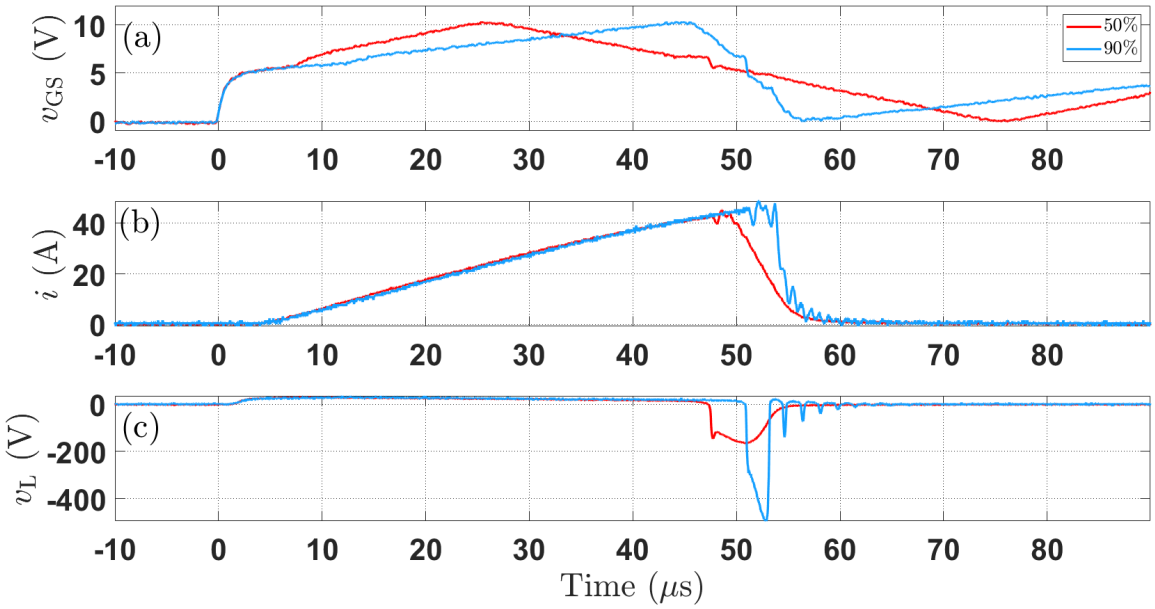

Fig. 9: MATLAB simulation results of 50% and 90% symmetry of the triangular gate voltage (10 kHz) given to S2 and its TMS coil current and voltage pulse respectively. 50% symmetry causes a current pulse of width 60 μs, rise-time of 47 μs and fall-time of 10 μs and voltage $\approx$ 200 V. Whereas, 90% symmetry gate voltage produces a current pulse of 55 μs width, 53 μs rise-time, 6 μs fall-time and $\approx$ 500 V voltage. Raw traces have been smoothed with a Whittaker filter [13] to reduce oscilloscope 8-bit digitization noise.

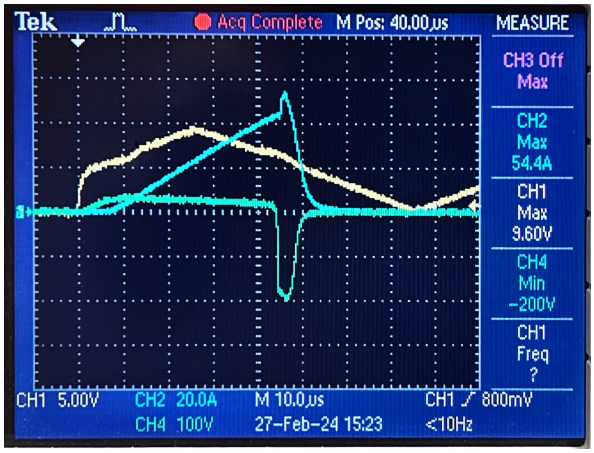

Fig. 10: Oscilloscope measurement of 50% triangular gate voltage (yellow), TMS coil current measured using Tektronix A622 (blue), voltage across the TMS coil (green)

requiring additional circuitry specifically designed for pulse shaping.

Given that this circuit is intended for TMS applications, we measured the magnetic field using an SS496A1 solid-state Hall effect sensor to confirm that we achieved the minimum magnetic field required to excite a small animal brain. Figure 8 depicts the current pulse and magnetic field of a 50% duty cycle pulse, showing a clipping at 100 mT magnetic field. Although the clipping suggests that the magnetic field may exceed 100 mT, it should be noted that the Hall-effect sensor has a limitation of measuring a maximum of 100 mT.

V. Effect of Triangular Gate Voltage to S2

After successfully experimenting with the filtered square gate voltage, we proceeded to test a triangular gate voltage (applied to S2) with a frequency of 10 kHz. Utilizing the adjustability feature provided by the variable slope of the triangle, we replicated the experimental setup using the triangular gate voltage.We charged the supercapacitor to 1 V and allowed the electrolytic capacitor to charge up to 35 V. Remarkably, even with 50% symmetry, we achieved a voltage of 190 V and peak instantaneous power of 9.5 kW for a period of 60 μs (pulse-width). This significant increase in voltage is attributed to the rapid drop in current during the negative-slope portion of the triangular gate voltage. Furthermore, by adjusting the symmetry to 90%, we observed an even more rapid negative slope, leading to a higher rate of change in current as MOSFET S2 turns off. This rapid change in current generates a voltage magnitude of 500 V and peak instantaneous power of 30 kW. Figure 9 illustrates the MATLAB-captured TMS pulse parameters at 50% and 90% symmetry. The variable symmetry of the triangular gate voltage thus provides ample scope for pulse shaping. The oscilloscope measurement of the TMS voltage and current pulse are depicted in Fig. 10.

Authorized licensed use limited to: Univ of Waikato. Downloaded on April 24,2025 at 06:31:49 UTC from IEEE Xplore. Restrictions apply.

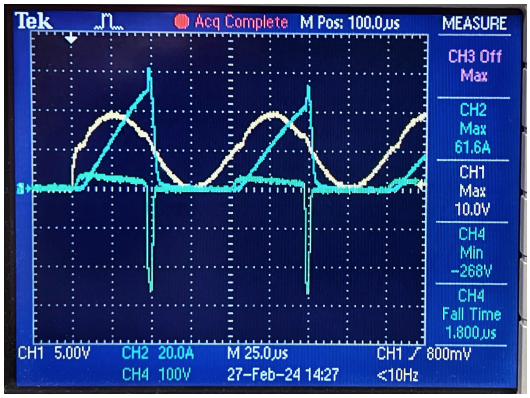

Fig. 11: Oscilloscope measurement of sinusoidal gate voltage (yellow), TMS coil current (blue), voltage across the TMS coil (green)

VI. Effect of sinusoidal gate voltage to S2

Given the smooth rise and fall time of a sinusoidal waveform at 10 kHz, we proceeded to test the experimental setup with sine waveform as well. Figure 11 displays the oscilloscope readings of the TMS parameters observed during coil energization. We recorded a voltage magnitude of 268 V and a current of 61 A using the same 1 V supercapacitor source. This voltage reading exceeds that achieved with the triangular 50% symmetry gate voltage.

VII. Conclusion and future work

In this project we have shown that by the use of precharged SC module followed by a traditional up-converter we can develop a useful pulse generator for TMS experiments on small animals. In order to shape the pulse, we have developed a unique low cost transistor drive circuit and tested it on the basic SC based pulse generator. Adjustable pulse parameters were easily achieved by the proposed wave shaping circuit based on a triangular waveform generator with symmetry adjustment. Further developments are in progress.

Acknowledgment

Authors gratefully acknowledge the University of Waikato Doctoral Scholarship for the research support.

References

[1] A. V. Peterchev, R. Jalinous, and S. H. Lisanby, "A transcranial magnetic stimulator inducing near-rectangular pulses with controllable pulse width (cTMS)," *IEEE Transactions on Biomedical Engineering*, vol. 55, no. 1, pp. 257–266, 2007.

[2] X. Zan, D. R. Torres, R. Kheirollahi, X. Lu, S. Zheng, F. Lu, and A.-T. Avestruz, "Medium voltage pulse power generator for accurate current interruption," *IEEE Transactions on Industrial Electronics*, vol. 70, no. 4, pp. 3604–3615, 2022.

[3] Z. Zhong, J. Rao, H. Liu, and L. Redondo, "Review on solid-state-based MARX generators," *IEEE Transactions on Plasma Science*, vol. 49, no. 11, pp. 3625–3643, 2021.

[4] J. Mankowski and M. Kristiansen, "A review of short pulse generator technology," *IEEE Transactions on Plasma Science*, vol. 28, no. 1, pp. 102–108, 2000.

[5] A. V. Peterchev and D. L. Murphy, "Controllable pulse parameter transcranial magnetic stimulator with enhanced pulse shaping," in *2013 6th International IEEE/EMBS Conference on Neural Engineering (NER)*, pp. 121–124. IEEE, 2013.

[6] A. D. Tang, K. Makowiecki, C. Bartlett, and J. Rodger, "Low intensity repetitive transcranial magnetic stimulation does not induce cell survival or regeneration in a mouse optic nerve crush model," *PloS one*, vol. 10, no. 5, p. e0126949, 2015.

[7] S. M. Goetz, M. Pfaeffl, J. Huber, M. Singer, R. Marquardt, and T. Weyh, "Circuit topology and control principle for a first magnetic stimulator with fully controllable waveform," in *2012 Annual International Conference of the IEEE Engineering in Medicine and Biology Society*, pp. 4700–4703. IEEE, 2012.

[8] L. M. Koponen and A. V. Peterchev, "Transcranial magnetic stimulation: principles and applications," *Neural Engineering*, pp. 245–270, 2020.

[9] F. A. Khokhar, L. J. Voss, D. A. Steyn-Ross, and M. T. Wilson, "Design and demonstration in vitro of a mouse-specific transcranial magnetic stimulation coil," *IEEE Transactions on Magnetics*, vol. 57, no. 7, pp. 1–11, 2021.

[10] M. Wilson, A. Tang, K. Iyer, H. McKee, J. Waas, and J. Rodger, "The challenges of producing effective small coils for transcranial magnetic stimulation of mice," *Biomedical Physics & Engineering Express*, vol. 4, no. 3, p. 037002, 2018.

[11] K. Ali, K. Wendt, M. M. Sorkhabi, M. Benjaber, T. Denison, and D. J. Rogers, "xTMS: A pulse generator for exploring transcranial magnetic stimulation therapies," in *2023 IEEE Applied Power Electronics Conference and Exposition (APEC)*, DOI 10.1109/APEC43580.2023.10131554, pp. 1875–1880, 2023.

[12] S. Raju, N. Kularatna, and M. Wilson, "Supercapacitor based adjustable high power pulse generator for medical research applications," in *IECON 2023-49th Annual Conference of the IEEE Industrial Electronics Society*, pp. 1–6. IEEE, 2023.

[13] H. L. Weinert, "Efficient computation for Whittaker–Henderson smoothing," *Computational Statistics & Data Analysis*, vol. 52, no. 2, pp. 959–974, 2007.

[14] A. Bungert, A. Antunes, S. Espenhahn, and A. Thielscher, "Where does TMS stimulate the motor cortex? Combining electrophysiological measurements and realistic field estimates to reveal the affected cortex position," *Cerebral Cortex*, vol. 27, no. 11, pp. 5083–5094, 2017.

Authorized licensed use limited to: Univ of Waikato. Downloaded on April 24,2025 at 06:31:49 UTC from IEEE Xplore. Restrictions apply.

Chapter 6

MATLAB simulation

This chapter explains the process of developing a MATLAB simulation to model a MOSFET, allowing predictions of its behavior and output of the developed prototype. Initially, here I outline the background study conducted for modeling and explain how I modified existing equations to function within the circuit. Subsequently, I describe the creation of the MATLAB model based on experimental data and then making a complete simulation MOSFET model which can predict the output TMS current and voltage as a function of time according to the gate voltage input as a function of time.

MOSFET principles are described in Chapter 3.

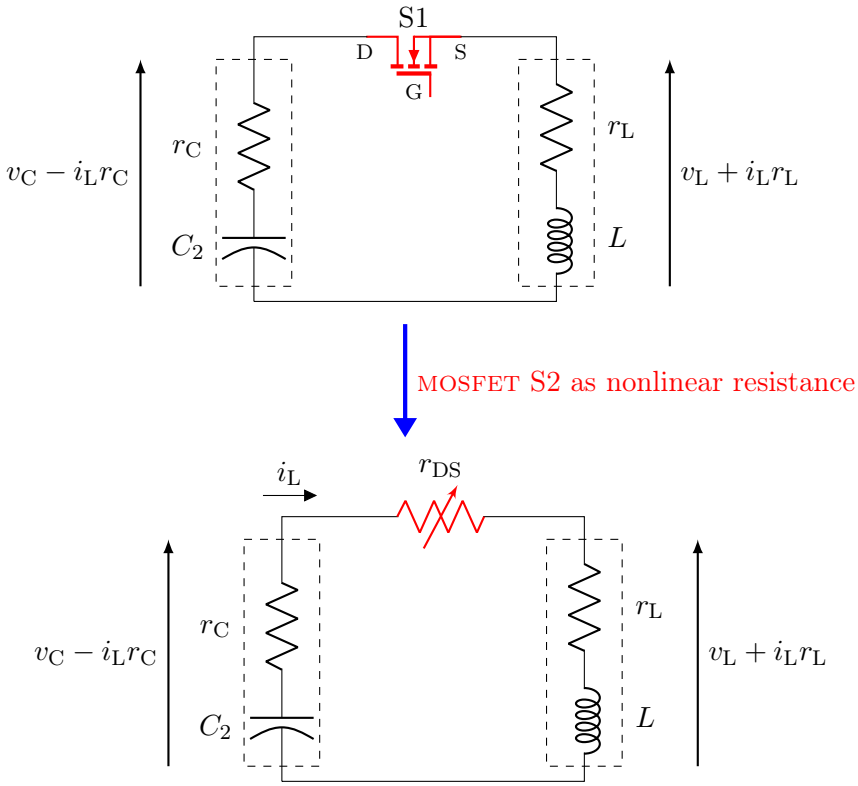

Figure 6.1: Equivalent model of RLC circuit in the prototype consisting the electrolytic capacitor C_2 with internal resistance r_C. For modeling, S2 is considered as a nonlinear resistance r_{DS}, where r_{DS} depends on the gate-source voltage, and TMS coil of inductance L with internal resistance r_L.

The TMS excitation circuit (RLC) is the last stage of the prototype which is illustrated in Fig. 6.1. The objective is to develop a model that solves the differential equation of the RLC circuit.

since

$$v_{\mathrm{C}} = v_{\mathrm{L}} + (r_{\mathrm{L}} + r_{\mathrm{C}} + r_{\mathrm{DS}})i_{\mathrm{L}} \tag{6.1}$$

where $v_{\mathrm{L}} = L\frac{di_{\mathrm{L}}}{dt}$

we obtain a differential equation for i_{L} from Eq. 6.1:

$$\frac{di_{\mathrm{L}}}{dt} = \frac{1}{L}\left[v_{\mathrm{C}} - (r_{\mathrm{L}} + r_{\mathrm{C}} + r_{\mathrm{DS}})i_{\mathrm{L}}\right] \tag{6.2}$$

Thus if we know r_{DS}, we can find $i_{\mathrm{L}}(t)$.

In these equations, I do not consider the MOSFET as a typical switching component. Instead, it is treated as analog, where the MOSFET behaves like a variable resistor controlled by the voltage applied to the gate. Thus, the main aim is to determine the resistance of the MOSFET at each instant whenever there is an input gate voltage and utilize it in the differential equation (Eq. 6.2). The following are the steps I took to develop the MOSFET MATLAB model:

1. Development of the drain-source current equation, $i_{\mathrm{L_{fit}}}$ as a function of v_{GS} (Section 6.1): No equation or expression determines the drain-source current at all the MOSFET regions (subthreshold, at the threshold, above-threshold). So I modified an existing equation used in the literature [178] to fit experimental results.

2. Computing the resistance of the MOSFET: After developing an equation for the current in step 1, the next step is to find the MOSFET drain-source voltage equation. To achieve this, experimental data of v_{DS} (drain-source voltage), v_{GS} (gate source voltage), and i_{L} (TMS coil current) is utilized. Curve fitting is employed on the graph of v_{DS} versus v_{GS} to obtain the v_{DSfit} equation. Curve fitting involves creating a mathematical function or curve that best fits the series of data points obtained from plotting v_{DS} versus v_{GS}. With the v_{DSfit} equation in hand, the $r_{\mathrm{DS_{fit}}}$ of the MOSFET can be determined by:

$$r_{\mathrm{DS_{fit}}} = \frac{v_{\mathrm{DS_{fit}}}(v_{\mathrm{GS}})}{i_{\mathrm{L_{fit}}}(v_{\mathrm{GS}})} \tag{6.3}$$

3. MATLAB model (Section 6.3): Now I can use this $r_{\mathrm{DS_{fit}}}$ in the differential Equation 6.2 as:

$$\frac{di_{\mathrm{L}}}{dt} = \frac{1}{L}\left[v_{\mathrm{C}} - (r_{\mathrm{L}} + r_{\mathrm{C}} + r_{\mathrm{DS_{fit}}}(v_{\mathrm{GS}}))i_{\mathrm{L}}\right] \tag{6.4}$$

   and solve it using any solver available in MATLAB for a given $v_{\mathrm{GS}}(t)$ profile. I have used `ode15s` to obtain good output results depending on the input gate voltage.

I have chosen the MATLAB platform for simulation instead of other options due to the need

for precise characterization of the MOSFET, specifically the IXFK120N65X2, used in the experiment. The circuit performance heavily depends on the MOSFET's turn-off behavior, particularly the dynamic change in resistance during switching.

It would be ideal to simulate the circuit with SPICE or another circuit simulator to demonstrate directly the need for an improved modelling approach. In the early stages of modeling, I explored both LTSPICE and PROTEUS. However, neither platform had the exact MOSFET model (IXFK120N65X2) available. In LTSPICE, the closest available model failed to turn on at the correct threshold voltage, and adjusting the parameters proved nontrivial. Similarly, Proteus did not offer the required device or allow sufficient customization for accurate behavioral representation. While further customization in LTSPICE may have been possible, I opted for MATLAB due to its flexibility in numerical modeling and the ability to implement custom equations and control over simulation logic. This approach allowed for detailed control of model behavior through code and produced simulation results that closely aligned with experimental observations.

To further improve model fidelity, I calculated the instantaneous resistance of the MOSFET using experimental data. Additionally, due to the absence of a unified drain-source current equation valid across all operating regions in existing literature, I developed a new equation to ensure continuous modeling across the cutoff, triode, and saturation regions.

While circuit-level simulations using conventional SPICE tools were considered, they were ultimately not pursued beyond preliminary trials, as they failed to reflect the critical switching characteristics of the actual device. The adopted MATLAB-based modeling provided a more accurate and adaptable framework for the study's objectives.

6.1 Expression for drain current of MOSFET

Here, I explain the stage-by-stage development of the drain-source current equation:

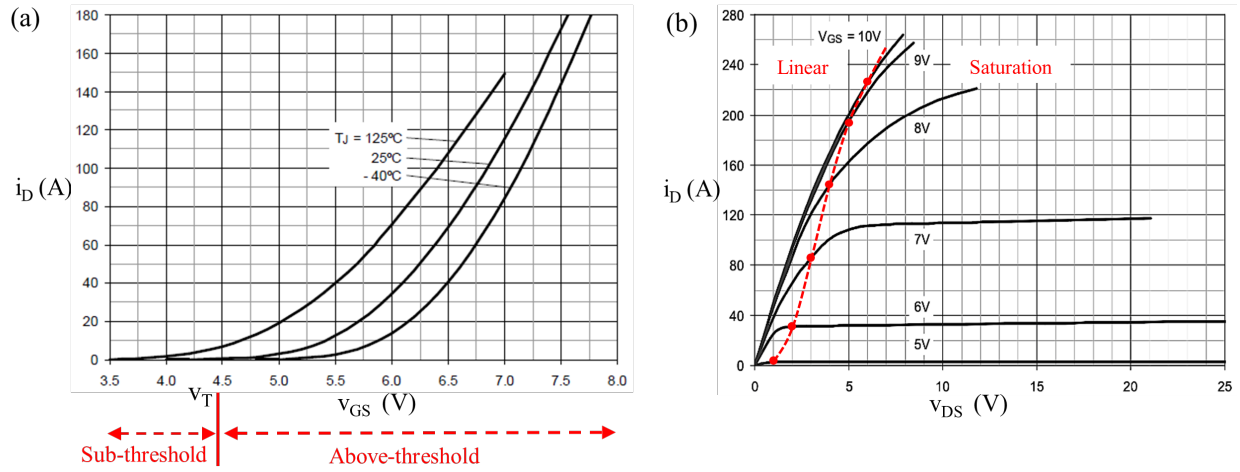

Figure 6.2: (a) Drain current against gate-source voltage for various temperatures and (b) drain current against the drain-source voltage for various gate source voltages of the MOSFET IXFK120N65X2 from data-sheet

A MOSFET operate across four distinct regions as shown in Fig. 6.2: subthreshold, at the threshold, above threshold in a linear manner, and above the threshold in saturation mode.

6.1.1 Subthreshold ($v_{\mathbf{GS}} < v_{\mathbf{T}}$)

In the subthreshold region, also known as the weak/cutoff region, the transistor remains in an "off" state with minimal conduction. The small current flow is described by an exponential function of v_{GS}:

$$i_{\mathrm{D}} \approx i_{\mathrm{D0}} \exp\left(\frac{v_{\mathrm{GS}} - v_{\mathrm{T}}}{\eta\, v_{\mathrm{Th}}}\right) \tag{6.5}$$

where applied gate voltage (v_{GS}), threshold voltage (v_{T}), thermal voltage (v_{Th}), and a subthreshold ideality factor (η) is used. The ideality factor accounts for the subthreshold division of the applied voltage between the gate insulator and the depletion layer [179].

6.1.2 Above-threshold ($v_{\mathbf{GS}} > v_{\mathbf{T}}$)

In above-threshold region where the MOSFET is turned on, there can be two region depending on the drain current characteristics with respect to drain-source voltage as in Fig 6.2(b). They are linear and saturation mode.

1. In triode/linear/ohmic mode ($v_{\mathrm{GS}} > v_{\mathrm{T}}, v_{DS} < (v_{\mathrm{GS}} - v_{\mathrm{T}})$), the MOSFET is fully turned on, and the channel is strongly formed, allowing current to flow easily between drain and source. In this region, the channel resistance is minimized and approximately constant, characterized by a low drain source resistance. The device behaves like a voltage-controlled resistor. The drain current in linear/ohmic mode is :

$$i_{\mathrm{D}} = \mu_n C_{\mathrm{ox}} \frac{W}{L}\left((v_{\mathrm{GS}} - v_{\mathrm{T}})v_{\mathrm{DS}} - \frac{{v_{\mathrm{DS}}}^2}{2}\right) \tag{6.6}$$

   where μ_n is the charge carrier effective mobility, C_{ox} is the gate oxide capacitance per unit area, gate width (W) and gate length (L) [180, 181]. According to this equation, when the drain voltage is small when compared with $(v_{\mathrm{GS}} - v_{\mathrm{T}})$, the drain current-voltage relationship becomes linear:

$$i_{\mathrm{D}} = \mu_n C_{\mathrm{ox}} \frac{W}{L}\left((v_{\mathrm{GS}} - v_{\mathrm{T}})v_{\mathrm{DS}}\right) \tag{6.7}$$

2. The saturation mode ($v_{\mathrm{GS}} > v_{\mathrm{T}}$, $v_{\mathrm{DS}} > (v_{\mathrm{GS}} - v_{\mathrm{T}})$), the MOSFET channel experiences pinch-off near the drain end. Although the drain-source voltage continues to increase, the current becomes relatively independent of v_{DS} and primarily depends on v_{GS}. The drain current in saturation mode is:

$$i_{\mathrm{D}} = \mu_n C_{\mathrm{ox}} \frac{W}{L}\left[v_{\mathrm{GS}} - v_{\mathrm{T}}\right]^2 \left[1 + \lambda v_{\mathrm{DS}}\right] \tag{6.8}$$

The parameter λ accounts for the impact of channel length modulation on drain current, known as the Early effect [182]. It represents the change in drain current with respect to drain voltage due to variations in the channel length. Combining both modes, the equations (Eq. 6.7 and 6.8) exhibits a linear behavior with saturation at the end. Fig. 6.2 shows the data-sheet version of input and output characteristics with different regions.

6.1.3 Near threshold

There is a commonly overlooked region in analysis and application of transistors, known as the threshold voltage region [183–186].

However, in my application, MOSFET operates at and near threshold region since the high voltage across TMS coil is achieved at the time of switch off (when gate voltage goes below threshold). Surprisingly, this region has not been thoroughly analyzed by researchers. Analytical solutions like the parallel plate charge control model and the unified charge control model exist [187–189], yet they lack precise analytical solutions for the subthreshold or near-threshold region. Finally for many applications, the approximate solution used from these models are :

$$i_{\mathrm{D}} = 2\ i_{\mathrm{o}} \ln\left[1 + \frac{1}{2}\exp\left(\frac{v_{\mathrm{GS}} - v_{\mathrm{T}}}{\eta\ v_{\mathrm{Th}}}\right)\right] \tag{6.9}$$

where i_0 is the current corresponding to the minority carriers at threshold. This equation can be further expressed in terms of a variable X:

$$i_{\mathrm{D}} = 2i_{\mathrm{o}} \ln\left[1 + \frac{X}{2}\right], \quad \text{where} \quad X = \exp\left(\frac{v_{\mathrm{GS}} - v_{\mathrm{T}}}{\eta\ v_{\mathrm{Th}}}\right). \tag{6.10}$$

Subthreshold region: In the subthreshold region ($v_{\mathrm{GS}} < v_{\mathrm{T}}$), where $X \ll 1$, we can approximate the exponential term for small values as:

$$\ln[1 + \frac{X}{2}] \approx \frac{X}{2} \quad \text{for small X.} \tag{6.11}$$

This simplifies Eq. 6.9:

$$i_{\mathrm{D}} \approx 2i_{\mathrm{o}}\left[\frac{X}{2}\right] = i_{\mathrm{o}} \exp\left(\frac{v_{\mathrm{GS}} - v_{\mathrm{T}}}{\eta v_{\mathrm{Th}}}\right). \tag{6.12}$$

Above-threshold region: In the above-threshold region ($v_{\mathrm{GS}} > v_{\mathrm{T}}$), where $X \gg 1$, the exponential term dominates. We can approximate it as:

$$\ln\left[1 + \frac{X}{2}\right] \approx \ln\left[\frac{X}{2}\right]. \tag{6.13}$$

and Eq. 6.9 simplifies to:

$$i_{\mathrm{D}} \approx 2i_{\mathrm{o}} \ln\left(\frac{1}{2}\right) + 2i_{\mathrm{o}} \frac{v_{\mathrm{GS}} - v_{\mathrm{T}}}{\eta v_{\mathrm{Th}}}. \tag{6.14}$$

At threshold: At the threshold ($v_{\mathrm{GS}} = v_{\mathrm{T}}$), we have:

$$X = 1, \tag{6.15}$$

so the equation becomes:

$$i_{\mathrm{D}} = 2i_{\mathrm{o}} \ln\left[1 + \frac{1}{2} \cdot 1\right] = 2i_{\mathrm{o}} \ln\left(\frac{3}{2}\right). \tag{6.16}$$

Thus threshold condition, the current i_{D} is not equal to i_{o}.

Equation 6.9 is suitable for both above and below the threshold but not near the threshold [178, 190, 191]. All analytical approaches available are designed for lower power and small-signal MOSFETs. But no analytical model have been developed for power MOSFETs. I initially tried to use Eq. (6.9) to fit the data points of the measured drain current versus gate voltage for power MOSFET, but failed. Thus I modified the drain current equation to read:

$$i_{\mathrm{D}} = \frac{i_{\mathrm{o}}}{\ln 2} \ln\left(1 + \left[\exp\left(\frac{v_{\mathrm{GS}} - v_{\mathrm{T}}}{\eta\ v_{\mathrm{Th}}}\right)\right]^{p}\right) \tag{6.17}$$

This equation can be further expressed in terms of a variable X:

$$i_{\mathrm{D}} = \frac{i_{\mathrm{o}}}{\ln 2} \ln[1 + X^{p}], \text{where } X = \exp\left(\frac{v_{\mathrm{GS}} - v_{\mathrm{T}}}{\eta\ v_{\mathrm{Th}}}\right). \tag{6.18}$$

Where, I have introduced a new parameter, the exponent p, and replaced the factor 2 in Eq. (6.9) with $\frac{1}{\ln 2}$.

Figure 6.3(a) illustrates the failed curve fit using Eq. 6.9, while Fig. 6.3(b) demonstrates the successful fit achieved by employing the modified equation (6.17), which aligns much better with the data points (black dotted points).

The reason for the modification become apparent by analyzing it in three different regions.

1. **SUBTHRESHOLD**: In the subthreshold region ($v_{\mathrm{GS}} < v_{\mathrm{T}}$), where $X \ll 1$, I use $p = 1$ (I have given the maximum value for the p since subthreshold region characteristics is of more exponential behavior):

$$i_{\mathrm{D}} = \frac{i_{\mathrm{o}}}{\ln 2} \ln[1 + X], \tag{6.19}$$

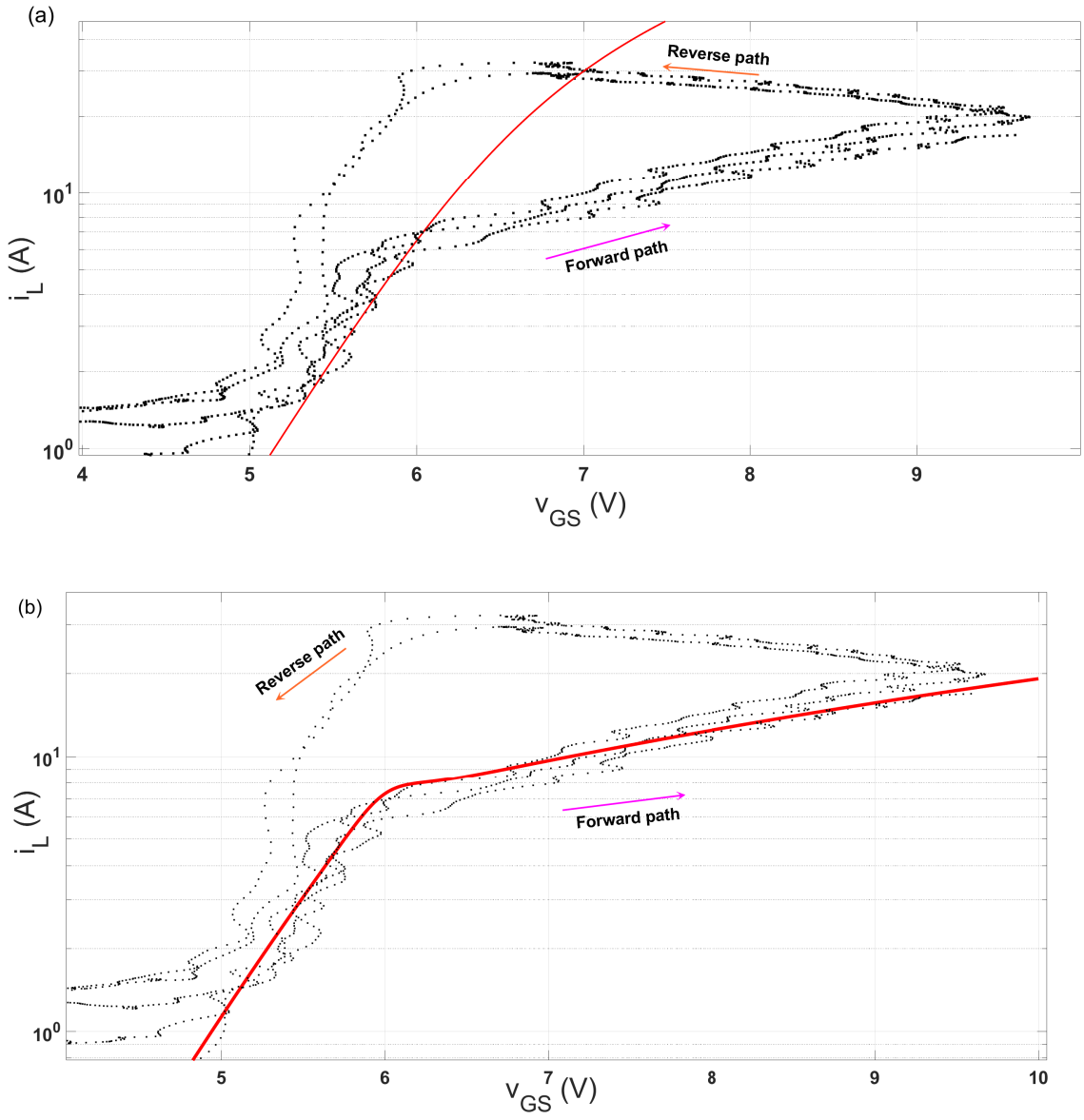

Figure 6.3: (a) Current curve fit (red line) of the data points (black dots) from experiment using Eq. 6.9 which failed to fit; (b) current curve fitting done using modified equation Eq. 6.17, which was a successful fit with the data points

and using

$$\ln[1+X] \approx X \quad \text{for small X} \tag{6.20}$$

we obtain

$$i_{\mathrm{D}} \approx \frac{i_{\mathrm{o}}}{\ln 2} \exp\left(\frac{v_{\mathrm{GS}} - v_{\mathrm{T}}}{\eta\, v_{\mathrm{Th}}}\right). \tag{6.21}$$

This equation resembles an exponential growth similar to general MOSFET characteristics, Eq. 6.5.

2. **ABOVE-THRESHOLD**: In the above-threshold region ($v_{\mathrm{GS}} > v_{\mathrm{T}}$), where $X \gg 1$ and I use $p \approx 0.2$ (the value of p reduces from below-threshold to above-threshold as we need the current curve to change from exponential to linear), i_{D} becomes a linear equation:

$$i_{\mathrm{D}} = \frac{i_{\mathrm{o}}}{\ln 2} \ln[1+X^p] \tag{6.22}$$

and using

$$\ln[1+X^p] \approx \ln X^p \quad \text{for large } X^p \tag{6.23}$$

we obtain

$$i_{\mathrm{D}} = \frac{i_{\mathrm{o}}}{\ln 2} \ln[X^p] = \frac{i_{\mathrm{o}}}{\ln 2} \ln\left[\exp\left(\frac{v_{\mathrm{GS}} - v_{\mathrm{T}}}{\eta\, v_{\mathrm{Th}}}\right)\right]^p \tag{6.24}$$

$$= p\frac{i_{\mathrm{o}}}{\ln 2}\left(\frac{v_{\mathrm{GS}} - v_{\mathrm{T}}}{\eta\, v_{\mathrm{Th}}}\right) \tag{6.25}$$

The equation (6.17) requires a gate-voltage dependent variable p to capture the changes occurring from subthreshold to above-threshold behaviors. Therefore, the addition of parameter p to the equation is justified.

3. **AT-THRESHOLD**: At threshold, when $v_{\mathrm{GS}} = v_T$, $X^p = 1$ for any value of p

$$i_{\mathrm{D}} = \frac{i_{\mathrm{o}}}{\ln 2} \ln[1+X^p] = i_{\mathrm{o}} \tag{6.26}$$

The modified term (ln 2) was added in Eq. 6.17, so that at threshold condition i_{D} should be equal to i_0.

By modifying the equation to depend solely on gate voltage, I achieved a consistent fit across

subthreshold, threshold, and above-threshold regions. The decision to introduce a gate-voltage-dependent parameter p was based on systematic analysis of experimental data, where standard models failed to capture the smooth transition from exponential to linear behavior. Setting $p \approx 1$ for subthreshold and reducing it to $p \approx 0.2$ above threshold allowed accurate interpolation between regions. The inclusion of the $\ln 2$ term ensured the model satisfied the boundary condition $i_{\mathrm{D}}(v_{\mathrm{GS}} = v_{\mathrm{T}}) = i_0$. These modifications were validated by improved fitting accuracy, as shown in Fig. 6.3(b), confirming their appropriateness both analytically and experimentally.

This approach treats the MOSFET as a variable resistance governed solely by the gate-source voltage, simplifying the analysis compared to treating it as a switch. However, it indirectly incorporates the influence of drain-source voltage on the resistance, thereby accounting for its effect in the model.

The crucial aspect of my application revolves around understanding MOSFET characteristics when the MOSFET is turning off, particularly the voltage and current across the TMS coil when the MOSFET is off. This necessitates a robust equation that accurately models behavior near, below and above the threshold. Through modification and analysis of experimental data, I derived the new equation (Eq. 6.17) capable of effectively modeling high-power MOSFET behavior, thus addressing the limitations of existing analytical approaches.

When the MOSFET transitions during switching events, the presence of an inductive load, such as the coil in this setup, significantly influences the current path. As shown in Fig. 6.3, a reverse current path is observed during switching events, which is an entirely expected outcome due to the inductive nature of the load. During turn-off, as the gate-source voltage (v_{GS}) drops below the threshold voltage (V_{Th}), the coil attempts to maintain current flow, leading to a temporary reverse current through the MOSFET's intrinsic body diode. Similarly, during turn-on, as v_{GS} crosses above V_{Th}, the channel reforms and restores forward conduction.

Additionally, the observed separation between forward and reverse switching trajectories can be attributed to hysteresis effects caused by asymmetric MOSFET switching behavior. During turn-on, the drain voltage is high, resulting in a small gate-drain (Miller) capacitance (C_{gd}), typically around 0.1 nF. This small capacitance enables rapid charging of the gate and fast channel formation. In contrast, during turn-off, the drain voltage is close to zero, leading to a much larger C_{gd} value (approximately 7 nF), significantly increasing the time required to discharge the gate. This asymmetry causes the effective gate control dynamics during turn-on and turn-off to differ, contributing to the observed loop behavior in the coil current waveform.

While the developed model primarily focuses on capturing the MOSFET's behavior through an effective, gate-voltage-dependent resistance, it does not explicitly model reverse conduction paths such as body diode effects. Nevertheless, the observed switching behavior confirms that the model provides a consistent and accurate representation of the device's dominant behavior during the transitions of interest, validating its suitability for the intended analysis.

The measured data (black dots) in Fig. 6.3 show considerable variability, including instances where v_{GS} appears to reverse with increasing i_{L}, particularly in the 5 V to 6 V gate voltage range. This variability is likely associated with the small "blips"—semi-circular deviations indicating a brief

rise and subsequent fall in gate voltage (Fig. 5.10). These anomalies are presumed to result from the Miller plateau effect [192], which becomes prominent during the MOSFET's turn-on and turn-off transitions. This effect may lead to irregularities in the measured v_{GS} for a given i_L, especially near the threshold region where gate capacitance dynamics are most sensitive.

6.2 Computing the resistance of the MOSFET

Now that the drain-source current equation that accurately fits the experimental data is developed, the next step is to determine the resistance of the MOSFET. To do so, the voltage fit equation is also required. Experimental data is utilized to understand the MOSFET behavior in the circuit prototype, observing how its drain current and drain-source voltage change at various gate voltages. Here is the method followed to obtain both voltage and current fits, which allow us to calculate the resistance fit. This information guided in developing an appropriate model.

Equation (6.17) was employed for current characteristics, and then aimed to derive equations for voltage and resistance characteristics by fitting curves using the hyperbolic tangent function. Here is a brief overview of different types of functions that can be employed in equations to fit the characteristics.

6.2.1 Sigmoid and hyperbolic tangent function

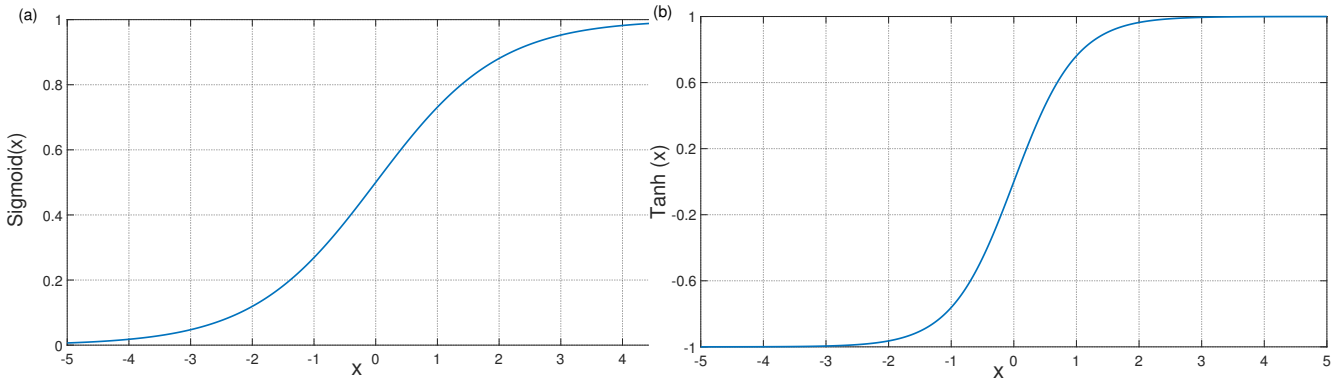

Figure 6.4: (a) Sigmoid and (b) Hyperbolic tangent function over the domain $-5 \leq x \leq 5$

The term "sigmoid function" typically refers to any function that has an S-shaped curve. In the context of machine learning and neural networks, the logistic sigmoid function is commonly used. It is a specific instance of a sigmoid function and shares similar properties with the hyperbolic tangent function. The logistic sigmoid function $\left(s(x) = \frac{1}{1+e^x}\right)$has an S-shaped curve that ranges from 0 to 1 as its input varies from negative to positive infinity. As its input approaches negative infinity, the sigmoid approaches 0, and as its input approaches positive infinity, sigmoid approaches 1. The logistic sigmoid function is commonly used in binary classification problems in machine learning as an activation function in the output layer or as a gating mechanism in recurrent neural networks.

The hyperbolic tangent function $\left(\tanh x = \frac{e^x - e^{-x}}{e^x + e^{-x}}\right)$, often abbreviated as tanh, is a mathematical function related to the regular tangent function but applicable to hyperbolic angles. With a

range of $(-1, 1)$, it proves particularly valuable in neural networks and various mathematical applications, commonly employed for mapping input values to a range suitable for activation functions. The tanh function has a characteristic S-shaped curve that ranges from -1 to 1 as its input varies from negative to positive infinity. It is an odd function, meaning that $\tanh(-x) = -\tanh(x)$. As its input approaches negative infinity, tanh(x) approaches -1, and as its input approaches positive infinity, tanh(x) approaches 1. The shape of the tanh function resembles that of the logistic sigmoid function, as illustrated in Fig. 6.4, yet its output values span from -1 to 1, distinct from the sigmoid range of 0 to 1. These operations provide flexibility in manipulating the tanh function to suit specific requirements, enabling adjustments in both position and range. Scaling and offsetting the tanh function allows us to ensure that the desired curve remains within a specific range, particularly if the graph exhibits the characteristic S-shaped or sigmoid curve.

In summary, both the hyperbolic tangent function and the sigmoid function share similar characteristics with their S-shaped curves and are commonly used in various applications, including machine learning, neural networks, and mathematical modeling.

6.2.2 Voltage fit

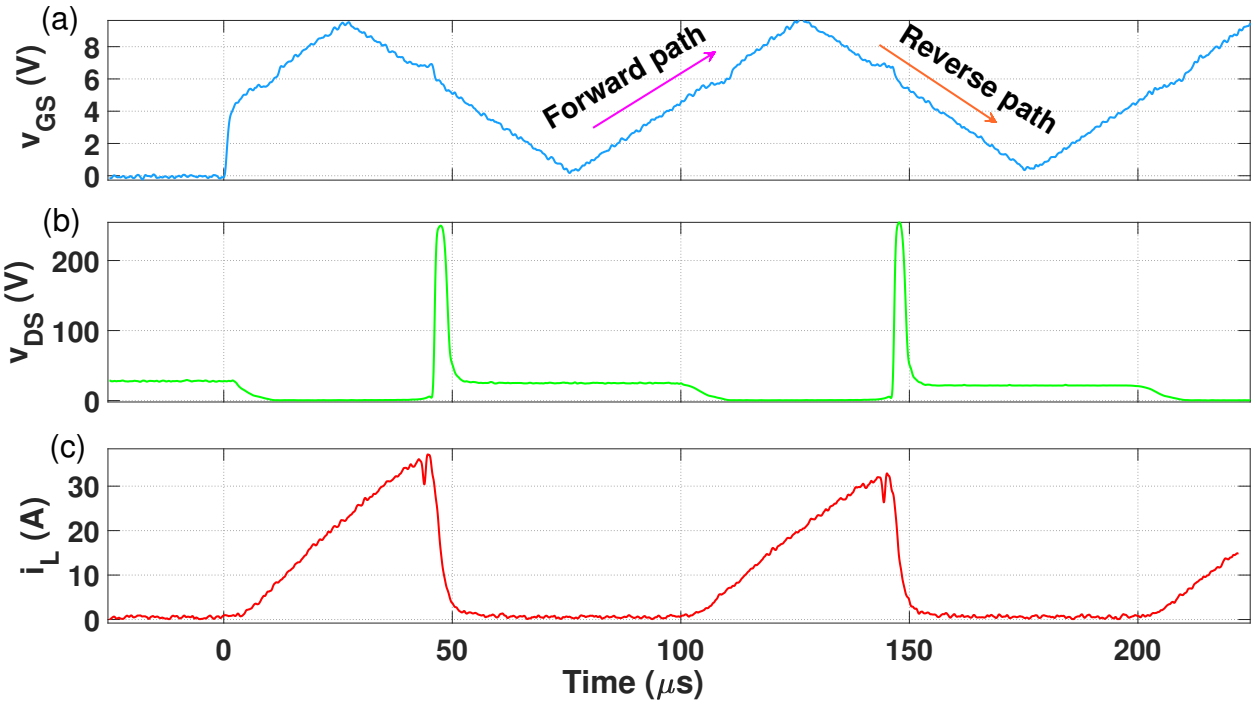

Figure 6.5: (a) 50% symmetry gate voltage with forward path (0 to 10 V) and reverse path (10 V to 0) marked (initial 25 μs of the triangular wave is not captured accurately due to the oscilloscope triggering configuration); (b) measured drain-source voltage and (c) coil current from the experimental setup used for the mosfet model (To correct for current probe delay, I advanced the measured current trace by 3 μs prior to plotting)

In my attempt to model the MOSFET S2 (Fig. 6.1) as a non-linear resistance, my goal is to calculate the resistance of the MOSFET at every instance when it is on or off. To do this, I measured

v_{DS} and i_{D} from the experimental setup using a triangle gate voltage as input.

Figure 6.5 shows the experimental drain-source voltage and coil current (equivalent to drain current) for a 50% symmetry triangular gate voltage. I then plotted the v_{DS} against v_{GS} using the experimental data points (blue dots) as shown in Fig 6.6. Here, only the forward path is modeled, which was sufficient for the analysis presented. The forward path varies from 0 V to 10 V, covering nearly the full range of gate-source voltages used in the experiment. Although the reverse current path was not explicitly modeled, its occurrence is expected due to the inductive nature of the load, as discussed earlier. The observed reverse behavior does not impact the validity of the forward-path-focused model developed here.

By analyzing the trajectory of the transfer characteristics (blue dots in Fig. 6.6), I found that it follows a hyperbolic tangent path since it has both upper and lower limit values. Therefore, I used the equation:

$$v_{\mathrm{DS_{fit}}} = \frac{1}{2}\left(D_1 + D_2 + (D_2 - D_1)\tanh\left(\frac{v_{\mathrm{GS}} - v_{\mathrm{T}}}{\eta_1\ v_{\mathrm{TH}}}\right)\right) \tag{6.27}$$

Here, D_1 and D_2 represent the upper and lower limits of the blue dotted curve in Fig 6.6. v_{T} is the threshold voltage, the gate-to-source voltage at which the S2 just begins to turn on and v_{TH} is the thermal voltage of the MOSFET. The term inside the hyperbolic tangent function is the argument of the tanh function. The tanh function is a sigmoidal or S-shaped curve that ranges from -1 to 1 as its input varies from negative to positive infinity. The input of the tanh function is the expression $\left(\frac{v_{\mathrm{GS}} - v_{\mathrm{T}}}{\eta_1\ v_{\mathrm{TH}}}\right)$.

When the gate-to-source voltage v_{GS} is far below the threshold voltage (subthreshold), the argument of the tanh function becomes very negative, causing the output of the tanh function to approach -1. Conversely, when v_{GS} is far above v_{T} (above-threshold), the argument becomes very positive, causing the output of the tanh function to approach 1. As v_{GS} approaches v_{T} (at threshold), the argument approaches 0, and the output of the tanh function approaches 0. The term $(D_2 - D_1)$ will be always negative which scales the range of the transition region and make the sigmoidal ranges from positive to negative. Finally, the entire expression is halved and added to upper and lower limits of the curve, likely for normalization purposes, ensuring that the output ranges from D_1 and D_2. In summary, the tanh curve (red curve in Fig 6.6) in this context represents the gradual transition of the drain-to-source voltage as the gate-to-source voltage varies around the threshold voltage of the MOSFET. The parameters used in curve fitting are provided in Table 6.1.

6.2.3 Current fit

From the experimental data of Fig. 6.5, the current versus gate voltage graph is illustrated in Fig. 6.8(a) with black dots, and fitted using Eq. 6.28. Typically, small-signal MOSFETs exhibit an η value ranging from 1 to 2. However, in this analysis, I selected the η values listed in Table 6.1 to achieve a more accurate fit, with η being treated as a fitting parameter. Choosing η values greater than 1 is required to attain a better alignment with the experimental data, particularly given the

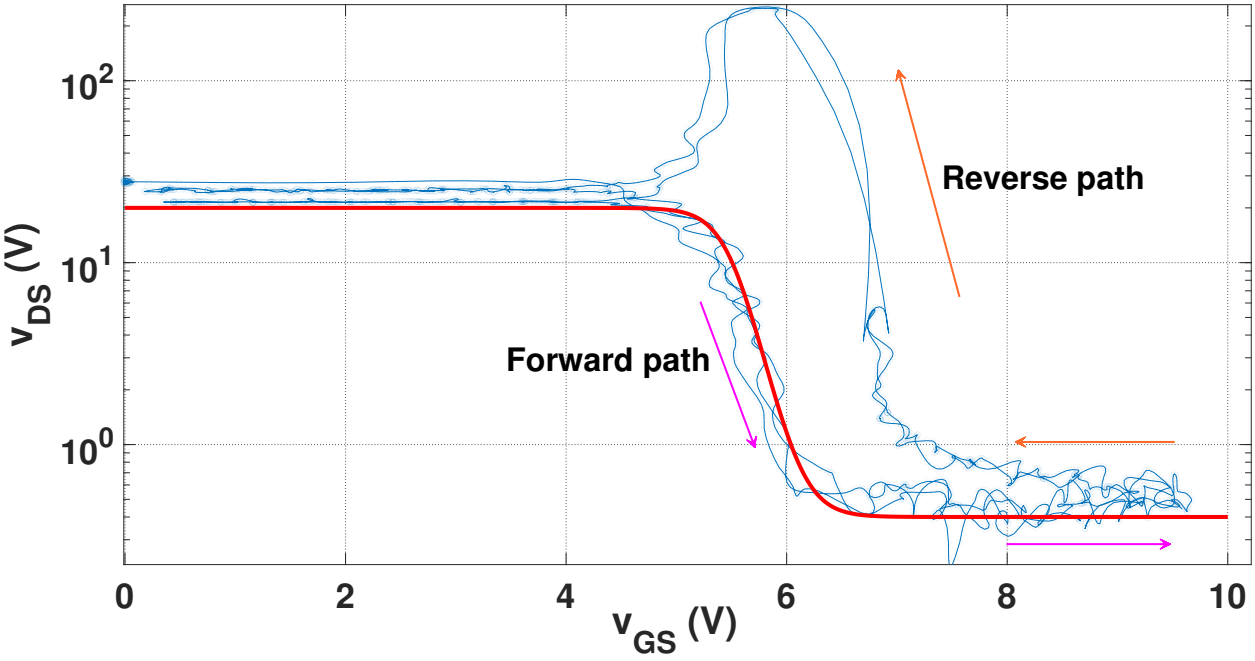

Figure 6.6: Drain-source voltage versus gate voltage of the experimental result (blue). Red colored curve shows the modeled drain-source voltage fitted curve in the forward path using the Eq. 6.27

specific behavior of power MOSFETs. Equation (6.17) is modified to read

$$i_{\mathrm{L_{fit}}} = \frac{i_{\mathrm{o}}}{\ln 2} \ln\left(1 + \left[\exp\left(\frac{v_{\mathrm{GS}} - v_{\mathrm{T}}}{\eta_2\ v_{\mathrm{TH}}}\right)\right]^{p_{\mathrm{fit}}}\right) \tag{6.28}$$

where the exponent $p \to p_{\mathrm{fit}}$ is now a tanh function of MOSFET gate voltage,

$$p_{\mathrm{fit}} = \frac{1}{2}\left(p_1 + p_2 + (p_2 - p_1)\tanh\left(\frac{v_{\mathrm{GS}} - v_{\mathrm{T}}}{\eta_3\ v_{\mathrm{TH}}}\right)\right) \tag{6.29}$$

The variation of p_{fit} against the gate voltage is shown in Fig. 6.7.

6.2.4 Resistance fit

Once we achieve an accurate fit for drain-source voltage and drain current, we can compute the MOSFET resistance as the ratio of voltage to current:

$$r_{\mathrm{DS_{fit}}} = \frac{v_{\mathrm{DS_{fit}}}}{i_{\mathrm{L_{fit}}}} \tag{6.30}$$

$$= \frac{\frac{1}{2}\left(D_1 + D_2 + (D_2 - D_1)\tanh\left(\frac{v_{\mathrm{GS}} - v_{\mathrm{T}}}{\eta_1\ v_{\mathrm{TH}}}\right)\right)}{\frac{i_{\mathrm{o}}}{\ln 2}\ln\left(1 + \left[\exp\left(\frac{v_{\mathrm{GS}} - v_{\mathrm{T}}}{\eta_2\ v_{\mathrm{TH}}}\right)\right]^{p_{\mathrm{fit}}}\right)} \tag{6.31}$$

As aimed, MOSFET is now modeled as a resistive element whose drain-source resistance r_{DS} is a

Table 6.1: Parameters and their values used for curve fitting equations

Parameters	Symbol	Values
Resistance of inductor	r_{L}	0.22 Ω
Inductance	L	0.22 μH
Internal resistance of C_1	r_{C}	0.22 Ω
Initial voltage of C_1	$v_{\mathrm{C}}(0)$	30 V
Thermal voltage	v_{Th}	26 mV
Threshold voltage	v_{T}	6.0 V
Parameters used in Equations		
$v_{\mathrm{DS_{fit}}}$ Eq. (6.27)	D_1, D_2, η_1	20, 0.4, 12
$i_{\mathrm{L_{fit}}}$ Eq. (6.28)	i_0, η_2	8, 16
p_{fit} Eq. (6.29)	p_1, p_2, η_3	1, 0.13, 10

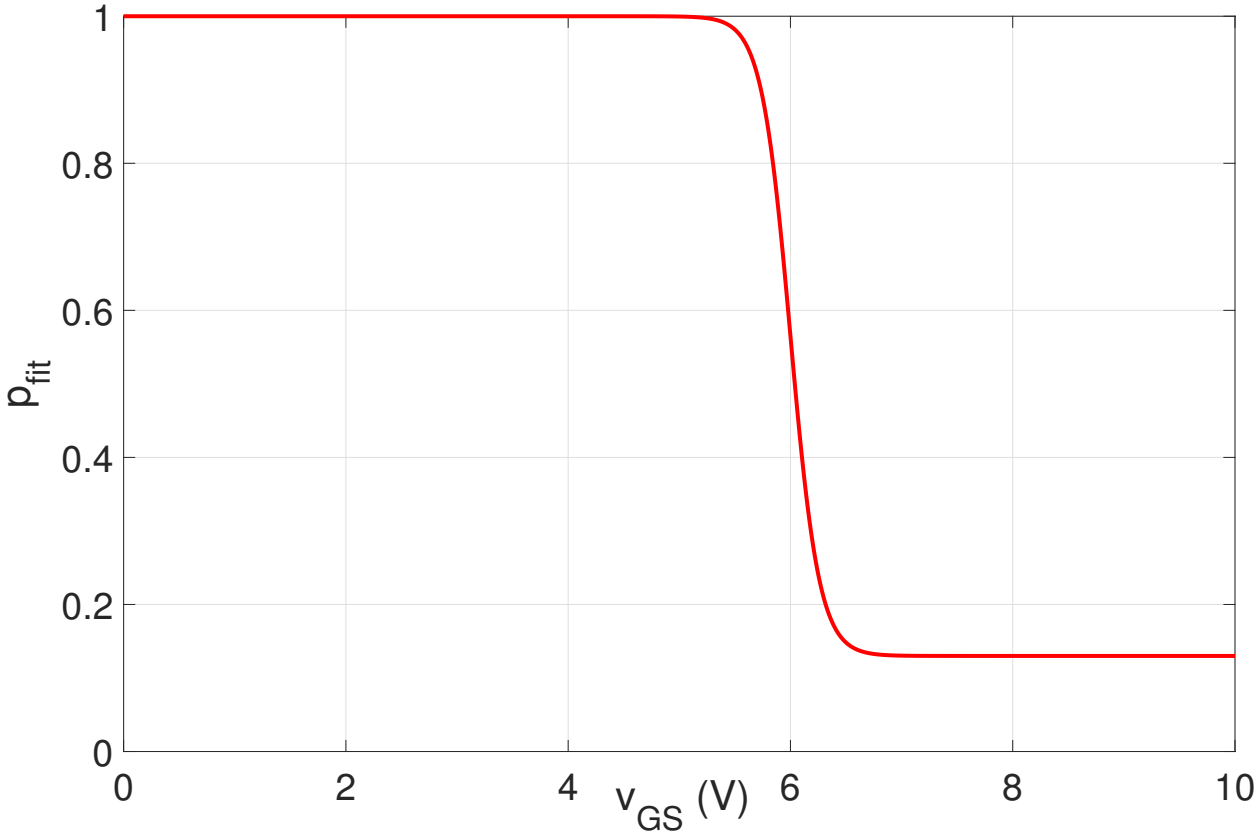

Figure 6.7: Variation of exponent p_{fit} variable with respect to the gate-source voltage (v_{GS})

nonlinear function of v_{GS} only.

$$r_{\mathrm{DS_{fit}}} = f(v_{\mathrm{GS}}) \tag{6.32}$$

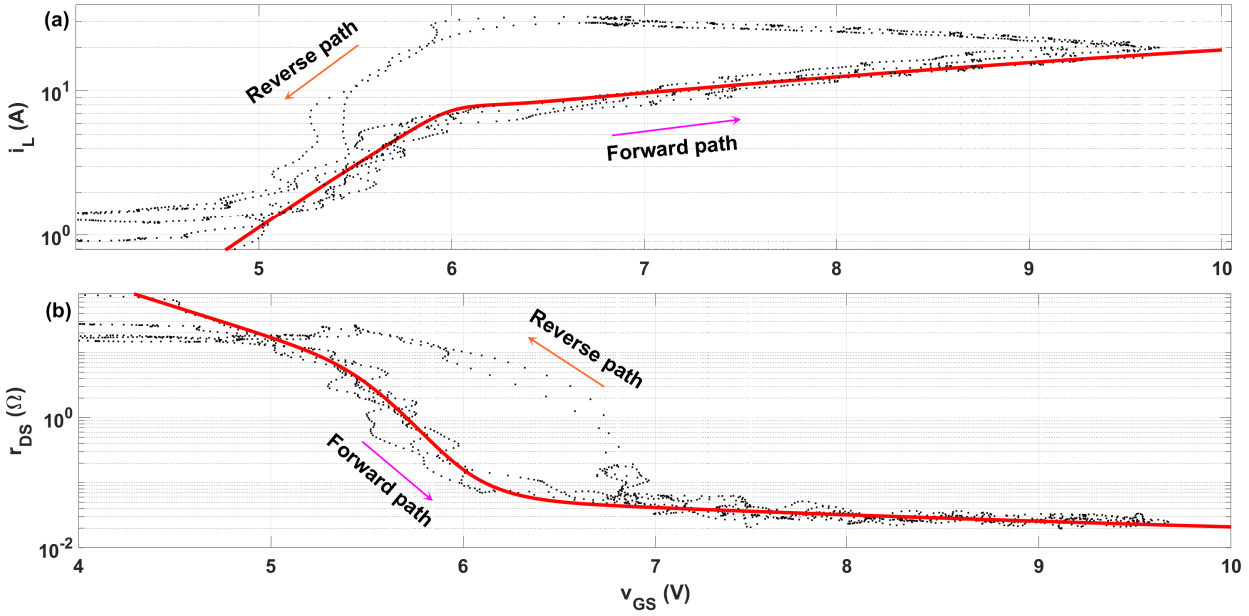

Figure 6.8: (a) Transfer characteristics with fitted current curve (red line) using the Eq. 6.28; (b) the input admittance characteristic with fitted drain-source resistance curve using the Eq. 6.31

Figure 6.8 shows the current fitted curve in the transfer characteristics and the resistance fit curve in the input admittance characteristics. With the knowledge of MOSFET resistance at different points, we can effectively solve the RLC circuit using the differential Eq. 6.33. This approach allows us to establish a MOSFET model grounded in experimental data, refining the equations accordingly. Such a model serves as a versatile tool for predicting MOSFET characteristics and, consequently, projecting the circuit output based on various input gate voltages applied to MOSFET S2.

This analysis is shown as a 3D plot in Fig. 6.9 illustrating relationships between gate-source voltage, drain-source voltage, and drain current or resistance, contributing to a thorough understanding of the MOSFETs behavior across different conditions.

6.3 MATLAB MOSFET model

By now, curve fitting and equations for the voltage, current, and resistance of the MOSFET have been obtained. The next step is to develop a fully simulated model that solves the RLC circuit with the MOSFET as shown in Figure 6.1. As mentioned earlier, the MOSFET is treated as a variable resistance defined by $r_{\mathrm{DS_{fit}}}$. The differential equation of the circuit is solved utilizing both Euler's method and the `ode15s` solver. The circuit differential equation is:

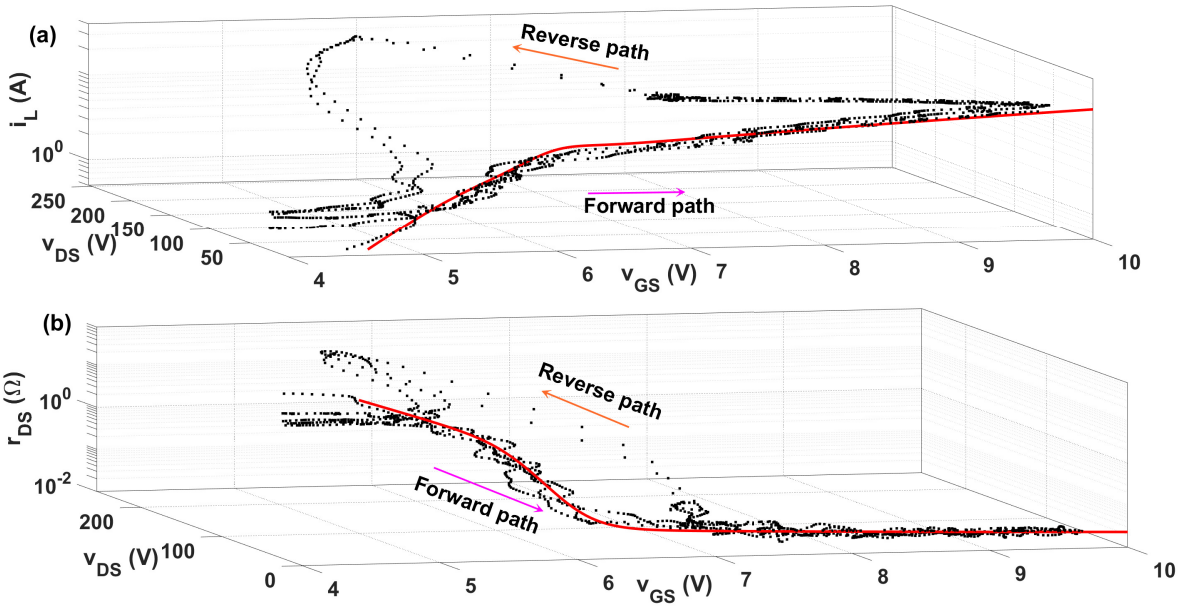

Figure 6.9: 3 dimensional view of the output characteristics of the MOSFET and dynamic resistance curve; (a) The output characteristics is shown in black dotted lines and red curve shows the fitted drain-source voltage in the forward path; (b) Black dotted lines represent the dynamic characteristics and red curve shows the fitted drain-source resistance.

$$\frac{di}{dt} = \frac{1}{L}\left[v_{\mathrm{C}} - (r_{\mathrm{L}} + r_{\mathrm{C}} + r_{\mathrm{DS_{fit}}})i_{\mathrm{L}}\right] \tag{6.33}$$

Any $v_{\mathrm{GS}}(t)$ sequence can be used to test the circuit. Here I generate a triangular gate voltage signal using a `pulsetran` MATLAB function, which simulates gate driving signals. The functions to model the drain-source voltage and drain-source current is explained as before based on experimental data using tanh and modified equation. By incorporating these equations, the code aims to accurately capture the behavior of the MOSFET within the RLC circuit, facilitating dynamic simulations of voltage and current waveform over time.

I solve the system using either `ode15s` or Euler's method. Euler's method is only used in the initial stage of the model development since it was an easier option. However, it was later only used to compare the results; it is not a better choice to use with this system due to its limitations.

Euler's Method is a simple numerical method for solving ordinary differential equations. It approximates the solution at each time step by using the derivative at the current time step to predict the value at the next time step. While it is straightforward to implement, it may not be as numerically accurate or stable as other methods, especially for stiff systems or when the time step is large. Stiff system means the dynamics of the system involve widely varying time scales in which some variables may change rapidly while others change slowly. Here, Euler's method calculates the capacitor voltage and loop current at each time step. The process involves computing the derivatives of the state variables (capacitor voltage and loop current) and then updating their

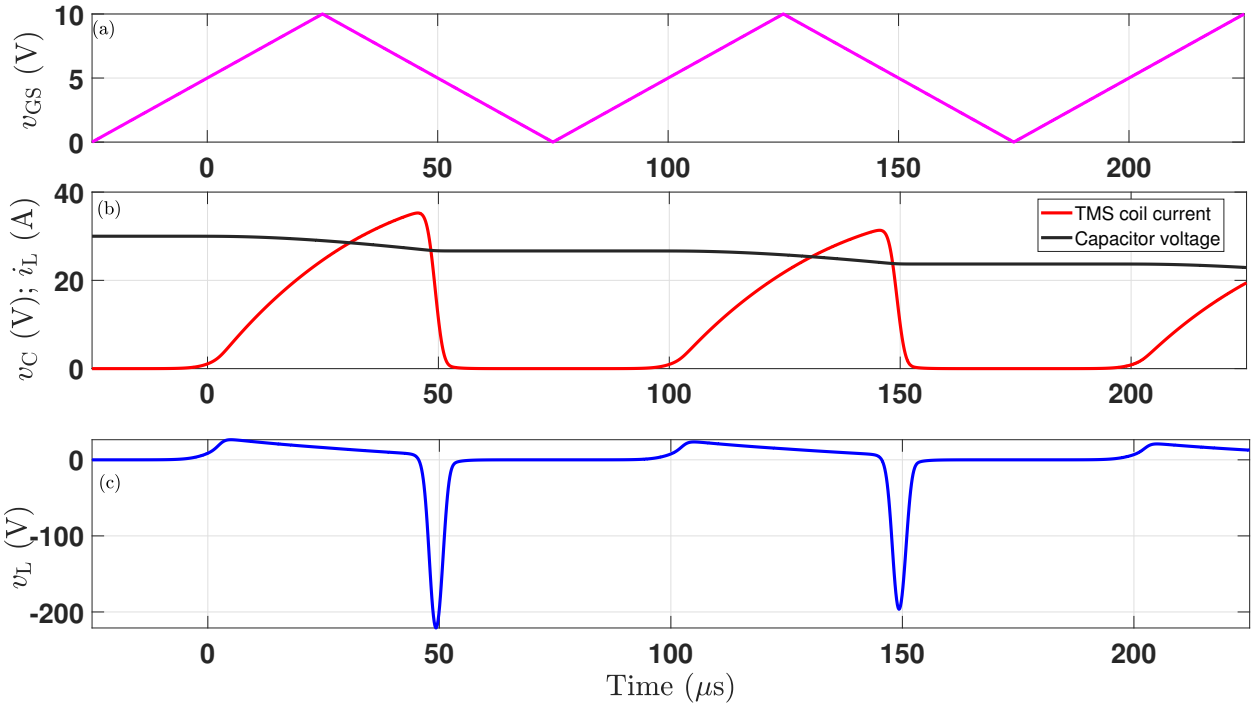

Figure 6.10: Euler method solution of the RLC differential equation; (a) Triangular gate control voltage of MOSFET S2 (magenta); (b) electrolytic capacitor voltage (black) and TMS coil current (red); (c) TMS coil voltage (blue)

values using these derivatives multiplied by the time step. This iterative process continues until the desired end time is reached.

`ode15s` solver is mainly used in this MATLAB model to solve the differential equation. `ode15s` solver is a MATLAB function that uses a variable-order solver based on the numerical differentiation formula (NDF) method for stiff and non-stiff systems. It is more robust and accurate than Euler's method, particularly for stiff systems where the stiffness ratio is high. It automatically adjusts the step size to control errors, making it more suitable for a wide range of ordinary differential equation (ODE) problems. `ode15s` adapts its time step dynamically throughout the simulation to control error, ensuring accuracy while maintaining stability. It achieves this by evaluating the derivatives at multiple time points within each time step and adjusting the step size accordingly. This solver is particularly advantageous for stiff systems, where the stiffness ratio is high, as it automatically adjusts the time step to capture rapid changes accurately without compromising stability. Here, `ode15s` is recommended for solving the RLC circuit due to its ability to handle stiff systems effectively, providing more accurate and reliable results compared to Euler's method, especially considering the potential stiffness of the RLC circuit with a MOSFET. However, Euler's method is also provided as an alternative for comparison if computational resources are limited.

Figures 6.10 and 6.11 shows the Euler method and `ode15s` solver solution results of the output TMS coil voltage and current respectively. MATLAB offers several other ODE solvers but `ode15s` worked well in this system with relatively accurate results which are close to the experimental values. The current probe used in the experiment has a bandwidth of DC-100 kHz, which leads to

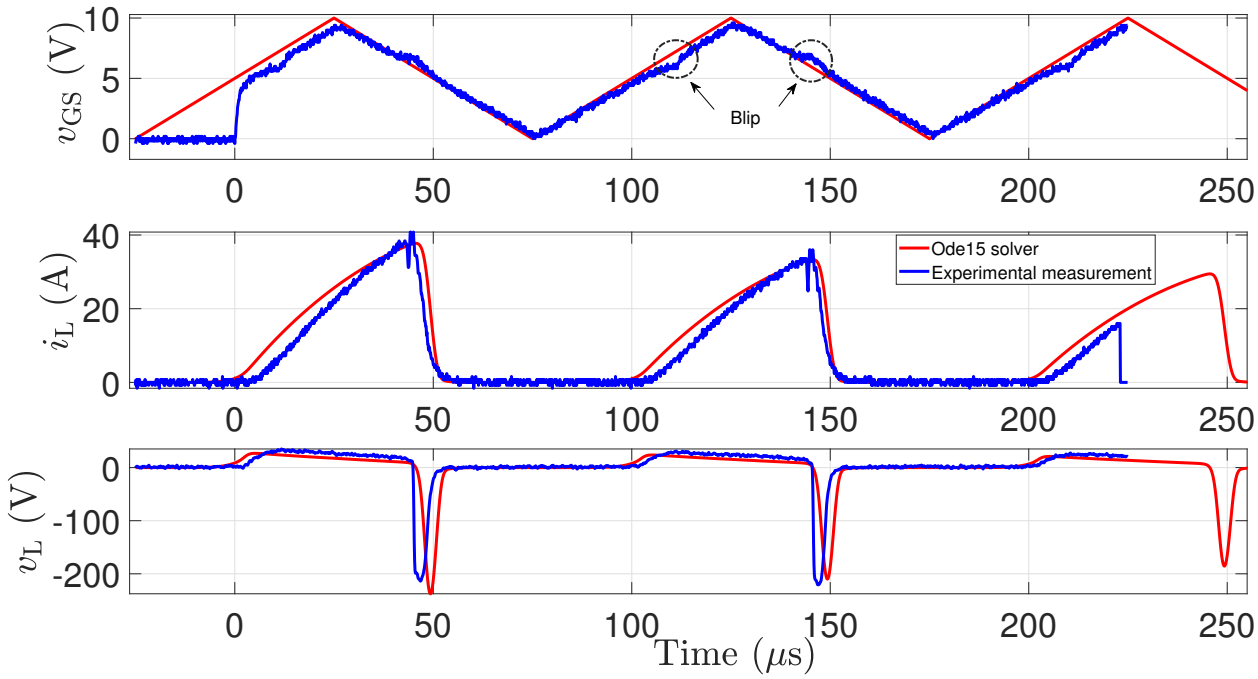

Figure 6.11: Comparison of `ode15s` solver solution of the differential equation with the measured experimental values. The experimental measurement is the MATLAB capture of the oscilloscope reading shown in Fig. 6.12.

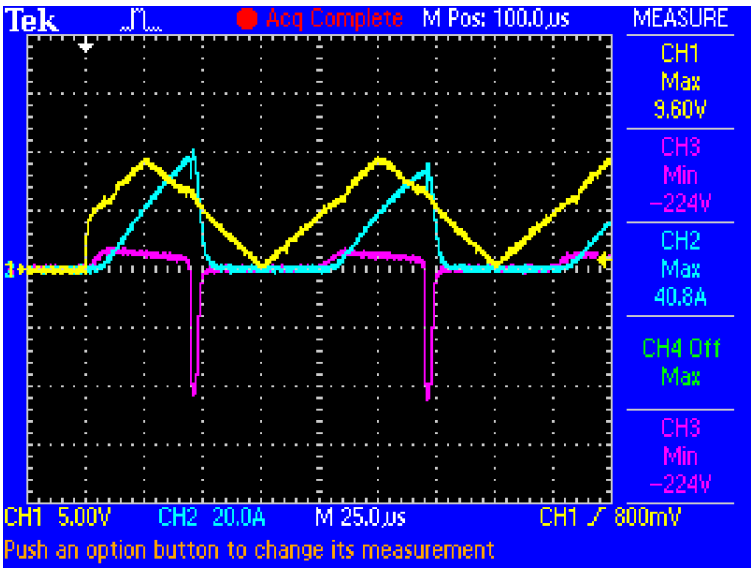

Figure 6.12: Oscilloscope measurement of MOSFET gate voltage (yellow), TMS coil voltage (magenta) and TMS coil current (blue). Gate voltage rise-fall symmetry is set at 50%.

a slow response time. In contrast, the oscilloscope used for $v_{\mathrm{L}}(t)$ voltage measurements, has a much higher bandwidth of 0-10 MHz. To correct for current probe delay, I have advanced the measured current trace by 3 μs prior to plotting (Fig. 6.5). This leftwards timing offset was also applied to the current traces displayed in MATLAB plots of Figures 6.11 and 6.13. Figure 6.11 shows a good match between experimental measurements and MATLAB model predictions for a triangular gate input voltage. Figure 6.12 shows the oscilloscope capture results of the same 50% symmetry gate voltage input used in simulation.

MATLAB simulations produce a perfect gate waveform without any distortion. However, in the experimental setup, the gate waveform exhibits minor distortions caused by the 8-bit quantization noise in digital oscilloscope captures. In Figure 6.11, the leading edge of the gate voltage shows a step discontinuity instead of the expected smooth voltage ramp. This discrepancy arises because the initial 25 μs of the triangular wave is not captured accurately due to the oscilloscope triggering configuration. However, focusing on the second pulse, I observe a good alignment between the simulation results and the circuit measurements. Since I have not modeled the charging and discharging of the gate-drain capacitance, this process causes a small blips (black circle) at the threshold voltage of the gate voltage, as shown in Fig. 6.11. These small imperfections can affect the current and voltage waveforms, making them slightly less precise compared to the ideal simulations. Despite these minor differences, the experimental waveforms match the MATLAB-generated output, confirming that the curve-fitting equations have successfully captured the nonlinear resistance behavior of the MOSFET.

This approach of modeling the mosfet and solving the circuit equation offers several advantages. Firstly, by incorporating a comprehensive mathematical model of MOSFET behavior, the simulation results are more accurate and reflective of real-world scenarios. Secondly, the flexibility of the code allows for easy modification and adaptation to different MOSFET specifications or circuit configurations. Overall, this code segment serves as a robust tool for analyzing RLC circuits with MOSFETs, enabling researchers to gain insights into circuit performance and behavior under varying conditions.

6.3.1 Testing the MOSFET model with different gate voltages

The developed MATLAB model was tested for versatility by applying different input gate voltages: a sinusoidal gate voltage and a triangular voltage with a dead-zone. A sinusoidal gate voltage of 10 kHz frequency with a 10 V_{pp} was used for testing. Solving the differential equation using the `ode15s` solver, I obtained TMS current and voltage waveform from the simulation. Figure 6.13 superimposes the simulation predictions against experimental measurements from the oscilloscope capture shown in Fig. 6.14. The experimental results closely matched the simulation results.

Furthermore, the model performance was evaluated using a triangular gate voltage input with a deadzone. This input signal also had a frequency of 10 kHz and an amplitude of 10 V. Utilizing the `ode15s` solver, I solved the differential equation and extracted the TMS current and voltage waveform from the simulation.

This test was conducted to assess whether pulses could be generated at wide intervals, as TMS

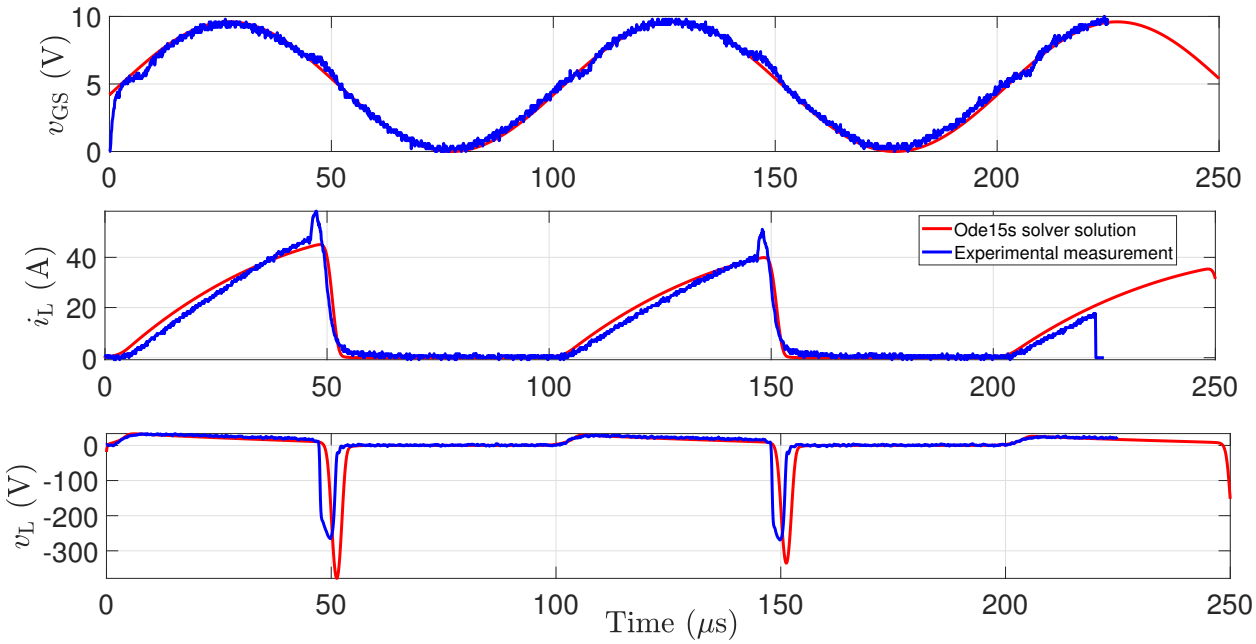

Figure 6.13: `ode15s` solver solution of the differential equation and experimental results with sinusoidal gate voltage input

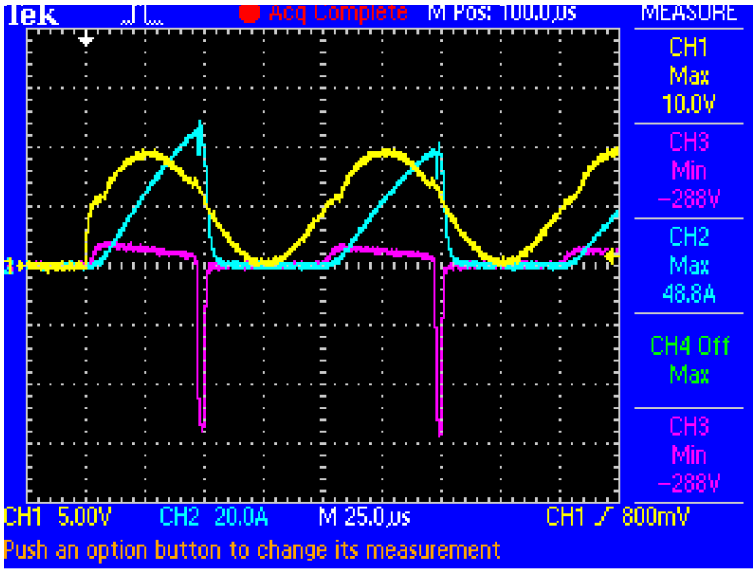

Figure 6.14: Oscilloscope measurement of sinusoidal gate voltage (yellow), TMS coil voltage (magenta) and TMS coil current (blue)

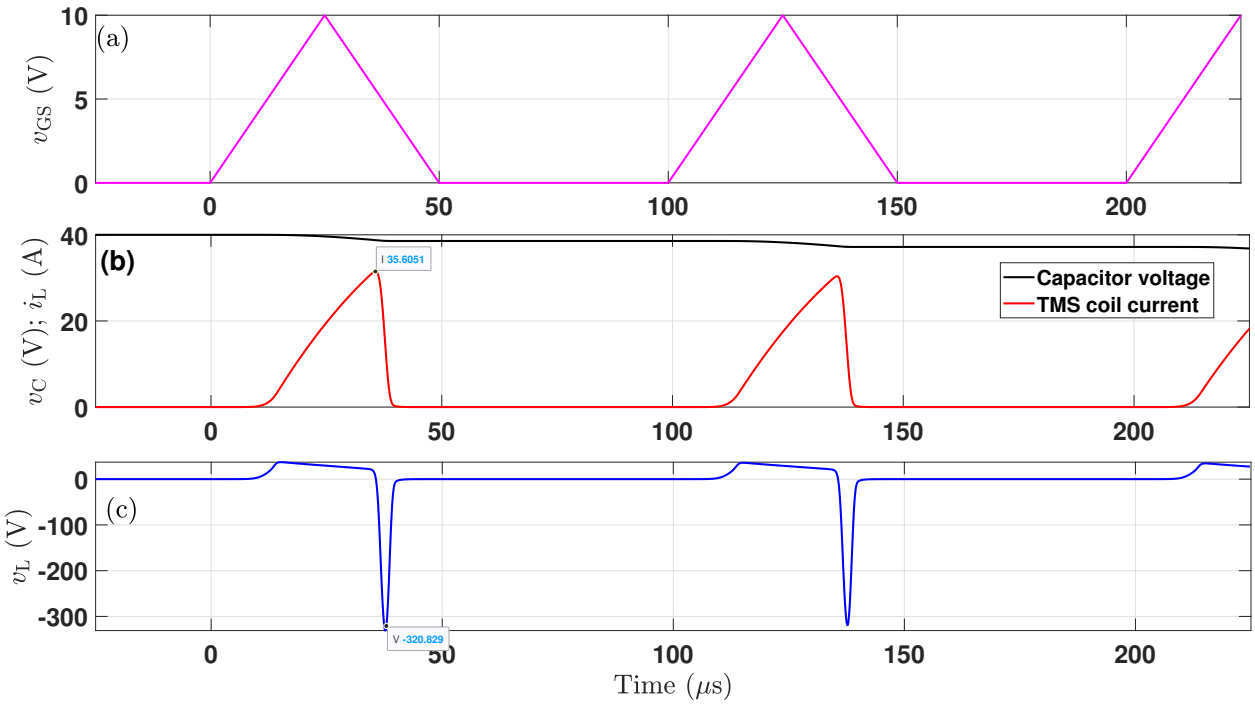

Figure 6.15: `ode15s` solver solution of the differential equation with triangle gate voltage with dead-zones

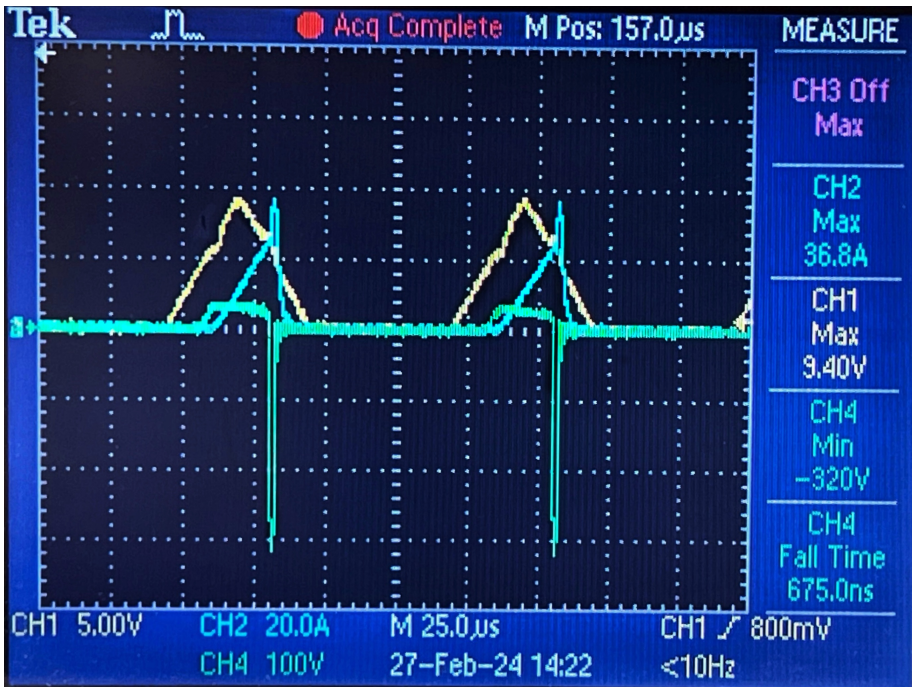

Figure 6.16: Oscilloscope measurement of triangle with dead zone gate voltage input (yellow), TMS coil voltage (green) and TMS coil current (blue)

operates at 200 ms repetition with three burst of 20 ms apart pulses. By adding a dead-zone to the triangular waveform, the same triangle was modified to create pulses spaced further apart. The model versatility was evaluated by applying this modified triangular gate voltage input, alongside a sinusoidal input, in the simulation. The obtained simulated TMS current and voltage waveform (Fig. 6.15) were compared with experimental results (Fig. 6.16), confirming the model accuracy under different input conditions. The close agreement between the experimental and simulation results demonstrates the model capability to accurately predict the TMS voltage and current pulse shape across a variety of input voltages.

6.4 Limitations and summary

A summary of the key aspects and challenges encountered during the development of the MATLAB model follows:

1. Data sheet limitations: The data sheets provided only the on-resistance value for the MOSFET. The model needed to account for the MOSFET behavior when turned off, particularly to calculate the maximum voltage across the TMS due to stored energy release. Accurate modeling required knowing the resistance at every instant, which was challenging due to limited data.

2. Gate capacitance exclusion: The current MATLAB model did not explicitly include gate capacitance, a parameter that typically affects the MOSFET's switching behavior. Surprisingly, the model still showed remarkable accuracy in predicting experimental results, though incorporating gate capacitance would add complexity to the model.

3. Measurement difficulty: During the MATLAB model development, accurately measuring the inductor voltage was a challenge. To overcome this, two probes were used to measure the TMS voltage; one for lower voltage levels and another for higher voltage levels. This approach helped in creating a more accurate model.

Despite the challenges, a robust MOSFET model was developed through full simulation. This model could predict the system's output with any input, and its predictions were verified against experimental data, showing strong alignment with the results. These aspects highlight the complexities of developing a MATLAB model for MOSFET behavior in TMS applications, particularly when dealing with incomplete data and unexpected experimental conditions.

Although explicit curve fitting for the reverse path has not yet been performed, the observed hysteresis-like separation between the forward and reverse trajectories is expected based on the switching behavior of the MOSFET with an inductive load. Specifically, as discussed earlier, the combination of the coil's stored magnetic energy during switching transitions and the strong voltage dependence of the gate-drain (Miller) capacitance (C_{gd}) introduces asymmetry between turn-on and turn-off dynamics. Despite focusing the modeling efforts solely on the forward path from 0 to 10 V, the developed model continues to provide a reliable prediction of the output behavior when compared to experimental results. This is attributed to the similarity in the overall shape of the resistance versus gate voltage relationship between the forward and reverse paths, as shown

in Fig. 6.8, despite the presence of a time shift. Consequently, even without explicit reverse path modeling, the simulation captures the essential features of the coil voltage waveform, including the negative phase during turn-off, in close agreement with experimental observations.

When the last RLC stage of the prototype was simulated in MATLAB Simulink and Proteus, the results were surprising. Even though Proteus has components that mimic actual hardware characteristics, the MOSFET did not behave like it did in the experiment. Since I have set the threshold, calculated resistance and curve fitted to match the experimental conditions, which resulted in a model that closely aligned with the experiment. I believe that the built-in component models in software will not replicate the results as accurately as the MOSFET MATLAB model.

While the RLC circuit appears simple, accurately capturing the MOSFET's characteristics and understanding its behavior is a complex task. I feels confident that this work on a single MOSFET model has provided a strong foundation, making it easier to create MATLAB models for new MOSFETs with minimal experimentation in the future.

6.5 Publications

6.5.1 Paper published in proceedings of APEC 2025

The following paper was presented at IEEE Applied Power Electronics Conference and Exposition (APEC), held from March 16-20, 2025, in Atlanta, USA, and will be published in the IEEE proceedings of the conference titled "Supercapacitor based TMS pulse generator design- Experimental results versus MATLAB MOSFET simulation model". I received a travel grant from the Neurological Foundation and the Hackett Memorial Trust to present this paper in the USA.

An attribution detailing the contributions from the authors is included in the Appendix E.

Supercapacitor based TMS pulse generator design-Experimental results versus MATLAB MOSFET simulation model

Soniya Raju
School of science
university of Waikato
Hamilton, New Zealand
sr231@students.waikato.ac.nz

Nihal Kularatna
School of Engineering
University of Waikato
Hamilton, New Zealand
nihalkul@waikato.ac.nz

Marcus Wilson
School of Science
University of Waikato
Hamilton, New Zealand
marcus.wilson@waikato.ac.nz

Alistair Steyn-Ross
School of Engineering
University of Waikato
Hamilton, New Zealand
alistair.steyn-ross@waikato.ac.nz

***Abstract*—Supercapacitors are ideal for short-term energy storage due to their high instantaneous power capability. Unlike traditional high-voltage DC power supplies typically used in transcranial magnetic stimulation (TMS) applications, a pre-charged supercapacitor module can serve as a cost-effective alternative for building a pulse generator with adjustable waveform capabilities. This approach utilizes a supercapacitor module with a capacitor bank rated at a few hundred farads and 10 V, combined with a step-up transformer-based converter and medium-voltage MOSFETs to meet TMS requirements. The output of this pulse generator, including the effects of varying gate voltages, can be accurately predicted using a robust model. This paper presents the design of a MOSFET model, incorporating a newly derived equation that effectively captures the subthreshold, near-threshold, and above-threshold regions of the MOSFET operation. Experimental results are provided and compared with MATLAB model simulations, demonstrating the model's accuracy and effectiveness.**

***Index Terms*—Electrical stimulation, Magnetic stimulation, Pulse circuits, Supercapacitors, Transcranial magnetic stimulation (TMS)**

I. Introduction

High-voltage and high-power pulse generators are essential for applications such as transcranial magnetic stimulation (TMS) [1–6], lightning surge simulators, and fence energizers [7]. Traditional designs, combining high-voltage DC sources with pulse-shaping circuits and high-voltage semiconductor switches, face significant challenges due to safety isolation requirements and high component costs [1, 6, 8–13]. Despite innovations like solid-state Marx generators and Tesla transformers aimed at enhancing efficiency, these systems remain complex, expensive, and require multiple stages and components. Most existing pulse generators also lack provisions for pulse shaping and demand high-voltage supplies or high-voltage capacitors, further complicating their use [14–21]. Additionally, TMS pulse generators, especially those for small animals, are underexplored, with limited dedicated circuits and simulation models. A supercapacitor-based pulse generator [22] offers a promising solution, leveraging higher energy density, rapid charging and discharging capabilities, and longer lifetimes. This approach could provide more efficient, cost-effective, and precise pulse control, advancing TMS research significantly.

Existing TMS circuitry uses MOSFET as switches, but they have the potential to shape coil current more precisely. This study introduces a model that predicts coil current by varying the gate applied to the MOSFET, incorporating a novel MOSFET drain current equation derived from real-time experimental results. Emphasizing MOSFET operation at and near the threshold region is critical for achieving high voltage across the TMS coil during switch-off. The model overcomes challenges such as limited-accurate data available from MOSFET datasheets.

II. Supercapacitor based Pulse generator (SCPG)

In a TMS pulse generator applications, the pulse generator is expected to drive certain amount of energy into the TMS coil and this may be in the range of few tens of joules to few hundred joules. With this requirement coming as primary requirement, we see that the commercially available supercapacitors (SC) could be easily configured into a pre-stored energy module to deliver multiple test pulses in one shot when required without using a continuously rated high-voltage DC power supply. The cost of this approach was found to be much less here due to the elimination of a high-voltage DC power supply.

The design approach for this TMS pulse generator leverages the capability of a charged supercapacitor to release a very high instantaneous current, which is predominantly controlled by the load side impedance rather than the SC's internal resistance. Considering a small supercapacitor module composed of 4 series-connected 380 F cells, this module has a short-circuit current capability of $\frac{10}{4\ \mathrm{ESR}}$, where the equivalent series resistance (ESR) of a single cell is approximately 3.2 mΩ. In cases where a larger storage module is required, using 3000 F cells with an ESR of 0.23 mΩ provides 14 times greater current capability. This straightforward practical consideration indicates that the primary loop current is mainly governed by

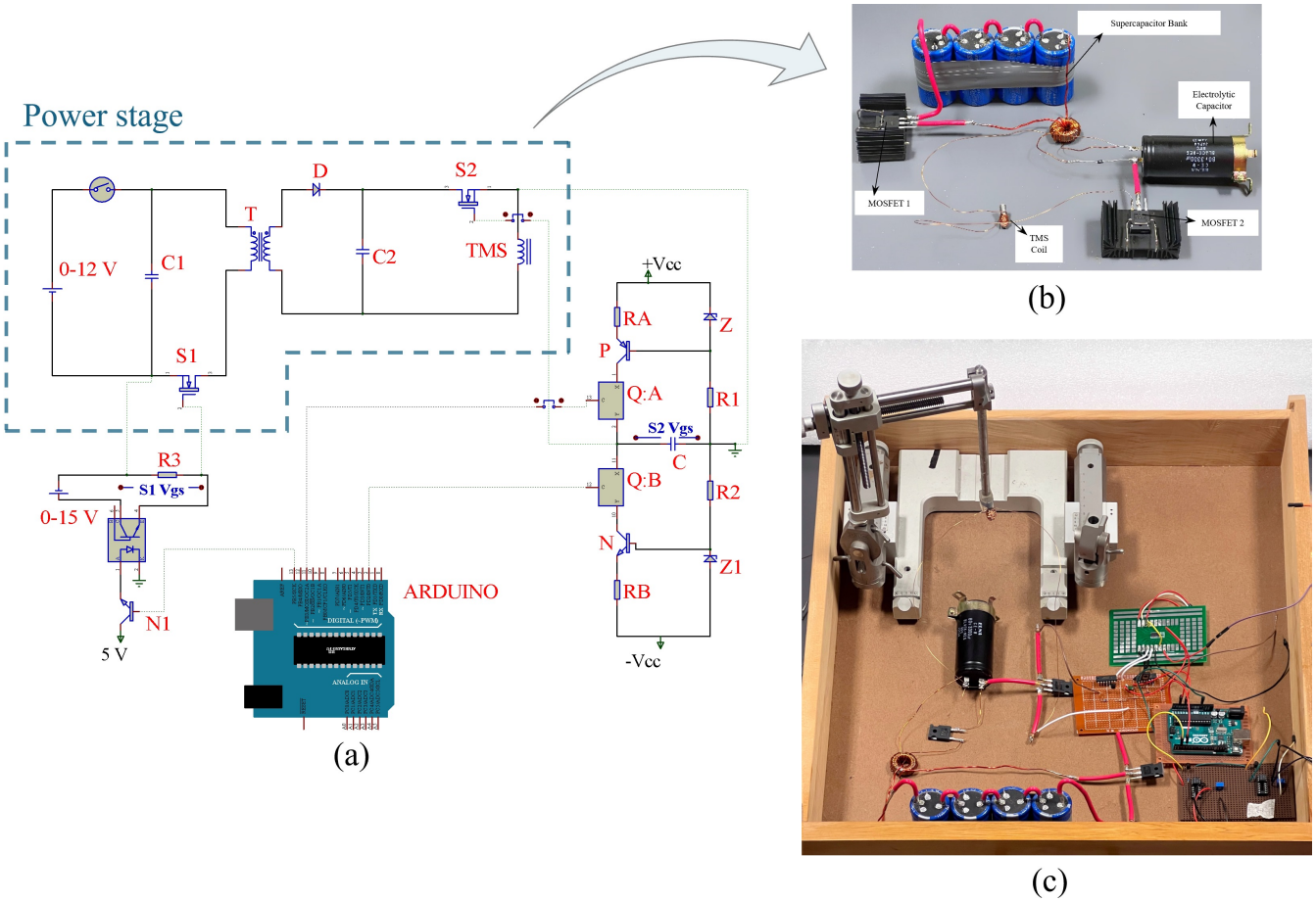

Fig. 1: Proof-of-concept of prototype- (a) Overall system showing external drivers to S1 from Arduino processor board and triangle voltage waveform generator for S2; (b) experimental power stage; (c) Full circuit prototype setup

the resistance and inductance parameters of the primary side of the step-up transformer.

Our team has successfully developed a supercapacitor-based pulse generator (SCPG) [22] as shown in Fig. 1, capable of producing a magnetic field of approximately 400 mT suitable for small animal brain excitation. This prototype can shape the output TMS current and voltage, crucially without needing additional external snubber or hardware setups like the existing topologies [6, 11]. The triangular gate input waveform, with its adjustable slope, enables a slower turn-on and turn-off than using MOSFET as switch, impacting the current and voltage pulses in the TMS coil system. Increasing the symmetry of the triangular waveform to 80% (80:20 rise-fall) resulted in a steeper fall slope as shown in Fig. 2, higher rate of change of current (di/dt), and a narrower pulse width of the voltage and current pulses. The developed MATLAB model of the MOSFET accurately predicts these outcomes, making it essential for future work in optimizing pulse shapes for TMS applications.

Using a 1 V input SC supply, we achieved a 250 V output TMS voltage pulse. For higher peak voltage of the output pulses we can proportionately increase the SC bank voltage. This can be further increased by adjusting the input triangle gate voltage symmetry. The results shown in Fig. 2 are for a 1 V input, which already produced a significant magnetic field (400 mT). Higher voltage outputs and pulse shaping are possible with change in optimal input gate voltage which can be determined through simulation models. Table I provides a breakdown of the cost of each component used

TABLE I: List of components and the associated costs

Label	Component	Nominal rating	Cost (USD)
C1	Electrolytic-capacitor	330 μF, 450 V	7
C2	Supercapacitor	380 F, 3 V, 3.2 mΩ	12
S1	Charging switch	40 V, 1.35 mΩ, 350 A	5
S2	Discharging switch	650 V, 24 mΩ, 120 A	24
D	High-frequency diode	1.2 kV, 75 A	5
T	Step-up transformer	1:60 Turns ratio	2
A	ARDUINO UNO	5 V, 14 digital I/O pin	30
	Others		20
		Total cost	105

(a) 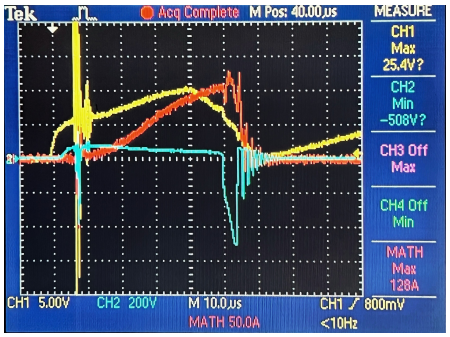

(b) 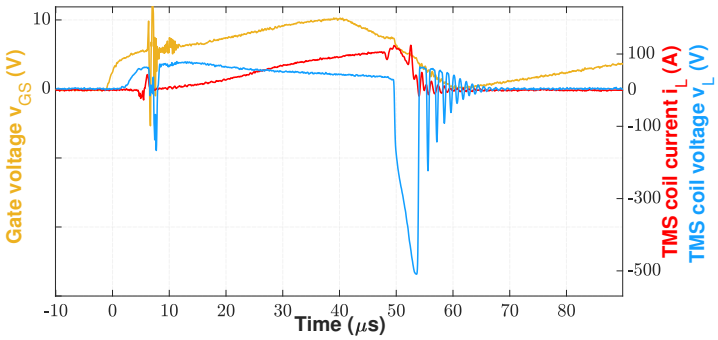

Fig. 2: (a) Oscilloscope measurement for gate voltage rise-fall symmetry set to 80:20. Note pronounced increase in peak coil voltage and emergence of ∼1 MHz oscillations arising from reduced gate-voltage fall time.; (b) MATLAB capture of oscilloscope traces shown in (a)

in the prototype, with the total amount reaching 105 USD, highlighting the affordability and cost-effectiveness of the design. The total cost of 105 USD demonstrates that the design is economically viable for research or small-scale manufacturing purposes.

One key advantage of this design is that the series-connected supercapacitor module can be pre-charged using any suitable laboratory power supply. This allows the SC module to deliver repeated pulse sets for a given experiment without requiring continuous connection to a DC power supply. Additionally, we have developed a new MOSFET equation that fills a gap in the literature, providing a model that closely aligns with experimental data.

III. Need for new equation

In our application, we require the MOSFET (S2 in Fig. 1) to operate at and near threshold point since the high voltage across the TMS coil is achieved at the time of switch off (when gate voltage goes below threshold). Surprisingly, this region has not been thoroughly analyzed by researchers. Analytical solutions such as the parallel plate charge control model and the unified charge control model exist [23–25], yet they lack precise analytical solutions for the sub-threshold or near-threshold region.

For many applications, the approximate solution for drain current used from these models is:

$$i_{\mathrm{D}} = 2\, i_{\mathrm{o}} \ln\left[1 + \frac{1}{2}\exp\left(\frac{v_{\mathrm{GS}} - v_{\mathrm{T}}}{\eta\, v_{\mathrm{Th}}}\right)\right] \tag{1}$$

where i_0 is the initial current (at threshold), applied gate voltage (v_{GS}), threshold voltage (v_{T}), thermal voltage (v_{Th}), and a sub-threshold ideality factor (η) is used. This solution is suitable for both above and below the threshold but not near the threshold [26–28]. All the analytical approaches available are designed for lower power and small-signal MOSFETs, whereas we are using a power MOSFET. There is no specific analytical calculation data available for power MOSFETs. We initially tried to use Equation (1) to fit the data points of the measured drain current versus gate voltage, but failed to do so as shown in Fig. 3(a). Thus we modified the drain current equation as a function of gate voltage only as:

$$i_{\mathrm{D}} = \frac{i_{\mathrm{o}}}{\ln 2} \ln\left(1 + \left[\exp\left(\frac{v_{\mathrm{GS}} - v_{\mathrm{T}}}{\eta\, v_{\mathrm{Th}}}\right)\right]^{p}\right) \tag{2}$$

where we have introduced a new parameter p to describe the transition from below-threshold to above-threshold as we need the current curve to change from exponential to linear. Figure 3(a) illustrates the failed curve fit using Eq. 1, while Fig. 3(b) demonstrates the successful fit achieved by employing the modified equation (2), which aligns much better with the data points (black dotted points).

The reason for the modification becomes apparent by analyzing Eq. (2) in three different regions.

The Eq. 2 can be further expressed in terms of a variable X:

$$i_{\mathrm{D}} = \frac{i_{\mathrm{o}}}{\ln 2} \ln[1 + X^{p}], \quad \text{where} \quad X = \exp\left(\frac{v_{\mathrm{GS}} - v_{\mathrm{T}}}{\eta\, v_{\mathrm{Th}}}\right). \tag{3}$$

A. Subthreshold

In the subthreshold region ($v_{\mathrm{GS}} < v_{\mathrm{T}}$), where $X \ll 1$, we use $p = 1$ (we have given the maximum value for the p since subthreshold region characteristics is of more exponential behavior):

$$i_{\mathrm{D}} = \frac{i_{\mathrm{o}}}{\ln 2} \ln[1 + X], \tag{4}$$

and using

$$\ln[1 + X] \approx X \quad \text{for small X}$$

we obtain

$$i_{\mathrm{D}} \approx \frac{i_{\mathrm{o}}}{\ln 2} \exp\left(\frac{v_{\mathrm{GS}} - v_{\mathrm{T}}}{\eta\, v_{\mathrm{Th}}}\right). \tag{5}$$

This equation resembles an exponential growth similar to general MOSFET characteristics [29].

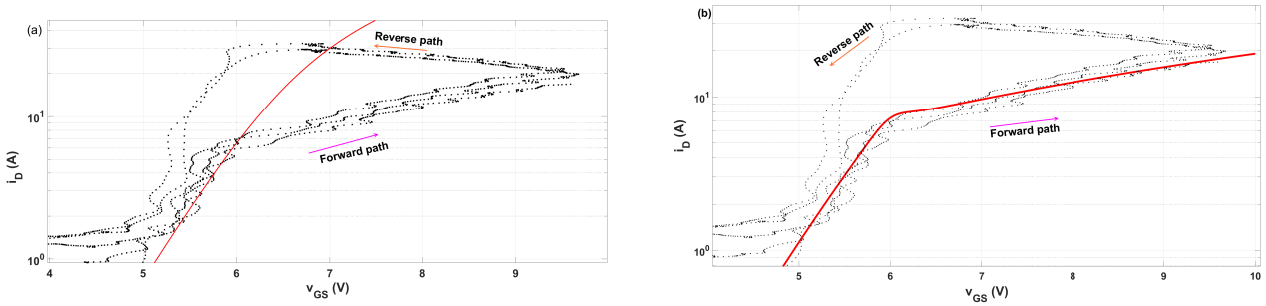

Fig. 3: (a) Current curve fit (red line) of the data points (black dots) from experiment using Eq. (1) which failed to fit; (b) current curve fitting done using modified equation Eq. (2), which was a successful fit with the forward data points

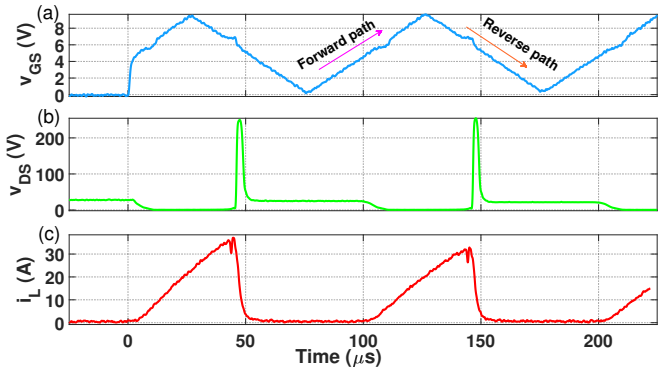

Fig. 4: Circuit parameters measured during TMS coil excitation- (a) Triangular control voltage of MOSFET 2 gate, 50% symmetry gate voltage with forward path (0 to 10 V) and reverse path (10 V to 0) marked (initial 25 μs of the triangular wave is not captured accurately due to the oscilloscope triggering configuration); (b) measured drain-source voltage and (c) coil current from the experimental setup used for the mosfet model

B. Above-threshold

In the above-threshold region ($v_{GS} > v_T$), where $X \gg 1$ and we use $p \approx 0.2$ (the value of p reduces from below-threshold to above-threshold as we need the current curve to change from exponential to linear), i_D becomes a linear equation:

$$i_D = \frac{i_o}{\ln 2} \ln[1 + X^p] \tag{6}$$

and using

$$\ln[1 + X^p] \approx \ln X^p \quad \text{for large } X^p$$

we obtain

$$\begin{aligned} i_D &= \frac{i_o}{\ln 2} \ln[X^p] = \frac{i_o}{\ln 2} \ln \left[\exp \left(\frac{v_{GS} - v_T}{\eta\, v_{Th}} \right) \right]^p \\ &= p \frac{i_o}{\ln 2} \left(\frac{v_{GS} - v_T}{\eta\, v_{Th}} \right) \end{aligned} \tag{7}$$

The equation (2) requires a gate-voltage dependent variable p to capture the changes occurring from subthreshold to above-threshold behaviors. Typically, small-signal MOSFETs exhibit an η value ranging from 1 to 2. However, in this analysis, we selected the η value to achieve a more accurate fit. In this context, η is treated as a fitting parameter. Thus, choosing η values greater than 1 is justified to attain a better alignment with the experimental data, particularly given the specific behavior of power MOSFETs.

C. At-threshold

At threshold, when $v_{GS} = v_T$, $X^p = 1$ for any value of p

$$i_D = \frac{i_o}{\ln 2} \ln[1 + X^p] = i_o \tag{8}$$

The modified term (ln 2) was added in Eq. (2), so that at threshold condition i_D should be equal to i_0.

The crucial aspect of our application revolves around understanding MOSFET characteristics during turn-off, particularly the voltage across and current through the inductor as the MOSFET transitions to its non-conducting state. This necessitates a robust equation that accurately models behavior below, near and above threshold. Through analysis of experimental data, we derived the new equation (Eq. 2) capable of effectively modeling high-power MOSFET behavior, thus addressing the limitations of existing analytical approaches.

By modifying the equation to depend solely on gate voltage, we achieved a successful fit that aligns with all operational regions. This method treats the MOSFET as a variable resistance controlled by gate-source voltage, simplifying analysis compared to switch-based models. It indirectly accounts for the influence of drain-source voltage on resistance, enhancing model accuracy.

IV. Development of Matlab model

The TMS excitation circuit (RLC) is the last stage of the prototype, illustrated in Fig. 1. The objective is to develop a model that solves the differential equation of the RLC circuit. since

$$v_C = v_L + (r_L + r_C + r_{DS}) i_L \tag{9}$$

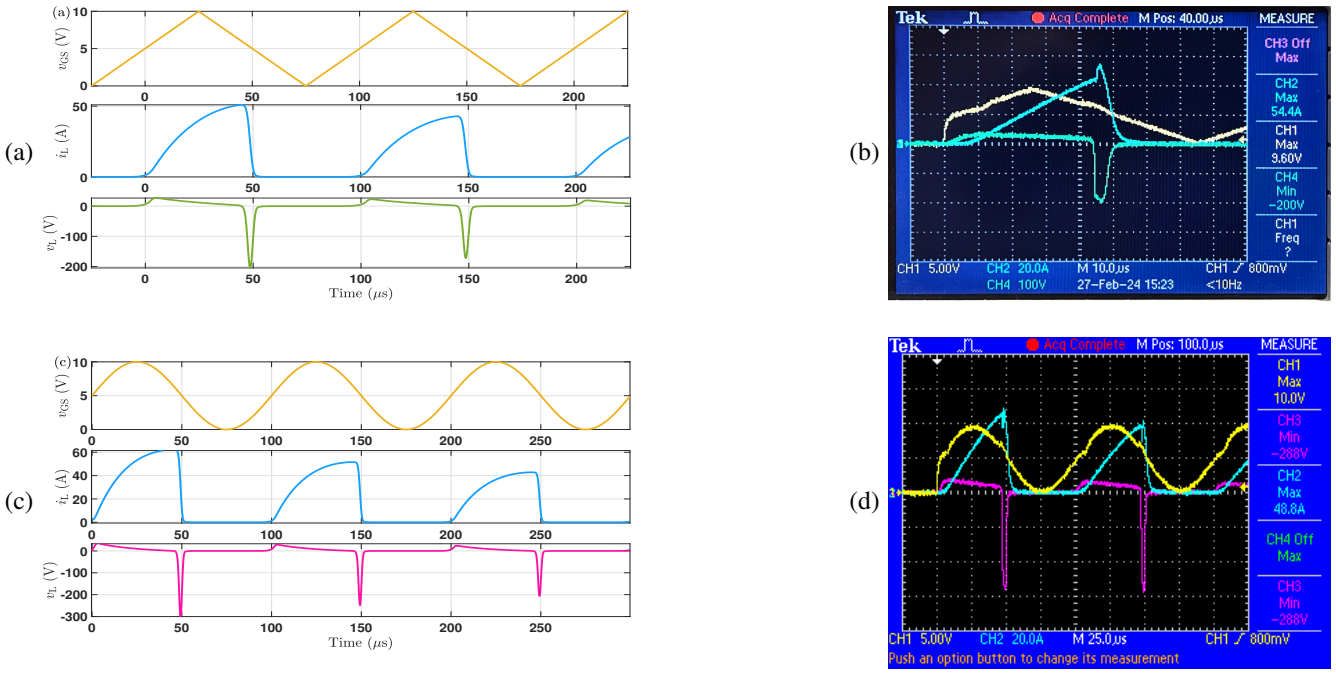

Fig. 5: (a) `ode15s` Solver solution of the differential equation with triangle gate voltage. The TMS voltage pulse has an amplitude of 200 V and current pulse with 50 A, which is almost identical to the oscilloscope output; (b) Oscilloscope measurement of MOSFET gate voltage (yellow), TMS coil voltage (green) and TMS coil current (blue). Gate voltage rise-fall symmetry is set at 50:50 (c) `ode15s` Solver solution of the differential equation with sinusoidal gate voltage input; (d) Oscilloscope measurement of sinusoidal gate voltage (yellow), TMS coil voltage (magenta) and TMS coil current (blue)

where r_{L} (internal resistance of the TMS coil), r_{C} (ESR of the capacitor C2), and L (inductance of the TMS coil) are known from experimental measurements. Given the measured values of v_{C} (C2 capacitor voltage) and v_{L} (inductor voltage), we can determine $i_{\mathrm{L}}(t)$. Our approach is as follows:

1) Development of the drain-source current equation, $i_{\mathrm{L_{fit}}} = i_{\mathrm{D}}$ as a function of v_{GS}: As in Eq. (2).
2) Computing the resistance of the MOSFET: Curve fitting is performed by plotting the measured v_{DS} versus v_{GS} (from Fig. 4) and deriving an equation for v_{DSfit} to fit the data points. Curve fitting involves creating a mathematical function or curve that best approximates the series of data points obtained from plotting v_{DS} versus v_{GS}. With the v_{DSfit} equation in hand, the $r_{\mathrm{DS_{fit}}}$ of the MOSFET can be determined by:

$$r_{\mathrm{DS_{fit}}} = \frac{v_{\mathrm{DS_{fit}}}(v_{\mathrm{GS}})}{i_{\mathrm{L_{fit}}}(v_{\mathrm{GS}})} \tag{10}$$

where

$$v_{\mathrm{DS_{fit}}} = \frac{1}{2}\left(D_1 + D_2 + (D_2 - D_1)\tanh\left(\frac{v_{\mathrm{GS}} - v_{\mathrm{T}}}{\eta_1\ v_{\mathrm{TH}}}\right)\right) \tag{11}$$

Equation (2) is modified to read as:

$$i_{\mathrm{L_{fit}}} = \frac{i_{\mathrm{o}}}{\ln 2}\ln\left(1 + \left[\exp\left(\frac{v_{\mathrm{GS}} - v_{\mathrm{T}}}{\eta_2\ v_{\mathrm{TH}}}\right)\right]^{p_{\mathrm{fit}}}\right) \tag{12}$$

where the exponent $p \to p_{\mathrm{fit}}$ is now a $\tanh$ function of MOSFET gate voltage,

$$p_{\mathrm{fit}} = \frac{1}{2}\left(p_1 + p_2 + (p_2 - p_1)\tanh\left(\frac{v_{\mathrm{GS}} - v_{\mathrm{T}}}{\eta_3\ v_{\mathrm{TH}}}\right)\right) \tag{13}$$

3) MATLAB model: Now we can use this $r_{\mathrm{DS_{fit}}}$ in the differential Equation. (9) as:

$$\frac{di_{\mathrm{L}}}{dt} = \frac{1}{L}\left[v_{\mathrm{C}} - (r_{\mathrm{L}} + r_{\mathrm{C}} + r_{\mathrm{DS_{fit}}}(v_{\mathrm{GS}}))i_{\mathrm{L}}\right] \tag{14}$$

and solve it for a given $v_{\mathrm{GS}}(t)$ profile. The circuit's performance hinges on the MOSFET's turn-off behavior, and relying solely on the on-resistance provided in datasheets or MOSFET models in simulation software like SPICE is inadequate. This model addresses the gap in the literature where a universal drain-source current equation applicable across all regions is missing, leading to the necessity of developing a new equation.

V. Verification

The MATLAB model for our supercapacitor-based pulse generator (SCPG) was validated using the `ode15s` solver,

aligning closely with experimental data. Figure 5(a) and 5(b) compares simulation and experimental results for a 50% symmetry gate voltage, demonstrating consistency. The MOSFET behavior was accurately captured through curve fitting. A 10 kHz, 10 V sinusoidal gate voltage (Fig. 5(c)) showed simulation results matching prototype tested results based on the oscilloscope outputs (Fig. 5(d)), affirming the model's accuracy in predicting TMS behavior under varied conditions.

VI. Conclusion

In conclusion, the developed prototype is a low-cost supercapacitor based pulse generator (SCPG) for TMS with pulse shaping capabilities, achieved without the need for any external snubber or additional wave-shaping circuit. The developed MATLAB model for our SCPG demonstrates robust accuracy in predicting TMS current and voltage waveforms under various input conditions. Through careful validation against experimental data, including sinusoidal and triangular gate voltages, the model reliably captures MOSFET behavior. This tool enhances understanding and optimization of pulse generator performance, offering valuable insights for future research and applications in neurostimulation and related fields.

Acknowledgment

The authors gratefully acknowledge the University of Waikato Doctoral Scholarship for research support, as well as the Neurological Foundation and the Hackett Memorial Trust for providing research funding and a travel grant.

References

[1] A. V. Peterchev, R. Jalinous, and S. H. Lisanby, "A transcranial magnetic stimulator inducing near-rectangular pulses with controllable pulse width (cTMS)," *IEEE Transactions on Biomedical Engineering*, vol. 55, no. 1, pp. 257–266, 2007.

[2] A. V. Peterchev, Z.-D. Deng, and S. M. Goetz, "Advances in transcranial magnetic stimulation technology," *Brain stimulation: methodologies and interventions*, pp. 165–189, 2015.

[3] J. Selvaraj, P. Rastogi, N. Prabhu Gaunkar, R. L. Hadimani, and M. Mina, "Transcranial magnetic stimulation: Design of a stimulator and a focused coil for the application of small animals," *IEEE Transactions on Magnetics*, vol. 54, no. 11, pp. 1–5, 2018.

[4] F. A. Khokhar, L. J. Voss, D. A. Steyn-Ross, and M. T. Wilson, "Design and demonstration in vitro of a mouse-specific transcranial magnetic stimulation coil," *IEEE Transactions on Magnetics*, vol. 57, no. 7, pp. 1–11, 2021.

[5] A. D. Tang, A. S. Lowe, A. R. Garrett, R. Woodward, W. Bennett, A. J. Canty, M. I. Garry, M. R. Hinder, J. J. Summers, R. Gersner *et al.*, "Construction and evaluation of rodent-specific rTMS coils," *Frontiers in neural circuits*, vol. 10, p. 47, 2016.

[6] A. V. Peterchev and D. L. Murphy, "Controllable pulse parameter transcranial magnetic stimulator with enhanced pulse shaping," in *2013 6th International IEEE/EMBS Conference on Neural Engineering (NER)*. IEEE, 2013, pp. 121–124.

[7] "Electric fencing basics," am.gallagher.com/en-US/Solutions/Case-Study-Listings/Electric-Fencing-Basics, accessed: 2022-02-15.

[8] J. Mankowski and M. Kristiansen, "A review of short pulse generator technology," *IEEE Transactions on plasma science*, vol. 28, no. 1, pp. 102–108, 2000.

[9] A. Elserougi, S. Ahmed, and A. Massoud, "A boost converter-based ringing circuit with high-voltage gain for unipolar pulse generation," *IEEE Transactions on Dielectrics and Electrical Insulation*, vol. 23, no. 4, pp. 2088–2094, 2016.

[10] X. Zan, D. R. Torres, R. Kheirollahi, X. Lu, S. Zheng, F. Lu, and A.-T. Avestruz, "Medium voltage pulse power generator for accurate current interruption," *IEEE Transactions on Industrial Electronics*, vol. 70, no. 4, pp. 3604–3615, 2023.

[11] S. M. Goetz, M. Pfaeffl, J. Huber, M. Singer, R. Marquardt, and T. Weyh, "Circuit topology and control principle for a first magnetic stimulator with fully controllable waveform," in *2012 Annual International Conference of the IEEE Engineering in Medicine and Biology Society*. IEEE, 2012, pp. 4700–4703.

[12] L. M. Koponen and A. V. Peterchev, "Transcranial magnetic stimulation: principles and applications," *Neural Engineering*, pp. 245–270, 2020.

[13] K. Ali, K. Wendt, M. M. Sorkhabi, M. Benjaber, T. Denison, and D. J. Rogers, "xTMS: A pulse generator for exploring transcranial magnetic stimulation therapies," in *2023 IEEE Applied Power Electronics Conference and Exposition (APEC)*, 2023, pp. 1875–1880.

[14] L. Pang, T. Long, K. He, Y. Huang, and Q. Zhang, "A compact series-connected sic mosfets module and its application in high voltage nanosecond pulse generator," *IEEE Transactions on Industrial Electronics*, vol. 66, no. 12, pp. 9238–9247, 2019.

[15] W. Zeng, C. Yao, S. Dong, Y. Wang, J. Ma, Y. He, and L. Yu, "Self-triggering high-frequency nanosecond pulse generator," *IEEE Transactions on Power Electronics*, vol. 35, no. 8, pp. 8002–8012, 2020.

[16] Y. Liu, R. Fan, X. Zhang, Z. Tu, and J. Zhang, "Bipolar high voltage pulse generator without h-bridge based on cascade of positive and negative marx generators," *IEEE Transactions on Dielectrics and Electrical Insulation*, vol. 26, no. 2, pp. 476–483, 2019.

[17] L. Cheng, K. Mei, Z. Chen, W. Jia, Y. Wang, H. Wang, L. Xie, S. Shen, and W. Ding, "High-voltage repetitive nanosecond pulse generator utilizing power synthesis of modified avalanche transistorized marx circuits," *IEEE Transactions on Instrumentation and Measurement*, vol. 71, pp. 1–16, 2022.

[18] J. Yan, S. Shen, and W. Ding, "High-power nanosecond pulse generators with improved reliability by adopting auxiliary triggering topology," *IEEE Transactions on*

Power Electronics, vol. 35, no. 2, pp. 1353–1364, 2020.

[19] L. Cheng, Z. Chen, H. Wang, F. Guo, G. Wu, L. Xie, J. Xiao, Y. Wang, S. Shen, and W. Ding, "A novel avalanche transistor-based nanosecond pulse generator with a wide working range and high reliability," *IEEE Transactions on Instrumentation and Measurement*, vol. 70, pp. 1–14, 2021.

[20] Y. Zhao, W. Xie, J. Jiang, L. Chen, S. Feng, M. Wang, and Z. Wang, "Replacement of marx generator by tesla transformer for pulsed power system reliability improvement," *IEEE Transactions on Plasma Science*, vol. 47, no. 1, pp. 574–580, 2019.

[21] L. Li, M. Ning, C. Dehuai, L. Lun, K. Qiang, L. Mingjia, C. Yong, and P. Yuan, "Study on double resonant performance of air-core spiral tesla transformer applied in repetitive pulsed operation," *IEEE Transactions on Dielectrics and Electrical Insulation*, vol. 22, no. 4, pp. 1916–1922, 2015.

[22] S. Raju, N. Kularatna, and M. Wilson, "Supercapacitor based adjustable high power pulse generator for medical research applications," in *IECON 2023-49th Annual Conference of the IEEE Industrial Electronics Society*. IEEE, 2023, pp. 1–6.

[23] N. D. Arora, *MOSFET models for VLSI circuit simulation: theory and practice*. Springer Science & Business Media, 2012.

[24] J. Brews, W. Fichtner, E. Nicollian, and S. Sze, "Generalized guide for mosfet miniaturization," in *1979 International Electron Devices Meeting*. IEEE, 1979, pp. 10–13.

[25] Y. Byun, K. Lee, and M. Shur, "Unified charge control model and subthreshold current in heterostructure field-effect transistors," *IEEE Electron Device Letters*, vol. 11, no. 1, pp. 50–53, 1990.

[26] T. Ytterdal, Y. Cheng, and T. A. Fjeldly, *Device modeling for analog and RF CMOS circuit design*. John Wiley & Sons, 2003.

[27] T. A. Fjeldly and M. Shur, "Threshold voltage modeling and the subthreshold regime of operation of short-channel mosfets," *IEEE Transactions on Electron Devices*, vol. 40, no. 1, pp. 137–145, 1993.

[28] T. A. Fjeldly, M. Shur, and T. Ytterdal, *Introduction to device modeling and circuit simulation*. John Wiley & Sons, Inc., 1997.

[29] P. van der Meer, A. van Staveren, and A. H. van Roermund, *Low-power deep sub-micron CMOS logic: sub-threshold current reduction*. Springer Science & Business Media, 2004, vol. 841.

6.5.2 IEEE Transactions on circuits and systems I: Regular papers

The following paper, "Dynamic nonlinear resistance model for a power MOSFET in an oscillatory RLC circuit," has been published in the IEEE journal, transactions on circuits and systems I: regular papers. An attribution detailing the contributions from the authors is included in the Appendix E.

This article has been accepted for inclusion in a future issue of this journal. Content is final as presented, with the exception of pagination.

Dynamic Nonlinear Resistance Model for a Power MOSFET in an Oscillatory RLC Circuit

Soniya Raju, *Member, IEEE*, D. Alistair Steyn-Ross, Marcus Wilson, and Nihal Kularatna, *Senior Member, IEEE*

***Abstract*— This paper presents the development of a new MATLAB MOSFET model specifically designed for RLC circuits. The key contribution is the formulation of a novel equation that accurately captures the device behavior across subthreshold, above-threshold regions and at threshold point, addressing limitations in existing models. The developed model treats the MOSFET as a variable resistance element, with the resistance changing dynamically at each instant, enabling the solution of differential equations governing the RLC circuit. Curve fitting and refinement were conducted based on experimental results, leading to a close match between the simulations and experimental data. The model was tested with triangle, sinusoidal and quadrilateral gate voltages, and the simulation results show good match with the experimental data, demonstrating the model's accuracy. It provides a straightforward way to predict performance, making it easier to refine and optimize the design gate voltage before physical implementation. This work provides a solid foundation for MOSFET modeling in oscillatory RLC circuits, which can be applied to a wide range of power electronics applications.**

***Index Terms*— Supercapacitors, transcranial magnetic stimulation (TMS), power semiconductor switches, pulse generator, magnetic stimulation, pulse circuits, nonlinear MOSFET model.**

I. Introduction

METAL-OXIDE semiconductor field effect transistor (MOSFET) models play a crucial role in simulating and understanding device behavior in power electronics. Various MOSFET models have been developed to accurately represent their characteristics in circuit simulations. These models fall into three broad categories: physics-based, analytical, and behavioral. Physics-based models, often used in technology computer-aided design (TCAD) simulations, focus on detailed internal phenomena such as electron mobility, channel length modulation, and threshold voltage shifts. While these models offer high accuracy, they can be computationally intensive and difficult to use for practical applications in power circuits due to the complexity of the physical phenomena being modeled [1], [2]. Analytical models, such as the Unified Charge Control Model (UCCM), rely on mathematical expressions to describe device behavior and to provide a clear relationship between key parameters like current, transconductance, and threshold voltage. Though more efficient for simulations than physics-based models, they can become complicated when high accuracy is required [3], [4].

Behavioral models, including widely-used SPICE models, are designed to simplify the simulation of MOSFETs for practical applications like power converters, automotive systems, and switching devices. These models focus on representing the overall electrical behavior of the MOSFET rather than the internal physical details. SPICE models are generally preferred for applications requiring fast and efficient simulation because they strike a balance between accuracy and simplicity. A SPICE model for a 6.5 kV SiC MOSFET was recently developed to closely match the device's static and dynamic characteristics, demonstrating how behavioral models can still achieve reasonable accuracy for power applications [5]. While behavioral models are simpler and more user-friendly, they can lack the precision needed for complex scenarios, particularly where parasitic elements (stray inductance and capacitance) or extreme operating conditions such as high switching frequencies or elevated temperatures come into play.

One of the major challenges in MOSFET modeling is the accurate simulation of switching behavior and parasitic effects. SiC MOSFETs offer lower on-state resistance than traditional silicon MOSFET, higher breakdown voltages, and faster switching speeds, making them suitable for high-voltage and high-frequency applications [6]. While several models have been proposed for SiC MOSFETs, such as the Hefner model and its derivatives [7], these models often require extensive parameter extraction from datasheets or experimental data, limiting their practical use in everyday circuit design. A recent approach involves using a modified Enz-Krumenacher-Vittoz (EKV) model [8] for SiC MOSFETs, which offers a single equation for the entire operating range, from weak to strong inversion. This model has been successfully applied to simulate SiC MOSFETs in high-frequency switching applications, with validation against experimental data.

Several studies have focused on modeling SiC power devices. PSpice is widely used for SiC MOSFET modeling, but its limitations in handling complex equations can affect accuracy [8]. MATLAB/Simulink, with superior simulation and data processing capabilities, offers an alternative. Tornello et al. [9] developed an analytical model for single and parallel SiC configurations, achieving accurate switching transient behavior and energy loss predictions

Received 27 November 2024; revised 26 January 2025; accepted 13 February 2025. This article was recommended by Associate Editor V. Lanza. *(Corresponding author: Soniya Raju.)*

Soniya Raju and Marcus Wilson are with the School of Science, University of Waikato, Hamilton 3240, New Zealand (e-mail: sr231@students.waikato.ac.nz).

D. Alistair Steyn-Ross and Nihal Kularatna are with the School of Engineering, University of Waikato, Hamilton 3240, New Zealand.

Digital Object Identifier 10.1109/TCSI.2025.3542754

1549-8328 © 2025 IEEE. All rights reserved, including rights for text and data mining, and training of artificial intelligence and similar technologies. Personal use is permitted, but republication/redistribution requires IEEE permission.
See https://www.ieee.org/publications/rights/index.html for more information.
Authorized licensed use limited to: Univ of Waikato. Downloaded on April 24,2025 at 06:32:33 UTC from IEEE Xplore. Restrictions apply.

This article has been accepted for inclusion in a future issue of this journal. Content is final as presented, with the exception of pagination.

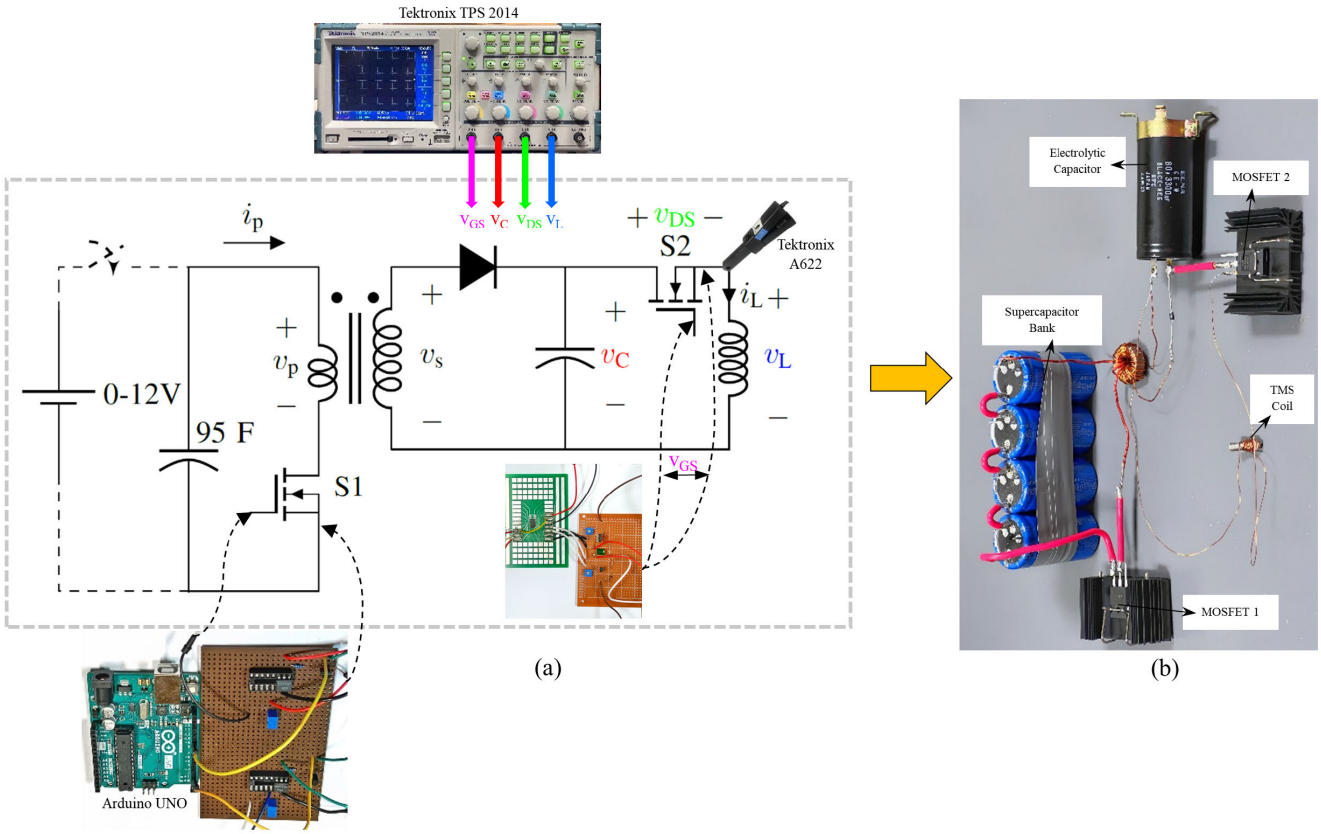

Fig. 1. Proof-of-concept prototype. Gate control signals for MOSFET S1 and S2 ensure that these switches are never ON at the same time. (a) Overall system with photos inserted showing external drivers to S1 from Arduino processor board, gate-drive waveform generator for S2 and oscilloscope; (b) experimental power stage.

compared to SPICE models using 2D and 1D Look-Up Tables (LUTs) for device characteristics. Ferretti et al. [10] implemented a MATLAB-based approach to create I-V-T maps (lookup tables), including operating regions not covered in datasheets. Zeng et al. [11] conducted modeling research on parasitic capacitances (C_{ds}) and (C_{gd}) using MATLAB Simulink, extracting values from datasheets and curve-fitting for accuracy. While these studies relied on datasheet-based modeling and simulation, none explored the internal MOSFET variations, such as dynamic resistance changes, highlighting a gap in the current research.

Wang et al. [12] proposed a modeling method using PSpice with a dual voltage-dependent lookup table approach based on the envelope of the switching trajectory. Their method defines the value ranges for gate-source voltage (v_{GS}) and drain-source voltage (v_{DS}) during interterminal capacitance operation periods, considering only essential data within the switching trajectory and discarding unnecessary information outside it. Talesara et al. [13] implemented an analytical subcircuit model for SiC MOSFETs into Synopsys Saber [14], validating it against measured DC characteristics. They employed distinct equations for sub-threshold and threshold regions instead of a unified equation and used a Simulink-based approach rather than a purely mathematical one. Yang et al. [15] employ small-signal oscillations, utilizing linear analysis without attempting to model the actual switching phase transition.

Despite these advancements, existing MOSFET models still face limitations when applied in circuit simulations, particularly in power electronics. Many models are either too complex for practical use or fail to accurately match experimental results, especially in scenarios involving parasitic inductance and capacitance, which are common in power circuits. Engineers often encounter difficulties when trying to use off-the-shelf MOSFETs for which detailed models are unavailable. For instance, while several SiC MOSFET models, such as the Hefner model and SPICE models, are available, they often require complex parameter extraction processes and do not always capture all the physical phenomena that occur at different operating temperatures or switching speeds [16]. This highlights the need for a more simplified and generalized MOSFET model that can closely match experimental data without the need for extensive parameter tuning.

This paper aims to address this gap by proposing a new MOSFET model, developed in MATLAB, which is based on experimental results and tailored for use in electrical RLC circuits as first trial step. The model introduces a new equation that simplifies the representation of MOSFET behavior, focusing on the static and dynamic characteristics that are critical for power electronics applications. Unlike

Authorized licensed use limited to: Univ of Waikato. Downloaded on April 24,2025 at 06:32:33 UTC from IEEE Xplore. Restrictions apply.

This article has been accepted for inclusion in a future issue of this journal. Content is final as presented, with the exception of pagination.

existing models that are either overly complex or limited in their accuracy, this model is designed to be easy to implement while maintaining close alignment with experimental results. This approach offers a practical solution for engineers looking to simulate MOSFETs in power converters, motor controllers, and other high-voltage applications, where both accuracy and simplicity are essential. By bridging the gap between detailed physics-based models and simplified behavioral models, the proposed model provides a more balanced solution for modern power electronics design [5], [6], [8], [16], [17].

This paper details the development of a MATLAB simulation to model a MOSFET, enabling predictions of its behavior and the output of an RLC circuit. This RLC circuit is integral to the supercapacitor-based TMS pulse generator [18], which has been developed and successfully tested. To advance the design further, a simulation model was essential to verify output pulses, perform precise pulse shaping, and assess the impact of varying gate voltages on TMS pulse characteristics. However, no existing MOSFET equation or model was suitable for this application, prompting us to derive a new equation and create a MATLAB MOSFET model tailored for in-depth analysis. The process begins with an overview of the background study conducted for modeling, followed by modifications to existing equations to ensure proper functionality within the circuit. The creation of the MATLAB model is then described, based on experimental data, resulting in a complete MOSFET simulation model capable of predicting output current and voltage as functions of time, in response to gate voltage input. Finally, a comparison between the modeling and experimental results for a different scenario is presented. This study presents a solution applicable to any oscillatory RLC circuit incorporating a MOSFET, offering insights and modeling techniques beneficial for a range of applications beyond TMS pulse generation.

II. Expression for Drain Current

Figure 1 shows the overall system, including the circuit diagram of the TMS pulse generator setup. This pulse generator [18] incorporates an RLC circuit in the final stage to excite the TMS coil. We developed this MOSFET model as part of our research study focused on pulse shaping capabilities and predicting the output TMS pulse. In this section, we discuss the modeling of the RLC part alone for a generic study.

Consider an RLC circuit containing an embedded MOSFET to control oscillatory current as shown in Fig. 2. We explicitly include the internal resistances of the capacitor (r_C) and the inductor (r_L).

Applying Kirchhoff's voltage law to Fig. 2,

$$v_C = v_L + (r_L + r_C + r_{DS})i_L \tag{1}$$

where the ideal inductor voltage is given by $v_L = L\frac{di_L}{dt}$

Equation (1) can be rewritten as a first-order differential equation,

$$\frac{di_L}{dt} = \frac{1}{L}\left[v_C - (r_L + r_C + r_{DS})i_L\right] \tag{2}$$

Thus if we know r_{DS}, we can numerically integrate Eq. (2) to find $i_L(t)$.

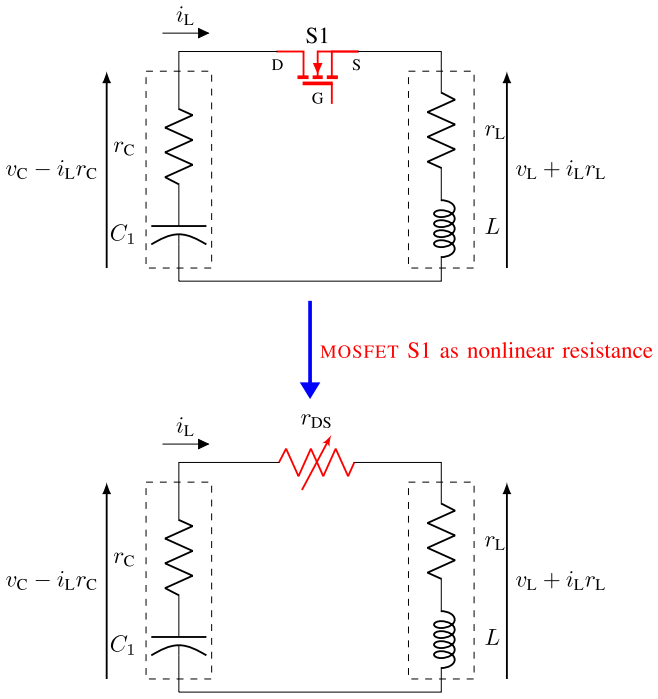

Fig. 2. The circuitry illustrates a RLC circuit, featuring the electrolytic capacitor C_1 along with its internal resistance r_C feeding an inductive load characterized by an inductance L and its internal resistance r_L. It includes a MOSFET switch represented as a nonlinear resistance r_{DS}, which depends on the gate-source voltage.

In these equations, we do not consider the MOSFET as a typical switching component. Instead, it is treated as an analog device, which behaves like a variable resistor controlled by the voltage applied to the gate. The challenge is to determine the time-varying resistance of the MOSFET as a function of input gate voltage for incorporation into differential equation (2).

By controlling the gate voltage v_{GS}, a MOSFET can be operated in distinct regions as shown in Fig. 3(a): subthreshold ($v_{GS} < v_T$), and above-threshold ($v_{GS} > v_T$). When gate voltage exceeds threshold, the MOSFET output characteristics moves from linear to saturation mode as v_{GS} increases. Our focus is on developing a unified description for MOSFET behavior that encompasses transition through threshold.

A. Subthreshold ($v_{GS} < v_T$)

In the subthreshold region, also known as the weak/cutoff region, the transistor remains in an 'off' state with minimal conduction. The small current flow into the drain is described by an exponential function of v_{GS}:

$$i_D \approx i_{D0} \exp\left(\frac{v_{GS} - v_T}{\eta\, v_{Th}}\right) \tag{3}$$

where applied gate voltage (v_{GS}), threshold voltage (v_T), thermal voltage (v_{Th}), and a subthreshold ideality factor (η) is used. The ideality factor accounts for the subthreshold division of the applied voltage between the gate insulator and the depletion layer [20].

Authorized licensed use limited to: Univ of Waikato. Downloaded on April 24,2025 at 06:32:33 UTC from IEEE Xplore. Restrictions apply.

This article has been accepted for inclusion in a future issue of this journal. Content is final as presented, with the exception of pagination.

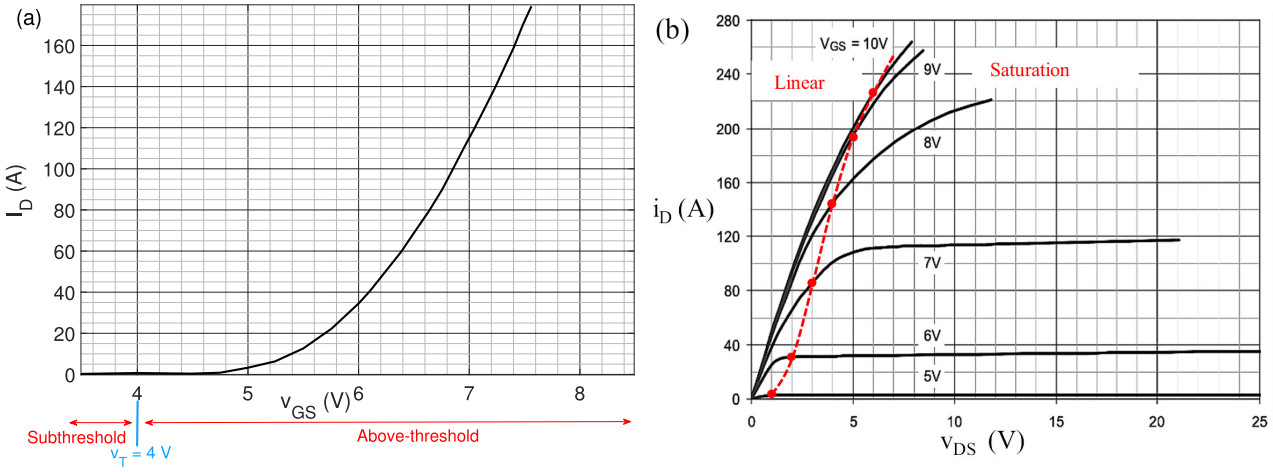

Fig. 3. (a) Drain current (I_D) against gate-source voltage (v_{GS}) of 25 °C and (b) drain current against the drain–source voltage for various gate voltages for MOSFET IXFK120N65 × 2 from data-sheet [19].The red dotted line in (b) indicates the above-threshold separation between linear and saturation modes, corresponding to v_{DS} being less or greater than ($v_{GS} - v_T$) respectively. The threshold voltage (v_T) is set to 4 V here for demonstration, as the datasheet specifies a range for v_T between 3 and 6 V.

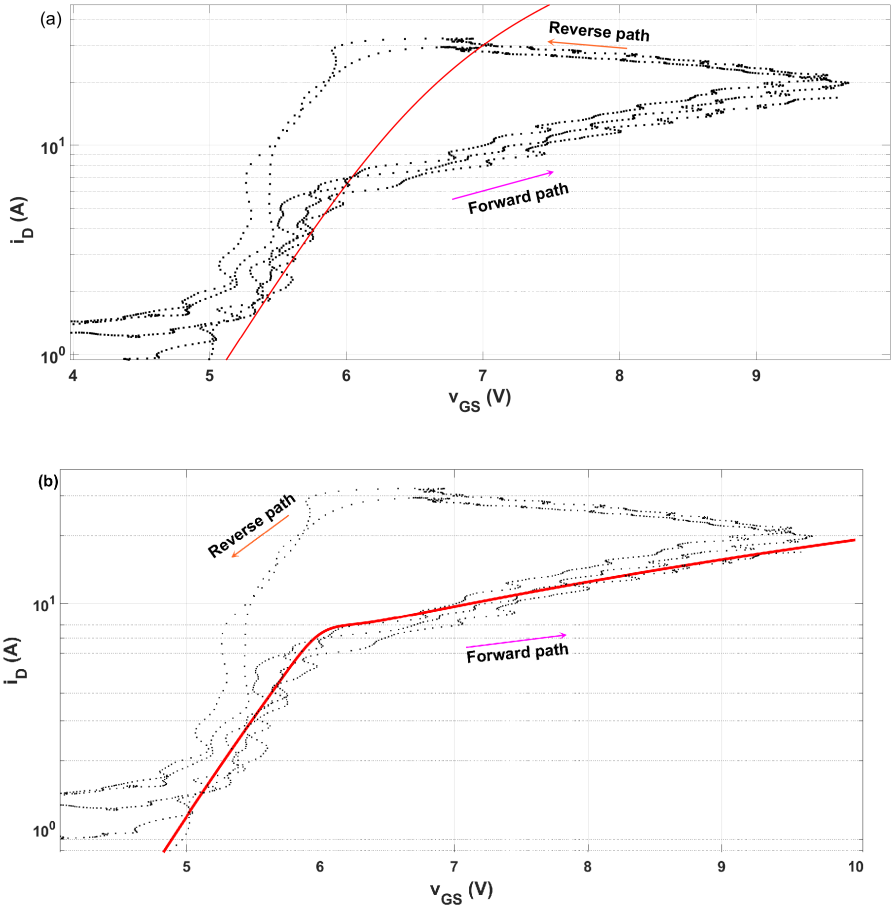

Fig. 4. (a) Curve fit (red line) for the MOSFET drain current i_L for data points (black dots) from experiment using Eq. (7) which failed to fit; (b) improved curve using equation Eq. (15), provided a good match for the forward-path measurements.

B. Above Threshold ($v_{GS} > v_T$)

In the above-threshold region, there are two operation modes depending on the drain-current characteristic with respect to drain-source voltage as in Fig 3(b). These are linear (also referred to as triode or ohmic), and saturation modes.

1) Linear mode ($v_{GS} > v_T, v_{DS} < (v_{GS} - v_T)$), the transistor activates, creating a narrow channel for current

Authorized licensed use limited to: Univ of Waikato. Downloaded on April 24,2025 at 06:32:33 UTC from IEEE Xplore. Restrictions apply.

This article has been accepted for inclusion in a future issue of this journal. Content is final as presented, with the exception of pagination.

to flow from drain to source. This region operates like a resistor, its conductance controlled by the gate-source voltage. The drain current in linear/ohmic mode consists of linear and quadratic terms as:

$$i_D = \mu_n C_{ox} \frac{W}{L} \left((v_{GS} - v_T) v_{DS} - \frac{{v_{DS}}^2}{2} \right) \quad (4)$$

where μ_n is the charge carrier effective mobility, C_{ox} is the gate oxide capacitance per unit area, gate width (W) and gate length (L) [21]. According to this equation, when the drain voltage is small, the drain current becomes a linear function of v_{DS}:

$$i_D = \mu_n C_{ox} \frac{W}{L} (v_{GS} - v_T) v_{DS}. \quad (5)$$

2) The saturation mode ($v_{GS} > v_T$, $v_{DS} > (v_{GS} - v_T)$), also above threshold, and since drain voltage is greater than the source voltage, it results in an increased electron dispersion and conduction through a broader channel. The drain current in saturation mode is:

$$i_D = \mu_n C_{ox} \frac{W}{L} [v_{GS} - v_T]^2 [1 + \lambda v_{DS}]. \quad (6)$$

The parameter λ accounts for the impact of channel length modulation on drain current, known as the Early effect, and it is measured in inverse volts (V^{-1}) [22]. It represents the change in drain current with respect to drain voltage due to variations in the channel length. Figure 3(b) shows the data-sheet version of input and output characteristics with the boundary between linear and saturation modes marked by the red line.

C. Near Threshold ($v_{GS} = v_T$)

In our application, we require the MOSFET to operate at and near threshold since the high voltage across the inductor coil is achieved at the time of switch off (when gate voltage goes below threshold). Surprisingly, this region has not been thoroughly analyzed by researchers [4], [23]. Analytical solutions like the parallel-plate charge-control model and the unified charge-control model exist [24], [25], [26], yet they lack precise analytical solutions for the subthreshold or near-threshold region. For many applications, an approximate solution used in these models is [4]:

$$i_D = 2\, i_o \ln \left[1 + \frac{1}{2} \exp \left(\frac{v_{GS} - v_T}{\eta\ v_{Th}} \right) \right] \quad (7)$$

where i_0 is the current corresponding to the minority carriers at threshold. This equation can be further expressed in terms of a variable X:

$$i_D = 2 i_o \ln \left[1 + \frac{X}{2} \right], \quad \text{where} \quad X = \exp \left(\frac{v_{GS} - v_T}{\eta\ v_{Th}} \right). \quad (8)$$

Equation 7 can be evaluated across different regions to determine its applicability for sub-threshold, above-threshold, and near-threshold regions.

1) Subthreshold Region: In the subthreshold region ($v_{GS} < v_T$), where $X \ll 1$, we can approximate the exponential term for small values as:

$$\ln[1 + \frac{X}{2}] \approx \frac{X}{2} \quad \text{for small X.} \quad (9)$$

This simplifies Eq. (7):

$$i_D \approx 2\ i_o \left[\frac{X}{2} \right] = i_o \exp \left(\frac{v_{GS} - v_T}{\eta v_{Th}} \right). \quad (10)$$

2) Above-Threshold Region: In the above-threshold region ($v_{GS} > v_T$), where $X \gg 1$, the exponential term dominates. We can approximate it as:

$$\ln \left[1 + \frac{X}{2} \right] \approx \ln \left[\frac{X}{2} \right]. \quad (11)$$

and Eq. (7) simplifies to:

$$i_D \approx 2\ i_o \ln \left(\frac{1}{2} \right) + 2\ i_o \frac{v_{GS} - v_T}{\eta v_{Th}}, \quad (12)$$

in agreement with Eq. (3).

3) At Threshold: At the threshold ($v_{GS} = v_T$), we have:

$$X = 1, \quad (13)$$

so the equation becomes:

$$i_D = 2\ i_o \ln \left[1 + \frac{1}{2} \cdot 1 \right] = 2\ i_o \ln \left(\frac{3}{2} \right). \quad (14)$$

Thus at the threshold condition, the current i_D is not equal to i_o.

Equation (7) is suitable for both above and below the threshold regions but not near the threshold region, as i_D is not equal to the initial current at the threshold point [27], [28], [29]. All analytical approaches available are designed for lower power and small-signal MOSFETs. But no analytical model have been developed for power MOSFETs. We initially tried to use Eq. (7) to fit the data points of the measured drain current versus gate voltage for our power MOSFET, but failed. Thus we modified the drain current equation to read:

$$i_D = \frac{i_o}{\ln 2} \ln \left(1 + \left[\exp \left(\frac{v_{GS} - v_T}{\eta\ v_{Th}} \right) \right]^p \right) \quad (15)$$

This equation can be further expressed in terms of a variable X:

$$i_D = \frac{i_o}{\ln 2} \ln[1 + X^p], \text{ where } X = \exp \left(\frac{v_{GS} - v_T}{\eta\ v_{Th}} \right). \quad (16)$$

Where, we have introduced a new parameter, the exponent p, and replaced the factor 2 in Eq. (7) with $\frac{1}{\ln 2}$ for reasons that will be explained in Section IV.

Figure 4(a) illustrates the failed curve fit using Eq. (7), while Fig. 4(b) demonstrates the successful fit achieved by employing the modified equation (15), which aligns much better with the data points (black dotted points).

Authorized licensed use limited to: Univ of Waikato. Downloaded on April 24,2025 at 06:32:33 UTC from IEEE Xplore. Restrictions apply.

This article has been accepted for inclusion in a future issue of this journal. Content is final as presented, with the exception of pagination.

III. Methodology

The following summarizes the steps we took to develop the MOSFET MATLAB model:

1) Development of the drain-source current equation, $i_{L_{fit}}$: No equation or expression determines the drain-source current at all the MOSFET regions (subthreshold, at the threshold, above-threshold). So we modified an existing equation used in the literature [27] to fit experimental results as shown Eq. 15.
2) Computing the resistance of the MOSFET: After developing an equation for the current in step 1, the next step is to find the MOSFET drain-source voltage equation. To achieve this, experimental data of v_{DS} (drain-source voltage), v_{GS} (gate source voltage), and i_L (TMS coil current) is utilized. Curve fitting is employed on the graph of v_{DS} versus v_{GS} to obtain the v_{DSfit} equation. Curve fitting involves creating a mathematical function or curve that best fits the series of data points obtained from plotting v_{DS} versus v_{GS}. With the v_{DSfit} equation in hand, the $r_{DS_{fit}}$ of the MOSFET can be determined by:
$$r_{DS_{fit}} = \frac{v_{DS_{fit}}(v_{GS})}{i_{L_{fit}}(v_{GS})} \tag{17}$$
3) MATLAB model: Now we can use this $r_{DS_{fit}}$ in the differential Equation 2 as:
$$\frac{di_L}{dt} = \frac{1}{L}\left[v_C - (r_L + r_C + r_{DS_{fit}}(v_{GS}))i_L\right] \tag{18}$$
and solve it using any solver available in MATLAB for a given $v_{GS}(t)$ profile. We have used `ode15s` to obtain good output results depending on the input gate voltage. We have chosen the MATLAB platform for simulation instead of other options because the need for precise characterization of the MOSFET, specifically the IXFK120N65×2, used in the experiment. As the circuit performance depends on the MOSFET turn-off behavior, relying solely on the on-resistance provided in the data sheet or MOSFET models in simulation software such as SPICE would not be adequate. Therefore, we have chosen to calculate the resistance of the particular MOSFET at every instant using the experimental data we have. Furthermore, there is a gap in the available literature, as there was no common drain-source current equation that could be used in all regions. Hence, we had to develop a new equation.

IV. Discussion of Model

We now explain the introduction of the ln 2 divisor and the exponent p in Eq. (15). It is critically important to note that p is itself a function of $(v_{GS} - v_T)$, as shown by the fitting in the next section.

A. Subthreshold

In the subthreshold region ($v_{GS} < v_T$), where $X \ll 1$, we set $p = 1$ (this is the maximum value for the p to capture the exponential characteristic of the subthreshold regime):
$$i_D = \frac{i_o}{\ln 2}\ln[1 + X], \tag{19}$$
and using
$$\ln[1 + X] \approx X \quad \text{for small X}$$
we obtain
$$i_D \approx \frac{i_o}{\ln 2}\exp\left(\frac{v_{GS} - v_T}{\eta\ v_{Th}}\right). \tag{20}$$
matching the Eq. (3), exponential form expected for MOSFETs.

B. Above Threshold

In the above-threshold region ($v_{GS} > v_T$) where $X \gg 1$, we use $p \approx 0.2$ (the value of p reduces from below-threshold to above-threshold as we need the current curve to change from exponential to linear), i_D becomes a linear equation:
$$i_D = \frac{i_o}{\ln 2}\ln[1 + X^p] \tag{21}$$
and using
$$\ln[1 + X^p] \approx \ln X^p \quad \text{for large } X^p$$
we obtain
$$\begin{aligned} i_D &= \frac{i_o}{\ln 2}\ln[X^p] = \frac{i_o}{\ln 2}\ln\left[\exp\left(\frac{v_{GS} - v_T}{\eta\ v_{Th}}\right)\right]^p \\ &= p\frac{i_o}{\ln 2}\left(\frac{v_{GS} - v_T}{\eta\ v_{Th}}\right) \end{aligned} \tag{22}$$
Equation (15) requires a gate-voltage dependent variable p to capture the transition from subthreshold to above-threshold behavior.

C. At Threshold

At threshold, when $v_{GS} = v_T$, $X^p = 1$ for any value of p
$$i_D = \frac{i_o}{\ln 2}\ln[1 + X^p] = i_o \tag{23}$$
The modified term (ln 2) was added in Eq. (15), so that at threshold i_D should be equal to i_0.

The exponent p is defined by a tanh function of MOSFET gate voltage,
$$p = \frac{1}{2}\left(p_1 + p_2 + (p_2 - p_1)\tanh\left(\frac{v_{GS} - v_T}{\eta\ v_{TH}}\right)\right). \tag{24}$$
By modifying the Eq. 7, we achieve a successful fit that aligns with the subthreshold, at threshold, and above threshold regions. This approach treats the MOSFET as a variable resistance governed solely by the gate-source voltage, simplifying the analysis compared to treating the MOSFET as a switch. Moreover, it indirectly incorporates the influence of drain-source voltage on the resistance, thereby accounting for its effect in the model.

The crucial aspect of our application revolves around understanding MOSFET characteristics during turn-off, particularly the voltage across and current through the inductor as the MOSFET transitions to its non-conducting state. This necessitates a robust equation that accurately models behavior below, near and above threshold. Through analysis of experimental data, we derived the new equation (Eq. 15) to model high-power MOSFET behavior, thus addressing the limitations of existing analytical approaches.

Authorized licensed use limited to: Univ of Waikato. Downloaded on April 24,2025 at 06:32:33 UTC from IEEE Xplore. Restrictions apply.

This article has been accepted for inclusion in a future issue of this journal. Content is final as presented, with the exception of pagination.

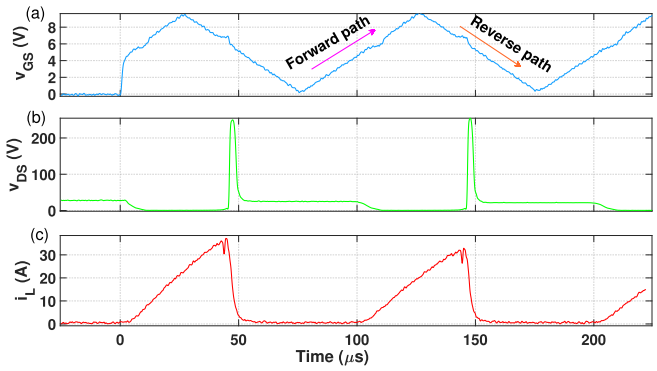

Fig. 5. (a) Gate voltage with forward path (0 to 10 V) and reverse path (10 V to 0) marked (the triangular wave is not captured for the initial 25 μs due to configuration of the triggering mechanism in the oscilloscope); (b) measured drain-source voltage and (c) coil current from the experimental setup used for the MOSFET model (To correct for current probe delay, we advanced the measured current trace by 3 μs prior to plotting).

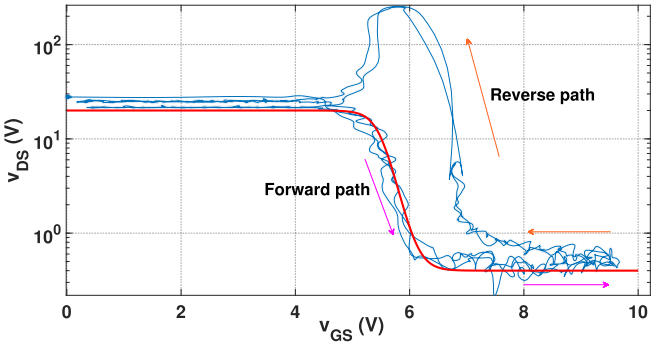

Fig. 6. Drain-source voltage versus gate voltage of the experimental result (blue). Red colored curve shows the modeled drain-source voltage fitted curve in the forward path using Eq. (25).

V. Computing the Resistance of the MOSFET

Now that the drain-source current equation that accurately fits the experimental data is developed, the next step is to determine the resistance of the MOSFET. To do so, the voltage fit equation is also required. Experimental data is utilized to understand the MOSFET behavior in the circuit, observing how the drain current and drain-source voltage vary with gate voltage. We now describe the method used to obtain both voltage and current fits, which allow us to calculate the resistance fit.

A. Voltage Fit

In our attempt to model the MOSFET S1 (Fig. 2) as a nonlinear resistance, our goal is to calculate the instantaneous dynamic resistance of the MOSFET at every instant throughout the oscillatory cycle. To do this, we measured v_{DS} and i_D from the experimental setup using a triangle gate voltage as input.

Figure 5 shows the experimental drain-source voltage (v_{DS}) and coil current (i_L) (equal to drain current i_D) for a triangular gate voltage. We then plotted v_{DS} against v_{GS} using the experimental data points (blue dots) as shown in Fig 6. Here, only the forward path is modeled, which was sufficient for the analysis. Additionally, the forward path varies from 0 to 10 V, which covers the full range of gate voltage used in the experiment. By analyzing the trajectory of the transfer characteristics (blue dots in Fig. 6), we found that it follows a hyperbolic tangent path since it has both upper and lower limit values. Therefore, we used the equation:

$$v_{\mathrm{DS_{fit}}} = \frac{1}{2}\left(D_1 + D_2 + (D_2 - D_1)\tanh\left(\frac{v_{GS} - v_T}{\eta_1\ v_{TH}}\right)\right) \quad (25)$$

The parameters used in curve fitting are provided in Table I.

B. Current Fit

From the experimental data of Fig. 5, the current versus gate voltage graph is illustrated in Fig. 8(a) with black dots, and fitted using Eq. (15). Typically, small-signal MOSFETs exhibit an η value ranging from 1 to 2. However, in this analysis, we selected the η values listed in Table I to achieve a more accurate fit, with η being treated as a fitting parameter. Choosing η values greater than 1 is required to attain a better alignment with the experimental data, particularly given the specific behavior of power MOSFETs.

TABLE I
Parameters and Their Values Used for Curve Fitting Equations

Measured parameters	Symbol	Values
Resistance of inductor	r_L	0.22 Ω
Inductance	L	0.22 μH
Internal resistance of C_1	r_C	0.22 Ω
Initial voltage of C_1	$v_C(0)$	30 V
Thermal voltage	v_{TH}	26 mV
Threshold voltage	v_T	6.0 V
Fitting parameters used in Equations		
$v_{\mathrm{DS_{fit}}}$ Eq. (25)	D_1, D_2, η_1	20, 0.4, 12
i_D Eq. (15)	i_0, η	8, 16
p_{fit} Eq. (26)	p_1, p_2, η_2	1, 0.13, 10

We use p as a function of $(v_{GS} - v_T)$, fitted to experimental data. Specifically the exponent of Eq. (15) is given by $p = p_{fit}(v_{GS} - v_T)$ where

$$p_{fit}(v_{GS} - v_T) = \frac{1}{2}\left(p_1 + p_2 + (p_2 - p_1)\tanh\left(\frac{v_{GS} - v_T}{\eta_2\ v_{TH}}\right)\right) \quad (26)$$

The variation of p_{fit} against the gate voltage is shown in Fig. 7.

C. Resistance Fit

Once we achieve an accurate fit for drain-source voltage and drain current, we can compute the MOSFET resistance as

Authorized licensed use limited to: Univ of Waikato. Downloaded on April 24,2025 at 06:32:33 UTC from IEEE Xplore. Restrictions apply.

This article has been accepted for inclusion in a future issue of this journal. Content is final as presented, with the exception of pagination.

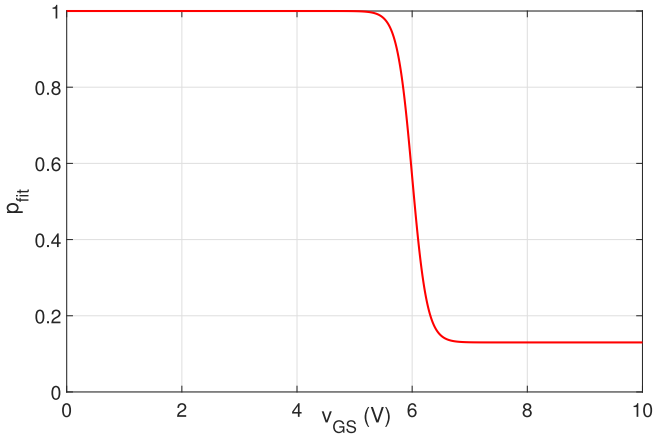

Fig. 7. Variation of exponent p_{fit} with respect to the gate-source voltage (v_{GS}).

the ratio of voltage to current:

$$r_{\text{DS}_{\text{fit}}} = \frac{v_{\text{DS}_{\text{fit}}}}{i_{\text{L}_{\text{fit}}}} \tag{27}$$

$$= \frac{\frac{1}{2}\left(D_1 + D_2 + (D_2 - D_1)\tanh\left(\frac{v_{\text{GS}} - v_{\text{T}}}{\eta_1\ v_{\text{TH}}}\right)\right)}{\frac{i_{\text{o}}}{\ln 2}\ln\left(1 + \left[\exp\left(\frac{v_{\text{GS}} - v_{\text{T}}}{\eta\ v_{\text{TH}}}\right)\right]^{p_{\text{fit}}}\right)} \tag{28}$$

The MOSFET is now modeled as a resistive element whose drain-source resistance r_{DS} is a nonlinear function of v_{GS} only,

$$r_{\text{DS}_{\text{fit}}} = f(v_{\text{GS}}) \tag{29}$$

Figure 8 shows fitting curves for current and resistance. The 3D plot in Fig. 9 illustrates the relationship between gate-source voltage, drain-source voltage, and drain current (top panel) or resistance (bottom panel).

VI. Modeling the RLC Circuit With Time-Varying MOSFET Resistance- MATLAB Solution

With the knowledge of the time-varying MOSFET resistance, we can model the RLC circuit using a first-order differential equation. This approach allows us to establish a dynamic MOSFET description grounded in experimental data. Such a model serves as a versatile tool that encapsulates MOSFET dynamics and allows prediction of the circuit output for arbitrary input voltage waveforms applied to MOSFET gate.

Once fitting parameters for the MOSFET voltage, current, and resistance equations have been obtained, the next step is to develop a simulation model that solves the MOSFET-controlled RLC circuit shown in Figure 2. The MOSFET is treated as a variable resistance $r_{\text{DS}_{\text{fit}}}$. The circuit differential equation is:

$$\frac{di}{dt} = \frac{1}{L}\left[v_{\text{C}} - \left(r_{\text{L}} + r_{\text{C}} + r_{\text{DS}_{\text{fit}}}(v_{\text{GS}})\right)i\right] \tag{30}$$

where r_{L}, r_{C}, v_{C} and L are given in Table I, and $r_{\text{DS}_{\text{fit}}}(v_{\text{GS}})$ is given in Eq. (27). Any $v_{\text{GS}}(t)$ waveform can be used to test the circuit. Here we use a triangular gate voltage generated by the `pulstran` MATLAB function to match the experimental setup shown in Fig. 5.

In this MATLAB model, Euler's method was initially used to solve the differential equations for capacitor voltage and loop current but was later replaced by the more robust `ode15s`. Euler's method, while simple, often struggles with accuracy and stability, especially in 'stiff' systems where variables change at different rates. `ode15s`, a variable-order solver, dynamically adjusts the time step for better error control and is more suited for handling the stiffness of the equations describing the MOSFET-controlled RLC circuit. While MATLAB offers a range of ODE solvers, `ode15s` proved to be the most effective for this system, delivering accurate results that closely match the experimental values.

We have implemented the simulation to replicate oscilloscope readings, where the time base resolution determines the displayed output. Using the `ode15` solver, a resolution of 0.04 μs corresponds to a total simulation duration of 0.4 ms, while a resolution of 0.2 μs allows viewing five output cycles over 1.6 ms. We observed that the Euler solver performs effectively only at smaller time base resolutions and struggles at higher resolutions where more than two cycles need to be visualized.

The current probe used in the experiment has a bandwidth of DC-100 kHz, which leads to a slow response time. In contrast, the oscilloscope used for $v_{\text{L}}(t)$ voltage measurements, has a much higher bandwidth of 0-10 MHz. To correct for current probe delay, we advanced the measured current trace by 3 μs prior to plotting (Fig. 5). This leftwards timing offset was also applied to the current traces displayed in MATLAB plots of Figures 10(a) and 11(a). Figure 10(a) shows a good match between experimental measurements and MATLAB model predictions for a triangular gate input voltage. Figure 10(b) shows the oscilloscope capture results of the same 50% symmetry gate voltage input used in simulation.

MATLAB simulations produce a perfect gate waveform without any distortion. However, in the experimental setup, the gate waveform exhibits minor distortions caused by the 8-bit quantization noise in digital oscilloscope captures. In Figure 10, the leading edge of the gate voltage shows a step discontinuity instead of the expected smooth voltage ramp. This discrepancy arises because the initial 25 μs of the triangular wave is not captured accurately due to the oscilloscope triggering configuration. However, focusing on the second pulse, we observe a good alignment between the simulation results and the circuit measurements. Since we have not modeled the charging and discharging of the gate capacitance, this process causes a small blips (black circle) at the threshold voltage of the gate voltage, as shown in Fig. 10. These small imperfections can affect the current and voltage waveforms, making them slightly less precise compared to the ideal simulations. Despite these minor differences, the experimental waveforms match the MATLAB-generated output, confirming that the curve-fitting equations have successfully captured the nonlinear resistance behavior of the MOSFET.

VII. Validation

As a test of the simulation equations, we replaced the triangular gate voltage with a 10 kHz 10 V_{pp} sinusoidal signal, but modeled with the same parameters as the triangle waveform we compared the output from the `ode15s` solver

Authorized licensed use limited to: Univ of Waikato. Downloaded on April 24,2025 at 06:32:33 UTC from IEEE Xplore. Restrictions apply.

This article has been accepted for inclusion in a future issue of this journal. Content is final as presented, with the exception of pagination.

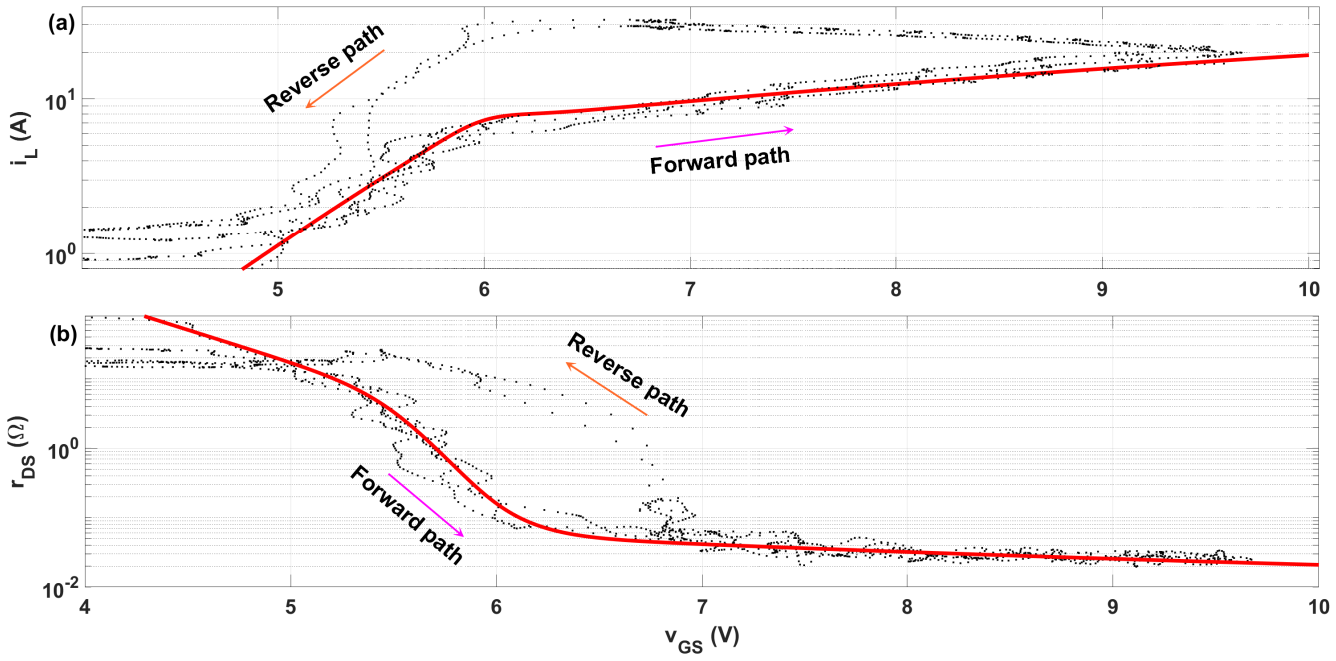

Fig. 8. (a) Transfer characteristics with fitted current curve (red line) and measured data (black dots) using Eq. (15); (b) drain-source resistance with fitted drain-source resistance curve using Eq. (27).

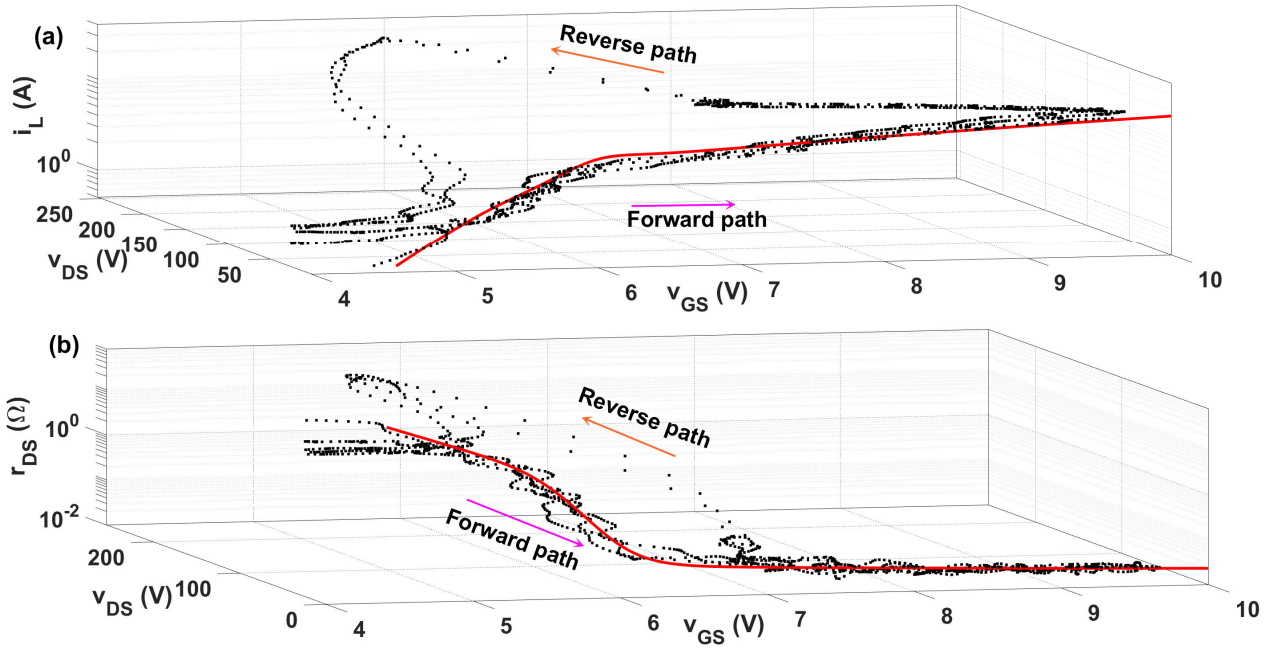

Fig. 9. Three dimensional view of the output characteristic of the MOSFET and dynamic resistance curve; (a) The measured output characteristic is shown in black dots, and the red curve shows the fitted drain-source voltage in the forward path; (b) black dots show the dynamic characteristic and, the red curve shows the fitted drain-source resistance.

with experimental measurements. Figure 11(a) superimposes the simulation predictions against experimental measurements from the oscilloscope capture shown in Fig. 11(b). It is interesting to observe that the output current and voltage waveforms are surprisingly insensitive to the shape (triangular or sinusoidal) of the input gate voltage drive signal. This is because the high voltage occurs near the threshold region primarily during turn-off, as the inductor coil only stores energy at that point. In both sinusoidal and triangular waveforms, the slope/points near the turn-off point around the threshold region is similar, resulting in comparable output behavior.

Figure 12 presents the experimental and MATLAB results for the quadrilateral gate voltage waveform. The results

Authorized licensed use limited to: Univ of Waikato. Downloaded on April 24,2025 at 06:32:33 UTC from IEEE Xplore. Restrictions apply.

This article has been accepted for inclusion in a future issue of this journal. Content is final as presented, with the exception of pagination.

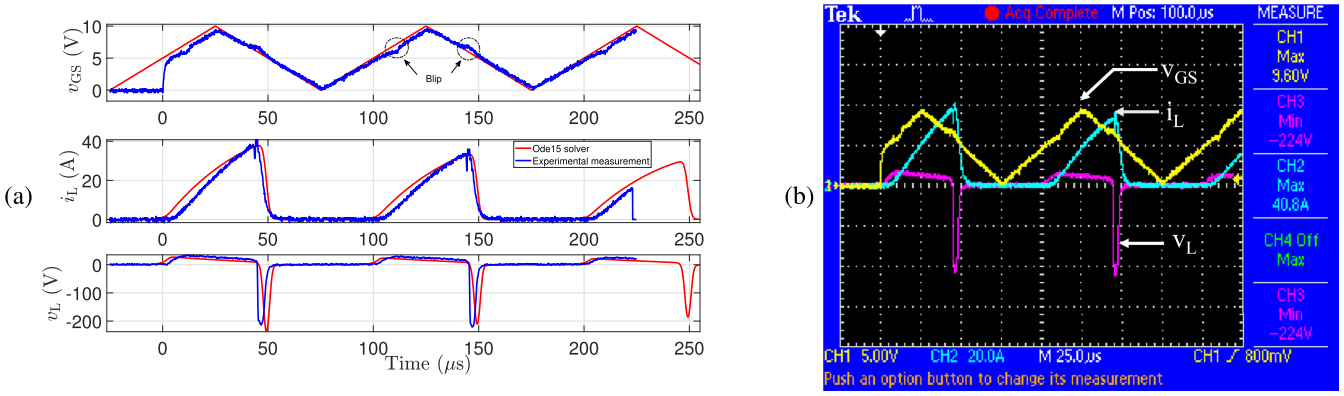

Fig. 10. Comparison of `ode15s` solver solution of the differential equation with the measured experimental values. The experimental measurement is the MATLAB of the oscilloscope view shown in (b). Blips due to charging and discharging of gate capacitance are highlighted (black circles). Note that the triangular wave is not accurately captured for the initial 25 μs due to the configuration of the triggering mechanism in the oscilloscope; (b) oscilloscope measurement of gate voltage (yellow), output coil voltage (magenta) and coil current (blue).

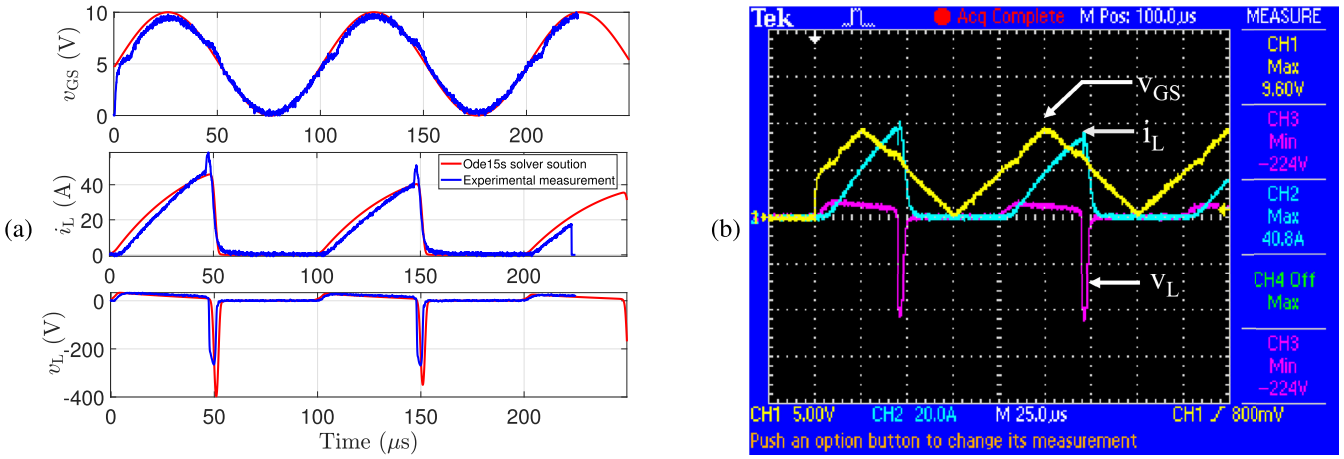

Fig. 11. (a) `ode15s` Solver solution of the differential equation (red) and experimental results (blue) with sinusoidal gate voltage input; (b) Oscilloscope measurement of sinusoidal gate voltage (yellow), output coil voltage (magenta) and coil current (blue).

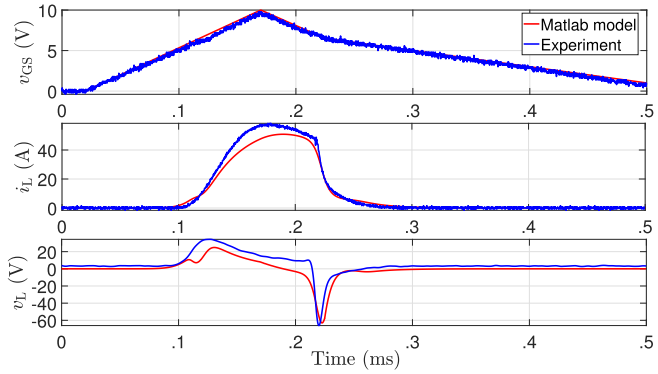

Fig. 12. Verification of experimental and MATLAB data with a quadrilateral gate voltage of 10 V amplitude.

indicate a good match between the TMS current and voltage pulses observed in the experimental setup and those from the MATLAB simulations.

VIII. DISCUSSION

This approach to MOSFET modeling offers two key advantages. Firstly, by incorporating a comprehensive mathematical model of MOSFET behavior, simulation results provide a good match to the real-world scenarios. Secondly, the flexibility of the code allows for easy modification and adaptation to different MOSFET specifications or circuit configurations. Overall, this code segment serves as a robust tool for analyzing MOSFETs-driven RLC circuits, enabling researchers to gain insights into circuit performance and behavior under varying conditions.

However, our approach is carried out in the context of an RLC circuit. Use of Equations (27)-(28) implicitly assumes particular voltage v_{DS} dynamics, and would likely need modifications for a different context. Here we have curve fitted with the parameter range that we got from the experimental data and also by looking the pattern. In contrast, variation of i_{DS} with v_{GS} near threshold is likely to be more robust, approximately independent of v_{DS} as shown in Fig. 3(b). Although we have not yet performed reverse path-curve fitting, Figures 8 and 9 shows a hysteresis separation from the forward path; we believe it is closely related to the gate capacitance charge and discharge dynamics [30]. Despite focusing solely on the forward path from 0 to 10 V, the model still offers a reliable prediction of the output compared to the experimental results. This accuracy can be attributed to the similarity in

Authorized licensed use limited to: Univ of Waikato. Downloaded on April 24,2025 at 06:32:33 UTC from IEEE Xplore. Restrictions apply.

This article has been accepted for inclusion in a future issue of this journal. Content is final as presented, with the exception of pagination.

shape between the forward and reverse paths in the resistance plot shown in Figure 8, despite a time shift. Consequently, even without explicitly modeling the reverse path, the negative phase of the voltage in the simulation aligns closely with the experimental results.

During experimental data collection, several measurement challenges were encountered. The oscilloscope resolution made it difficult to capture the full range of data with the maximum number of points for both high and low voltage levels. When using a 100X probe, the minimum voltage values lacked accuracy. To address this, two probes were employed: a 100X probe for higher voltage levels and a 10X probe for lower voltage levels. The data from both probes were then combined in the MATLAB model.

Additionally, the resolution of the current probe and the oscilloscope differed, and we were unable to calibrate the zero-current setting on the probe. As a result, the initial inductor current values (i_L) were not zero or very small, as expected. These imperfections will be addressed in the next stage of the model, where the gate capacitance will be considered. The energy dissipated and power delivered during the tests were lower than the rated values specified in the datasheet. Additionally, the MOSFET did not heat up during testing, indicating minimal thermal stress. As a result, the temperature effect has not been considered in the current analysis.

Existing studies on SiC MOSFET modeling, such as those by Tornello [9], Ferretti [10], and Wang [12], emphasize datasheet-based methods, lookup tables, and linear analyses without considering switching transients. However, they often overlook internal variations like dynamic resistance changes. Our approach addresses this gap by modeling the MOSFET as a dynamically varying resistor, considering smoothing phase transition between the sub threshold and above threshold region rather than piecewise analysis offering deeper insights into device behavior and predicting the output.

IX. Conclusion

The development of the analytical model for nonlinear MOSFET dynamics faced several challenges, including limited data from datasheets, unexpected experimental observations, and measurement difficulties. Despite these hurdles, the model was successfully refined to accurately predict system behavior. The neglect of gate capacitance effects, although simplifying the model, did not significantly impact the accuracy of the results, which closely matched experimental data. The complexity of modeling MOSFET dynamics in the RLC circuit became evident, particularly when simulation tools like Proteus failed to replicate real-world results. However, by fine-tuning resistance, threshold values, and utilizing curve fitting based on a physical descriptions of the near threshold region, the MATLAB model provided reliable predictions. This work offers a strong physical foundation for power MOSFET modeling, allowing for more accurate simulations with minimal additional experimentation.

This study can be significant because, in the existing literature, there are primarily Simulink block models or subthreshold equations, with no dedicated equation available to cover the full operating range of a MOSFET. Our approach can serve as a valuable tool for other researchers to evaluate circuits where the MOSFET is treated as a dynamically varying element.

X. Future Work

In future work, we are working to incorporate stray inductance and capacitance effects into the model, as these factors play a critical role in circuit performance. While this study focuses on the initial development stage, we recognize the importance of addressing these elements and will include them in the next phase.

Acknowledgment

The authors gratefully acknowledge the University of Waikato Doctoral Scholarship for the research support.

References

[1] Z. Feng, A. Berry, P. Ellis, and W. Lawson, "SPICE models for predicting EMC performance of a MOSFET based half-bridge configuration," in *Proc. IEEE 1st Int. Power Electron. Appl. Symp. (PEAS)*, Nov. 2021, pp. 1–5.

[2] D. G. A. Neto, G. Maranhão, M. C. Schneider, and C. Galup-Montoro, "A design-oriented single-piece short-channel MOSFET model," in *Proc. IEEE Int. Symp. Circuits Syst. (ISCAS)*, May 2024, pp. 1–5, doi: 10.1109/ISCAS58744.2024.10558311.

[3] K. Lee, M. Shur, T. A. Fjeldly, and T. Ytterdal, *Semiconductor Device Modeling for VLSI*. Upper Saddle River, NJ, USA: Prentice-Hall, 1993.

[4] M. Shur, T. A. Fjeldly, T. Ytterdal, and K. Lee, "Unified MOSFET model," *Solid-State Electron.*, vol. 35, no. 12, pp. 1795–1802, Dec. 1992.

[5] J. Xie et al., "An accurate and effective spice model of 6.5kV SiC MOSFET with parasitic parameters analysis in medium-voltage power module," in *Proc. IEEE 10th Int. Power Electron. Motion Control Conf. (IPEMC-ECCE Asia)*, May 2024, pp. 3487–3492, doi: 10.1109/IPEMC-ECCEASIA60879.2024.10567836.

[6] F. Wang, S. Kher, T. Fichtner, and J. Aurich, "A new power MOSFET model and an easy to use characterization tool using device datasheet," in *Proc. IEEE 14th Workshop Control Model. Power Electron. (COMPEL)*, Jun. 2013, pp. 1–5, doi: 10.1109/COMPEL.2013.6626471.

[7] M. Mudholkar, M. Saadeh, and H. A. Mantooth, "A datasheet driven power MOSFET model and parameter extraction procedure for 1200 V, 20A SiC MOSFETs," in *Proc. 14th Eur. Conf. Power Electron. Appl.*, Aug. 2011, pp. 1–10.

[8] A. Ghulam et al., "Accurate & complete behaviourial SPICE modelling of commercial SiC power MOSFET OF 1200 V, 75A," in *Proc. 25th Int. Conf. Thermal, Mech. Multi-Physics Simul. Experiments Microelectron. Microsystems (EuroSimE)*, Apr. 2024, pp. 1–4.

[9] L. D. Tornello, M. G. Spitaleri, G. Scarcella, and M. Cacciato, "An analytical model of a SiC MOSFETs in parallel configuration," in *Proc. ELEKTRO (ELEKTRO)*, May 2024, pp. 1–6.

[10] J. Ferretti, G.-P. Schiapparelli, E. Sangiorgi, and A. N. Tallarico, "SiC MOSFETs performance modeling in simulink simscape environment," in *Proc. IEEE 10th Workshop Wide Bandgap Power Devices Appl. (WiPDA)*, Dec. 2023, pp. 1–6.

[11] P. Zeng, S. Wu, Y. Luo, and X. Xiao, "Research on SiC MOSFET model based on simulink," in *Proc. 7th Int. Conf. Comput. Inf. Sci. Appl. Technol. (CISAT)*, Jul. 2024, pp. 679–682.

[12] N. Wang and J. Zhang, "Nonlinear capacitance model of SiC MOSFET considering envelope of switching trajectory," *IEEE Trans. Power Electron.*, vol. 37, no. 7, pp. 7977–7988, Jul. 2022.

[13] V. Talesara et al., "Dynamic switching of SiC power MOSFETs based on analytical subcircuit model," *IEEE Trans. Power Electron.*, vol. 35, no. 9, pp. 9680–9689, Sep. 2020.

[14] C. Wang, H. Chen, H. Wang, Z. Wang, and X. Ye, "Refined electrical modelling of power MOSFETs based on physical information," in *Proc. 5th Int. Conf. Syst. Rel. Saf. Eng. (SRSE)*, Oct. 2023, pp. 164–169.

[15] X. Yang, J. Li, Y. Ding, M. Xu, X.-F. Zhu, and J. Zhu, "Observation of transient parity-time symmetry in electronic systems," *Phys. Rev. Lett.*, vol. 128, no. 6, Feb. 2022, Art. no. 065701.

Authorized licensed use limited to: Univ of Waikato. Downloaded on April 24,2025 at 06:32:33 UTC from IEEE Xplore. Restrictions apply.

This article has been accepted for inclusion in a future issue of this journal. Content is final as presented, with the exception of pagination.

[16] Q. Liu, P. Sun, G. Peng, and X. Ma, "A semi-physical model of SiC MOSFETs for improved static characteristic," in *Proc. IEEE 7th Int. Electr. Energy Conf. (CIEEC)*, May 2024, pp. 1842–1845, doi: 10.1109/CIEEC60922.2024.10583229.

[17] Y. Mukunoki et al., "Modeling of a silicon-carbide MOSFET with focus on internal stray capacitances and inductances, and its verification," in *Proc. IEEE Appl. Power Electron. Conf. Expo. (APEC)*, Mar. 2017, pp. 2671–2677, doi: 10.1109/APEC.2017.7931076.

[18] S. Raju, N. Kularatna, and M. Wilson, "Supercapacitor based adjustable high power pulse generator for medical research applications," in *Proc. 49th Annu. Conf. IEEE Ind. Electron. Soc.*, Oct. 2023, pp. 1–6.

[19] Littelfuse. (2024). *Discrete MOSFETs N-Channel Ultra Junction IXF120N65X2 Datasheet*. Accessed: Sep. 26, 2024. [Online]. Available: https://shorturl.at/09f62

[20] P. van der Meer, A. van Staveren, and A. H. van Roermund, *Low-Power Deep Sub-Micron CMOS Logic: Sub-Threshold Current Reduction*, vol. 841. Berlin, Germany: Springer, 2004.

[21] B. J. Baliga, *Silicon RF Power MOSFETs*. Singapore: World Scientific, 2005.

[22] R. C. Jaeger, T. N. Blalock, and B. J. Blalock, *Microelectronic Circuit Design*, vol. 97. New York, NY, USA: McGraw-Hill, 1997.

[23] M. Shur and J. Singh, "Physics of semiconductor devices," *Phys. Today*, vol. 43, no. 10, pp. 98–99, doi: 10.1063/1.2810727.

[24] N. D. Arora, *MOSFET Models for VLSI Circuit Simulation: Theory and Practice*. Berlin, Germany: Springer, 2012.

[25] J. R. Brews, W. Fichtner, E. H. Nicollian, and S. M. Sze, "Generalized guide for MOSFET miniaturization," in *IEDM Tech. Dig.*, Dec. 1979, pp. 10–13.

[26] Y. H. Byun, K. Lee, and M. Shur, "Unified charge control model and subthreshold current in heterostructure field-effect transistors," *IEEE Electron Device Lett.*, vol. 11, no. 1, pp. 50–53, Jan. 1990, doi: 10.1109/55.46928.

[27] T. Ytterdal, Y. Cheng, and T. A. Fjeldly, *Device Modeling for Analog and RF CMOS Circuit Design*. Hoboken, NJ, USA: Wiley, 2003.

[28] T. A. Fjeldly and M. Shur, "Threshold voltage modeling and the subthreshold regime of operation of short-channel MOSFETs," *IEEE Trans. Electron Devices*, vol. 40, no. 1, pp. 137–145, Jan. 1993.

[29] T. A. Fjeldly, M. Shur, and T. Ytterdal, *Introduction to Device Modeling and Circuit Simulation*. Hoboken, NJ, USA: Wiley, 1997.

[30] M. Xu, X. Yang, and J. Li, "C-RC snubber optimization design for improving switching characteristics of SiC MOSFET," *IEEE Trans. Power Electron.*, vol. 37, no. 10, pp. 12005–12016, Oct. 2022, doi: 10.1109/TPEL.2022.3180387.

Soniya Raju (Member, IEEE) was born in Kerala, India. She received the degree (Hons.) in electrical and electronics engineering from Mahatma Gandhi University, Kerala, in 2014, and the master's degree in power electronics and drives with a specialization in power electronics application in power systems from Karunya University, Tamil Nadu, in 2016. She is currently pursuing the Ph.D. degree with The University of Waikato. She was an Assistant Professor for five years in India. Her research interests encompass a diverse range, including power electronics, circuit designing, transcranial magnetic stimulation, and supercapacitors.

D. Alistair Steyn-Ross received the B.Sc., M.Sc., and Ph.D. degrees in physics from the University of Waikato (UoW), Hamilton, New Zealand, in 1975, 1977, and 2002, respectively. He is currently an Associate Professor with the School of Engineering, UoW. He has supervised a substantial number of Ph.D. projects in the application of supercapacitors to renewable-energy storage and the design of robust, energy-efficient dc power supplies, and has coauthored more than 50 papers on supercapacitor-related topics. His research expertise is the application of computational physics and mathematics to the modeling of nonlinear stochastic systems during close approach to phase transition critical points.

Marcus Wilson received the degree (Hons.) in physics and theoretical physics from the University of Cambridge, U.K., in 1992, and the Ph.D. degree in theoretical solid state physics from the University of Bristol, U.K., in 1995. He is currently a Senior Lecturer in physics and emistry with the Te Aka Mātuatua, School of Science, The University of Waikato, Hamilton, New Zealand. He has worked in numerical modeling of physics processes in industry in U.K. and in academia in New Zealand, the latter since 2004. His research interests include electric properties and dynamics of the human brain, transcranial magnetic stimulation, and more recently batteries.

Nihal Kularatna (Senior Member, IEEE) received the D.Sc. degree in electronic engineering in 2015. Prior to moving to academia in New Zealand, he was the CEO of the Arthur C Clarke Institute for Modern Technologies, Sri Lanka. He is currently an Associate Professor with The University of Waikato, Hamilton, New Zealand. He is research-active in supercapacitor applications and power electronics. He has authored ten reference books and research monographs, and contributed more than 175 publications. He was a recipient of the Post Graduate Research Supervision Excellence Award from The University of Waikato in 2021. For developing supercapacitor-assisted (SCA) techniques, he won the NZ Engineering Innovator of the Year 2013 Award.

Authorized licensed use limited to: Univ of Waikato. Downloaded on April 24,2025 at 06:32:33 UTC from IEEE Xplore. Restrictions apply.

(INTENTIONALLY BLANK)

Chapter 7

Pulse shaping

Introduction

This chapter explores the optimization of TMS pulses through parameter adjustments in a developed pulse generator prototype and a corresponding MATLAB model. The primary focus is on understanding how changes in the C2 capacitor voltage and capacitance, gate voltage amplitude, and symmetry impact the TMS output pulses. By leveraging these modifications, the chapter aims to provide insights into extended pulse duration, and customized pulse shapes, thereby enhancing the effectiveness and flexibility of TMS protocols. Also I validated the modified triangular voltage waveform with four distinct points and tested various possibilities by changing the on time and off time slopes. This exploration aimed to understand their effects on TMS output pulses. I conducted experimental validations and compared the results with MATLAB simulations, demonstrating a high degree of correlation between the two. Additionally, a comprehensive analysis of the pulse shaping capacity of the circuit is provided, offering deeper insights into optimizing TMS pulse characteristics for more effective applications.

7.1 Parameter changes

In the pursuit of advancing TMS technology, a pulse generator prototype has been successfully developed and tested. This prototype demonstrates the ability to create and control TMS pulses. Additionally, a MATLAB model has been developed that relatively accurately replicates the experimental results. The MATLAB model serves as a powerful tool for simulating and analyzing the TMS pulse output under various conditions. By adjusting different attributes of the prototype within the model such as component values, frequency, and gate voltage, we can observe the resulting TMS pulse characteristics.

In the previous chapters, I have focused on experimenting with a 100 μs gate waveform pulse width. This choice is based on using a 1 V input to charge the C2 capacitor to 30 V, which serves as the basis for all initial testing. Increasing the input voltage to the supercapacitor (SC) and consequently raising the voltage on the C2 capacitor would result in higher voltage and current pulses in the TMS coil. This chapter will discuss these effects in more detail.

For safety reasons and to ensure the MOSFET operates within safe limits, I have maintained the same voltage settings used in the test prototype. In my experiments, I took precautions to avoid stressing the components with higher voltages, which could potentially damage the circuit. Such damage would necessitate replacing and rewiring the entire setup, posing a risk of loosening the TMS coil winding and altering its inductance.

Therefore, I have not altered the test setup. Instead, I have used a MATLAB model to predict the outcomes of parameter changes. Some of these predictions have been experimentally verified using the test setup, and the results are similar. This consistency indicates that the MATLAB model is reliable for predicting the relationship between gate voltage and TMS output pulse. Exploring the effects of changing components and operating parameters in the model offers significant advantages. It enables the ability to predict and analyze the outcomes of modifications without the need for extensive physical experimentation. This approach not only saves time and resources but also broadens the scope for experimentation, facilitating the exploration of various configurations and enhancements. By leveraging the MATLAB model, I can investigate various scenarios without physically altering the test setup, ensuring the integrity of the components and the accuracy of the coil inductance. This approach provides a safe and effective means of understanding and optimizing the circuit performance.

I conceived the idea to use a triangular gate voltage waveform due to its ability to induce transitions between on and off states through its varying slopes. By adjusting the symmetry of the triangular waveform, which refers to the rise-to-fall ratio, I can effectively modify the output pulse shape. For instance, a 60% symmetry implies a 60:40 rise-to-fall ratio. By varying the symmetry, I can achieve different pulse shapes, allowing for control over the output TMS pulse. Initially, I experimented with a standard triangular waveform to understand its effects. Later, I explored modifications to the triangular waveform to further refine and control the TMS output pulse.

7.1.1 Effect of C2 voltage and capacitance

The following analysis explores how changes in the C2 capacitor voltage affect the output pulse in a TMS circuit. The parameters used in this section are provided in Table 7.1.

Firstly, consider the scenario where the voltage of the C2 capacitor is increased to a higher value. For instance, when the voltage is raised to 500 V, the output voltage is significantly higher compared to the initial prototype condition where the capacitor voltage is 30 V.

Table 7.1: Parameters and their values used in subsection 7.1.1

Parameters	Values
Capacitance (C2)	1500 μF
C2 voltage	500 V

The relationship between the capacitor voltage (V) and the energy stored (E) is given by the

equation:

$$E = \frac{1}{2}CV^2 \tag{7.1}$$

This equation (Eq. 7.1) indicates that the energy stored in the capacitor increases quadratically with the voltage. Therefore, a higher initial voltage in the C2 capacitor results in a substantially greater energy reserve, which translates into higher and more numerous output pulses.

Another significant parameter to consider is the capacitance of the C2 capacitor. Replacing the C2 capacitor with one of higher capacitance results in a greater number of pulses per discharge cycle. This is because a larger capacitance allows the capacitor to store more energy at the same voltage, thereby sustaining the pulse generation for a longer duration until the amplitude drops below the set minimum.

Figure 7.1 demonstrates the output parameters of TMS when the C2 capacitor is replaced with a capacitance of 1500 μF and charged to 500 V , showing that increasing the capacitance and voltage of C2 leads to a higher number of pulses.

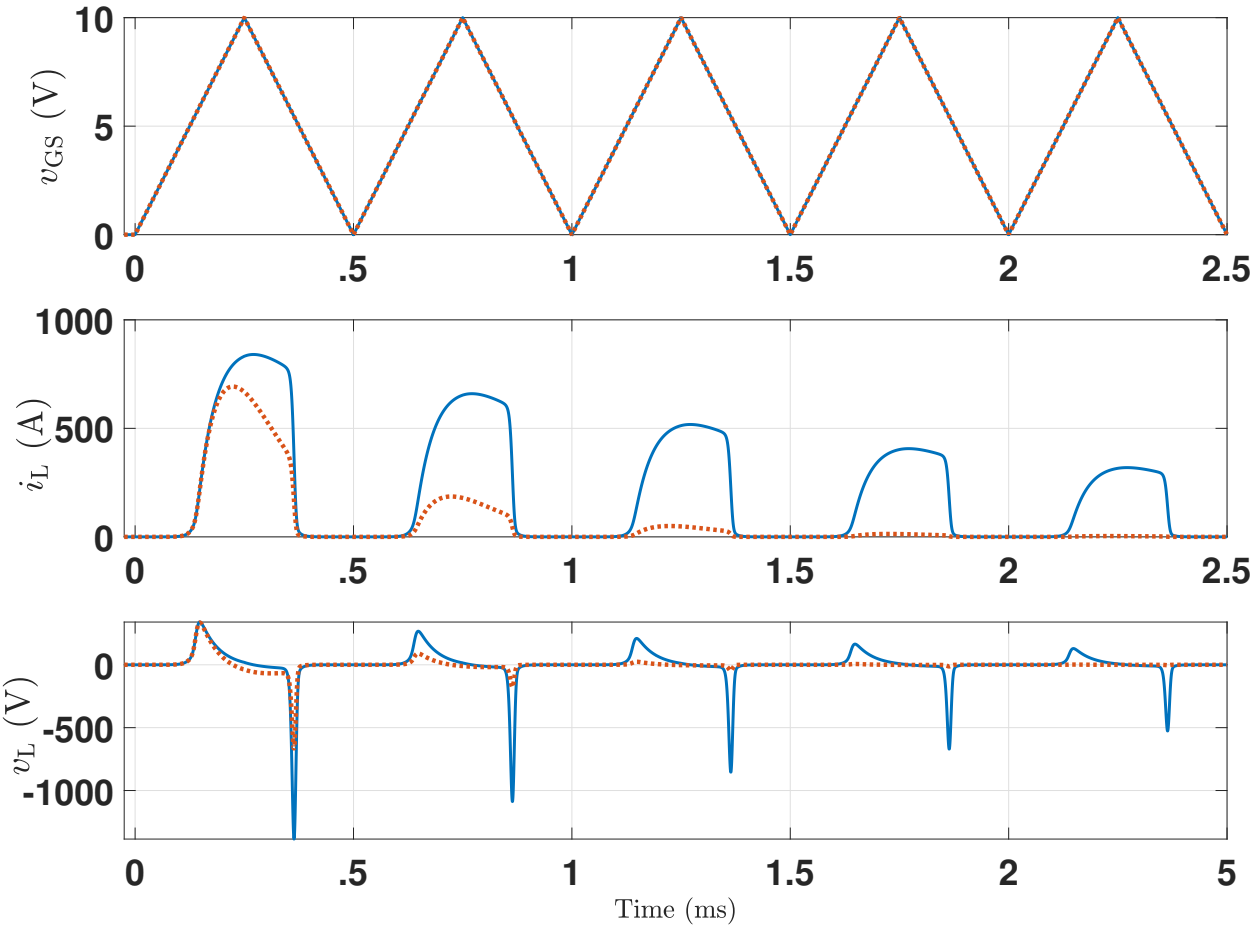

Figure 7.1: TMS output parameters when the C2 capacitor (330 μF- orange dotted lines) is replaced with 1500 μF (blue) and charged to 500 V, showing that increasing the capacitance and voltage of C2 contributes to a higher number of pulses

The energy stored in a capacitor, as in Eq. 7.1, is dependent on both the capacitance and the voltage. By increasing the capacitance (C), the total energy available for discharge increases, given

the same initial voltage. This results in a prolonged discharge period, during which more pulses can be generated.

To enhance the charging rate of C2, several strategies can be implemented. Firstly, by increasing the voltage of the SC (C1) capacitor from 1 V to 10 V or higher, the charging speed of C2 can be significantly improved. Additionally, I employed an 8 kHz gate voltage with a 50% duty cycle for S1. By adjusting the duty cycle and frequency, the charging time can be further optimized, allowing for faster charging rates. Moreover, the charging rate can be expedited by reducing the resistance in the circuit, which involves selecting an SC with a low ESR. Capacitors with higher capacitance typically exhibit very low ESR, making them ideal for this purpose. Therefore, C1 can be replaced with any low ESR capacitors available.

As discussed in the Section 4.4.1, higher capacitance SC not only have lower voltage loss and reduced ESR but can also withstand and efficiently charge C2 without the need for frequent recharging. This ensures a more stable and rapid charging process, improving the overall performance and reliability of the TMS system.

To summarize, the analysis reveals that increasing either the voltage or the capacitance of the C2 capacitor in a TMS circuit significantly enhances the output pulse characteristics. Higher initial voltage increases the amplitude and number of pulses, particularly when coupled with higher gate voltage symmetry. Similarly, a higher capacitance extends the duration of pulse generation, providing a greater number of pulses per discharge cycle. These adjustments to the C2 capacitor parameters are crucial for optimizing TMS output and exploring the full potential of the prototype.

7.2 Usefulness of the prototype in cTBS pattern

Continuous theta burst stimulation (cTBS) has become a standard procedure in TMS applications [49, 50, 57, 77, 193, 194]. The cTBS pattern consists of bursts of high-frequency pulses delivered in a rhythmic pattern, typically at theta frequency (5 Hz). Typically cTBS consist of burst of three pulses 20 ms apart repeated every 200 milliseconds (5 Hz burst rate). Often 600 or 1200 pulses are delivered , although the total number of pulses can vary [195–200]. The parameters used in this section are provided in Table 7.2.

Table 7.2: Parameters and their values used in subsection 7.2

Parameters	Values
Supercapacitor input	1 V
Capacitance (C2)	330 μF
C2 voltage	30 V

Testing the cTBS burst pattern with the initial prototype parameters (30 V C2 capacitor voltage) revealed an initial pulse voltage amplitude of 200 V. This demonstrates the potential of the prototype to produce existing pulse pattern even with basic parameters. However, modifying these parameters, as previously discussed, can yield higher voltages and sustain pulse production for a longer duration.

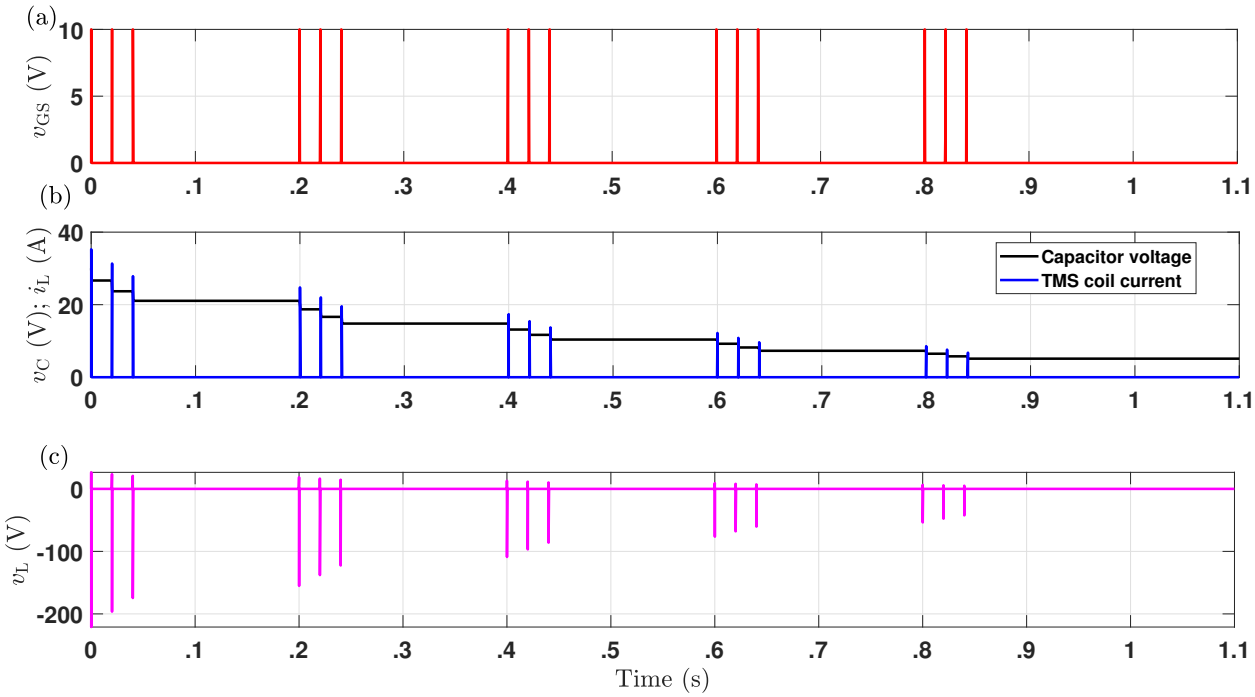

Figure 7.2: Demonstrates the cTBS sequence produced by the MATLAB model. cTBS delivers bursts of three pulses 20ms apart, repeated at every 200 milliseconds (a burst rate at 5 Hz in the theta range) with the pattern continuing for a total duration typically ranging from 20 seconds to several minutes.

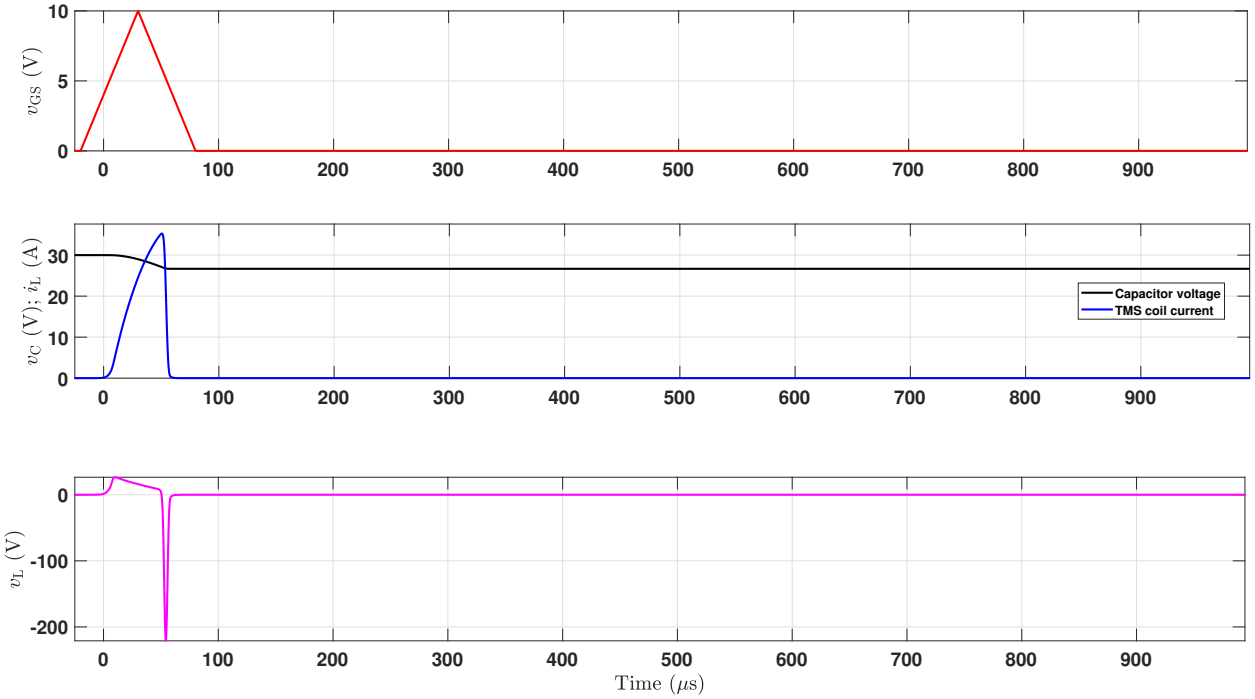

Figure 7.3: A zoomed-in view of a single pulse within the cTBS pattern shown in Fig. 7.2, providing enhanced illustration and clarity of the pulse characteristics.

Figure 7.4: Oscilloscope capture of a single pulse within the cTBS pattern shown in Fig. 7.2, providing enhanced illustration and clarity of the pulse characteristics. Yellow represents the gate voltage, green depicts the TMS current pulse, and magenta illustrates the TMS voltage pulse in the experimental setup.

The tested cTBS pattern used a 100 μs triangle pulse-width with bursts occurring every 20 ms and repeated every 200 ms. The pulse parameters can be modified by adjusting the amplitude and symmetry of the gate voltage, allowing for further customization of the pulse shape. Changes in the triangle sequence of the gate voltage can also produce different phase patterns, enhancing the flexibility of the stimulation protocol.

Figures 7.2 and 7.3 show the pulse pattern of cTBS produced by a MATLAB model. It demonstrates that the model accurately replicates the pulse patterns used in TMS, including the capability to generate high coil voltage pulses with a prototype. Figure 7.3 offers a detailed zoom-in on a single pulse within the continuous theta burst stimulation (cTBS) pattern. Additionally, Figure 7.4 presents the single pulse obtained from the laboratory setup, providing a clearer and more illustrative depiction of the pulse characteristics.

The initial test setup used a 100 μs pulse-width, which is significantly faster than the typical cTBS pulse. Despite this, the pattern has been illustrated using the same pulse width for consistency. However, it is possible to reproduce the cTBS pattern with a pulse width of 500 μs for each gate voltage.

Using the test setup parameters, such as a C2 voltage of 30 V and a capacitance of 330 μF, the pulses do not last long due to the limited energy stored in C2. For validation, Figure 7.5 presents the 500 μs pulse-width gate voltage tested with the prototype setup. To address this, we can adjust the values in the MATLAB model. Figure 7.6 demonstrates the cTBS pattern with a 500 μs pulse width, where the C2 voltage is increased to 150 V and the capacitance is raised to

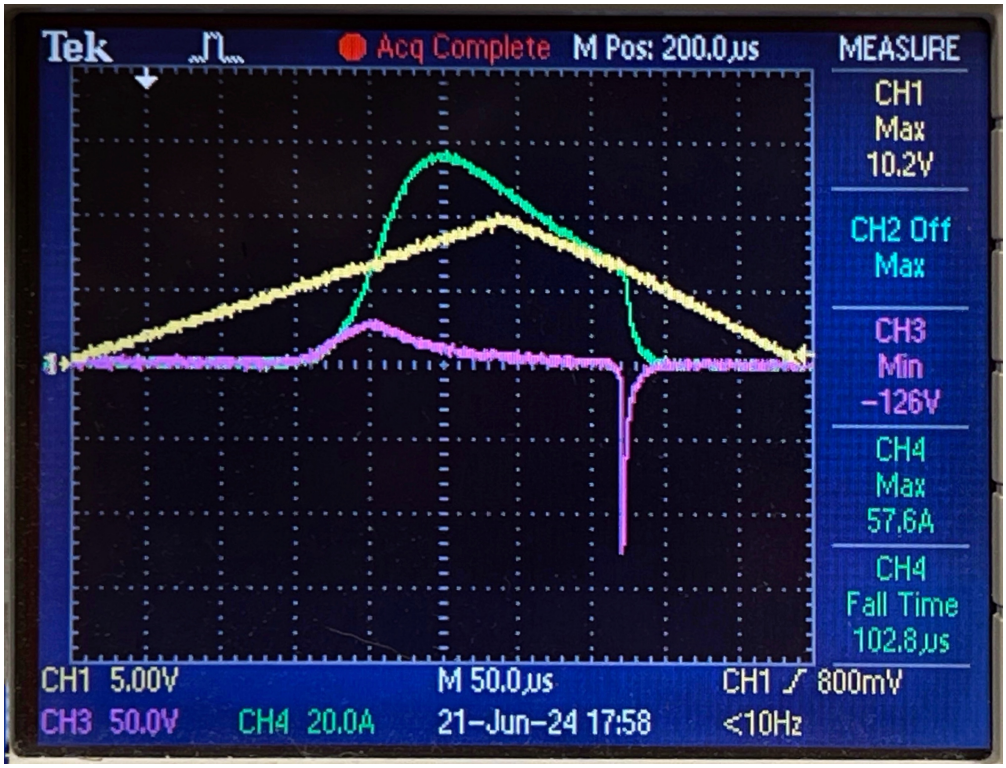

Figure 7.5: This figure demonstrates the cTBS pulse generated by the MATLAB model with a 500 μs pulse width, shown with the experimental test setup. Yellow represents the gate voltage, green depicts the TMS current pulse, and magenta illustrates the TMS voltage pulse in the experimental setup.

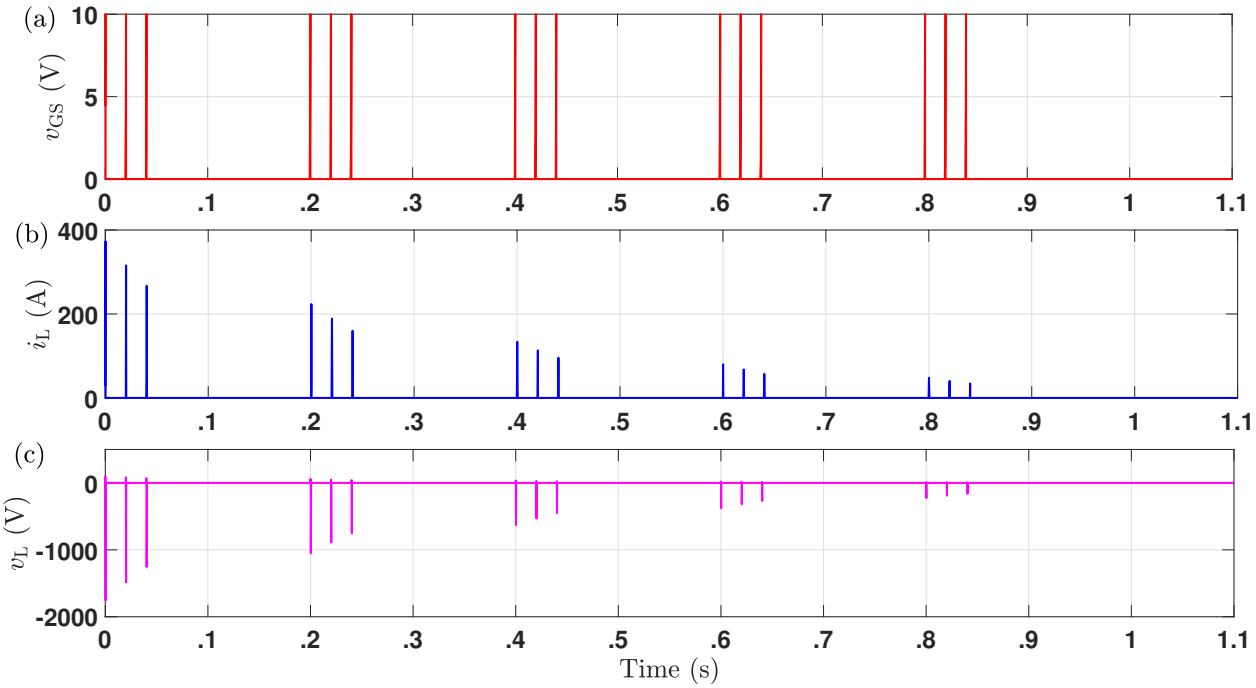

Figure 7.6: Demonstrates the cTBS pulse generated by the MATLAB model with a 500 μs pulse width. The prolonged and higher amplitude pulses result from adjusting the capacitance of C2 to 1500 μF and increasing the voltage to 150 V.

1500 μF. This modification shows that the same prototype can be adapted to various setups by changing the component values or increasing the capacitor voltage to handle higher amplitude or a greater number of pulses. This experimental data suggests the system is capable of adapting to different pulse widths by appropriately adjusting the voltage and capacitance of C2.

By varying the pulse width and adjusting the circuit parameters accordingly, the system demonstrates flexibility in generating different cTBS patterns, ensuring compatibility with various experimental requirements. This approach highlights the importance of component selection and configuration in achieving desired pulse characteristics while maintaining the integrity and performance of the circuit.

These figures and their corresponding explanations provide insights into various aspects of TMS, including pulse patterns, parameter variations, and model capabilities. The prototype demonstrated the ability to produce high-voltage, sustained pulses with the cTBS pattern, confirming its potential for effective modification. By leveraging these adjustments, the TMS prototype can be optimized to produce higher voltages and more sustained pulses, offering greater control over the stimulation parameters. This flexibility is crucial for tailoring TMS treatments to individual needs and exploring new therapeutic possibilities [119, 201, 202].

7.3 Triangle gate voltage- summary

By utilizing a triangular gate voltage waveform, I observed significant effects on the characteristics of the TMS pulses, depending on the waveform symmetry. When employing a 10% symmetry, the TMS current pulse exhibited an extended fall time, resulting in a longer decay phase, while the peak current was slightly reduced. Conversely, with a 90% symmetry, the TMS current pulse demonstrated a shorter fall time and a slightly higher peak current. Importantly, the overall pulse width—defined as the duration from the current rising from effective zero to when it returns to effective zero—remained relatively unchanged. Instead, what was controlled was primarily the fall time of the current pulse, affecting the shape of the pulse rather than its width. Correspondingly, in the voltage pulse, the fall time and peak voltage were influenced in a consistent manner. Figure 7.7 illustrates the impact of modifying the symmetry and amplitude of the gate voltage waveform on the TMS output voltage and current pulses.

Therefore, adjusting the symmetry of the triangular gate voltage waveform is an effective method for varying the fall time of the current TMS pulse. If the goal is to achieve a longer fall time and pulse width in the voltage TMS pulse, a lower symmetry (such as 10%) should be used. Conversely, for a shorter fall time in the current TMS pulse and reduced voltage pulse width, a higher symmetry (such as 90%) is beneficial.

Additionally, changing the amplitude of the gate voltage pulse has a direct impact on the pulse characteristics. Increasing the amplitude of the gate voltage pulse leads to an increase in the pulse width, rise time, and fall time of the current TMS pulse.

The current through the TMS inductor coil is directly influenced by the gate voltage waveform applied to the MOSFET as discussed here. Variations in the gate voltage shape and timing affect the

rate at which the current changes, its peak value, and its duration. Also voltage across the TMS inductor coil is similarly affected by the gate voltage waveform. Adjusting the waveform can control the coil voltage pulse rise and fall times, amplitude, and width, impacting the induced magnetic field strength and temporal characteristics.

In summary, by manipulating the symmetry and amplitude of the gate voltage waveform, we can control the rise time, fall time, and pulse width of both current and voltage TMS pulses. These adjustments provide valuable flexibility in optimizing TMS pulses for various applications.

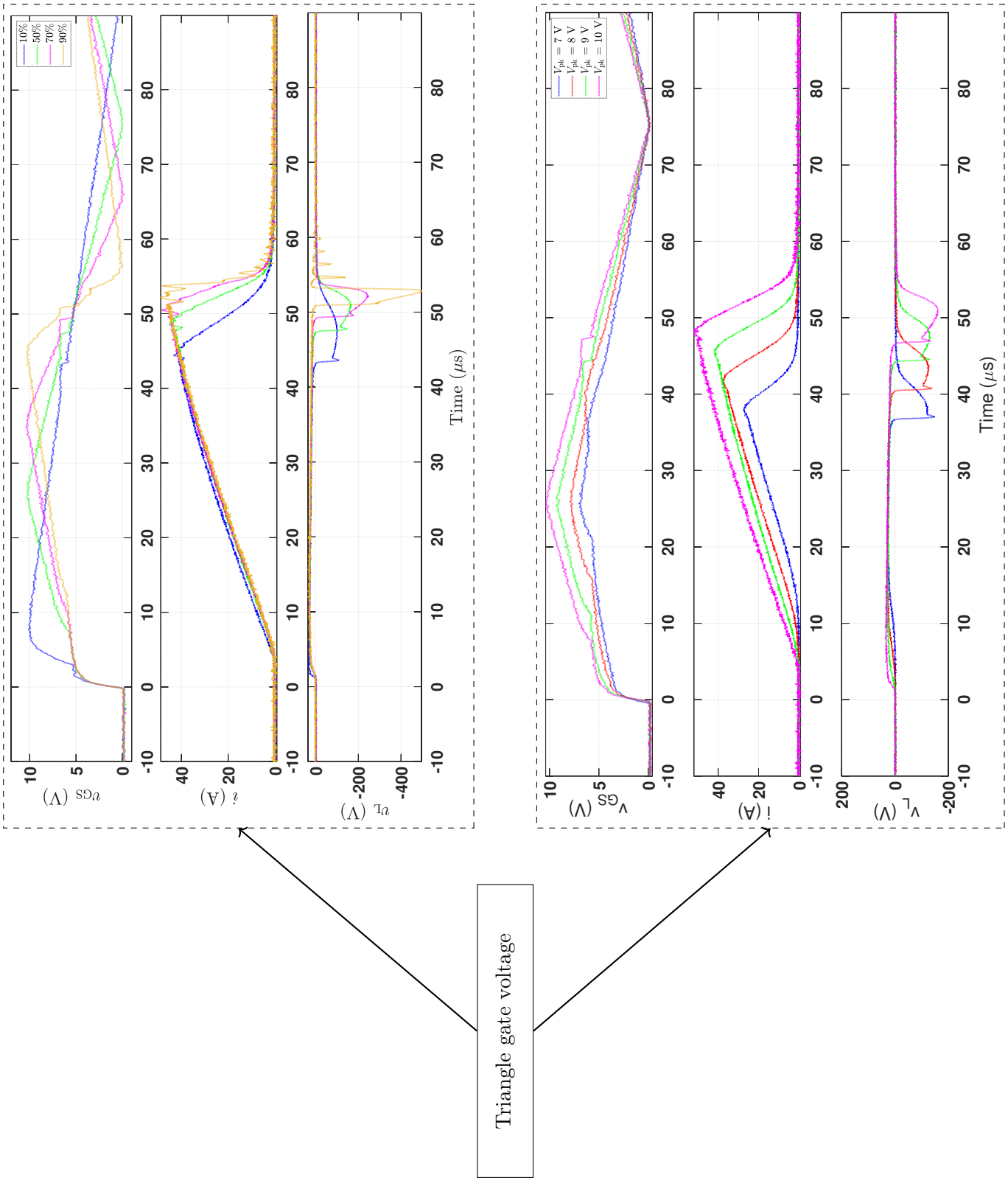

Figure 7.7: Illustrates the effect of symmetry and amplitude modification of gate voltage on TMS pulse

7.4 Modification of triangle gate voltage

So far, I have explored the effects of triangular gate voltage on the TMS coil, discussing how the symmetry and amplitude of the triangular gate voltage influence TMS pulse parameters such as rise time, fall time, and pulse width. In this section, I will examine the impact of quadrilateral gate voltage on the TMS coil and how varying the points within the quadrilateral can affect the shaping of the TMS voltage and current pulses. The parameters used in the following sections are provided in Table 7.3. Refer to the Fig. 7.8 illustrating the quadrilateral with four points labeled P1, P2, P3, and P4, defined at different voltages (V1, V2, V3, V4) and times (T1, T2, T3, T4).

Table 7.3: Parameters and their values used in subsections 7.4 to 7.6

Parameters	Values
Supercapacitor input	1 V
Capacitance (C2)	330 μF
C2 voltage	30 V

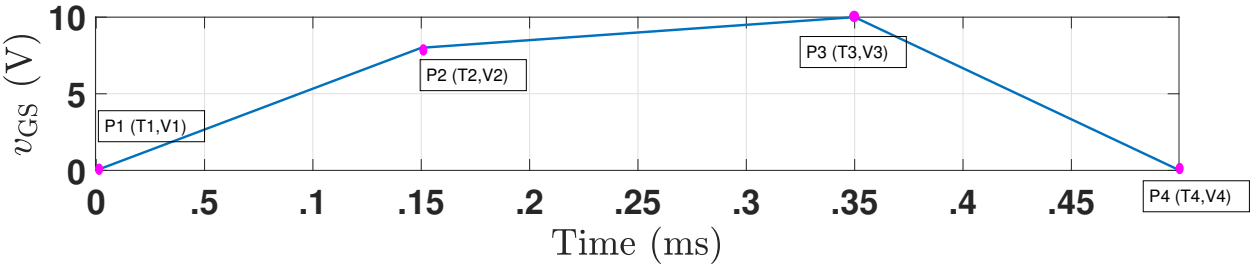

Figure 7.8: Point defined in a quadrilateral gate waveform

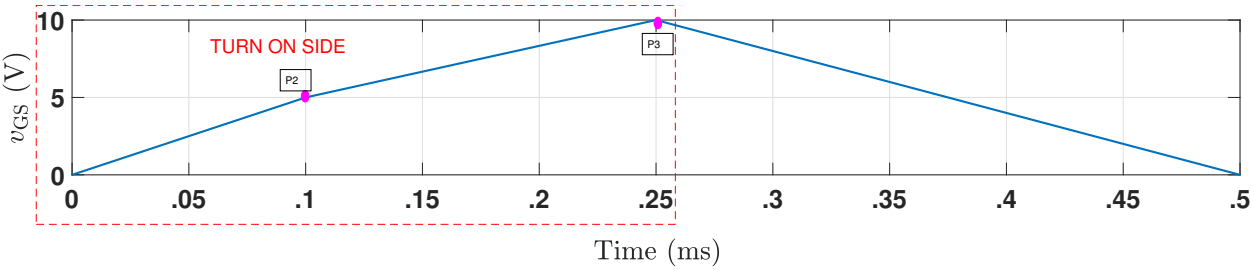

Figure 7.9: Turn-on slope representation in a quadrilateral waveform

In Fig 7.9, P2 and P3 are positioned on the left side of the quadrilateral, allowing for the adjustment of P2 around the turn-on threshold voltage to observe the effects on pulse shaping. Additionally, in Fig. 7.10, P3 is placed to the right and P2 at the center, enabling the modification of P3 to alter the turn-off timing and voltage, and thereby analyze the resulting effects. Lastly, another condition is examined, which involves the hold-on time. In this scenario (Fig. 7.11), P2 and P3 are maintained on either sides with respect to the center. This approach allows for delaying the turn-off time, resulting in a longer pulse width for the TMS pulse.

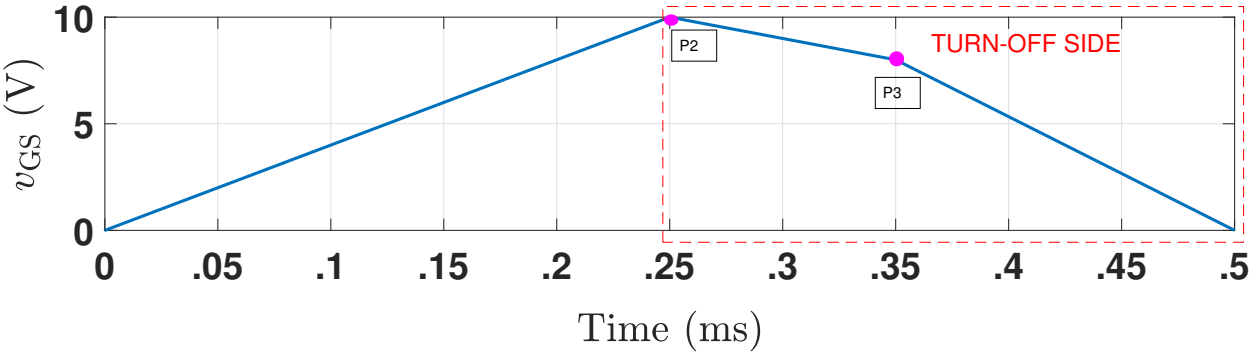

Figure 7.10: Turn-off side representation in a quadrilateral waveform

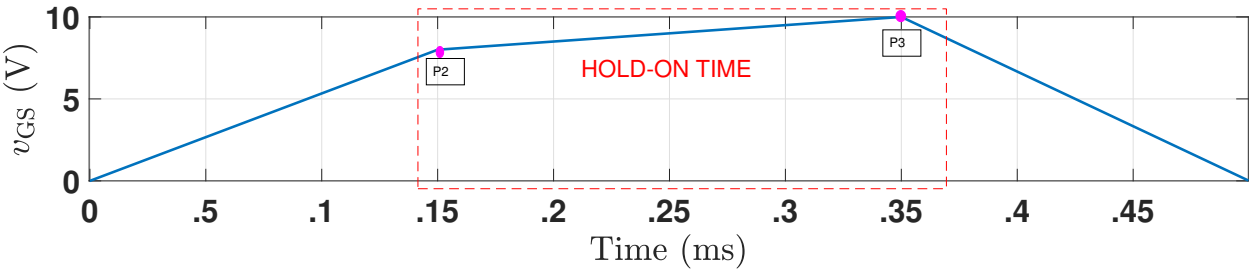

Figure 7.11: Hold-on time representation in a quadrilateral waveform

7.4.1 Effects of turn-on variations

In this analysis, the focus is on the points P2 and P3, primarily P2. The turn-off side is kept constant (Fig. 7.9), and its effects are not considered in this examination.

I have varied the P2 point with respect to voltage while keeping it at the same time instant as shown in Fig. 7.12 (first plot). This P2 variation occurs around the threshold region, specifically from 4.5 V to 6 V. As a result, the current pulse width increased, and the starting time of the TMS voltage pulse shifted due to the changing turn-on times. Additionally, the current rise/fall slope variations influenced the amplitude of the coil voltage pulse. These adjustments had a significant impact on the current rise time, which in turn affected the pulse width of the voltage pulse. A faster turn on in gate voltage led to a quicker rise time for the current, shortening the voltage pulse width. This occurs because a steeper slope allows the current to reach its peak value faster, resulting in a shorter duration for the voltage pulse. Conversely, a more gradual gate voltage turn on extending the rise time, leading longer coil voltage pulse width. In this case, the current takes longer to reach its peak value, thereby elongating the voltage pulse.

Fig. 7.12 is examined, where the violet graph shows a faster turn-on, leading to a quicker rise time of the current pulse as the transition from turn-on to maximum gate voltage is faster. The rise time here is measured at 80 μs (violet). In contrast, the blue waveform turns on at 0.05 ms, while the violet turns on at 0.02 ms. This delay in turn-on is due to the slope change from P1 to P2. The gradual slope change from turn-on to the maximum gate voltage at P3 results in a slower rise time, measured at 120 μs (blue). This slower rise time causes a difference in pulse shape and pulse width in the TMS voltage pulse. In the third plot, the positive phase of the violet TMS voltage pulse has

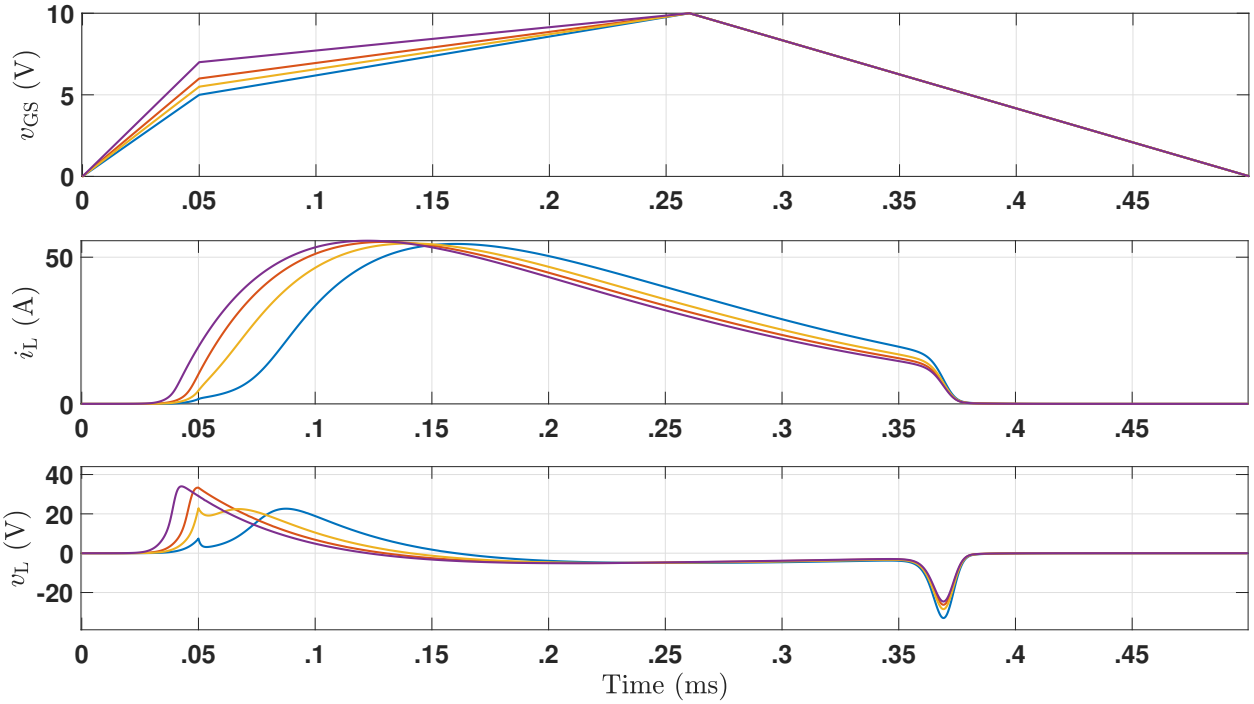

Figure 7.12: Modified triangular voltage waveform adjusted to a quadrilateral shape, with variation in the "on" time and its effect on the resulting TMS voltage and current pulses.

a width of 80 μs, while the blue waveform has an elongated positive phase of 120 μs. From this, we can see that if an elongated positive phase of the TMS voltage pulse is needed, the slope between P2 and P3 should be gradual, allowing the MOSFET to slowly build up the current.

By focusing on the turn-on side, the initial characteristics of the pulse can be effectively controlled and modified. Therefore, any modifications aimed at improving or tailoring the positive part of the voltage waveform should concentrate on the turn-on side.

7.4.2 Effects of turn-off variations

In this analysis, the focus is on the turn-off side, with the turn-on side kept constant to isolate the effects of changes in the turn-off region. Specifically, I have shifted the P3 point within the range of 4.5 V to 6 V, near the threshold region, allowing for different turn-off timings as shown in Fig. 7.13.

Figure 7.13 shows the analysis of the experiment. After point P2, the gate voltage starts to decrease, as seen in the gate voltage plot (first plot). As the gate voltage decreases, the MOSFET's resistance increases, causing the current to reduce. This current reduction depends on the gate voltage variation from 6 V to 4.5 V, which is the threshold region. At 6 V, the MOSFET begins to turn off, and it is completely off at 4.5 V. The fall time depends on how gradually or slowly the gate voltage varies between P2 and P3 and also between P3 and P4. In the violet graph, the turn-off occurs later than in the other graphs because its V3 is at 6 V, meaning it fully turns off only after the P3 point. Due to the gradual decrease in gate voltage from P2 to P4, the fall time of the violet current pulse is 60 μs, which affects the negative phase of the coil voltage pulse. This results in the violet voltage pulse being broader and delayed compared to other pulses. On the other hand, the

blue graph has a current fall time of 20 μs, making the blue voltage pulse rapid and shorter. These experiments revealed that by keeping the turn-on side constant and varying P2 and P3, the pulse width of the voltage and the current fall time can be effectively controlled.

This capability is essential for customizing TMS pulses to meet specific requirements, such as achieving precise amplitude, longer pulse width, and quick or slower rise/fall times. Additionally, by adjusting the turn-off side, we can primarily influence the shape of the negative phase of the voltage pulse.

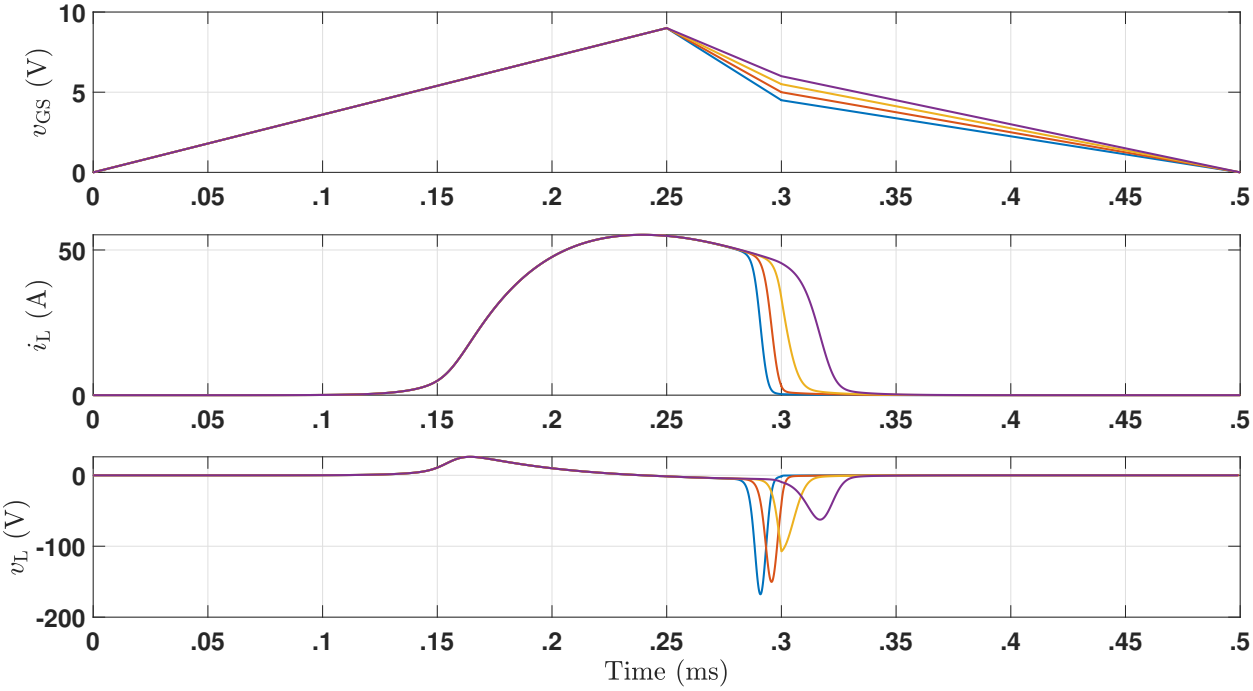

Figure 7.13: Modified triangular voltage waveform adjusted to a quadrilateral shape, with variation in the "turn off" time and its effect on the resulting TMS voltage and current pulses.

7.4.3 Investigation of hold-on time variations

In my investigation of hold-on time variations, adjustments were made by fine-tuning the P2 and P3 points in the waveform (Fig. 7.14). This method of controlling the spacing between these points allowed for changes in the pulse width. By varying the time between the P2 and P3 points, the duration of the pulse could be effectively adjusted, directly impacting the amount of energy stored in the TMS coil.

A greater time between these points resulted in a longer pulse width, enabling the coil to store more energy, while a shorter interval led to a shorter pulse width. Figure 7.14 illustrates the results with different hold-on timings. Each variation in timing was analyzed to observe its effect on the TMS voltage and current pulse shapes. In Figure 7.14, the blue graph shows a larger time interval between P2 and P3, resulting in a longer current pulse width of 450 μs, while the yellow graph results in a current pulse width of 400 μs. The main idea behind the hold-on time is to increase the pulse width of the current and voltage waveforms. If an elongated pulse is needed in the positive

or negative phase of the pulse, hold-on points can be introduced. During this time, no switching occurs, allowing more time for energy buildup, which leads to a longer pulse. The usage of hold-on time will be explained further in the next sections.

The data revealed how changing the hold-on time influenced the duration of the pulses, highlighting the relationship between timing adjustments and energy storage within the TMS system.

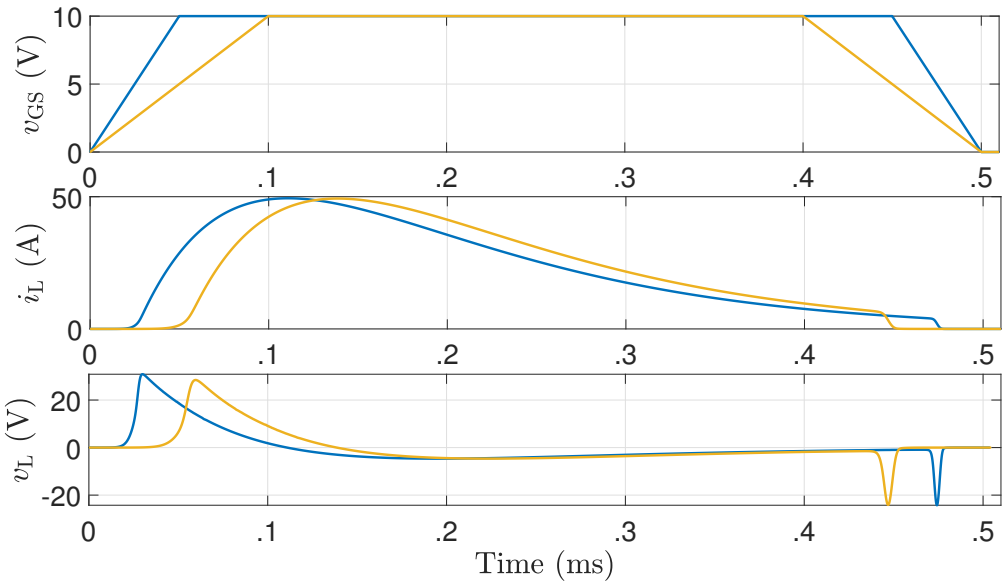

Figure 7.14: Modified triangular voltage waveform adjusted to a quadrilateral shape, with variation in the "hold on" time and its effect on the resulting TMS voltage and current pulses.

These findings provide valuable insights into optimizing TMS pulse characteristics by manipulating hold-on times, thereby enhancing control over energy delivery and overall pulse performance.

This research emphasizes the importance of a dedicated gate voltage waveform generator capable of producing the precise waveform required. It is crucial that the output waveform remains undistorted when applied to the gate of a MOSFET. In my setup, the triangle waveform generator initially produced a good triangular voltage waveform output. However, when this output was connected to the MOSFET gate and measured, slight distortions were observed in the waveform. These distortions are attributed to the combined effects of the inherent gate capacitance of the MOSFET, which alters the intended triangular waveform, and imperfections in the arbitrary waveform generator output, which was found to be neither fully clean nor perfectly accurate. As a result, the gate-source voltage (v_{GS}) waveform deviated from the ideal triangular shape, introducing variations in the TMS pulse characteristics observed in the experiments.

Even when using an arbitrary waveform generator in the lab, capable of creating standard triangle, sine, and square waveforms, generating a waveform with more than three points proved to be imprecise. This lack of precision can impact the accuracy of the TMS pulses. Despite these challenges, the experimental setup yielded promising results. My research suggests that fine-tuning the gate voltage waveform can effectively shape the pulse width and waveform of TMS pulses. This underscores the need for a perfect, undistorted gate voltage waveform to achieve consistent and accurate results.

7.5 Analysis of the gate voltage modification

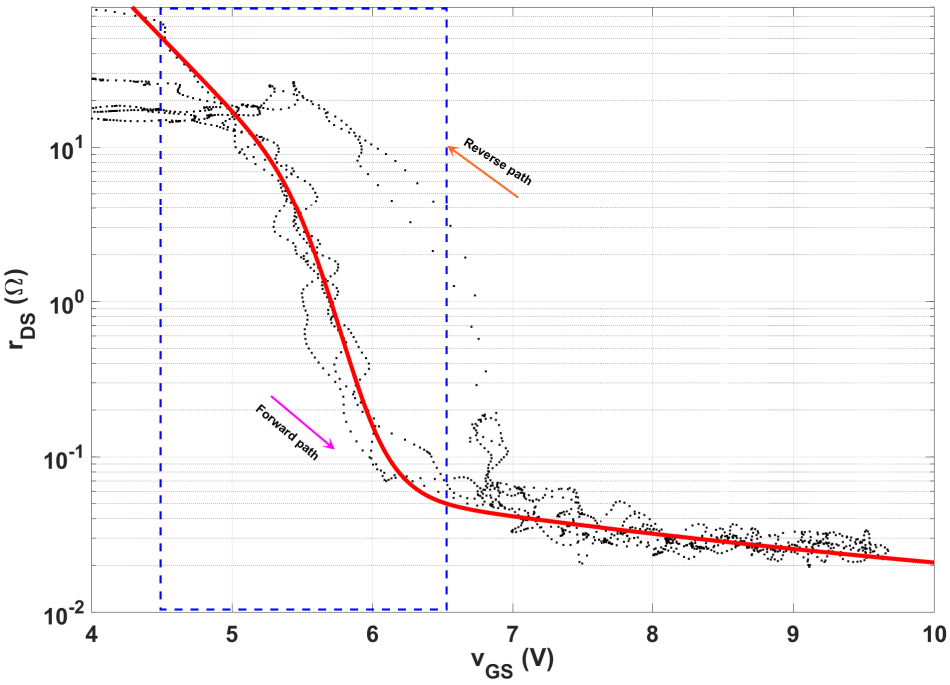

Figure 7.15: Input admittance characteristic with curve fitting (red) and blue box shows the variable resistance region of the MOSFET

The findings so far discussed underscore the critical role of waveform shape and timing in controlling the characteristics of TMS pulses. By fine-tuning the gate voltage waveform, particularly the timing of key points, it is possible to achieve control over the pulse width and amplitude of both coil current and voltage pulses to a certain extent. However, the question arises: what can be done beyond this with the current prototype? In this section, I will discuss modifications to the gate voltage and explore various adjustments that can be made, as well as identifying the optimal operating regions for the MOSFET to achieve better pulse shaping.

The point adjustments had a limited effect on the overall pulse shape. It became apparent that more substantial modifications to the pulse shape could be achieved by focusing on the gate voltage amplitude, particularly around the threshold region where the MOSFET resistance is varying significantly. From the Fig. 7.15, it was observed that the MOSFET resistance changes more noticeably within the gate voltage range of 4.5 V to 6.5 V. In this range, the resistance is not constant, which provides a more dynamic control point for pulse shaping. By adjusting the gate voltage within this critical range, we can achieve more pronounced changes in the pulse characteristics.

The next section provides a comprehensive analysis of this approach, exploring various options and their impacts on pulse shaping. Specifically, it examines how varying the gate voltage within the 4.5 V to 6.5 V range can be utilized to fine-tune the pulse width, rise time, fall time, and overall shape of both the voltage and current TMS pulses. This approach allows for more precise control over the pulse parameters, making it possible to tailor the TMS pulses to meet specific requirements.

For instance, by focusing on this threshold region, we can more effectively control the amplitude of the pulse, extending or shortening the pulse width, and adjusting the rise and fall times to achieve the desired pulse shape. This method provides a greater degree of flexibility and precision compared to simply altering the slopes or points of the quadrilateral waveform.

In summary, while the initial experiments with point adjustments provided some control over the pulse shape, the most effective way to achieve significant and precise modifications is by varying the gate voltage around the threshold region where the MOSFET resistance varies. This insight allows more advanced pulse shaping techniques, as detailed in the following section.

7.6 Summary table

In the following analysis, I explore various waveform changes and their corresponding observations related to turn-on and turn-off times, amplitude variations, and gate voltage effects on TMS pulses. The observations detail how these changes influence pulse width, rise and fall times, and the overall shape of the voltage and current pulses. Table 7.4 summarizes the key findings from this analysis:

Table 7.4: Effects of gate voltage alteration on TMS output voltage and current pulse

Parameters	**Waveforms**	**Observations**
Row 1 v_{GS} i_L v_L	Amplitude variation around threshold 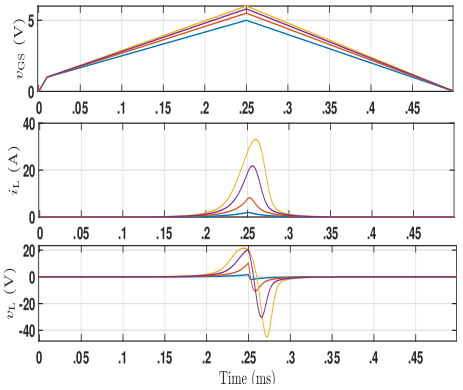 	• Low amplitude of v_{GS} makes pulse with low amplitude of i_L and v_L. • A higher amplitude of the gate voltage, v_{GS}, increases the rise time of the current pulse. • The yellow trace shows a rise time of 65 μs, while the blue trace shows 50 μs.
Row 2 v_{GS} i_L v_L	Delaying the turn-on time 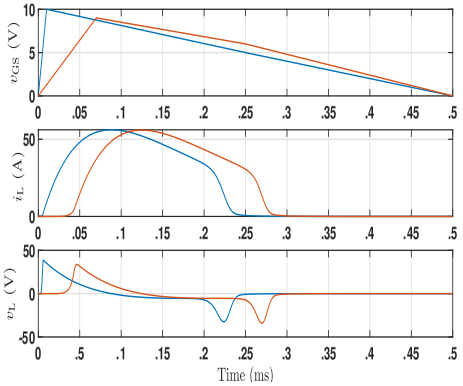 	• Delayed turn-on (orange): Increases current pulse width (270 μs) with a less steep current rise time (100 μs). Whereas blue has rise time of 80 μs. • Faster turn-on (blue): Steeper voltage pulse rise time (3 μs) in TMS.

Parameters	Waveforms	Observations
Row 3 v_{GS} i_L v_L	P2, P3 voltage varies, but occurs at the same time instant. 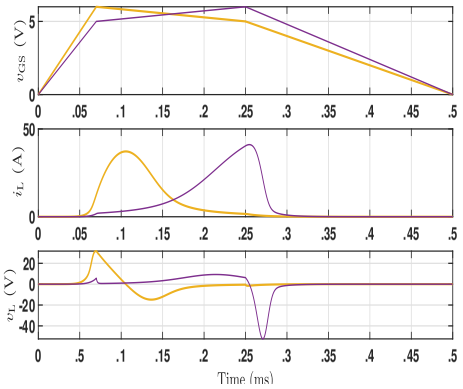	• P2 (5V) to P3 (6V) increases (purple): Slower current pulse rise time (200 μs) with a faster fall time (50 μs). • P2 (6V) to P3 (5V) decreases (yellow): Quicker rise (50 μs) and slow fall time (100 μs) for current pulse. • Yellow voltage pulse width is 150 μs and violet is 250 μs. • Yellow has a narrowed positive voltage phase, whereas violet has a elongated positive phase. • The elongated positive phase (violet) can be attained with the hold-on time from 5 V to 6 V. Similarly, negative phase voltage portion can be elongated by the hold-on time from 6 V to 5 V.

Parameters	Waveforms	Observations
Row 4 v_{GS} i_L v_L	Same as Row 3, but with points shifted later in time 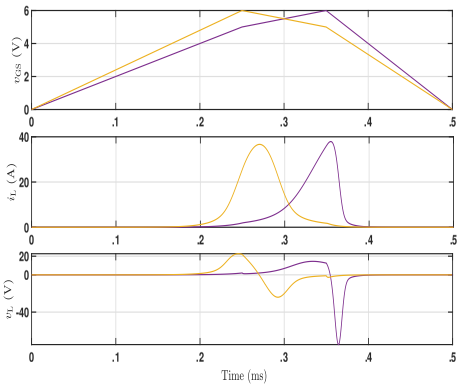	• Delayed output pulse. • shorter hold on time than Row 3 graph causes shorter pulse-width.
Row 5 v_{GS} i_L v_L	Variation in P2 and P3 the threshold. 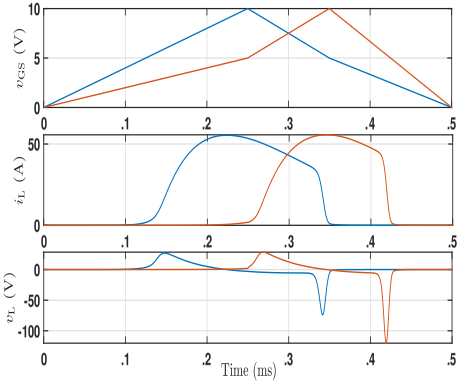	• The starting point of the current and voltage pulses can be controlled by adjusting when the gate voltage crosses the threshold. • The blue pulse begins at 0.13 ms because the blue gate voltage crosses the 5 V (threshold) at 0.13 ms. • Orange TMS pulse, on the other hand, starts at 0.25 ms. • Similarly, the pulse end instant can also be controlled by adjusting when the gate voltage falls back below the threshold.

Parameters	Waveforms	Observations
Row 6 v_{GS} i_L v_L	Turn-off side variation 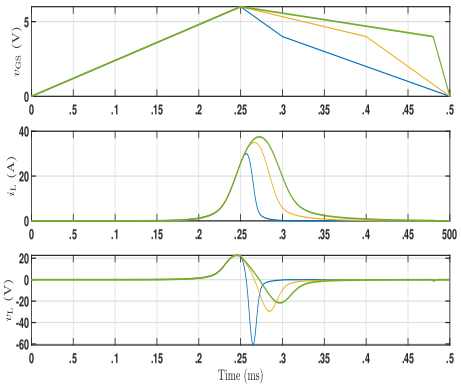	• P3 is varied to adjust turn-off timing • Increased turn-off time leads to a wider current pulse. Green current and voltage pulse is 200 μs while blue is 100 μs long • Slower turn off results in more symmetric pulses with a broader pulse width.
Row 7 v_{GS} i_L v_L	Effects if the P4 is not at 0V 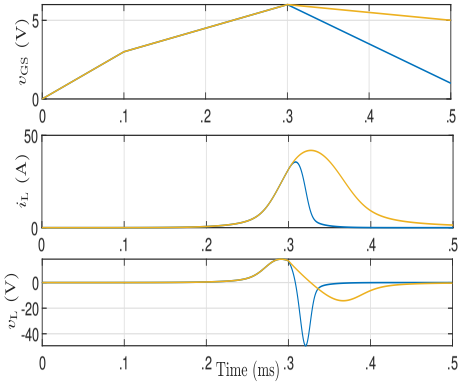	• The yellow TMS voltage and current pulse is 250 μs long, while the blue TMS pulse is 130 μs long. • The yellow pulse has P4 at 5 V, and the blue pulse has P4 at 1 V, which affects the turn-off time instant, resulting in the difference in pulse width.

Parameters	Waveforms	Observations
Row 8 v_{GS} i_L v_L	5- point gate voltage waveform 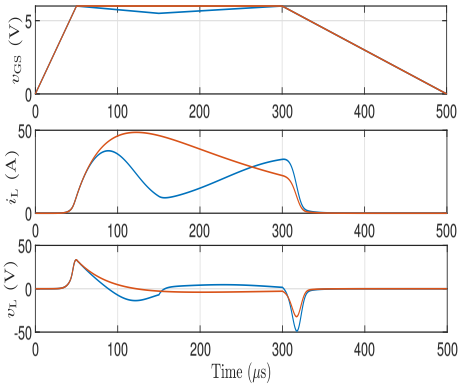 	•A comparison is made between the 4-point (orange) and 5-point (blue) graphs. • In the 5-point graph, the voltage shifts from 6 V to 5.5 V and then back to 6 V, all within the MOSFET threshold region. • The MOSFET begins turning off at 6 V, but as the gate voltage rises again from 5.5 V to 6 V, the MOSFET turns back on with the same gate voltage. • The advantage of operating the gate voltage with 5 points and within the threshold is that it allows the generation of two positive and two negative voltage pulse phases using a single gate voltage input. • The blue waveform demonstrates the MOSFET turning on and off twice within a single gate voltage cycle. • The current TMS pulse shape is now more complex, featuring two rises and falls, unlike the previous (Row 1-7) simpler single rise and fall waveform.

7.7 Verification of experimental data with MOSFET model

In this section, I conducted an experimental verification of the gate voltage waveform by comparing it with the simulated waveform generated in MATLAB MOSFET model. The comparison revealed that the pulse shapes and pulse widths were identical between the experimental results and the MATLAB simulations. The parameters used in this section are provided in Table 7.5.

Table 7.5: Parameters and their values used in subsections 7.7

Parameters	Experiment	Simulation
Supercapacitor input	1 V	1 V
Capacitance (C2)	330 μF	330 μF
C2 voltage	30 V	30 V

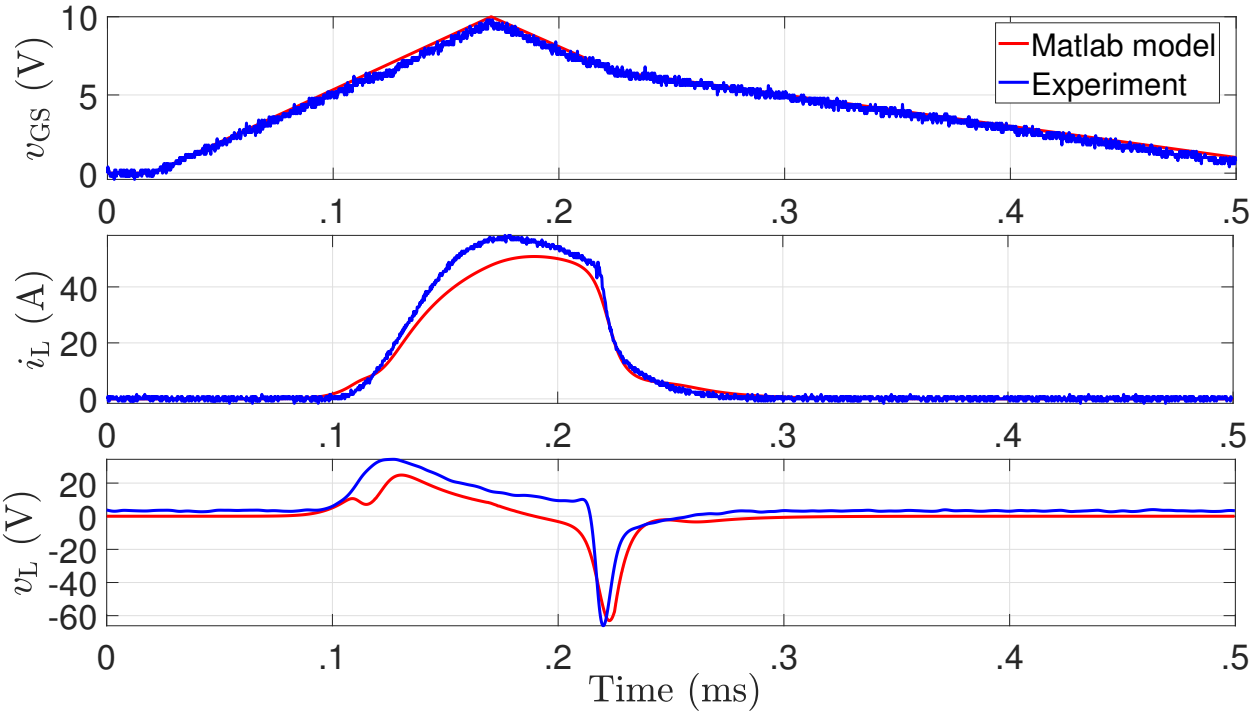

Figure 7.16: Verification of experimental and MATLAB data with a quadrilateral gate voltage of 10 V amplitude

The current probe used in the experiment has a bandwidth of DC-100 kHz, which leads to a slower response time compared to the MATLAB simulations. In contrast, the oscilloscope used for voltage measurements, specifically for $v_L(t)$, has a much higher bandwidth of 0-10 MHz. This difference in bandwidth capabilities explains the variations in response times observed between the current and voltage measurements. These delays have been corrected and plotted. Figures 7.16 and 7.17 present the experimental and MATLAB results of the modified triangular gate voltage waveform. The results indicate that the TMS current and voltage pulses are identical between the experimental

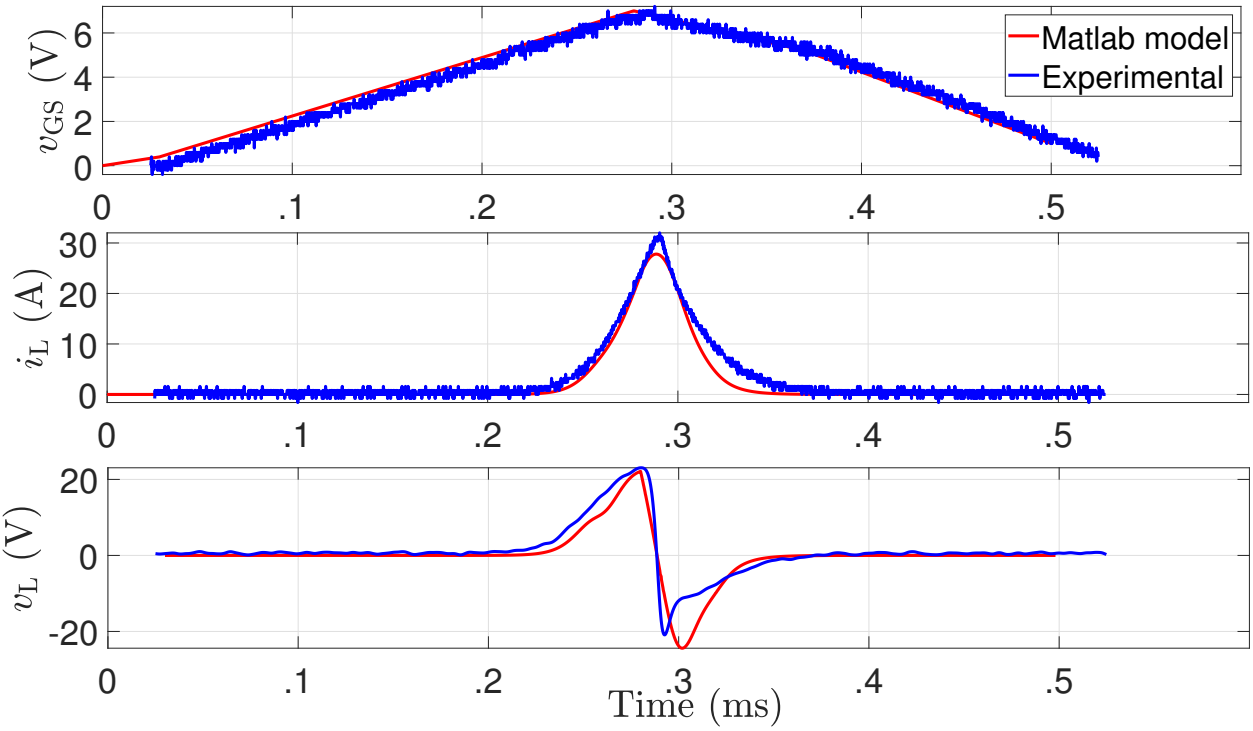

Figure 7.17: Verification of experimental and MATLAB data with a gate voltage of 7 V amplitude

setup and the MATLAB simulations. This comparison underscores the high degree of accuracy and consistency achieved in the experimental setup despite minor discrepancies in the waveform slopes. By re-plotting the oscilloscope photos in MATLAB, the comparison becomes clearer. This detailed comparison highlights the importance of considering the bandwidth and response times of measurement instruments in experimental setups, as they can significantly influence the observed results.

MATLAB simulations produce a perfect gate waveform without any distortion, characterized by sharp slopes. These ideal conditions significantly impact the current and voltage waveforms, resulting in precise and well-defined pulses. However, in the experimental setup, while the gate waveform is nearly identical to the MATLAB-generated waveform, it exhibits minor distortions and less sharp slopes. These small imperfections can affect the current and voltage waveforms, making them slightly less precise compared to the ideal simulations.

The discrepancies between the experimental and simulated results in Fig. 7.16(a–c) can be attributed to several factors, both in model assumptions and experimental conditions. First, the model parameters were originally tuned for a triangular gate voltage input, and the same set was used for trapezoidal waveform simulations without re-optimization. While this was done under the assumption that the change in waveform would result in minimal variation, the flat-top regions of the trapezoidal gate voltage introduce differences in MOSFET switching dynamics and coil response that are not fully captured by the initial model.

In addition, the output from the arbitrary waveform generator used in the experiments was found to be imperfect, introducing noise and deviations from the ideal trapezoidal shape. Notably,

the gate-source voltage (v_{GS}) shows visible distortion around 0.125 ms, likely affecting the switching behavior of the MOSFET and contributing to further mismatch between simulation and measurement.

These conditions lead to observable discrepancies: in the experimental data (Fig. 7.16), the inductor current (i_L) reaches a higher peak than in the simulated result, and the peak occurs earlier. A similar trend is observed in the inductor voltage (v_L), which also shows a higher and earlier peak compared to the model. This conclusion is drawn from the fact that the v_{GS} distortion alone does not fully account for the earlier and higher peaks seen in both i_L and v_L, suggesting an underlying mismatch in model dynamics. Conversely, even with a clean waveform, using parameters optimised for a triangular input would not capture the altered switching behaviour introduced by the flat regions of the trapezoidal signal. Therefore, the discrepancies likely result from the combined influence of both factors.

7.8 Pulse shape comparison and replication strategy

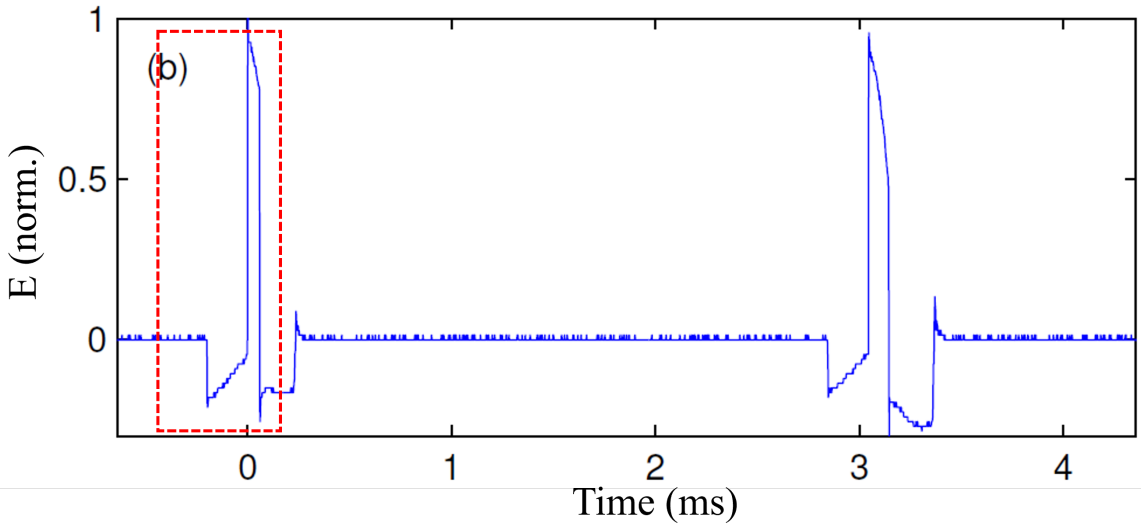

Figure 7.18: Existing TMS pulse generated by the pulse generator used in [134] © 2014 IOP Publishing Ltd. The red dotted rectangle represents the pulse portion I intend to replicate using my prototype. Electric field (E) is expected to be nearly proportional to v_L.

In this discussion, I will examine the pulse shape characteristics produced by existing TMS circuits, as referenced in Peterchev et al. (2014) [134]. These circuits, currently used for human TMS, generate specific pulse shapes that I aim to replicate with my pulse generator prototype designed for a mouse coil. At present, my prototype is configured to generate only monophasic pulses, which limits its capability to reproduce only half of the existing pulse shape, as depicted in Figure 7.18. This figure illustrates the existing TMS pulse shape of the electric field (E), which is proportional to the TMS coil voltage. The red-highlighted area in the figure indicates the portion of the waveform that I aim to replicate, producing a coil voltage pulse with both negative and positive phases, with a positive phase pulse width of 60 μs and a negative phase pulse width of 100 μs. The

pulse (Fig. 7.18) was digitized and used as a reference for the replication steps. The parameters used in this section are provided in Table 7.6.

Table 7.6: Parameters and their values used in subsections 7.8

Parameters	Values
Supercapacitor input	1 V
Capacitance (C2)	330 μF
C2 voltage	30 V

I am unable to precisely replicate both the amplitude and pulse width of the reference pulse in my prototype circuit. It is possible to independently control either pulse-width or amplitude of the TMS pulse. As a result, I am focusing on controlling the pulse width rather than the amplitude. The amplitude can be easily adjusted by changing the voltage across the C2 capacitor, which directly influences the energy stored in the circuit. This allows for easier manipulation of the amplitude without affecting the pulse width significantly.

7.8.1 Step-1: Initial Configuration

I began the process by applying a triangular gate voltage with an amplitude of 10 V and a pulse width of 500 μs. The results are shown in Fig. 7.19. I then compared the obtained TMS voltage pulse shape to the reference pulse as shown in Fig. 7.19(b). The negative phase of the voltage waveform (-v_L) matched the reference pulse width, but the positive phase exhibited a delayed rise compared to the reference. This observation led me to conclude that adjustments were needed primarily in the turn-off region of the pulse, as explained in Section 7.4.2. Specifically, points P2 and P3 in the quadrilateral need to be shifted to the right side to influence the turn-off portion of the pulse effectively.

The term "pulse-width" refers to the duration of the pulse measured between the points where the signal crosses the zero-voltage line. Specifically, the positive pulse width is the time interval during which the signal remains positive, starting from when the signal first crosses zero as it enters the positive phase, and ending when it crosses zero again at the end of the positive phase.

As shown in Fig. 7.19, the positive pulse width is indicated by the section between the initial zero crossing, where the signal moves into the positive phase, and the final zero crossing, where the positive phase ends. The concept also applies to the negative phase, where the negative pulse width is similarly defined as the duration between the start of the negative phase (when the signal crosses zero) and the end of the negative phase (when it crosses zero again).

7.8.2 Step-2: Refining the Pulse Width

In this step, I set point P2 at (250 μs, 10 V) because this serves as one vertex of the triangular voltage waveform in step-1. Next, I positioned P3 where the pulse should end. To do this, I added 60 μs to the 250 μs (T2), resulting in T3 being set at 310 μs. The 60 μs interval corresponds to the

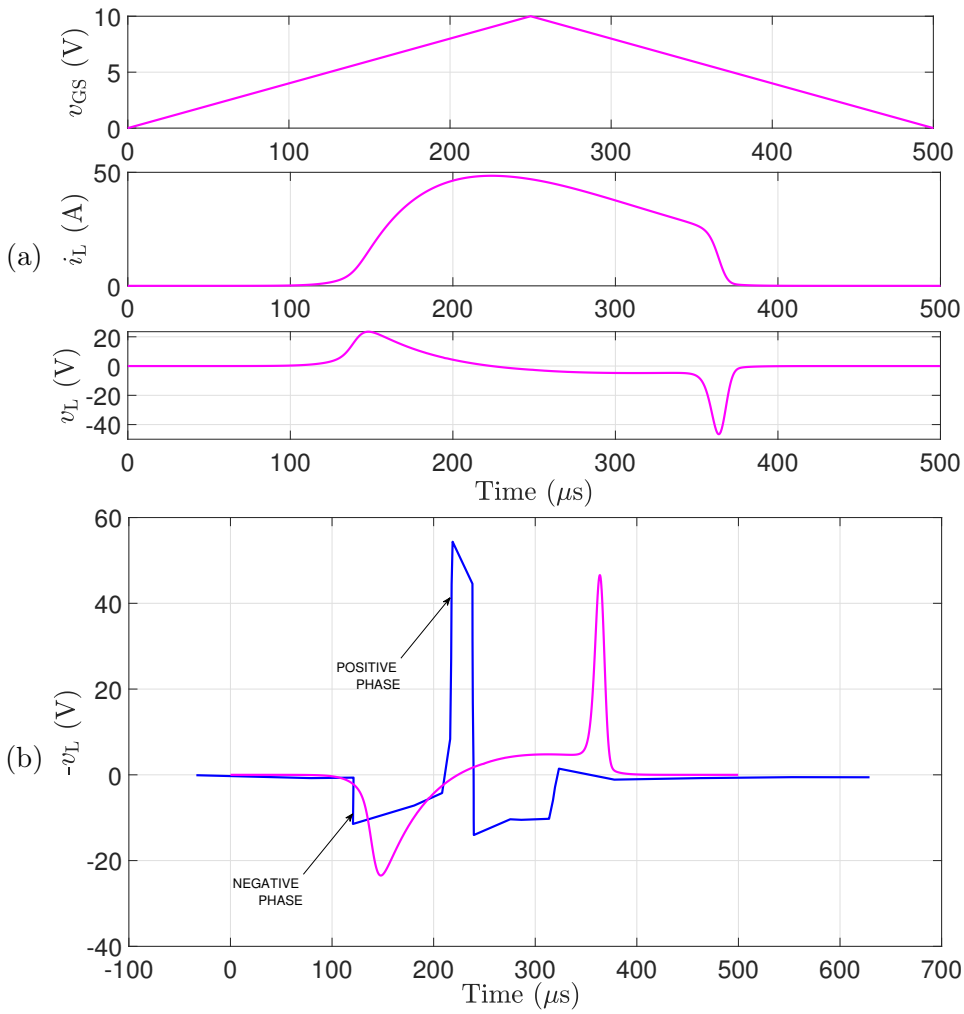

Figure 7.19: (a) TMS pulse parameters from the Step-1 results; (b) comparison between the reference shape (blue) and the TMS pulse shape obtained in Step-1 (magenta).

Table 7.7: Time and voltage values at specific gate voltage points in step-2

Points	(**Time (μs)**, **Voltage (V)**)	
	Attempt 1	**Attempt 2**
P1	(0, 0)	(0, 0)
P2	(250, 10)	(250, 8)
P3	(310, 5)	(310, 6)
P4	(500, 0)	(500, 0)

positive phase pulse width of the reference waveform. For the voltage at V3, I set it to 5 V, which is close to the MOSFET's threshold voltage, the point where the MOSFET turns off. This configuration produces a rapid voltage pulse, as shown in Fig. 7.20 (black waveform).

For the next attempt (attempt 2), I aimed to reduce the slope between P2 and P3 which makes the turn off slower, as the previous result was abrupt. This was achieved by lowering the gate voltage amplitude, setting V2 to 8 V and V3 to 6 V (Fig. 7.20 red waveform). Both attempts are shown in Figure 7.20, with the corresponding parameters detailed in Table 7.7.

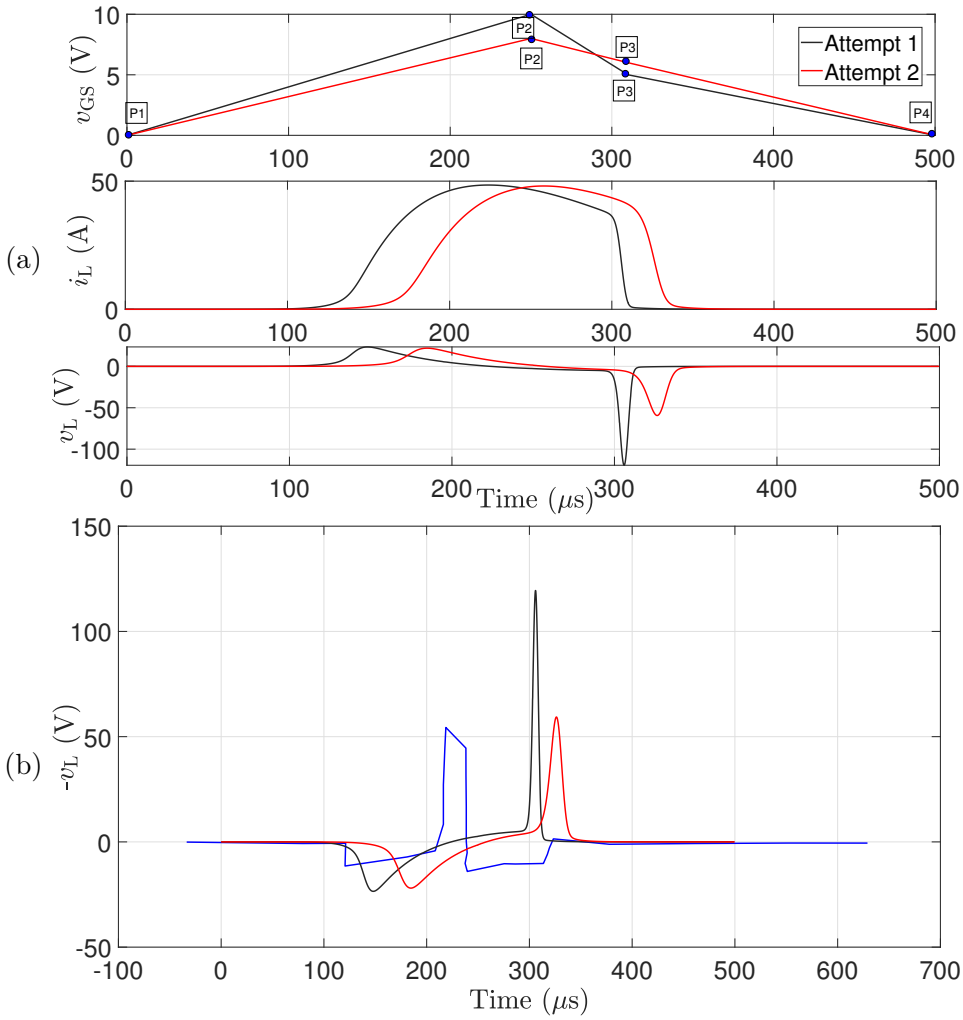

Figure 7.20: (a) TMS pulse parameters from the Step-2 results; (b) comparison between the reference shape (blue) and the TMS pulse shape obtained in Step-2.

7.8.3 Step-3: Alignment of Positive Portion

After step 2, the result (Fig. 7.20 red waveform) closely resembles the reference waveform (Fig. 7.20, blue waveform). However, there is a timing discrepancy. My prototype's pulse was delayed compared to the reference. To correct this, I shifted T2 backward by 50 μs, adjusting T2 to 200 μs. Similarly, I shifted T3 backward by 95 μs, resulting in T3 being set to 215 μs. These differences can be observed

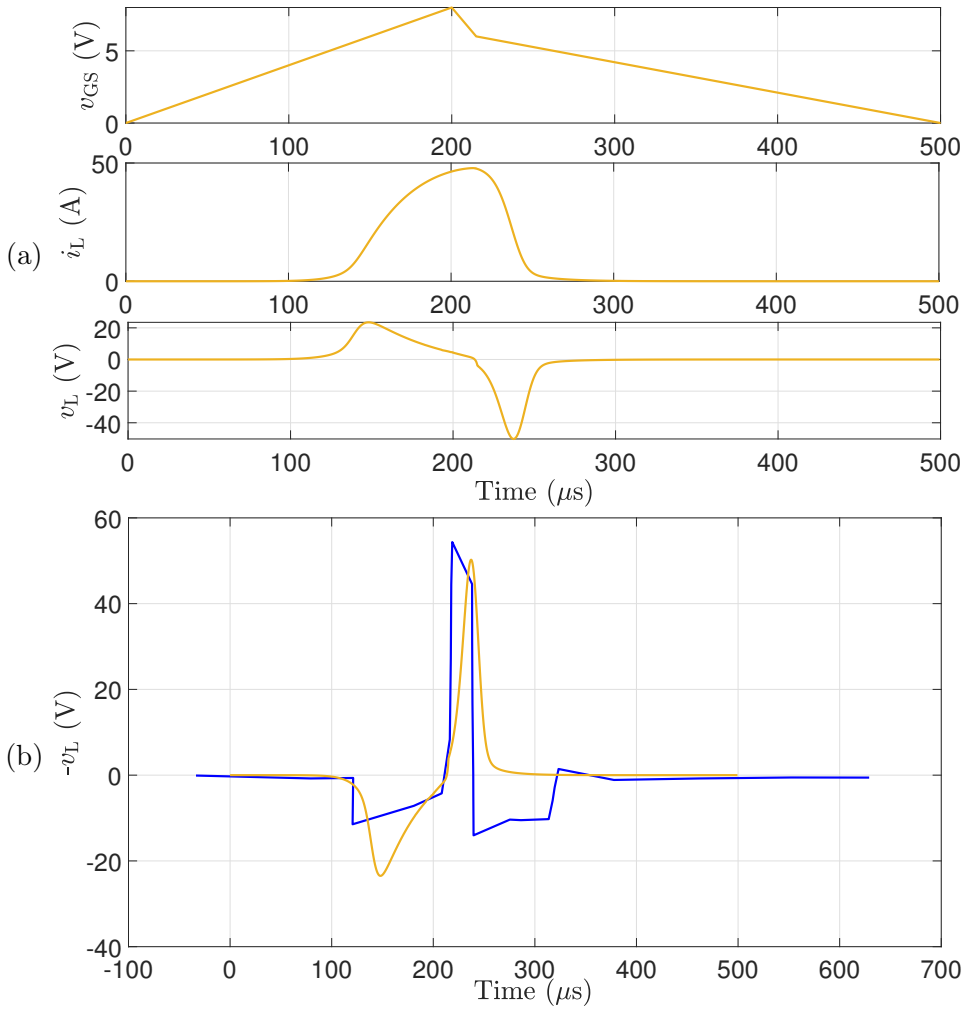

Figure 7.21: (a) TMS pulse parameters from the Step-3 results; (b) comparison between the reference shape (blue) and the TMS pulse shape obtained in Step-3 (yellow).

in the comparison graphs (Fig. 7.20). The resultant TMS parameters and their comparison with the reference are shown in Fig.7.21, with the corresponding parameters detailed in Table 7.8.

Table 7.8: Time and voltage values at specific gate voltage points in step-3

Points	(**Time (μs)**, **Voltage (V)**)
P1	(0, 0)
P2	(200, 8)
P3	(215, 6)
P4	(500, 0)

7.8.4 Step-4: Final Adjustments

At this stage, the alignment was good, but fine-tuning is necessary. The positive phase of the -v_L waveform is slightly delayed. To correct this, I made small adjustments to V2 and V3, with increments or decrements of 0.1 V. The final settings were V2 at 8.5 V and V3 at 5.8 V, resulting in a steeper slope from P2 to P3 compared to Step-3 as shown in Fig 7.22. This adjustment aligned the positive portion of the -v_L waveform more closely with the reference. Achieving this alignment required two or three iterations with 0.1 V variations, as the deviation from the reference was minimal.

The parameters used in Step 4 is detailed in Table 7.9. A comparison with the reference waveform is illustrated in Fig. 7.23. In this replication process, the focus was on achieving pulse shape accuracy with respect to pulse width only, the amplitude of the pulse was not taken into consideration.

I also tested the same gate voltage with the points in Table 7.9 in the experimental setup of the prototype, and the results closely matched those of the MATLAB model. Additionally, the pulse width was consistent with that of the reference pulse. The experimental results are presented in Fig. 7.24.

Table 7.9: Time and voltage values at specific gate voltage points in step-4

Points	(**Time (μs)**, **Voltage (V)**)
P1	(0, 0)
P2	(200, 8.5)
P3	(215, 5.8)
P4	(500, 0)

It is evident that I was not able to recreate the second negative phase in the reference Fig. 7.18. Since my circuit does not generate a biphasic current waveform, I was unable to replicate the exact same pulse. However, I was successful in recreating both the first negative phase and the positive phase accurately.

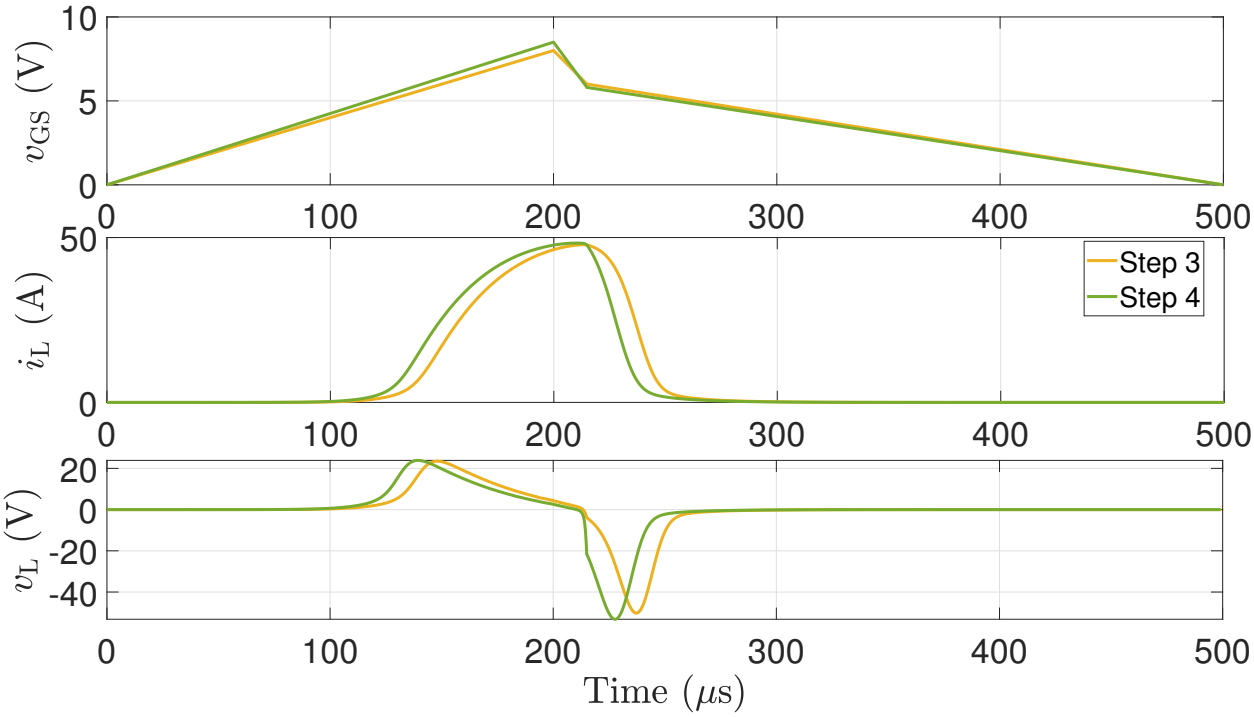

Figure 7.22: TMS pulse parameters from the Step-3 and Step-4 results

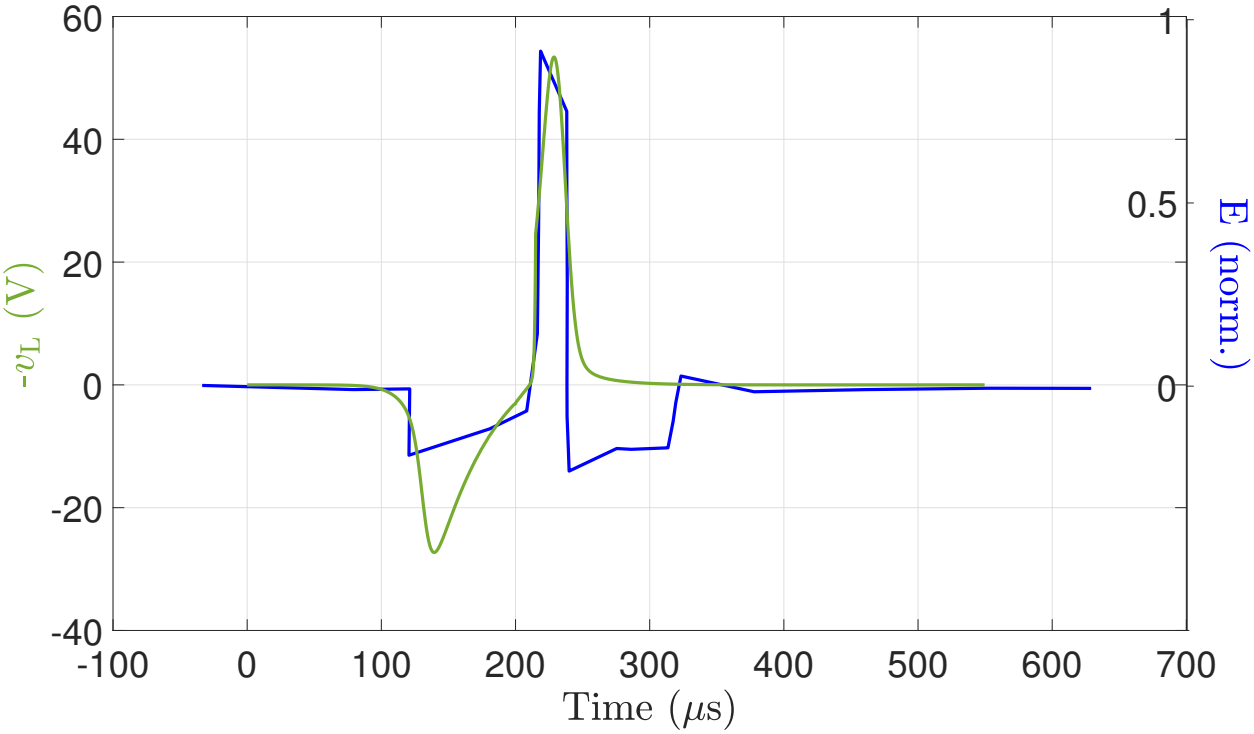

Figure 7.23: Comparison between the reference shape (blue) and the TMS pulse shape (simulated) obtained in Step-4 (green)

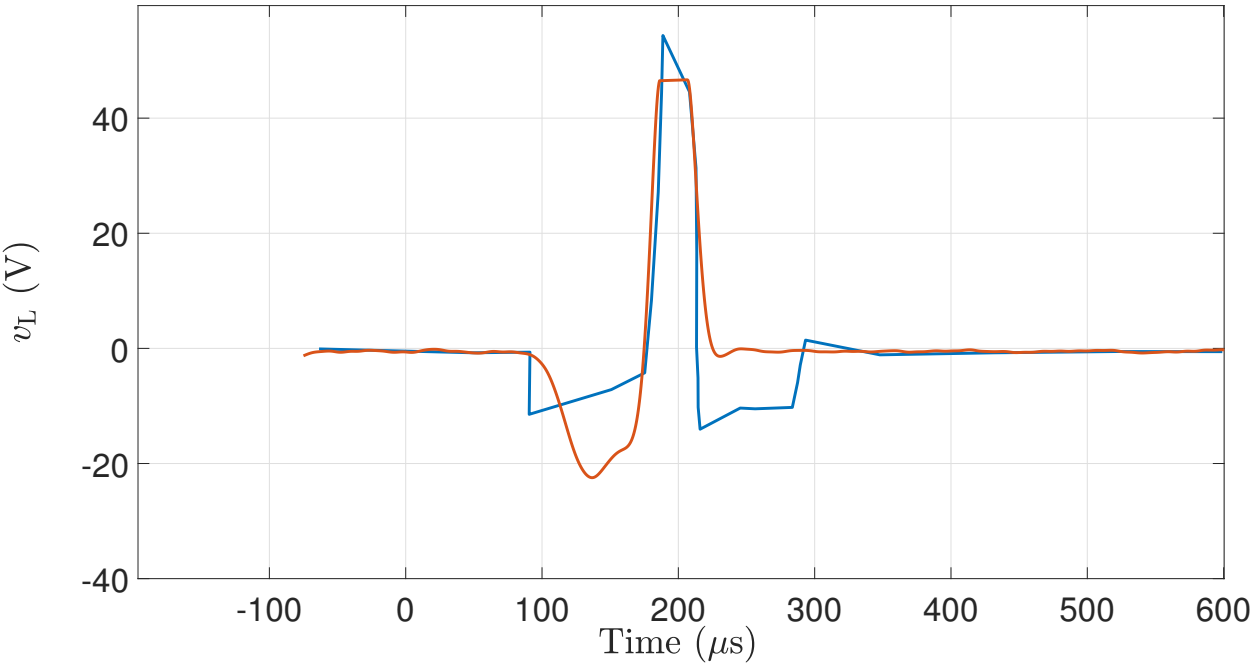

Figure 7.24: Comparison between the reference shape (blue) and the experimental TMS pulse shape obtained using Step-4 points (orange)

7.9 Exploring alternative pulse configurations

I have successfully replicated another pulse from [134] (Fig. 7.25 (blue waveform)) using a different approach than starting with a triangle gate voltage. By understanding how the gate voltage works and using the data from the summary table in Section 7.6, it becomes easier to replicate any desired pulse shape using the prototype.

7.9.1 Step-1

I began by redrawing the target pulse using MATLAB digitization, which served as a reference as shown in Fig. 7.26. The pulse has three main points, in addition to the starting point P1 (0,0) and the endpoint P2 (250 μs, 0) as marked in Fig. 7.26. Point (2) is where the gradient of v_L starts to fall. This corresponds to the P2 point in the gate voltage waveform. According to the summary table in Section 7.6, Row 2, there is a similar TMS pulse result with quick rise time. That is why I kept P2 very near to P1, so that I could achieve a quick rise time. I used a 10 V amplitude for all the gate voltages throughout this research, so I am maintaining the same voltage amplitude as in my initial attempt. So P2 was set at (20 μs, 10), since point (2) is located at 20 μs in the reference figure. The positive phase drops at point (3), where the MOSFET begins to turn off. I set P3 at (40 μs, 6), corresponding to the point where the MOSFET starts to turn off. Finally, P4 is where the MOSFET completely turns off, so I set it at (150 μs, 5).

The resistance variation discussed in the Section 7.5 showed a change from 4.5 to 6.5 V, with a significant resistance change between 5 V and 6 V. Therefore, I initially used 5 V when I needed to turn on or completely turn off the MOSFET instead of 4.5 V and 6 V to start the turn-off instead of

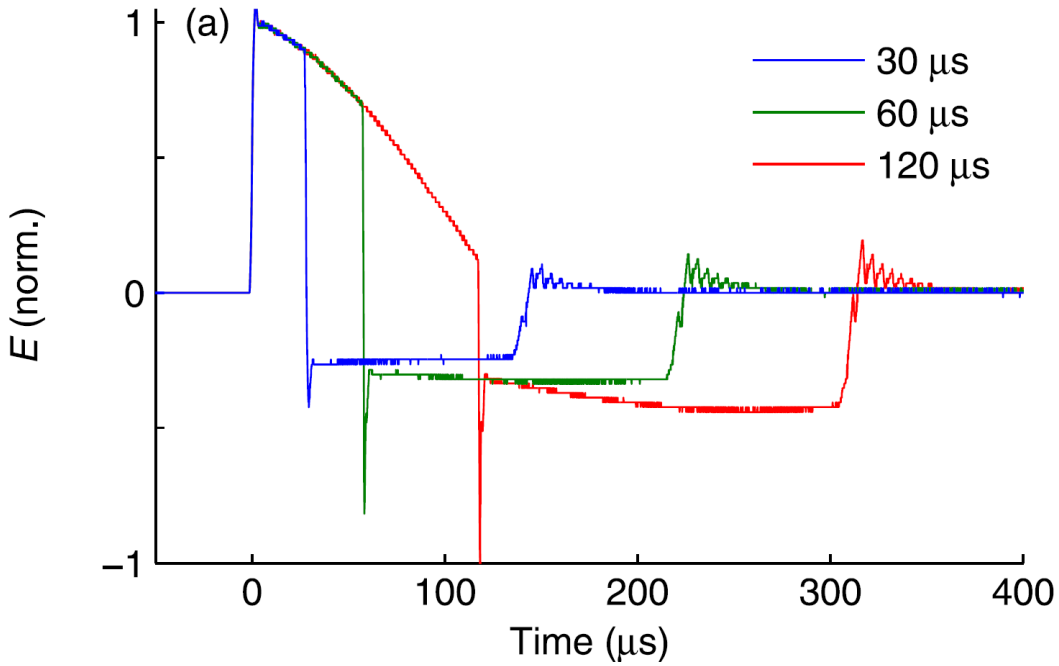

Figure 7.25: The existing TMS pulse generated by the pulse generator used in [134] ©2014 IOP Publishing Ltd. features a blue waveform with a 30 μs positive phase and a 100 μs negative phase. This pulse (blue) is the one I am recreating in my work.

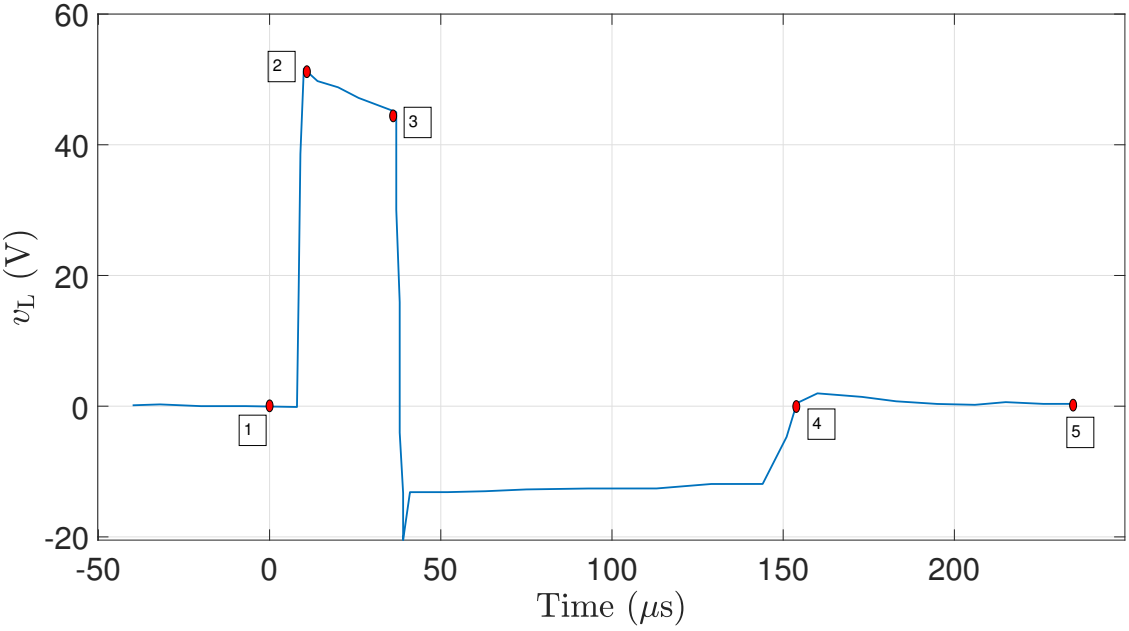

Figure 7.26: The reference pulse shape digitized using MATLAB.

6.5 V. Also based on the summary table (Section 7.6) in Row 3, I tried variations from 6 V to 5 V, which resulted in a wider negative phase of the voltage pulse.

Table 7.10: Time and voltage values at specific gate voltage points in step-2

Points	(**Time (μs)**, **Voltage (V)**)
P1	(0, 0)
P2	(20, 10)
P3	(40, 6)
P4	(150, 5)
P4	(250, 0)

Table 7.11: Time and voltage values at specific gate voltage points in step-3

Points	(**Time (μs)**, **Voltage (V)**)	
	Attempt 1	**Attempt 2**
P1	(0, 0)	(0, 0)
P2	(20, 10)	(20, 10)
P3	(40, 5.5)	(39, 5.7)
P4	(150, 5)	(150, 5)
P4	(250, 0)	(250, 0)

7.9.2 Step-2

With the points in Step-1, I tested the gate voltage waveform as shown in the Fig. 7.27 with the points in Table 7.10. The initial rise was accurate, but the turn-off was not abrupt, and the end position of the pulse-shape was also correct. The points to adjust were the voltages at P3 and P4.

7.9.3 Step-3

To achieve an abrupt fall from P3, I adjusted the slope between P2 and P3 by changing V3 to 5.5 V. This resulted in an abrupt voltage drop, but the negative phase was not wide enough (green in the Fig. 7.28). In the second attempt, I set V3 to 5.7 V to smooth the slope between P2 and P3. This resulted in the fall time aligning more closely with the reference and achieving a wider negative phase (magenta waveform in Fig. 7.28) with the same pulse width. These results are shown in Fig. 7.28 and the point details in Table 7.11.

The final result of the pulse replication, compared with the reference pulse, is shown in Fig. 7.29.

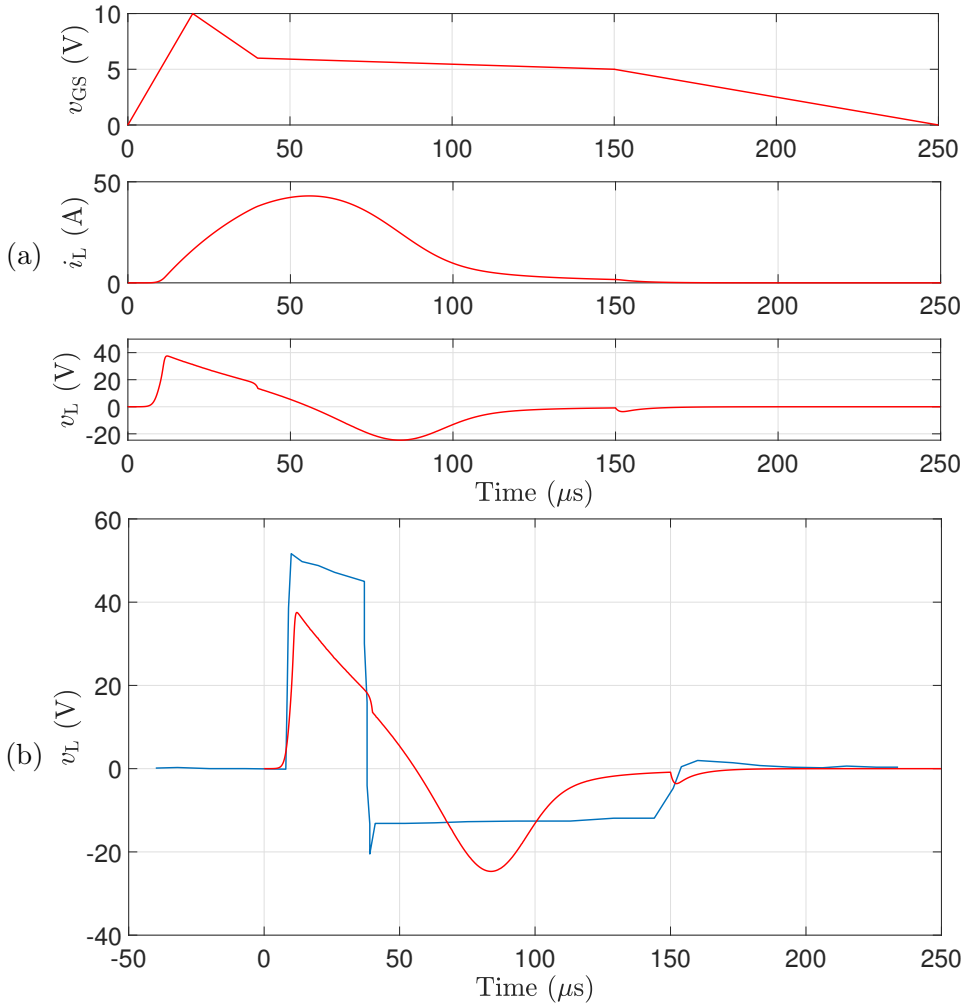

Figure 7.27: (a) TMS pulse parameters from the Step-2 results; (b) comparison between the reference shape (blue) and the TMS pulse shape obtained in Step-2 (red)

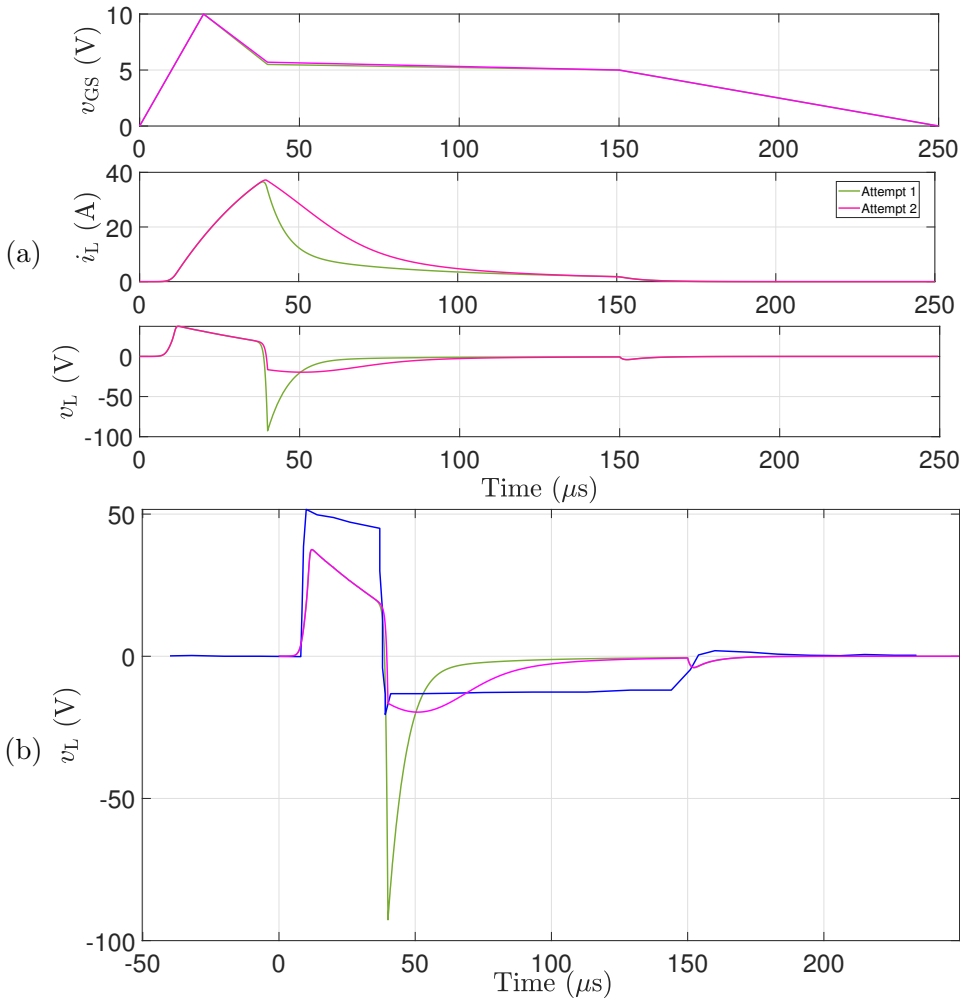

Figure 7.28: (a) TMS pulse parameters from the Step-3 results; (b) comparison between the reference shape (blue) and the TMS pulse shape obtained in Step-3.

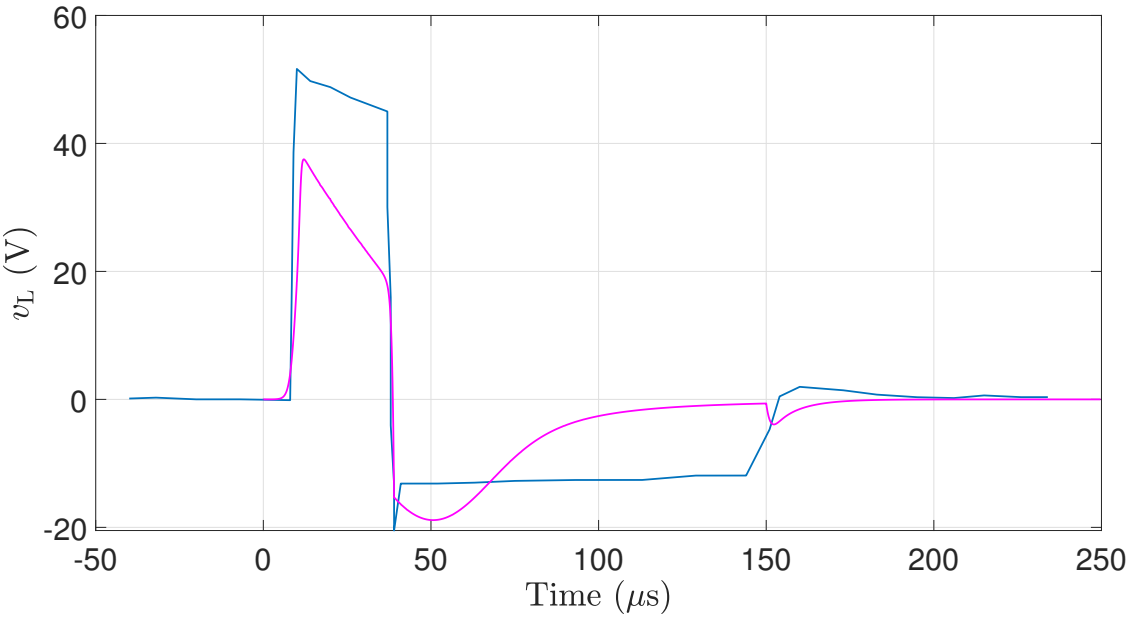

Figure 7.29: Comparison between the reference shape (blue) and the TMS pulse shape obtained in Step-3 attempt 2 (magenta)

7.9.4 Inference from the pulse recreation

In conclusion, based on the pulse shape recreation analysis in the previous sections, my prototype recreated the pulse shapes except the second negative phase and widths that have been proven effective for human stimulation. Due to the limitations within my circuit, such as the specific values of the resistance, capacitor, and inductor, I am unable to generate a biphasic current pulse that can reproduce the exact reference pulse (Fig. 7.18). While it is possible to achieve a biphasic current pulse by adjusting the component values, for the purpose of this study, I have used the fixed component values in my circuit. Within these constraints, I have achieved the maximum pulse shaping possible with the current prototype. Except for the second negative portion in Fig. 7.23, the pulse shape closely matches the reference.

The main challenge lies in extending the duration and width of the negative phase of the voltage pulse in the reference Fig. 7.25. To address this, in the next section, I will explore incorporating an R-diode combination snubber, which many researchers add for discharge path when MOSFET is off, and I will discuss its effects on pulse shaping.

Additionally, using a simple lab generator and an Arduino-based pulse system, similar excitation and neural stimulation have been achieved in mouse coils [59, 136]. My circuit prototype is capable of generating the pulse shapes and widths that have already been shown to be effective for stimulation. Furthermore, the circuit can produce higher amplitude pulses and modify pulse shapes, widths, and timings by adjusting the gate voltage. This flexibility is a valuable feature, as it allows the circuit to generate a variety of pulse types, including new shapes and widths, which can be used to test and evaluate their effects in TMS applications. This prototype will be highly suitable for a TMS mouse study because it enables testing with existing pulse shapes as well as the development of new pulse shapes for further experimentation.

7.10 Enhanced pulse shaping with resistor-diode combinations

In my circuit prototype, I utilized an RLC-like topology, incorporating a switch (S2) at the last stage of the circuit. Existing TMS circuits [59, 105, 120, 136] often employ inverters or RLC configurations to achieve the desired pulse shapes. However, my approach goes a step further by leveraging the MOSFET not only as a switch but also as a wave-shaping control tool. This dual-purpose use of the MOSFET allows for significant control over the entire pulse width of the TMS pulse by adjusting the frequency of the gate voltage. Specifically, it enables fine-tuning of the pulse width for both the positive and negative phase of the pulse, as explained in previous sections.

Most TMS circuits incorporate a discharge path into the TMS coil circuit. This is often for the purpose of preventing high voltages over the switches, but also has the advantages that, the circuit gains additional control over the energy release from the coil, allowing for more precise manipulation of the pulse characteristics, such as width, amplitude, and overall shape. In this section, I explain the options made available by inclusion of a discharge path.

The parameters used in this chapter are provided in Table 7.12

Table 7.12: Parameters and their values used in Section 7.10

Parameters	Values
Supercapacitor input	1 V
Capacitance (C2)	330 μF
C2 voltage	30 V

7.10.1 Circuit modification

In my TMS prototype, the addition of a resistor-diode combination in parallel with the TMS coil as in Fig. 7.30 serves a role in controlling the discharge rate of the coil when the MOSFET (S2) is turned off. This setup functions similarly to a snubber circuit, which is commonly used in electronic circuits to protect components and shape waveforms by controlling the voltage and current transitions.

When the switch S2 is on, the current flows through the TMS coil, storing energy in the magnetic field of the inductor. Without the R-diode, upon turning off the switch S2, the current flow through the coil would typically drop rapidly leading to a high, potentially damaging voltage over S2. However the diode D1 allows the current to continue flowing through the resistor, rather than abruptly stopping. This creates a path for the inductor's stored energy to discharge more gradually. The resistor in the combination sets the rate at which the energy is dissipated. A higher resistance shortens the time it takes for the current to decay to zero, manifested through the $\frac{L}{R}$ time constant. Conversely, a lower resistance results in a more prolonged discharge. This controlled discharge extends the duration of the negative phase of the voltage waveform across the TMS coil, allowing you to shape the pulse more effectively.

In Figure 7.31, the TMS pulse output is analyzed using different resistor values in the R-diode

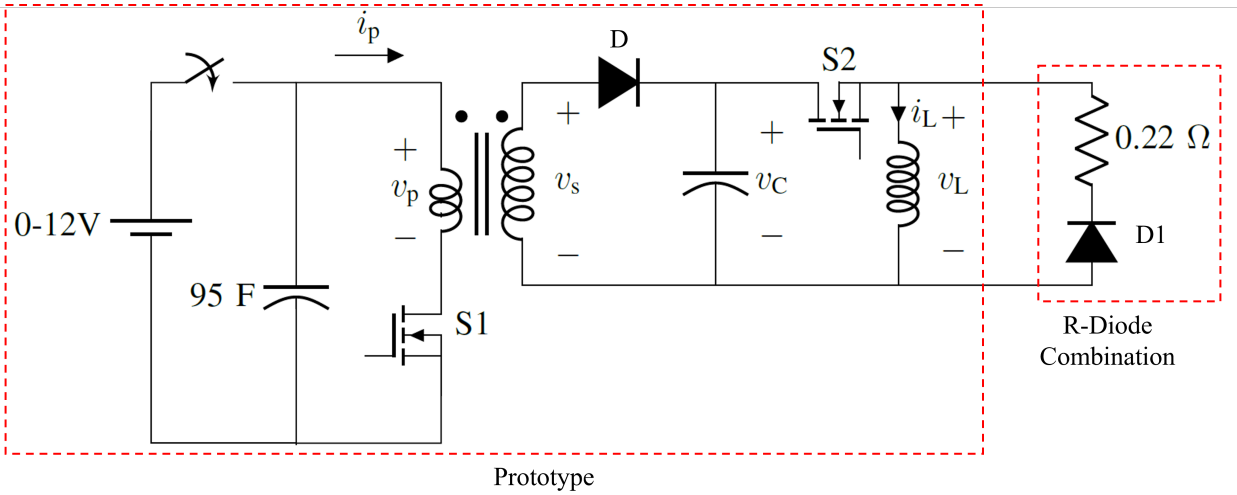

Figure 7.30: Circuit modification with R-diode combination connected in parallel to the existing prototype

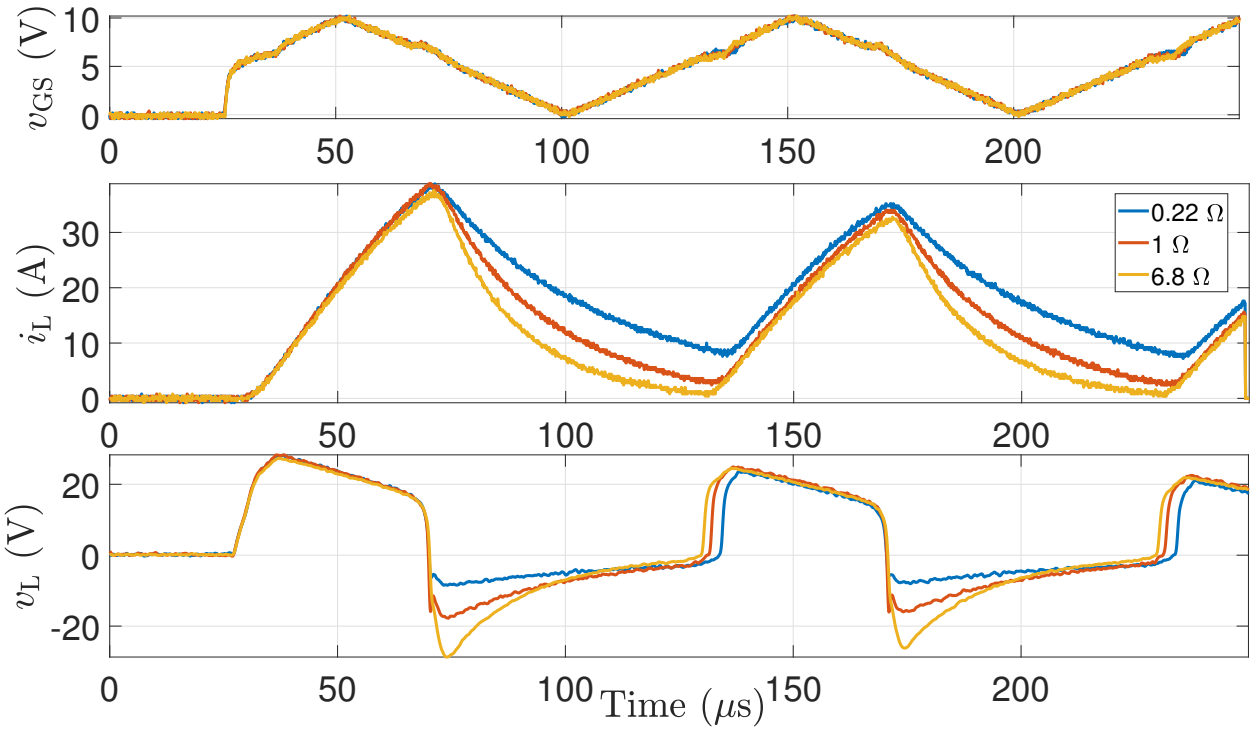

Figure 7.31: Circuit modification with R-diode combination tested with different resistor values

combination block. From this analysis, I opted for a 0.22 Ω resistor in the discharge path because it provided the longer pulse width. Specifically, with the 0.22 Ω resistor (blue trace), I obtained a 100 μs long negative voltage phase, compared to 50 μs with a 1 Ω resistor (red) and 30 μs with a 6.8 Ω resistor (yellow). Given that the 0.22 Ω resistor offered longer negative phase and had a power rating of 10 W, it was suitable for the pulse duration in the microsecond range. Thus, using the 0.22 Ω resistor was both safe and effective for this application.

Note that a pulse width in the negative phase of the voltage pulse is achieved using the triangular gate voltage, where I had previously obtained only a 25 μs pulse width (refer to Section 7.3). However, with the quadrilateral gate voltage, a larger negative voltage pulse width (80 μs) can be achieved (Section 7.6). This section analyzes the usage of the R-diode path in detail, as this block is commonly used in most TMS circuits.

By controlling the rate of current decay, you can prolong the negative phase of the voltage pulse and shape the overall waveform more precisely. This is particularly useful in TMS applications, where precise control over the pulse shape can significantly impact the effectiveness of the stimulation. Additional benefits of using the resistor-diode combination in your TMS prototype include:

1. Prolonged negative voltage pulse: By adjusting the resistor value, the duration of the negative phase of the pulse can be effectively controlled. This adjustment allows for a prolonged waveform compared to what was achieved in the prototype without the R-Diode combination. This capability can be particularly beneficial in certain TMS applications where a longer duration of stimulation is desired.

2. Enhanced control: The ability to fine-tune the discharge rate provides more control over the pulse shape, enabling the creation of custom waveforms tailored to specific experimental.

3. Improved energy management: By carefully managing how the energy is dissipated, the pulse can deliver the necessary amount of energy while minimizing unnecessary stress on the components. This approach leads to more reliable and consistent performance, enhancing the longevity of the circuit and ensuring that it operates efficiently under various conditions.

4. Increased component longevity: By avoiding sudden current and voltage changes, the resistor-diode combination reduces stress on the MOSFET and other circuit components, potentially extending their operational lifespan.

7.10.2 Challenges with rapid MOSFET switching

One of the challenges encountered with the prototype was the rapid switching of the MOSFET, which limited the level of control over the pulse shape. This rapid switching caused the current fall-off time to be excessively fast. The Fig. 7.32 shows a comparison between the RLC prototype and an enhanced version where a resistor-diode combination was added, as shown in the circuit diagram (Fig 7.30).

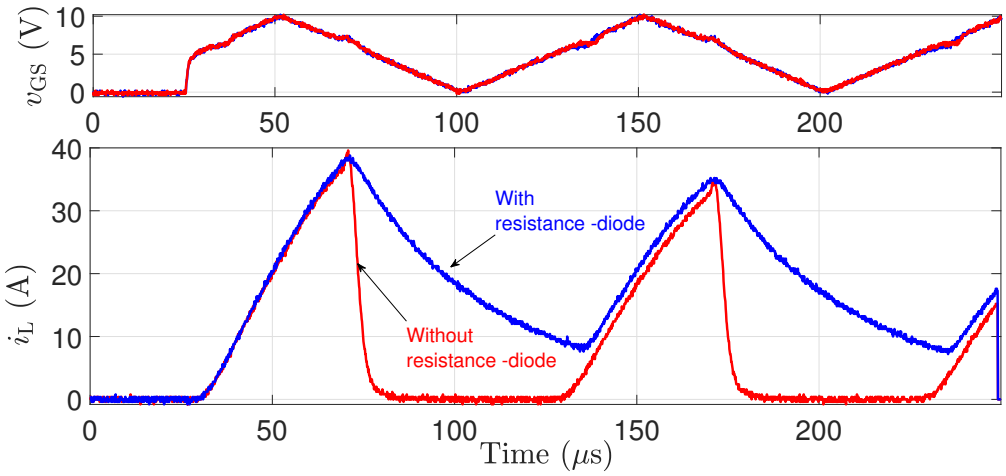

Figure 7.32: Comparison of the TMS current pulse between the original RLC prototype and an enhanced version with a resistor (0.22 Ω)-diode combination added.

When the MOSFET turns off, or when the gate voltage reduces from 10 V, the added resistance and diode provide a path for the current in the TMS coil to circulate. This design prevents a sudden drop in current, instead allowing for a gradual reduction due to the controlled decay path provided by the resistor and diode. This configuration effectively delays the current drop, ensuring a smoother and more controlled pulse shape. This delay is crucial because it allows for more gradual current reduction, thereby extending the fall time of the current in the inductor. This extension in fall time directly impacts the shape and duration of the negative phase of the TMS voltage pulse.

7.10.3 Pulse shape control with resistor-diode combinations

The rise time of the pulse can be altered by adjusting the turn-on timing of the MOSFET S2. However, this is limited by the time constant of the circuit. The voltage across the inductor is governed by the relationship ($V = L\frac{dI}{dt}$, where L is the inductance and $\frac{dI}{dt}$ is the rate of change of current. Since the inductance of the TMS coil is constant, the voltage primarily depends on how quickly the current changes.

Despite these limitations, the prototype demonstrates that the rise time can still be influenced by adjusting the specific points (P2 and P3) in the waveform, as detailed in the summary Table 7.4 (Rows 3, 4, 6) in Section 7.6. These adjustments allow for some control over the initial characteristics of the pulse, but the most significant improvement comes from modifying the current reduction phase.

By incorporating a resistor (0.22 Ω) and a diode (IN4007) in parallel with the TMS coil, the current reduction in the inductor can be slowed down, effectively lengthening the duration of the current drop. This increased width of the negative phase of the voltage pulse suggests that the TMS pulse can deliver more energy during the negative phase. Additionally, it provides the flexibility to shape the negative phase with different pulse widths compared to the original prototype. Since the original prototype only had a small negative voltage pulse width, adjusting within that pulse width was limited. With the new setup, having a larger pulse width for the negative phase now allows

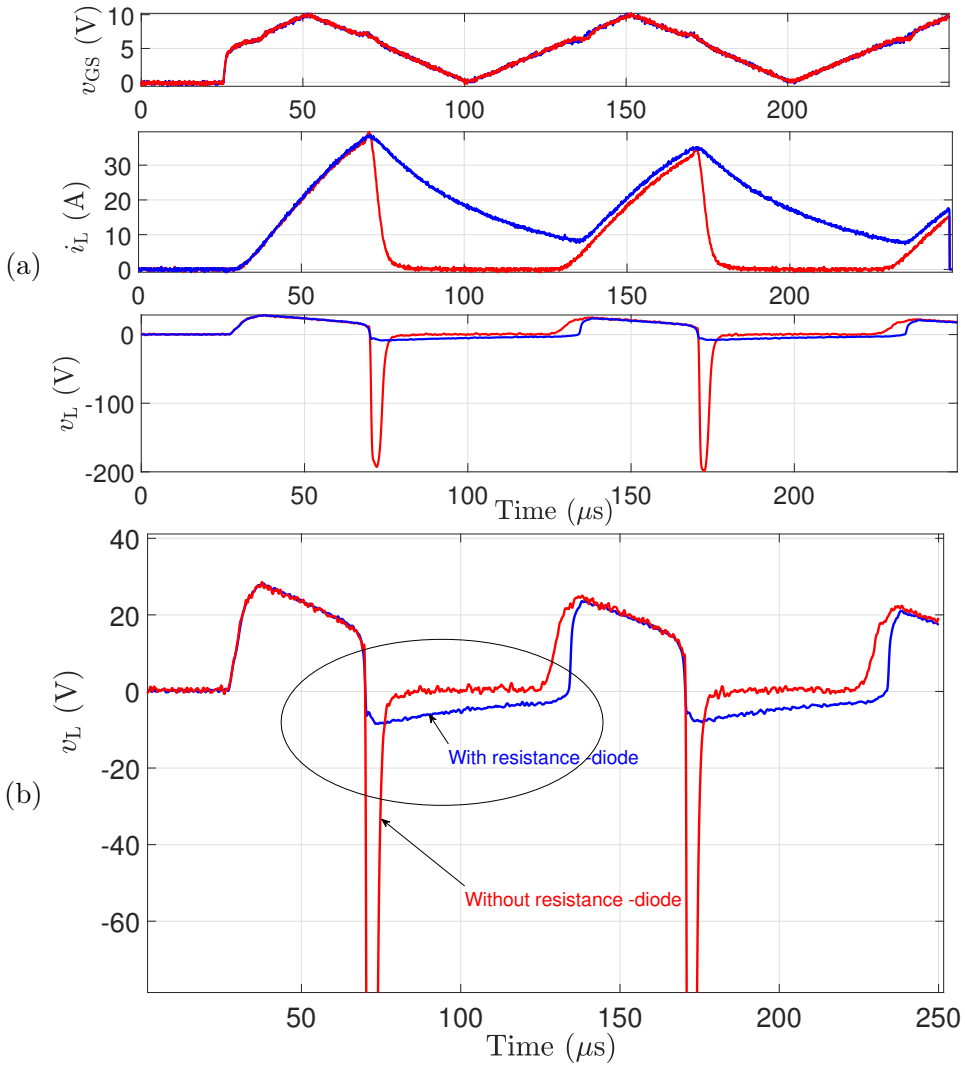

Figure 7.33: (a) Voltage Pulse TMS comparison between RLC prototype and enhanced version with resistor-diode combination (b) The zoomed-in view of the negative phase is presented, comparing the waveform with and without the resistor-diode combination.

for more flexibility. You can fine-tune the negative phase to achieve specific pulse shapes, which enhances the overall capability of the TMS system.

The Figure 7.33 clearly shows the difference between the original prototype and the modified circuit with the resistor-diode combination. When the MOSFET S2 turns off, the current drop is delayed, allowing for more gradual energy dissipation. This delay in current reduction translates into a longer-lasting and more controllable negative phase of the TMS pulse.

The next section will delve into the effects of the resistor-diode combination in parallel with the TMS coil, discussing the additional improvements achieved in pulse shaping.

7.10.4 Analysis

The Table 7.13 presents a variety of waveforms that were modified by adjusting the turn-on and turn-off timings, as detailed in Section 7.6. These adjustments directly influence the pulse width of the TMS pulses. By varying the points at which the gate voltage turns on and off, different pulse shapes and duration were achieved. This also illustrates how incorporating the resistor-diode combination into the circuit provides additional flexibility in shaping the pulse. This modification allows for more precise control over the pulse characteristics, enabling further adjustments to the pulse width and shape.

Table 7.13: Effects of gate voltage alteration on TMS output voltage and current pulse

Parameters	Waveforms	Observations
v_{GS} i_L v_L	Turn-on side variation 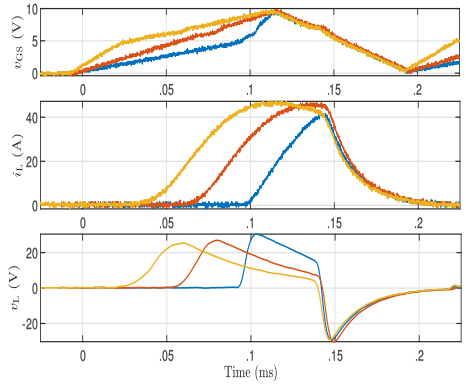	• Turn on side variation result in different turn on time. • Yellow has a rise time of 110 μs whereas blue has 45 μs. • Positive phase pulse-width of voltage pulse is increased with delayed turn on • Pulse-width of current pulse decrease with delayed turn on • Yellow current pulsewidth is 170 μs and blue is 100 μs.
v_{GS} i_L v_L	Turn-off side variation 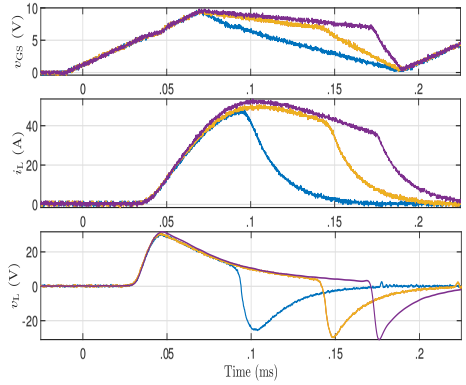	• Delay in turn-off time increases the current pulse width. Violet current pulse is 260 μs whereas blue is 140 μs • Turn-off timing affects the negative pulse width of the voltage waveform. • Blue voltage pulse is 80 μs long, whereas violet is 120 μs long • Positive phase of voltage pulse width also differs. Blue positive phase is 60 μs, whereas violet is 140 μs

Parameters	Waveforms	Observations
v_{GS} i_L v_L	Pulse-width change in voltage & current pulse 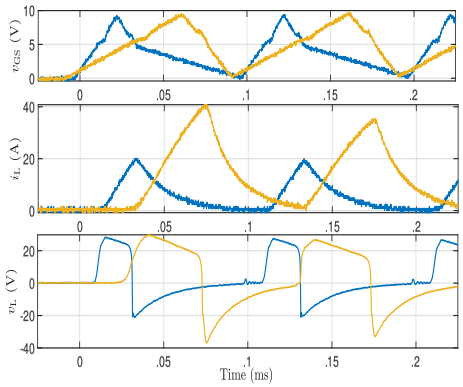	• Voltage pulse width differs between both waveforms. • The blue waveform has a smaller voltage positive pulse phase (20 μs) compared to the yellow (50 μs). • The yellow voltage waveform has a larger positive phase and larger current pulsewidth because its v_{GS} remains above the threshold for a longer time compared to the blue.

Based on the analysis, it is evident that the circuit requires a snubber circuit in parallel with the TMS coil, particularly to shape the negative phase of the TMS voltage pulse. Additionally, protection for the MOSFET against high switching voltages is necessary, and a resistor-diode (R-D1) combination can be beneficial. The analysis highlighted a significant difference in the pulse width of the negative phase when using a triangular gate voltage (Fig. 7.33).

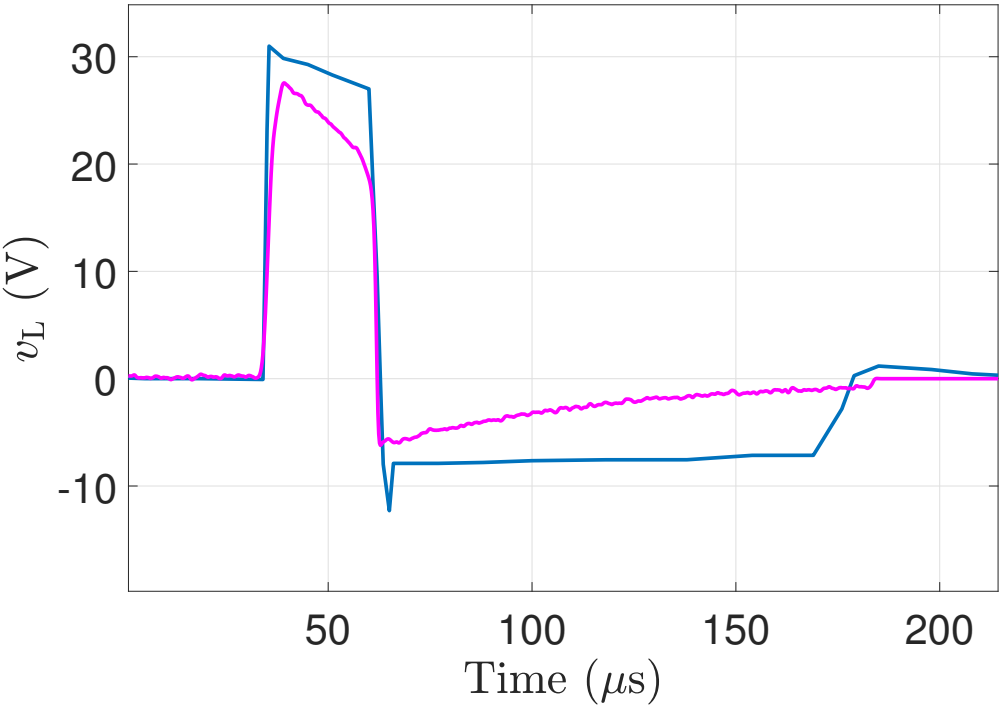

Figure 7.34: Comparison between the reference shape (blue) and the Experimental TMS pulse shape (magenta) obtained from the prototype (1 V input and 30 V C2 voltage) with R (0.22 Ω)-diode combination with the gate voltage points from Table 7.11 Attempt 2.

To evaluate the necessity of the R-diode combination, I attempted to replicate the pulse from Section 7.9 using the same 0.22 Ω resistor and diode configuration, with points outlined in Table 7.11 Attempt 2. Initially, the setup was configured with a 1 V input and the capacitor C2 charged to 30 V, showing the resulting pulse in Fig. 7.34. To investigate whether increasing the input voltage would enhance the pulse amplitude in the negative portion, the input was raised to 4 V, with C2 charged to 100 V. The experimental results, presented in Figure 7.35, demonstrate that incorporating the R-diode combination significantly broadened the negative phase of the voltage pulse compared to Figure 7.29.

From the Fig. 7.35(b), the positive phase of the TMS voltage pulse (magenta) is larger compared to the negative portion, leading to a situation where the area of the v_L voltage graph is not zero. The experimental output of the TMS voltage and current measurements is presented in Fig. 7.35(a). The area can be found by integrating the voltage over time:

$$\text{Area} = \int_{t'=0}^{t} v_{\text{L}}(t')dt', \tag{7.2}$$

where $t' = 0$ represents the start of the pulse and t denotes the time at the end of the pulse. The non-zero area suggests an imbalance in the pulse phases, which corresponds to a significant resistance of the TMS coil. The voltage across the inductor v_{L} can be expressed using the standard inductor equation:

$$v_{\mathrm{L}} = L\frac{di_{\mathrm{L}}}{dt} + i_{\mathrm{L}}r_{\mathrm{L}}, \tag{7.3}$$

thus,

$$\int_{t'=0}^{t} v_{\mathrm{L}}dt' = \int_{t'=0}^{t} Ldi_{\mathrm{L}} + r_{\mathrm{L}}\int_{t'=0}^{t} i_{\mathrm{L}}dt' \tag{7.4}$$

The first term on the right-hand side vanishes because i_{L} is zero at the limits. Thus, if $\int_{t'=0}^{t} v_{\mathrm{L}}dt'$ is non-zero, it indicates that the resistance r_{L} is significant. Here, the areas under the waveforms in Fig. 7.35(a) were calculated using the MATLAB function trapz, which performs numerical integration using the trapezoidal method. The resulting values for the area are:

$$\int_{t'=0}^{t} v_{\mathrm{L}}dt' = 0.00171700 \text{ Vs}; \tag{7.5}$$

$$\int_{t'=0}^{t} i_{\mathrm{L}}dt' = 0.00786400 \text{ As}; \tag{7.6}$$

and substituting in Eq. 7.4, I obtain $r_{\mathrm{L}} = 218$ mΩ, which is consistent with the measured value of 212 mΩ, as reported by Khokhar et al. [136] and in Table 6.1.

The role of the R-diode combination becomes relevant when the circuit's parameters, such as resistance, capacitance, or inductor values, are fixed and cannot be adjusted further to achieve the desired pulse width. In such cases, where constraints limit the ability to adjust the negative phase of the pulse, the R-diode combination provides an effective solution to extend the width of the negative portion. By incorporating this combination, it compensates for the limitations of the circuit and allows for better pulse shaping, particularly in the negative phase.

However, there is a limit to expanding the negative phase of the voltage pulse. This limitation arises due to the time constant in the discharge path, given by $\frac{L}{R}$, where L is the inductance and R is the combined resistance of the mouse TMS coil (r_{L}) and the resistor in the R-diode path. The time constant cannot be increased beyond a limit $\frac{L}{r_{\mathrm{L}}}$ because the resistance of the TMS coil (r_{L}) is fixed. In this case, the coil's resistance is approximately 212 mΩ, which imposes a restriction on lengthening the negative phase of the pulse. This makes it challenging to achieve a more extended negative phase beyond 100 μs without significantly altering the coil design or circuit design.

Even if the coil design is changed, reducing the resistance while maintaining sufficient magnetic field strength remains a significant challenge. Increasing the number of turns in the coil to increase B-field for a given current would lead to more wire length, which inherently adds resistance. Additionally, using thicker wire or materials with lower resistivity might reduce resistance, but this

approach has practical limitations, such as making the coil bulkier [58]. Moreover, reducing the number of turns would diminish the coil's ability to generate the necessary magnetic field strength for effective TMS, as the induced magnetic field is proportional to the number of turns. Therefore, striking a balance between resistance reduction and maintaining adequate magnetic field strength becomes difficult, further limiting the flexibility to shape the negative phase of the pulse.

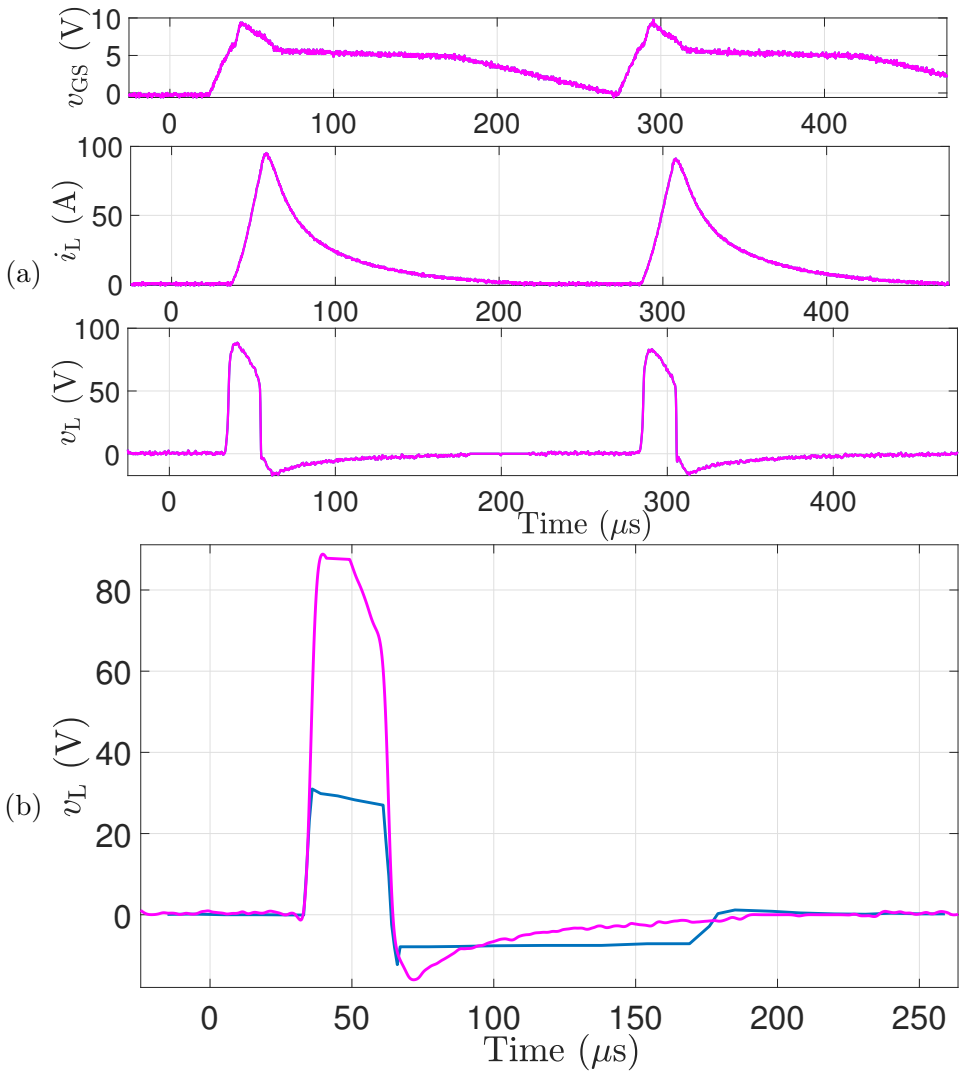

Figure 7.35: (a) TMS voltage and current pulse obtained from the prototype (4 V input and 100 V C2 voltage) with R-diode combination with the gate voltage points from Table 7.11 Attempt 2; (b) Comparison between the reference shape (blue) and the Experimental TMS voltage pulse shape (magenta)

Discussion & Conclusion

In conclusion, this chapter demonstrated the impact of increasing the capacitance C2 and voltage, leading to the generation of more pulses. This finding highlights the scalability of the same circuit, indicating its potential use in larger-scale applications. The prototype has shown it can generate cTBS pulses, emphasizing its practical value in TMS applications. Further modifications to the

triangular gate waveform, by introducing four points to form a quadrilateral gate shape, were explored. A summary table (Table 7.4) was provided to explain the effects of changing each point in the quadrilateral waveform, illustrating how these adjustments influence the TMS output pulse.

With my current circuit configuration, I was not fully successful in reproducing the exact pulse shape used in human TMS. This is because my prototype, in its present configuration, cannot generate a biphasic current pulse. As a result, I was unable to produce the second negative phase of the pulse shown in Fig 7.18. Consequently, the current pulse generated by my circuit remains monophasic, and further modifications are required to achieve the desired biphasic pulse shape. In the second attempt to reproduce an another pulse (Fig. 7.25), the negative voltage phase was not significantly extended or widened. To address this, I experimented with using an R-diode combination to extend the discharge time, aiming to increase the pulse width of the negative phase. Despite these efforts, the resistance of the coil ultimately limits the pulse shaping capacity. The inherent resistance of the coil imposes a constraint on achieving the desired pulse width, making it challenging to extend the negative phase beyond a 100 μs. As a result, further modifications are required to overcome this limitation and achieve the intended pulse shape. These modifications include using a different C2 capacitor, which may generate a biphasic current pulse, as illustrated in Fig. 5.16. Adjusting components with varying values could influence the damping characteristics, potentially resulting in damped or underdamped current pulses, which would affect the overall pulse shape. Additionally, testing with an alternative TMS coil can also be explored to optimize the current pulse characteristics.

Alternatively, treating the MOSFET as a variable switch could also be explored. This technique can be applied in inverter topologies (Fig. 2.6), where the MOSFET's behavior could be fine-tuned for more precise control of pulse shaping. Furthermore, if necessary, the power source for the inverter topology could be based on a supercapacitor, similar to the design of my prototype. This approach could potentially be used to implement the innovative concepts introduced by my prototype into existing inverter or cascaded circuits [120, 147, 157]. Additionally, applying triangular gate pulses to the MOSFET in inverter topologies could offer further control and refinement in shaping the output pulse.

I have developed comprehensive guidelines for generating the gate voltage required to achieve specific TMS pulse shapes, utilizing the full capabilities of the prototype. However, complete success in replicating the desired pulse shapes has not yet been achieved. This work highlights the prototype's versatility and emphasizes the importance of fine-tuning the gate voltage to meet desired pulse characteristics. The R-diode combination was tested to improve pulse shaping and provide MOSFET protection during high-voltage switching. Incorporating the R-diode combination has significantly enhanced pulse shaping, especially by improving the width and performance of the negative phase compared to the original prototype without the R-diode combination. However, despite these improvements, the circuit has not yet fully succeeded in recreating a full range of desired negative phase pulse widths.

Despite challenges in replicating the existing pulse shapes, this prototype is effective for generating some new pulse waveforms and widths, facilitating valuable testing of their effects and TMS

outcomes. Although the exact shapes may not be perfectly achieved, the prototype and model enable extensive studies on TMS with varying pulse characteristics, contributing to a deeper understanding of TMS applications.

Chapter 8

Conclusion

In this research, my goal was to design and evaluate electronic circuitry for shaping current pulses suitable for small-scale TMS applications. The circuit was specifically designed for small animal coils, and I was able to generate a magnetic field ranging from 200 mT to 400 mT with just a 1 V input. Furthermore, by increasing the input voltage, the strength of the magnetic field is enhanced, providing flexibility depending on the application requirements.

High-voltage (HV) generation is a fundamental requirement for various TMS applications, including the system developed in this work. Traditional pulse generators typically rely on high-voltage DC power supplies combined with voltage multipliers to achieve the necessary operating voltages of several thousand volts. However, such approaches increase system complexity, cost, and pose challenges in terms of safety, insulation, and energy efficiency, particularly for compact designs such as those intended for small-animal TMS. In contrast, the method developed here achieves the required high voltage in a more compact and cost-effective manner by utilizing a pre-charged supercapacitor as the energy source. This approach maintains the necessary voltage levels while significantly simplifying the circuit architecture, improving safety, and reducing both the physical footprint and component costs typically associated with conventional high-voltage systems.

First, I developed a supercapacitor-based pulse generator, which serves as a stable voltage source capable of producing a sufficient number of pulses for TMS treatment. This pulse generator is not only cost-effective but also compact in size, making it a practical option for TMS systems. The use of supercapacitors has proven to be an excellent choice, offering a continuous and reliable source of voltage for the pulse generator. In contrast to the more complex and costly approaches, I use a pre-charged supercapacitor followed by a step-up transformer and associated output circuitry to develop an inexpensive and flexible high-voltage pulse generator. This new approach is to use the high-power delivery capability of commercial supercapacitors in TMS applications.

Second, moving on to pulse shaping, I aimed to shape the pulses without introducing unnecessary complexity in the circuit. Throughout my experiments, I explored various approaches, starting with a square gate voltage waveform and transitioning to a triangular gate voltage. While square gate voltages are commonly used, the triangular gate voltage provided a smoother turn-on and turn-off transition for the MOSFET switch, allowing for more precise control over the rise time, fall time, and pulse width of the output pulses. By adjusting the symmetry of the triangular waveform, I was

able to fine-tune the ratio between the rise and fall times. In my circuit, the S2 switch is treated as a dynamic element rather than a typical on-off switch. This innovative dynamic approach allows me to use the MOSFET (S2) as a dynamically varying resistive element, offering greater control and flexibility in the circuit behavior.

Third, in addition to the experimental results, I developed a MATLAB model of the MOSFET to predict the TMS output pulse behavior based on the input gate voltage supplied to the MOSFET in the circuit. This MATLAB model is the first of its kind for TMS applications and other applications, and no similar model has been found in the existing literature. The model offers a powerful tool to predict output pulse shape for a given input. Through detailed analysis and experimentation, the MATLAB model has shown strong agreement with experimental data, enabling control over the pulse width and amplitude based on the gate voltage inputs. This model may serve as a guiding tool to design and shape pulses tailored to specific needs in TMS applications.

My circuit prototype can replicate proven pulse shapes and widths for effective stimulation, while also generating higher amplitude pulses and adjusting shapes, widths, and timings by modifying the gate voltage. In addition, the circuit can generate new pulse shapes, enabling tests to determine their applicability for TMS or explore whether improved pulses might be more effective. This makes it a valuable tool for analyzing and studying TMS in greater detail. This flexibility makes it ideal for TMS mouse studies, allowing both the use of existing pulses and the creation of new pulse shapes for further experimentation.

In summary, I have developed a prototype pulse generator for small coil TMS applications, utilizing a supercapacitor as the energy source. My aim was to design a circuit with a budget of 500 NZD, as outlined in the Section 2.4. However, I successfully developed the circuit at a significantly lower cost of just 170 NZD (Table 4.1). Moreover, the MATLAB model I developed based on the prototype accurately predicts the output pulse characteristics, providing a valuable tool for designing new pulse shapes. This combined approach opens up opportunities for further exploration in TMS research, allowing the creation of novel pulse shapes and enabling targeted research on small animal to enhance scientific studies of TMS effects and mechanism. This research marks an advancement in the field of TMS, particularly for small animal studies, and lays the foundation for future developments in pulse shaping and neural stimulation.

Chapter 9

Future work

Building on the current research, several key areas for future investigation could significantly enhance the effectiveness and applicability of the pulse generator.

The first critical step is Neural Stimulation Testing, as the effectiveness of the design and pulse patterns can only be validated by demonstrating their ability to stimulate brain tissue. Pulses of varying widths can be applied to mouse brain tissue *in vitro* to assess their potential for inducing spontaneous seizures, seizure-like events (SLE), or epileptiform activity. In future experiments, a protocol similar to Khokhar et al. [136] can be followed to assess the effects of TMS on spontaneous seizure-like events in brain slices, focusing on both amplitude and inter-event frequency. For each experiment, around 20 brain slices can be used, sourced from approximately 5 mice. As in previous work [136], each slice can receive both stimulation and sham treatments in a randomized order. This allows for a balanced comparison between actual TMS effects and sham conditions. The ability of the pulse generator to reliably deliver pulse patterns should be tested by stimulating the mouse brain tissue *in vitro*, and potential biophysical changes can be monitored over a time course of up to 30 minutes post-stimulation. Any changes in SLE activity and the response of evoked potentials will be crucial in determining the effectiveness of these protocols.

A wide range of pulse widths and shapes should be explored to identify the most effective configurations for neural stimulation. The supercapacitor (SC) module can be charged to higher voltages, such as 12 V, and the electrolytic capacitor (C2) can be tested at higher voltages, potentially reaching 200 V or more, to increase pulse strength and enhance stimulation power in TMS systems. Additionally, experiments can include testing the pulse generator's ability to deliver theta-burst stimulation (TBS) and other pulse sequences to further explore their neural effects. This neural testing is essential for optimizing the pulse patterns, as parameter adjustments to the circuit may be necessary based on the observed stimulation responses.

Once successful neural stimulation is demonstrated, further circuit modifications can be explored to optimize performance. The primary goal will be to assess how effectively the high-voltage pulses generated by the current circuit stimulate neural tissue. After validating its impact, parameters such as coil inductance and resistance can be varied to study their effects on pulse shape and magnetic field strength. Since only one coil has been tested so far, experimenting with different mouse-specific coils and re-evaluating neural activity will provide crucial insights into optimizing the system.

Developing a dedicated gate voltage waveform generator for your TMS system requires precise control over MOSFET switching to optimize pulse shape, rise/fall times, and energy efficiency. The generator must cater to the MOSFET's gate voltage requirements (typically 5 V to 15 V) and allow fine adjustment of waveform parameters such as pulse width, frequency, and amplitude, ensuring accurate and effective neural stimulation. Microcontrollers (MCU) or digital signal processors (DSP), like STM32 or Texas Instruments C2000, offer flexibility through programmable pulse-width modulation (PWM) outputs for precise control. For even higher precision and complex waveform needs, field-programmable gate arrays (FPGAs) are ideal though it need more advanced design knowledge. To convert digital signals into analog gate voltages, a digital-to-analog converter (DAC) can be integrated, enabling programmable, real-time waveform adjustments. We can also incorporate feedback control systems to adjust the waveform in real-time based on the observed performance of the TMS circuit.

Further enhancements to the MATLAB simulation can be achieved by incorporating gate capacitance dynamics and accurately modeling the MOSFET's reverse conduction path. Specifically, the gate-source capacitance could be integrated into the model by calculating the charge accumulated during the deviations (or blips) observed in the gate voltage waveform and comparing these to an ideal gate voltage profile. Currently, the simulation aligns well with experimental measurements; however, the reverse conduction path has not yet been curve-fitted. While this addition may not result in significant differences, given the already strong match, it would further improve the model's accuracy and remove the blips, bringing it even closer to experimental outcomes. While gate capacitance has been modeled in SPICE/ANSYS Simplorer software [185, 186], we can try incorporate this into the MOSFET model within the MATLAB environment to improve simulation accuracy.

This research lays the foundation for the development of an innovative pulse generator, advanced pulse-shaping techniques, and comprehensive simulation models. Future work will deepen our understanding of TMS pulse generation, optimize neural stimulation outcomes, and contribute to designing more efficient and powerful TMS systems.

Appendix A

Posters presented

This appendix showcases the posters presented at three major conferences, where key research findings from this thesis were shared with the scientific community.

- **NZIP & PHYSIKOS 2023 conference**: Presented at Massey University's Albany Campus, Auckland, from July 3-5, 2023, this poster highlighted the early stages of research on TMS pulse shaping and initial experimental results.
- **Australasian winter conference on brain research**: Held in Queenstown, New Zealand, from August 26-30, 2023, this poster focused on advancements in TMS technology and shared experimental findings relevant to brain research applications.
- **IEEE IECON 2024 - 50th annual conference of the IEEE industrial electronics society (IES)**: Presented in Chicago, Illinois, from November 3-6, 2024, this poster showcased the latest developments in TMS pulse generator design.

NZIP & PHYSIKOS 2023 Conference, Albany, 3-5 July 2023

Electronic circuitry for shaping current pulses for small scale transcranial magnetic stimulation coils

Soniya Raju, Marcus Wilson, Nihal Kularatna

THE UNIVERSITY OF WAIKATO
Te Whare Wānanga o Waikato

INTRODUCTION

TMS, Transcranial Magnetic Stimulation, works on the principle of Faraday's law of electromagnetic induction. A coil carrying a time-varying current is placed on the surface of the scalp to produce a magnetic field. This magnetic field which permeates a conductive medium (e.g., brain tissue), can induce an electric current sufficient to stimulate the axon hillock of each neuron. TMS is used clinically to treat depression, obsessive-compulsive disorder (OCD), anxiety, Parkinson's disease, multiple sclerosis, etc.

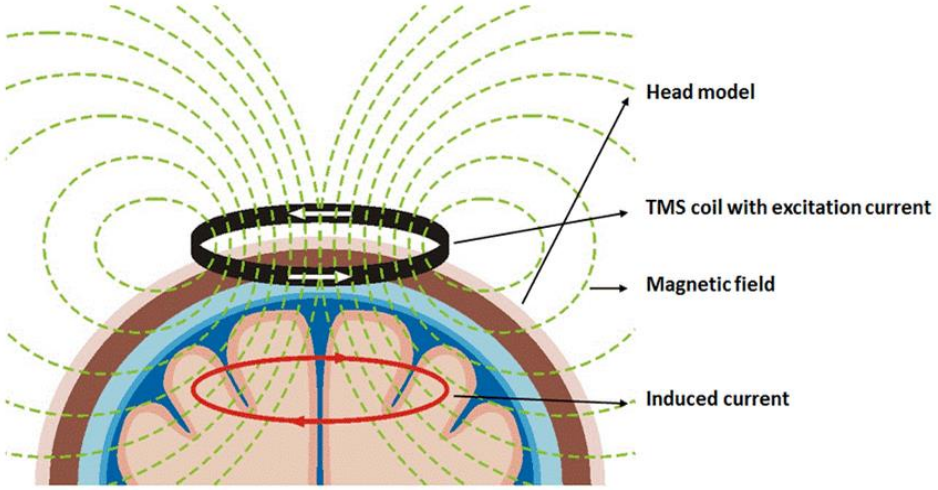

WHY?

TMS is well explored & studied in the human brain. But some mechanisms are still unknown. To help investigate these, we need to carry out TMS experiments in small animals.

- How to develop a current pulse circuit with pulse shaping that can produce a sufficient field strength for TMS in small animals?
- Can this study arrive at a relation between the pulse shape, field and heating so that we can optimize pulse parameters (in all aspects like time, shape, and duration) for a particular TMS application?

GAPS

- Commercial animal coils stimulate the entire body of a mouse
- Existing stimulator cannot produce different pulses of width and shapes within the circuit

BENEFITS

- A specific mouse TMS circuit is suitable for pre-clinical studies and for fast prototyping and testing.
- The TMS stimulator design for animals may improve efficacy of TMS application.
- This will increase the incentive for animal studies that might reveal the mode of action and improve TMS.

BLOCK DIAGRAM (supercapacitor-based pulse generator)

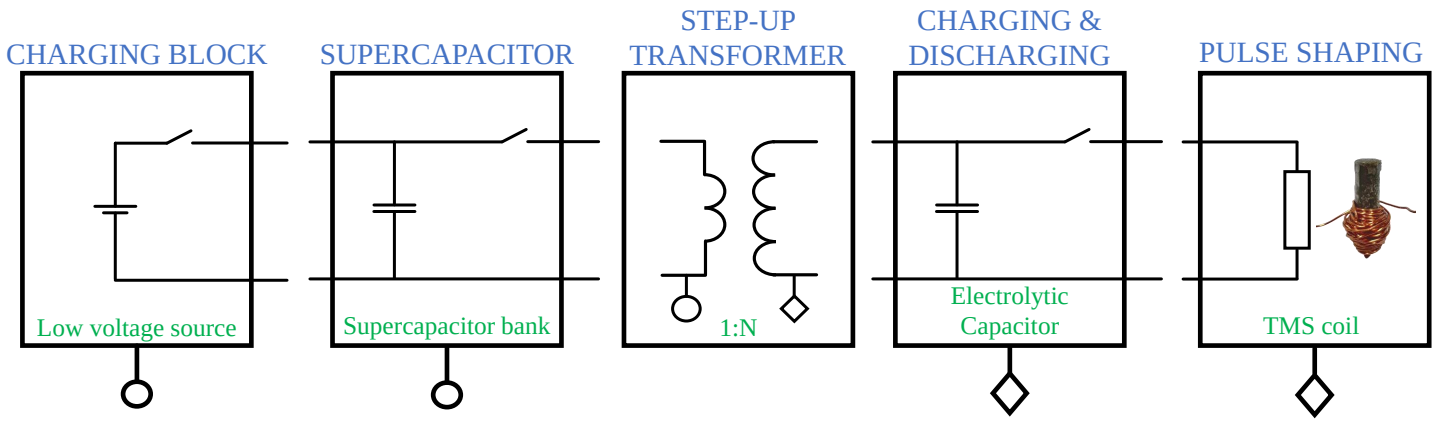

PULSE ANALYSIS

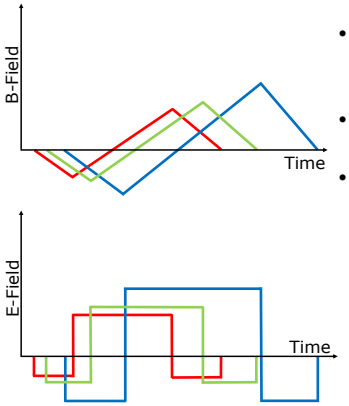

**Straight lines in waveforms are only used to depict the fields clearly

- Producing different pulse pattern, pulses with different widths, shapes, and sizes.
- Analysing their effect on the coil performance.
- Analyses of magnetic and electric field produced by each type of pulses.

Scan Me

WHAT NEXT ?

- Considering the heating of the coil.
- Optimize the possibilities and produce a current pulse circuit for the TMS coil.
- Maximize the effect of pulse shaping analysis for TMS application.
- Opens many avenues for research on the stimulation of animal brains.

sraju@waikato.ac.nz

Australasian Winter Conference on Brain Research (AWCBR), QUEENSTOWN, 26-30 AUGUST 2023

Electronic circuitry for shaping current pulses for small scale transcranial magnetic stimulation coils

Soniya Raju[1], Marcus Wilson[1], Nihal Kularatna[2]
[1]Te Aka Mātuatua -School of Science, University of Waikato
[2]School of Engineering, University of Waikato

THE UNIVERSITY OF WAIKATO
Te Whare Wānanga o Waikato

INTRODUCTION

TMS, Transcranial Magnetic Stimulation is a procedure in which a coil carrying a time-varying current is placed on the surface of the scalp to produce a magnetic field that can induce an electric current sufficient to stimulate neurons.

GAPS

- ❑ Commercial animal coils stimulate the entire body of a mouse.
- ❑ Existing stimulator cannot produce different pulses of width and shapes within the circuit.

WHY?

Small animal TMS coil circuits

- ❑ are less explored.
- ❑ helpful for pre-clinical studies and for fast prototyping and testing.

BENEFITS

TMS stimulator design

- ❑ improves the efficacy of TMS application.
- ❑ will increase the incentive for animal studies that might reveal the mode of action and improve TMS.

ACHIEVEMENTS

- ✓ Simple and inexpensive circuit.
- ✓ Can produce 500+ pulses from a single charged supercapacitor bank.
- ✓ Successful pulse shaping with fall time and pulse width control.
- ✓ Magnetic field and current across the coil is linear.
- ✓ 150mT magnetic field is obtained 2mm below the TMS coil

BLOCK DIAGRAM (supercapacitor-based pulse generator)

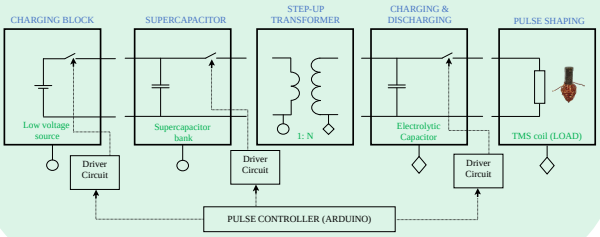

DEPRESSION

PARKINSON'S DISEASE

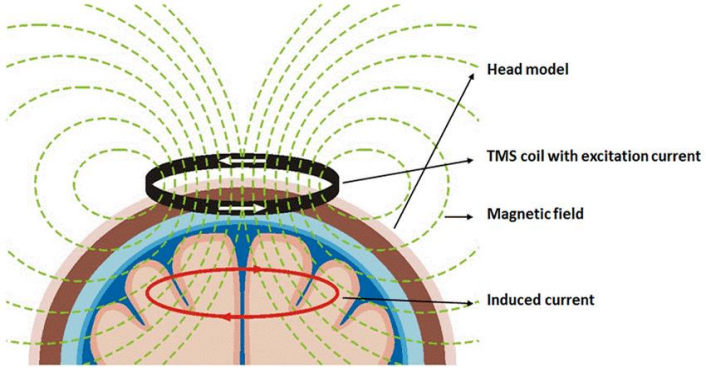

ANXIETY

PULSE ANALYSIS

(1)

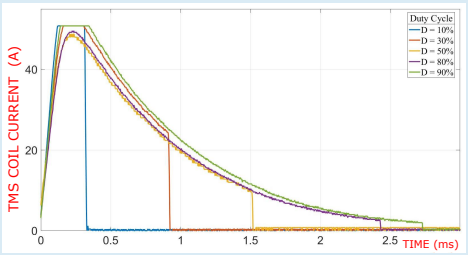

- ✓ Graph 1 shows the pulse width variation by controlling the switch's duty cycle within the circuit.
- ✓ We have attained Control over Fall time and pulse width by which pulse shaping is done.
- ✓ The variation in pulse width is proportional to the duty cycle (Graph 2).

(2)

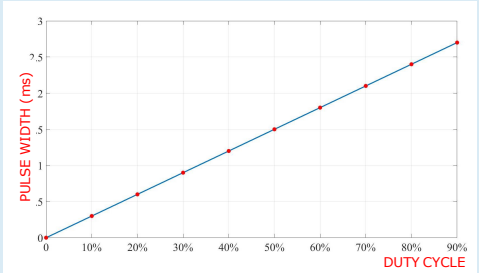

(3)

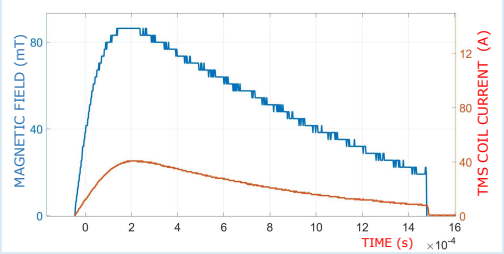

- ✓ Current and magnetic fields are proportional implying the core is linear.
- ✓ Graph 3 shows 10V charged capacitor can deliver 20A current and 90mT magnetic field. TMS coil was excited with these parameters. This can be scaled up by increasing the voltage.

WHAT NEXT?

- ➢ Producing a bidirectional magnetic field
- ➢ Attain Control over rise time
- ➢ Speeding up the pulse rate (50 Hz)
- ➢ Maximize the effect of pulse shaping analysis for TMS application.
- ➢ Opens many avenues for research on the stimulation of animal brains.

REFERENCE

1. F. A. Khokhar, L. J. Voss, D. A. Steyn-Ross and M. T. Wilson, "Design and Demonstration In Vitro of a Mouse-Specific Transcranial Magnetic Stimulation Coil," in IEEE Transactions on Magnetics, vol. 57, no. 7, pp. 1-11, July 2021, Art no. 5800511, doi: 10.1109/TMAG.2021.3077976.
2. M. T. Wilson, A. D. Tang, K. Iyer, H. McKee, J. Waas, and J. Rodger, "The challenges of producing effective small coils for transcranial magnetic stimulation of mice," Biomed. Phys. Eng. Exp., vol. 4, no. 3, Apr. 2018, Art. no. 037002, doi: 10.1088/2057-1976/aab525.

Scan Me

sraju@waikato.ac.nz

Effects of Triggering Mechanisms on TMS Pulse Shaping with Supercapacitor Storage

Soniya Raju[1], Nihal Kularatna[2], Marcus Wilson[1], Alistair Steyn-Ross[2]

[1]School of Science, University of Waikato, New Zealand, [2] School of Engineering, University of Waikato, New Zealand

50th IECON ANNUAL CONFERENCE OF THE IEEE INDUSTRIAL ELECTRONICS SOCIETY
Chicago | Illinois, November 3-6, 2024

Introduction

• **Transcranial Magnetic Stimulation (TMS):** is a non-invasive method that uses rapid magnetic field changes to stimulate neurons in the brain. A coil on the scalp delivers brief, high-intensity pulses, inducing electrical activity in specific brain areas.
• **Focus on Small Animal TMS:** Our project aims to develop a prototype specifically for small animal TMS studies.
• **Innovative Design**: We replace expensive high-voltage supplies with a pre-charged low-voltage supercapacitor, step-up converter, and pulse-shaping circuit, reducing costs.
• **Pulse Shaping Flexibility**: The system allows precise control over pulse parameters (amplitude, width, rise/fall times) via a triangular gate voltage, offering more customization than conventional TMS systems.

Block Diagram

- **Charging Stage**: Supplies energy to a pre-storage energy source in preparation for pulse generation.
- **Step-Up Transformer**: Boosts voltage to the required level for effective stimulation.
- **High-Power Output Stage**: Delivers the boosted voltage to the TMS coil.
- **Pulse Shaping**: Managed by a triangle gate voltage generator, which shapes the output pulse for precise control.

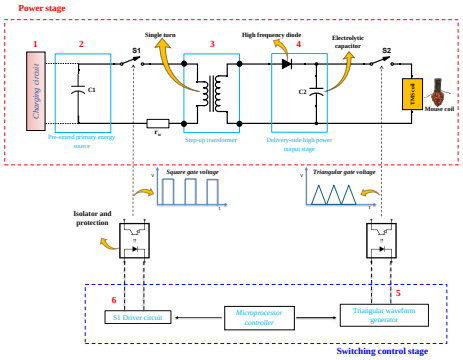

Fig 1: Block diagram of prototype TMS pulse generator. Power stage (high voltage/current) and switching control stage (low voltage) highlighted by red and blue dotted rectangles. An opto-isolator isolates the stages for protection and safety

Supercapacitor (SC) as a reliable source

- Lower Cost
- Longer Lifespan
- No Dedicated Power Supply
- Stable Output
- High Power Delivery

Table 1: Comparison of representative supercapacitors and electrolytic capacitors

	Capacitance (F)	Rated Volage (V)	ESR (mΩ)	Max. Current (A)	Short circuit Current (A)	Max Power (W)	Max Energy (J)
Supercapacitor	25	3	30	21	100	75	112.5
	100	3	8	78	375	281	450
	380	3	3.2	250	937.5	703	1800
	3000	3	0.23	2663	13 k	9.7 k	13.5 k
Normal capacitor	220 µ	450	1206	2.34	0.37 k	42 k	22.3
	680 µ	200	36	4.15	11.1 k	277.7 k	13.6
	2200 µ	400	60	16	6.7 k	666.7 k	176

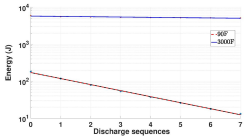

Fig. 2: Energy discharge of 90 F and 3000 F supercapacitor with 2 V initial voltage

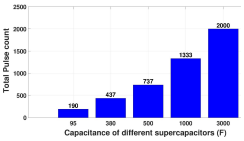

Fig 3: Total pulse count of the respective supercapacitors with initial voltage of 2 V

• **Energy Efficiency:** SC efficiently discharge energy at low voltages, making them ideal for TMS pulse generation (Fig. 2).
• **Pulse Count Advantage:** Larger supercapacitors can generate more pulses per charge cycle (Fig. 3), with less voltage drop.

Effect of triangle gate voltage

- The prototype (Fig. 4) was tested with a filtered square gate with varying dutycycles, producing TMS current pulses (Fig. 5).
- After charging the supercapacitor (C1) to 1 V and the electrolytic capacitor (C2) to 35 V, a peak instantaneous power of 9.5 kW was achieved at 190 V with 50% symmetry; at 90% symmetry, the voltage increased to 500 V with a peak power of 30 kW (Fig. 6).
- 50% symmetry causes a current pulse of width 60 µs, rise-time of 47 µs and fall-time of 10 µs and voltage ≈ 200 V. Whereas, 90% symmetry gate voltage produces a current pulse of 55 µs width, 53 µs rise-time, 6 µs fall-time and ≈ 500 V voltage.

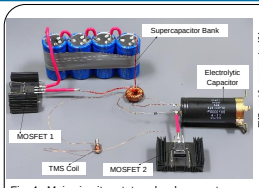

Fig. 4: Main circuit prototype hardware setup

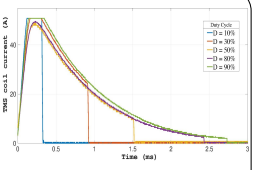

Fig. 5: The pulse width variation by controlling the S2 duty cycle (filtered square gate voltage) within the circuit

Effect of sinusoidal gate voltage

- Tested the experimental setup with a sinusoidal waveform at 10 kHz due to its smooth rise and fall time (Fig. 7).
- The recorded voltage magnitude was 268 V with a current of 61 A from a 1 V supercapacitor source, generating a TMS current pulse with a width of 50 µs, rise-time of 40 µs, fall-time of 10 µs.

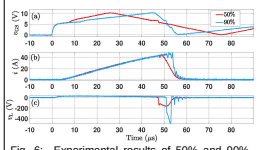

Fig. 6: Experimental results of 50% and 90% symmetry of the triangular gate voltage (10 kHz) given to S2 and its TMS coil current and voltage pulse respectively.

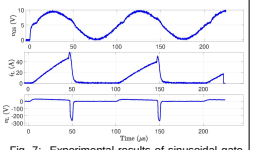

Fig. 7: Experimental results of sinusoidal gate voltage (10 kHz) given to S2 and its TMS coil current and voltage pulse respectively.

Conclusion

- Used a precharged supercapacitor (SC) and traditional up-converter to create a TMS pulse generator for small animals.
- Developed a low-cost circuit for pulse shaping, successfully tested with the SC pulse generator.
- Achieved adjustable pulse parameters using a triangular waveform generator with symmetry adjustment.

Reference

1. S. Raju, N. Kularatna, and M. Wilson, "Supercapacitor based adjustable high power pulse generator for medical research applications," in IECON 2023-49th Annual Conference of the IEEE Industrial Electronics Society, pp. 1–6. IEEE, 2023
2. F. A. Khokhar, L. J. Voss, D. A. Steyn-Ross, and M. T. Wilson, "Design and demonstration in vitro of a mouse-specific transcranial magnetic stimulation coil," IEEE Transactions on Magnetics, vol. 57, no. 7, pp. 1–11, 2021.
3. M. T. Wilson, A. D. Tang, K. Iyer, H. McKee, J. Waas, and J. Rodger, "The challenges of producing effective small coils for transcranial magnetic stimulation of mice," Biomed. Phys. Eng. Expr., vol. 4, no. 3, Apr. 2018, Art. no. 037002, doi: 10.1088/2057-1976/aab525.

Appendix B

MATLAB code for the MOSFET model from the experimental data

This MATLAB code is implementing a model of a MOSFET based on experimental data. It begins by loading experimental data from files, defining parameters such as inductance and resistance, and applying smoothing techniques. The code then calculates theoretical predictions for various quantities such as loop current and resistance/conductance of the MOSFET. Subsequently, it computes nonlinear resistance and conductance of the MOSFET, fits exponential and tanh functions to the data, and generates 3D plots illustrating the relationship between gate-source voltage, drain-source voltage, and current or conductance. It includes fitting functions to match experimental data, as well as visualization of the results through 2D and 3D plots. This code is to characterize the behavior of the MOSFET based on the experimental and theoretical data to develop a MOSFET model.

```
function RLC_MOSFET_330uF_expt_12
datapath = '_data/';
fnames = {
    'RLC_12_330uF_0p04us'                    ... 1
    'RLC_12_330uF_0p1us'                     ... 2
    'RLC_12_330uF_0p2us'                     ... 3
    'RLC_12_330uF_0p4us'                     ....4
};
which_file = 2;

load([datapath fnames{which_file} '.mat'])

L = 22e-6;      % coil inductance (22 uH)
r_L = 0.22;     % coil dc resistance (ohm)
t_us = 1e6*t;
dt = diff(t(1:2));
```

```
17          dt_us = diff(t_us(1:2))
18          N = length(t_us);
19
20          % apply Whittaker smoothing
21          smoo = 1e-6;
22          v_GS_smo = whittaker(v_GS, 1/dt, smoo);
23          v_DS_smo = whittaker(v_DS, 1/dt, smoo);
24          v_L_smo = whittaker(v_L, 1/dt, smoo);
25          i_L_smo = whittaker(i_L, 1/dt, smoo);
26
27          % compensate for current-probe delay
28          % current probe seems to show ~3 us delay?
29          delay_iL = 3.0;
30          o_iL = round(delay_iL/dt_us);       % index offset
31          i_L_adv = nan(size(i_L));
32          i_L_adv(1 : end-o_iL+1) = i_L_smo(o_iL : end); % time-advanced
               copy of i_L
33          % ensure i_L_adv never goes to zero
34          i_L_adv(i_L_adv < 0.1) = 0.1;
35
36          % compare theoretical prediction for loop current vs measured
               value
37          i_theor = zeros(size(t_us));
38          i_theor(1) = 0.1;       % no current initially
39          v_L_dc_offset = mean(v_L_smo(t_us < 0))
40
41          for k = 1 : N - 1
42          i_theor(k+1) = i_theor(k) + dt/L * ...
43          (v_L_smo(k) - i_theor(k)*r_L - v_L_dc_offset + 0.4);
44          if (abs(i_theor(k+1)) > 200)
45          break;
46          end
47          end
48
49          % nonlinear resistance and conductance of DS channel
50          r_DS = v_DS_smo ./ i_theor;
51          G_DS = 1 ./ r_DS;
52          % try exponential fit to subthreshold current
53          v_GS_dom = linspace(0, 10, 1001);
54          v_therm = 0.026;
```

```
55          I0 = 8.0;
56          v_T2 = 6;
57          n2 = 16;
58          i_fit = I0*exp((v_GS_dom - v_T2)/(n2*v_therm));
59
60          % try tanh() fit to v_DS vs v_GS
61          D1 = 20;
62          D2 = 0.4;
63          v_T3 = 5.5;
64          n3 = 12;
65          v_DS_fit = 0.5*(D1 + D2 + (D2 - D1)*tanh((v_GS_dom -
               v_T3)/(n3*v_therm)));
66
67          % consider power-law exponent p that follows a tanh law with
               v_GS to be
68          p1 = 1;
69          p2 = 0.13;
70          v_Tp = 6.0;
71          n_p = 10;
72          p_fit = 0.5*(p1 + p2 + (p2 - p1)*tanh((v_GS_dom -
               v_Tp)/(n_p*v_therm)));
73          i_fit3 = (I0/log(2)) * log(1 + (i_fit/I0).^p_fit);
74          r_DS_fit = v_DS_fit ./ i_fit3;
75          G_DS_fit = 1 ./ (r_DS_fit);
76
77          % figure(3)
78          if 1
79          figure(3); clf;
80          subplot(1,1,1);
81          zoom on; grid on; hold on;
82          plot(v_GS_smo, v_DS_smo, '-o');
83          plot(v_GS_dom, v_DS_fit, '-r');
84          xlabel('v_{GS} (V)');
85          ylabel('v_{DS} (V)')
86          axis tight;
87          set(gca, 'yscale', 'log');
88          end
89
90          % 3D plots
91          % set up some viewing angles for 3D plots
```

```
92          az_set = [0   90   -14];
93          el_set = [0    0    25];
94
95          which_view = 3;          % <<<<---  choose 1, 2, or 3
96          want_conductance = 0;    % 0 for r_DS; 1 for G_DS
97          want_logplot = 1;
98          [az, el] = deal(az_set(which_view), el_set(which_view));
99
100         figure(2); clf;
101         subplot(2,1,1);
102         plot3(v_GS_smo, v_DS_smo, i_theor, '.k');
103         grid on; hold on;
104         plot3(v_GS_dom, v_DS_fit, i_fit, 'g');
105         plot3(v_GS_dom, v_DS_fit, i_fit3, 'r');
106         axis tight;
107         zlim([0.5   40]);
108         xlim([4   10]);
109         if want_logplot
110         set(gca, 'zscale', 'log');
111         end
112         xlabel('v_{GS} (V)'); ylabel('v_{DS} (V)'); zlabel('i_L (A)');
113         title('(a) Drain-source current');
114         view(az, el);
115         subplot(2,1,2);
116         if want_conductance
117         plot3(v_GS_smo, v_DS_smo, G_DS, '.k');
118         grid on; hold on;
119         plot3(v_GS_dom, 0*v_GS_dom,   G_DS_fit, '-r');
120         plot3(v_GS_dom, 0*v_GS_dom,   i_fit ./ v_DS_fit, '-g');
121         z_lab = 'G_{DS} (S)';
122         title_b = '(b) Nonlinear conductance';
123         zlim([0.001   80]);
124         xlim([4   10]);
125         else
126         plot3(v_GS_smo, v_DS_smo, r_DS, '.k');
127         grid on; hold on;
128         plot3(v_GS_dom, 0*v_GS_dom,   r_DS_fit, '-r');
129         plot3(v_GS_dom, 0*v_GS_dom, v_DS_fit ./ i_fit, '-g');
130         z_lab = 'r_{DS} (\Omega)';
131         title_b = '(b) Nonlinear resistance';
```

```
132         zlim([0.01  80]);
133         xlim([4  10]);
134         end
135         if want_logplot
136         set(gca, 'zscale', 'log');
137         end
138         xlabel('v_{GS} (V)'); ylabel('v_{DS} (V)'); zlabel(z_lab);
139         title(title_b);
140         view(az, el);
```

(INTENTIONALLY BLANK)

Appendix C

MATLAB simulation code for the MOSFET model

This covers the code related to modeling the MOSFET characteristics and calculating the dynamic resistance. It is designed to simulate the behavior of an RLC circuit with MOSFET, utilizing both Euler's method and the `ode15s` solver for Ordinary Differential Equations (ODEs)

```
function solve_RLC_mosfet_de

WANT_EULER = 0;      % 0 ==> ode15s (recommended);  1 ==> Euler

V0 = 30;                % initial capacitor voltage
L = 22e-6;              % henry
C = 330*1e-6;           % farad; rating = 450 V
r_L = 0.22;             % ohm
r_C = 0.25;             % ohm
V_th = 0.026;           % thermal voltage at 25 degC

% which scope time-base do we wish to simulate?
which_tb = 4;           % <<<----- choose from [1 : 4]
dt_scope_set = [0.04  0.1  0.2  0.4 0.8 4]/1e6; % timebase
   resolution on scope
dt_scope = dt_scope_set(which_tb);
duration = 2500*dt_scope    % 2500 time-points captured
t = linspace(-0.1*duration, 0.9*duration, 1 + 2e6)';
t_us = 1e6*t;
dt = diff(t(1:2))           % timebase resolution (s)
dt_us = dt*1e6;
N = length(t);

```

```
23          D = 0 : 100/1e6:t(end);
24          wid = 100/1e6;
25          skew = 0;       % -1 <= skew <= +1
26          o = 25/1e6;     % time offset
27          v_GS_tri = 10*pulstran(t - o, D, @tripuls, wid, skew);
28          % scalar version of v_GS_tri (for use with ode solvers)
29          v_GS_t_fn = @(x) 10*pulstran(x - o, D, @tripuls, wid, skew);
30          v_G = v_GS_tri;     % triangular gate voltage (V)
31
32
33          % tanh() fit to v_DS (forward path only; reverse path ignored)
34          D1 = 20;
35          D2 = 0.4;
36          v_T_DS = 5.5;
37          eta_DS = 12;
38          v_DS_fit_fn = @(x) 0.5*(D1 + D2 + (D2 - D1)*tanh((x -
               v_T_DS)/(eta_DS*V_th)));
39
40          % diode-law exponential kernel for drain-source current
41          v_T_dio = 6;
42          eta_dio = 16;
43          i_kernel_fn = @(x) exp((x - v_T_dio)/(eta_dio*V_th));
44
45          % power-law tuning to be applied to Ytterdal's
               exponential-linear blend cfor MOSFET transition from below-
               to above-threshold
46          p1 = 1;
47          p2 = 0.13;
48          v_T_p = 6.0;
49          eta_p = 10;
50          p_fit_fn = @(x) 0.5*(p1 + p2 + (p2 - p1)*tanh((x -
               v_T_p)/(eta_p*V_th)));
51
52          % Ytterdal expression for drain-source current
53           (modified from Eq. 3.8)
54          I0 = 8.0;
55          i_fit_Ytt_fn = @(x) (I0/log(2)) * log(1 +
               (i_kernel_fn(x)).^p_fit_fn(x));
56
57          % MOSFET dynamic resistance (assumed to be a function of
```

```
          gate-source voltage only
58        r_DS_fit_fn = @(x) v_DS_fit_fn(x) ./ i_fit_Ytt_fn(x);
59        r_DS_fit = r_DS_fit_fn(v_G);
60        [max(r_DS_fit)  min(r_DS_fit)]
61
62        if WANT_EULER
63        % need to impose a max drain-source resistance otherwise Euler
            simulation becomes unstable
64        r_max = 1e5;                % 100 kohm
65        r_DS_fit(r_DS_fit > r_max) = r_max;
66        end
67        G_DS = 1 ./ r_DS_fit;       % conductance (S)
68        v_C = zeros(size(t));       % ideal capacitor voltage (V)
69        i_L = zeros(size(t));       % loop current (A)
70
71        % initial conditions
72        v_C(1)  = V0;               % capacitor is fully charged
73        i_L(1) = V0 / (r_DS_fit(1) + r_C + r_L);
74
75        % solve RLC-mosfet DEs
76        %-----------------------------------------------
77        function dydt = ode_MOSFET_fn(t, y)
78        [vC, iL] = deal(y(1), y(2));
79        dvC_dt = -1/C * iL;
80        di_dt = 1/L*(vC - iL*(r_L + r_C + r_DS_fit_fn(v_GS_t_fn(t))));
81        dydt = [dvC_dt; di_dt];
82        end
83        %-----------------------------------------
84
85        if ~WANT_EULER                  % i.e., NOT Euler ==> ode15s
86        opts = odeset('RelTol',1e-10,'AbsTol',1e-12,
            'MaxStep',100/1e6);
87        [t_ode, y] = ode15s...
88        (@ode_MOSFET_fn, [t(1), t(end)], [v_C(1), i_L(1)], opts);
89        [vC_ode, iL_ode] = deal(y(:,1), y(:,2));
90        vL_ode = L * cdiff(iL_ode) ./ cdiff(t_ode);
91        vGS_ode = v_GS_t_fn(t_ode);
92
93        figure(7); clf;                         %ode15s solver
            solution figure
```

```
94          pp(1) = subplot(5,1,1);
95          zoom on; grid on; hold on;
96          plot(t_ode*1e6, vGS_ode, '-');
97          pp(2) = subplot(5,1,2:5);
98          zoom on; grid on; hold on;
99          plot(t_ode*1e6, [vC_ode, iL_ode, vL_ode], '-');
100         title('ode15s solution', 'FontSize',20);
101         xlabel('Time (us)');
102         linkaxes(pp, 'x');
103         xlim([t_ode(1) t_ode(end)]*1e6);
104         lh = legend('v\_C', 'i\_L', 'v\_L');
105         set(lh, 'Fontsize', 16, 'location', 'best');
106         clear pp;
107
108         return
109         %----------------------------------------
110
111         else
112         % run Euler instead of ode15s
113         tic
114         for k = 1 : N - 1
115         R = r_L + r_C + r_DS_fit(k);
116         v_C(k+1) = v_C(k) - dt/C * i_L(k);
117         i_L(k+1) = i_L(k) + dt/L * (v_C(k) - i_L(k)*R);
118         if (abs(v_C(k+1)) > 100) || (abs(i_L(k+1)) > 100)
119         break;
120         end
121         end
122         toc
123         end
124
125         % estimate measured (non-ideal) v_C, v_L
126         v_C_meas = v_C - r_C * i_L;
127         v_L_meas = v_L + r_L * i_L;
128
129         figure(5); clf;                          % Euler solution
              figure
130         pp(1) = subplot(5,1,1);
131         hold on; grid on; zoom on;
132         plot(t_us, v_GS_tri, 'b');
```

```
133         %   plot(t_us, log10(r_DS_fit), '--k');
134         plot(t_us, r_DS_fit/1e4, '--k');
135         plot(t_us, G_DS/max(G_DS)*10, '-.g');
136         lab(1) = title('Gate voltage');
137         lab(2) = ylabel('$v_{\rm{}GS}$ (V)');
138
139         pp(2) = subplot(5,1,2:3);
140         hold on; grid on; zoom on;
141         plot(t_us, i_L, 'r');
142         plot(1e6*t, v_C_meas, '-.g');
143         plot(t_us, v_C, '-b');
144         %   lab(3) = xlabel('Time ($\mu$s)');
145         %   ylim([-10 50])
146         lab(3) = ylabel('$v_{\rm{}C}$ (V);  $i_{\rm{}L}$ (A)');
147         lab(4) = title('Capacitor voltage (green/blue); Loop current
               (red)');
148
149         pp(3) = subplot(5,1,4:5);
150         hold on; grid on; zoom on;
151         plot(t_us, v_DS, 'b');
152         plot(t_us, v_DS2, '--m');
153         plot(t_us, v_L, 'r');
154         %   plot(1e6*t, v_L_meas, '-.g');
155         lab(5) = xlabel('Time ($\mu$s)');
156         lab(6) = ylabel('$v_{\rm{DS}}$;  $v_{\rm{L}}$ (V)');
157         lab(7) = title('Drain-source voltage (blue); Inductor voltage
               (red)');
158         %   ylim([-200 200]);
159         set(lab, 'interp','latex', 'fontsize',18)
160         linkaxes(pp, 'x')
161         xlim([t_us(1) t_us(end)])
162         end
```

(INTENTIONALLY BLANK)

Appendix D

Component datasheets

This appendix includes the datasheets for the components used in the circuit design and measurements.

International
IOR Rectifier

IRFP4004PbF

HEXFET® Power MOSFET

Applications
- High Efficiency Synchronous Rectification in SMPS
- Uninterruptible Power Supply
- High Speed Power Switching
- Hard Switched and High Frequency Circuits

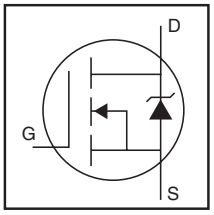

V_{DSS}	40V
$R_{DS(on)}$ typ.	1.35mΩ
max.	1.70mΩ
I_D (Silicon Limited)	350A①
I_D (Package Limited)	195A

Benefits
- Improved Gate, Avalanche and Dynamic dv/dt Ruggedness
- Fully Characterized Capacitance and Avalanche SOA
- Enhanced body diode dV/dt and dI/dt Capability

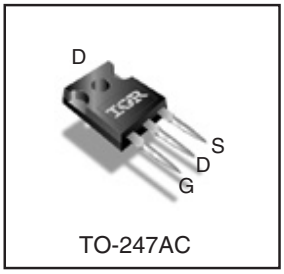

TO-247AC

G	D	S
Gate	Drain	Source

Absolute Maximum Ratings

Symbol	Parameter	Max.	Units
I_D @ T_C = 25°C	Continuous Drain Current, VGS @ 10V (Silicon Limited)	350①	A
I_D @ T_C = 100°C	Continuous Drain Current, V_{GS} @ 10V (Silicon Limited)	250①	
I_D @ T_C = 25°C	Continuous Drain Current, V_{GS} @ 10V (Wire Bond Limited)	195	
I_{DM}	Pulsed Drain Current ②	1390	
P_D @T_C = 25°C	Maximum Power Dissipation	380	W
	Linear Derating Factor	2.5	W/°C
V_{GS}	Gate-to-Source Voltage	± 20	V
dv/dt	Peak Diode Recovery ④	2.0	V/ns
T_J T_{STG}	Operating Junction and Storage Temperature Range	-55 to + 175	°C
	Soldering Temperature, for 10 seconds (1.6mm from case)	300	
	Mounting torque, 6-32 or M3 screw	10lb·in (1.1N·m)	

Avalanche Characteristics

$E_{AS\ (Thermally\ limited)}$	Single Pulse Avalanche Energy ③	290	mJ
I_{AR}	Avalanche Current ②	See Fig. 14, 15, 22a, 22b	A
E_{AR}	Repetitive Avalanche Energy ⑤		mJ

Thermal Resistance

Symbol	Parameter	Typ.	Max.	Units
$R_{\theta JC}$	Junction-to-Case ⑨	—	0.40	°C/W
$R_{\theta CS}$	Case-to-Sink, Flat Greased Surface	0.24	—	
$R_{\theta JA}$	Junction-to-Ambient ⑧⑨	—	40	

IXYS

X2-Class HiPerFET™ Power MOSFET

IXFK120N65X2
IXFX120N65X2

V_{DSS} = 650V
I_{D25} = 120A
$R_{DS(on)}$ ≤ 24mΩ

N-Channel Enhancement Mode
Avalanche Rated
Fast Intrinsic Diode

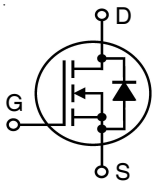

TO-264 (IXFK)

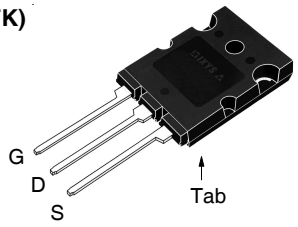

PLUS247 (IXFX)

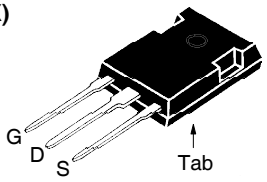

G = Gate D = Drain
S = Source Tab = Drain

Symbol	Test Conditions	Maximum Ratings	
V_{DSS}	T_J = 25°C to 150°C	650	V
V_{DGR}	T_J = 25°C to 150°C, R_{GS} = 1MΩ	650	V
V_{GSS}	Continuous	± 30	V
V_{GSM}	Transient	± 40	V
I_{D25}	T_C = 25°C	120	A
I_{DM}	T_C = 25°C, Pulse Width Limited by T_{JM}	240	A
I_A	T_C = 25°C	15	A
E_{AS}	T_C = 25°C	3.5	J
P_D	T_C = 25°C	1250	W
dv/dt	$I_S \le I_{DM}$, $V_{DD} \le V_{DSS}$, $T_J \le 150°C$	50	V/ns
T_J		-55 ... +150	°C
T_{JM}		150	°C
T_{stg}		-55 ... +150	°C
T_L	Maximum Lead Temperature for Soldering	300	°C
T_{SOLD}	1.6 mm (0.062in.) from Case for 10s	260	°C
M_d	Mounting Torque (TO-264)	1.13/10	Nm/lb.in
F_C	Mounting Force (PLUS247)	20..120 /4.5..27	N/lb
Weight	TO-264	10	g
	PLUS247	6	g

Symbol	Test Conditions (T_J = 25°C Unless Otherwise Specified)	Characteristic Values Min.	Typ.	Max.	
BV_{DSS}	V_{GS} = 0V, I_D = 3mA	650			V
$V_{GS(th)}$	$V_{DS} = V_{GS}$, I_D = 8mA	3.5		5.0	V
I_{GSS}	V_{GS} = ± 30V, V_{DS} = 0V			± 100	nA
I_{DSS}	$V_{DS} = V_{DSS}$, V_{GS} = 0V			50	μA
	T_J = 125°C			5	mA
$R_{DS(on)}$	V_{GS} = 10V, $I_D = 0.5 \bullet I_{D25}$, Note 1			24	mΩ

Features

- International Standard Packages
- Low Q_G
- Avalanche Rated
- Low Package Inductance

Advantages

- High Power Density
- Easy to Mount
- Space Savings

Applications

- Switch-Mode and Resonant-Mode Power Supplies
- DC-DC Converters
- PFC Circuits
- AC and DC Motor Drives
- Robotics and Servo Controls

© 2020 IXYS CORPORATION, All Rights Reserved

Green-Cap (ELECTRIC DOUBLE LAYER CAPACITORS)

DA Snap-in Terminal Type, High Voltage Series

· Endurance : 3.0V 65˚C 1500 hours
· The middle size and high capacitance, low resistance
· Charge and discharge efficiency are higher than in batteries

DB ⇨ DA
High Voltage

Item	Characteristics	
Operating temperature range	-40 ~ +65˚C	
Rated Voltage	3.0 VDC	
Capacitance tolerance	0% ~ +20%	
Temperature characteristics	Capacitance change	Within ±5% of initial value at +20˚C
	Internal resistance change	Within 50% of initial value at +20˚C
Endurance (65˚C)	Test time	1500 hours
	Capacitance change	Within ±30% of specified value
	Internal resistance change	Less than 100% of specified value
Shelf life (65˚C)	After 1000 hours no load test same as endurance	
Life Time at RT(1)	10 years	(1) I△CI < 30% and △ESR < 100% of specified value, respectively and LC < specified value
Cycle Life (25˚C)(1)(2)	500,000 cycles	(2) Cycle : between rated voltage and half rated voltage under constant current at 25˚C

DRAWING

Unit : mm

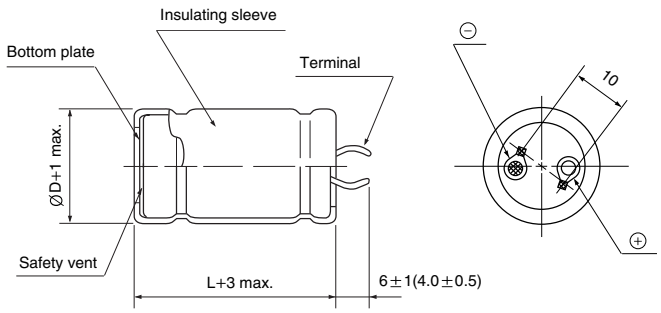

PC Board Mounting Holes

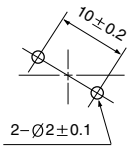

Terminal

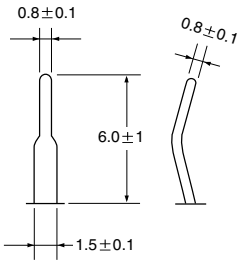

CHARACTERISTIC LIST & DIMENSIONS

Rated Voltage	Capacitance (F)	ESR, 1KHz (mΩ)	ESR, DC (mΩ)	LC (72hr) (mA)	Max Continuous Current(A)		Max Peak Current(A)	Specific Energy		Weight (g)	Volume (ml)	Dimension ØD×L(mm)
					△T=15˚C	△T=40˚C		(Wh/kg)	(Wh/L)			
3.0	100	7.0	9.0	0.30	12.5	20.0	79	5.95	7.31	21	17	22×45
	200	6.0	8.0	0.60	13.0	21.0	115	6.58	7.86	38	32	30×45
	300	3.5	5.0	0.90	16.0	26.5	180	6.58	7.80	57	48	35×50
	360	3.2	3.8	1.08	23.0	38.0	228	6.43	7.80	70	58	35×60
	380	3.0	3.2	1.00	25.0	40.0	257	6.60	8.23	72	58	35×60
	430	2.8	3.0	1.00	25.0	40.0	282	6.72	8.59	80	63	35×65
	480	2.8	3.0	1.00	25.0	40.0	295	6.82	8.91	88	67	35×70

TEL (714) 970-9400
USA (800) 356-5977
FAX (714) 970-0400

DATA SHEET

Part Number: P1224-340/9

Description: Iron Powder Plain Core

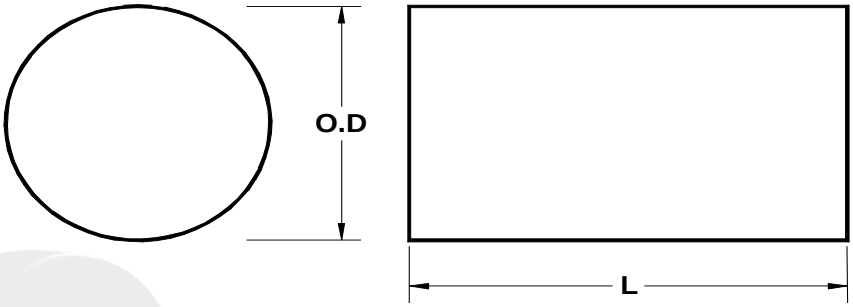

Dimensions:	inches	(millimeters)
Outside Diameter:	0.190 / 0.185	(4.83 / 4.70)
Length:	0.765 / 0.735	(19.43 / 18.67)

Material Characteristics:

Material Type:	Micrometals Mix-40
μ_i(reference)	60 (reference)
Temperature Stability	+950ppm/K typical
Finish:	None

Note: Core surface will rust if exposed to high humidity and rain or not handled with cotton gloves. The Thermal Aging properties of Micrometals Mix –40 are unique to Micrometals alone and not our competitors. Other material properties as described in Micrometals Power Conversion Catalog, Issue L, February 2007. Micrometals Iron Powder Cores comply with the EU Directives 2002/95/EC and 2003/11/EC. Any possible unintentional RoHS trace elements present are less than 100 ppm.

MAGNETICS ®
A Division of Spang & Company

Specification for:

ZW42207TC

110 Delta Drive
Pittsburgh, PA 15238
Phone: 412/696-1333
Fax: 412/696-0333
Email:magnetics@spang.com

DIMENSIONS

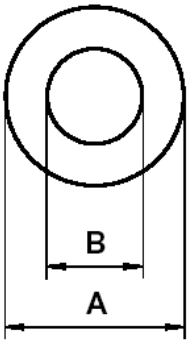

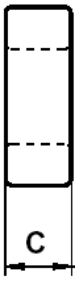

(mm)	Uncoated Nominal:	Coated Min:	Coated Max:
O.D. (A)	22.1	21.63	23.07
I.D. (B)	13.7	12.75	14.19
Ht. (C)	7.8	7.75	8.69

Eff. Parameters		
A_e mm^2	l_e mm	V_e mm^3
32.1	54.1	1740

INDUCTANCE

AL value (nH/T^2)	Test conditions
7400 ± 30%	10 kHz, 0.5 mT (For N = 5, use 0.25 mA), 25°C

ELECTRICAL LOSSES

tan δ / μ_i	Production lot limit Average	Test conditions	
≤ 3.5·10^{-6}	≤ 3 ·10^{-6}	10 kHz	0.5 mT, 25ºC
≤ 55·10^{-6}	≤ 45·10^{-6}	100 kHz	

COATING

Epoxy rated for 200°C continuous operation.
Voltage breakdown rating 2,000 V_{DC} Min Wire-to-Wire.

NOTE

Spec. Modifications	Previous	Revised
2005.12.16	Breakdown voltage > 1,000 V LF: General W material	Breakdown voltage > 2,000 V_{DC} LF: Detail as indicated
2007.01.11	Ht Nom = 7.9	Ht Nom = 7.8

Solid State Hall Effect Sensors

High Performance Miniature Ratiometric Linear *SS490 Series*

SPECIFICATIONS (V_s = 5.0 v, t_a = -40 to +125°C, unless otherwise noted)

Catalog Listing Type		SS495A	SS495A1	SS495A2	SS495B	SS496A	SS496A1	SS496B
Supply Voltage (VDC)		4.5 to 10.5						
Supply Current @ 25°C (mA)	Typ.	7.0						
	Max.	8.7						
Output Type (Sink or Source)		Ratiometric						
Output Current (mA)								
Typ. Sink or Source	Vs > 4.5 V	1.5						
Min. Source	Vs > 4.5 V	1.0						
Min. Sink	Vs > 4.5 V	0.6						
Min. Sink	Vs > 5.0 V	1.0						
Operating Temperature		-40 to +150°C (-40 to +302°F)						
Magnetic Range, Gauss	Typ.	± 670	± 670	± 670	± 670	± 840	± 840	± 840
	Min.	± 600	± 600	± 600	± 600	± 750	± 750	± 750
Output Voltage Span	Typ.	0.2 to (Vs-0.2)						
	Min.	0.4 to (Vs-0.4)						
Null (Output @ 0 Gauss, V)		2.50 ±0.075	2.50 ±0.075	2.50 ±0.100	2.50 ±0.150	2.50 ±0.075	2.50 ±0.075	2.50 ±0.150
Sensitivity (mV/G)		3.125 ±0.125	3.125 ±0.094	3.125 ±0.156	3.125 ±0.250	2.50 ±0.100	2.50 ±0.075	2.50 ±0.200
Linearity,	Typ.	-1.0						
% of Span)	Max.	-1.5						
Temperature Error								
Null Drift	(%/°C)	± 0.06	± 0.04	± 0.07	± 0.08	± 0.048	± 0.03	± 0.06
Sensitivity Drift	(%/°C)							
≥ 25°C Max.		-0.01, +0.05	-0.02, +0.06	-0.02, +0.06	-0.01, +0.05	- 0.01, +0.05	-0.01, +0.05	- 0.02, +0.06
< 25°C Max.		0.0, +0.06	0.0, +0.06	- 0.01, +0.07	- 0.02, +0.06	0.0, +0.06	0.0, +0.06	- 0.02, +0.06

BLOCK DIAGRAM

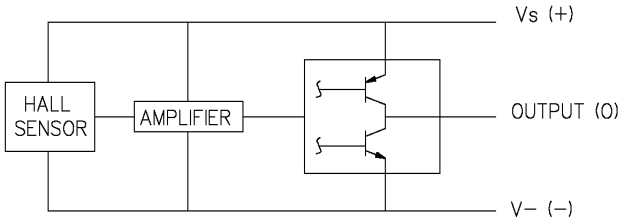

TRANSFER CHARACTERISTICS at Vs = 5.0 VDC

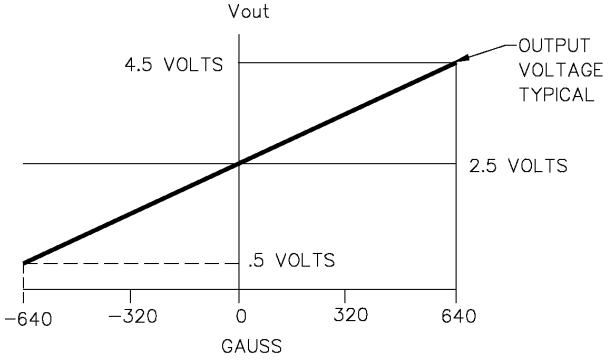

MAXIMUM SUPLY VOLTAGE vs. TEMPERATURE

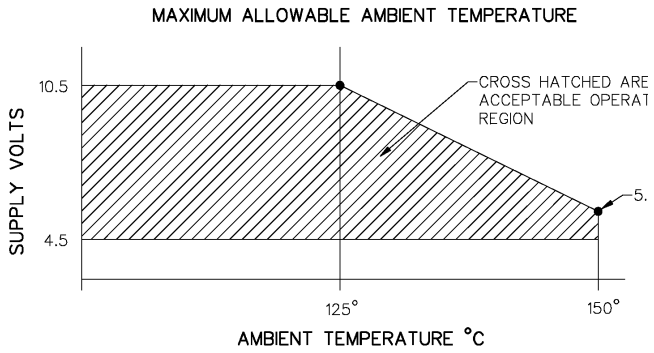

Current Probes

A621 & A622 Datasheet

The A600 Series current probes are specifically designed to support measurements with the TekMeter® or oscilloscope.

Features and benefits

- A621
  - AC – 5 Hz to 50 kHz
  - 100 mA to 2000 A peak
  - For DMMs and oscilloscopes
  - Clamp on
- A622
  - AC/DC – 100 kHz
  - 50 mA to 100 A peak
  - For DMMs and oscilloscopes

Applications

- Motor drives
- Inverters
- Power supplies
- Avionics

A621 2000 Amp AC Current probe/BNC

This industrial-style clamp-on probe has a BNC connector and can be used with a shrouded banana plug adapter [1] so it can be used on digital multimeters, TekMeter, and oscilloscopes. The A621 can measure AC currents from 100 mA to 2000 A peak over a frequency range of 5 Hz to 50 kHz. It provides a 1 mV, 10 mV, or 100 mV output for each Amp measured.

A622 100 Amp AC DC Current probe/BNC

This "long nose" style clamp-on probe uses a Hall Effect current sensor to provide a voltage output to oscilloscopes. It has a BNC connector and can be used with a shrouded banana plug adapter [1] so it can also be used on digital multimeters, TekMeter, and oscilloscopes. The A622 can measure AC/DC currents from 50 mA to 100 A peak over a frequency range of DC to 100 kHz. It provides 10 mV or 100 mV output for each Amp measured.

Recommended products

TPS2000, TDS1000B, TDS2000C, and TDS3000C Series oscilloscopes and DMM4020 [1], DMM4040 [1], and DMM4050 [1] digital multimeters.

1 For instruments with banana jack inputs, Tektronix part number 012-1450-00 Female BNC to banana lead adapter is required.

Appendix E

Co-authorship forms

This appendix includes the author attribution forms for the publications presented in this thesis, detailing the contributions of each author to the associated publications.

THE UNIVERSITY OF WAIKATO
Te Whare Wānanga o Waikato

Co-Authorship Form

School of Graduate Research
The University of Waikato
Private Bag 3105
Hamilton 3240, New Zealand
Phone +64 7 838 5096
Email: SGR@waikato.ac.nz
Website: http://www.waikato.ac.nz/students/research-degree

This form is to accompany the submission of any PhD that contains research reported in published or unpublished co-authored work. **Please include one copy of this form for each co-authored work**. Completed forms should be included in your appendices for all the copies of your thesis submitted for examination and library deposit (including digital deposit).

Please indicate the chapter/section/pages of this thesis that are extracted from a co-authored work and give the title and publication details or details of submission of the co-authored work.

Appendix A
Poster Presented at Australasian Winter Conference on Brain Research (AWCBR), QUEENSTOWN, 26-30 AUGUST 2023

Nature of contribution by PhD candidate	Design and Content writing
Extent of contribution by PhD candidate (%)	90%

CO-AUTHORS

Name	Nature of Contribution
Marcus Wilson	Review & Editing
Nihal Kularatna	Review

Certification by Co-Authors

The undersigned hereby certify that:

- the above statement correctly reflects the nature and extent of the PhD candidate's contribution to this work, and the nature of the contribution of each of the co-authors; and
- that the candidate wrote all or the majority of the text.

Name	Signature	Date
Marcus Wilson		11 October 2024
Nihal Kularatna		11 / oct / 2024

THE UNIVERSITY OF WAIKATO
Te Whare Wānanga o Waikato

Co-Authorship Form

School of Graduate Research
The University of Waikato
Private Bag 3105
Hamilton 3240, New Zealand
Phone +64 7 838 5096
Email: SGR@waikato.ac.nz
Website: http://www.waikato.ac.nz/students/research-degree

This form is to accompany the submission of any PhD that contains research reported in published or unpublished co-authored work. **Please include one copy of this form for each co-authored work.** Completed forms should be included in your appendices for all the copies of your thesis submitted for examination and library deposit (including digital deposit).

Please indicate the chapter/section/pages of this thesis that are extracted from a co-authored work and give the title and publication details or details of submission of the co-authored work.

Appendix A
Poster Presented at NZIP & PHYSIKOS 2023 Conference, Albany, 3-5 July 2023

Nature of contribution by PhD candidate	Design and Content writing
Extent of contribution by PhD candidate (%)	90%

CO-AUTHORS

Name	Nature of Contribution
Marcus Wilson	Review & Editing
Nihal Kularatna	Review

Certification by Co-Authors

The undersigned hereby certify that:

- the above statement correctly reflects the nature and extent of the PhD candidate's contribution to this work, and the nature of the contribution of each of the co-authors; and
- that the candidate wrote all or the majority of the text.

Name	Signature	Date
Marcus Wilson	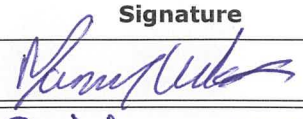	11 October 2024
Nihal Kularatna	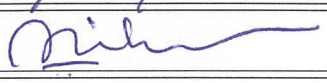	11/oct/2024

THE UNIVERSITY OF WAIKATO
Te Whare Wānanga o Waikato

Co-Authorship Form

School of Graduate Research
The University of Waikato
Private Bag 3105
Hamilton 3240, New Zealand
Phone +64 7 838 5096
Email: SGR@waikato.ac.nz
Website: http://www.waikato.ac.nz/students/research-degree

This form is to accompany the submission of any PhD that contains research reported in published or unpublished co-authored work. **Please include one copy of this form for each co-authored work.** Completed forms should be included in your appendices for all the copies of your thesis submitted for examination and library deposit (including digital deposit).

Please indicate the chapter/section/pages of this thesis that are extracted from a co-authored work and give the title and publication details or details of submission of the co-authored work.

Appendix A

Poster presented at IEEE IECON 2024 conference, 3-6 November 2024 in Chicago, USA

Nature of contribution by PhD candidate	Methodology, Experimental analysis and measurements, Designing and content writing
Extent of contribution by PhD candidate (%)	90%

CO-AUTHORS

Name	Nature of Contribution
Nihal Kularatna	Review
Marcus Wilson	Review and editing
Alistair Steyn-Ross	Review

Certification by Co-Authors

The undersigned hereby certify that:

- the above statement correctly reflects the nature and extent of the PhD candidate's contribution to this work, and the nature of the contribution of each of the co-authors; and
- that the candidate wrote all or the majority of the text.

Name	Signature	Date
Nihal Kularatna		11/Nov/2024
Marcus Wilson		8 Nov 2024
Alistair Steyn-Ross	A Steyn-Ross	11 Nov 2024

THE UNIVERSITY OF WAIKATO
Te Whare Wānanga o Waikato

Co-Authorship Form

School of Graduate Research
The University of Waikato
Private Bag 3105
Hamilton 3240, New Zealand
Phone +64 7 838 5096
Email: SGR@waikato.ac.nz
Website: http://www.waikato.ac.nz/students/research-degree

This form is to accompany the submission of any PhD that contains research reported in published or unpublished co-authored work. **Please include one copy of this form for each co-authored work.** Completed forms should be included in your appendices for all the copies of your thesis submitted for examination and library deposit (including digital deposit).

Please indicate the chapter/section/pages of this thesis that are extracted from a co-authored work and give the title and publication details or details of submission of the co-authored work.

Chapter 4, Section 4.5.1
Supercapacitor based adjustable high power pulse generator for medical research applications published in IECON 2023- 49th Annual Conference of the IEEE Industrial Electronics Society, Singapore, Singapore, 2023, pp. 1-6

Nature of contribution by PhD candidate	Conceptualization, Methodology, making experimental measurements and analysis, development of theory, data interpretation
Extent of contribution by PhD candidate (%)	70%

CO-AUTHORS

Name	Nature of Contribution
Marcus Wilson	Overall guidance, analysis of experimental data
Nihal Kularatna	Conceptualization of work, guidance, contribution to writing

Certification by Co-Authors

The undersigned hereby certify that:

- the above statement correctly reflects the nature and extent of the PhD candidate's contribution to this work, and the nature of the contribution of each of the co-authors; and
- that the candidate wrote all or the majority of the text.

Name	Signature	Date
Marcus Wilson		11 October 2024
Nihal Kularatna		11/oct/2024

THE UNIVERSITY OF WAIKATO
Te Whare Wānanga o Waikato

Co-Authorship Form

School of Graduate Research
The University of Waikato
Private Bag 3105
Hamilton 3240, New Zealand
Phone +64 7 838 5096
Email: SGR@waikato.ac.nz
Website: http://www.waikato.ac.nz/students/research-degree

This form is to accompany the submission of any PhD that contains research reported in published or unpublished co-authored work. **Please include one copy of this form for each co-authored work**. Completed forms should be included in your appendices for all the copies of your thesis submitted for examination and library deposit (including digital deposit).

Please indicate the chapter/section/pages of this thesis that are extracted from a co-authored work and give the title and publication details or details of submission of the co-authored work.

Chapter 5, Section 5.6
Effects of different triggering mechanisms on pulse shaping of a TMS pulse generator based on supercapacitor energy storage will be published in IECON 2024- 50th Annual Conference of the IEEE Industrial Electronics Society, USA, 2024.

Nature of contribution by PhD candidate	Conceptualization, Methodology, making experimental measurements and analysis, development of theory, data interpretation
Extent of contribution by PhD candidate (%)	80%

CO-AUTHORS

Name	Nature of Contribution
Marcus Wilson	Overall guidance
Nihal Kularatna	Guidance and corrections
Alistair Steyn-Ross	Corrections

Certification by Co-Authors

The undersigned hereby certify that:

- the above statement correctly reflects the nature and extent of the PhD candidate's contribution to this work, and the nature of the contribution of each of the co-authors; and
- that the candidate wrote all or the majority of the text.

Name	Signature	Date
Marcus Wilson		11 October 2024
Nihal Kularatna		11/Oct/2024
Alistair Steyn-Ross	A Steyn-Ross	21 Oct 2024

THE UNIVERSITY OF WAIKATO
Te Whare Wānanga o Waikato

Co-Authorship Form

School of Graduate Research
The University of Waikato
Private Bag 3105
Hamilton 3240, New Zealand
Phone +64 7 838 5096
Email: SGR@waikato.ac.nz
Website: http://www.waikato.ac.nz/students/research-degree

This form is to accompany the submission of any PhD that contains research reported in published or unpublished co-authored work. **Please include one copy of this form for each co-authored work.** Completed forms should be included in your appendices for all the copies of your thesis submitted for examination and library deposit (including digital deposit).

Please indicate the chapter/section/pages of this thesis that are extracted from a co-authored work and give the title and publication details or details of submission of the co-authored work.

Chapter 6, Section 6.5
Supercapacitor based TMS pulse generator design- Experimental results versus MATLAB MOSFET simulation model will be published in APEC 2025, IEEE Applied Power Electronics Conference and Exposition.

Nature of contribution by PhD candidate	Methodology, making experimental measurements and analysis, development of theory, data interpretation
Extent of contribution by PhD candidate (%)	70%

CO-AUTHORS

Name	Nature of Contribution
Nihal Kularatna	Conceptualization of work, guidance
Marcus Wilson	Overall guidance, analysis of experimental data
Alistair Steyn-Ross	Conceptualization, overall guidance, data interpretation, Software development

Certification by Co-Authors

The undersigned hereby certify that:

- the above statement correctly reflects the nature and extent of the PhD candidate's contribution to this work, and the nature of the contribution of each of the co-authors; and
- that the candidate wrote all or the majority of the text.

Name	Signature	Date
Nihal Kularatna		11 Nov 2024
Marcus Wilson		8 Nov 2024
Alistair Steyn-Ross		11 Nov 2024

THE UNIVERSITY OF WAIKATO
Te Whare Wānanga o Waikato

Co-Authorship Form

School of Graduate Research
The University of Waikato
Private Bag 3105
Hamilton 3240, New Zealand
Phone +64 7 838 5096
Email: SGR@waikato.ac.nz
Website: http://www.waikato.ac.nz/students/research-degree

This form is to accompany the submission of any PhD that contains research reported in published or unpublished co-authored work. **Please include one copy of this form for each co-authored work.** Completed forms should be included in your appendices for all the copies of your thesis submitted for examination and library deposit (including digital deposit).

Please indicate the chapter/section/pages of this thesis that are extracted from a co-authored work and give the title and publication details or details of submission of the co-authored work.

Chapter 4, Section 4.5.2
Supercapacitor-based pulse generator with waveform adjustment capability for small animal Transcranial Magnetic Stimulation (TMS) submitted to Biomedical Physics & Engineering Express.

Nature of contribution by PhD candidate	Conceptualization, Methodology, making experimental measurements and analysis, development of theory, data interpretation
Extent of contribution by PhD candidate (%)	70%

CO-AUTHORS

Name	Nature of Contribution
Marcus Wilson	Overall guidance, analysis of experimental data
Nihal Kularatna	Conceptualization of work, guidance, contribution to writing
Alistair Steyn-Ross	Overall guidance, data interpretation

Certification by Co-Authors

The undersigned hereby certify that:

- the above statement correctly reflects the nature and extent of the PhD candidate's contribution to this work, and the nature of the contribution of each of the co-authors; and
- that the candidate wrote all or the majority of the text.

Name	Signature	Date
Marcus Wilson		11 October 2024
Nihal Kularatna		11/oct/2024
Alistair Steyn-Ross		21 oct 2024

THE UNIVERSITY OF WAIKATO
Te Whare Wānanga o Waikato

Co-Authorship Form

School of Graduate Research
The University of Waikato
Private Bag 3105
Hamilton 3240, New Zealand
Phone +64 7 838 5096
Email: SGR@waikato.ac.nz
Website: http://www.waikato.ac.nz/students/research-degree

This form is to accompany the submission of any PhD that contains research reported in published or unpublished co-authored work. **Please include one copy of this form for each co-authored work**. Completed forms should be included in your appendices for all the copies of your thesis submitted for examination and library deposit (including digital deposit).

Please indicate the chapter/section/pages of this thesis that are extracted from a co-authored work and give the title and publication details or details of submission of the co-authored work.

Chapter 6, Section 6.6
Dynamic nonlinear resistance model for a power MOSFET in an oscillatory RLC circuit submitted to IEEE Transactions on Industry Applications

Nature of contribution by PhD candidate	Methodology, making experimental measurements and analysis, development of theory, data interpretation
Extent of contribution by PhD candidate (%)	60%

CO-AUTHORS

Name	Nature of Contribution
Alistair Steyn-Ross	Conceptualization, overall guidance, data interpretation, Software development
Marcus Wilson	Overall guidance, analysis of experimental data
Nihal Kularatna	Conceptualization of work, guidance

Certification by Co-Authors

The undersigned hereby certify that:

- the above statement correctly reflects the nature and extent of the PhD candidate's contribution to this work, and the nature of the contribution of each of the co-authors; and
- that the candidate wrote all or the majority of the text.

Name	Signature	Date
Alistair Steyn-Ross	A Steyn-Ross	11 NOV 2024
Marcus Wilson		20 Nov 2024
Nihal Kularatna		15 NOV 2024

(INTENTIONALLY BLANK)

References

[1] A. T. Barker, R. Jalinous, and I. L. Freeston, "Non-invasive magnetic stimulation of human motor cortex," *The Lancet*, vol. 325, no. 8437, pp. 1106–1107, 1985.

[2] A. Barker, C. Garnham, and I. Freeston, "Magnetic nerve stimulation: the effect of waveform on efficiency, determination of neural membrane time constants and the measurement of stimulator output." *Electroencephalography and clinical neurophysiology. Supplement*, vol. 43, pp. 227–237, 1991.

[3] D. A. Spampinato, J. Ibanez, L. Rocchi, and J. Rothwell, "Motor potentials evoked by transcranial magnetic stimulation: interpreting a simple measure of a complex system," *The Journal of Physiology*, vol. 601, no. 14, pp. 2827–2851, 2023.

[4] M. Sabé, A. Sulstarova, C. Chen, J. Hyde, E. Poulet, A. Aleman, J. Downar, V. Brandt, L. Mallet, O. Sentissi *et al.*, "A century of research on neuromodulation interventions: A scientometric analysis of trends and knowledge maps," *Neuroscience & Biobehavioral Reviews*, vol. 152, p. 105300, 2023.

[5] E. M. Wassermann, "Risk and safety of repetitive transcranial magnetic stimulation: report and suggested guidelines from the international workshop on the safety of repetitive transcranial magnetic stimulation, june 5–7, 1996," *Electroencephalography and Clinical Neurophysiology/Evoked Potentials Section*, vol. 108, no. 1, pp. 1–16, 1998.

[6] S. Rossi, M. Hallett, P. M. Rossini, A. Pascual-Leone, S. of TMS Consensus Group *et al.*, "Safety, ethical considerations, and application guidelines for the use of transcranial magnetic stimulation in clinical practice and research," *Clinical neurophysiology*, vol. 120, no. 12, pp. 2008–2039, 2009.

[7] E. M. Wassermann and T. Zimmermann, "Transcranial magnetic brain stimulation: therapeutic promises and scientific gaps," *Pharmacology & therapeutics*, vol. 133, no. 1, pp. 98–107, 2012.

[8] A. Aleman, "Use of repetitive transcranial magnetic stimulation for treatment in psychiatry," *Clinical Psychopharmacology and Neuroscience*, vol. 11, no. 2, p. 53, 2013.

[9] D. J. Stultz, S. Osburn, T. Burns, S. Pawlowska-Wajswol, and R. Walton, "Transcranial magnetic stimulation (TMS) safety with respect to seizures: A literature review," *Neuropsychiatric disease and treatment*, pp. 2989–3000, 2020.

[10] L. Y. Cabrera and O. A. van den Heuvel, "Ethical considerations regarding the use of transcranial magnetic stimulation in mental health practice," *Biological Psychiatry*, vol. 95, no. 6, pp. 491–493, 2024.

[11] S. H. Lisanby, "Transcranial magnetic stimulation in psychiatry: Historical reflections and future directions," *Biological Psychiatry*, vol. 95, no. 6, pp. 488–490, 2024.

[12] M. S. George and R. H. Belmaker, "Transcranial magnetic stimulation in clinical psychiatry," 2007.

[13] A. H. Iglesias, "Transcranial magnetic stimulation as treatment in multiple neurologic conditions," *Current neurology and neuroscience reports*, vol. 20, pp. 1–9, 2020.

[14] F. A. Somaa, T. A. de Graaf, and A. T. Sack, "Transcranial magnetic stimulation in the treatment of neurological diseases," *Frontiers in Neurology*, vol. 13, p. 793253, 2022.

[15] F. S. Bersani, A. Minichino, P. G. Enticott, L. Mazzarini, N. Khan, G. Antonacci, R. Raccah, M. Salviati, R. Delle Chiaie, G. Bersani *et al.*, "Deep transcranial magnetic stimulation as a treatment for psychiatric disorders: A comprehensive review," *European Psychiatry*, vol. 28, no. 1, pp. 30–39, 2013.

[16] F. Maeda and A. Pascual-Leone, "Transcranial magnetic stimulation: studying motor neurophysiology of psychiatric disorders," *Psychopharmacology*, vol. 168, pp. 359–376, 2003.

[17] H. Ozturk and S. Venugopal, "Transcranial magnetic stimulation as a therapeutic option for neurologic diseases and psychiatric disorders: A systematic review," *Cureus*, vol. 14, no. 8, 2022.

[18] T. D. Kim, G. Hong, J. Kim, and S. Yoon, "Cognitive enhancement in neurological and psychiatric disorders using transcranial magnetic stimulation (TMS): A review of modalities, potential mechanisms and future implications," *Experimental Neurobiology*, vol. 28, no. 1, p. 1, 2019.

[19] S. Machado, O. Arias-Carrión, F. Paes, R. T. Vieira, L. Caixeta, F. Novaes, T. Marinho, L. F. Almada, A. C. Silva, and A. E. Nardi, "Repetitive transcranial magnetic stimulation for clinical applications in neurological and psychiatric disorders: an overview," *The Eurasian journal of medicine*, vol. 45, no. 3, p. 191, 2013.

[20] J.-P. Miron, V. D. Jodoin, P. Lespérance, and D. M. Blumberger, "Repetitive transcranial magnetic stimulation for major depressive disorder: basic principles and future directions," *Therapeutic Advances in Psychopharmacology*, vol. 11, p. 20451253211042696, 2021.

[21] M. S. George, S. H. Lisanby, D. Avery, W. M. McDonald, V. Durkalski, M. Pavlicova, B. Anderson, Z. Nahas, P. Bulow, P. Zarkowski *et al.*, "Daily left prefrontal transcranial magnetic stimulation therapy for major depressive disorder: A sham-controlled randomized trial," *Archives of general psychiatry*, vol. 67, no. 5, pp. 507–516, 2010.

[22] L. Menzies, S. R. Chamberlain, A. R. Laird, S. M. Thelen, B. J. Sahakian, and E. T. Bullmore, "Integrating evidence from neuroimaging and neuropsychological studies of obsessive-compulsive disorder: the orbitofronto-striatal model revisited," *Neuroscience & Biobehavioral Reviews*, vol. 32, no. 3, pp. 525–549, 2008.

[23] D. M. McLoughlin, A. Mogg, S. Eranti, G. Pluck, R. Purvis, D. Edwards, S. Landau, R. Brown, S. Rabe-Heskith, R. Howard *et al.*, "The clinical effectiveness and cost of repetitive transcranial magnetic stimulation versus electroconvulsive therapy in severe depression: A multicentre pragmatic randomised controlled trial and economic analysis." *Health technology assessment (Winchester, England)*, vol. 11, no. 24, pp. 1–54, 2007.

[24] G. d'Andrea, G. Mancusi, M. C. Santovito, C. Marrangone, F. Martino, M. Santorelli, A. Miuli, F. Di Carlo, M. S. Signorelli, M. Clerici *et al.*, "Investigating the role of maintenance tms protocols for major depression: systematic review and future perspectives for personalized interventions," *Journal of Personalized Medicine*, vol. 13, no. 4, p. 697, 2023.

[25] S. J. Van Rooij, A. R. Arulpragasam, W. M. McDonald, and N. S. Philip, "Accelerated TMS-moving quickly into the future of depression treatment," *Neuropsychopharmacology*, vol. 49, no. 1, pp. 128–137, 2024.

[26] A. Modak and P. B. Fitzgerald, "Personalising transcranial magnetic stimulation for depression using neuroimaging: A systematic review," *The World Journal of Biological Psychiatry*, vol. 22, no. 9, pp. 647–669, 2021.

[27] I. Cheng, A. Sasegbon, and S. Hamdy, "Dysphagia treatments in Parkinson's disease: A systematic review and meta-analysis," *Neurogastroenterology & Motility*, vol. 35, no. 8, p. e14517, 2023.

[28] J. Madrid and D. H. Benninger, "Non-invasive brain stimulation for Parkinson's disease: Clinical evidence, latest concepts and future goals: A systematic review," *Journal of Neuroscience Methods*, vol. 347, p. 108957, 2021.

[29] F. Fregni, D. Simon, A. Wu, and A. Pascual-Leone, "Non-invasive brain stimulation for Parkinson's disease: A systematic review and meta-analysis of the literature," *Journal of Neurology, Neurosurgery & Psychiatry*, vol. 76, no. 12, pp. 1614–1623, 2005.

[30] K. Dong, X. Zhu, W. Xiao, C. Gan, Y. Luo, M. Jiang, H. Liu, and X. Chen, "Comparative efficacy of transcranial magnetic stimulation on different targets in Parkinson's disease: A bayesian network meta-analysis," *Frontiers in Aging Neuroscience*, vol. 14, p. 1073310, 2023.

[31] A. E. Isroilovich, R. M. Muxammedjanovna, and A. S. Abduvaxobovich, "Transcranial magnetic stimulation therapy in early and late stages of parkinson's disease," *European journal of modern medicine and practice*, vol. 3, no. 1, pp. 31–36, 2023.

[32] M. Starosta, N. Cichoń, J. Saluk-Bijak, and E. Miller, "Benefits from repetitive transcranial magnetic stimulation in post-stroke rehabilitation," *Journal of clinical medicine*, vol. 11, no. 8, p. 2149, 2022.

[33] M.-C. Smith and C. M. Stinear, "Transcranial magnetic stimulation (TMS) in stroke: ready for clinical practice?" *Journal of Clinical Neuroscience*, vol. 31, pp. 10–14, 2016.

[34] A. Dionisio, I. C. Duarte, M. Patricio, and M. Castelo-Branco, "The use of repetitive transcranial magnetic stimulation for stroke rehabilitation: A systematic review," *Journal of stroke and cerebrovascular diseases*, vol. 27, no. 1, pp. 1–31, 2018.

[35] M. N. McDonnell and C. M. Stinear, "TMS measures of motor cortex function after stroke: A meta-analysis," *Brain stimulation*, vol. 10, no. 4, pp. 721–734, 2017.

[36] L. Li, S. Zhang, H. Wang, F. Zhang, B. Dong, J. Yang, and X. Liu, "Multi-scale modeling to investigate the effects of transcranial magnetic stimulation on morphologically-realistic neuron with depression," *Cognitive Neurodynamics*, pp. 1–18, 2024.

[37] J. Yan, Y. Zhang, J. Wang, G. Zhu, and K. Fang, "Effects of transcranial magnetic stimulation on sleep structure and quality in children with autism," *Frontiers in Psychiatry*, vol. 15, p. 1413961, 2024.

[38] Q. Ding, J. Chen, S. Zhang, S. Chen, X. Li, Y. Peng, Y. Chen, J. Chen, K. Chen, G. Cai *et al.*, "Neurophysiological characterization of stroke recovery: A longitudinal TMS and EEG study," *CNS Neuroscience & Therapeutics*, vol. 30, no. 3, p. e14471, 2024.

[39] H. M. Kolbinger, G. Höflich, A. Hufnagel, H.-J. Müller, and S. Kasper, "Transcranial magnetic stimulation (TMS) in the treatment of major depression—a pilot study," *Human Psychopharmacology: Clinical and Experimental*, vol. 10, no. 4, pp. 305–310, 1995.

[40] T. Paus and J. Barrett, "Transcranial magnetic stimulation (TMS) of the human frontal cortex: implications for repetitive TMS treatment of depression," *Journal of Psychiatry and Neuroscience*, vol. 29, no. 4, pp. 268–279, 2004.

[41] J. Cadwell, "Optimizing magnetic stimulator design." *Electroencephalography and clinical neurophysiology. Supplement*, vol. 43, pp. 238–248, 1991.

[42] R. Jalinous, "Technical and practical aspects of magnetic nerve stimulation." *Journal of clinical neurophysiology: official publication of the American Electroencephalographic Society*, vol. 8, no. 1, pp. 10–25, 1991.

[43] L. J. Gomez, S. M. Goetz, and A. V. Peterchev, "Design of transcranial magnetic stimulation coils with optimal trade-off between depth, focality, and energy," *Journal of neural engineering*, vol. 15, no. 4, p. 046033, 2018.

[44] C. M. Epstein and K. R. Davey, "Iron-core coils for transcranial magnetic stimulation," *Journal of Clinical Neurophysiology*, vol. 19, no. 4, pp. 376–381, 2002.

[45] H. Lorenzen and T. Weyh, "Practical application of the summation method for 3-D static magnetic field calculation of a setup of conductive and ferromagnetic material," *IEEE transactions on magnetics*, vol. 28, no. 2, pp. 1481–1484, 1992.

[46] N. J. Tachas and T. Samaras, "The effect of head and coil modeling for the calculation of induced electric field during transcranial magnetic stimulation," *International journal of psychophysiology*, vol. 93, no. 1, pp. 167–171, 2014.

[47] A. Pascual-Leone, J. R. Gates, and A. Dhuna, "Induction of speech arrest and counting errors with rapid-rate transcranial magnetic stimulation," *Neurology*, vol. 41, no. 5, pp. 697–702, 1991.

[48] T. Wagner, M. Zahn, A. Grodzinsky, and A. Pascual-Leone, "Three-dimensional head model simulation of transcranial magnetic stimulation," *IEEE Transactions on Biomedical Engineering*, vol. 51, no. 9, pp. 1586–1598, 2004.

[49] M. Kobayashi and A. Pascual-Leone, "Transcranial magnetic stimulation in neurology," *The Lancet Neurology*, vol. 2, no. 3, pp. 145–156, 2003.

[50] S. M. Goetz and Z.-D. Deng, "The development and modelling of devices and paradigms for transcranial magnetic stimulation," *International Review of Psychiatry*, vol. 29, no. 2, pp. 115–145, 2017.

[51] N. Lang, H. R. Siebner, N. S. Ward, L. Lee, M. A. Nitsche, W. Paulus, J. C. Rothwell, R. N. Lemon, and R. S. Frackowiak, "How does transcranial dc stimulation of the primary motor cortex alter regional neuronal activity in the human brain?" *European Journal of Neuroscience*, vol. 22, no. 2, pp. 495–504, 2005. [Online]. Available: https://onlinelibrary.wiley.com/doi/abs/10.1111/j.1460-9568.2005.04233.x

[52] S. Groppa, A. Oliviero, A. Eisen, A. Quartarone, L. Cohen, V. Mall, A. Kaelin-Lang, T. Mima, S. Rossi, G. Thickbroom, P. Rossini, U. Ziemann, J. Valls-Solé, and H. Siebner, "A practical guide to diagnostic transcranial magnetic stimulation: Report of an IFCN committee," *Clinical Neurophysiology*, vol. 123, no. 5, pp. 858–882, 2012. [Online]. Available: https://www.sciencedirect.com/science/article/pii/S1388245712000569

[53] B. Wang, A. V. Peterchev, G. Gaugain, R. J. Ilmoniemi, W. M. Grill, M. Bikson, and D. Nikolayev, "Quasistatic approximation in neuromodulation," *Journal of neural engineering*, vol. 21, no. 4, p. 041002, 2024.

[54] G. M. Noetscher, D. Tang, A. R. Nummenmaa, C. S. Bingham, C. C. McIntyre, and S. N. Makaroff, "Estimations of charge deposition onto convoluted axon surfaces within extracellular electric fields," *IEEE Transactions on Biomedical Engineering*, 2023.

[55] S. N. Makaroff, A. R. Nummenmaa, G. M. Noetscher, Z. Qi, C. C. McIntyre, and C. S. Bingham, "Influence of charges deposited on membranes of human hyperdirect pathway axons on depolarization during subthalamic deep brain stimulation," *Journal of Neural Engineering*, vol. 20, no. 4, p. 044001, 2023.

[56] T. A. Wagner, M. Zahn, A. J. Grodzinsky, and A. Pascual-Leone, "Three-dimensional head model simulation of transcranial magnetic stimulation," *IEEE Transactions on Biomedical Engineering*, vol. 51, no. 9, pp. 1586–1598, 2004.

[57] A. V. Peterchev, Z.-D. Deng, and S. M. Goetz, "Advances in transcranial magnetic stimulation technology," *Brain stimulation: methodologies and interventions*, pp. 165–189, 2015.

[58] M. Wilson, A. Tang, K. Iyer, H. McKee, J. Waas, and J. Rodger, "The challenges of producing effective small coils for transcranial magnetic stimulation of mice," *Biomedical Physics & Engineering Express*, vol. 4, no. 3, p. 037002, 2018.

[59] A. Tang, G. Thickbroom, and J. Rodger, "Repetitive transcranial magnetic stimulation of the brain: mechanisms from animal and experimental models," *The Neuroscientist*, vol. 23, no. 1, pp. 82–94, 2017.

[60] S. Rossi, M. Hallett, P. M. Rossini, and A. Pascual-Leone, "Safety, ethical considerations, and application guidelines for the use of transcranial magnetic stimulation in clinical practice and research," *Clinical Neurophysiology*, vol. 120, no. 12, pp. 2008–2039, 2009. [Online]. Available: https://www.sciencedirect.com/science/article/pii/S1388245709005197

[61] S. Rossi, A. Antal, S. Bestmann, M. Bikson, C. Brewer, J. Brockmöller, L. L. Carpenter, M. Cincotta, R. Chen, J. D. Daskalakis, V. Di Lazzaro, M. D. Fox, M. S. George, D. Gilbert, V. K. Kimiskidis, G. Koch, R. J. Ilmoniemi, J. P. Lefaucheur, L. Leocani, S. H. Lisanby, C. Miniussi, F. Padberg, A. Pascual-Leone, W. Paulus, A. V. Peterchev, A. Quartarone, A. Rotenberg, J. Rothwell, P. M. Rossini, E. Santarnecchi, M. M. Shafi, H. R. Siebner, Y. Ugawa, E. M. Wassermann, A. Zangen, U. Ziemann, and M. Hallett, "Safety and recommendations for TMS use in healthy subjects and patient populations, with updates on training, ethical and regulatory issues: Expert guidelines," *Clinical Neurophysiology*, vol. 132, no. 1, pp. 269–306, 2021. [Online]. Available: https://www.sciencedirect.com/science/article/pii/S1388245720305149

[62] A. Antal, I. Alekseichuk, M. Bikson, J. Brockmöller, A. Brunoni, R. Chen, L. Cohen, G. Dowthwaite, J. Ellrich, A. Flöel, F. Fregni, M. George, R. Hamilton, J. Haueisen, C. Herrmann, F. Hummel, J. Lefaucheur, D. Liebetanz, C. Loo, C. McCaig, C. Miniussi, P. Miranda, V. Moliadze, M. Nitsche, R. Nowak, F. Padberg, A. Pascual-Leone,

W. Poppendieck, A. Priori, S. Rossi, P. Rossini, J. Rothwell, M. Rueger, G. Ruffini, K. Schellhorn, H. Siebner, Y. Ugawa, A. Wexler, U. Ziemann, M. Hallett, and W. Paulus, "Low intensity transcranial electric stimulation: Safety, ethical, legal regulatory and application guidelines," *Clinical Neurophysiology*, vol. 128, no. 9, pp. 1774–1809, 2017. [Online]. Available: https://www.sciencedirect.com/science/article/pii/S1388245717302122

[63] D. Durand, A. S. Ferguson, and T. Dalbasti, "Induced electric fields by magnetic stimulation in non-homogeneous conducting media," in *Images of the Twenty-First Century. Proceedings of the Annual International Engineering in Medicine and Biology Society,*. IEEE, 1989, pp. 1252–1253.

[64] M. Stöhr, R. Pfister, and P. Reilich, *Klinische Elektromyographie und Neurographie: Lehrbuch und Atlas*. Kohlhammer Verlag, 2022.

[65] P. Kaluskar, D. Bharadwaj, K. S. Iyer, C. Dy, M. Zheng, and D. M. Brogan, "A systematic review to compare electrical, magnetic, and optogenetic stimulation for peripheral nerve repair," *Journal of Hand Surgery Global Online*, 2024.

[66] J. Mankowski and M. Kristiansen, "A review of short pulse generator technology," *IEEE Transactions on plasma science*, vol. 28, no. 1, pp. 102–108, 2000.

[67] H. R. Siebner, K. Funke, A. S. Aberra, A. Antal, S. Bestmann, R. Chen, J. Classen, M. Davare, V. Di Lazzaro, P. T. Fox *et al.*, "Transcranial magnetic stimulation of the brain: What is stimulated?–A consensus and critical position paper," *Clinical Neurophysiology*, vol. 140, pp. 59–97, 2022.

[68] A. S. Aberra, B. Wang, W. M. Grill, and A. V. Peterchev, "Simulation of transcranial magnetic stimulation in head model with morphologically-realistic cortical neurons," *Brain stimulation*, vol. 13, no. 1, pp. 175–189, 2020.

[69] E. Manassero, G. Concina, M. C. C. Caraig, P. Sarasso, A. Salatino, R. Ricci, and B. Sacchetti, "Medial anterior prefrontal cortex stimulation downregulates implicit reactions to threats and prevents the return of fear," *Elife*, vol. 13, p. e85951, 2024.

[70] J. M. Van Dam, L. Graetz, J. B. Pitcher, and M. R. Goldsworthy, "The effects of age and biological sex on the association between I-wave recruitment and the response to cTBS: An exploratory study," *Brain Research*, vol. 1810, p. 148359, 2023.

[71] A. Merkin, S. Sghirripa, L. Graetz, A. E. Smith, B. Hordacre, R. Harris, J. Pitcher, J. Semmler, N. C. Rogasch, and M. Goldsworthy, "Do age-related differences in aperiodic neural activity explain differences in resting EEG alpha?" *Neurobiology of Aging*, vol. 121, pp. 78–87, 2023.

[72] T. M. Hutton, S. T. Aaronson, L. L. Carpenter, K. Pages, D. Krantz, L. Lucas, B. Chen, and H. A. Sackeim, "Dosing transcranial magnetic stimulation in major depressive disorder: relations between number of treatment sessions and effectiveness in a large patient registry," *Brain Stimulation*, vol. 16, no. 5, pp. 1510–1521, 2023.

[73] D. Levi, S. Vignati, E. Guida, A. Oliva, P. Cecconi, A. Sironi, A. Corso, and G. Broggi, "Tailored repetitive transcranial magnetic stimulation for depression and addictions," *Progress in Brain Research*, vol. 270, no. 1, pp. 105–121, 2022.

[74] I. Laakso, T. Murakami, A. Hirata, and Y. Ugawa, "Where and what TMS activates: Experiments and modeling," *Brain Stimulation*, vol. 11, no. 1, pp. 166–174, 2018. [Online]. Available: https://www.sciencedirect.com/science/article/pii/S1935861X17309038

[75] F. Houde, R. Butler, E. St-Onge, M. Martel, V. Thivierge, M. Descoteaux, K. Whittingstall, and G. Leonard, "Anatomical measurements and field modeling to assess transcranial magnetic stimulation motor and non-motor effects," *Neurophysiologie Clinique*, vol. 54, no. 6, p. 103011, 2024. [Online]. Available: https://www.sciencedirect.com/science/article/pii/S0987705324000698

[76] I. Laakso, K. Tani, J. Gomez-Tames, A. Hirata, and S. Tanaka, "Small effects of electric field on motor cortical excitability following anodal tDCS," *Iscience*, vol. 27, no. 2, 2024.

[77] L. M. Koponen and A. V. Peterchev, "Transcranial magnetic stimulation: principles and applications," *Neural Engineering*, pp. 245–270, 2020.

[78] A. V. Peterchev, R. Jalinous, and S. H. Lisanby, "A transcranial magnetic stimulator inducing near-rectangular pulses with controllable pulse width (cTMS)," *IEEE Transactions on Biomedical Engineering*, vol. 55, no. 1, pp. 257–266, 2007.

[79] S. Raju, N. Kularatna, and M. Wilson, "Supercapacitor based adjustable high power pulse generator for medical research applications," in *IECON 2023-49th Annual Conference of the IEEE Industrial Electronics Society*. IEEE, 2023, pp. 1–6.

[80] A. D. Tang, A. S. Lowe, A. R. Garrett, R. Woodward, W. Bennett, A. J. Canty, M. I. Garry, M. R. Hinder, J. J. Summers, R. Gersner *et al.*, "Construction and evaluation of rodent-specific rTMS coils," *Frontiers in neural circuits*, vol. 10, p. 47, 2016.

[81] A. D. Tang, K. Makowiecki, C. Bartlett, and J. Rodger, "Low intensity repetitive transcranial magnetic stimulation does not induce cell survival or regeneration in a mouse optic nerve crush model," *PloS one*, vol. 10, no. 5, p. e0126949, 2015.

[82] A. D. Tang, W. Bennett, C. Hadrill, J. Collins, B. Fulopova, K. Wills, A. Bindoff, R. Puri, M. I. Garry, M. R. Hinder *et al.*, "Low intensity repetitive transcranial magnetic stimulation modulates skilled motor learning in adult mice," *Scientific reports*, vol. 8, no. 1, p. 4016, 2018.

[83] J. Zhai, J. Wang, H. Cui, Q. Chen, J. Lin, D. Pan, and L. Li, "Rodent transcranial magnetic stimulation coil structure with controllable induction electric field direction," *IEEE Access*, vol. 12, pp. 67 189–67 198, 2024.

[84] G. S. Pell, Y. Roth, and A. Zangen, "Modulation of cortical excitability induced by repetitive transcranial magnetic stimulation: influence of timing and geometrical parameters and underlying mechanisms," *Progress in neurobiology*, vol. 93, no. 1, pp. 59–98, 2011.

[85] U. Najib and J. C. Horvath, "Transcranial magnetic stimulation (TMS) safety considerations and recommendations," *Transcranial magnetic stimulation*, pp. 15–30, 2014.

[86] S. Anand and J. Hotson, "Transcranial magnetic stimulation: neurophysiological applications and safety," *Brain and cognition*, vol. 50, no. 3, pp. 366–386, 2002.

[87] R. Taylor, V. Galvez, and C. Loo, "Transcranial magnetic stimulation (TMS) safety: A practical guide for psychiatrists," *Australasian Psychiatry*, vol. 26, no. 2, pp. 189–192, 2018.

[88] P. Merton and H. Morton, "Stimulation of the cerebral cortex in the intact human subject," *Nature*, vol. 285, no. 5762, pp. 227–227, 1980.

[89] S. Silva, P. Basser, and P. Miranda, "Elucidating the mechanisms and loci of neuronal excitation by transcranial magnetic stimulation using a finite element model of a cortical sulcus," *Clinical neurophysiology*, vol. 119, no. 10, pp. 2405–2413, 2008.

[90] E. M. Wassermann, J. Grafman, C. Berry, C. Hollnagel, K. Wild, K. Clark, and M. Hallett, "Use and safety of a new repetitive transcranial magnetic stimulator," *Electroencephalography and Clinical Neurophysiology/Electromyography and Motor Control*, vol. 101, no. 5, pp. 412–417, 1996.

[91] J. Rothwell, P. Thompson, B. Day, S. Boyd, and C. Marsden, "Stimulation of the human motor cortex through the scalp," *Experimental Physiology: Translation and Integration*, vol. 76, no. 2, pp. 159–200, 1991.

[92] C. M. Epstein, D. G. Schwartzberg, K. R. Davey, and D. B. Sudderth, MD, "Localizing the site of magnetic brain stimulation in humans," *Neurology*, vol. 40, no. 4, pp. 666–666, 1990.

[93] E. Marg and D. Rudiak, "Phosphenes induced by magnetic stimulation over the occipital brain: description and probable site of stimulation," *Optometry and Vision Science*, vol. 71, no. 5, pp. 301–311, 1994.

[94] A. Zangen, Y. Roth, B. Voller, and M. Hallett, "Transcranial magnetic stimulation of deep brain regions: evidence for efficacy of the H-coil," *Clinical neurophysiology*, vol. 116, no. 4, pp. 775–779, 2005.

[95] T. Fadini, L. Matthäus, H. Rothkegel, M. Sommer, F. Tergau, A. Schweikard, W. Paulus, and M. A. Nitsche, "H-coil: Induced electric field properties and input/output curves on healthy volunteers, comparison with a standard figure-of-eight coil," *Clinical Neurophysiology*, vol. 120, no. 6, pp. 1174–1182, 2009.

[96] J. Rodger and R. M. Sherrard, "Optimising repetitive transcranial magnetic stimulation for neural circuit repair following traumatic brain injury," *Neural regeneration research*, vol. 10, no. 3, p. 357, 2015.

[97] Z. Nahas, C. C. Teneback, A. Kozel, A. M. Speer, C. DeBrux, M. Molloy, L. Stallings, K. M. Spicer, G. Arana, D. E. Bohning *et al.*, "Brain effects of TMS delivered over prefrontal cortex in depressed adults: Role of stimulation frequency and coil–cortex distance," *The Journal of neuropsychiatry and clinical neurosciences*, vol. 13, no. 4, pp. 459–470, 2001.

[98] W. Klomjai, R. Katz, and A. Lackmy-Vallée, "Basic principles of transcranial magnetic stimulation (TMS) and repetitive TMS (rTMS)," *Annals of physical and rehabilitation medicine*, vol. 58, no. 4, pp. 208–213, 2015.

[99] P. S. Sachdev, R. McBride, C. Loo, P. M. Mitchell, G. S. Malhi, and V. Croker, "Effects of different frequencies of transcranial magnetic stimulation (TMS) on the forced swim test model of depression in rats," *Biological psychiatry*, vol. 51, no. 6, pp. 474–479, 2002.

[100] E. Houdayer, A. Degardin, F. Cassim, P. Bocquillon, P. Derambure, and H. Devanne, "The effects of low-and high-frequency repetitive TMS on the input/output properties of the human corticospinal pathway," *Experimental brain research*, vol. 187, pp. 207–217, 2008.

[101] Z.-D. Deng, S. H. Lisanby, and A. V. Peterchev, "Coil design considerations for deep transcranial magnetic stimulation," *Clinical Neurophysiology*, vol. 125, no. 6, pp. 1202–1212, 2014.

[102] M. Talebinejad and S. Musallam, "Effects of TMS coil geometry on stimulation specificity," in *2010 Annual International Conference of the IEEE Engineering in Medicine and Biology*. IEEE, 2010, pp. 1507–1510.

[103] R. M. Hardwick, E. Lesage, and R. C. Miall, "Cerebellar transcranial magnetic stimulation: the role of coil geometry and tissue depth," *Brain stimulation*, vol. 7, no. 5, pp. 643–649, 2014.

[104] J. O. Nieminen, A. S. Pospelov, L. M. Koponen, P. Yrjölä, A. Shulga, S. Khirug, and C. Rivera, "Transcranial magnetic stimulation set-up for small animals," *Frontiers in Neuroscience*, vol. 16, p. 935268, 2022.

[105] J. Selvaraj, P. Rastogi, N. Prabhu Gaunkar, R. L. Hadimani, and M. Mina, "Transcranial magnetic stimulation: Design of a stimulator and a focused coil for the application of small animals," *IEEE Transactions on Magnetics*, vol. 54, no. 11, pp. 1–5, 2018.

[106] A. M. Vahabzadeh-Hagh, P. A. Muller, A. Pascual-Leone, F. E. Jensen, and A. Rotenberg, "Measures of cortical inhibition by paired-pulse transcranial magnetic stimulation in anesthetized rats," *Journal of neurophysiology*, vol. 105, no. 2, pp. 615–624, 2011.

[107] K. Hoppenrath and K. Funke, "Time-course of changes in neuronal activity markers following iTBS-TMS of the rat neocortex," *Neuroscience letters*, vol. 536, pp. 19–23, 2013.

[108] R. Gersner, E. Kravetz, J. Feil, G. Pell, and A. Zangen, "Long-term effects of repetitive transcranial magnetic stimulation on markers for neuroplasticity: differential outcomes in anesthetized and awake animals," *Journal of Neuroscience*, vol. 31, no. 20, pp. 7521–7526, 2011.

[109] K. Makowiecki, A. R. Harvey, R. M. Sherrard, and J. Rodger, "Low-intensity repetitive transcranial magnetic stimulation improves abnormal visual cortical circuit topography and upregulates BDNF in mice," *Journal of Neuroscience*, vol. 34, no. 32, pp. 10 780–10 792, 2014.

[110] J. Rodger, C. Mo, T. Wilks, S. A. Dunlop, and R. M. Sherrard, "Transcranial pulsed magnetic field stimulation facilitates reorganization of abnormal neural circuits and corrects behavioral deficits without disrupting normal connectivity," *The FASEB Journal*, vol. 26, no. 4, pp. 1593–1606, 2012.

[111] S. Grehl, H. M. Viola, P. I. Fuller-Carter, K. W. Carter, S. A. Dunlop, L. C. Hool, R. M. Sherrard, and J. Rodger, "Cellular and molecular changes to cortical neurons following low intensity repetitive magnetic stimulation at different frequencies," *Brain stimulation*, vol. 8, no. 1, pp. 114–123, 2015.

[112] M. Colella, R. M. Laher, D. Z. Press, C. E. McIlduff, S. B. Rutkove, A. Pascual-Leone, F. Apollonio, M. Liberti, and G. Bonmassar, "Ultra-focal magnetic stimulation using a μTMS coil: A computational study," in *2019 41st Annual International Conference of the IEEE Engineering in Medicine and Biology Society (EMBC)*. IEEE, 2019, pp. 3987–3990.

[113] G. Bonmassar and P. Serano, "MRI-induced heating of coils for microscopic magnetic stimulation at 1.5 tesla: An initial study," *Frontiers in human neuroscience*, vol. 14, p. 53, 2020.

[114] Q. Meng, L. Jing, J. P. Badjo, X. Du, E. Hong, Y. Yang, H. Lu, and F.-S. Choa, "A novel transcranial magnetic stimulator for focal stimulation of rodent brain," *Brain Stimulation: Basic, Translational, and Clinical Research in Neuromodulation*, vol. 11, no. 3, pp. 663–665, 2018.

[115] C. C. Sánchez, J. J. J. García, M. R. Cabello, and M. F. Pantoja, "Design of coils for lateralized TMS on mice," *Journal of Neural Engineering*, vol. 17, no. 3, p. 036007, 2020.

[116] S. Minusa, S. Muramatsu, H. Osanai, and T. Tateno, "A multichannel magnetic stimulation system using submillimeter-sized coils: system development and experimental application to rodent brain in vivo," *Journal of neural engineering*, vol. 16, no. 6, p. 066014, 2019.

[117] Y. Shirota, M. Sommer, and W. Paulus, "Strength-duration relationship in paired-pulse transcranial magnetic stimulation (TMS) and its implications for repetitive TMS," *Brain Stimulation*, vol. 9, no. 5, pp. 755–761, 2016.

[118] H. Rothkegel, M. Sommer, W. Paulus, and N. Lang, "Impact of pulse duration in single pulse tms," *Clinical neurophysiology*, vol. 121, no. 11, pp. 1915–1921, 2010.

[119] M. Hamada, R. Hanajima, Y. Terao, N. Arai, T. Furubayashi, S. Inomata-Terada, A. Yugeta, H. Matsumoto, Y. Shirota, and Y. Ugawa, "Quadro-pulse stimulation is more effective than paired-pulse stimulation for plasticity induction of the human motor cortex," *Clinical neurophysiology*, vol. 118, no. 12, pp. 2672–2682, 2007.

[120] A. V. Peterchev and D. L. Murphy, "Controllable pulse parameter transcranial magnetic stimulator with enhanced pulse shaping," in *2013 6th International IEEE/EMBS Conference on Neural Engineering (NER)*. IEEE, 2013, pp. 121–124.

[121] S. M. Goetz, C. N. Truong, M. G. Gerhofer, A. V. Peterchev, H.-G. Herzog, and T. Weyh, "Analysis and optimization of pulse dynamics for magnetic stimulation," *PLoS One*, vol. 8, no. 3, p. e55771, 2013.

[122] Q. He, C. F. Geißler, M. Ferrante, G. Hartwigsen, and M. A. Friehs, "Effects of transcranial magnetic stimulation on reactive response inhibition," *Neuroscience & Biobehavioral Reviews*, vol. 157, p. 105532, 2024.

[123] D. Veniero, D. Brignani, G. Thut, and C. Miniussi, "Alpha-generation as basic response-signature to transcranial magnetic stimulation (TMS) targeting the human resting motor cortex: A TMS/EEG co-registration study," *Psychophysiology*, vol. 48, no. 10, pp. 1381–1389, 2011.

[124] M. C. Pellicciari, D. Veniero, and C. Miniussi, "Characterizing the cortical oscillatory response to TMS pulse," *Frontiers in cellular neuroscience*, vol. 11, p. 38, 2017.

[125] J. Daligadu, B. Murphy, J. Brown, B. Rae, and P. Yielder, "TMS stimulus–response asymmetry in left-and right-handed individuals," *Experimental brain research*, vol. 224, pp. 411–416, 2013.

[126] A. Curra, N. Modugno, M. Inghilleri, M. Manfredi, M. Hallett, and A. Berardelli, "Transcranial magnetic stimulation techniques in clinical investigation," *Neurology*, vol. 59, no. 12, pp. 1851–1859, 2002.

[127] Y. Terao and Y. Ugawa, "Basic mechanisms of TMS," *Journal of clinical neurophysiology*, vol. 19, no. 4, pp. 322–343, 2002.

[128] A. Antal, T. Z. Kincses, M. A. Nitsche, O. Bartfai, I. Demmer, M. Sommer, and W. Paulus, "Pulse configuration-dependent effects of repetitive transcranial magnetic stimulation on visual perception," *Neuroreport*, vol. 13, no. 17, pp. 2229–2223, 2002.

[129] J. L. Taylor and C. K. Loo, "Stimulus waveform influences the efficacy of repetitive transcranial magnetic stimulation," *Journal of affective disorders*, vol. 97, no. 1-3, pp. 271–276, 2007.

[130] I. Mogyoros, M. C. Kiernan, and D. Burke, "Strength-duration properties of human peripheral nerve," *Brain*, vol. 119, no. 2, pp. 439–447, 04 1996. [Online]. Available: https://doi.org/10.1093/brain/119.2.439

[131] A. V. Peterchev, D. L. Murphy, and S. H. Lisanby, "Repetitive transcranial magnetic stimulator with controllable pulse parameters (cTMS)," in *2010 Annual International Conference of the IEEE Engineering in Medicine and Biology*. IEEE, 2010, pp. 2922–2926.

[132] A. V. Peterchev, S. M. Goetz, G. G. Westin, B. Luber, and S. H. Lisanby, "Pulse width dependence of motor threshold and input–output curve characterized with controllable pulse parameter transcranial magnetic stimulation," *Clinical Neurophysiology*, vol. 124, no. 7, pp. 1364–1372, 2013.

[133] K. D Ostilio, S. M. Goetz, R. Hannah, M. Ciocca, R. Chieffo, J.-C. A. Chen, A. V. Peterchev, and J. C. Rothwell, "Effect of coil orientation on strength–duration time constant and i-wave activation with controllable pulse parameter transcranial magnetic stimulation," *Clinical Neurophysiology*, vol. 127, no. 1, pp. 675–683, 2016.

[134] A. V. Peterchev, K. D Ostilio, J. C. Rothwell, and D. L. Murphy, "Controllable pulse parameter transcranial magnetic stimulator with enhanced circuit topology and pulse shaping," *Journal of neural engineering*, vol. 11, no. 5, p. 056023, 2014.

[135] T. Kammer, S. Beck, A. Thielscher, U. Laubis-Herrmann, and H. Topka, "Motor thresholds in humans: A transcranial magnetic stimulation study comparing different pulse waveforms, current directions and stimulator types," *Clinical neurophysiology*, vol. 112, no. 2, pp. 250–258, 2001.

[136] F. A. Khokhar, L. J. Voss, D. A. Steyn-Ross, and M. T. Wilson, "Design and demonstration in vitro of a mouse-specific transcranial magnetic stimulation coil," *IEEE Transactions on Magnetics*, vol. 57, no. 7, pp. 1–11, 2021.

[137] W. Gerschlager, H. R. Siebner, and J. C. Rothwell, "Decreased corticospinal excitability after subthreshold 1 Hz rTMS over lateral premotor cortex," *Neurology*, vol. 57, no. 3, pp. 449–455, 2001.

[138] M. Sommer, N. Lang, F. Tergau, and W. Paulus, "Neuronal tissue polarization induced by repetitive transcranial magnetic stimulation?" *Neuroreport*, vol. 13, no. 6, pp. 809–811, 2002.

[139] T. Tings, N. Lang, F. Tergau, W. Paulus, and M. Sommer, "Orientation-specific fast rTMS maximizes corticospinal inhibition and facilitation," *Experimental brain research*, vol. 164, pp. 323–333, 2005.

[140] N. Arai, S. Okabe, T. Furubayashi, Y. Terao, K. Yuasa, and Y. Ugawa, "Comparison between short train, monophasic and biphasic repetitive transcranial magnetic stimulation (rTMS) of the human motor cortex," *Clinical neurophysiology*, vol. 116, no. 3, pp. 605–613, 2005.

[141] N. André-Obadia, P. Mertens, A. Gueguen, R. Peyron, and L. Garcia-Larrea, "Pain relief by rTMS: differential effect of current flow but no specific action on pain subtypes," *Neurology*, vol. 71, no. 11, pp. 833–840, 2008.

[142] H. Rothkegel, M. Sommer, and W. Paulus, "Breaks during 5 Hz rTMS are essential for facilitatory after effects," *Clinical neurophysiology*, vol. 121, no. 3, pp. 426–430, 2010.

[143] K. Kujirai, T. Kujirai, T. Sinkjaer, and J. C. Rothwell, "Associative plasticity in human motor cortex during voluntary muscle contraction," *Journal of neurophysiology*, vol. 96, no. 3, pp. 1337–1346, 2006.

[144] A. Suppa, E. Ortu, N. Zafar, F. Deriu, W. Paulus, A. Berardelli, and J. C. Rothwell, "Theta burst stimulation induces after-effects on contralateral primary motor cortex excitability in humans," *The Journal of physiology*, vol. 586, no. 18, pp. 4489–4500, 2008.

[145] P. Talelli, B. J. Cheeran, J. Teo, and J. C. Rothwell, "Pattern-specific role of the current orientation used to deliver theta burst stimulation," *Clinical Neurophysiology*, vol. 118, no. 8, pp. 1815–1823, 2007.

[146] N. Zafar, W. Paulus, and M. Sommer, "Comparative assessment of best conventional with best theta burst repetitive transcranial magnetic stimulation protocols on human motor cortex excitability," *Clinical Neurophysiology*, vol. 119, no. 6, pp. 1393–1399, 2008.

[147] S. M. Goetz, M. Pfaeffl, J. Huber, M. Singer, R. Marquardt, and T. Weyh, "Circuit topology and control principle for a first magnetic stimulator with fully controllable waveform," in *2012 Annual International Conference of the IEEE Engineering in Medicine and Biology Society*. IEEE, 2012, pp. 4700–4703.

[148] M. M. Sorkhabi, M. Benjaber, K. Wendt, T. O. West, D. J. Rogers, and T. Denison, "Programmable transcranial magnetic stimulation: A modulation approach for the generation of controllable magnetic stimuli," *IEEE Transactions on Biomedical Engineering*, vol. 68, no. 6, pp. 1847–1858, 2021.

[149] David.F.Peelo, *Current Interruption Transients Calculation*. John Wiley & Sons, Ltd, 2020.

[150] L. Moura and I. Darwazeh, *Introduction to linear circuit analysis and modelling: from DC to RF*. Elsevier, 2005.

[151] D. Senda, H. Strong, D. Hines, R. Hines, and R. J. Baker, "A compact 1200 V, 700 A, IGBT-based pulse generator for repetitive transcranial magnetic stimulation in vivo laboratory experiments on small animals," *Review of Scientific Instruments*, vol. 92, no. 8, 2021.

[152] M. H. Rashid, *Electric renewable energy systems*. Academic Press, 2015.

[153] M. H. .Rashid, *Power electronics handbook*. Butterworth-Heinemann, 2017.

[154] N. Mohan, T. M. Undeland, and W. P. Robbins, *Power electronics: converters, applications, and design*. John Wiley & Sons, 2003.

[155] M. Plonus, *Electronics and communications for scientists and engineers*. Butterworth-Heinemann, 2020.

[156] A. V. Peterchev, D. L. Murphy, and S. H. Lisanby, "Repetitive transcranial magnetic stimulator with controllable pulse parameters," *Journal of neural engineering*, vol. 8, no. 3, p. 036016, 2011.

[157] A. V. Peterchev, "Circuit topology comparison and design analysis for controllable pulse parameter transcranial magnetic stimulators," in *2011 5th International IEEE/EMBS Conference on Neural Engineering*, 2011, pp. 646–649.

[158] I. M. Reti, "Brain stimulation: Methodologies and interventions, edited by," *Brain Stimulation*, vol. 8, p. 1243, 2015.

[159] S. M. Goetz, N. C. Truong, M. G. Gerhofer, A. V. Peterchev, H.-G. Herzog, and T. Weyh, "Optimization of magnetic neurostimulation waveforms for minimum power loss," in *2012 Annual International Conference of the IEEE Engineering in Medicine and Biology Society*. IEEE, 2012, pp. 4652–4655.

[160] K. Ali, K. Wendt, M. M. Sorkhabi, M. Benjaber, T. Denison, and D. J. Rogers, "xTMS: A pulse generator for exploring transcranial magnetic stimulation therapies," in *2023 IEEE Applied Power Electronics Conference and Exposition (APEC)*, 2023, pp. 1875–1880.

[161] I. Halawa, Y. Shirota, A. Neef, M. Sommer, and W. Paulus, "Neuronal tuning: selective targeting of neuronal populations via manipulation of pulse width and directionality," *Brain Stimulation*, vol. 12, no. 5, pp. 1244–1252, 2019.

[162] J. O. Nieminen, H. Sinisalo, V. H. Souza, M. Malmi, M. Yuryev, A. E. Tervo, M. Stenroos, D. Milardovich, J. T. Korhonen, L. M. Koponen *et al.*, "Multi-locus transcranial magnetic stimulation system for electronically targeted brain stimulation," *Brain stimulation*, vol. 15, no. 1, pp. 116–124, 2022.

[163] N. Kularatna and K. Gunawardane, *Energy Storage Devices for Renewable Energy-Based Systems: Rechargeable Batteries and Supercapacitors*. Academic Press, 2021.

[164] N. Kularatna, *Digital and analogue instrumentation: testing and measurement*. IET, 2003, no. 11.

[165] N. Kularatna and D. Jayananda, "Supercapacitor-based long time-constant circuits: A unique design opportunity for new power electronic circuit topologies," *IEEE Industrial Electronics Magazine*, vol. 14, no. 2, pp. 40–56, 2020.

[166] T. Christen and M. W. Carlen, "Theory of Ragone plots," *Journal of power sources*, vol. 91, no. 2, pp. 210–216, 2000.

[167] V. C. Valchev and A. Van den Bossche, *Inductors and transformers for power electronics*. CRC press, 2018.

[168] A. Elserougi, S. Ahmed, and A. Massoud, "A boost converter-based ringing circuit with high-voltage gain for unipolar pulse generation," *IEEE Transactions on Dielectrics and Electrical Insulation*, vol. 23, no. 4, pp. 2088–2094, 2016.

[169] X. Zan, D. R. Torres, R. Kheirollahi, X. Lu, S. Zheng, F. Lu, and A.-T. Avestruz, "Medium voltage pulse power generator for accurate current interruption," *IEEE Transactions on Industrial Electronics*, vol. 70, no. 4, pp. 3604–3615, 2023.

[170] S. T. S. Udayanga, S. Kokuhennadige, J. Fernando, N. Kularatna, and D. A. Steyn-Ross, "Supercapacitor assisted surge absorber (SCASA) technique: Selection of magnetic components based on permeance," in *2021 IEEE Applied Power Electronics Conference and Exposition (APEC)*. IEEE, 2021, pp. 2299–2304.

[171] N. Kularatna, K. Subasinghage, K. Gunawardane, D. Jayananda, and T. Ariyarathna, "Supercapacitor-assisted techniques and supercapacitor-assisted loss management concept: New design approaches to change the roadmap of power conversion systems," *Electronics*, vol. 10, no. 14, p. 1697, 2021.

[172] T. Ariyarathna, D. Jayananda, N. Kularatna, and D. A. Steyn-Ross, "Potential of supercapacitors in novel power converters as semi-ideal lossless voltage droppers," in *IECON 2017-43rd Annual Conference of the IEEE Industrial Electronics Society*. IEEE, 2017, pp. 1429–1434.

[173] N. Kularatna, J. Fernando, A. Pandey, and S. James, "Surge capability testing of supercapacitor families using a lightning surge simulator," *IEEE transactions on Industrial Electronics*, vol. 58, no. 10, pp. 4942–4949, 2011.

[174] V. Molahalli, C. K, M. K. Singh, M. Agrawal, S. G. Krishnan, and G. Hegde, "Past decade of supercapacitor research – lessons learned for future innovations," *Journal of Energy Storage*, vol. 70, p. 108062, 2023. [Online]. Available: https://www.sciencedirect.com/science/article/pii/S2352152X23014597

[175] H. Taha, G. Dousoky, and H. Hamed, "Energy management for EV review," 12 2017.

[176] H. L. Weinert, "Efficient computation for Whittaker–Henderson smoothing," *Computational Statistics & Data Analysis*, vol. 52, no. 2, pp. 959–974, 2007.

[177] P. H. Eilers, "A perfect smoother," *Analytical chemistry*, vol. 75, no. 14, pp. 3631–3636, 2003.

[178] T. Ytterdal, Y. Cheng, and T. A. Fjeldly, *Device modeling for analog and RF CMOS circuit design*. John Wiley & Sons, 2003.

[179] P. van der Meer, A. van Staveren, and A. H. van Roermund, *Low-power deep sub-micron CMOS logic: sub-threshold current reduction*. Springer Science & Business Media, 2004, vol. 841.

[180] C. Galup-Montoro *et al.*, *MOSFET modeling for circuit analysis and design*. World scientific, 2007.

[181] B. J. Baliga, *Silicon RF Power MOSFETs*. World Scientific, 2005.

[182] R. C. Jaeger, T. N. Blalock, and B. J. Blalock, *Microelectronic circuit design.* McGraw-Hill New York, 1997, vol. 97.

[183] M. Shur, "Physics of semiconductor devices, prentice hall," *Inc., Englewood Cliffs, New Jersey*, p. 680, 1990.

[184] M. Shur, T. A. Fjeldly, T. Ytterdal, and K. Lee, "Unified MOSFET model," *Solid-state electronics*, vol. 35, no. 12, pp. 1795–1802, 1992.

[185] A. Ghulam, "Accurate & complete behaviourial SPICE modelling of commercial SiC power MOSFET of 1200V, 75A," *2024 25th International Conference on Thermal, Mechanical and Multi-Physics Simulation and Experiments in Microelectronics and Microsystems (EuroSimE)*, pp. 1–4, 2024.

[186] Y. Mukunoki, Y. Nakamura, K. Konno, T. Horiguchi, Y. Nakayama, A. Nishizawa, M. Kuzumoto, and H. Akagi, "Modeling of a silicon-carbide mosfet with focus on internal stray capacitances and inductances, and its verification," *IEEE Transactions on Industry Applications*, vol. 54, no. 3, pp. 2588–2597, 2018.

[187] N. D. Arora, *MOSFET models for VLSI circuit simulation: theory and practice.* Springer Science & Business Media, 2012.

[188] J. Brews, W. Fichtner, E. Nicollian, and S. Sze, "Generalized guide for MOSFET miniaturization," in *1979 International Electron Devices Meeting.* IEEE, 1979, pp. 10–13.

[189] Y. Byun, K. Lee, and M. Shur, "Unified charge control model and subthreshold current in heterostructure field-effect transistors," *IEEE Electron Device Letters*, vol. 11, no. 1, pp. 50–53, 1990.

[190] T. A. Fjeldly and M. Shur, "Threshold voltage modeling and the subthreshold regime of operation of short-channel mosfets," *IEEE Transactions on Electron Devices*, vol. 40, no. 1, pp. 137–145, 1993.

[191] T. A. Fjeldly, M. Shur, and T. Ytterdal, *Introduction to device modeling and circuit simulation.* John Wiley & Sons, Inc., 1997.

[192] R. McArthur, "Making use of gate charge information in mosfet and igbt data sheets," *Application Note APT0103 Advanced Power Technology*, 2001.

[193] T. Kishi, T. Ikuta, K. Sakuma, M. Hatano, Y. Matsuda, J. Wilkening, R. Goya-Maldonado, M. Tik, N. R. Williams, S. Kito *et al.*, "Theta burst stimulation for depression: A systematic review and network and pairwise meta-analysis," *Molecular psychiatry*, pp. 1–7, 2024.

[194] R. S. Kelkar, V. S. Sreeraj, U. M. Mehta, A. A. Patwardhan, J. Thirthalli, and D. M. Blumberger, "Generalized seizure induced by continuous theta-burst stimulation (cTBS) in a patient with bipolar depression: A case report," *Brain Stimulation: Basic, Translational, and Clinical Research in Neuromodulation*, vol. 16, no. 3, pp. 693–694, 2023.

[195] Y.-Z. Huang, J. C. Rothwell, R.-S. Chen, C.-S. Lu, and W.-L. Chuang, "The theoretical model of theta burst form of repetitive transcranial magnetic stimulation," *Clinical Neurophysiology*, vol. 122, no. 5, pp. 1011–1018, 2011.

[196] T. Nyffeler, D. Cazzoli, P. Wurtz, M. Lüthi, R. Von Wartburg, S. Chaves, A. Déruaz, C. W. Hess, and R. M. Müri, "Neglect-like visual exploration behaviour after theta burst transcranial magnetic stimulation of the right posterior parietal cortex," *European Journal of Neuroscience*, vol. 27, no. 7, pp. 1809–1813, 2008.

[197] A. V. Chistyakov, B. Kreinin, S. Marmor, B. Kaplan, A. Khatib, N. Darawsheh, D. Koren, M. Zaaroor, and E. Klein, "Preliminary assessment of the therapeutic efficacy of continuous theta-burst magnetic stimulation (cTBS) in major depression: A double-blind sham-controlled study," *Journal of affective disorders*, vol. 170, pp. 225–229, 2015.

[198] D. V. Ott, M. Ullsperger, G. Jocham, J. Neumann, and T. A. Klein, "Continuous theta-burst stimulation (cTBS) over the lateral prefrontal cortex alters reinforcement learning bias," *Neuroimage*, vol. 57, no. 2, pp. 617–623, 2011.

[199] N. Valchev, B. Ćurčić-Blake, R. J. Renken, A. Avenanti, C. Keysers, V. Gazzola, and N. M. Maurits, "cTBS delivered to the left somatosensory cortex changes its functional connectivity during rest," *Neuroimage*, vol. 114, pp. 386–397, 2015.

[200] C. J. Lowe, F. Manocchio, A. B. Safati, and P. A. Hall, "The effects of theta burst stimulation (TBS) targeting the prefrontal cortex on executive functioning: A systematic review and meta-analysis," *Neuropsychologia*, vol. 111, pp. 344–359, 2018.

[201] S. W. Wu, N. Shahana, D. A. Huddleston, and D. L. Gilbert, "Effects of 30 Hz theta burst transcranial magnetic stimulation on the primary motor cortex," *Journal of neuroscience methods*, vol. 208, no. 2, pp. 161–164, 2012.

[202] Y.-Z. Huang and J. C. Rothwell, "The effect of short-duration bursts of high-frequency, low-intensity transcranial magnetic stimulation on the human motor cortex," *Clinical neurophysiology*, vol. 115, no. 5, pp. 1069–1075, 2004.